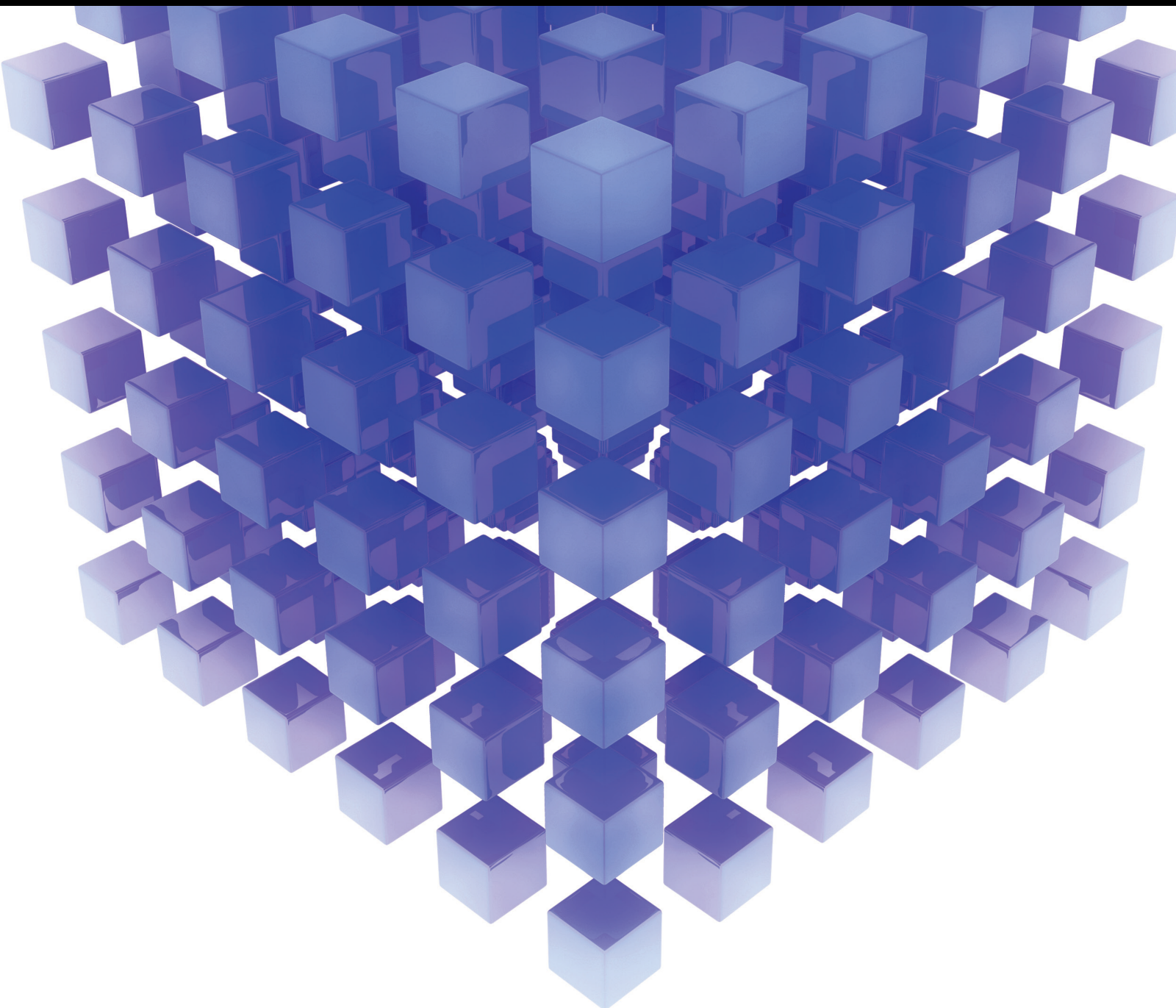


Mathematical Problems in Engineering

Artificial Intelligence for Civil Engineering

Lead Guest Editor: Zheng-zheng Wang

Guest Editors: Di-yuan Li, Yu-Sheng Shen, and Danial Jahed Armaghani





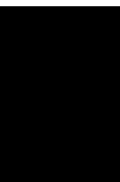
Artificial Intelligence for Civil Engineering

Mathematical Problems in Engineering

Artificial Intelligence for Civil Engineering

Lead Guest Editor: Zheng-zheng Wang


Guest Editors: Di-yuan Li, Yu-Sheng Shen, and
Danial Jahed Armaghani



Copyright © 2021 Hindawi Limited. All rights reserved.

This is a special issue published in “Mathematical Problems in Engineering.” All articles are open access articles distributed under the Creative Commons Attribution License, which permits unrestricted use, distribution, and reproduction in any medium, provided the original work is properly cited.

Chief Editor

Guangming Xie , China

Academic Editors

Kumaravel A , India
Waqas Abbasi, Pakistan
Mohamed Abd El Aziz , Egypt
Mahmoud Abdel-Aty , Egypt
Mohammed S. Abdo, Yemen
Mohammad Yaghoub Abdollahzadeh
Jamalabadi , Republic of Korea
Rahib Abiyev , Turkey
Leonardo Acho , Spain
Daniela Addessi , Italy
Arooj Adeel , Pakistan
Waleed Adel , Egypt
Ramesh Agarwal , USA
Francesco Aggogeri , Italy
Ricardo Aguilar-Lopez , Mexico
Afaq Ahmad , Pakistan
Naveed Ahmed , Pakistan
Elias Aifantis , USA
Akif Akgul , Turkey
Tareq Al-shami , Yemen
Guido Ala, Italy
Andrea Alaimo , Italy
Reza Alam, USA
Osamah Albahri , Malaysia
Nicholas Alexander , United Kingdom
Salvatore Alfonzetti, Italy
Ghous Ali , Pakistan
Nouman Ali , Pakistan
Mohammad D. Aliyu , Canada
Juan A. Almendral , Spain
A.K. Alomari, Jordan
José Domingo Álvarez , Spain
Cláudio Alves , Portugal
Juan P. Amezcua-Sanchez, Mexico
Mukherjee Amitava, India
Lionel Amodeo, France
Sebastian Anita, Romania
Costanza Arico , Italy
Sabri Arik, Turkey
Fausto Arpino , Italy
Rashad Asharabi , Saudi Arabia
Farhad Aslani , Australia
Mohsen Asle Zaem , USA

Andrea Avanzini , Italy
Richard I. Avery , USA
Viktor Avrutin , Germany
Mohammed A. Awadallah , Malaysia
Francesco Aymerich , Italy
Sajad Azizi , Belgium
Michele Bacciocchi , Italy
Seungik Baek , USA
Khaled Bahlali, France
M.V.A Raju Bahubalendruni, India
Pedro Balaguer , Spain
P. Balasubramaniam, India
Stefan Balint , Romania
Ines Tejado Balsera , Spain
Alfonso Banos , Spain
Jerzy Baranowski , Poland
Tudor Barbu , Romania
Andrzej Bartoszewicz , Poland
Sergio Baselga , Spain
S. Caglar Baslamisli , Turkey
David Bassir , France
Chiara Bedon , Italy
Azeddine Beghdadi, France
Andriette Bekker , South Africa
Francisco Beltran-Carbajal , Mexico
Abdellatif Ben Makhlof , Saudi Arabia
Denis Benasciutti , Italy
Ivano Benedetti , Italy
Rosa M. Benito , Spain
Elena Benvenuti , Italy
Giovanni Berselli, Italy
Michele Betti , Italy
Pietro Bia , Italy
Carlo Bianca , France
Simone Bianco , Italy
Vincenzo Bianco, Italy
Vittorio Bianco, Italy
David Bigaud , France
Sardar Muhammad Bilal , Pakistan
Antonio Bilotta , Italy
Sylvio R. Bistafa, Brazil
Chiara Boccaletti , Italy
Rodolfo Bontempo , Italy
Alberto Borboni , Italy
Marco Bortolini, Italy

Paolo Boscariol, Italy
Daniela Boso , Italy
Guillermo Botella-Juan, Spain
Abdesselem Boulkroune , Algeria
Boulaïd Boulkroune, Belgium
Fabio Bovenga , Italy
Francesco Braghin , Italy
Ricardo Branco, Portugal
Julien Bruchon , France
Matteo Bruggi , Italy
Michele Brun , Italy
Maria Elena Bruni, Italy
Maria Angela Butturi , Italy
Bartłomiej Błachowski , Poland
Dhanamjayulu C , India
Raquel Caballero-Águila , Spain
Filippo Cacace , Italy
Salvatore Caddemi , Italy
Zuowei Cai , China
Roberto Caldelli , Italy
Francesco Cannizzaro , Italy
Maosen Cao , China
Ana Carpio, Spain
Rodrigo Carvajal , Chile
Caterina Casavola, Italy
Sara Casciati, Italy
Federica Caselli , Italy
Carmen Castillo , Spain
Inmaculada T. Castro , Spain
Miguel Castro , Portugal
Giuseppe Catalanotti , United Kingdom
Alberto Cavallo , Italy
Gabriele Cazzulani , Italy
Fatih Vehbi Celebi, Turkey
Miguel Cerrolaza , Venezuela
Gregory Chagnon , France
Ching-Ter Chang , Taiwan
Kuei-Lun Chang , Taiwan
Qing Chang , USA
Xiaoheng Chang , China
Prasenjit Chatterjee , Lithuania
Kacem Chehdi, France
Peter N. Cheimets, USA
Chih-Chiang Chen , Taiwan
He Chen , China

Kebing Chen , China
Mengxin Chen , China
Shyi-Ming Chen , Taiwan
Xizhong Chen , Ireland
Xue-Bo Chen , China
Zhiwen Chen , China
Qiang Cheng, USA
Zeyang Cheng, China
Luca Chiapponi , Italy
Francisco Chicano , Spain
Tirivanhu Chinyoka , South Africa
Adrian Chmielewski , Poland
Seongim Choi , USA
Gautam Choubey , India
Hung-Yuan Chung , Taiwan
Yusheng Ci, China
Simone Cinquemani , Italy
Roberto G. Citarella , Italy
Joaquim Ciurana , Spain
John D. Clayton , USA
Piero Colajanni , Italy
Giuseppina Colicchio, Italy
Vassilios Constantoudis , Greece
Enrico Conte, Italy
Alessandro Contento , USA
Mario Cools , Belgium
Gino Cortellessa, Italy
Carlo Cosentino , Italy
Paolo Crippa , Italy
Erik Cuevas , Mexico
Guozeng Cui , China
Mehmet Cunkas , Turkey
Giuseppe D'Aniello , Italy
Peter Dabnichki, Australia
Weizhong Dai , USA
Zhifeng Dai , China
Purushothaman Damodaran , USA
Sergey Dashkovskiy, Germany
Adiel T. De Almeida-Filho , Brazil
Fabio De Angelis , Italy
Samuele De Bartolo , Italy
Stefano De Miranda , Italy
Filippo De Monte , Italy

José António Fonseca De Oliveira
Correia , Portugal
Jose Renato De Sousa , Brazil
Michael Defoort, France
Alessandro Della Corte, Italy
Laurent Dewasme , Belgium
Sanku Dey , India
Gianpaolo Di Bona , Italy
Roberta Di Pace , Italy
Francesca Di Puccio , Italy
Ramón I. Diego , Spain
Yannis Dimakopoulos , Greece
Hasan Dinçer , Turkey
José M. Domínguez , Spain
Georgios Dounias, Greece
Bo Du , China
Emil Dumic, Croatia
Madalina Dumitriu , United Kingdom
Premraj Durairaj , India
Saeed Eftekhar Azam, USA
Said El Kafhali , Morocco
Antonio Elipe , Spain
R. Emre Erkmen, Canada
John Escobar , Colombia
Leandro F. F. Miguel , Brazil
FRANCESCO FOTI , Italy
Andrea L. Facci , Italy
Shahla Faisal , Pakistan
Giovanni Falsone , Italy
Hua Fan, China
Jianguang Fang, Australia
Nicholas Fantuzzi , Italy
Muhammad Shahid Farid , Pakistan
Hamed Faruqi, Iran
Yann Favennec, France
Fiorenzo A. Fazzolari , United Kingdom
Giuseppe Fedele , Italy
Roberto Fedele , Italy
Baowei Feng , China
Mohammad Ferdows , Bangladesh
Arturo J. Fernández , Spain
Jesus M. Fernandez Oro, Spain
Francesco Ferrise, Italy
Eric Feulvarch , France
Thierry Floquet, France

















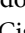








Eric Florentin , France
Gerardo Flores, Mexico
Antonio Forcina , Italy
Alessandro Formisano, Italy
Francesco Franco , Italy
Elisa Francomano , Italy
Juan Frausto-Solis, Mexico
Shujun Fu , China
Juan C. G. Prada , Spain
HECTOR GOMEZ , Chile
Matteo Gaeta , Italy
Mauro Gaggero , Italy
Zoran Gajic , USA
Jaime Gallardo-Alvarado , Mexico
Mosè Gallo , Italy
Akemi Gálvez , Spain
Maria L. Gandarias , Spain
Hao Gao , Hong Kong
Xingbao Gao , China
Yan Gao , China
Zhiwei Gao , United Kingdom
Giovanni Garcea , Italy
José García , Chile
Harish Garg , India
Alessandro Gasparetto , Italy
Stylianios Georgantzinou, Greece
Fotios Georgiades , India
Parviz Ghadimi , Iran
Ştefan Cristian Gherghina , Romania
Georgios I. Giannopoulos , Greece
Agathoklis Giaralis , United Kingdom
Anna M. Gil-Lafuente , Spain
Ivan Giorgio , Italy
Gaetano Giunta , Luxembourg
Jefferson L.M.A. Gomes , United Kingdom
Emilio Gómez-Déniz , Spain
Antonio M. Gonçalves de Lima , Brazil
Qunxi Gong , China
Chris Goodrich, USA
Rama S. R. Gorla, USA
Veena Goswami , India
Xunjie Gou , Spain
Jakub Grabski , Poland

Antoine Grall , France
George A. Gravvanis , Greece
Fabrizio Greco , Italy
David Greiner , Spain
Jason Gu , Canada
Federico Guarracino , Italy
Michele Guida , Italy
Muhammet Gul , Turkey
Dong-Sheng Guo , China
Hu Guo , China
Zhaoxia Guo, China
Yusuf Gurefe, Turkey
Salim HEDDAM , Algeria
ABID HUSSANAN, China
Quang Phuc Ha, Australia
Li Haitao , China
Petr Hájek , Czech Republic
Mohamed Hamdy , Egypt
Muhammad Hamid , United Kingdom
Renke Han , United Kingdom
Weimin Han , USA
Xingsi Han, China
Zhen-Lai Han , China
Thomas Hanne , Switzerland
Xinan Hao , China
Mohammad A. Hariri-Ardebili , USA
Khalid Hattaf , Morocco
Defeng He , China
Xiao-Qiao He, China
Yanchao He, China
Yu-Ling He , China
Ramdane Hedjar , Saudi Arabia
Jude Hemanth , India
Reza Hemmati, Iran
Nicolae Herisanu , Romania
Alfredo G. Hernández-Díaz , Spain
M.I. Herreros , Spain
Eckhard Hitzer , Japan
Paul Honeine , France
Jaromir Horacek , Czech Republic
Lei Hou , China
Yingkun Hou , China
Yu-Chen Hu , Taiwan
Yunfeng Hu, China
Can Huang , China
Gordon Huang , Canada
Linsheng Huo , China
Sajid Hussain, Canada
Asier Ibeas , Spain
Orest V. Iftime , The Netherlands
Przemyslaw Ignaciuk , Poland
Giacomo Innocenti , Italy
Emilio Insfran Pelozo , Spain
Azeem Irshad, Pakistan
Alessio Ishizaka, France
Benjamin Ivorra , Spain
Breno Jacob , Brazil
Reema Jain , India
Tushar Jain , India
Amin Jajarmi , Iran
Chiranjibe Jana , India
Łukasz Jankowski , Poland
Samuel N. Jator , USA
Juan Carlos Jáuregui-Correa , Mexico
Kandasamy Jayakrishna, India
Reza Jazar, Australia
Khalide Jbilou, France
Isabel S. Jesus , Portugal
Chao Ji , China
Qing-Chao Jiang , China
Peng-fei Jiao , China
Ricardo Fabricio Escobar Jiménez , Mexico
Emilio Jiménez Macías , Spain
Maolin Jin, Republic of Korea
Zhuo Jin, Australia
Ramash Kumar K , India
BHABEN KALITA , USA
MOHAMMAD REZA KHEDMATI , Iran
Viacheslav Kalashnikov , Mexico
Mathiyalagan Kalidass , India
Tamas Kalmar-Nagy , Hungary
Rajesh Kaluri , India
Jyotheeswara Reddy Kalvakurthi, India
Zhao Kang , China
Ramani Kannan , Malaysia
Tomasz Kapitaniak , Poland
Julius Kaplunov, United Kingdom
Konstantinos Karamanos, Belgium
Michal Kawulok, Poland

Irfan Kaymaz , Turkey
Vahid Kayvanfar , Qatar
Krzysztof Kecik , Poland
Mohamed Khader , Egypt
Chaudry M. Khalique , South Africa
Mukhtaj Khan , Pakistan
Shahid Khan , Pakistan
Nam-Il Kim, Republic of Korea
Philipp V. Kiryukhantsev-Korneev ,
Russia
P.V.V Kishore , India
Jan Koci , Czech Republic
Ioannis Kostavelis , Greece
Sotiris B. Kotsiantis , Greece
Frederic Kratz , France
Vamsi Krishna , India
Edyta Kucharska, Poland
Krzysztof S. Kulpa , Poland
Kamal Kumar, India
Prof. Ashwani Kumar , India
Michal Kunicki , Poland
Cedrick A. K. Kwuimy , USA
Kyandoghere Kyamakya, Austria
Ivan Kyrchei , Ukraine
Márcio J. Lacerda , Brazil
Eduardo Lalla , The Netherlands
Giovanni Lancioni , Italy
Jaroslaw Latalski , Poland
Hervé Laurent , France
Agostino Lauria , Italy
Aimé Lay-Ekuakille , Italy
Nicolas J. Leconte , France
Kun-Chou Lee , Taiwan
Dimitri Lefebvre , France
Eric Lefevre , France
Marek Lefik, Poland
Yaguo Lei , China
Kauko Leiviskä , Finland
Ervin Lenzi , Brazil
ChenFeng Li , China
Jian Li , USA
Jun Li , China
Yueyang Li , China
Zhao Li , China































Zhen Li , China
En-Qiang Lin, USA
Jian Lin , China
Qibin Lin, China
Yao-Jin Lin, China
Zhiyun Lin , China
Bin Liu , China
Bo Liu , China
Heng Liu , China
Jianxu Liu , Thailand
Lei Liu , China
Sixin Liu , China
Wanquan Liu , China
Yu Liu , China
Yuanchang Liu , United Kingdom
Bonifacio Llamazares , Spain
Alessandro Lo Schiavo , Italy
Jean Jacques Loiseau , France
Francesco Lolli , Italy
Paolo Lonetti , Italy
António M. Lopes , Portugal
Sebastian López, Spain
Luis M. López-Ochoa , Spain
Vassilios C. Loukopoulos, Greece
Gabriele Maria Lozito , Italy
Zhiguo Luo , China
Gabriel Luque , Spain
Valentin Lychagin, Norway
YUE MEI, China
Junwei Ma , China
Xuanlong Ma , China
Antonio Madeo , Italy
Alessandro Magnani , Belgium
Toqeer Mahmood , Pakistan
Fazal M. Mahomed , South Africa
Arunava Majumder , India
Sarfranz Nawaz Malik, Pakistan
Paolo Manfredi , Italy
Adnan Maqsood , Pakistan
Muazzam Maqsood, Pakistan
Giuseppe Carlo Marano , Italy
Damijan Markovic, France
Filipe J. Marques , Portugal
Luca Martinelli , Italy
Denizar Cruz Martins, Brazil

Francisco J. Martos , Spain
Elio Masciari , Italy
Paolo Massioni , France
Alessandro Mauro , Italy
Jonathan Mayo-Maldonado , Mexico
Pier Luigi Mazzeo , Italy
Laura Mazzola, Italy
Driss Mehdi , France
Zahid Mehmood , Pakistan
Roderick Melnik , Canada
Xiangyu Meng , USA
Jose Merodio , Spain
Alessio Merola , Italy
Mahmoud Mesbah , Iran
Luciano Mescia , Italy
Laurent Mevel , France
Constantine Michailides , Cyprus
Mariusz Michta , Poland
Prankul Middha, Norway
Aki Mikkola , Finland
Giovanni Minafò , Italy
Edmondo Minisci , United Kingdom
Hiroyuki Mino , Japan
Dimitrios Mitsotakis , New Zealand
Ardashir Mohammadzadeh , Iran
Francisco J. Montáns , Spain
Francesco Montefusco , Italy
Gisele Mophou , France
Rafael Morales , Spain
Marco Morandini , Italy
Javier Moreno-Valenzuela , Mexico
Simone Morganti , Italy
Caroline Mota , Brazil
Aziz Moukrim , France
Shen Mouquan , China
Dimitris Mourtzis , Greece
Emiliano Mucchi , Italy
Taseer Muhammad, Saudi Arabia
Ghulam Muhiuddin, Saudi Arabia
Amitava Mukherjee , India
Josefa Mula , Spain
Jose J. Muñoz , Spain
Giuseppe Muscolino, Italy
Marco Mussetta , Italy

Hariharan Muthusamy, India
Alessandro Naddeo , Italy
Raj Nandkeolyar, India
Keivan Navaie , United Kingdom
Soumya Nayak, India
Adrian Neagu , USA
Erivelton Geraldo Nepomuceno , Brazil
AMA Neves, Portugal
Ha Quang Thinh Ngo , Vietnam
Nhon Nguyen-Thanh, Singapore
Papakostas Nikolaos , Ireland
Jelena Nikolic , Serbia
Tatsushi Nishi, Japan
Shanzhou Niu , China
Ben T. Nohara , Japan
Mohammed Nouari , France
Mustapha Nourelfath, Canada
Kazem Nouri , Iran
Ciro Núñez-Gutiérrez , Mexico
Włodzimierz Ogryczak, Poland
Roger Ohayon, France
Krzysztof Okarma , Poland
Mitsuhiro Okayasu, Japan
Murat Olgun , Turkey
Diego Oliva, Mexico
Alberto Olivares , Spain
Enrique Onieva , Spain
Calogero Orlando , Italy
Susana Ortega-Cisneros , Mexico
Sergio Ortobelli, Italy
Naohisa Otsuka , Japan
Sid Ahmed Ould Ahmed Mahmoud , Saudi Arabia
Taoreed Owolabi , Nigeria
EUGENIA PETROPOULOU , Greece
Arturo Pagano, Italy
Madhumangal Pal, India
Pasquale Palumbo , Italy
Dragan Pamučar, Serbia
Weifeng Pan , China
Chandan Pandey, India
Rui Pang, United Kingdom
Jürgen Pannek , Germany
Elena Panteley, France
Achille Paolone, Italy

George A. Papakostas , Greece
Xosé M. Pardo , Spain
You-Jin Park, Taiwan
Manuel Pastor, Spain
Pubudu N. Pathirana , Australia
Surajit Kumar Paul , India
Luis Payá , Spain
Igor Pažanin , Croatia
Libor Pekař , Czech Republic
Francesco Pellicano , Italy
Marcello Pellicciari , Italy
Jian Peng , China
Mingshu Peng, China
Xiang Peng , China
Xindong Peng, China
Yuxing Peng, China
Marzio Pennisi , Italy
Maria Patrizia Pera , Italy
Matjaz Perc , Slovenia
A. M. Bastos Pereira , Portugal
Wesley Peres, Brazil
F. Javier Pérez-Pinal , Mexico
Michele Perrella, Italy
Francesco Pesavento , Italy
Francesco Petrini , Italy
Hoang Vu Phan, Republic of Korea
Lukasz Pieczonka , Poland
Dario Piga , Switzerland
Marco Pizzarelli , Italy
Javier Plaza , Spain
Goutam Pohit , India
Dragan Poljak , Croatia
Jorge Pomares , Spain
Hiram Ponce , Mexico
Sébastien Poncet , Canada
Volodymyr Ponomaryov , Mexico
Jean-Christophe Ponsart , France
Mauro Pontani , Italy
Sivakumar Poruran, India
Francesc Pozo , Spain
Aditya Rio Prabowo , Indonesia
Anchasa Pramuanjaroenkij , Thailand
Leonardo Primavera , Italy
B Rajanarayan Prusty, India

Krzysztof Puszynski , Poland
Chuan Qin , China
Dongdong Qin, China
Jianlong Qiu , China
Giuseppe Quaranta , Italy
DR. RITU RAJ , India
Vitomir Racic , Italy
Carlo Rainieri , Italy
Kumbakonam Ramamani Rajagopal, USA
Ali Ramazani , USA
Angel Manuel Ramos , Spain
Higinio Ramos , Spain
Muhammad Afzal Rana , Pakistan
Muhammad Rashid, Saudi Arabia
Manoj Rastogi, India
Alessandro Rasulo , Italy
S.S. Ravindran , USA
Abdolrahman Razani , Iran
Alessandro Reali , Italy
Jose A. Reinoso , Spain
Oscar Reinoso , Spain
Haijun Ren , China
Carlo Renno , Italy
Fabrizio Renno , Italy
Shahram Rezapour , Iran
Ricardo Rianza , Spain
Francesco Riganti-Fulginei , Italy
Gerasimos Rigatos , Greece
Francesco Ripamonti , Italy
Jorge Rivera , Mexico
Eugenio Roanes-Lozano , Spain
Ana Maria A. C. Rocha , Portugal
Luigi Rodino , Italy
Francisco Rodríguez , Spain
Rosana Rodríguez López, Spain
Francisco Rossomando , Argentina
Jose de Jesus Rubio , Mexico
Weiguo Rui , China
Rubén Ruiz , Spain
Ivan D. Rukhlenko , Australia
Dr. Eswaramoorthi S. , India
Weichao SHI , United Kingdom
Chaman Lal Sabharwal , USA
Andrés Sáez , Spain

Bekir Sahin, Turkey
Laxminarayan Sahoo , India
John S. Sakellariou , Greece
Michael Sakellariou , Greece
Salvatore Salamone, USA
Jose Vicente Salcedo , Spain
Alejandro Salcido , Mexico
Alejandro Salcido, Mexico
Nunzio Salerno , Italy
Rohit Salgotra , India
Miguel A. Salido , Spain
Sinan Salih , Iraq
Alessandro Salvini , Italy
Abdus Samad , India
Sovan Samanta, India
Nikolaos Samaras , Greece
Ramon Sancibrian , Spain
Giuseppe Sanfilippo , Italy
Omar-Jacobo Santos, Mexico
J Santos-Reyes , Mexico
José A. Sanz-Herrera , Spain
Musavarah Sarwar, Pakistan
Shahzad Sarwar, Saudi Arabia
Marcelo A. Savi , Brazil
Andrey V. Savkin, Australia
Tadeusz Sawik , Poland
Roberta Sburlati, Italy
Gustavo Scaglia , Argentina
Thomas Schuster , Germany
Hamid M. Sedighi , Iran
Mijanur Rahaman Seikh, India
Tapan Senapati , China
Lotfi Senhadji , France
Junwon Seo, USA
Michele Serpilli, Italy
Silvestar Šesnić , Croatia
Gerardo Severino, Italy
Ruben Sevilla , United Kingdom
Stefano Sfarra , Italy
Dr. Ismail Shah , Pakistan
Leonid Shaikhet , Israel
Vimal Shanmuganathan , India
Prayas Sharma, India
Bo Shen , Germany
Hang Shen, China

Xin Pu Shen, China
Dimitri O. Shepelsky, Ukraine
Jian Shi , China
Amin Shokrollahi, Australia
Suzanne M. Shontz , USA
Babak Shotorban , USA
Zhan Shu , Canada
Angelo Sifaleras , Greece
Nuno Simões , Portugal
Mehakpreet Singh , Ireland
Piyush Pratap Singh , India
Rajiv Singh, India
Seralathan Sivamani , India
S. Sivasankaran , Malaysia
Christos H. Skiadas, Greece
Konstantina Skouri , Greece
Neale R. Smith , Mexico
Bogdan Smolka, Poland
Delfim Soares Jr. , Brazil
Alba Sofi , Italy
Francesco Soldovieri , Italy
Raffaele Solimene , Italy
Yang Song , Norway
Jussi Sopanen , Finland
Marco Spadini , Italy
Paolo Spagnolo , Italy
Ruben Specogna , Italy
Vasilios Spitas , Greece
Ivanka Stamova , USA
Rafał Stanisławski , Poland
Miladin Stefanović , Serbia
Salvatore Strano , Italy
Yakov Strelniker, Israel
Kangkang Sun , China
Qiuqin Sun , China
Shuaishuai Sun, Australia
Yanchao Sun , China
Zong-Yao Sun , China
Kumarasamy Suresh , India
Sergey A. Suslov , Australia
D.L. Suthar, Ethiopia
D.L. Suthar , Ethiopia
Andrzej Swierniak, Poland
Andras Szekrenyes , Hungary
Kumar K. Tamma, USA

Yong (Aaron) Tan, United Kingdom
Marco Antonio Taneco-Hernández , Mexico
Lu Tang , China
Tianyou Tao, China
Hafez Tari , USA
Alessandro Tasora , Italy
Sergio Teggi , Italy
Adriana del Carmen Téllez-Anguiano , Mexico
Ana C. Teodoro , Portugal
Efstathios E. Theotokoglou , Greece
Jing-Feng Tian, China
Alexander Timokha , Norway
Stefania Tomasiello , Italy
Gisella Tomasini , Italy
Isabella Torcicollo , Italy
Francesco Tornabene , Italy
Mariano Torrisi , Italy
Thang nguyen Trung, Vietnam
George Tsiatas , Greece
Le Anh Tuan , Vietnam
Nerio Tullini , Italy
Emilio Turco , Italy
Ilhan Tuzcu , USA
Efstratios Tzirtzilakis , Greece
FRANCISCO UREÑA , Spain
Filippo Ubertini , Italy
Mohammad Uddin , Australia
Mohammad Safi Ullah , Bangladesh
Serdar Ulubeyli , Turkey
Mati Ur Rahman , Pakistan
Panayiotis Vafeas , Greece
Giuseppe Vairo , Italy
Jesus Valdez-Resendiz , Mexico
Eusebio Valero, Spain
Stefano Valvano , Italy
Carlos-Renato Vázquez , Mexico
Martin Velasco Villa , Mexico
Franck J. Vernerey, USA
Georgios Veronis , USA
Vincenzo Vespri , Italy
Renato Vidoni , Italy
Venkatesh Vijayaraghavan, Australia

Anna Vila, Spain
Francisco R. Villatoro , Spain
Francesca Vipiana , Italy
Stanislav Vitek , Czech Republic
Jan Vorel , Czech Republic
Michael Vynnycky , Sweden
Mohammad W. Alomari, Jordan
Roman Wan-Wendner , Austria
Bingchang Wang, China
C. H. Wang , Taiwan
Dagang Wang, China
Guoqiang Wang , China
Huaiyu Wang, China
Hui Wang , China
J.G. Wang, China
Ji Wang , China
Kang-Jia Wang , China
Lei Wang , China
Qiang Wang, China
Qingling Wang , China
Weiwei Wang , China
Xinyu Wang , China
Yong Wang , China
Yung-Chung Wang , Taiwan
Zhenbo Wang , USA
Zhibo Wang, China
Waldemar T. Wójcik, Poland
Chi Wu , Australia
Qihong Wu, China
Yuqiang Wu, China
Zhibin Wu , China
Zhizheng Wu , China
Michalis Xenos , Greece
Hao Xiao , China
Xiao Ping Xie , China
Qingzheng Xu , China
Binghan Xue , China
Yi Xue , China
Joseph J. Yame , France
Chuanliang Yan , China
Xinggang Yan , United Kingdom
Hongtai Yang , China
Jixiang Yang , China
Mijia Yang, USA
Ray-Yeng Yang, Taiwan


Zaoli Yang , China
Jun Ye , China
Min Ye , China
Luis J. Yebra , Spain
Peng-Yeng Yin , Taiwan
Muhammad Haroon Yousaf , Pakistan
Yuan Yuan, United Kingdom
Qin Yuming, China
Elena Zaitseva , Slovakia
Arkadiusz Zak , Poland
Mohammad Zakwan , India
Ernesto Zambrano-Serrano , Mexico
Francesco Zammori , Italy
Jessica Zangari , Italy
Rafal Zdunek , Poland
Ibrahim Zeid, USA
Nianyin Zeng , China
Junyong Zhai , China
Hao Zhang , China
Haopeng Zhang , USA
Jian Zhang , China
Kai Zhang, China
Lingfan Zhang , China
Mingjie Zhang , Norway
Qian Zhang , China
Tianwei Zhang , China
Tongqian Zhang , China
Wenyu Zhang , China
Xianming Zhang , Australia
Xuping Zhang , Denmark
Yinyan Zhang, China
Yifan Zhao , United Kingdom
Debao Zhou, USA
Heng Zhou , China
Jian G. Zhou , United Kingdom
Junyong Zhou , China
Xueqian Zhou , United Kingdom
Zhe Zhou , China
Wu-Le Zhu, China
Gaetano Zizzo , Italy
Mingcheng Zuo, China

Contents



Gray Relation Analysis for Optimal Selection of Bridge Reinforcement Scheme Based on Fuzzy-AHP Weights

Yanbin Tan, Zhe Zhang, Huili Wang , and Shaobo Zhou
Research Article (8 pages), Article ID 8813940, Volume 2021 (2021)









Predicting the Healthy Operation of Heavy Oil Well Casings in Permafrost Regions

Tiecheng Sun , Cancan Liu, Zurun Yue, Tianfei Hu, and Yiming Liao
Research Article (10 pages), Article ID 8893159, Volume 2021 (2021)



Semantic-Segmentation-Based Rail Fastener State Recognition Algorithm

Liming Li , Rui Sun, Shuguang Zhao , Xiaodong Chai, Shubin Zheng, and Ruichao Shen
Research Article (15 pages), Article ID 8956164, Volume 2021 (2021)



Influence of Data Splitting on Performance of Machine Learning Models in Prediction of Shear Strength of Soil

Quang Hung Nguyen , Hai-Bang Ly , Lanh Si Ho , Nadhir Al-Ansari , Hiep Van Le , Van Quan Tran , Indra Prakash , and Binh Thai Pham 
Research Article (15 pages), Article ID 4832864, Volume 2021 (2021)


Mechanical Parameter Identification of Hydraulic Engineering with the Improved Deep Q-Network Algorithm

Wei Ji , Xiaoqing Liu , Huijun Qi , Xunnan Liu, Chaoning Lin, and Tongchun Li
Research Article (20 pages), Article ID 6404819, Volume 2020 (2020)


Evolution Laws for Frozen Wall Formation under Conditions of Sudden Seepage

Song Zhang , Zurun Yue, Tiecheng Sun , Yufu Han, Wei Gao, Tianfei Hu, and Yunxi Han
Research Article (13 pages), Article ID 8836149, Volume 2020 (2020)

Application of PS-INSAR Technique on Health Diagnosis of the Deformable Body on Front Slope beside Mountain Tunnel Portal

Jiaxin Jia 
Research Article (7 pages), Article ID 8823382, Volume 2020 (2020)

Research on Design Parameters and Fatigue Life of Tunnel Bottom Structure of Single-Track Ballasted Heavy-Haul Railway Tunnel with 40-Ton Axle Load

W. B. Ma, J. F. Chai , Z. L. Han, Z. G. Ma, X. X. Guo, W. H. Zou, Z. L. An, T. F. Li, and Y. B. Niu
Research Article (9 pages), Article ID 3181480, Volume 2020 (2020)

Intelligent Classification Method for Tunnel Lining Cracks Based on PFC-BP Neural Network

Hao Ding , Xinghong Jiang , Ke Li , Hongyan Guo , and Wenfeng Li 
Research Article (12 pages), Article ID 8838216, Volume 2020 (2020)





An Improved Nondestructive Semantic Segmentation Method for Concrete Dam Surface Crack Images with High Resolution

Jun Zhang  and Jia Zhang 
Research Article (14 pages), Article ID 5054740, Volume 2020 (2020)


Experimental Study on Structural Mechanics of Asphalt Pavement by Digital Speckle Correlation Methods

Hailiang Xu , Hehuan Ren , Jining Qin , and Xu Guo 
Research Article (10 pages), Article ID 8857369, Volume 2020 (2020)

Evaluating Construction Risks of Modified Shield Machine Applicable to Soft Soils Based on Fuzzy Comprehensive Evaluation Method

Qingfei Luo , Wei Li , Honglin Su , and Xinru Chen 
Research Article (15 pages), Article ID 8861801, Volume 2020 (2020)








Concrete Cracks Detection Using Convolutional Neural Network Based on Transfer Learning

Chao Su and Wenjun Wang 
Research Article (10 pages), Article ID 7240129, Volume 2020 (2020)

Projection of Future Hydropower Generation in Samanalawewa Power Plant, Sri Lanka

Bhabishya Khaniya , Chamaka Karunanayake , Miyuru B. Gunathilake , and Upaka Rathnayake 
Research Article (11 pages), Article ID 8862067, Volume 2020 (2020)

Improving Voting Feature Intervals for Spatial Prediction of Landslides

Binh Thai Pham , Tran Van Phong , Mohammadtaghi Avand , Nadhir Al-Ansari , Sushant K. Singh , Hiep Van Le , and Indra Prakash 
Research Article (15 pages), Article ID 4310791, Volume 2020 (2020)


The Optimization Research of Diesel Cylinder Gasket Parameters Based on Hybrid Neural Network and Improved Grey Wolf Algorithm

Yi Dong, Jianmin Liu, Yanbin Liu , Xinyong Qiao , Xiaoming Zhang, Qi Kang, and Tianqi Wang
Research Article (16 pages), Article ID 3718174, Volume 2020 (2020)

Study on the Intelligent Evaluation System of Tunnel Frost Damage in Cold Regions Based on the Fuzzy Comprehensive Evaluation Model

Dao-yuan Wang , Yong-quan Zhu, Guang-yao Cui , Yong-jun Luan, Hai-long Cui, Liang Sun, Yong-jie Sun, Yue Wang, and Jin-xiu Yuan 
Research Article (8 pages), Article ID 3153670, Volume 2020 (2020)

Applications of the RST Algorithm to Nonlinear Systems in Real-Time Hybrid Simulation

Yu Tang and Hui Qin 
Research Article (13 pages), Article ID 5734720, Volume 2020 (2020)

Research Article

Gray Relation Analysis for Optimal Selection of Bridge Reinforcement Scheme Based on Fuzzy-AHP Weights

Yanbin Tan,¹ Zhe Zhang,¹ Huili Wang ^{1,2} and Shaobo Zhou¹

¹National & Local Joint Engineering Laboratory of Bridge and Tunnel Technology, Dalian University of Technology, Dalian 116023, China

²State Key Laboratory of Structural Analysis for Industrial Equipment, Dalian University of Technology, Dalian 116023, China

Correspondence should be addressed to Huili Wang; wanghuili@dlut.edu.cn

Received 16 September 2020; Accepted 6 July 2021; Published 23 July 2021

Academic Editor: Yung-Chung Wang

Copyright © 2021 Yanbin Tan et al. This is an open access article distributed under the Creative Commons Attribution License, which permits unrestricted use, distribution, and reproduction in any medium, provided the original work is properly cited.

In order to solve the problem on optimal selection of old bridge reinforcement schemes, a decision-making method of gray relation analysis based on fuzzy-AHP weights is proposed. Firstly, the fuzzy-AHP is used to develop the decision index system of old bridge reinforcement schemes and determine the weight of decision indexes. The 0.1–0.9 scale method is introduced as the index judgment criterion, and the weight judgment matrix is established. Through the consistency test, the relative weight vector of each decision index in the index layer is calculated. Secondly, according to the gray relation model of the old bridge reinforcement schemes, the decision matrix is constructed, and the gray relation coefficient matrix is calculated to obtain the gray relation coefficient corresponding to the ideal optimal scheme. Finally, the optimal scheme is determined. Through an engineering example, the reinforcement scheme of a concrete-filled steel tube arch bridge deck system is calculated and analyzed, and the best reinforcement scheme is selected. The optimal selection result is consistent with the actual reinforcement scheme available for the bridge. The decision-making method of gray relation analysis based on fuzzy-AHP weights make the evaluation system more organized and systematic and the index weight more operable and quantitative, reduce the subjective evaluation impact, and make the evaluation result more objective and reliable. Considering the fuzzy and gray information of comparison and selection, the optimal scheme with high feasibility and applicability is selected by the gray relation method.

1. Introduction

With the operation of in-service bridges, due to the increase of traffic volume and vehicle load, the influence of unfavorable factors in the surrounding environment, and the natural aging of materials, the bridge structure is faced with performance degradation during its life cycle, resulting in the weakening of its function. In order to meet the traffic development needs, ensure the safety of bridge structure, satisfy the use function, and extend the service life, it is necessary to reconstruct and reinforce the old bridges. Many bridge reinforcement methods are now available, such as reinforcing the main girder cross section, reducing the dead load, and changing the structural system. These methods comprehensively consider the bearing capacity, durability, impact of traffic interruption, economic

rationality of reinforcement cost, and complexity of reinforcement technology. The determination of the reinforcement scheme is the key to the success of the reconstruction and reinforcement, especially the feasibility, reliability, and economy of the reinforcement scheme. The optimal selection process of the old bridge reinforcement scheme is a multiobjective decision-making process. The multiobjective decision-making is characterized by the conflicting objectives, inconsistent objective dimensions, and adjustable “optimal solution,” making the decision-making process more complicated [1]. Dağdeviren and Yüksel developed the evaluation index system of bridge reinforcement schemes based on the analytic hierarchy process (AHP) and performed the optimal selection analysis [2]. Nguyen et al. established a two-level fuzzy optimal selection model and used the nonstructural fuzzy

decision-making theory for the bridge scheme comparison and selection [3]. Maghrabie et al. proposed a multilayer and multiobjective fuzzy optimal selection model and applied it to the comparison and optimal selection of bridge schemes [4]. Thakur and Ramesh combined the AHP method and the entropy method to weigh the evaluation indexes and established the gray relation method based on the combined weight for the optimal selection of bridge reinforcement schemes [5]. Li and Chen proposed to improve the fuzzy belief structure method to determine the weight and established the gray relation optimal selection model for the optimal selection research of bridge reinforcement schemes [6]. Kalemci et al. used the combined weight method to establish a simplified gray wolf optimization algorithm method model for the optimal selection of bridge reinforcement schemes [7]. For this reason, according to the characteristics of the old bridge reinforcement scheme evaluation, this paper organically combines the fuzzy theory [8–11] with AHP, proposes a method to determine the index weight, and adopts the gray relation method [12] to realize the comprehensive evaluation of each reinforcement alternative and thus the selection of optimal scheme, making the optimal selection process more simple, objective, reasonable, and reliable. Therefore, it is necessary to carry out the optimal selection of bridge reinforcement schemes in order to achieve the basic objectives in technical feasibility, reliability, economic rationality, construction simplicity, and quality assurance.

In this paper, four bridge reinforcement schemes for an old bridge are carried out. Many factors need to be considered, such as the aging and disease degree of the original structure, the technical feasibility, and the impact of traffic interruption, which are more risky and difficult compared with the new bridge construction. In order to solve the problem on optimal selection of old bridge reinforcement schemes, a decision-making method of gray relation analysis based on fuzzy-AHP weights is proposed.

2. Evaluation Index System

Since several optimal selection indexes need to be comprehensively considered in the decision-making process for optimal selection of old bridge reinforcement schemes, the fuzzy-AHP [13] shall be firstly used to organize and hierarchize the optimal selection problem, thus developing a hierarchy-based optimal selection index system, as shown in Table 1. The system is divided into three layers: the first layer mainly includes the optimal selection purpose or desirable result, that is, to determine the optimal reinforcement scheme; the second layer includes the subordinate indexes of the upper layer, which represent the optimal selection index factors to be satisfied before the optimal selection purpose is achieved; the third layer is the basic index layer, which includes the most basic decomposition indexes of the optimal selection problem and directly reflects the comprehensive attribute information of each reinforcement scheme.

3. Decision Index Weight Determined by Fuzzy-AHP

3.1. Construction of Fuzzy Complementary Judgment Matrix. Based on the principle of fuzzy-AHP, the mutual priority relationship among the decision indexes is determined, and the 0.1–0.9 scale method [14] is used as the judgment criterion for the pairwise comparison of the indexes to establish the weight judgment matrix $C = (c_{ij})_{n \times n}$:

$$C = \begin{bmatrix} c_{11} & c_{12} & \cdots & c_{1n} \\ c_{21} & c_{22} & \cdots & c_{2n} \\ \cdots & \cdots & \cdots & \cdots \\ c_{n1} & c_{n2} & \cdots & c_{nn} \end{bmatrix}, \quad (1)$$

where c_{ij} is the relative weight vector based on the j th decision index than the i th decision.

3.2. Consistency Check of Judgment Matrix. The weight vector of matrix C is obtained by solving the judgment matrix with the formula derived in [15] $W = [w_1 \ w_2 \ \cdots \ w_n]^T$:

$$w_i = \frac{\sum_{j=1}^n c_{ij} + (n/2) - 1}{n(n-1)}. \quad (2)$$

Set

$$w_{ij} = \frac{w_i}{w_i + w_j}, \quad (i, j = 1, 2, \dots, n). \quad (3)$$

Then, the N -order matrix $S = (w_{ij})_{n \times n}$ is taken as the characteristic matrix of the judgment matrix C . The compatibility index of C and S is

$$I(C, S) = \frac{1}{n^2} \sum_{i=1}^n \sum_{j=1}^n |c_{ij} + w_{ij} - 1|. \quad (4)$$

With regard to the attitude α of the decision maker, when the compatibility index $I(C, S) \leq \alpha$, the judgment matrix is considered to be satisfactorily consistent. The smaller the α , the higher the consistency requirement for the matrix, which is generally taken as $\alpha = 0.2$.

Assuming there are k experts, then the fuzzy judgment matrix $C_k = (c_{ij}^k)_{n \times n}$; when $k = 1, 2, \dots, t$, the corresponding weight vector set $W_k = [W_1 \ W_2 \ \cdots \ W_t]$ [15], and the characteristic matrix $S_k = (w_{ij}^k)_{n \times n}$. If t judgment matrices $B(k)$ and other judgment matrices are of satisfactory consistency, the fuzzy-AHP weight is

$$W = \frac{1}{t} \sum_{k=1}^t W_k. \quad (5)$$

3.3. Total Hierarchical Sorting. Assuming that, in a decision index system with r layers, the relative weight vector based on the h th decision index is $P_h^{(r)} = [p_{1h}^{(r)} \ p_{2h}^{(r)} \ \cdots \ p_{n,h}^{(r)}]^T$; when $h = 1, 2, \dots, n_{r-1}$, then $n_r \times n_{r-1}$ order matrix is

TABLE 1: Evaluation index system of old bridge reinforcement scheme.

Decision set	Factor set	Index set
Optimal selection of bridge reinforcement scheme C	Structural functionality S	Satisfaction of bearing capacity
		Satisfaction of durability
	Economic rationality E	Satisfaction of vibratility
		Satisfaction of safety
		Reinforcement cost
Technical feasibility F	Reinforcement period	
	Subsequent maintenance cost	
	Utilization degree of original structure	
	Reliability of reinforcement technology	
Structural aesthetics A	Applicability of reinforcement technology	
	Complexity of reinforcement technology	
	Degree of impact of reinforcement on traffic	
	Structural aesthetics	
	Environmental friendliness	
	Environmental impact	
	Traffic impact	

$$P^{(r)} = [P_1^{(r)} \ P_2^{(r)} \ \dots \ P_{n_{r-1}}^{(r)}]^T, \quad (6)$$

where $p_{nh}^{(r)}$ is the relative weight vector based on the h th decision index than the h th decision.

If the comprehensive weight vector matrix of all decision indexes from the $r - 1$ layer to the decision layer is $W^{(r-1)} = [W_1^{(r-1)} \ W_2^{(r-1)} \ \dots \ W_{n_{r-1}}^{(r-1)}]^T$ [16], then the comprehensive weight of all decision indexes from the r layer to the decision layer is

$$W^{(r)} = [W_1^{(r)} \ W_2^{(r)} \ \dots \ W_{n_r}^{(r)}]^T = P^{(r)}W^{(r-1)}. \quad (7)$$

Generally,

$$W^{(r)} = P^{(r)}P^{(r-1)} \dots P^{(3)}W^{(2)}, \quad (8)$$

where $W^{(2)}$ is actually the same as the relative weight vector under the single hierarchical sorting.

4. Gray Relation Analysis Model

It is difficult to obtain the optimal scheme by a gray system composed of known information and nondeterministic information. The gray relation analysis method [17] is a method to measure the relation degree among factors based on their similarity or dissimilarity in the development trend [18], which is suitable for solving the problem on multi-objective optimal selection decision-making of old bridge reinforcement design schemes.

4.1. Construction of Decision Matrix. Assuming that there are a total of m old bridge reinforcement schemes and a total of n decision indexes and x_{ij} represents the attribute value of the j th index of the i th beam design scheme, then the initial decision matrix is

$$X = \begin{bmatrix} x_{11} & x_{12} & \dots & x_{1n} \\ x_{21} & x_{22} & \dots & x_{2n} \\ \dots & \dots & \dots & \dots \\ x_{m1} & x_{m2} & \dots & x_{mn} \end{bmatrix}. \quad (9)$$

In the decision-making objectives of the old bridge reinforcement design schemes, for the decision index value corresponding to the bearing capacity, the higher is better, while for the decision index value corresponding to the economic indexes such as construction period and cost, the lower is better. Moreover, the different dimensions and orders of magnitude among decision indexes have a large impact on the evaluation and optimal selection of the beam design scheme. Therefore, in order to facilitate the gray relation analysis, all decision indexes of the beam design scheme are normalized [19].

4.1.1. Quantitative Index Processing. In the evaluation index system of old bridge reinforcement scheme, some evaluation indexes can be expressed by numerical values and directly used as quantitative indexes of the scheme, such as the reinforcement cost and construction period. Quantitative indexes can be processed as follows. For benefit indexes (the larger the attribute value is, the better), the dimensionless value is

$$y'_{ij} = \begin{cases} 0, & y_{ij} \leq y_{i \min}, \\ \frac{y_{ij} - y_{i \min}}{y_{i \max} - y_{i \min}}, & y_{i \min} < y_{ij} < y_{i \max}, \\ 1, & y_{ij} \geq y_{i \max}. \end{cases} \quad (10)$$

For cost indexes (the smaller the attribute value is, the better), the dimensionless value is

$$y'_{ij} = \begin{cases} 0, & y_{ij} \geq y_{i \max}, \\ \frac{y_{i \max} - y_{ij}}{y_{i \max} - y_{i \min}}, & y_{i \min} < y_{ij} < y_{i \max}, \\ 1, & y_{ij} \leq y_{i \min}. \end{cases} \quad (11)$$

where y_{ij} is the index value of the i th index for the j th scheme to be evaluated, y'_{ij} is the normalized value, $y_{i \min}$ is

the minimum index value in the i th evaluation index of each scheme, i.e., $y_{i\min} = \min(y_{i1} \ y_{i2} \ \dots \ y_{im})$, and $y_{i\max}$ is the maximum index value in the i th evaluation index of each scheme, i.e., $y_{i\max} = \max(y_{i1} \ y_{i2} \ \dots \ y_{im})$, where $i = 1, 2, 3, \dots, n$ and $j = 1, 2, 3, \dots, m$.

4.1.2. Qualitative Index Processing. Some evaluation indexes in the evaluation index system of old bridge reinforcement scheme belong to qualitative indexes which can only be used for qualitative estimation and judgment. According to the needs of old bridge reinforcement, a 9-level factor set [20] is adopted, $E = (\text{worst, very poor, poor, relatively poor, medium, relatively good, good, very good, best})$, and the qualitative index language gray number is quantified by the linear gray number whitening weight function [21]. The quantification results are shown in Table 2.

4.2. Construction of Gray Relation Coefficient Matrix. Due to the relativity of bridge reinforcement scheme decision during comparison, an ideal reference scheme [22] is firstly constructed as $y_0 = [y_{01} \ y_{02} \ \dots \ y_{0m}]$, where

$$y_{0j} = \max(y_{1j}, y_{2j}, \dots, y_{mj}), \quad (12)$$

where y_{mj} is the relative vector based on the j th decision index than the i th decision.

The ideal reference scheme can be understood as taking the best value of the corresponding evaluation index in all candidate design schemes as the reference sequence. The attribute values of decision indexes of m design schemes are, respectively, taken as the comparison sequences, and the relation coefficient is used to measure the closeness of the data relationship between the reference sequence and the comparison sequence. The calculation formula of the relation coefficient of each decision index under different design schemes is

$$\varepsilon_{ij} = \frac{\min_i \min_j |y_{0j} - y_{ij}| + \rho \max_i \max_j |y_{0j} - y_{ij}|}{|y_{0j} - y_{ij}| + \rho \max_i \max_j |y_{0j} - y_{ij}|}, \quad (13)$$

where ε_{ij} is the relation coefficient between the i th comparison sequence and the j th index in the reference sequence y_0 , $i = 1, 2, \dots, m$ and $j = 1, 2, \dots, n$, and ρ is the identification coefficient ($\rho \in [0, 1]$) and is generally taken as $\rho = 0.5$.

4.3. Calculation of Gray Relation Degree. Combined with the fuzzy-AHP, the comprehensive weight vector matrix of all decision indexes at the third layer of the decision index system of the old bridge reinforcement scheme is determined as $W^{(3)} = [W_1^{(3)} \ W_2^{(3)} \ \dots \ W_n^{(3)}]^T$, and the comprehensive weight vector of n decision indexes to the decision layer in the decision index system is

$$W^{(3)} = [w_1^{(3)} \ w_2^{(3)} \ \dots \ w_n^{(3)}]^T, \quad (14)$$

where $w_n^{(3)}$ is the relative vector based on the n th decision index than all decision indexes at the third layer of the decision.

Let w_k be the combined weight of the k th index, and $\sum_{k=1}^n W_k^3 = 1$ [23]. So, the gray relation degree γ_{i0} between the old bridge reinforcement scheme and the ideal scheme is

$$\gamma_{i0} = \sum_{j=1}^n \varepsilon_{ij} w_j^{(3)}, \quad (15)$$

where ε_{ij} is the calculation formula of the relation coefficient of each decision index under different design schemes and $w_j^{(3)}$ is the relative vector based on the j th decision index than all decision indexes at the third layer of the decision.

4.4. Determination of Optimal Scheme. Firstly, according to the gray correlation degree, the evaluation schemes are sorted and optimized: the larger the relation degree is, the closer the reinforcement scheme is to the ideal scheme, and thus, the better the reinforcement scheme is, so as to determine the optimal scheme in the old bridge reinforcement schemes.

According to the gray relation axiom, gray relation degree γ_{i0} satisfies

- (1) Normative $0 < \gamma_{i0} \leq 1$, $\gamma_{i0} = 1 \Leftrightarrow i = 0$
- (2) The smaller the proximity $|i - 0|$, the greater the $\gamma(i, 0)$

Normativeness limits the value of gray correlation degree within the interval of $[0, 1]$. Proximity indicates that the closer the two behaviors are, the more similar their changing trends are.

The evaluated schemes are sorted for optimal selection according to the gray relation degree: the larger the relation degree, the closer the reinforcement scheme is to the ideal scheme, and thus the better the reinforcement scheme, so as to determine the optimal scheme in the old bridge reinforcement schemes.

5. Example of Decision-Making for Optimal Selection of Old Bridge Reinforcement Schemes

5.1. General Situation and Reinforcement Schemes of Old Bridge. This paper takes the deck system reinforcement design schemes of a certain reinforced concrete ribbed arch bridge as an example, uses the fuzzy-AHP to determine the weight and gray relation analysis model for the optimal selection, and obtains the optimal reinforcement scheme, as well as verifies the effectiveness and practicability of the gray relation analysis method for the optimal selection of bridge reinforcement schemes based on fuzzy-AHP weights.

The bridge is a concrete-filled steel tube arch bridge, which was completed in July 1997, as shown in Figure 1.

TABLE 2: Quantification results of qualitative index.

Level	Worst	Very poor	Poor	Relatively poor	Medium	Relatively good	Good	Very good	Best
Value	0	0.125	0.250	0.375	0.500	0.625	0.750	0.875	1.000

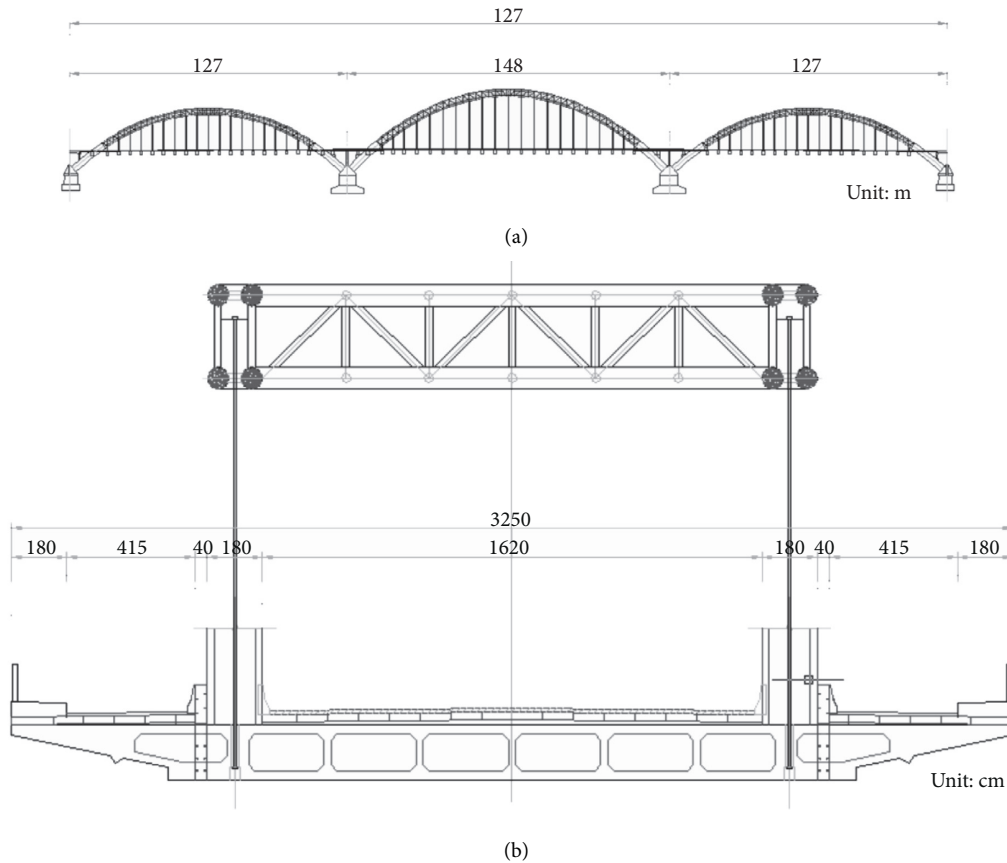


FIGURE 1: Bridge structure diagram. (a) Bridge elevation. (b) Bridge section view.

With the development of the city and the increase of traffic volume, the original design has approached the bearing capacity limit; the structure vibration is more obvious in actual use. Later, the bridge has been reinforced, with a hope to improve the dynamic characteristics and reduce the structural vibration response, but the reinforcement effect was not obvious. A total of four bridge deck reinforcement schemes are proposed this time: scheme 1, replace the overall bridge deck; scheme 2, add longitudinal concrete beams; scheme 3, add longitudinal steel beams; scheme 4, add longitudinal steel box-concrete composite beams, as shown in Figure 2.

5.2. *Determination of Comprehensive Weight of Decision Indexes.* As for determination on the relative weight of decision indexes at each layer of the old bridge reinforcement scheme, the pairwise comparison of structural functionality S , economic rationality E , technical feasibility F , and structural aesthetics A are conducted according to the 0.1–0.9 scale method, to obtain the fuzzy complementary judgment matrix, see Table 3, for details.

According to formulas (1) and (2), the relative weight vector of the factor set is calculated as

$$W_1 = (0.308, 0.242, 0.258, 0.192). \tag{16}$$

According to formulas (3) and (4), the compatibility index of C_1 and S_1 is obtained as $I(C_1, S_1) = 0.104 < 0.2$, and the distribution of the relative weight vector W_1 of the corresponding objective layer is reasonable. Therefore, it is believed that the fuzzy judgment matrices are satisfactorily compatible. In conclusion, it is reasonable and reliable to use the mean value of the relative weight set as the relative weight vector of the objective layer. The relative weight vector of the objective layer is $W = (0.308, 0.242, 0.258, 0.192)$.

Similarly, by constructing the fuzzy judgment matrix of the index layer, the relative weight vector of each decision index of the index layer is calculated, and thus, the comprehensive weight is calculated by formulas (6)~(8), as shown in Table 4.

5.3. *Calculation of Gray Relation Degree.* According to formulas (9)~(11), a decision matrix is established to select the optimal value of each index and determine the optimal scheme:

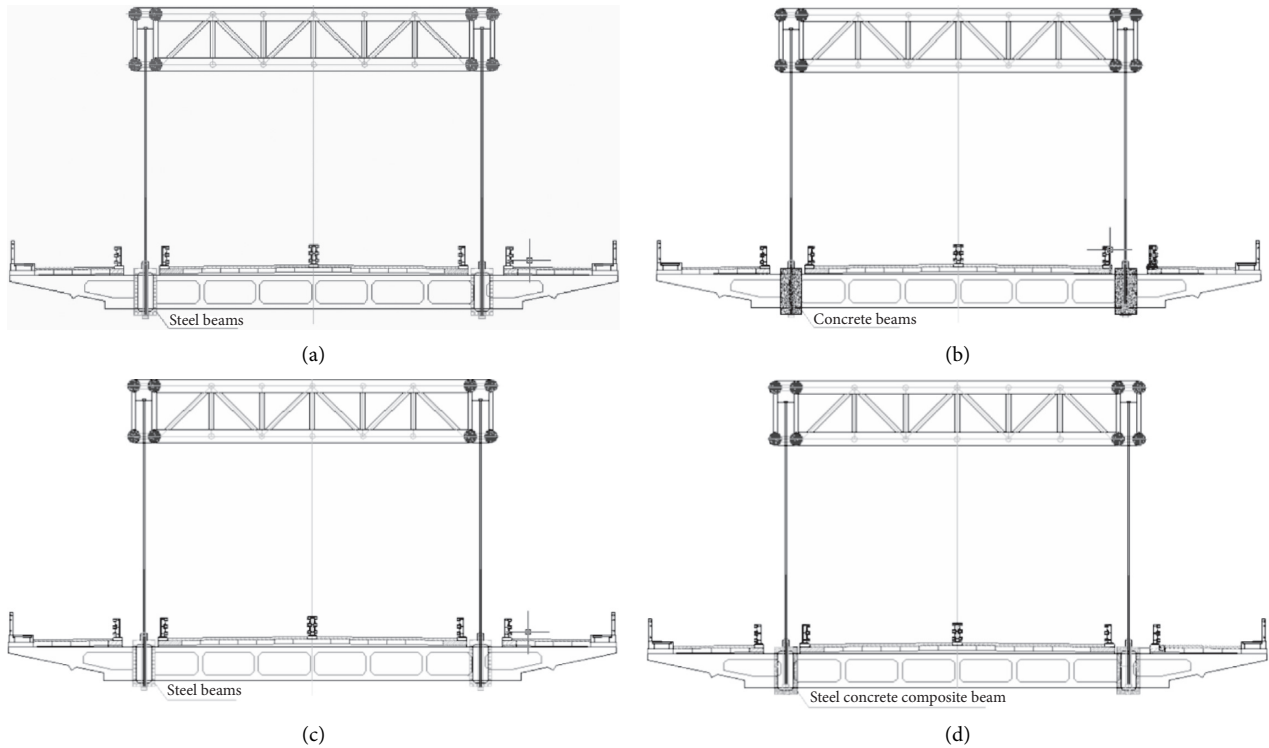


FIGURE 2: Bridge reinforcement schemes. (a) Scheme 1: replace the overall bridge deck. (b) Scheme 2: add longitudinal concrete beams. (c) Scheme 3: add longitudinal steel beams. (d) Scheme 4: add longitudinal steel box-concrete composite beams.

TABLE 3: Factor set importance evaluation matrix.

Factor set	Structural functionality S	Economic rationality E	Technical feasibility F	Structural aesthetics A
Structural functionality S	0.5	0.7	0.7	0.8
Economic rationality E	0.3	0.5	0.4	0.7
Technical feasibility F	0.3	0.6	0.5	0.7
Structural aesthetics A	0.2	0.3	0.3	0.5

TABLE 4: Relative weights and comprehensive weights of decision indexes at various layers.

Objective layer	Relative weight	Index layer	Relative weight	Comprehensive weight
Structural functionality S	0.308	Bearing capacity	0.258	0.080
		Durability	0.208	0.064
		Vibratility	0.283	0.087
		Safety	0.250	0.077
Economic rationality E	0.242	Reinforcement cost	0.267	0.064
		Reinforcement period	0.275	0.066
		Maintenance cost	0.242	0.058
		Utilization degree of original structure	0.217	0.052
Technical feasibility F	0.258	Reliability	0.267	0.069
		Practicality	0.233	0.060
		Complexity	0.233	0.060
		Traffic impact	0.267	0.069
Structural aesthetic A	0.192	Structural aesthetics	0.267	0.051
		Environmental friendliness	0.233	0.045
		Environmental impact	0.233	0.045
		Traffic impact	0.267	0.051

$$y_0 = \{1 \ 0.875 \ 1 \ 1 \ 0.75 \ 1 \ 0.875 \ 0.75 \ 0.875 \ 0.875 \ 0.75 \ 0.875 \ 1 \ 0.875 \ 0.5 \ 0.875\}. \quad (17)$$

The gray relation coefficient matrix is calculated by formulas (12) and (13):

$$\epsilon_{ij} = \begin{bmatrix} 0.400 & 0.500 & 0.400 & 0.333 & 0.500 & 1.000 & 0.667 & 0.400 & 0.400 & 1.000 & 1.000 & 0.500 & 1.000 & 1.000 & 0.667 & 0.400 \\ 0.500 & 1.000 & 0.500 & 0.333 & 0.500 & 0.286 & 1.000 & 1.000 & 0.500 & 0.667 & 0.500 & 0.400 & 1.000 & 1.000 & 0.667 & 0.400 \\ 0.667 & 0.500 & 0.400 & 1.000 & 1.000 & 0.500 & 0.400 & 0.667 & 1.000 & 0.667 & 0.667 & 0.667 & 0.667 & 0.667 & 1.000 & 1.000 \\ 1.000 & 0.667 & 1.000 & 0.667 & 0.667 & 0.400 & 0.500 & 0.667 & 1.000 & 0.667 & 0.500 & 1.000 & 1.000 & 0.667 & 1.000 & 0.667 \end{bmatrix}. \quad (18)$$

According to the comprehensive weight of decision index obtained in Table 4, the gray relation degree between each old bridge reinforcement scheme and the ideal optimal scheme is calculated by formulas (14) and (15):

$$\begin{aligned} \gamma_{10} &= 0.612, \\ \gamma_{20} &= 0.614, \\ \gamma_{30} &= 0.708, \\ \gamma_{40} &= 0.763. \end{aligned} \quad (19)$$

It can be seen that the gray relation degree between scheme 4 and ideal optimal scheme is the largest, so scheme 4 “add longitudinal steel box-concrete composite beams” is the optimal scheme. The optimum selection result is consistent with the actual reinforcement scheme adopted.

6. Conclusion

- (1) The fuzzy-AHP is used to construct the decision index system of the old bridge reinforcement scheme and determine the weight of the decision index, which makes the evaluation system more organized and systematic, and the index weight is more operable and quantitative, reducing the subjective evaluation impact and making the evaluation result more objective and reliable
- (2) Fully considering the fuzzy and gray information of comparison and selection, the gray relation method is used for calculation and analysis of old bridge reinforcement schemes, thus selecting the optimal reinforcement scheme
- (3) For the optimal selection of bridge reinforcement schemes, the gray relation analysis based on fuzzy-AHP weights can select the optimal reinforcement scheme as a reference for the bridge reinforcement project and has a certain practical application value

Data Availability

All data, models, and codes generated or used during the study are included within the article.

Conflicts of Interest

The authors declare that they have no potential conflicts of interest with respect to the research, authorship, and/or publication of this article.

Acknowledgments

This work was supported by the Natural Science Foundation Projects of Liaoning Province (2019-ZD-0006 and 2019-ZD-0145).

References

- [1] Y. Kuo, T. Yang, and G.-W. Huang, “The use of grey relational analysis in solving multiple attribute decision-making problems,” *Computers & Industrial Engineering*, vol. 55, no. 1, pp. 80–93, 2008.
- [2] M. Dağdeviren and İ. Yüksel, “Developing a fuzzy analytic hierarchy process (AHP) model for behavior-based safety management,” *Information Sciences*, vol. 178, no. 6, pp. 1717–1733, 2008.
- [3] H.-T. Nguyen, S. Z. M. Dawal, Y. Nukman, and H. Aoyama, “A hybrid approach for fuzzy multi-attribute decision making in machine tool selection with consideration of the interactions of attributes,” *Expert Systems With Applications*, vol. 41, no. 6, pp. 3078–3090, 2014.
- [4] H. F. Maghrabie, Y. Beauregard, and A. Schiffauerova, “Grey-based multi-criteria decision analysis approach: addressing uncertainty at complex decision problems,” *Technological Forecasting and Social Change*, vol. 146, pp. 366–379, 2019.
- [5] V. Thakur and A. Ramesh, “Healthcare waste disposal strategy selection using grey-AHP approach,” *Benchmarking: An International Journal*, vol. 24, no. 3, pp. 735–749, 2017.
- [6] Z. Li and L. Chen, “A novel evidential FMEA method by integrating fuzzy belief structure and grey relational projection method,” *Engineering Applications of Artificial Intelligence*, vol. 77, pp. 136–147, 2019.
- [7] E. N. Kalemci, S. B. İkizler, T. Dede, and Z. Angın, “Design of reinforced concrete cantilever retaining wall using grey wolf optimization algorithm,” *Structures*, vol. 23, pp. 245–253, 2020.
- [8] A. Hafezalkotob, A. Hafezalkotob, H. Liao, and F. Herrera, “An overview of MULTIMOORA for multi-criteria decision-making: theory, developments, applications, and challenges,” *Information Fusion*, vol. 51, pp. 145–177, 2019.

- [9] M. S. A. Khan and S. Abdullah, "Interval-valued pythagorean fuzzy GRA method for multiple-attribute decision making with incomplete weight information," *International Journal of Intelligent Systems*, vol. 33, no. 8, pp. 1689–1716, 2018.
- [10] H. Naderpour, M. Mirrashid, and K. Nagai, "An innovative approach for bond strength modeling in FRP strip-to-concrete joints using adaptive neuro-fuzzy inference system," *Engineering with Computers*, vol. 36, no. 3, pp. 1083–1100, 2020.
- [11] Z. Z. Wang and C. Chen, "Fuzzy comprehensive Bayesian network-based safety risk assessment for metro construction projects," *Tunnelling and Underground Space Technology*, vol. 70, pp. 330–342, 2017.
- [12] J. L. Deng, "Introduction to Grey system theory," *Journal of Grey System*, vol. 1, no. 1, pp. 1–24, 1989.
- [13] L. A. Zadeh, "Fuzzy sets as a basis for a theory of possibility," *Fuzzy Sets and Systems*, vol. 100, no. 1, pp. 9–34, 1999.
- [14] H. D. Cheng, J.-R. Chen, C. Glazier et al., "Novel approach to pavement cracking detection based on fuzzy set theory," *Journal of Computing in Civil Engineering*, vol. 13, no. 4, pp. 270–280, 1999.
- [15] Q. Zhou and V. V. Thai, "Fuzzy and grey theories in failure mode and effect analysis for tanker equipment failure prediction," *Safety Science*, vol. 83, pp. 74–79, 2016.
- [16] A. M. Sefidian and N. Daneshpour, "Missing value imputation using a novel grey based fuzzy c-means, mutual information based feature selection, and regression model," *Expert Systems With Applications*, vol. 115, pp. 68–94, 2019.
- [17] I. Bayane, A. Mankar, E. Brühwiler, and J. D. Sørensen, "Quantification of traffic and temperature effects on the fatigue safety of a reinforced-concrete bridge deck based on monitoring data," *Engineering Structures*, vol. 196, Article ID 109357, 2019.
- [18] S. Liu, Y. Yang, N. Xie, and J. Forrest, "New progress of grey system theory in the new millennium," *Grey Systems: Theory and Application*, vol. 6, no. 1, pp. 2–31, 2016.
- [19] H. Wang, Y.-M. Zhang, and Z. Yang, "A risk evaluation method to prioritize failure modes based on failure data and a combination of fuzzy sets theory and grey theory," *Engineering Applications of Artificial Intelligence*, vol. 82, pp. 216–225, 2019.
- [20] M. Yazdani, C. Kahraman, P. Zarate, and S. C. Onar, "A fuzzy multi attribute decision framework with integration of QFD and grey relational analysis," *Expert Systems With Applications*, vol. 115, pp. 474–485, 2019.
- [21] S. Sasmal, K. Ramanjaneyulu, S. Gopalakrishnan, and N. Lakshmanan, "Fuzzy logic based condition rating of existing reinforced concrete bridges," *Journal of Performance of Constructed Facilities*, vol. 20, no. 3, pp. 261–273, 2006.
- [22] L. Di Sarno, C. Del Vecchio, G. Maddaloni, and A. Prota, "Experimental response of an existing RC bridge with smooth bars and preliminary numerical simulations," *Engineering Structures*, vol. 136, pp. 355–368, 2017.
- [23] J. Xue, P. H. A. J. M. Van Gelder, G. Reniers, E. Papadimitriou, and C. Wu, "Multi-attribute decision-making method for prioritizing maritime traffic safety influencing factors of autonomous ships' maneuvering decisions using grey and fuzzy theories," *Safety Science*, vol. 120, pp. 323–340, 2019.

Research Article

Predicting the Healthy Operation of Heavy Oil Well Casings in Permafrost Regions

Tiecheng Sun ^{1,2,3}, Cancan Liu,³ Zurun Yue,^{1,2,3} Tianfei Hu,^{1,2,3} and Yiming Liao³

¹State Key Laboratory of Mechanical Behavior and System Safety of Traffic Engineering Structures, Shijiazhuang Tiedao University, Shijiazhuang 050043, China

²Key Laboratory of Roads and Railway Engineering Safety Control (Shijiazhuang Tiedao University), Ministry of Education, Shijiazhuang 050043, China

³School of Civil Engineering, Shijiazhuang Tiedao University, Shijiazhuang 050043, China

Correspondence should be addressed to Tiecheng Sun; sjz_sti@stdu.edu.cn

Received 18 September 2020; Revised 6 November 2020; Accepted 30 November 2020; Published 26 March 2021

Academic Editor: Yu-Sheng Shen

Copyright © 2021 Tiecheng Sun et al. This is an open access article distributed under the Creative Commons Attribution License, which permits unrestricted use, distribution, and reproduction in any medium, provided the original work is properly cited.

This study explores the distribution of stress and deformation on casings in heavy oil recovery wells and the distribution of stress in the thaw bulb in permafrost areas. Considering the expansion of the thaw bulb, the simulation analysis method is used to explore the internal mechanisms of vertical settlement displacement development and stress redistribution within thawed soil and casing. Calculation results show the following: (a) The maximum settlement of the thawed soil and the casing was positively correlated with the expansion of the thaw bulb. Although the settlement of the thawed soil was greater than that of the casing, the initial increase in maximum settlement difference between the thawed soil and the casing eventually tended to be constant due to stabilization of the thaw bulb's expansion. (b) The size of the thaw bulb directly affects the redistribution of internal stress in thawed soil, leading to different distribution rules for the vertical displacement of thawed soil and casing with depth. (c) Beyond a certain formation depth, the vertical stress of thawed soil gradually transits from a tensile stress state to a compressive stress state. The depth of a soil layer whose horizontal stress value is initially greater than its vertical stress value will gradually deepen with an increase in thaw bulb radius. (d) There is no significant negative friction on the lateral wall of casing in yield state, but significant negative friction exists on the lateral wall of casing in elastic state. The vertical stress of casing in elastic state increased gradually with the increase of casing depth, due to the existence of continuous negative friction and dead weight.

1. Introduction

With the gradual increase of the global temperature, large-scale development of Arctic oil and gas resources has become possible. In the late 1960s, a large number of oil wells began to appear in the Arctic region. Many of them are still in operation. In the process of heavy oil production, large bending and shear deformation of oil well casings made it difficult to operate the oil wells. Excessive strain leads to breakage at casing joints, which eventually leads to failure of the oil well [1–5]. Casing damage and tubing deformation [6] are shown in Figure 1. Scientists have carried out fruitful research on how to reduce casing deformation by examining the causes of casing stress [7–10], casing design methodology [11–16], oil well construction techniques, and the

technology of heavy oil recovery [17–21]. However, in terms of factors affecting casing stress, there has been little research on the interactions between soil layer and oil well casing.

Oil well casing in polar permafrost areas employs a thaw bulb with positive temperature between the casing and the permafrost. The size of the thaw bulb will change with the extension of oil well operation time. The continuous expansion of the thaw bulb complicates stress and deformation exerted on the casing. In order to deeply understand the interactions between the thawed soil and the casing in the thaw bulb and to further explore the internal mechanisms of casing settlement deformation, this paper uses the simulation analysis method to analyze and predict the stress and deformation of a single oil well casing. Stress distribution

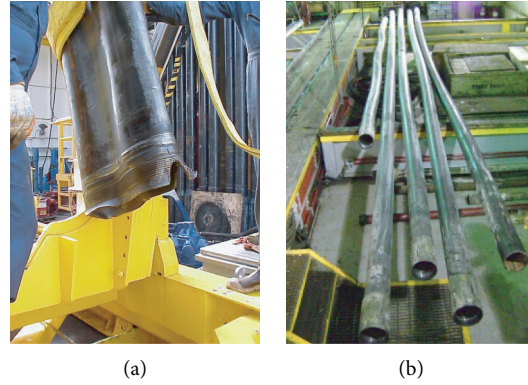


FIGURE 1: Deformation of the oil well components: (a) the casing and (b) the tubing.

laws within the thaw bulb are analyzed on the basis of changes occurring within the thaw bulb. As such, this research may provide a theoretical reference for the design of new oil wells and important technical support for settlement control measures for existing oil wells. At the same time, it will provide technical suggestions for China's participation in oil and gas development in polar permafrost regions. Although China is an extraterritorial country in the Arctic region, the country can participate in the development and utilization of resources in the region according to "The Svalbard Treaty."

2. Model

2.1. Assumptions. To simplify analysis, the following assumptions were made:

- (1) In the analysis of casing stress and deformation, additional stress caused by casing connection errors was considered negligible. That is, to allow for simple analysis of the friction between the soil layer and the casing, the casing was assumed to be a linear pipe body.
- (2) The thermal properties of thawed soil layer, permafrost soil layer, and casing were not considered. It has been assumed that there was no heat transfer inside the thaw bulb, in the permafrost region, between the thawed soil and the casing or between the thaw bulb and the permafrost. The model boundary was assumed to be adiabatic.
- (3) The model did not take the moisture field of the soil layer into account; that is, it assumed that no water migration occurred in the soil layer.

2.2. Geometric Parameters. According to the measurements of an existing oil well [22], a casing with an inner diameter of 22.3 cm, an outer diameter of 24.5 cm, and a wall thickness of 1.1 cm was used. On the basis of data from a field investigation report [6], the soil layer in the model was divided into 14 layers to reflect conditions on the ground. The type and thickness of each soil layer are shown in Table 1 and 2. Matthews et al. [6] carried out an ice-melting assessment for a single well model with an average radius R_{TB} for the thaw

bulb represented by the change of thaw bulb over time. The thaw bulb radius R_{TB} was 1.0 m, 3.0 m, 5.0 m, and 7.5 m, which corresponded to the thaw bulb radius over the course of the oil well operation period at 1 year, 5 years, 10 years, and more than 20 years, respectively. According to these data, a cylindrical model with a radius of 22.5 m and a vertical depth of 171 m was determined for calculation and analysis. The model grid number was 166460. The casing was modeled using the 8-node quadrilateral in-plane general-purpose continuum shell element (SC8R). The soil was modeled using 8-node linear brick elements (C3D8R) or 6-node linear triangular prism elements (C3D6). The specifics of the model are illustrated in Figure 2.

2.3. Physical and Mechanical Parameters. In actual oil well engineering, casing adopts J55 steel pipe. For the model, the pipe's physical and mechanical properties were obtained by referring to relevant literature [23]. Specific parameters are listed in Table 3.

The physical and mechanical parameters for each soil layer were determined partly on the basis of existing literature [24]. The remaining parameters [25] were obtained through indoor tests. The physical and mechanical parameters of the soil layers are shown in Tables 2 and 3.

Contact surfaces were set up between the casing and the thawed soil and the thawed soil and the permafrost. Contact parameters were measured through laboratory testing and are listed in Table 4.

2.4. Model Constitutive and Others. Through experimentation, it was found that thawed soil formed by the thawing of permafrost demonstrated strong nonlinearity. For this reason, the Mohr-Coulomb model was selected to calculate nonlinearity in the numerical simulation. According to the literature [26], the relationship between Young's modulus for soil and the confining pressure is shown in

$$E = E_0 \left(\frac{P}{P_\alpha} \right)^\alpha, \quad (1)$$

where E_0 is Young's modulus at a reference pressure, P is the mean confining pressure, P_α is the reference pressure (usually a standard atmospheric pressure), and α is the

TABLE 1: Soil layer division and physical and mechanical parameters.

Layer	Soil type	Depth (m)	Density (kg/m ³)	Internal friction angle (°)		Dilatancy angle (°)		Cohesive force (kPa)	
				F^*	T^+	F	T	F	T
1	Gravel and sand	0~30	1900	30	32	10	5	1000	5
2	Silt	30~54	1800	15	20	5	5	2000	40
3	Silty sand	54~63	1900	15	22	5	5	2000	35
4	Clay	63~69	1750	5	10	0.1	0.1	2000	100
5	Sand	69~81	1900	25	30	10	5	1000	35
6	Clayey silt	81~90	1850	10	17	5	5	2000	50
7	Silty clay	90~96	1900	5	12	0.1	0.1	2000	75
8	Silt	96~102	1800	15	20	5	5	2000	40
9	Sand	102~135	1950	25	30	10	5	1000	35
10	Silt	135~147	1800	15	20	5	5	2000	40
11	Sand	147~153	1950	25	30	10	5	1000	30
12	Clay	153~156	1750	5	10	0.1	0.1	2000	100
13	Silty sand	156~162	1900	15	22.5	10	5	1000	35
14	Clay	162~171	1750	5	10	0.1	0.1	2000	100

F^* indicates permafrost and T^+ indicates thawed soil.

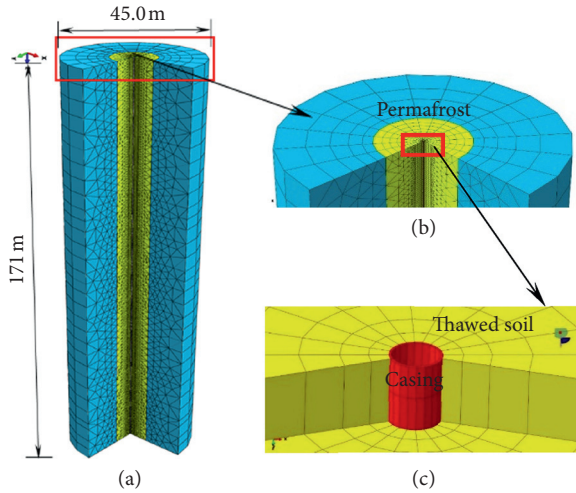


FIGURE 2: Size and detailed structure of the model: (a) mesh of the whole model, (b) local mesh of the model, and (c) local mesh of the casing.

confining pressure index. The confining pressure index can generally be taken as 0.5.

The change in casing stress state occurring during the thawing of frozen soil is closely related to the friction force generated by thawed soil on its contact surface. The friction properties of the contact surface between the casing and the thawed soil were taken to be a key parameter for calculation and analysis. This parameter was necessary to more accurately obtain value of the friction force and to better understand its distribution laws as they apply to the outer contact surface of the casing. In the analysis, the linear attenuation traction-separation model [27] was used to analyze contact behavior.

The model boundary was an adiabatic boundary and a normally fixed constraint was adopted on each surface. In calculation and analysis, the influence of confining pressure on Young's modulus of soil was realized by using a

subroutine. The gravity field and the initial tensile stress of the casing were added to the calculation model, and the model was also adjusted to account for the stress balance which occurs to eliminate the initial displacement and deformation caused by the gravity field. The shrinkage/expansion coefficient (determined by strain caused by the thawing of the visible ice lens of the total ice lens in each soil layer and the strain caused by the soil thawing and consolidation in the consolidation test [28]) was used to account for changes to the volume of the soil layer within the thaw bulb. Taking into account the semi-infinite nature of soil in the horizontal direction, its horizontal shrinkage becomes very small due to strong constraints. Therefore, the horizontal shrinkage was ignored in the present analysis. Only the vertical shrinkage of the soil layer was considered.

3. Analysis of Calculation Results

3.1. Maximum Settlement and Deformation. The maximum settlement deformation SC_{\max} and ST_{\max} of the ground surface and the casing appeared at the top of the casing and the thawed ground surface adjacent to the casing, respectively. The change curve with respect to the thaw bulb radius R_{TB} is shown in Figure 3.

As illustrated by the graphs in Figure 3, the maximum settlement of the thawed soil and the casing increases slowly alongside the gradual expansion of the thaw bulb. Moreover, the settlement of thawed soil is greater than that of the casing. The settlement difference between the thawed soil and the casing increases initially before decreasing during the process of the gradual expansion of the thaw bulb. Eventually, thaw bulb expansion within the actual oil well project tends to stabilize, and the settlement difference between the thawed soil and the casing tends towards a constant state.

In the preliminary stage of permafrost thawing, ice lens thawing and thawed soil consolidation cause initial settlement deformation within the thawed soil. The magnitude of

TABLE 2: Soil layer division and other physical and mechanical parameters.

Layer	Soil type	Depth (m)	Poisson's ratio		Young's modulus (MPa)		Confining pressure correlation index a	Coefficient of shrinkage of thawed soil (%)
			F	T	F	T		
1	Gravel & sand	0~30	0.30	0.35	777.0	58.0	0.499	1.81
2	Silt	30~54	0.35	0.40	767.0	84.0	0.2	2.09
3	Silty sand	54~63	0.30	0.35	777.0	58.0	0.499	1.99
4	Clay	63~69	0.40	0.45	737.5	62.0	0.1	3.21
5	Sand	69~81	0.30	0.35	777.0	58.0	0.499	1.10
6	Clayey silt	81~90	0.35	0.40	767.0	84.0	0.2	3.13
7	Silty clay	90~96	0.40	0.45	737.5	62.0	0.1	3.35
8	Silt	96~102	0.35	0.40	767.0	84.0	0.2	2.02
9	Sand	102~135	0.30	0.35	777.0	64.0	0.447	1.31
10	Silt	135~147	0.35	0.40	767.0	84.0	0.2	1.07
11	Sand	147~153	0.30	0.35	777.0	54.5	0.532	1.47
12	Clay	153~156	0.40	0.45	737.5	62.0	0.1	1.66
13	Silty sand	156~162	0.3	0.35	777.0	54.5	0.532	1.24
14	Clay	162~171	0.4	0.45	737.5	62.3	0.1	1.75

TABLE 3: Physical and mechanical parameters of the casing.

Grade	Density (kg/m ³)	Young's modulus (GPa)	Poisson's ratio	Yield stress (MPa)		Strain corresponding to the maximum yield strength (%)
				Minimum value	Maximum value	
J55	7805	210	0.3	380	517	3

TABLE 4: Parameters of the contact properties.

Layer	Soil type	Tangential direction		Cohesive force (MPa)	Damage		
		Friction coefficient	Elastic sliding		Initial value	Evolution	Stability coefficient
1	Gravel and sand	0.624	0.05	0.1	0.05	0.1	0.001
2	Silt	0.531	0.1	0.4	0.1	0.2	0.001
3	Silty sand	0.624	0.05	0.75	0.05	0.1	0.001
4	Clay	0.268	0.1	1.0	0.1	0.2	0.001
5	Sand	0.624	0.05	0.75	0.05	0.1	0.001
6	Clayey silt	0.531	0.1	0.5	0.1	0.2	0.001
7	Silty clay	0.268	0.1	0.75	0.1	0.2	0.001
8	Silt	0.531	0.1	0.4	0.1	0.2	0.001
9	Sand	0.624	0.05	0.75	0.05	0.1	0.001
10	Silt	0.531	0.1	0.4	0.1	0.2	0.001
11	Sand	0.624	0.05	0.6	0.05	0.1	0.001
12	Clay	0.268	0.1	1.0	0.1	0.2	0.001
13	Silty sand	0.624	0.05	0.75	0.05	0.1	0.001
14	Clay	0.268	0.1	1.0	0.1	0.2	0.001

the deformation value is related to the material properties of permafrost and thawed soil, as well as the degree of restraint the permafrost and casing demonstrates to the thawed soil. As a result of various material properties of the casing and thawed soil, negative friction on the outer wall of the casing will gradually appear and increase with the increase of thawed soil deformation. Casing settlement deformation will occur under the combined action of dead weight and negative friction. As the rigidity of casing material is greater than that of thawed soil, the settlement deformation of the casing is always less than that of thawed soil.

With the gradual expansion of the thaw bulb, constraints exerted on thawed soil by the permafrost and casing gradually weaken, while the settlement deformation of thawed soil gradually increases. When casing stress is in an elastic stage, the settlement and deformation difference value between the top of the casing and the base of the thawed soil and the negative friction acting on the casing increase gradually. These increases cause an increase in casing settlement and deformation. After the casing stress enters the plastic stage, approximate synchronous settlement and deformation occur between the thawed soil and the casing. At

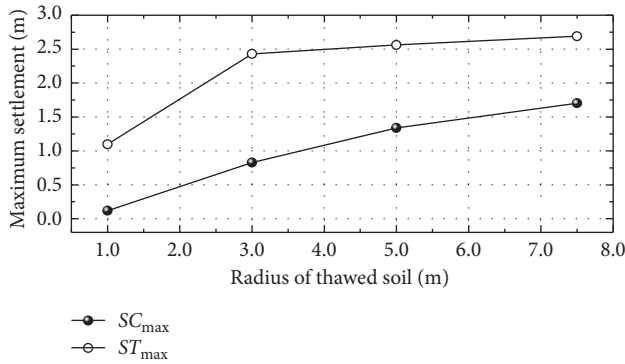


FIGURE 3: Curve of maximum settlement deformation with the expansion of the thaw bulb radius.

this time, the friction force on the lateral wall of casing in the plastic stage does not change much when compared with casing in the ultimate elastic state. The maximum settlement deformation difference between the thawed soil and the casing remains basically unchanged.

After the casing of heavy oil wells has been in operation for more than 20 years, the thaw bulb radius is about 7.5 m and remains basically unchanged. At this time, the casing will become stable under the influence of the thawed soil. Therefore, it is necessary to monitor the health state of heavy oil well casing operation during the first 20 years.

3.2. Analysis of Vertical Displacement. To study interactions between thawed soil and casing, casing wall and the soil adjacent to the outer wall of the casing were examined; the vertical displacement D_V is distributed along the depth direction as shown in Figure 4.

The following conclusions can be drawn from Figure 4:

- (1) The variation in vertical displacement of the thawed soil and the casing with depth are greatly affected by the size of the thaw bulb.

The vertical displacement distribution of the thawed soil is obviously nonlinear with depth, while that of the casing is approximately linear with depth when the thaw bulb radius R_{TB} reaches 1.0 m. The vertical displacement of the thawed soil is approximately linearly distributed with depth. That of the casing has an obvious inflection point with depth when $R_{TB} \geq 3.0$ m.

- (2) With the gradual expansion of the thaw bulb, the curve inflection point of the casing's vertical displacement with depth gradually approaches the ground surface. On both sides of the inflection point, the casing's vertical displacement with depth is approximately linear.

It can be seen from the analysis that the location of the deformation inflection point on the casing is the location where the stress yield occurs under the effect of negative friction. On the side where the casing strength has not reached the yield state, the settlement deformation of casing in the elastic stage

gradually accumulates, while the casing's vertical displacement with depth is approximately linear. On the other side of the casing, where the strength has reached its yield state, the settlement deformation reflects the settlement deformation of the thawed soil. Therefore, the vertical displacement curve for casing with depth is similar to that of the external thawed soil, but there is a certain difference near the point where the casing strength begins to yield. Besides, due to the gradual expansion of the thaw bulb, the negative friction acting on the casing increases, which eventually leads the casing's stress yield inflection point to gradually approach the ground surface. This phenomenon is discussed in detail in the subsequent analysis of casing stress. For the casing's vertical displacement curve with depth, the depth of the deformation inflection point also becomes shallower with the expansion of the thaw bulb.

- (3) When the thaw bulb radius is small, the thawed soil's vertical displacement fluctuates rapidly near the boundaries of some of the soil layers.

After the thawing of permafrost, the volume of thawed soil will be smaller than that of the permafrost due to ice disappearance and thawed soil consolidation. Without lateral restraint, the gradual accumulation of settlement deformation in the thawed soil leads to the largest settlement deformation at the top of the thaw bulb surface. In theory, the thawed soil is bound to be constrained by the frozen soil and the casing, creating a tension stress state in some parts of the thawed soil. Existing survey data [22] have confirmed that when the tensile stress in the thawed soil exceeds its tensile limit state, an internal cavity will form in the thawed soil, and its vertical displacement will create an abrupt change on both sides of the cavity. There is no cavity in the thawed soil because the fracture failure behaviors of the soil are not considered in the model calculation. However, when the thaw bulb radius is small ($R_{TB} = 1.0$ m), there are strong constraints on the settlement process of the thawed soil between the permafrost and thawed soil and between the casing and the thawed soil. The curve of the vertical displacement of thawed soil with depth changes abruptly near the boundary of some soil layers. It can be seen that there is a large thaw bulb with a tensile stress state in the subsequent analysis of thawed soil stress. While the thaw bulb radius is large ($R_{TB} \geq 3.0$ m), the thawed soil is less restrained by permafrost and casing during settlement. Settlement deformation accumulates gradually; hence, the curve of the vertical displacement with depth demonstrates an approximately linear distribution.

3.3. Analysis of Thawed Soil Stress. Stress redistribution in the thaw bulb is crucial for understanding the mechanical behaviour of casing during ground subsidence. Figure 5 shows the vertical and horizontal stresses of the soil layer near the casing as the thaw bulb expands.

The following can be seen from Figure 5:

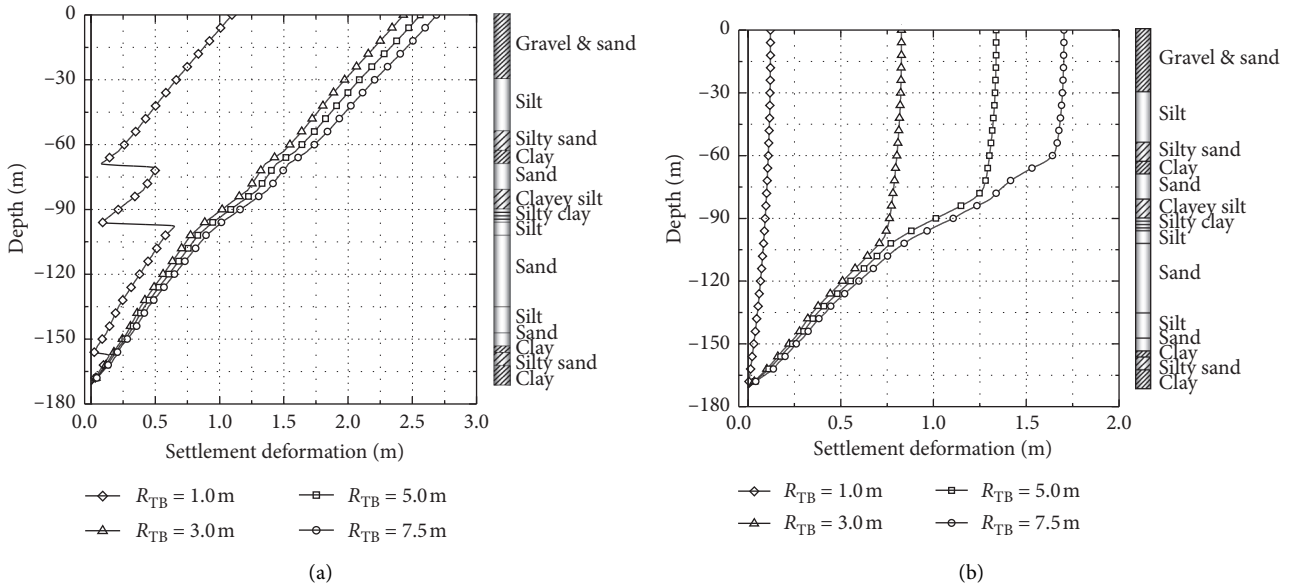


FIGURE 4: Vertical displacement distribution of the thawed soil and the casing with depth: (a) vertical displacement of thawed soil and (b) vertical displacement of casing.

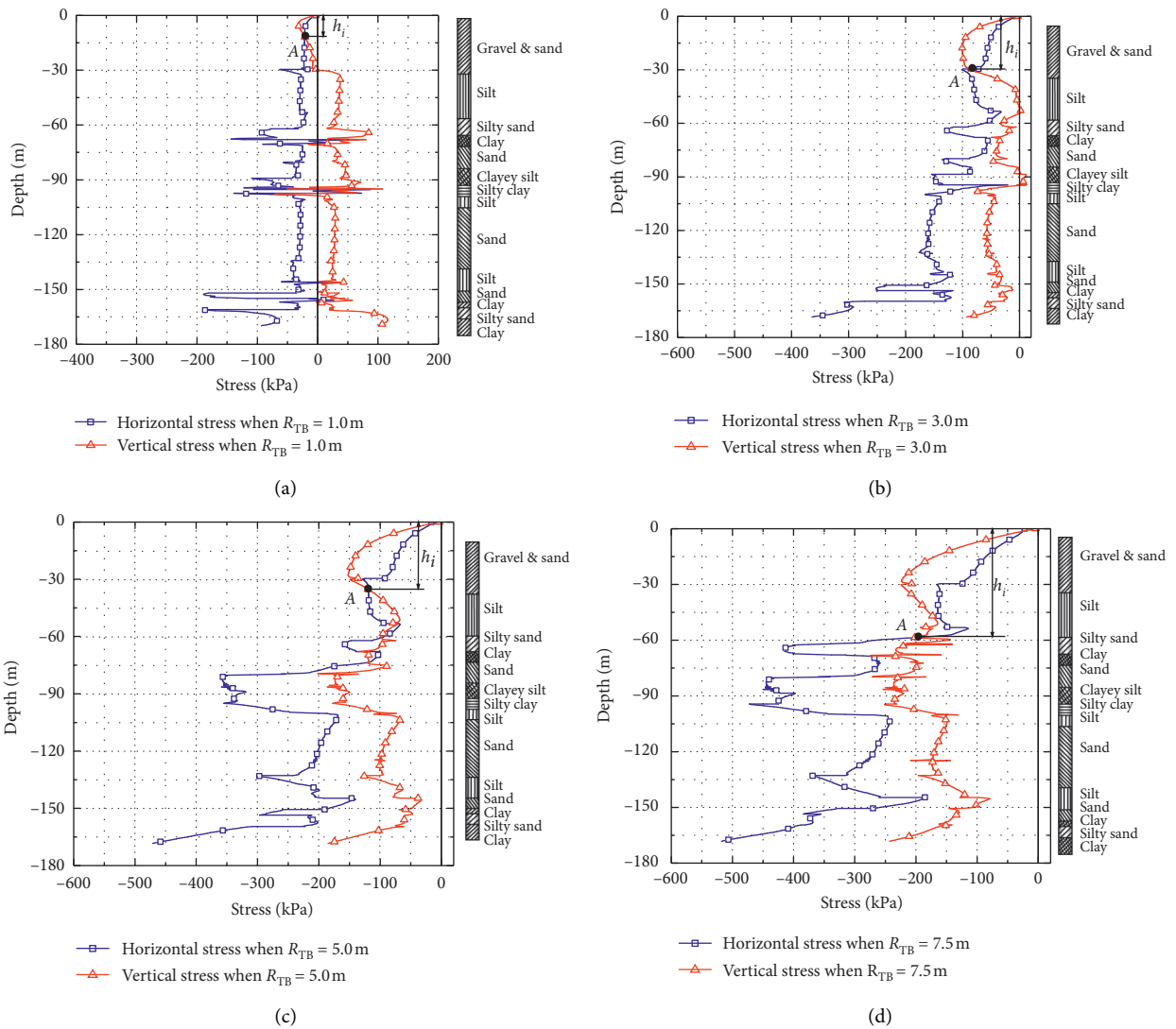


FIGURE 5: Continued.

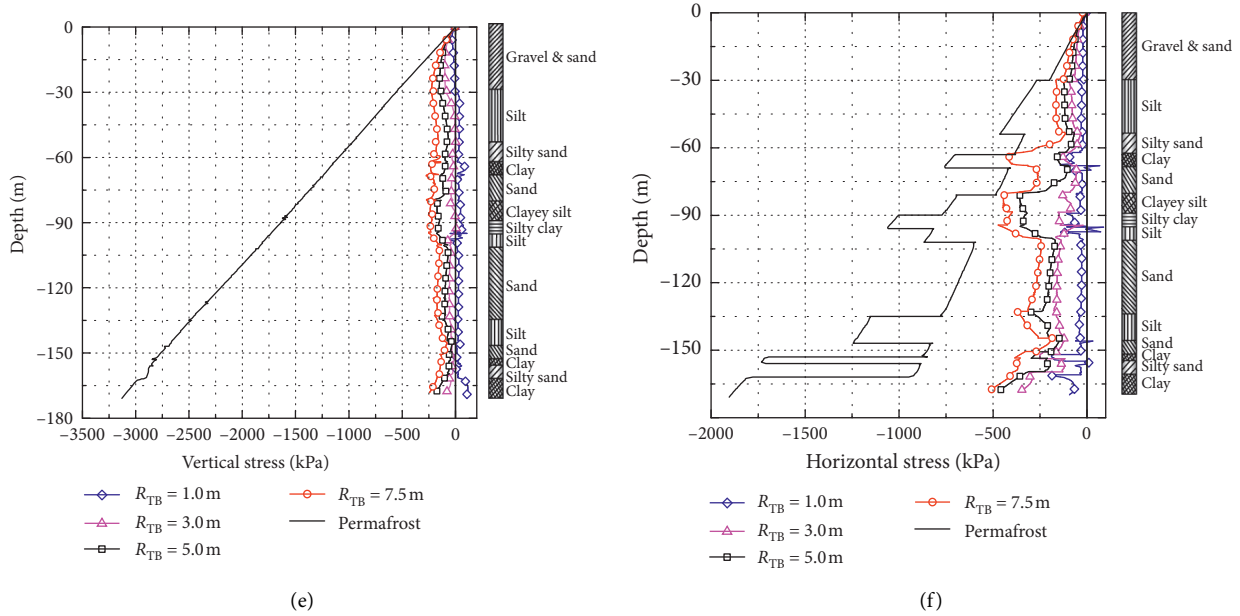


FIGURE 5: Distribution curve for thawed soil stress with depth: (a) $R_{TB} = 1.0$ m, (b) $R_{TB} = 3.0$ m, (c) $R_{TB} = 5.0$ m, (d) $R_{TB} = 7.5$ m, (e) vertical stress on the thawed soil, and (f) horizontal stress of the thawed soil.

(1) The vertical stress at the permafrost boundary increases linearly with an increase in soil depth, and the horizontal stress changes abruptly at the soil layer boundary. This latter change is due to the influence of Poisson’s ratio. Figures 5(e) and 5(f) can clearly observe the above phenomenon.

(2) The sensitivity of the thawed soil vertical stress to depth is higher than that of its horizontal stress.

The melting of ice lenses and pore ice in the permafrost causes soil volume shrinkage, ground settlement deformation, a decrease in Young’s modulus of thawed soil, and the development of friction force on the casing’s lateral walls. According to classical soil mechanics, the horizontal stress value of the soil should be less than its vertical stress value. However, in Figures 5(a)–5(d), it can be clearly observed that when the depth of thawed soil exceeds a certain value, the vertical stress value of the thawed soil is less than its horizontal stress value. In addition, it can be seen from Figure 5(d) that when the thaw bulb radius reaches 7.5 m, the vertical stress of the thawed soil at 171.0 m decreases from about 3.0 MPa to about 0.25 MPa, and the horizontal stress decreases from about 2.0 MPa to about 0.5 MPa. Obviously, the vertical stress of thawed soil is more sensitive to the changing of soil depth than horizontal stress.

(3) The vertical stress on the thawed soil gradually transits from a tensile stress state to a compressive stress state with the expansion of the thaw bulb radius, and the value of vertical stress increases continuously, while the horizontal stress of the thawed soil is always in the compressive stress state. Soil depth h_i , where the horizontal stress value is at first greater than the vertical stress

value, gradually deepens as the thaw bulb radius expands.

It can be seen from Figure 5(a) that the horizontal stress on the thawed soil is compressive stress when the thaw bulb radius reaches 1.0 m, while the vertical stress is more tensile. The vertical stress and horizontal stress of the soil layer in the thaw bulb are both compressive when the thaw bulb radius is greater than 1.0 m. Moreover, at point A, the vertical stress value of the thawed soil is greater than that of horizontal stress when its depth is less than h_i away from the ground surface. Conversely, the value horizontal stress on the thawed soil is greater than the vertical stress when depth is greater than h_i .

The vertical stress at the permafrost boundary is greater than the horizontal stress, and compressive stress prevails in both directions, in conformation with classical soil mechanics theory. However, in the thaw bulb, the vertical stress value on the thawed soil is greater than the horizontal stress value only in the formation depth h_i near the ground surface, while the vertical stress value of thawed soil is less than the horizontal stress value beyond the formation depth h_i . When the thaw bulb radius is smaller, the soil layer’s vertical stress exhibits a tensile state over a large range. These stress phenomena in the thaw bulb are mainly a result of the fact that the finite element model did not account for the fracture failure criteria in the soil’s constitutive properties and stress redistribution in the thaw bulb. The depth h_i is related to the physical properties of permafrost and thawed soil, the size of the thaw bulb, and the vertical deformation of the casing. As h_i gradually increases with the increase of R_{TB} , the internal laws of these interactions are a necessary object of future study.

3.4. Analysis of the Vertical Stress and Negative Friction on Casing. The change law for the casing’s vertical stress with the expansion of the thaw bulb is shown in Figure 6(a). The

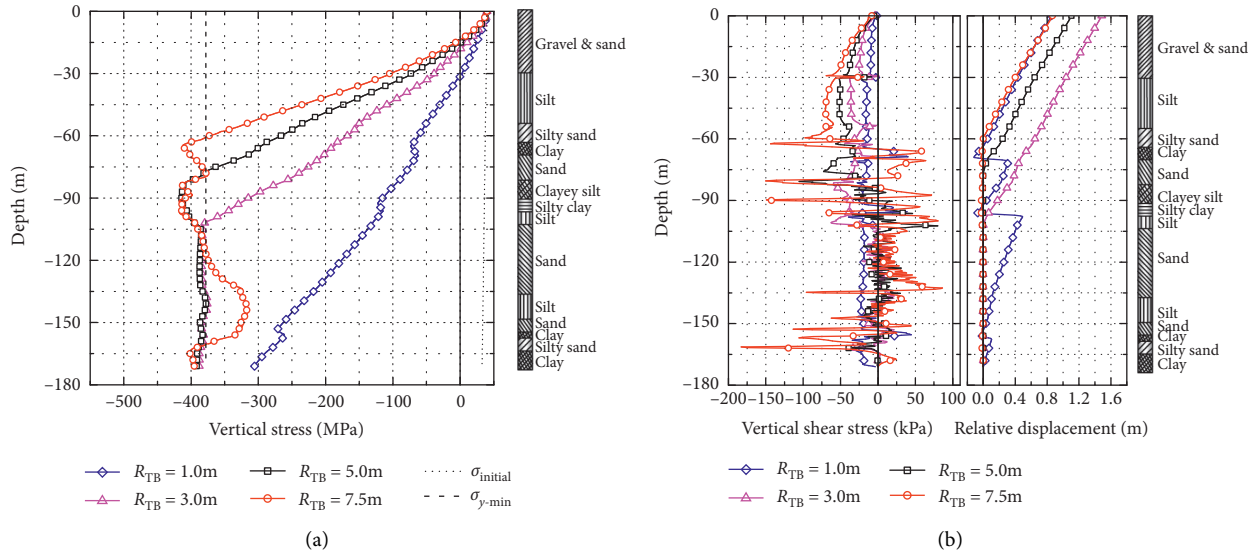


FIGURE 6: Distribution curve for casing vertical stress and its shear stress with depth: (a) vertical stress and (b) vertical shear stress and relative displacement.

curve of the J55 API casing's minimum plastic yield stress $\sigma_{y-\text{min}}$ and the change curve of the casing's initial construction tensile stress σ_{initial} with depth are shown in Figure 6(a). In order to facilitate analysis, the curves for the vertical shear stress on the casing's lateral wall with depth and the relative displacement of the casing and soil layer with depth are plotted in Figure 6(b).

The graphs illustrate the following:

- (1) Due to the existence of the casing initial stress σ_{initial} , the casing's vertical stress presents a tensile stress state within a certain depth range from the ground. As the depth gradually increases, the casing's vertical stress gradually changes to a compressive stress state.
- (2) When $R_{TB} = 1.0\text{m}$, due to the continuous negative friction and deadweight acting on the lateral casing wall, the casing's vertical stress increases almost linearly with depth.
- (3) When $R_{TB} > 1.0\text{m}$, the casing's vertical stress exceeds the minimum plastic yield stress. As it begins to yield, the location of the casing's initial stress yield gradually becomes shallower with the expansion of the thaw bulb. Before the casing has yielded, there is obvious negative friction on the lateral casing wall, but after the casing has yielded, there is no significant negative friction.

It can be seen from Figure 6(a) that when $R_{TB} = 3.0\text{m}$, the depth of the casing strength yield is about 100 m, while when $R_{TB} = 5.0\text{m}$ and 7.5m , it is about 75 m and 60 m, respectively. The distribution law for casing strength yielding depth with R_{TB} is similar to the law for the inflection point of casing vertical displacement changes with R_{TB} . As can be seen from Figure 6(b), the gravity stress on the casing is the same at the same depth. The negative friction on the lateral casing wall increases with the expansion of the thaw bulb, as does the vertical stress on the casing. When the vertical stress

reaches or exceeds its yield stress, the casing begins to yield. As vertical stress of casing with a large thaw bulb reaches the yield state, the depth where the casing yields gradually becomes shallower with the expansion of the thaw bulb. Due to the interaction between the casing and the surrounding soil, the vertical stress on the casing fluctuates slightly adjacent to its yield stress $\sigma_{y-\text{min}}$.

4. Limitations of the Model

Due to the lack of physical and mechanical parameters after the formation depth exceeds 171 m and the fact that the casing failure depth is mainly within 150 m, the simulation analysis model only considered the casing stress state within a depth of 171 m. Based on the technology employed in constructing heavy oil wells, a certain thickness was presumed for the cement grouting layer on the lateral casing wall. After the grouting layer is solidified, the casing's buckling resistance improves and its risk of settlement deformation is reduced. Because the thickness of the cement grouting layer and the parameters of its contact interface with the surrounding permafrost are difficult to determine, the cement grouting layer was ignored in the model calculation process. However, the mechanical behaviour of the interface between the frozen soil and the concrete will also have a certain impact on the force and deformation of the structure [29]. Thus, it should be noted that ignoring the cement grouting layer will not produce calculation results which exactly reflect the real state.

The actual production process of heavy oil includes injection well casing and production well casing. These two casings do not have identical temperature fields and stress states. In order to facilitate production management, in general, multiple heavy oil production well casings are concentrated in one place at a horizontal distance of about 5.5 m. The influence of the interaction between casings on

the thawing settlement of permafrost and the healthy operation of the casings is complicated. This paper has examined simple working conditions and only considers single production well casing, but it still provides a reference for future analyses of the interactions between multiple adjacent well casings.

To analyze the major factors influencing the healthy operating status of the casing, the model made three assumptions which resulted in inflated calculation results for casing stress and deformation. Use of these calculation results must therefore remain conservative.

Given the above-mentioned shortcomings of the analysis model, the analysis model will continue to be improved, hoping that the research results can provide more reference for actual production.

5. Conclusion

Based on the simulation calculation of a single oil casing in a producing well in a permafrost region, the deformation and stress distribution of casing and thawed soil with the different thaw bulb in permafrost have been analyzed. The internal mechanisms of vertical settlement displacement development and stress redistribution for thawed soil and casing were also discussed. The following conclusions can be drawn:

- (1) The maximum settlement of thawed soil and casing was positively related to the gradual expansion of the thaw bulb. The settlement of thawed soil was larger than that of the casing. Though the maximum settlement difference between thawed soil and casing increased first, it then decreased and finally tended to be constant due to stabilization of the thaw bulb's expansion, meaning that actual oil well project tends to stabilize over time.
- (2) When the thaw bulb was small, the vertical displacement curve for the thawed soil with depth fluctuated acutely due to stress redistribution. The law for vertical displacement of the casing with depth demonstrated a positive correlation and linear distribution. As the thaw bulb gradually expands, the vertical displacement of the thawed soil increases linearly with depth. The inflection point appears in the vertical displacement curve of the casing with depth, and the location of the inflection point gradually approaches the ground surface with the expansion of the thaw bulb. In addition, the casing's vertical displacement with depth on both sides of the inflection point changed approximately linearly, but the stress state of the casing was completely different.
- (3) The vertical stress on the thawed soil gradually transitioned from tensile stress to compressive stress with the expanding of the thaw bulb, while the horizontal stress was always in the compressive state. The depth h_i of the soil layer where the horizontal stress value was greater than the vertical stress value for the first time gradually deepened with the increase of the thaw bulb radius. In addition, the thawed soil's vertical stress with soil depth was more sensitive to change than was its horizontal stress.
- (4) When the vertical stress of the casing exceeded the minimum plastic yield stress, the casing began to yield. The location where the casing stress began to reach the yield state gradually became shallower with the expansion of the thaw bulb. In addition, though there was no significant negative friction on the lateral of casing wall when the casing strength reached yield, there was obvious negative friction on the lateral of casing wall when the casing strength was in an elastic stress state. Due to the existence of continuous negative friction and deadweight, the vertical value stress on the casing increased gradually as the casing location deepened.

In short, the thaw bulb around the casing of a single heavy oil-producing oil well in an Arctic permafrost region examined in this study basically no longer expanded after 20 years of operation due to heat balance. As such, the casing will become stable under the influence of thawed soil. These analysis results can be used to predict the final healthy operating status of oil well casings, provide theoretical references for the design of new oil wells, and provide technical support for the treatment of casing subsidence in existing oil wells.

Data Availability

The data used to support the findings of this study are included within the article.

Conflicts of Interest

The authors declare no conflicts of interest.

Acknowledgments

This scientific research program was supported by the National Natural Science Foundation of China (no. 42001059) and the Natural Science Foundation of Hebei Province, China (E2020210044).

References

- [1] L. J. Yang, X. M. Wang, and Z. D. Cui, "Current and comprehensive regulation measures of casing damage in Jidong oilfield," *Oil Drilling & Production Technology*, vol. 25, no. 2, pp. 79–82 + 92, 2003.
- [2] L. Yu and M. Bo, "New technology for casing damage prevention and cure of thermal production wells in Liaohe oilfield," *Petroleum Exploration and Development*, vol. 32, no. 1, pp. 116–118, 2005.
- [3] P. Q. Li, "Analysis of causes responsible for damages of casings occurring during oil/gas field exploration stage—"standard study, failure analysis and typical cases of oil tubing/casing" (2)," *Steel Pipe*, vol. 35, no. 5, pp. 53–60, 2006.
- [4] A. I. Mohammed, B. Oyeneyin, B. Atchison et al., "Casing structural integrity and failure modes in a range of well types—a review," *Journal of Natural Gas Science and Engineering*, vol. 68, 2019.

- [5] T. Wang, S. I. Yang, W. H. Zhu et al., "Law and countermeasures for the casing damage of oil production wells and water injection wells in Tarim oilfield," *Petroleum Exploration and Development Online*, vol. 38, no. 3, pp. 352–161, 2011.
- [6] C. M. Matthews, T. Dessein, and S. Yuen, "Comprehensive thaw subsidence assessments for Kuparuk DS-2A," in *Draft Final Report to ConocoPhillips Alaska Inc C-FER Technologies*, Edmonton, Canada, 2015.
- [7] G. Xu, P. Liu, Q. L. Zhang et al., "Analysis of casing damage on typical wells in bohai oilfield," *Surface Technology*, vol. 46, no. 7, pp. 168–172, 2017.
- [8] J. H. Jia, "Casing failure mechanism of thermal production wells and casing strength optimization design," *Journal of Safety Science and Technology*, vol. 7, no. 9, pp. 121–125, 2011.
- [9] F. Yin and D. Gao, "Mechanical analysis and design of casing in directional well under in-situ stresses," *Journal of Natural Gas Science And Engineering*, vol. 20, pp. 285–291, 2014.
- [10] Q. J. Zhu and J. Chen, "Deformation analysis and fracture mechanism of steel casing in oil wells," *Applied Mechanics and Materials*, vol. 467, pp. 317–322, 2013.
- [11] J. J. Wang, L. H. Han, X. Z. Yan et al., "Analysis of the casing string prestressed relaxation effect in heavy oil steam injection well," *China Petroleum Machinery*, vol. 41, no. 8, pp. 65–67, 2013.
- [12] R. J. Xie, S. J. Liu, Y. Wu et al., "Study on the casing string mechanics and feasibility of pre-stressed cementing in offshore thermal recovery wells," *China Offshore Oil and Gas*, vol. 27, no. 3, pp. 113–118 + 125, 2015.
- [13] L. J. Lu, S. B. Feng, and B. Zhang, "Method for designing casing stem strength in heavy-oil steam injection wells," *Journal of Oil and Gas Technology*, vol. 31, no. 2, pp. 364–366 + 18, 2009.
- [14] R. Mitchell (Halliburton), "Casing design with flowing fluids," *SPE Drilling & Completion*, vol. 26, no. 3, pp. 432–435, 2011.
- [15] J. Wu (Chevron ETC), "Improve casing design for WCD in deepwater wells," in *Proceedings of the SPE Annual Technical Conference and Exhibition*, New Orleans, LA, USA, September 2013.
- [16] C. Y. Hu, C. Ai, F. Y. Tao, F. Wang, and M. Yan, "Optimization of well completion method and casing design parameters to delay casing impairment caused by formation slippage," in *Proceedings of the SPE/IADC Middle East Drilling Technology Conference and Exhibition*, Abu Dhabi, UAE, January 2016.
- [17] L. D. Yu, "Distribution of world heavy oil reserves and its recovery technologies and future," *Special Oil & Gas Reservoirs*, vol. 8, no. 2, pp. 98–103 + 110, 2001.
- [18] S. J. Jiang, X. D. Tang, Y. Y. Zhang et al., "Adaptability of air-injection low-temperature catalytic oxidation technology in heavy oil production," *Special Oil & Gas Reservoirs*, vol. 21, no. 5, pp. 130–133 + 157–158, 2014.
- [19] Z. H. Zhu, M. Du, and H. Y. Han, "New technique of shallow-layer super-viscous oil production in Karamay oilfield," *Journal of Oil and Gas Technology*, no. 3, pp. 441–443 + 521, 2007.
- [20] A. Shafiei and M. B. Dusseault, "Geomechanics of thermal viscous oil production in sandstones," *Journal of Petroleum Science and Engineering*, vol. 103, pp. 121–139, 2013.
- [21] W. Guan, X. Zhang, C. Xi et al., "Displacement and development characteristics of fire flooding of vertical wells in old heavy oil areas," *Petroleum Research*, vol. 3, no. 2, pp. 165–179, 2018.
- [22] API (American Petroleum Institute), *Specification for Casing and Tubing: API Specification 5CT/ISO 11960*, American Petroleum Institute, Washington, DC, USA, 8th edition, 2005.
- [23] N. Morita and S. Shiozawa, "Stability analysis of casings during plastic deformation," in *Proceedings of the SPE Deepwater Drilling and Completion Conference*, pp. 129–142, Galveston, TX, USA, September 2014.
- [24] F. Zhang, Z. Yang, B. Still et al., "Elastic properties of saline permafrost during thawing by bender elements and bending disks," *Cold Regions Science and Technology*, vol. 146, pp. 60–71, 2018.
- [25] Z. H. Yang, T. C. Sun, J. H. Wang et al., "Well casing subsidence in thawing permafrost: a case study," *Journal of Cold Regions Engineering*, vol. 34, no. 2, 2020.
- [26] N. Janbu, "Soil compressibility as determined by oedometer and triaxial tests," in *Proceedings of European Conference on Soil Mechanics and Foundation Engineering (ECSMFE)*, pp. 19–25, Wiesbaden, Germany, 1963.
- [27] ABAQUS, *ABAQUS Analysis User's Guide*, Dassault Systèmes, Providence, RI, USA, 2016.
- [28] EBA, "Kuparuk deep core permafrost project: core descriptions," EBA File: E14103016. Electronic File Issued by EBA, A Tetra Tech Company, Technical Report to CPAI, EBA, Paris, France, 2013.
- [29] T. C. Sun, X. J. Gao, Z. R. Yue et al., "Experimental study on the adfreezing strength of the interface between silt and concrete," *Chinese Journal of Rock Mechanics and Engineering*, vol. 39, no. 5, pp. 1032–1039, 2020.

Research Article

Semantic-Segmentation-Based Rail Fastener State Recognition Algorithm

Liming Li ^{1,2}, Rui Sun,² Shuguang Zhao ¹, Xiaodong Chai,² Shubin Zheng,² and Ruichao Shen²

¹School of Information Science and Technology, Donghua University, Shanghai 201620, China

²School of Urban Railway Transportation, Shanghai University of Engineering Science, Shanghai 201620, China

Correspondence should be addressed to Shuguang Zhao; sgzhao@dhu.edu.cn

Received 13 June 2020; Revised 10 September 2020; Accepted 13 February 2021; Published 3 March 2021

Academic Editor: Zheng-zheng Wang

Copyright © 2021 Liming Li et al. This is an open access article distributed under the Creative Commons Attribution License, which permits unrestricted use, distribution, and reproduction in any medium, provided the original work is properly cited.

Rail fastener status recognition and detection are key steps in the inspection of the rail area status and function of real engineering projects. With the development of and widespread interest in image processing techniques and deep learning theory, detection methods that combine the two have yielded promising results in practical detection applications. In this paper, a semantic-segmentation-based algorithm for the state recognition of rail fasteners is proposed. On the one hand, we propose a functional area location and annotation method based on a salient detection model and construct a novel slab-fastclip-type rail fastener dataset. On the other hand, we propose a semantic-segmentation-framework-based model for rail fastener detection, where we detect and classify rail fastener states by combining the pyramid scene analysis network (PSPNet) and vector geometry measurements. Experimental results prove the validity and superiority of the proposed method, which can be introduced into practical engineering projects.

1. Introduction

As shown in Figure 1, a rail fastener is a fixed coupling part that prevents horizontal and vertical offsets in rails. Thus, rail fastener detection can be used for maintaining the stability of railway systems and ensuring the safety of trains. Figure 1 shows that the slab fastclip (SFC) type of rail fastener is used for coupling steel rails and sleepers in ballast and ballastless rail scenarios, respectively. Traditional rail fasteners detection requires workers to walk along the railroad to determine the state of the rail fasteners and other functional components; this method has low detection efficiency and precision and is dangerous [1]. Therefore, automatic rail fastener detection has attracted increasing attention from researchers.

To address the limitation of traditional detection methods, many automatic detection methods using machine vision and image processing technology have been proposed and achieved good experimental results [1–11]. Recently, deep learning theory has received increasing attention in

target detection and image segmentation works and has been successfully applied to rail fastener detection [12–14]. However, these efforts are often heavily dependent on time-consuming and expensive manual annotations.

Thus, this paper proposes a semantic-segmentation-based rail fastener state recognition algorithm. Our research was conducted in three main aspects. First is the construction of a functional area marker model for rail fasteners based on significance detection. In this model, the fastclip parts in the rail fastener image are regionally localized by the significance detection model. Then, the different functional parts in the image are semiautomatically labeled by constructing pseudolabels. Finally, a SFC-type rail fastener dataset is constructed based on the labeling results and the true state information. This method can effectively avoid the tedious manual collection and labeling of fastener samples and can compete in fastener detection. Second, we creatively propose a semantic-segmentation-based method for detecting rail fasteners. The functional regions in the input rail fastener image are segmented by a semantic

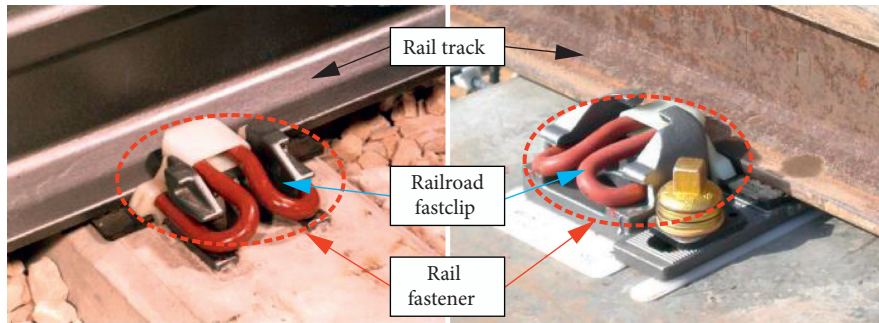


FIGURE 1: SFC-type rail fastener.

segmentation network model, and a fastener state detection method based on vector geometry relationships was designed based on the segmentation results. Third, the overall model of the proposed system is an end-to-end detection model that can detect and complete the classification of the rail fastener status in the raw input image, which can have excellent advantages in actual engineering projects.

The rest of this paper is organized as follows. Section 2 introduces related works on current rail fastener detection. Section 3 describes the overall framework and methods. Section 4 discusses the experimental results and analysis. Finally, the conclusion and future work are presented in Section 5.

2. Related Work

With the development of computer vision and image processing technologies, researchers have been committed to the research of rail fastener detection using two-dimensional visual images. In most of the studies, the primary purpose of the rail fastener inspection task is to check for missing fasteners on both sides of a rail. In [1], the top-down detection method is proposed to detect the fastener region and predict its status. In [2], an automatic and configurable real-time vision system is proposed to detect the presence/absence of rail fasteners. In [3], a fastener location and detection method based on the combination of wavelet transform and template matching is proposed; the method can accurately locate fasteners and predict their status. In [4], the authors present a method based on image processing and pattern recognition techniques, which can be customized to detect the absence of fasteners. In [5], wavelet transformation and principal component analysis are combined to detect fasteners. In [6], a method based on line local binary mode coding is proposed; the authors comprehensively considered the correlation between the image center point and its neighborhood nodes. In [7], the from-coarse-to-fine strategy is proposed to detect and recognize broken rail fasteners with a method based on Haar-like features and the Adaboost algorithm. In [8], the probabilistic structure topic model is proposed for simultaneously learning the probabilistic representations of different objects using unlabeled samples. In [9], a fastener detection method

based on the combination of the Shi–Tomasi and Harris–Stephen feature detection algorithms is proposed; the method can successfully detect the presence of fasteners. In [10], an autonomous visual rail fastener inspection system is proposed; in the system, the histogram of oriented gradient features and the linear support vector machine (SVM) classifiers' method are utilized to inspect the defect situation and classify fasteners.

Several laser detection methods have also been proposed. For example, in [15], a real-time rail fastener detection system is proposed using laser ranging, which can effectively reduce the calculation cost. In [16], a fastener detection method based on the light sensor mechanism is proposed; the method uses a decision tree classifier and the centerline extraction method to detect the incomplete state and loose fasteners. In [17], a structured light method based on motion image for the moving object inspection method is proposed, offering a fresh perspective when inspecting missing fastening components on high-speed railways. In [18], the authors proposed a structured-light-based system to evaluate the rail gauge and detect missing rail fasteners.

A rail fastener image, which contains some functional parts, can be further divided into the rail, fastener, and background regions. In [19], unlike in traditional rail fastener detection methods, attention is also given to the location and detection of the hexagonal nut in a rail fastener image.

In recent years, with the increasing application of deep learning technologies, some researchers have also applied deep learning to rail fastener detection. For example, in [12], the authors proposed a template matching classification method to automatically collect and annotate fastener samples and further deployed a similarity-based deep convolutional neural network (DCNN) to estimate the fastener state. In [13], a real-time inspection system for ballast railway fasteners based on point cloud deep learning was developed, demonstrating excellent accuracy and efficiency in field testing on ballastless tracks. In [14], a fastener detection method based on visual rail inspection is proposed using material classification and semantic segmentation with DCNN to, respectively, identify and segment the different functional parts in a rail fastener image. In [20], the authors proposed Yolo v3, which is deployed and trained as a deep learning model for detecting the state of rail fasteners. In

[21], an end-to-end abnormal fastener detection method, which can identify abnormal fasteners from a rail scene image, is proposed.

In summary, we consider the following major problems of previous approaches:

- (1) Although good results can be achieved in rail fastener detection through deep learning frameworks, the detection methods based on existing supervised learning are heavily dependent on the manual pixel-level annotation of image data. Annotating large-scale rail fastener image datasets one by one through manual methods is extremely tedious, time-consuming, and expensive.
- (2) Existing rail fastener detection methods are mainly focused on the missing state of rail fasteners in images. The main body of the detection target generally determines the missing state only for the overall area of the fastener, rather than performing specific state detection based on local functional areas. The positioning results and status of rail fasteners can only be considered from a qualitative analysis perspective, and no unified quantitative evaluation criteria exist for the accurate description and comparison of the effects of the detection method.
- (3) Rail fastener detection is a standard data sample imbalance problem in which the positive sample data images of fasteners taken and collected in actual railway scenes are generally much larger than the negative samples. Unbalanced training and experimental samples can affect the accuracy of experimental results.

To solve the problems of existing approaches, we present a novel semantic-segmentation-based rail fastener state recognition algorithm. The contributions of our work are as follows:

- (1) To reduce the reliance of traditional deep learning methods on manual annotation, we provide a semiautomatic method for locating and annotating rail fasteners based on saliency detection. The experimental results show that the method can accurately locate and segment fastener pop-up regions and generate accurate pixel-level annotations of the rail fastener image, reducing the cost of the manual annotation of functional regions and improving the efficiency by 25 times that of the traditional manual annotation process.
- (2) We further classify the fastener state into five specific situations based on a priori knowledge of the geometric relationships between the different functional regions in the fastener image. Meanwhile, we shift the attention of detection to specific functional structural regions (i.e., the fastener fastclip and rail regions). We propose a semantic-segmentation-based rail fastener detection method and introduce new quantitative

evaluation metrics to describe and evaluate the results of fastener positioning experiments. The experimental results prove that the fastener cartridge positioning effect and state detection results of this method have obvious accuracy and superiority.

- (3) To solve the problem of data imbalance, a new standard dataset based on the SFC-type fastener is constructed by the method in Contribution 1, and the image's negative sample data is reasonably augmented in the construction process. To some extent, the problem of dataset imbalance is alleviated, and the overall performance of the detection method framework is improved.

3. Proposed Method

First, we perform localization and semiautomatic labeling of the functional regions in the original images using a salient detection model (SDM). Then, we propose a semantic-segmentation-based rail fastener state detection method, which is based on the semantic information and spatial relationships among the functional parts in the rail fastener image, to achieve the accurate detection and monitoring of the rail fastener state.

3.1. Positioning and Marking of Functional Areas.

Figure 2 describes in detail a specific implementation of the method for locating and labeling rail fasteners based on significance detection, which enables the interactive automatic labeling of the functional areas in the input image. Our overall approach consists of three main modules. First, the fastener region in the input image is positioned by the salient detection model to obtain the original rail saliency map corresponding to each original rail image. Then, the target region segmentation model is used to locate and segment the fastener regions on both sides of the rails in the image to obtain the corresponding position of the rail fastener image, which mainly contains the rails and fastener fastclip regions that we are interested in. Finally, a salient detection model is used to further locate and correct the fastener fastclip areas in the saliency map, and a pseudolabel construction model is used to semiautomatically label the functional areas in the image to generate the corresponding interactive pseudolabels for each rail fastener image. The following section discusses these three main modules in detail. In addition, we constructed a special dataset of SFC rail fasteners using the above method. This dataset includes the rail fastener images obtained by salient detection and target area segmentation, the corresponding functional area pseudolabeling, the ground truth, and the labeled real fastener states.

3.1.1. Salient Detection Model (SDM). We first perform the salient detection of the original rail fastener image by setting up a sliding processing window based on the comparison of regional features. As shown in Figure 3, sliding image processing window W is defined with an adjustable window

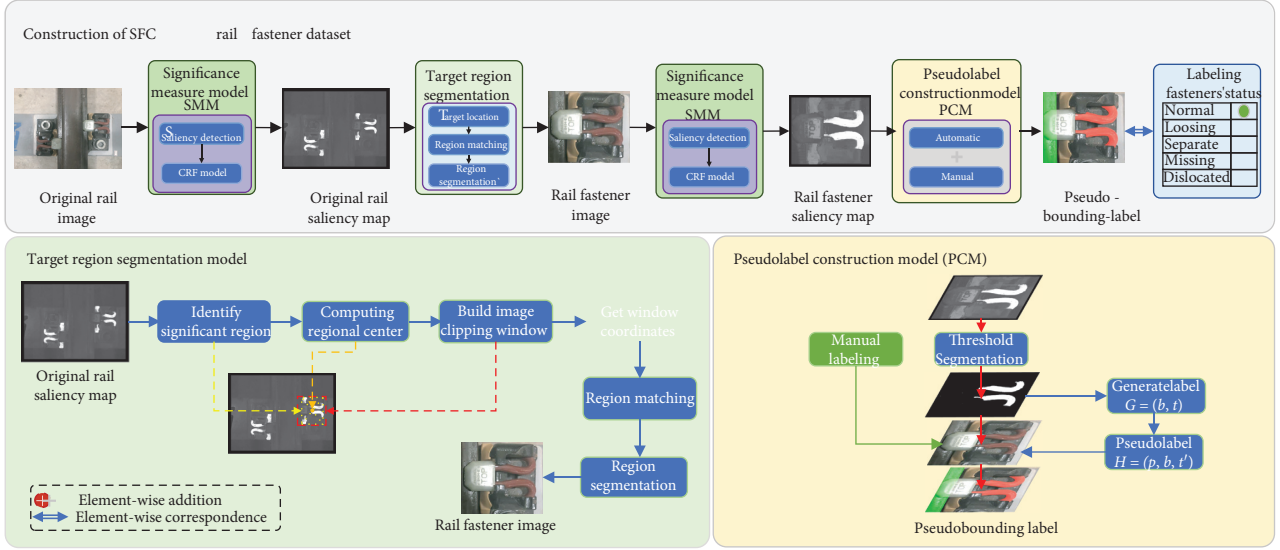


FIGURE 2: Overall framework of the rail functional area positioning and labeling method: (a) details of the target region segmentation model and (b) details of PCM.

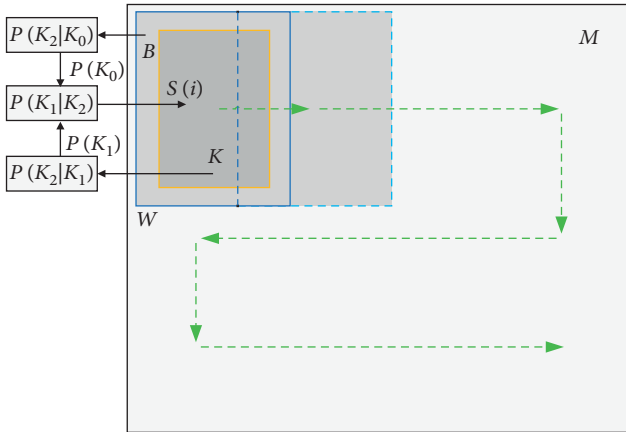


FIGURE 3: Detailed diagram of the sliding processing window in SDM.

scale in the input image, and image processing window W is divided into processing kernel K and outer frame B . Random variable $i \in \mathbf{R}^2$ represents a pixel node in image processing window W , and a specific characteristic attribute of the node is defined as $f(i)$. The characteristic properties of the described pixel node are measured by computing the intensity and color features of the image to measure the significance of the node. This salient detection mechanism is similarly defined in the literature [22].

For pixel node i in the sliding image processing frame, window W , we assume that events H_0 and H_1 indicate that pixel node i is located in processing kernel K and outer frame B , and event H_2 indicates that pixel node i is a significant pixel node. The significant measure ($S(i)$) of pixel node i can be expressed by the following Bayesian formula:

$$S(i) = P(H_0|H_2) = \frac{P(H_2|H_0)P(H_0)}{P(H_2|H_0)P(H_0) + P(H_2|H_1)P(H_1)} \quad (1)$$

In addition, to further calculate the significance metric value ($S(i)$) for each pixel node i in sliding image processing window W , we assume that the probability of the existence of the above event (H_0) is p , which ranges from (0,1). To reduce the error interference during the calculation of the saliency measure, we introduce a normalized regular histogram to enhance the robustness and stability of the algorithm. Second, we represent $P(K_2|K_0)$ and $P(K_2|K_1)$ in equation (1) by feature histograms $h_K(i)$ and $h_B(i)$ and use $\mathbf{h}_F(i)$ and $\mathbf{h}_B(i)$ to represent the products of the pixels in the corresponding histograms in the CIELAB color space. Finally, the significant metric value of pixel node i that meets the requirements of the specific feature attributes in sliding image processing frame window W is

$$S(i) = \frac{\mathbf{h}_K(i)p}{\mathbf{h}_K(i)p + \mathbf{h}_B(i)(1-p)} \quad (2)$$

We construct the feature histograms of any window in different position cases by moving different proportions of the sliding image processing frame window in the original image of the rail fastener and measuring the significance of the pixel nodes within the sliding image processing frame window according to equation (2).

On this basis, we label and segment the pixel nodes by the minimization energy function in the conditional random field (CRF) [23] to perform the target-level foreground segmentation of the significant regions in the rail fastener image. Suppose that input image M contains n pixel nodes i ; we first define array $X = (x_1, x_2, \dots, x_n)$ to represent the set

of all pixel nodes i in image M . Then, let array $Y = (y_1, y_2, \dots, y_n)$ represent the significant metric value of pixel node i . Finally, we assume that a binary segmentation label that can label pixel node i exists, where $y_i \in \{F, B\}$ indicates that pixel node i is a salient and non-salient label. The mathematical description of the CRF model we constructed based on salient detection is

$$p(Y|X, s) = \frac{1}{Z(X)} \exp\left(-\sum_n E(y, x, s)\right), \quad (3)$$

where $Z(x)$ is the normalization factor. We estimate the label attribute (y_i) of a pixel node in an image by using the energy function in the minimized CRF model, and the mathematical representation is

$$\hat{Y} = (\hat{y}_1, \hat{y}_2, \dots, \hat{y}_n) = \arg \min E(y, x, s). \quad (4)$$

Energy function E in the CRF model consists of three feature models: two one-dimensional U^S terms based on saliency feature model U^S , color feature model U^C for a particular pixel node, and a two-dimensional term based on spatial relationship model Q for neighboring pixels. The mathematical expression is

$$E(y, x, s) = \sum_{i=1}^n (w_s U^S(y_i, s_i) + w_c U^C(y_i, x_i)) + \sum_{(h,j) \in X} Q(y_h, y_j, x_h, x_j), \quad (5)$$

where parameters w_s and w_c are the weighting factors that control the corresponding feature models. Their specific values are determined by the method described in the literature [24]. x_h and x_j are adjacent pixel nodes in rail fastener image M .

For the original rail images in Figure 2, we first optimally estimate the labeling of pixel points by the energy minimization function of the CRF model and label the pixel nodes as significant and nonsignificant feature nodes. The image is then segmented into significant foreground and nonsignificant background areas based on the significant feature contrast of adjacent pixel nodes. In this approach, the fastclip areas on the rail fastener image can be marked and highlighted as prominent foreground areas, and the original rail salient maps can be generated.

3.1.2. Target Region Segmentation Model. Considering that the original rail image input contains some irrelevant regions and backgrounds in addition to our fastener regions of interest, we propose a target region segmentation module. In this module, we first divide the localization results of saliency detection into left and right subimages and then segment and extract the corresponding target regions in the subimages.

As shown in Figure 2a, the coordinates of the center pixel of the significant region are first calculated and discriminated based on the spatial geometric prior information of the saliency positioning module results. Subsequently, a specific size image clipping frame is constructed with the central

pixel as the coordinate origin. Then, the boundary coordinates of the clipping frame are mapped and matched with the original rail image by obtaining the clipping frame. Finally, by segmenting the matching region in the original image, we finally obtain our desired rail fastener image.

We first define array $T = \{N_{1,1}, N_{1,2}, \dots, N_{n,m}\}$ to represent the set of all pixel nodes $N_{i,j}$ in the original rail saliency map (M_S). Then, we perform the binary segmentation of saliency map M_S and define function $F_s(N_{i,j})$ to represent the saliency eigenvalue of pixel node $N_{i,j}$. The value of the function is 1 when the pixel node is the significant foreground and 0 for the background node. The coordinates of pixel node $N_{i,j}$ are represented by (x_i, y_j) . We can calculate the value of the coordinates of the center of the significant region ($C(X, Y)$) as follows:

$$\begin{cases} X = \bar{x} = \frac{1}{MN} \sum_{i=1}^M \sum_{j=1}^N x_i F_s(x_i, y_i), \\ Y = \bar{y} = \frac{1}{MN} \sum_{i=1}^M \sum_{j=1}^N y_i F_s(x_i, y_i), \end{cases} \quad (6)$$

where the value of function $F_s(x_i, y_i)$ is 1 and M and N are the respective lengths and widths of the significant regions derived by statistical operations.

Based on the coordinates ($C(X, Y)$) of the centroids of the significant regions obtained from the above equation, we can reconstruct an image crop frame ($Z = (C, V)$) containing all significant regions based on our a priori knowledge, where C is the coordinates of the centroids of the regions and V represents the size of the reconstructed crop frame. To facilitate the subsequent image computation and processing, the range of the V values is positioned here as [470,520] pixels. Through this method of randomly generating crop frames of variable size in the parameter interval, the negative sample data of the input image can be randomly augmented. Consequently, the data samples can be maintained at a relatively balanced level as much as possible. To a certain extent, the imbalance of the dataset of rail fasteners is alleviated and solved, improving the overall performance and accuracy of the algorithm.

Finally, by obtaining the boundary coordinates of the image clipping frame for coordinate mapping and matching with the original rail image, we can obtain an image that contains only the rail fasteners and rail edges of ROI (region of interest), completing the task of segmenting the foreground target area.

3.1.3. Pseudolabel Construction Module (PCM). Given the irregular shape characteristics of the fastener bar area in the rail fastener image, the bar area in the image must be manually marked at a high cost when using the traditional supervised learning method to detect a specific bar area in the rail fastener image, whereas the shape characteristics of the rail travel area in the image are usually significant and a regular rectangular area, which can be marked using the manual marking method. Therefore, this work attempts to construct image target-level pseudolabels instead of pixel-level manual annotations for the

rail fasteners' bullet regions and combine the results of manual annotations for the rail walk regions to learn and train the labels of different rail functional regions in the image through weak supervised learning.

Our model for constructing pseudolabels for the automatic labeling of fastener fastclip regions is inspired by the literature [25]. Ultimately, accurate target classification and semantic segmentation can be implemented for the different classes of track-functional fasteners in the image.

As shown in Figure 2b, we first construct an image target-level pseudolabel for the rail functional area in the rail fastener image positioned by the saliency area. First, let $M'_s \in \mathbb{R}^{w \times h \times 3}$ represent the segmentation result of the significant map, where w and h are the height and width of the input image, respectively. Suppose that T represents the set of different functional area categories in rail fastener image M_O ; then, the significant map of the rail fasteners generated by the SDM is transformed into a binarized image by threshold segmentation. Assuming the existence of binarized label t to label the fastclip and background regions, the pixel value of the significant region in the segmentation result is set to 1 and the background pixel to 0. Then, image-level label G is constructed for the pixels in the fastener fastclip region, which is mathematically expressed as

$$G = (b, t), \quad t \in T, \quad (7)$$

where b is the boundary segmentation box for a significant foreground region. When the value of t is 1, G denotes the set of pixels in the bounding box where the fastener striping region of the figure is calibrated.

Second, we assume that marker vector t' has a similar definition as t : 0 and 1 denote the pixel properties of the background and the pop-up bar region of the graph. In addition, the rail region pixel property is set to 2. Then, the mathematical expression for constructing pseudolabel H is

$$H = \begin{cases} (p, b', t') \leftarrow G(b, t) & t' = t = 1, \\ (b', t'), t' = 2, \end{cases} \quad (8)$$

where parameter p represents the probability that the bounding box belongs to the fastener fastclip area. According to equation (8), we perform a pixel-level annotation of the rail regions in the rail fastener image manually ($t' = 2$) and jointly construct the pseudolabeling (H) of the image functional regions with the fastener bullet image-level labels (G) obtained by the above automatic annotation method ($t' = 1$).

This semiautomatic image labeling method is used to generate the proposed pseudolabel in this work. The pseudolabeling structure consists of the target-level labeling of the fastclip region and the pixel-set labeling of the rail region. Consequently, we can finally obtain complete semantic labels for the different functional regions of the rail fastener image. Furthermore, as shown in Figure 2, we construct a new rail fastener image dataset, which includes the cropped rail fastener image, the generated pseudolabels, and the real state of the fastener.

3.2. Semantic Segmentation and Defect Detection. In this section, we first describe in detail the overall architecture of a vision-based rail fastener defect detection system. The system detects and outputs the state of the rail fastener in the raw input rail image via an end-to-end detection model. Second, we elaborate and discuss the semantic segmentation-based fastener defect detection algorithm within the system.

3.2.1. Overall System Architecture. As shown in Figure 4, the objective of this study is to photograph and collect original rail images in real engineering applications. Our proposed detection system is an end-to-end rail fastener detection system. The acquired original input rail image is first localized regionally, and the target region is segmented based on the SDM to obtain rail fastener images that contain only useful functional region features. Then, a semantic segmentation-based defect detection method for rail fasteners, which utilizes a semantic segmentation model and a state detection method based on vector geometry measurements, is proposed to detect and judge the state of rail fasteners. The results of the rail fastener defect detection and the status classification are finalized and generated.

3.2.2. Status Detection Method. Figure 5 presents the overall architecture of our semantic-segmentation-based approach to the rail fastener defect detection proposed in the detection method. In our designed detection method, we first perform an accurate semantic segmentation of the rails and fastener fastclip in the input rail fastener image using a semantic segmentation model. A fastener defect detection algorithm based on vector geometry parameters is then designed based on the segmentation results of the different functional regions to realize the detection and classification of fastener defects and states.

Functional region segmentation is an important part of this method. In this part, the input rail fastener image of the rail, the fastener bar, and the background region of our interest are segmented using the semantic segmentation model to obtain the semantic segmentation result of the corresponding region. The semantic segmentation model involves the accurate prediction and segmentation of the different functional regions in the rail fastener image by detecting the semantic segmentation network involved in the system.

For the rail fastener images taken and collected in the actual engineering scene, this paper uses PSPNet [26] to learn the context information and key details between the pseudolabels constructed for the different region categories in the global scene of the input image to finally achieve the semantic segmentation of different functional regions in the image. PSPNet can fuse semantic and detailed information features in different network layers. The diverse positions, shapes, and sizes of different functional areas in the rail fastener image can be used in rail fastener detection.

We use the pseudolabeled rail fastener images of different functional regions as training data, extract the underlying features of the input images, and generate the

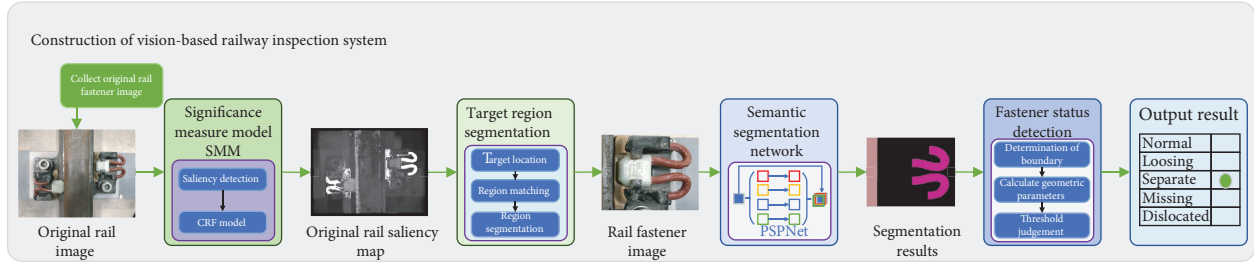


FIGURE 4: Overall architecture of our detection system.

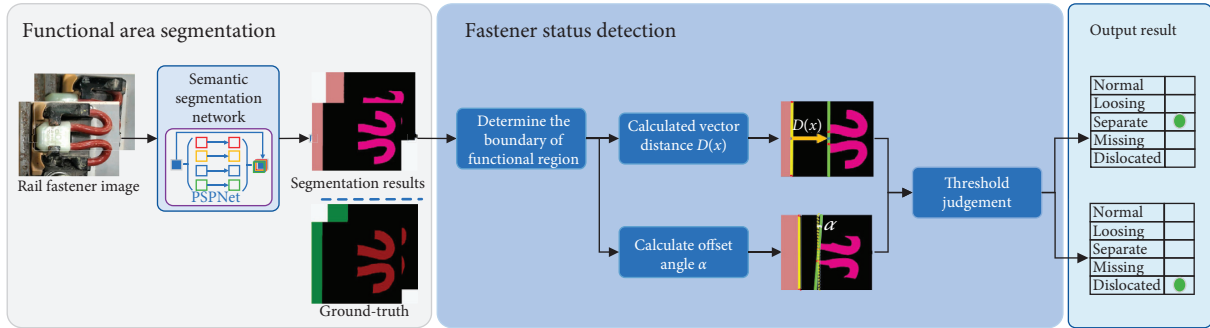


FIGURE 5: Overall architecture of our detection method.

corresponding feature maps using the pretrained deep residual network (ResNet) [27] and the expansion convolution strategies [28, 29] in the PSPNet split network architecture used in this study. ResNet can achieve good network classification and identification by deepening the training network depth; the expansion convolution strategy can expand the size of the receiving field to a certain extent without changing the feature layer scale to obtain more global image information by expansion convolution on the basis of completing the original network structure. Second, we use the pyramid pooling module to learn and acquire contextual information about the different regional category labels in the image based on the full use of the captured global image features. The pyramid pool module in the PSPNet network architecture integrates four pyramid sub-models of different scales to sample and output feature elements of different dimensions from low to high dimensions and then fuses the different dimensions to obtain the global context of the pyramid pool. As shown in the figure, the pyramidal pool module involved in this study contains pyramidal submodels with 1×1 , 2×2 , 3×3 , and 6×6 dimensions. Finally, the accurate segmentation of the different functional areas in the original rail fastener image is achieved by fusing and convolutionalizing the multidimensional feature elements with the original feature map to generate the final segmentation result map.

Fastener status detection is a detection method based on the vector geometry computation proposed based on the a priori knowledge embodied in the semantic segmentation results of the functional regions. From the semantic segmentation results, we can derive the following information. (1) Regardless of the angle of the input image, the edge of the rail region in the image is always a straight line. (2) The

thresholds for the vector pixel distances between different functional regions can be divided by experimentally measuring the images of rail fasteners in different states. (3) If no rail fastener fastclip area is detected in the image prediction results, then the rail fastener is in an unhealthy missing state.

On the basis of the a priori information obtained from the above experimental experience, this paper proposes a method for fastener defect detection and state classification based on vector geometry relationships. The method calculates the vector geometry relationship between the functional regions processed by the semantic segmentation model, determines the threshold of different states according to the specific vector distance, and finally classifies the states according to the defective state of the obtained rail fasteners. The implementation is as follows. First, we determine the linear boundaries of the different functional regions by a least squares linear fitting algorithm. The vector distance and the offset angle from the rail region boundary to the rail fastener region boundary are then calculated. Finally, the defect detection and classification results of the final rail fastener state are obtained by comparing and judging the calculated results with the empirical threshold.

Figure 6 shows two images of rail fasteners in a non-healthy state and the corresponding state detection principle. For the images of unhealthy rail fasteners in the detached and offset states presented in Figures 6(a) and 6(b), we determine the working state of the fasteners in the images by calculating the vector distance and offset angle of the rail and fastclip boundaries, respectively. Let M represent the semantic segmentation results obtained by the above method, and w and h represent the length and width of the image, respectively, with a range of $[0, 473]$ pixels. Given the regular and smooth rectangle rail region in the image, we

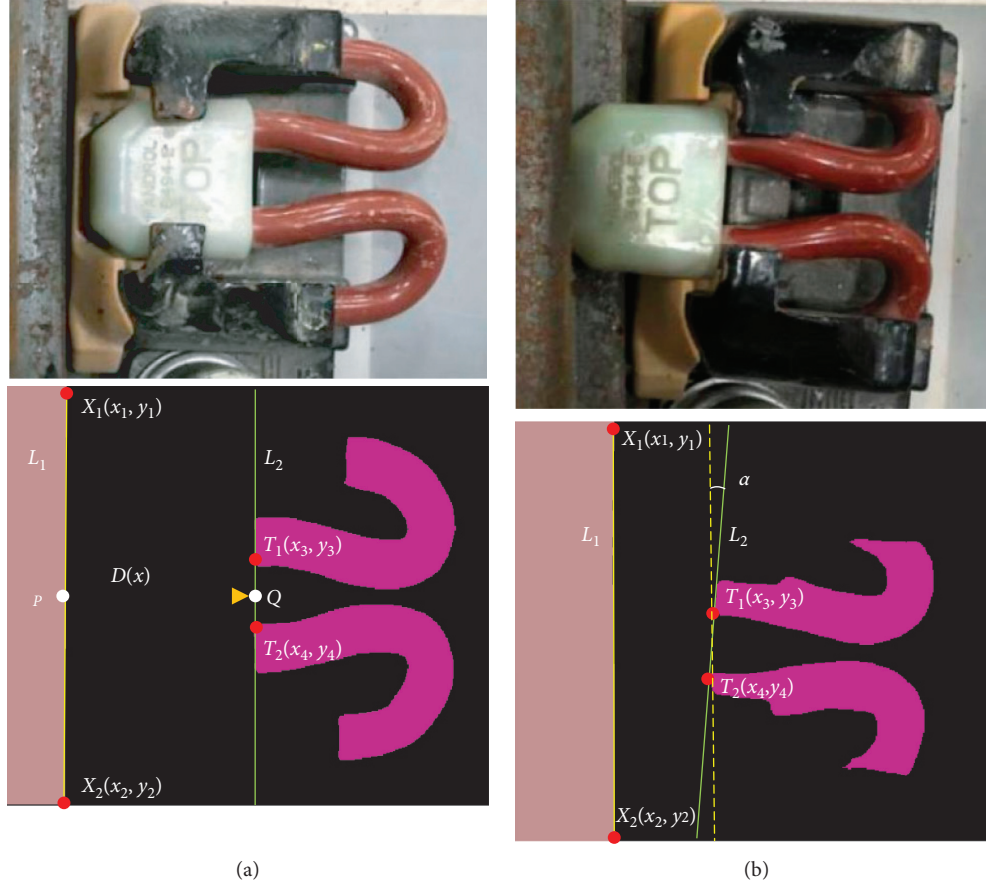


FIGURE 6: Schematic of a state detection method based on vector geometry.

obtain the linear equation ($L_1: y = ax + b$) for the border of the rail region by defining two pixel points ($X_1(x, 0)$ and ($X_2(x, 473)$) as the locus points for the border of the rail region, which are calculated from the coordinates of the two locus points, as shown by the yellow solid line in Figure 6. In addition, we select 30 discrete pixel nodes $T_i(x, y)$ with the smallest value of transverse coordinate x in the fastener region as the locator, where $i \in [1, 30]$, and then, use the least squares linear fitting algorithm to determine the linear equation ($L_2: y = cx + d$) for the near-rail side boundary of the rail fastener, as shown by the green solid line in Figure 6. The error term is defined as $S(c, d) = \sum (y_i - (cx + b))^2$. According to the principle of least squares, S must be of minimum value, and the condition for obtaining the minimum value of S is $(\partial S / \partial c) = (\partial S / \partial d)$, which gives

$$\begin{pmatrix} \sum_{i=1}^n x_i^2 & -\sum_{i=1}^n x_i \\ -\sum_{i=1}^n x_i & n \end{pmatrix} = \begin{pmatrix} c \\ d \end{pmatrix} \begin{pmatrix} -\sum_{i=1}^n x_i y_i \\ \sum_{i=1}^n y_i \end{pmatrix}. \quad (9)$$

By substituting the coordinates of the location point to the value of parameter c and d , the following equations are derived:

$$c = \frac{n \sum_{i=1}^n x_i y_i - \sum_{i=1}^n x_i \sum_{i=1}^n y_i}{n \sum_{i=1}^n x_i^2 - (\sum_{i=1}^n x_i)^2}, \quad (10)$$

$$d = \frac{\sum_{i=1}^n x_i^2 \sum_{i=1}^n y_i - \sum_{i=1}^n x_i \sum_{i=1}^n x_i y_i}{n \sum_{i=1}^n x_i^2 - (\sum_{i=1}^n x_i)^2}.$$

As shown in Figure 6(a), the linear fitting equation (L_2) for the near-rail measurement boundary of the rail fastener region is obtained by the above method. Defining parameter $D(x)$ as the vector distance from the rail region boundary to the fastener region boundary and assuming that $P(x_{L_1}, y_{L_1})$ and $Q(x_{L_2}, y_{L_2})$ are the pixel points on rail region line L_1 and fastener region boundary line L_2 , respectively, $D(x)$ is calculated as

$$D(x) = \sqrt{(x_{L_2} - x_{L_1})^2 + (y_{L_2} - y_{L_1})^2}. \quad (11)$$

To simplify the calculation of the equation, we set y to 236. Empirically, if the vector distance between the line of the fastener near the pixels on the side of the rail and the rail in the predicted result is less than 100 pixels, then the rail fastener is in the normal state; if the vector distance between the two is in the range of 100–160 pixels, then the rail

fastener is in an unhealthy loose state; if the vector distance between the two is greater than 160 pixels, then the rail fastener is in an unhealthy separate state. If the fastener sling area is not detected, the rail fastener is in the missing state.

In addition, we calculate the degree of deflection of the rail fasteners relative to the rails by calculating the angle of clamping (α) of the two boundary lines (L_1 and L_2), as shown in Figure 6(b). According to the experimental test, if $\alpha \in [5^\circ, 90^\circ]$, then the rail fastener is in the dislocated state; otherwise, it is in the normal state within a reasonable error. Parameter α is calculated as

$$\alpha = \arccos \left| \frac{1 + ac}{\sqrt{1 + a^2} \sqrt{1 + c^2}} \right|. \quad (12)$$

Calculated vector distance parameter $D(x)$ and angular offset α are compared with a predetermined threshold, and the rail fasteners are subjected to defect detection and state classification by threshold judgment. Furthermore, to avoid detection errors due to the simultaneous action of two geometric parameters on the experimental results, the rail fasteners in the unhealthy state satisfy only one of the dislocated or other nonnormal states, prioritizing the influence of the vector distance parameter on the detection results during the experiment.

4. Experiments and Analysis

In this section, we first construct a SFC rail fastener dataset by the method described in Section 4.1. A new evaluation metric is then proposed to quantitatively characterize the effect of rail fastener fastclip region positioning based on a significance detection model. In addition, by conducting experiments on the rail fastener image dataset, the results of the experiments performed on the present algorithm are qualitatively and quantitatively validated.

4.1. Dataset. Our experimental data were derived from original rail images taken and captured in real railway project scenarios, and we segmented the fastener regions on both sides of the steel rail in the original images and constructed the SFC-type rail fastener dataset using the method described in Section 3.1. Our dataset contains images of rail fasteners on the left and right sides of the tracks, pseudo-labels corresponding to the images, the ground truth, and the true state of the fasteners in the images. In addition, we classified the type of fasteners according to the state of the rail fasteners into positive and negative data samples, where the positive samples include the image data of the rail fasteners in the normal state, and the negative samples include the image data of the rail fasteners in the loose, detached, missing, and dislocated states.

The SFC rail fastener dataset contains 2000 positive sample data in the normal state and 2000 negative sample datasets with defects (including 500 negative sample data in each of the three different states). In addition, we divided the equal amount of rail fastener image data for different state conditions in the dataset into a training set and a test set by random selection, with 2400 samples for training and 1600 samples for testing.

4.2. Analysis of Experimental Results. We first quantitatively evaluated the positioning effect of the rail fastener fastclip region and then conducted extensive experiments on the rail fastener image dataset to further qualitatively and quantitatively validate the experimental results of the detection system designed in this work.

4.2.1. Experimental Analysis of Fastener Railroad Fastclip Positioning. In existing studies on the positioning of the rail fastener area by computer vision and image processing techniques, existing methods can usually only qualitatively describe and evaluate the results of fastener positioning experiments. Given the lack of uniform evaluation criteria for the positioning results of the rail fastener images, the experimental results of the fastener region positioning are difficult to quantitatively evaluate and compare. Thus, we introduced the evaluation parameters in the visual attention mechanism [30–34].

The Precision-Recall curve, the F-measure [35], and the mean absolute error (MAE) are used as indicators for evaluating the accuracy of fastener positioning for the effective evaluation and analysis of the accuracy of positioning results from a quantitative perspective.

In the fastener fastclip image dataset, a corresponding ground truth was first constructed for each rail fastener image in the dataset by manual labeling at the pixel level. Then, the resultant diagram of the fastener fastclip region localization obtained by this method was threshold selected as a binary segmentation from 0 to 255. Finally, for each threshold condition, the fastclip positioning results plot was compared pixel-by-pixel with the true value plot, and the evaluation parameters of the positioning results relative to the ground truth were calculated. The experimental results on the positioning of the fastener fastclips were evaluated from a quantitative point of view. Precision represents the ratio of the correctly positioned area of the fastener fastclip in the positioning result map to the actual overall area of the fastclip in the positioning result, and Recall represents the ratio of the correctly positioned area of the fastener fastclip in the positioning result map to the theoretical area of the fastclip in the true value map. The F-measure is a comprehensive indicator for evaluating the final positioning result. The MAE is used to measure the positioning error of the positioning result relative to the true value image, which is calculated as follows:

$$\text{Precision} = \frac{T_p}{T_p + F_p}, \quad (13)$$

$$\text{Recall} = \frac{T_p}{T_p + F_N}, \quad (14)$$

$$F_\lambda = \frac{(1 + \lambda^2) \text{Precision} \times \text{Recall}}{\lambda^2 \text{Precision} + \text{Recall}}, \quad (15)$$

$$\text{MAE} = \frac{1}{WH} \sum_{x=1}^W \sum_{y=1}^H |\bar{S}(x, y) - \bar{G}(x, y)|. \quad (16)$$

In formulas (13) and (14), T_p represents the pixel sample data of the real fastener area located, and F_p and F_N , respectively, indicate the false and missed pixel data samples of the positioning experiment results relative to the theoretical railroad fastclip area in the truth map. In formula (15), the value of λ^2 is 0.3 [35]. W and H in formula (16) are used to represent the length and width of the input rail fastener image to be processed, and parameters x and y represent the horizontal and vertical coordinates of the pixel node in the image, respectively.

We quantitatively evaluated the results of the localization of the fastclip region on a dataset of 200 images of rail fasteners in different states. In addition, the fastener positioning results obtained by this method were compared with the positioning effects of several other classical target saliency detection algorithms on rail fasteners, including the SER [36], SWD [37], SIM [38], SS [39], MR [40], RCRR [41], and ACM [42] algorithms. The representative serial numbers in Figure 7 are 2–8, respectively, and the graphs of the Precision-Recall curve, F-measure, and MAE of various algorithms for locating the fastclip area in the rail fastclip image are presented.

As shown in Figure 7(a), the localization experiments performed for the fast clip region significantly outperform several other saliency detection algorithms. The results show that the proposed localization method achieves the best accuracy of more than 0.9. Although the background region in the localization results was clearly separated from the foreground fastclip region, which can effectively meet the localization and segmentation needs of the postexperiment, the recall values below 0.4 do not correspond to the ideal situation (high accuracy value of 0.9) and show an increasing trend because they were not treated by the model as completely irrelevant black backgrounds. In addition, all methods converged toward an accuracy value of 0.12 when a threshold value near 255 was selected for the maximum recall value. During the convergence of the curves, the accuracy of the methods was significantly better than that of the other algorithms at any Recall value. The experimental results show that the fastener fastclip location effect of the proposed method is more accurate than those of the other methods and has a lower false alarm rate and robustness. Figures 7(b) and 7(c) show an F-measure and MAE of 0.5632 and 0.1302, respectively, for the experimental results obtained by this method. The positioning area of the rail fasteners obtained by this method is more accurate than the positioning effect of several other algorithms, and the average absolute errors of the positioning results are smaller than those of other methods, indicating that this method can position rail fasteners more precisely.

4.2.2. Functional Region Semantic Segmentation Results.

We validated the detection effect of the proposed method on the constructed SFC-type rail fastener dataset. The segmentation network was modeled and trained on the training set based on the pseudolabeling of each image sample, namely, the semantics and segmentation of the “rail” and “fastclip” regions of the image with different properties.

Next, we fed 1600 rail fastener image samples from the test set into a trained semantic segmentation model for automatic region identification and semantic segmentation, enabling accurate targeting and segmentation tasks for specific functional regions in the image samples.

The images of rail fasteners in four different states for the dataset were constructed. Accurate regional localization and semantic segmentation can be performed through the proposed method. The experimental results are shown in Figure 8. Figure 8(a) shows the rail fastener images of the five different fastener state types obtained by this method, where the rail fastener image in the normal, loose, separate, missing, and dislocated states are shown from the top to bottom; Figure 8(b) shows the rail fastener remarkable images for the completed fastclip remarkable area positioning; Figure 8(c) shows the functional area ground truths for the manually labeled multiple fastener images; Figure 8(d) shows the target-level pseudolabels for the rail fastener image constructed by this method, where the red and green areas are the labels for the fastclip and rail areas in the image, respectively; Figure 8(e) shows the predicted functional area results for the rail fastener image for different state types, where the gray area represents the predicted rail area, the white area represents the predicted fastclip area, and the other background and unrelated functional areas are black. In addition, Figures 8(f)–8(j) show the corresponding schematic of the fastener image data on the other side of the rail.

The experimental results in Figure 8 indicate that the functional region semantic segmentation results obtained by this method and shown in Figures 8(e) and 8(j) have an excellent experimental effect compared to the corresponding ground truth shown in Figures 8(c) and 8(h). The experimental results show that our segmentation results are accurate and automatic for the functional areas of interest in all five types of rail fastener images and can effectively filter out other areas and complex backgrounds. Therefore, the region segmentation method established in this work has significant validity and accuracy for rail fastener images.

4.2.3. Rail Fastener State Detection Results. In the field of rail fastener detection, the performance of rail fastener detection and classification methods is an important factor in confirming system reliability. For the 800 data samples in the test set used for algorithm validation in different states, we detected and classified the states of the rail fasteners using the proposed vector-based geometry measurement method. In the test results obtained by this method, we assumed that parameter T_p indicates the number of samples of true positives detected by this method, T_N indicates the number of samples of true negatives detected, F_p indicates the number of samples of false positive data detected, and F_N indicates the number of samples of false negative data detected. The Precision, Recall, and F-measure of the state detection and classification results of the rail fasteners were, respectively, calculated by equations (13)–(15) (the value of parameter λ in equation (15) is set to 1 in this experiment), and the accuracy of the experimental results was evaluated in

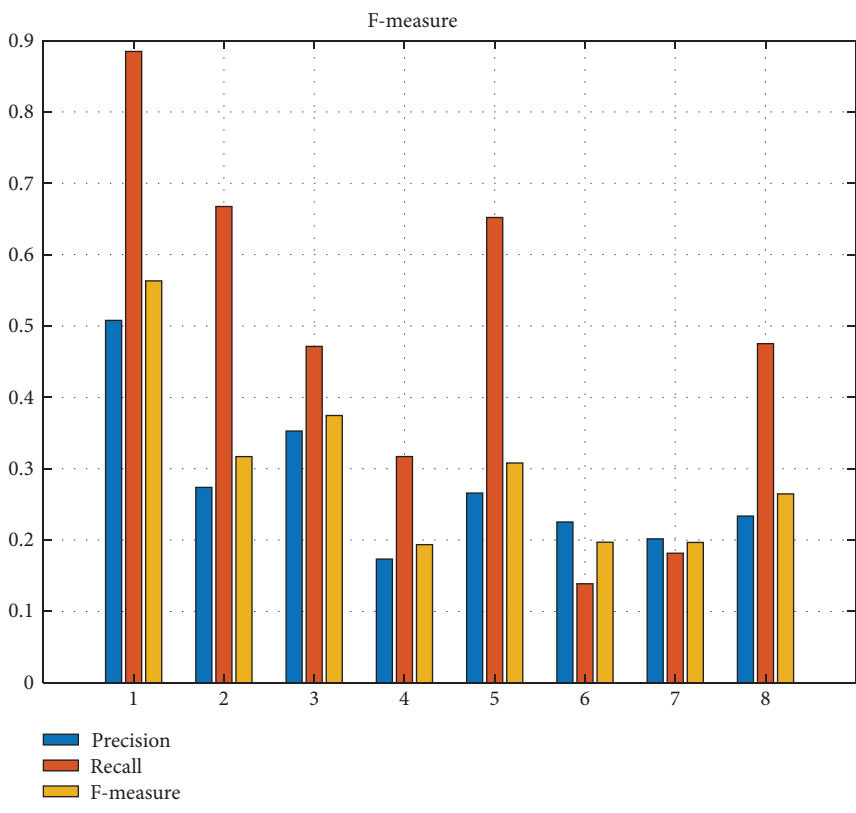
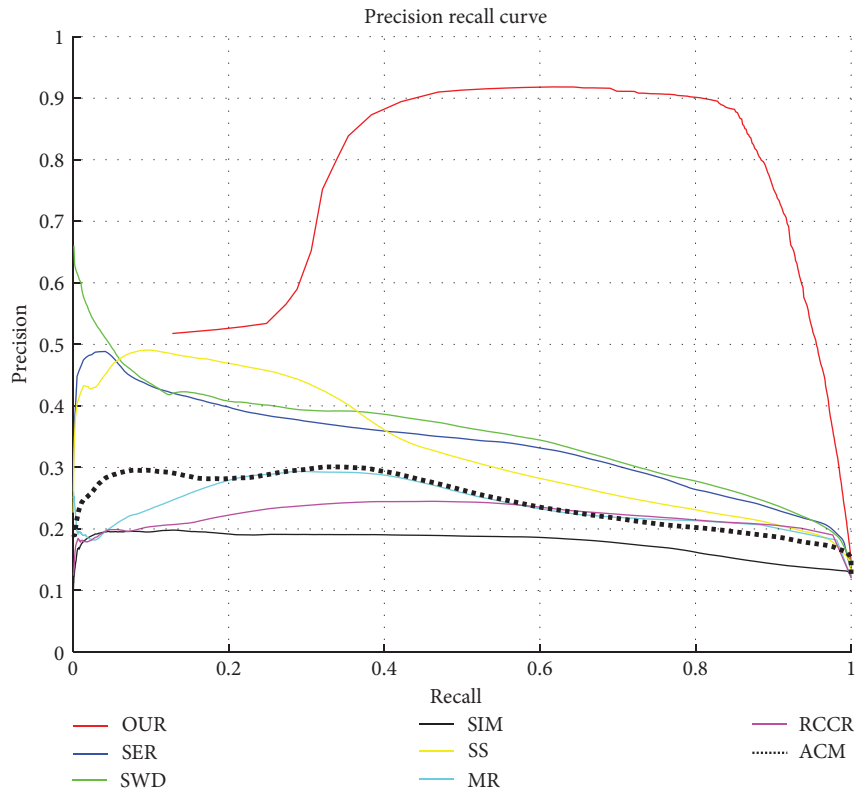


FIGURE 7: Continued.

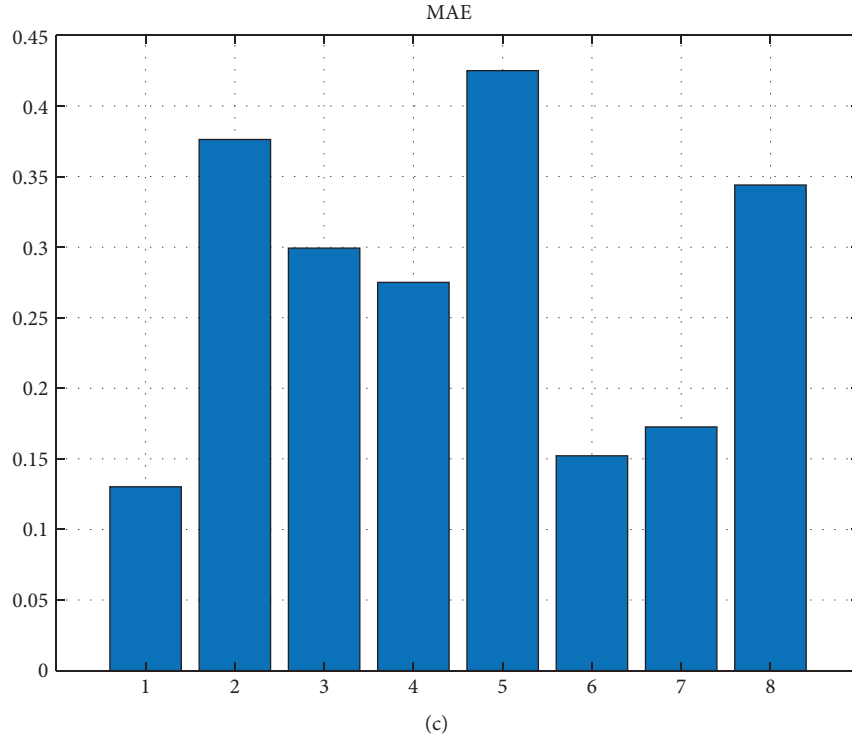


FIGURE 7: Evaluation curve of the results of the positioning of the fastener fastclip area.

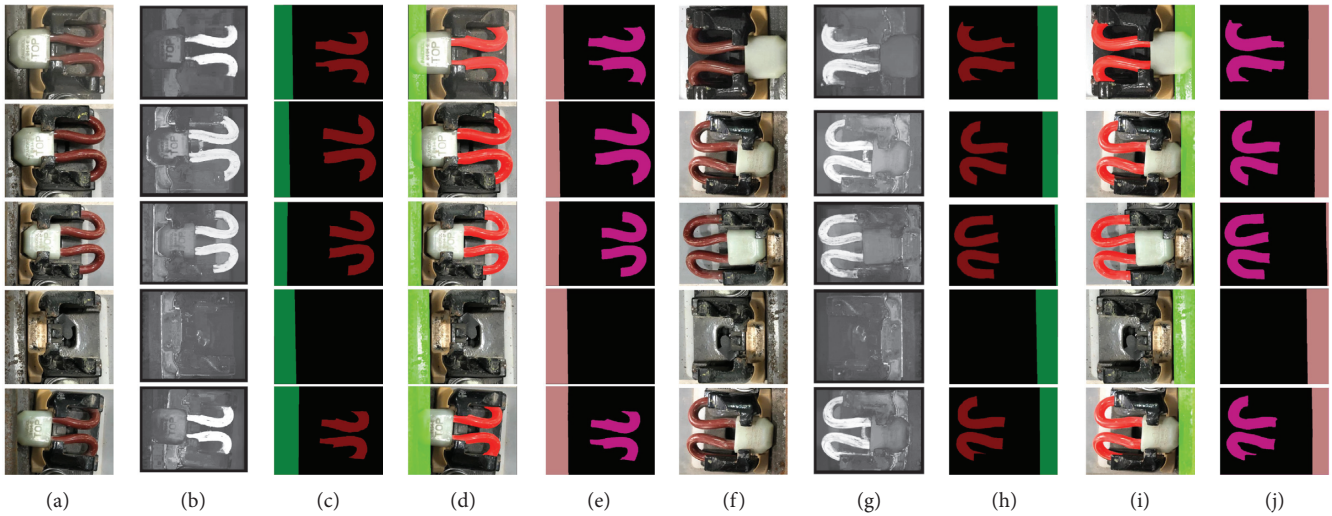


FIGURE 8: Schematic of the prediction results of semantic segmentation of rail fastener images for five state types.

conjunction with the Accuracy index. The mathematical expression of the Accuracy indicator is

$$\text{Accuracy} = \frac{T_P + T_N}{T_P + T_N + F_P + F_N}. \quad (17)$$

The experimental results are shown in Table 1, and the proposed rail fastener detection method can achieve 93.13% Accuracy on the validation dataset (contains 800 positive samples and 800 negative samples of various data types).

Average Accuracy and Recall rates of 92.17% and 90.50% were achieved for the five different states of the rail fastener image data in the validation set, with an average F-measure of 0.9127. In addition, the experimental results indicate that the proposed method can obtain more accurate detection results for samples of rail fasteners in the normal, losing, separate, missing, and dislocated states.

The experimental results indicate that the rail fastener detection system and proposed method obtain good experimental results on the SFC-type rail fastener dataset.

TABLE 1: Detection and classification results of rail fasteners in five state types.

Fastener status	Type	Experimental results					Evaluation index			
		Normal	Loosing	Separate	Missing	Dislocated	Precision (%)	Recall (%)	<i>F</i> -measure	Accuracy (%)
Real sample	Normal	780	11	4	0	5	94.43	97.50	0.9594	93.13
	Loosing	18	158	15	0	9	85.41	79.00	0.8208	
	Separate	4	9	184	1	2	90.20	92.00	0.9109	
	Missing	0	0	0	200	0	99.50	100.00	0.9975	
	Dislocated	24	7	1	0	168	91.30	84.00	0.8750	

TABLE 2: Accuracy results of state detection of multiple detection methods in SFC-type rail fasteners.

Method	Ours (%)	DCNN [19] (%)	PHOG + SVR [1]	HOG + SVM [10]
Accuracy	93.31	88.79	85.67%	79.29%

Specimens of rail fasteners in normal, loosing, missing, and dislocated states can be obtained with high accuracy in the experiment, but the accuracy against the loose state of the fasteners is only 85.41%. The difference between the characteristics of the image samples of rail fasteners in the loosened state and the normal and disengaged state is small that even experienced professional inspectors cannot accurately determine whether the rail fasteners are in the loosened state in the inspection work. Consequently, detecting rail fasteners in a loose state is difficult and challenging, so the accuracy of the results of testing the state of rail fasteners in the loose state is affected compared to several other samples of state rail fasteners. However, considering the overall experimental results, the proposed method can be used to conduct an accurate state inspection of rail fasteners in different states with obvious accuracy and reliability and can achieve better inspection results in practical engineering applications.

To demonstrate the validity of our method, the detection accuracy metrics of different detection methods were calculated and compared on the validation dataset constructed above. Table 2 shows the total accuracy of different methods for SFC-type fastener images. The table shows that our method significantly outperforms several other detection methods mainly because the other schemes do not consider the state detection of the offset fastener during design and implementation, producing unsatisfactory experimental results and accuracy for this part of the negative sample detection. In addition, the difficulty of detecting the negative sample data in the loose state also affects the detection performance of other methods and can thus affect the overall performance of the detection method to some extent.

To test the performance of the detection method, the proposed algorithm was tested on a dataset of SFC-type rail fastener images taken and constructed in a real railway scenario. The proposed semantic-segmentation-based rail fastener detection method was executed on a computer equipped with an Intel Xeon W-2150B processor (10 cores and 10 threads). Experimental calculations indicate that the time to detect the state and classification of each rail fastener using the proposed method is 1.135 s, which can meet the requirements of practical engineering inspection tasks. In addition, we evaluated the efficiency of our semiautomatic labeling method by randomly selecting 50

images of rail fasteners from several types of data. The average time for the semiautomatic annotation of a single image in the dataset was 5.256 s, while the average time for manual annotation was 132 s. This method is 25 times more efficient than the manual method in annotating all the images. In summary, this method can effectively reduce the cost of manual annotation and has very reliable detection performance and a good generalization ability, which can meet the accuracy and efficiency requirements of engineering inspection scenarios.

5. Conclusions and Future Work

In this study, we aim to address the limitations of traditional rail fastener detection methods and deep learning theory in engineering applications. A semantic segmentation-based rail fastener state recognition algorithm is proposed. First, we propose a functional area positioning and labeling method based on the salient detection model in the system, and a novel SFC-type rail fastener dataset was constructed by labeling and constructing pseudolabels for fastclip and rail regions through an interactive semiautomatic labeling method. Then, the fastener state in the original rail image was classified and produced by the detection system designed in this study. Second, a rail fastener state detection method based on the semantic segmentation model was designed, and the fastener state was detected by the semantic segmentation network and vector distance calculation method. The experimental results show that the proposed method has good accuracy and robustness while effectively saving cost and can achieve good experimental results in practical application scenarios.

Although the proposed method was validated by numerous effective experiments on our dataset and achieved promising results, it can still be improved. Although the results based on the saliency detection model satisfy the requirements of the algorithm, the model can be further optimized and improved. Moreover, detecting the state of the rail fastener image of the loose fastclip is still challenging and difficult. In future work, we plan to address some of the above limitations. Nevertheless, we believe that the proposed inspection method is a major step forward in the automation of rail inspection and has significant implications for practical engineering applications.

Data Availability

The data used to support the findings of this study are available from the corresponding author upon request.

Conflicts of Interest

The authors declare that there are no conflicts of interest regarding the publication of this paper.

Acknowledgments

This work was supported by the National Natural Science Foundation of China (no. 51975347 and 51907117) and Key Science and Technology Support Project of the Shanghai Science and Technology Commission (no.18030501300).

References

- [1] T. Prasongpongchai, T. H. Chalidabhongse, and S. Leelhapantu, "A vision-based method for the detection of missing rail fasteners," in *Proceedings of the 2017 IEEE International Conference on Signal and Image Processing Applications (ICSIPA)*, pp. 419–424, Kuching, Malaysia, September 2017.
- [2] P. De Ruvo, A. Distanto, E. Stella, and F. Marino, "A GPU-based vision system for real time detection of fastening elements in railway inspection," in *Proceedings of the 2009 16th IEEE International Conference on Image Processing (ICIP)*, pp. 2333–2336, Cairo, Egypt, November 2009.
- [3] X. Yuan, B. Liu, and H. Chen, "Algorithm and program design for fastener locating and detection using wavelet transformation and template matching," in *Proceedings of the 2017 IEEE 17th International Conference on Communication Technology (ICCT)*, pp. 1116–1121, Chengdu, China, October 2017.
- [4] J. Yang, W. Tao, M. Liu, Y. Zhang, H. Zhang, and H. Zhao, "An efficient direction field-based method for the detection of fasteners on high-speed railways," *Sensors*, vol. 11, no. 8, pp. 7364–7381, 2011.
- [5] E. Stella, P. Mazzeo, M. Nitti et al., "Visual recognition of missing fastening elements for railroad maintenance," in *Proceedings of the IEEE 5th International Conference on Intelligent Transportation Systems*, pp. 94–99, Singapore, September 2002.
- [6] H. Fan, P. C. Cosman, Y. Hou, and B. Li, "High-speed railway fastener detection based on a line local binary pattern," *IEEE Signal Processing Letters*, vol. 25, no. 6, pp. 788–792, 2018.
- [7] Y. Xia, F. Xie, and Z. Jiang, "Broken railway fastener detection based on Adaboost algorithm," in *Proceedings of the 2010 International Conference on Optoelectronics and Image Processing*, pp. 313–316, Haikou, China, November 2010.
- [8] H. Feng, Z. Jiang, F. Xie, P. Yang, J. Shi, and L. Chen, "Automatic fastener classification and defect detection in vision-based railway inspection systems," *IEEE Transactions on Instrumentation and Measurement*, vol. 63, no. 4, pp. 877–888, 2014.
- [9] R. A. Khan, S. Islam, and R. Biswas, "Automatic detection of defective rail anchors," in *Proceedings of the 17th International IEEE Conference on Intelligent Transportation Systems (ITSC)*, pp. 1583–1588, Qingdao, China, October 2014.
- [10] X. Gibert, V. M. Patel, and R. Chellappa, "Robust fastener detection for autonomous visual railway rail inspection," in *Proceedings of the 2015 IEEE Winter Conference on Applications of Computer Vision*, pp. 694–701, Waikoloa, HI, USA, January 2015.
- [11] W. F. Zhu, X. J. Chen, Z. W. Li et al., "A SAFT method for the detection of void defectin side a ballastless rail structure using ultrasonic array sensors," *Sensors*, vol. 19, no. 21, p. 15, 2019.
- [12] X. Gibert, V. M. Patel, and R. Chellappa, "Deep multitask learning for railway track inspection," *IEEE Transactions on Intelligent Transportation Systems*, vol. 18, no. 1, pp. 153–164, 2017.
- [13] H. Cui, J. Li, Q. Hu, and Q. Mao, "Real-time inspection system for ballast railway fasteners based on point cloud deep learning," *IEEE Access*, vol. 8, pp. 61604–61614, 2020.
- [14] X. Giben, V. M. Patel, and R. Chellappa, "Material classification and semantic segmentation of railway rail images with deep convolutional neural networks," in *Proceedings of the 2015 IEEE International Conference on Image Processing (ICIP)*, pp. 621–625, Quebec, Canada, September 2015.
- [15] C. Aytekin, Y. Rezaeitabar, S. Dogru, and I. Ulusoy, "Railway fastener inspection by real-time machine vision," *IEEE Transactions on Systems, Man, and Cybernetics: Systems*, vol. 45, no. 7, pp. 1101–1107, 2015.
- [16] Q. Mao, H. Cui, Q. Hu, and X. Ren, "A rigorous fastener inspection approach for high-speed railway from structured light sensors," *ISPRS Journal of Photogrammetry and Remote Sensing*, vol. 143, pp. 249–267, 2018.
- [17] H. Zhang, J. Yang, W. Tao, and H. Zhao, "Vision method of inspecting missing fastening components in high-speed railway," *Applied Optics*, vol. 50, no. 20, pp. 3658–3665, 2011.
- [18] Z. Peng, C. Wang, Z. Ma et al., "A multifeature hierarchical locating algorithm for hexagon nut of railway fasteners," *IEEE Transactions on Instrumentation and Measurement*, vol. 69, no. 3, 2019.
- [19] J. Liu, Y. Huang, Q. Zou et al., "Learning visual similarity for inspecting defective railway fasteners," *IEEE Sensors Journal*, vol. 52, 2019.
- [20] Y. Lin, C. Hsieh, W. Huang, S. Hsieh, and W. Hung, "Railway rail fasteners fault detection using deep learning," in *Proceedings of the 2019 IEEE Eurasia Conference on IOT, Communication and Engineering (ECICE)*, pp. 187–190, Yunlin, Taiwan, October 2019.
- [21] B. Dong, Q. Li, J. Wang, W. Huang, P. Dai, and S. Wang, "An end-to-end abnormal fastener detection method based on data synthesis," in *Proceedings of the 2019 IEEE 31st International Conference on Tools with Artificial Intelligence (ICTAI)*, pp. 149–156, Portland, OR, USA, November 2019.
- [22] E. Rahtu and J. Heikkilä, "A simple and efficient saliency detector for background subtraction," in *Proceedings of the 2009 IEEE 12th International Conference on Computer Vision Workshops*, pp. 1137–1144, Kyoto, Japan, October 2009.
- [23] A. Criminisi, G. Cross, A. Blake et al., "Bilayer segmentation of live video," in *Proceedings of the 2006 IEEE Computer Society Conference on Computer Vision and Pattern Recognition (CVPR'06)*, pp. 53–60, New York, NY, USA, June 2006.
- [24] M. Szummer, P. Kohli, and D. Hoiem, "Learning CRFs using graph cuts," in *Proceedings of the European Conference on Computer Vision. railroad fastcliper*, pp. 582–595, Berlin, Heidelberg, April 2008.
- [25] N. Inoue, R. Furuta, T. Yamasaki, and K. Aizawa, "Cross-domain weakly-supervised object detection through progressive domain adaptation," in *Proceedings of the 2018 IEEE/CVF Conference on Computer Vision and Pattern Recognition*, pp. 5001–5009, Salt Lake City, UT, USA, June 2018.

- [26] H. Zhao, J. Shi, X. Qi et al., "Pyramid scene parsing network," in *Proceedings of the IEEE Conference on Computer Vision and Pattern Recognition*, pp. 2881–2890, Honolulu, HI, USA., July 2017.
- [27] K. He, X. Zhang, S. Ren et al., "Deep residual learning for image recognition," in *Proceedings of the IEEE Conference on Computer Vision and Pattern Recognition*, pp. 770–778, Las Vegas, ND, USA, July 2016.
- [28] F. Yu and V. Koltun, "Multi-scale context aggregation by dilated convolutions," 2015, <https://arxiv.org/abs/1511.07122>.
- [29] L. C. Chen, G. Papandreou, I. Kokkinos et al., "DeepLab: semantic image segmentation with deep convolutional nets, atrous convolution, and fully connected crfs," *IEEE Transactions on Pattern Analysis and Machine Intelligence*, vol. 40, no. 4, pp. 834–848, 2017.
- [30] L. Itti, C. Koch, and E. Niebur, "A model of saliency-based visual attention for rapid scene analysis," *IEEE Transactions on Pattern Analysis and Machine Intelligence*, vol. 20, no. 11, pp. 1254–1259, 1998.
- [31] J. Harel, C. Koch, and P. Perona, "Graph-based visual saliency," in *Proceedings of the Advances in Neural Information Processing Systems*, pp. 545–552, Columbia, UK, May 2007.
- [32] G. Li, Y. Xie, T. Wei et al., "Flow guided recurrent neural encoder for video salient object detection," in *Proceedings of the IEEE Conference on Computer Vision and Pattern Recognition*, pp. 3243–3252, Salt Lake City, UT, USA, June 2018.
- [33] X. Zhang, T. Wang, J. Qi et al., "Progressive attention guided recurrent network for salient object detection," in *Proceedings of the IEEE Conference on Computer Vision and Pattern Recognition*, pp. 714–722, Salt Lake City, UT, USA, June 2018.
- [34] W. Wang, J. Shen, X. Dong et al., "Salient object detection driven by fixation prediction," in *Proceedings of the IEEE Conference on Computer Vision and Pattern Recognition*, pp. 1711–1720, Salt Lake City, UT, USA, June 2018.
- [35] R. Achanta, S. Hemami, F. Estrada, and S. Susstrunk, "Frequencytuned salient region detection," in *Proceedings of the IEEE Conference on Computer Vision and Pattern Recognition*, pp. 1597–1604, Miami, FL, USA, June 2009.
- [36] H. J. Seo and P. Milanfar, "Nonparametric bottom-up saliency detection by self-resemblance," in *2009 IEEE Computer Society Conference On Computer Vision and Pattern Recognition Workshops*, pp. 45–52, Miami, FL, USA, June 2009.
- [37] L. Duan, C. Wu, J. Miao et al., "Visual saliency detection by spatially weighted dissimilarity," in *Proceedings of the IEEE Conference on Computer Vision and Pattern Recognition CVPR 2011*, pp. 473–480, Colorado Springs, CO, USA, June 2011.
- [38] S. Goferman, L. Zelnik-Manor, and A. Tal, "Context-aware saliency detection," *IEEE Transactions on Pattern Analysis and Machine Intelligence*, vol. 34, no. 10, pp. 1915–1926, 2012.
- [39] X. Hou, J. Harel, and C. Koch, "Image signature: highlighting sparse salient regions," *IEEE Transactions on Pattern Analysis and Machine Intelligence*, vol. 34, no. 1, pp. 194–201, 2012.
- [40] C. Yang, L. Zhang, H. Lu, X. Ruan, and M. Yang, "Saliency detection via graph-based manifold ranking," in *Proceedings of the 2013 IEEE Conference on Computer Vision and Pattern Recognition*, pp. 3166–3173, Portland, OR, USA, June 2013.
- [41] Y. Yuan, C. Li, J. Kim, W. Cai, and D. D. Feng, "Reversion correction and regularized random walk ranking for saliency detection," *IEEE Transactions on Image Processing*, vol. 27, no. 3, pp. 1311–1322, 2018.
- [42] Q. Zhang, L. Zhang, W. Shi, and Y. Liu, "Airport extraction via complementary saliency analysis and saliency-oriented active contour model," *IEEE Geoscience and Remote Sensing Letters*, vol. 15, no. 7, pp. 1085–1089, 2018.

Research Article

Influence of Data Splitting on Performance of Machine Learning Models in Prediction of Shear Strength of Soil

Quang Hung Nguyen ¹, Hai-Bang Ly ², Lanh Si Ho ^{2,3}, Nadhir Al-Ansari ⁴,
Hiep Van Le ⁵, Van Quan Tran ², Indra Prakash ⁶, and Binh Thai Pham ²

¹Thuyloi University, Hanoi 100000, Vietnam

²University of Transport Technology, Hanoi 100000, Vietnam

³Civil and Environmental Engineering Program, Graduate School of Advanced Science and Engineering, Hiroshima University, 1-4-1, Kagamiyama, Higashi-Hiroshima, Hiroshima 739-8527, Japan

⁴Department of Civil, Environmental and Natural Resources Engineering, Lulea University of Technology, 971 87 Lulea, Sweden

⁵Institute of Research and Development, Duy Tan University, Da Nang 550000, Vietnam

⁶Bhaskaracharya Institute for Space Applications and Geo-Informatics (BISAG), Gandhinagar 382002, India

Correspondence should be addressed to Quang Hung Nguyen; hungwuhan@tlu.edu.vn, Hai-Bang Ly; banglh@utt.edu.vn, Nadhir Al-Ansari; nadhir.alansari@ltu.se, and Binh Thai Pham; binhpt@utt.edu.vn

Received 24 June 2020; Revised 17 December 2020; Accepted 27 January 2021; Published 8 February 2021

Academic Editor: Yu-Sheng Shen

Copyright © 2021 Quang Hung Nguyen et al. This is an open access article distributed under the Creative Commons Attribution License, which permits unrestricted use, distribution, and reproduction in any medium, provided the original work is properly cited.

The main objective of this study is to evaluate and compare the performance of different machine learning (ML) algorithms, namely, Artificial Neural Network (ANN), Extreme Learning Machine (ELM), and Boosting Trees (Boosted) algorithms, considering the influence of various training to testing ratios in predicting the soil shear strength, one of the most critical geotechnical engineering properties in civil engineering design and construction. For this aim, a database of 538 soil samples collected from the Long Phu 1 power plant project, Vietnam, was utilized to generate the datasets for the modeling process. Different ratios (i.e., 10/90, 20/80, 30/70, 40/60, 50/50, 60/40, 70/30, 80/20, and 90/10) were used to divide the datasets into the training and testing datasets for the performance assessment of models. Popular statistical indicators, such as Root Mean Squared Error (RMSE), Mean Absolute Error (MAE), and Correlation Coefficient (R), were employed to evaluate the predictive capability of the models under different training and testing ratios. Besides, Monte Carlo simulation was simultaneously carried out to evaluate the performance of the proposed models, taking into account the random sampling effect. The results showed that although all three ML models performed well, the ANN was the most accurate and statistically stable model after 1000 Monte Carlo simulations (Mean $R=0.9348$) compared with other models such as Boosted (Mean $R=0.9192$) and ELM (Mean $R=0.8703$). Investigation on the performance of the models showed that the predictive capability of the ML models was greatly affected by the training/testing ratios, where the 70/30 one presented the best performance of the models. Concisely, the results presented herein showed an effective manner in selecting the appropriate ratios of datasets and the best ML model to predict the soil shear strength accurately, which would be helpful in the design and engineering phases of construction projects.

1. Introduction

Soil is a crucial material in civil engineering, as most of the structures are built on soil ground [1]. The failure of the ground and collapse of the buildings are often associated with soil shear strength. Under different loading conditions, the soil shear strength, or the shear resistance, is dependent

on the cohesion, friction, and interlocking between particles [1]. The mechanical property of soil is complex due to the fact that soil often contains different particle sizes, high water content, and large voids [1]. Soil shear strength is dominated by basic parameters such as soil mineralogy, overburden pressure, water content, density, and void. Commonly, the soil shear strength is calculated by

determining the effective stress and soil parameters, such as internal friction angle and cohesion [1, 2]. These soil parameters can be determined in the field by Standard Penetration Test (SPT) or shear vane test and in the laboratory by conducting direct shear test, ring shear test, triaxial test, and unconfined compression [3, 4]. These tests are time-consuming and involve a lot of cost on conducting tests on an important number of samples.

Over the last decades, many researchers have tried to improve and find alternative methods to determine the shear strength of soil [3, 5–10]. Nam et al. [11] used a multistage direct shear test for determining the shear strength of unsaturated and saturated soils. Such a method could reduce some disadvantages of conventional direct shear tests and produced high accuracy results. Besides, many researchers have attempted to establish a relationship between soil indexes, such as clay fraction, liquid limit, plastic limit, and clay mineralogy [9, 12]. Also, many efforts have been made to evaluate the shear strength of soil through other soil parameters, such as establishing a correlation between suction and shear strength [10, 13]. In addition, several conventional procedures were introduced to estimate the shear strength of soil, where the relationship between the water content and suction is employed as a tool in the prediction process of unsaturated soil shear strength [6, 14–16]. Another effort has been carried out to estimate the soil shear strength in situ through shear wave velocity [16–18]. Overall, the conventional and traditional techniques possess some disadvantages and limitations, such as limitations in using basic soil parameters or considering a small range of soils. As an example, Kaya [2] indicated that the empirical formula, as suggested by Wright [19], is only limited to the soil containing a clay fraction superior to 50%.

In the recent time, Machine Learning (ML) techniques have been developed expeditiously and successfully applied in many fields of civil engineering [20–27] and Earth sciences [28–31], including geotechnical engineering such as landslide susceptibility [32–41] and estimation of soil parameters [42–47] including shear strength of soil [47–52]. In the work of Das et al. [53], the authors successfully applied an Artificial Neural Network (ANN) for estimating the residual friction angle of tropical soil in a specified area. Besides, it is found that the Support Vector Machine (SVM) showed a better performance than ANN for estimating the shear strength of soil using basic soil parameters, such as liquid limit, plastic limit, and clay fraction. In another work, Besalatpour et al. [54] showed that Adaptive-Network-based Fuzzy Inference System (ANFIS) and ANN models had higher ability than conventional regression methods. In another study, three new optimization techniques, namely, the Dragonfly Algorithm (DA), Invasive Weed Optimization (IWO), and Whale Optimization Algorithm (WOA), were employed to optimize the weights and biases of an ANN structure in estimating the shear strength of soil [50], where it was noticed that the learning error was significantly decreased. Thus, the IWO-ANN hybrid algorithm was found to be promising model instead of conventional methods in solving soil shear strength problems. Further, Moayedi et al. [49] used four neural-metaheuristic models for estimating

the shear strength of soil and stated that the Salp Swarm Algorithm-Multilayer Perceptron (SSA-MLP) model is a potential alternative method for estimating the soil shear strength. In general, ML techniques have significantly improved the prediction ability compared to conventional methods.

Despite significant growing of researches in applying ML algorithms in soil science, it is surprising how few of these suggestions are dedicated to the investigation of the performance assessment under a combination of factors during the model development phase. These factors could be the choice of data splitting, the selection of sampling technique, or the ML algorithm. For instance, a study on the comparison of ML techniques in digital soil mapping found that sample design and model choice significantly affected the outputs [55]. With regard to the data splitting, the data sample is often divided into two datasets, including a training set for model training and a testing set for model validation. Many researchers proposed a ratio of 70/30 or 80/20 (training/testing set) for producing datasets in landslide susceptibility problems [56–61]. Regarding studies on estimating the residual strength of soil using ML algorithms, previous works mainly used ratios of 70/30, 80/20, and 90/10 (training/testing) for generating datasets [22, 43, 47–49, 51–53]. Recently, Pham et al. [47] conducted a study on estimating the shear strength of soil in varying the training dataset size from 30% to 90% using the Random Forest (RF) algorithm. The study revealed that the increase in the size of the training dataset improved the training performance and made the model more stable. For the testing performance, the increase in the training set's size from 30% to 80% could also enhance the testing performance. However, when training size increased from 80% to 90%, the opposite trend was found in testing performance. In general, the training set size had an important effect on the prediction ability of the ML models [62].

The main objective of the present study is to evaluate the performance of ML models considering different ratios of soil data splitting for the prediction of soil shear strength. In this research, three ML techniques, namely, ANN, Extreme Learning Machine (ELM), and Boosting algorithm, were adopted to estimate the soil shear strength based on different splitting ratios of input data for the training and testing phases. The main difference of this study compared with the previously published works is that it is the first time the influence of splitting strategy of training and testing datasets used in ML models was investigated to predict the soil shear strength. Results were evaluated using standard statistical measures, namely Mean Absolute Error (MAE), Correlation Coefficient (R), and Root Mean Squared Error (RMSE), for the selection of the best model in predicting the soil shear strength and study the influence of different ratios of training and testing data on the performance of models.

2. Research Significance

ML, which includes advanced soft computing based techniques, has been developed and applied successfully and efficiently to solve a lot of real-world problems [63–68].

The main advantage of ML is that it can subjectively analyze unlimited amounts of data and give reliable outcomes and assessment [69]. However, its performance depends significantly on the quality of data and the strategy of using the data [70–72]. Therefore, assessment of the influence of data splitting on ML models' performance has a high significance, which will pave the way on how to select a suitable data splitting for better ML-based modeling. In this study, we have selected three popular ML models, namely, ANN, ELM, and Boosted, for modeling. In addition, we have selected a research problem, "the prediction of soil shear strength," which is an important geotechnical engineering task [43, 46, 47, 73]. This will help the construction engineers and managers to quickly and accurately predict the soil shear strength, which can be used for the design and verification of construction projects.

3. Data Used

Soil investigation data of the Long Phu 1 power plant project, located in Soc Trang province, Vietnam (longitude of $9^{\circ}59'07.3''\text{N}$ and latitude of $106^{\circ}04'48.0''\text{E}$), was used in this study for the development of the ML models. The construction of this power plant was started in June 2015, reflecting a key project under the Vietnamese Government's 2011–2020 National Power Development Plan [73]. A database of 538 soil samples was used to build the training and testing data sets. Soil parameters such as clay content (%), void ratio, moisture content (%), liquid limit (%), plastic limit (%), and specific gravity were used as input variables, whereas the soil shear strength (kg/cm^2) determined by direct shear test under the Undrain and Unconsolidated (UU) scheme was used as the output variable.

Statistical analysis of the input variables suggests that, in the samples, the clay content varied from 0 to 65 (%), plastic limit from 15 to 35 (%), liquid limit from 20 to 65 (%), specific gravity from 2.6 to 2.7, and void ratio from 0.5 to 1.0 (Figures 1(a)–1(g)), whereas the output variable varied from 0.45 to 0.7 (kg/cm^2) (Figure 1(g)).

Considering different ranges of variables (Figure 1), these values were scaled in the range of [0, 1] to avoid unexpected jumps and reduce fluctuations within the datasets used for modeling.

4. Methods Used

4.1. Artificial Neural Network (ANN). ANN has been known as a popular and powerful machine learning technique (computational model) [74, 75], based on structures and functions of biological neural networks: the nervous system of the human brain [20, 76–78]. This method has been used successfully in solving a wide range of civil engineering problems, including geotechnical engineering problems. ANN method is used to identify the relationship between input and output neurons in both linear and nonlinear patterns [21, 22, 79]. Thus, ANN could make a decision by analyzing patterns and relationships in data by itself [2, 43, 80]. In this study, a multilayered perceptron neural

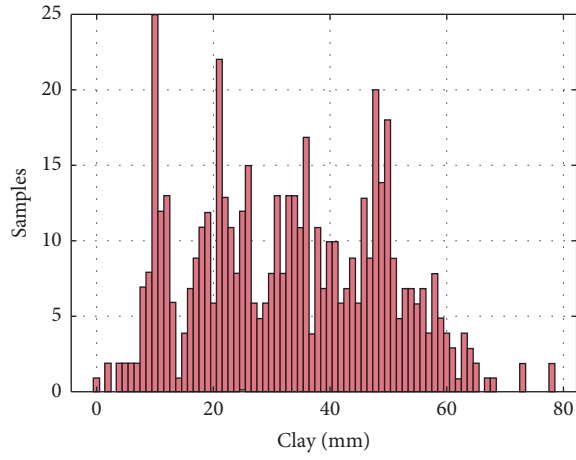
network, a popular ANN [81], was employed as a regression technique to estimate the soil shear strength.

4.2. Boosting Trees (Boosted). Boosted (Trees) is a hybrid method that combines the decision trees and boosting method. In this ensemble-type method, decision trees are employed to link input and output variables through recursive dual separations, while the boosting method is adopted to associate many individual models for improving the performance of the hybrid model [82]. The Boosted method, having the merits of tree-based techniques, can overcome the disadvantages of a sole tree model because of the following reasons. Firstly, this ensemble can choose a proper variable to match the appropriate functions. Secondly, it is suitable for various types of data using random boosting, and finally, this method can mitigate both bias and variance via model averaging [83].

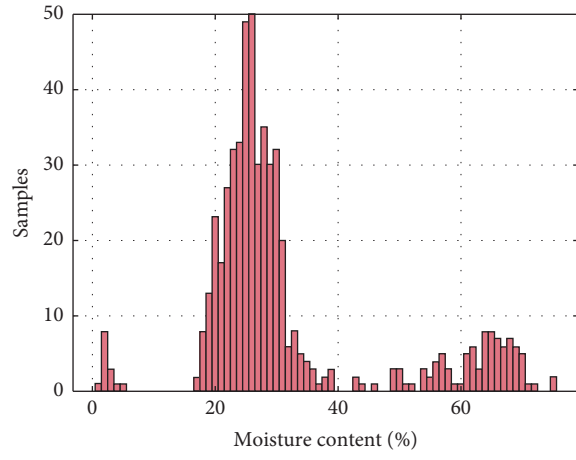
4.3. Extreme Learning Machine (ELM). ELM was firstly suggested by Huang et al. [84, 85], which is a modern algorithm and employed as a Single hidden Layer Feedforward Neuron Network (SLFN) [86]. ELM algorithm produces better performance in terms of learning speed compared to a conventional algorithm, for instance, backpropagation and least-square support vector machine [61, 84, 87]. The main aim of ELM is to get the smallest norm of weights on which the smallest training error can be reached for optimization of the model performance. A detailed description of ELM algorithm is available in published papers [84, 88–90].

4.4. Monte Carlo Approach. Monte Carlo method has been widely introduced to solve problems relating to the variability of input parameters in various fields, including geotechnical engineering [45, 91, 92]. Monte Carlo methods are a broad class of computational algorithms that rely on the repeated random sampling process to obtain numerical results. Basically, this technique could produce a high ability to compute, statistically, the relationship in data for both linear and nonlinear problems [45, 91]. Monte Carlo technique is implemented by repeating randomly input variables based on the distribution of probability density, and the outputs are computed correspondingly via a simulated model [93, 94]. A concept of the Monte Carlo method includes the following: (i) variability of input parameter could be completely spread by predetermined models and (ii) sensitivity analysis of inputs can be evaluated using statistical analysis of the output results.

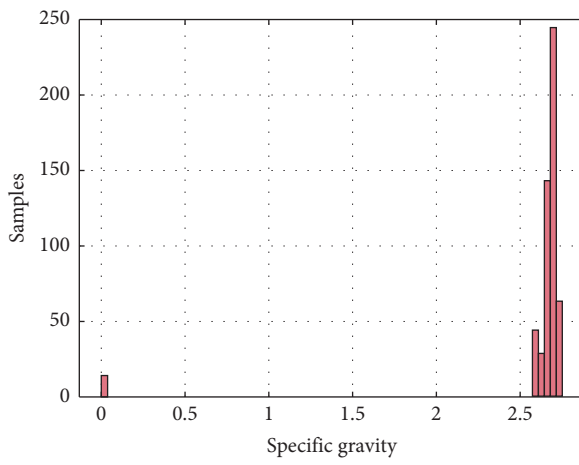
4.5. Performance Evaluation Criteria. In this paper, standard statistical measures, namely, Root Mean Square Error (RMSE), Mean Absolute Error (MAE), and Correlation Coefficient (R), were used to compare and validate the performance of ML models [47, 95]. In general, RMSE is the mean squared difference between the estimated and actual values, while MAE is the mean amplitude of errors. Lower values of RMSE and MAE mean higher prediction ability of the models. Besides, R is employed to evaluate the



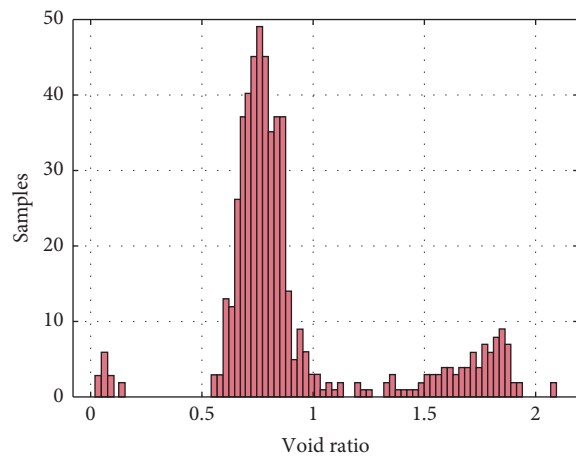
(a)



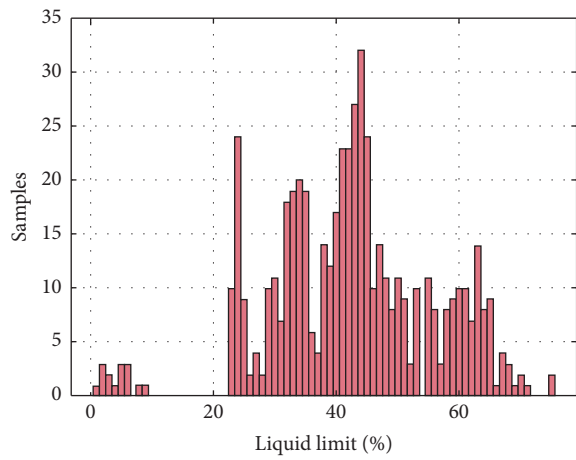
(b)



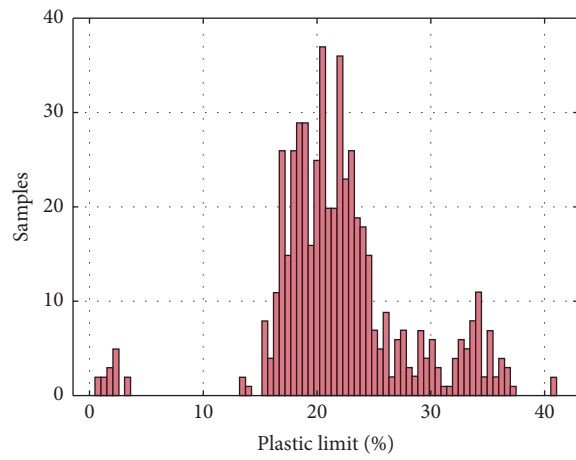
(c)



(d)



(e)



(f)

FIGURE 1: Continued.

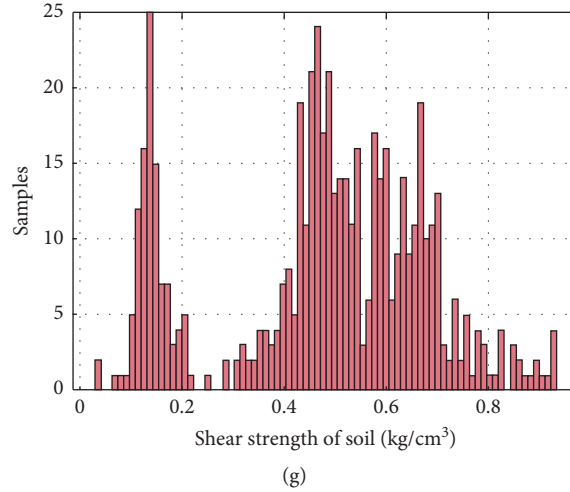


FIGURE 1: Histograms of the parameters used in this study: (a) clay; (b) moisture content; (c) specific gravity; (d) void ratio; (e) liquid limit; (f) plastic limit; (g) shear strength of soil.

correlation of the predicted and actual values of soil shear strength. The values of R are between -1 and $+1$, where the absolute values of R close to 1 mean higher prediction ability. These indicators can be computed using the following formulas [45, 96]:

$$R = \frac{\sum_{i=1}^n (y_{coi} - \overline{y_{co}})(y_{aci} - \overline{y_{ac}})}{\sqrt{\sum_{i=1}^n (y_{coi} - \overline{y_{co}})^2 (y_{aci} - \overline{y_{ac}})^2}}$$

$$RMSE = \sqrt{\frac{1}{n} \sum_{i=1}^n (y_{coi} - y_{aci})^2}, \quad (1)$$

$$MAE = \frac{1}{n} \sum_{i=1}^n |y_{coi} - y_{aci}|,$$

where y_{coi} and $\overline{y_{co}}$ represent the output value of the i th sample and the corresponding output mean value computed by the ML model, respectively; y_{aci} and $\overline{y_{ac}}$ denote the measured value of the i th sample and the measured mean value, respectively; and n indicates the total number of samples.

5. Results and Analysis

In this section, the prediction results of the soil shear strength are presented using various ML models (ANN, ELM, and Boosted). In the modeling, clay content, void ratio, moisture content, liquid limit, plastic limit, and specific gravity were considered as input variables, whereas soil shear strength was considered as the output variable. As a first step, the influence of training and testing ratio on the performance of the ML models is presented, followed by the study of the random sampling effects on the performance of ML models, and finally, comparisons of different ML models are performed.

5.1. Influence of Different Training and Testing Ratios on the Performance of the ML Models. To evaluate the influence of different ratios on the performance of ML models, ANN model was used to select the best train-to-test ratio for the estimation of soil shear strength. Using ANN to perform the study, six parameters (Table 1) were selected using trial and error tests to train the model. The dataset was divided into two parts, with different ratios: 10:90, 20:80, 30:70, 40:60, 50:50, 60:40, 70:30, 80:20, and 90:10 train/test split. Basically, a training dataset was used to construct the model, whereas the testing dataset was used to assess the model's predictive capability. Finally, the performance of ANN model on different ratio-based training and testing datasets using various statistical indices was evaluated, as shown in Figure 2.

It can be seen that as the number of data in the training datasets increased, the errors (RMSE and MAE) of the ANN model increased, and R values of the ANN model decreased, showing the accuracy of ANN decreased (Figures 2(a), 2(c), and 2(e)). In contrast, as the number of data in the testing datasets increased, the errors (RMSE and MAE) of ANN decreased, and R values increased, reflecting an increase of the ANN accuracy (Figures 2(b), 2(d), and 2(f)). It can be observed that the performance of the ANN model on both training and testing datasets was the best on the training/testing ratio of 70/30, based on the values of mean, standard deviation, and quantile levels of the three criteria.

5.2. Random Sampling Effects on the Performance of ANN. To validate the random sampling effects on the performance of the ML models, the ANN model was used and trained on different training/testing ratios using Monte Carlo simulation. In this process, the 1000 simulation was carried out to validate the statistical convergence of the model, as shown in Figure 3. It can be seen that RMSE and MAE values were stable at 10% of the average values with only 10 iterations,

TABLE 1: Parameters of the ANN algorithm used in this study.

No.	Parameters	Setting
1	Number of hidden layers	1
2	Number of neurons in the hidden layer	8
3	Activation function for the hidden layer	Sigmoid
4	Activation function for the output layer	Linear
5	Training algorithm	Levenberg-Marquardt
6	Cost function	MSE

whereas these values were stable at 5% average from 20 Monte Carlo iterations. Besides, the values of R were statistically stable at 2% average with 8 iterations and at 1% average from 50 iterations.

In addition, the analysis of the probability density of R , RMSE, and MAE values was also carried out to study the random sampling effects on the performance of ANN model (Figure 4). It can be observed that the distribution of the probability density of R , RMSE, and MAE values was different on various training/testing ratios.

In general, it can be stated that the performance of the ANN model is sensitive to the random selection of data in the datasets used for training and validating the model. In this study, the ANN model was converged with above 700 Monte Carlo simulations, and the train-to-test ratio of 70:30 was found as the best option for ML modeling.

5.3. Validation and Comparison of Different ML Models.

Validation and comparison of three ML models (i.e., ANN, ELM, and Boosted) were conducted using the best ratio of 70/30 of training and testing datasets. The ANN was trained with the parameters provided in Table 1, whereas ELM was trained with the network constructed by one input layer (6 neurons), one hidden layer (8 neurons), and one output (1 neuron). Regarding Boosted algorithm, the minimum leaf size was taken as 8, the number of learning cycles was 20, and the learning rate was set at 0.1. Values of R , RMSE, and MAE of the models using the testing dataset are shown in Figures 4–6. On the basis of RMSE indicator, it can be observed that the range of RMSE of ANN model was from about 0.05 to 0.1, whereas this value ranged from about 0.08 to 0.125 for Boosted algorithm and from 0.07 to 0.3 for ELM model over 1000 Monte Carlo simulations (Figure 5). Regarding MAE indicator, it can be seen that the range of MAE of ANN model was from 0.04 to 0.07, whereas this value ranged from 0.06 to 0.09 for the Boosted model and from 0.075 to 0.25 for ELM model over 1000 Monte Carlo simulations (Figure 6). In terms of R indicator, ANN model had the R values ranging from 0.95 to 0.97, from 0.88 to 0.95 for Boosted model, and from 0.62 to 0.95 for ELM model (Figure 7). Based on these results, it can be generally seen that the ANN model got the lowest error values (RMSE and MAE) and highest R values compared with other models (Boosted and ELM), whereas the ELM got the most unstable values of RMSE, MAE, and R . ELM also got the highest values of errors and lowest values of R over 1000 Monte Carlo simulations. A summary of the main results of the three methods is presented in Table 2. Overall, it can be stated that the ANN model is the best and most stable model

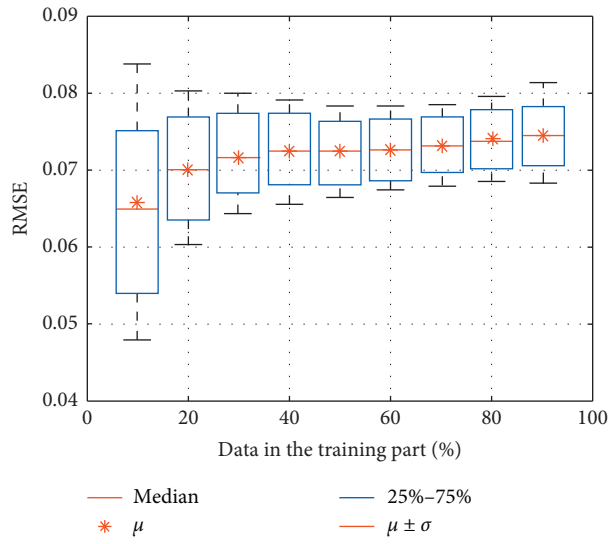
compared with other models (Boosted and ELM) for the prediction of soil shear strength.

6. Discussion

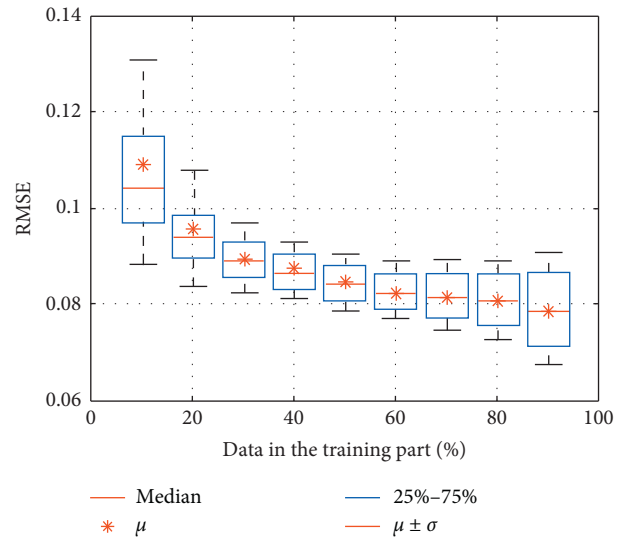
ML models are known as advanced techniques and approaches for quick and accurate prediction of real-world problems. These models, based on the objective computational algorithms, can handle complex relationships between input and output variables [97]. However, it is observed that ML models are quite sensitive to the quality of data and the way they are used in the modeling process, especially the ratio used to divide the datasets for training and validating the ML models [98]. In this study, this problem is analyzed by investigating the influence of training/testing ratio on the performance of three different popular ML models, namely, ANN, EML, and Boosted, to predict the soil shear strength.

Overall, the results showed that the ML models' performance was significantly changed under different training/testing ratios. The results showed that the training/testing ratio of 70/30 was the most suitable one for training and validating the ML models. This finding is in line with other published works, such as Pham et al. [99], who investigated different training/testing ratios for training and validating various ML models (SVM, Logistic Regression, ANN, and Naive Bayes) for spatial prediction of landslides and proved that 70/30 was the best training/testing ratio for getting the best performance of the ML models. Other studies and researches also confirmed the finding of this study [100–105]. In addition, it is noticed that when the percentage of data in the training dataset increased, the errors (RMSE and MAE) of the models increased, and R values decreased. Thus, an increase of data (or samples) in the training dataset might have a negative influence on the prediction accuracy and difficulty in applying the models.

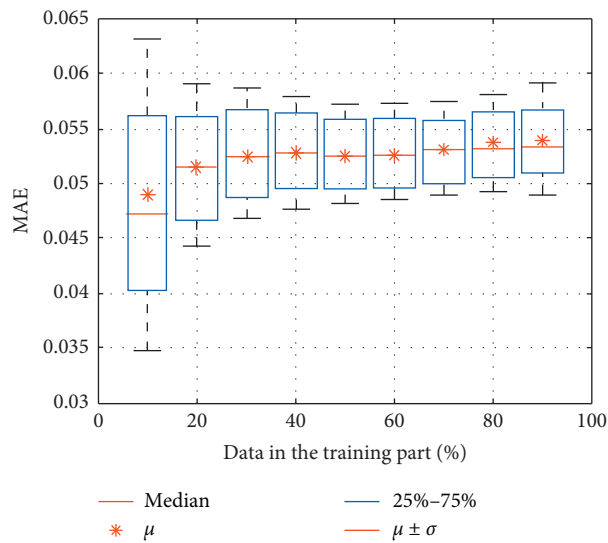
Besides, the validation and comparison results showed that all the ML models performed well, but ANN was the best model for the prediction of soil shear strength. It can be stated that ANN model has been reaffirmed as the best single ML model for solving most of the real-world problems [106, 107]. ANN has several advantages compared with other ML models, such as (i) capable of extracting the essential process information from data for analyzing and prediction, (ii) an ability of generalization of data, (iii) able to correctly process information that only broadly resembles the original training data, and (iv) its essential features being related to nonlinearity, fault tolerance, independent assumptions, and universality. Thus, ANN algorithm is particularly reasonable for extremely complex data. Last but not least, ANN is an



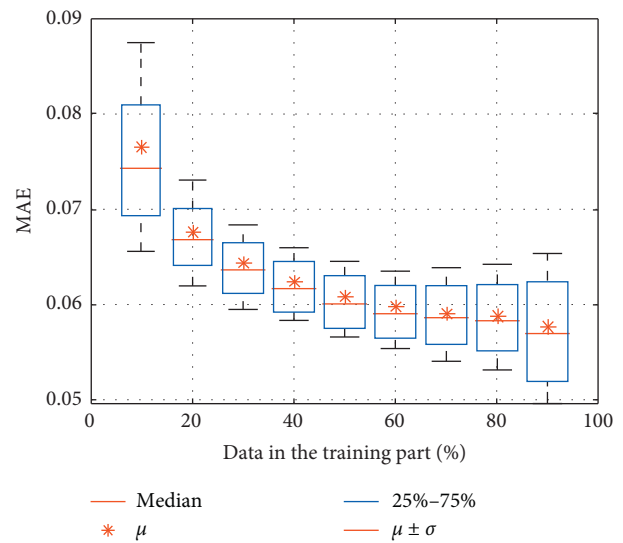
(a)



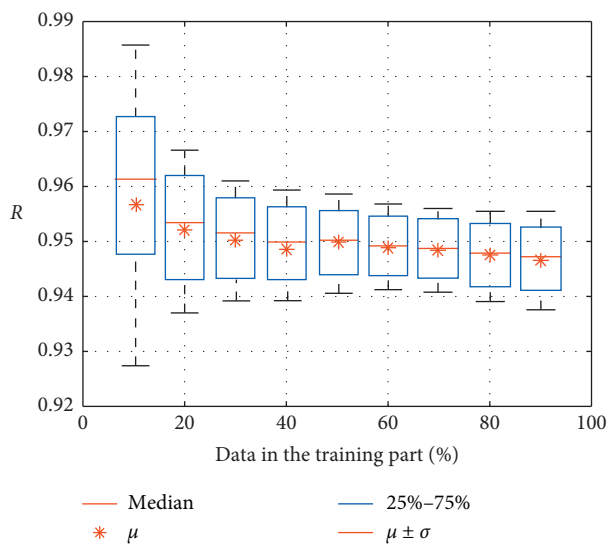
(b)



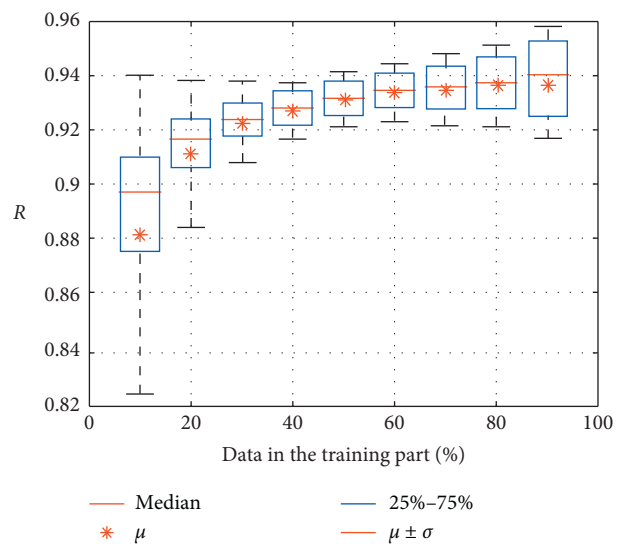
(c)



(d)



(e)



(f)

FIGURE 2: Validation of the ANN model's performance under different ratio (percentage) of data in the training part: (a) RMSE for the training part; (b) RMSE for the testing part; (c) MAE for the training part; (d) MAE for the testing part; (e) R for the training part; and (f) R for the testing part.

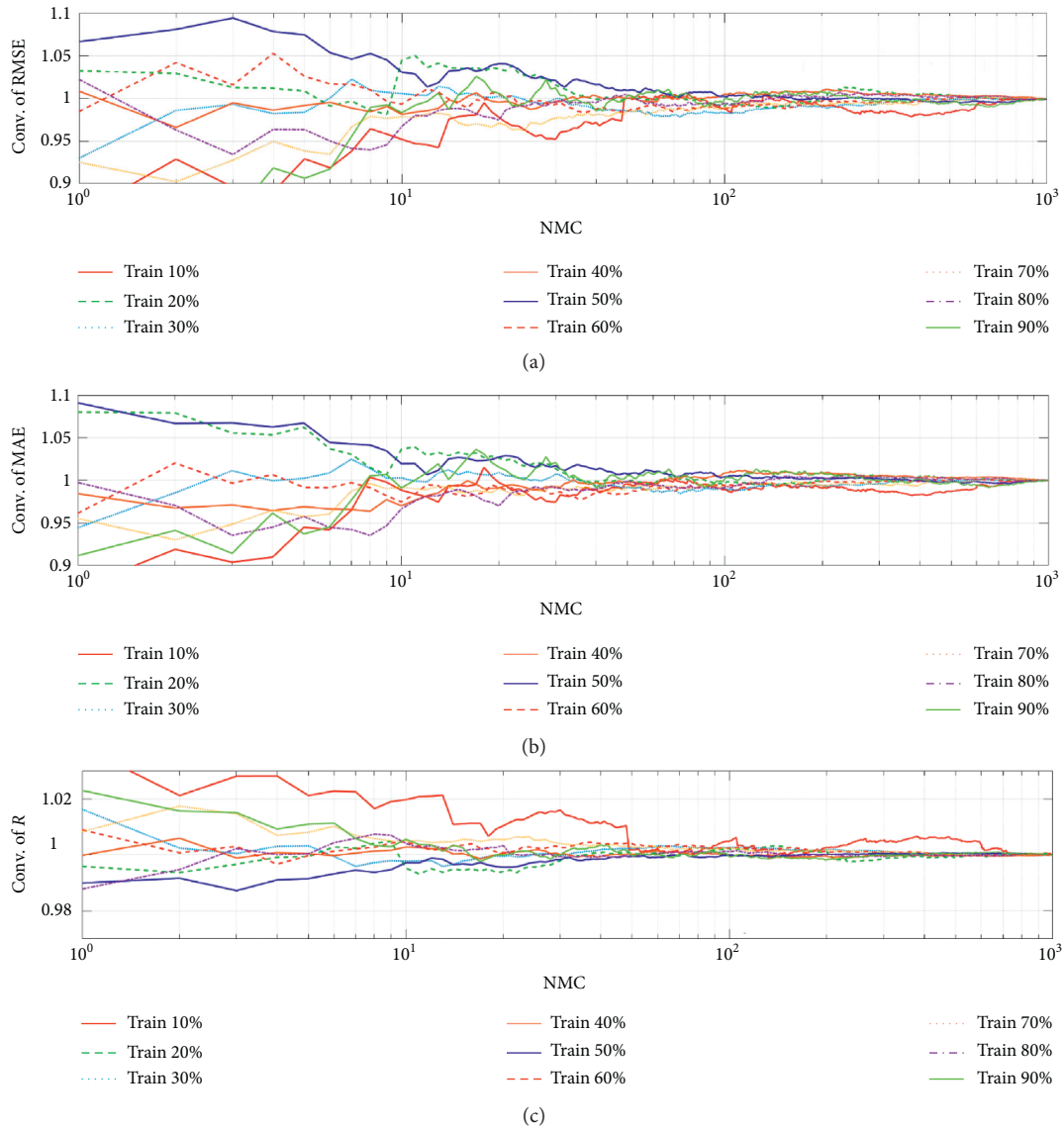


FIGURE 3: Statistical convergence results for 1000 Monte Carlo simulations for the testing part: (a) RMSE; (b) MAE; and (c) R .

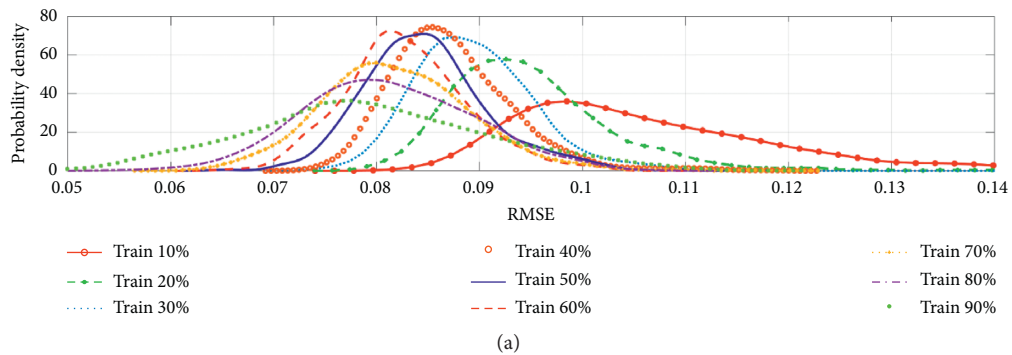


FIGURE 4: Continued.

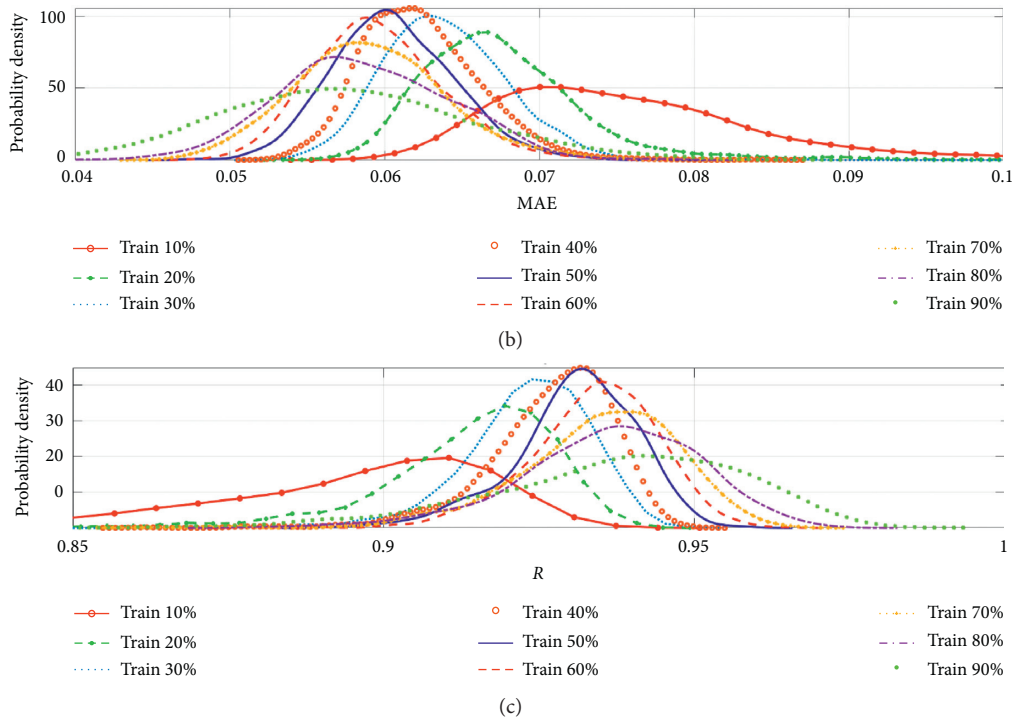


FIGURE 4: Probability density results for 1000 Monte Carlo simulations for the testing part with different indicators: (a) RMSE; (b) MAE; and (c) R . It should be noticed that the legends, for instance, Train 10%, indicates that the results obtained with 10% of the total data were used to construct the training dataset.

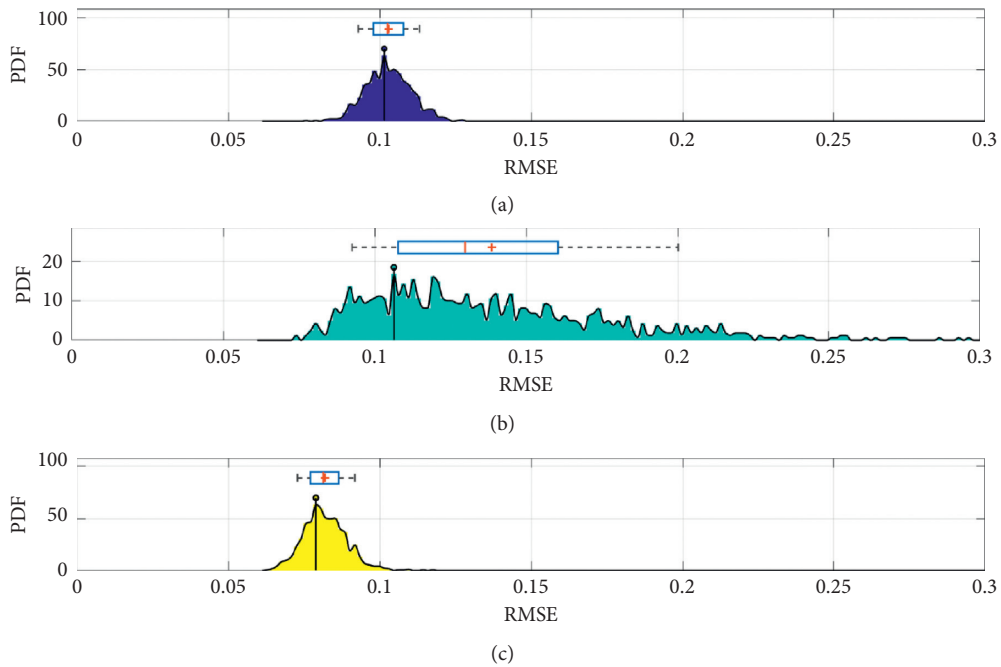


FIGURE 5: Comparison of Boosted, ELM, and ANN in terms of probability density results for 1000 Monte Carlo simulations for the testing part in terms of RMSE.

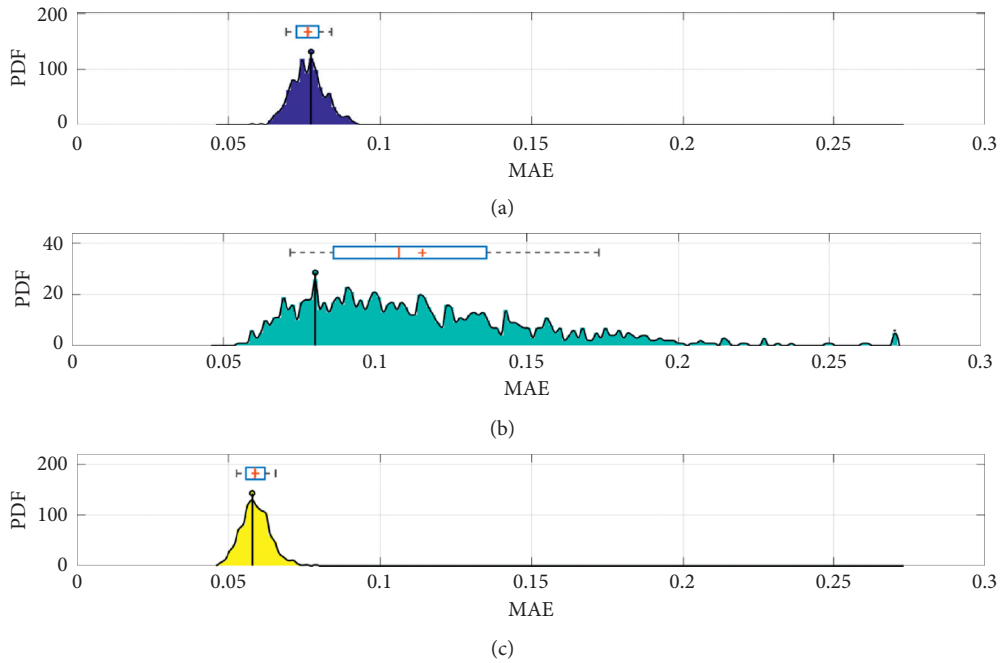


FIGURE 6: Comparison of Boosted, ELM, and ANN in terms of probability density results for 1000 Monte Carlo simulations for the testing part in terms of MAE.

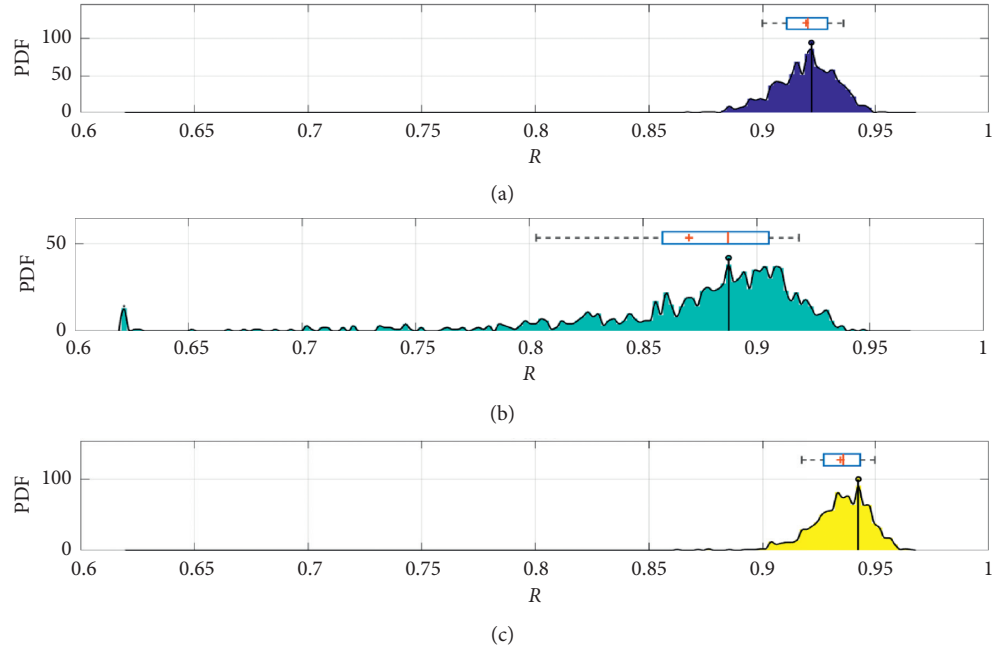


FIGURE 7: Comparison of Boosted, ELM, and ANN in terms of probability density results for 1000 Monte Carlo simulations for the testing part in terms of R .

TABLE 2: Summary of the results obtained over 1000 Monte Carlo simulations for ANN, Boosted, and ELM algorithms in this study.

Criteria	ANN	Boosted	ELM
Mean R	0.9348	0.9192	0.8703
Std. R	0.0129	0.0134	0.0624
Mean RMSE	0.0820	0.1029	0.1386
Std. RMSE	0.0073	0.0076	0.0412
Mean MAE	0.0591	0.0763	0.1157
Std. MAE	0.0049	0.0056	0.0388

adaptive algorithm, so that the learning process can be more effective [108, 109]. Therefore, it can be stated that the ANN was the best predictor for the prediction of soil shear strength.

7. Conclusions

Soil shear strength is one of the most critical geotechnical engineering properties used for designing and constructing civil engineering structures and constructions. Prediction of this parameter using advanced ML models might help in saving time and reducing cost for construction projects. In this study, three popular ML models, including ANN, ELM, and Boosted, were applied and compared to predict the soil shear strength using a database collected from Long Phu 1 power plant project, Vietnam. In addition, the performance of these models was also investigated under the influence of different training and testing ratios over 1000 Monte Carlo simulations.

Validation and comparison results showed that even the performance of all models was good and the performance of ANN was the best compared with other models. It can also be observed that the performance of the models was significantly changed under the different training and testing ratios used for training and validating the models. Based on the statistical analysis, a ratio of 70/30 for training and testing datasets was considered as the best ratio for training and validating the models. In addition, Monte Carlo simulations showed that the performance of the models is different under the random sampling effect over 1000 simulations. ANN was found as the best and most stable method under the variability of the input space.

In short, civil engineers can use the results of this study for quick and accurate prediction of soil shear strength for designing purposes, for instance, road, bridges, retaining walls, and other geotechnical and civil structures. Although the one group of data used in this study is sufficient for the development of the ML models, it is recommended that these ML models should be applied and validated with various data in different regions for better justification and verification. However, it is noticed that these applied models are considered as black-box models and do not provide the equations for engineer's calculation; therefore, other ML models like GEP, GMDH, and EPR, which can provide the equations, can be considered for future application and comparison.

Data Availability

The data used to support the findings of this study are available from the corresponding author upon request.

Conflicts of Interest

The authors declare that they have no conflicts of interest.

Acknowledgments

This research was funded by the Ministry of Transport, project titled "Building Big Data and Development of Machine Learning Models Integrated with Optimization Techniques for Prediction of Soil Shear Strength Parameters for Construction of Transportation Projects" under Grant no. DT 203029.

References

- [1] B. M. Das and K. Sobhan, *Principles of Geotechnical Engineering*, Cengage Learning, Boston, MA, USA, 2013.
- [2] A. Kaya, "Residual and fully softened strength evaluation of soils using artificial neural networks," *Geotechnical and Geological Engineering*, vol. 27, no. 2, pp. 281–288, 2009.
- [3] H. Hettiarachchi and T. Brown, "Use of SPT blow counts to estimate shear strength properties of soils: energy balance approach," *Journal of Geotechnical and Geoenvironmental Engineering*, vol. 135, no. 6, pp. 830–834, 2009.
- [4] H. Motaghedi and A. Eslami, "Analytical approach for determination of soil shear strength parameters from CPT and CPTu data," *Arabian Journal for Science and Engineering*, vol. 39, no. 6, pp. 4363–4376, 2014.
- [5] M. Cha and G.-C. Cho, "Shear strength estimation of sandy soils using shear wave velocity," *Geotechnical Testing Journal*, vol. 30, no. 6, pp. 484–495, 2007.
- [6] E. A. Garven and S. K. Vanapalli, "Evaluation of empirical procedures for predicting the shear strength of unsaturated soils," in *Proceedings of the Fourth International Conference on Unsaturated Soils*, pp. 2570–2592, Carefree, AZ, USA, April 2006.
- [7] B.-S. Kim, S. Shibuya, S.-W. Park, and S. Kato, "Application of suction stress for estimating unsaturated shear strength of soils using direct shear testing under low confining pressure," *Canadian Geotechnical Journal*, vol. 47, no. 9, pp. 955–970, 2010.
- [8] J. O. Ohu, G. S. V. Raghavan, E. McKyes, and G. Mehuys, "Shear strength prediction of compacted soils with varying added organic matter contents," *Transactions of the ASAE*, vol. 29, no. 2, pp. 351–355, 1986.
- [9] B. Tiwari and H. Marui, "A new method for the correlation of residual shear strength of the soil with mineralogical composition," *Journal of Geotechnical and Geoenvironmental Engineering*, vol. 131, no. 9, pp. 1139–1150, 2005.
- [10] O. M. Vilar, "A simplified procedure to estimate the shear strength envelope of unsaturated soils," *Canadian Geotechnical Journal*, vol. 43, no. 10, pp. 1088–1095, 2006.

- [11] S. Nam, M. Gutierrez, P. Diplas, and J. Petrie, "Determination of the shear strength of unsaturated soils using the multistage direct shear test," *Engineering Geology*, vol. 122, no. 3-4, p. 272, 2011.
- [12] A. W. Skempton, "Residual strength of clays in landslides, folded strata and the laboratory," *Géotechnique*, vol. 35, no. 1, pp. 3-18, 1985.
- [13] D. W. Rassam and D. J. Williams, "A relationship describing the shear strength of unsaturated soils," *Canadian Geotechnical Journal*, vol. 36, no. 2, pp. 363-368, 1999.
- [14] M. A. Tekinsoy, C. Kayadelen, M. S. Keskin, and M. Söylemez, "An equation for predicting shear strength envelope with respect to matric suction," *Computers and Geotechnics*, vol. 31, no. 7, pp. 589-593, 2004.
- [15] Y. F. Xu, "Fractal approach to unsaturated shear strength," *Journal of Geotechnical and Geoenvironmental Engineering*, vol. 130, no. 3, pp. 264-273, 2004.
- [16] Y. F. Xu and D. A. Sun, "A fractal model for soil pores and its application to determination of water permeability," *Physica A: Statistical Mechanics and Its Applications*, vol. 316, no. 1-4, pp. 56-64, 2002.
- [17] C. R. McGann, B. A. Bradley, M. L. Taylor, L. M. Wotherspoon, and M. Cubrinovski, "Development of an empirical correlation for predicting shear wave velocity of Christchurch soils from cone penetration test data," *Soil Dynamics and Earthquake Engineering*, vol. 75, pp. 66-75, 2015.
- [18] M. S. Nam and C. Vipulanandan, "Roughness and unit side resistances of drilled shafts socketed in clay shale and limestone," *Journal of Geotechnical and Geoenvironmental Engineering*, vol. 134, no. 9, pp. 1272-1279, 2008.
- [19] S. G. Wright, *Evaluation of Soil Shear Strengths for Slope and Retaining Wall Stability Analyses with Emphasis on High Plasticity Clays*, Federal Highway Administration, Washington, DC, USA, 2005.
- [20] H.-B. Ly, T.-T. Le, H.-L. T. Vu, V. Q. Tran, L. M. Le, and B. T. Pham, "Computational hybrid machine learning based prediction of shear capacity for steel fiber reinforced concrete beams," *Sustainability*, vol. 12, no. 7, p. 2709, 2020.
- [21] D. V. Dao, H.-B. Ly, H.-L. T. Vu, T.-T. Le, and B. T. Pham, "Investigation and optimization of the C-ANN structure in predicting the compressive strength of foamed concrete," *Materials*, vol. 13, no. 5, p. 1072, 2020.
- [22] D. V. Dao, H. Adeli, H.-B. Ly et al., "A sensitivity and robustness analysis of GPR and ANN for high-performance concrete compressive strength prediction using a Monte Carlo simulation," *Sustainability*, vol. 12, no. 3, p. 830, 2020.
- [23] T.-T. Le, B. T. Pham, H.-B. Ly, A. Shirzadi, and L. M. Le, "Development of 48-hour precipitation forecasting model using nonlinear autoregressive neural network," in *CIGOS 2019, Innovation for Sustainable Infrastructure*, pp. 1191-1196, Springer, Berlin, Germany, 2020.
- [24] H.-B. Ly, L. M. Le, L. V. Phi et al., "Development of an AI model to measure traffic air pollution from multisensor and weather data," *Sensors*, vol. 19, no. 22, p. 4941, 2019.
- [25] H.-B. Ly, B. T. Pham, D. V. Dao, V. M. Le, L. M. Le, and T.-T. Le, "Improvement of ANFIS model for prediction of compressive strength of manufactured sand concrete," *Applied Sciences*, vol. 9, no. 18, p. 3841, 2019.
- [26] H.-B. Ly, T.-T. Le, L. M. Le et al., "Development of hybrid machine learning models for predicting the critical buckling load of I-shaped cellular beams," *Applied Sciences*, vol. 9, no. 24, p. 5458, 2019.
- [27] B. T. Pham, L. M. Le, T.-T. Le et al., "Development of advanced artificial intelligence models for daily rainfall prediction," *Atmospheric Research*, vol. 237, Article ID 104845, 2020.
- [28] W. Chen, Y. Li, W. Xue et al., "Modeling flood susceptibility using data-driven approaches of naïve Bayes tree, alternating decision tree, and random forest methods," *Science of the Total Environment*, vol. 701, Article ID 134979, 2020.
- [29] V.-H. Nhu, A. Mohammadi, H. Shahabi et al., "Landslide susceptibility mapping using machine learning algorithms and remote sensing data in a tropical environment," *International Journal of Environmental Research and Public Health*, vol. 17, no. 14, p. 4933, 2020.
- [30] W. Chen, B. Pradhan, S. Li et al., "Novel hybrid integration approach of bagging-based Fisher's linear discriminant function for groundwater potential analysis," *Natural Resources Research*, vol. 28, no. 4, pp. 1239-1258, 2019.
- [31] Y. Wang, H. Hong, W. Chen et al., "Flood susceptibility mapping in Dingnan County (China) using adaptive neuro-fuzzy inference system with biogeography based optimization and imperialistic competitive algorithm," *Journal of Environmental Management*, vol. 247, pp. 712-729, 2019.
- [32] M. Abedini, B. Ghasemian, A. Shirzadi et al., "A novel hybrid approach of bayesian logistic regression and its ensembles for landslide susceptibility assessment," *Geocarto International*, vol. 34, no. 13, pp. 1427-1457, 2019.
- [33] Pham, Shirzadi, Shahabi et al., "Landslide susceptibility assessment by novel hybrid machine learning algorithms," *Sustainability*, vol. 11, no. 16, p. 4386, 2019.
- [34] Nguyen, Tuyen, Shirzadi et al., "Development of a novel hybrid intelligence approach for landslide spatial prediction," *Applied Sciences*, vol. 9, no. 14, p. 2824, 2019.
- [35] B. T. Pham, I. Prakash, K. Khosravi et al., "A comparison of support vector machines and Bayesian algorithms for landslide susceptibility modelling," *Geocarto International*, vol. 34, no. 13, pp. 1385-1407, 2019.
- [36] B. T. Pham and I. Prakash, "A novel hybrid model of Bagging-based Naïve Bayes Trees for landslide susceptibility assessment," *Bulletin of Engineering Geology and the Environment*, vol. 78, no. 3, pp. 1911-1925, 2019.
- [37] T. V. Phong, T. T. Phan, I. Prakash et al., "Landslide susceptibility modeling using different artificial intelligence methods: a case study at Muong Lay district, Vietnam," *Geocarto International*, pp. 1-24, 2019.
- [38] B. T. Pham, T. V. Phong, T. Nguyen-Thoi et al., "Ensemble modeling of landslide susceptibility using random subspace learner and different decision tree classifiers," *Geocarto International*, pp. 1-23, 2020.
- [39] V.-H. Nhu, A. Mohammadi, H. Shahabi et al., "Landslide detection and susceptibility modeling on cameron highlands (Malaysia): a comparison between random forest, logistic regression and logistic model tree algorithms," *Forests*, vol. 11, no. 8, p. 830, 2020.
- [40] V.-H. Nhu, A. Shirzadi, H. Shahabi et al., "Shallow landslide susceptibility mapping by random forest base classifier and its ensembles in a semi-arid region of Iran," *Forests*, vol. 11, no. 4, p. 421, 2020.
- [41] G. Wang, X. Lei, W. Chen, H. Shahabi, and A. Shirzadi, "Hybrid computational intelligence methods for landslide susceptibility mapping," *Symmetry*, vol. 12, no. 3, p. 325, 2020.
- [42] M. D. Nguyen, B. T. Pham, T. T. Tuyen et al., "Development of an artificial intelligence approach for prediction of consolidation coefficient of soft soil: a sensitivity analysis," *The Open Construction and Building Technology Journal*, vol. 13, no. 1, p. 178, 2019.

- [43] B. T. Pham, L. H. Son, T.-A. Hoang, D.-M. Nguyen, and D. Tien Bui, "Prediction of shear strength of soft soil using machine learning methods," *Catena*, vol. 166, pp. 181–191, 2018.
- [44] B. T. Pham, M. D. Nguyen, K.-T. T. Bui, I. Prakash, K. Chapi, and D. T. Bui, "A novel artificial intelligence approach based on Multi-layer Perceptron Neural Network and Biogeography-based Optimization for predicting coefficient of consolidation of soil," *Catena*, vol. 173, pp. 302–311, 2019.
- [45] B. T. Pham, M. D. Nguyen, D. V. Dao et al., "Development of artificial intelligence models for the prediction of Compression Coefficient of soil: an application of Monte Carlo sensitivity analysis," *Science of the Total Environment*, vol. 679, pp. 172–184, 2019.
- [46] H.-B. Ly and B. T. Pham, "Prediction of shear strength of soil using direct shear test and support vector machine model," *The Open Construction and Building Technology Journal*, vol. 14, no. 1, p. 41, 2020.
- [47] B. T. Pham, C. Qi, L. S. Ho et al., "A novel hybrid soft computing model using random forest and particle swarm optimization for estimation of undrained shear strength of soil," *Sustainability*, vol. 12, no. 6, p. 2218, 2020.
- [48] D. T. Bui, N.-D. Hoang, and V.-H. Nhu, "A swarm intelligence-based machine learning approach for predicting soil shear strength for road construction: a case study at Trung Luong National Expressway Project (Vietnam)," *Engineering with Computers*, vol. 35, no. 3, pp. 955–965, 2019.
- [49] H. Moayedi, M. Gör, M. Khari, L. K. Foong, M. Bahiraei, and D. T. Bui, "Hybridizing four wise neural-metaheuristic paradigms in predicting soil shear strength," *Measurement*, vol. 156, Article ID 107576, 2020.
- [50] H. Moayedi, D. Tien Bui, A. Dounis, L. Kok Foong, and B. Kalantar, "Novel nature-inspired hybrids of neural computing for estimating soil shear strength," *Applied Sciences*, vol. 9, no. 21, p. 4643, 2019.
- [51] H. Moayedi, D. Bui, D. Anastasios, and B. Kalantar, "Spotted hyena optimizer and ant lion optimization in predicting the shear strength of soil," *Applied Sciences*, vol. 9, no. 22, p. 4738, 2019.
- [52] V.-H. Nhu, N.-D. Hoang, V.-B. Duong, H.-D. Vu, and D. T. Bui, "A hybrid computational intelligence approach for predicting soil shear strength for urban housing construction: a case study at Vinhomes Imperia project, Hai Phong City (Vietnam)," *Engineering with Computers*, vol. 36, no. 2, pp. 1–14, 2019.
- [53] S. Das, P. Samui, S. Khan, and N. Sivakugan, "Machine learning techniques applied to prediction of residual strength of clay," *Open Geosciences*, vol. 3, no. 4, pp. 449–461, 2011.
- [54] A. Besalatpour, M. A. Hajabbasi, S. Ayoubi, M. Afyuni, A. Jalalian, and R. Schulin, "Soil shear strength prediction using intelligent systems: artificial neural networks and an adaptive neuro-fuzzy inference system," *Soil Science and Plant Nutrition*, vol. 58, no. 2, pp. 149–160, 2012.
- [55] B. Heung, H. C. Ho, J. Zhang, A. Knudby, C. E. Bulmer, and M. G. Schmidt, "An overview and comparison of machine-learning techniques for classification purposes in digital soil mapping," *Geoderma*, vol. 265, pp. 62–77, 2016.
- [56] D. T. Bui, B. Pradhan, O. Lofman, I. Revhaug, and O. B. Dick, "Landslide susceptibility mapping at Hoa Binh province (Vietnam) using an adaptive neuro-fuzzy inference system and GIS," *Computers & Geosciences*, vol. 45, pp. 199–211, 2012.
- [57] W. Chen, J. Peng, H. Hong et al., "Landslide susceptibility modelling using GIS-based machine learning techniques for Chongren County, Jiangxi Province, China," *Science of the Total Environment*, vol. 626, pp. 1121–1135, 2018.
- [58] F. Huang, K. Yin, J. Huang, L. Gui, and P. Wang, "Landslide susceptibility mapping based on self-organizing-map network and extreme learning machine," *Engineering Geology*, vol. 223, pp. 11–22, 2017.
- [59] B. T. Pham, D. Tien Bui, H. R. Pourghasemi, P. Indra, and M. B. Dholakia, "Landslide susceptibility assessment in the Uttarakhand area (India) using GIS: a comparison study of prediction capability of naïve bayes, multilayer perceptron neural networks, and functional trees methods," *Theoretical and Applied Climatology*, vol. 128, no. 1–2, pp. 255–273, 2017.
- [60] K. Taalab, T. Cheng, and Y. Zhang, "Mapping landslide susceptibility and types using Random Forest," *Big Earth Data*, vol. 2, no. 2, pp. 159–178, 2018.
- [61] N. N. Vasu and S.-R. Lee, "A hybrid feature selection algorithm integrating an extreme learning machine for landslide susceptibility modeling of Mt. Woomyeon, South Korea," *Geomorphology*, vol. 263, pp. 50–70, 2016.
- [62] C. Qi, A. Fourie, Q. Chen, and Q. Zhang, "A strength prediction model using artificial intelligence for recycling waste tailings as cemented paste backfill," *Journal of Cleaner Production*, vol. 183, pp. 566–578, 2018.
- [63] J. Zhou, P. G. Asteris, D. J. Armaghani, and B. T. Pham, "Prediction of ground vibration induced by blasting operations through the use of the Bayesian Network and random forest models," *Soil Dynamics and Earthquake Engineering*, vol. 139, Article ID 106390, 2020.
- [64] S. Lu, M. Koopialipoor, P. G. Asteris, M. Bahri, and D. J. Armaghani, "A novel feature selection approach based on tree models for evaluating the punching shear capacity of steel fiber-reinforced concrete flat slabs," *Materials*, vol. 13, no. 17, p. 3902, 2020.
- [65] D. J. Armaghani and P. G. Asteris, "A comparative study of ANN and ANFIS models for the prediction of cement-based mortar materials compressive strength," *Neural Computing and Applications*, pp. 1–32, 2020.
- [66] P. G. Asteris, "A novel heuristic algorithm for the modeling and risk assessment of the COVID-19 pandemic phenomenon," *Computer Modeling in Engineering & Sciences*, vol. 125, no. 2, pp. 815–828, 2020.
- [67] D. J. Armaghani, E. Momeni, and P. Asteris, "Application of group method of data handling technique in assessing deformation of rock mass," *Applied Metaheuristic Computing*, vol. 1, pp. 1–18, 2020.
- [68] D. Jahed Armaghani, P. G. Asteris, B. Askarian, M. Hasanipanah, R. Tarinejad, and V. V. Huynh, "Examining hybrid and single SVM models with different kernels to predict rock brittleness," *Sustainability*, vol. 12, no. 6, p. 2229, 2020.
- [69] J. Qiu, Q. Wu, G. Ding, Y. Xu, and S. Feng, "A survey of machine learning for big data processing," *EURASIP Journal on Advances in Signal Processing*, vol. 2016, no. 1, p. 67, 2016.
- [70] P. G. Asteris, "On the metaheuristic models for the prediction of cement-metakaolin mortars compressive strength," *Metaheuristic Computing and Applications*, vol. 1, no. 1, p. 063, 2020.
- [71] M. Apostolopoulou, P. G. Asteris, D. J. Armaghani et al., "Mapping and holistic design of natural hydraulic lime mortars," *Cement and Concrete Research*, vol. 136, Article ID 106167, 2020.
- [72] H.-B. Ly, B. T. Pham, L. M. Le, T.-T. Le, V. M. Le, and P. G. Asteris, "Estimation of axial load-carrying capacity of concrete-filled steel tubes using surrogate models," *Neural Computing and Applications*, pp. 1–22, 2020.

- [73] B. T. Pham, T. Nguyen-Thoi, H.-B. Ly et al., "Extreme learning machine based prediction of soil shear strength: a sensitivity analysis using Monte Carlo simulations and feature backward elimination," *Sustainability*, vol. 12, no. 6, p. 2339, 2020.
- [74] M. Alizadeh, E. Alizadeh, S. Asadollahpour Kotenaee et al., "Social vulnerability assessment using artificial neural network (ANN) model for earthquake hazard in Tabriz city, Iran," *Sustainability*, vol. 10, no. 10, p. 3376, 2018.
- [75] P. G. Asteris and V. G. Mokos, "Concrete compressive strength using artificial neural networks," *Neural Computing and Applications*, pp. 1–20, 2019.
- [76] B. T. Pham, S. K. Singh, and H.-B. Ly, "Using Artificial Neural Network (ANN) for prediction of soil coefficient of consolidation," *Vietnam Journal of Earth Sciences*, vol. 42, 2020.
- [77] V. M. Le, B. T. Pham, T.-T. Le, H.-B. Ly, and L. M. Le, "Daily rainfall prediction using nonlinear autoregressive neural network," *Micro-Electronics and Telecommunication Engineering*, pp. 213–221, 2020.
- [78] T.-T. Le, B. T. Pham, V. M. Le, H.-B. Ly, and L. M. Le, "A robustness analysis of different nonlinear autoregressive networks using Monte Carlo simulations for predicting high fluctuation rainfall," in *Micro-electronics and Telecommunication Engineering*, pp. 205–212, Springer, Berlin, Germany, 2020.
- [79] T. A. Pham, H.-B. Ly, V. Q. Tran, L. V. Giap, H.-L. T. Vu, and H.-A. T. Duong, "Prediction of pile axial bearing capacity using artificial neural network and random forest," *Applied Sciences*, vol. 10, no. 5, p. 1871, 2020.
- [80] M. A. Behrang, E. Assareh, A. Ghanbarzadeh, and A. R. Noghrehabadi, "The potential of different artificial neural network (ANN) techniques in daily global solar radiation modeling based on meteorological data," *Solar Energy*, vol. 84, no. 8, pp. 1468–1480, 2010.
- [81] K. K. Peh, C. P. Lim, S. S. Quek, and K. H. Khoh, "Use of artificial neural networks to predict drug dissolution profiles and evaluation of network performance using similarity factor," *Pharmaceutical Research*, vol. 17, no. 11, pp. 1384–1389, 2000.
- [82] M. Zięba, S. K. Tomczak, and J. M. Tomczak, "Ensemble boosted trees with synthetic features generation in application to bankruptcy prediction," *Expert Systems with Applications*, vol. 58, pp. 93–101, 2016.
- [83] J. Elith, J. R. Leathwick, and T. Hastie, "A working guide to boosted regression trees," *Journal of Animal Ecology*, vol. 77, no. 4, pp. 802–813, 2008.
- [84] G.-B. Huang, Q.-Y. Zhu, and C.-K. Siew, "Extreme learning machine: theory and applications," *Neurocomputing*, vol. 70, no. 1–3, pp. 489–501, 2006.
- [85] G. Bin Huang, H. Zhou, X. Ding, and R. Zhang, "Extreme learning machine for regression and multiclass classification," *IEEE Transactions on Systems, Man, and Cybernetics, Part B: Cybernetics*, vol. 42, no. 2, pp. 513–529, 2012.
- [86] A. Shirzadi, S. Asadi, H. Shahabi et al., "A novel ensemble learning based on Bayesian Belief Network coupled with an extreme learning machine for flash flood susceptibility mapping," *Engineering Applications of Artificial Intelligence*, vol. 96, Article ID 103971, 2020.
- [87] D. T. Bui, P.-T. T. Ngo, T. D. Pham et al., "A novel hybrid approach based on a swarm intelligence optimized extreme learning machine for flash flood susceptibility mapping," *Catena*, vol. 179, pp. 184–196, 2019.
- [88] G.-B. Huang, H. Zhou, X. Ding, and R. Zhang, "Extreme learning machine for regression and multiclass classification," *IEEE Transactions on Systems, Man, and Cybernetics, Part B (Cybernetics)*, vol. 42, no. 2, pp. 513–529, 2011.
- [89] G.-B. Huang, Q.-Y. Zhu, and C.-K. Siew, "Extreme learning machine: a new learning scheme of feedforward neural networks," in *Proceedings of the 2004 IEEE International Joint Conference on Neural Networks (IEEE Cat. No. 04CH37541)*, vol. 2, pp. 985–990, Budapest, Hungary, July 2004.
- [90] H.-B. Ly, P. G. Asteris, and B. T. Pham, "Accuracy assessment of extreme learning machine in predicting soil compression coefficient," *Vietnam Journal of Earth Sciences*, vol. 42, 2020.
- [91] L. M. Le, H.-B. Ly, B. T. Pham et al., "Hybrid artificial intelligence approaches for predicting buckling damage of steel columns under axial compression," *Materials*, vol. 12, no. 10, p. 1670, 2019.
- [92] X. Wang, Z. Yang, and A. P. Jivkov, "Monte Carlo simulations of mesoscale fracture of concrete with random aggregates and pores: a size effect study," *Construction and Building Materials*, vol. 80, pp. 262–272, 2015.
- [93] J. Guillemot and C. Soize, "Generalized stochastic approach for constitutive equation in linear elasticity: a random matrix model," *International Journal for Numerical Methods in Engineering*, vol. 90, no. 5, pp. 613–635, 2012.
- [94] S. Mordechai, *Applications of Monte Carlo Method in Science and Engineering*, InTechOpen, Rijeka, Croatia, 2012.
- [95] H.-B. Ly, E. Monteiro, T.-T. Le et al., "Prediction and sensitivity analysis of bubble dissolution time in 3D selective laser sintering using ensemble decision trees," *Materials*, vol. 12, no. 9, p. 1544, 2019.
- [96] H.-L. Nguyen, B. T. Pham, L. H. Son et al., "Adaptive network based fuzzy inference system with meta-heuristic optimizations for international roughness index prediction," *Applied Sciences*, vol. 9, no. 21, p. 4715, 2019.
- [97] H. Q. Nguyen, H.-B. Ly, V. Q. Tran, T.-A. Nguyen, T.-T. Le, and B. T. Pham, "Optimization of artificial intelligence system by evolutionary algorithm for prediction of axial capacity of rectangular concrete filled steel tubes under compression," *Materials*, vol. 13, no. 5, p. 1205, 2020.
- [98] S. P. Mohanty, D. P. Hughes, and M. Salathé, "Using deep learning for image-based plant disease detection," *Frontiers in Plant Science*, vol. 7, p. 1419, 2016.
- [99] B. T. Pham, I. Prakash, A. Jaafari, and D. T. Bui, "Spatial prediction of rainfall-induced landslides using aggregating one-dependence estimators classifier," *Journal of the Indian Society of Remote Sensing*, vol. 46, no. 9, pp. 1457–1470, 2018.
- [100] C. Verma and Z. Illés, "Attitude prediction towards ICT and mobile technology for the real-time: an experimental study using machine learning," in *Proceedings of the 15th eLearning and Software for Education Conference - eLSE 2019*, vol. 3, pp. 247–254, Bucharest, Romania, April 2019.
- [101] D. V. Dao, A. Jaafari, M. Bayat et al., "A spatially explicit deep learning neural network model for the prediction of landslide susceptibility," *Catena*, vol. 188, p. 104451, 2020.
- [102] C. Qi, H.-B. Ly, Q. Chen, T.-T. Le, V. M. Le, and B. T. Pham, "Flocculation-dewatering prediction of fine mineral tailings using a hybrid machine learning approach," *Chemosphere*, vol. 244, Article ID 125450, 2020.
- [103] B. T. Pham, M. Avand, S. Janizadeh et al., "GIS based hybrid computational approaches for flash flood susceptibility assessment," *Water*, vol. 12, no. 3, p. 683, 2020.

- [104] P. T. Nguyen, D. H. Ha, M. Avand et al., "Soft computing ensemble models based on logistic regression for groundwater potential mapping," *Applied Sciences*, vol. 10, no. 7, p. 2469, 2020.
- [105] P. T. Nguyen, D. H. Ha, A. Jaafari et al., "Groundwater potential mapping combining artificial neural network and real AdaBoost ensemble technique: the DakNong province case-study, Vietnam," *International Journal of Environmental Research and Public Health*, vol. 17, no. 7, p. 2473, 2020.
- [106] W. Chen, H. R. Pourghasemi, A. Kornejady, and N. Zhang, "Landslide spatial modeling: introducing new ensembles of ANN, MaxEnt, and SVM machine learning techniques," *Geoderma*, vol. 305, pp. 314–327, 2017.
- [107] Z. H. Khan, T. S. Alin, and M. A. Hussain, "Price prediction of share market using artificial neural network (ANN)," *International Journal of Computer Applications*, vol. 22, no. 2, pp. 42–47, 2011.
- [108] J. C. Gertrudes, V. G. Maltarollo, R. A. Silva, P. R. Oliveira, K. M. Honorio, and A. B. F. Da Silva, "Machine learning techniques and drug design," *Current Medicinal Chemistry*, vol. 19, no. 25, pp. 4289–4297, 2012.
- [109] A.-L. Milac, S. Avram, and A.-J. Petrescu, "Evaluation of a neural networks QSAR method based on ligand representation using substituent descriptors: application to HIV-1 protease inhibitors," *Journal of Molecular Graphics and Modelling*, vol. 25, no. 1, pp. 37–45, 2006.

Research Article

Mechanical Parameter Identification of Hydraulic Engineering with the Improved Deep Q-Network Algorithm

Wei Ji ¹, Xiaoqing Liu ¹, Huijun Qi ², Xunnan Liu,¹ Chaoning Lin,^{1,3} and Tongchun Li¹

¹College of Water Conservancy and Hydropower Engineering, Hohai University, Nanjing 210098, Jiangsu, China

²College of Computer and Information, Hohai University, Nanjing 210098, Jiangsu, China

³Faculty of Technology, Policy, and Management, Delft University of Technology, Delft 2628 BX, Netherlands

Correspondence should be addressed to Xiaoqing Liu; lxqhhu@163.com and Huijun Qi; qihuijun@hhu.edu.cn

Received 30 July 2020; Accepted 29 November 2020; Published 28 December 2020

Academic Editor: Zheng-zheng Wang

Copyright © 2020 Wei Ji et al. This is an open access article distributed under the Creative Commons Attribution License, which permits unrestricted use, distribution, and reproduction in any medium, provided the original work is properly cited.

During the long-term operating period, the mechanical parameters of hydraulic structures and foundation deteriorated gradually because of the environmental factors. In order to evaluate the overall safety and durability, these parameters should be calculated by some accurate analysis methods, which are hindered by slow computational efficiency and optimization performance. The improved deep Q-network (DQN) algorithm combined with the deep neural network (DNN) surrogate model was proposed in this paper to ameliorate the above problems. Through the study cases of different zoning in the dam body and the actual engineering foundation, it is shown that the improved DQN algorithm has a good application effect on inversion analysis of material mechanical parameters in this paper.

1. Introduction

The premier task is to monitor the safe status of structures during the operating period. There have been catastrophes of engineer crash from time to time around the world due to the lack of overall monitoring methods and the low analysis accuracy of calculating methods. A disastrous example is that the dam Edenville broke, and the leaking flood shattered both Smallwood dam and Sanford dam subsequently in the downstream position, which caused serious damage to surrounding cities.

The hydraulic project crashes happen mainly because of the collapse of the dam body and the sliding of the foundation or abutment. During the operating term, the concrete dam is affected by environmental factors obviously. At the microlevel, there are physical and chemical reactions in the parameters of the dam body material and foundation material, so their mechanical parameters deteriorated gradually, leading to the increase of structure displacement or leakage at the macrolevel. Both the deformation of the dam body or foundation and the leakage of the concrete structure are key monitoring targets. The deformation monitoring includes

forward analysis and inversion analysis. The former is to map the linear or nonlinear relation between environmental loads and displacement by establishing a regress model [7–9], whose target is predicting the status of the engineering and environment nearby in the future. The latter is to check the strength and the stability according to the mechanical parameters of structures or foundations by calculating the data of structural operating state combined with the data of the environmental variation [10].

Because the constitutive models of practical engineering are all nonlinear, it is impossible to work out the problems directly. By calculating the maximum or minimum value of target functions, the heuristic algorithms became the main methods to optimize parameters in the feasible region. Particle swarm optimization (PSO) algorithm and genetic algorithm were applied to optimize the structural parameters in the early time [11]. Kang introduced the artificial bee algorithm in 2013 [12]. And he optimized the models by combining heuristic algorithm with machine learning algorithm in 2016 [13–15]. After that, he improved firework algorithm and obtained better effect in identifying parameters [16]. Besides, Lin carried out inversion calculation with

wolf pack algorithm, and the resultant accuracy was higher than whale optimization algorithm.

There are two main problems existing in the inversion analysis of hydraulic structures. The first one is that the current displacement inversion method is based on the finite element method (FEM). Under the combination of different mechanical parameters and environmental loads, the nodes' displacements are calculated by the finite element model. With the growing number of parameters, the calculating dimensions rise synchronously. Besides, the time complexity of the finite element model increases sharply with more grids. The two factors could lead to the result that the calculating convergence time is so long that the feasibility of application in the practical project is low. The second one is that although so many heuristic algorithms provide the possibility to implement global search in the feasible region, these methods calculate and compare the target values after sampling practical points in the parameter space, so they could not guarantee the best consequence in the multidimensional parameter space and have poor convergence in practice.

Recently, machine learning algorithm with a positive developing trend includes three parts, which are supervised learning, unsupervised learning, and reinforcement learning (RL) [17]. As the cutting-edge branch, RL differs from the other ones. It is a learning algorithm with delay effect, seeking the best policy with dynamic programming [17]. The core idea is that the agent tries different policies to select corresponding actions under diverse state from the environment during the interactive process between the agent and the environment, so the agent could find the best action to maximize the reward when facing different states after the learning stage [18]. RL adopts the way of exploring from the beginning time and then utilizing the exploratory experience to complete the trail-and-error process [19]. Bellman proposed a dynamic method to deal with the value function based on the information from the systematic state [20], but the curse of dimensionality occurred when the method was applied, which was solved effectively by Mes and Rivera [21]. Some scholars introduced the function approximation method to access the value when the state and action were consecutive, such as the linear function and artificial neural network [23, 24]. With the gradual development of RL theory, these relative technologies had made great progress in the industry. Zhiang Zhang et al. reduced the indoor energy consumption by 16.7% by optimizing the HVAC system with deep reinforced learning algorithm [25]. Zhe Wang and Hong discussed the contribution and current obstacles when RL was adopted in controlling buildings [26]. The industry of robot employed RL to control the mechanical action accurately [27–30]. Fangyuan Chang et al. achieved the goal of reducing cost in the charging battery by combining RL and LSTM [31].

To improve two inversion problems with machine learning mentioned above in the paper, the DNN surrogate model and reinforcement learning are introduced into the structural inversion calculation for the first time. The deep neural network completes the learning stage with training samples which are the calculating results from the FEM,

which makes the DNN model replace the finite element model to map the target points' displacements approximately and improve the convergence efficiency greatly under the premise of ensuring the calculating accuracy. The basic theory of reinforcement learning guarantees the convergence of the algorithm. The inversion calculation of structural material parameters with monitoring data is a Markov process. Its core is working out the best value of a nonlinear function in the global parameter space. Taking the monitoring data as a part of the observable environmental state, the inversion calculation and optimization of structural material parameters can be realized through reinforcement learning combined with the engineering's deep learning surrogate model. This paper adopts the punitive idea which is a negative reinforcement mode to form deep reinforcement learning algorithm by combining the target of inversion calculation and the DNN surrogate model with reinforcement learning. Besides, the interactive mode of information between the agent and the environment is improved to adapt to the optimization of material parameters of engineering structures and the surrounding foundation. The last part is to employ a new mode to express the displacement relativity among different monitoring points from the same structural sections to make the deep reinforcement learning algorithm adapt to the inversion calculation of multiple zones, to ensure the coordination among the parameters among all zones in the same section, so that this algorithm could get a wider application to introduce a new mode for the hydraulic inversion analysis.

2. Theory

2.1. The Inversion Theory of Mechanical Parameters. The elastic modulus is calculated inversely by the relation between the monitoring data of dam deformation and those of the environment. According to the monitoring theory [32], the displacement along the river of the dam body, $disp$, consists of the water pressure component δ_H , time-dependent component δ_T , and temperature component δ_θ .

The water pressure component δ_H is strongly related to the upstream water head, mechanical parameters of the structure and foundation, and the coordinates of target points. The constitutive model of the concrete dam reads

$$u_c = \mathbf{F}(\mathbf{E}, \mathbf{H}, x, y), \quad (1)$$

$$\mathbf{E} = [E_1, E_2, \dots, E_n]. \quad (2)$$

\mathbf{F} maps the relation between the displacements of finite element nodes and the state combined by different material parameters and environmental loads. \mathbf{E} is a vector consisting of different material parameters in every zone from the finite element model. \mathbf{H} is the water head. (x, y) is a group of nodes' coordinate. u_c is the displacement of target finite element nodes calculated by the constitutive model F with the target mechanical parameter E when facing different environmental loads.

The inversion analysis is to seek the suitable mechanical parameters to minimize the error f_e which is produced by

the displacement series of target nodes and water pressure component δ_H separated from displacement monitored by measuring instruments. The error f_e reads

$$f_e = \|u_c - \delta_H\|_2^2 \quad (3)$$

2.2. DNN Surrogate Model. A three-layer network structure with a suitable activation function could approximate any function infinitely in theory with reasonable number of iterative epochs [33]. According to equation (1), the factors affecting the displacement of nodes u_c are the material mechanical parameters E , water level H , and the coordinate of nodes (x, y) , so the form of the sample is $[E, H, x, y : u_c]$, which indicates that the input vector is $[E, H, x, y]$ and the calculating target of output node O is u_c , shown in Figure 1 and equation (4). f represents the mapping relation between input data and output data. After the input layer and output layer are determined, the number of layers and nodes in the hidden layer need to be determined by trail calculation according to the specific demand. The output error J results from equations (4) and (5). W and b are weights and biases, respectively, connecting these layers.

$$O = f(E, H, x, y), \quad (4)$$

$$J(E, H, x, y, W, b) = \frac{1}{2} \|u_c - O\|_2^2 \quad (5)$$

The neural network adopts the gradient descent method to minimize the output error J and upgrade the network parameters W and b . By selecting reasonable number of samples each time, the minibatch gradient descent method could not only ensure the representativeness of each group of samples to reduce the negative impact of noise points on network and ensure the convergence but also prompt the velocity of network convergence to reach a better learning model, so this method meets the requirements of this paper.

The process of producing DNN samples needs the following steps:

Input: constitutive model F , m groups of material mechanical parameters E , and n groups of reasonable water level H

Output: sample of finite element node displacement $[E, H, x, y : u_c]$

start:

for $i = 1$ to m :

for $j = 1$ to n :

calculate displacement of nodes by model F

$$u_c = F(E, H, x, y)$$

store sample $[E, H, x, y : u_c]$

output all samples.

end

The process of constructing the DNN surrogate model is shown in the following steps:

Input: the number of network layers, the node number of each layer, activation function, loss function, the maximum epoch N , and m samples from each batch

Output: DNN model with fixed weights W and biases b start:

initialize the weight coefficient matrix W and bias vector b randomly

for iter = 1 to N :

input vector $[E, H, x, y]$ into nodes of input layer
forward propagation calculation

$$O = f(E, H, x, y)$$

calculating the loss

$$J(E, H, x, y, W, b) = (1/2) \|u_c - O\|_2^2$$

back propagation calculation according to the loss of the last step

upgrade weight matrix W and bias vector b

output the DNN model with fixed network structure and parameters

end

The fixed DNN model could map the relation between input nodes and output nodes in a very short time which overcomes the problem that the calculating velocity of the finite element model is too slow, so replacing the constitutive model with the network is reasonable for inversion analysis.

2.3. Optimization Capability of DQN. According to Figure 2, the framework of reinforcement learning consists of five parts: agent, environment, state, action, and reward (the abbreviations are Agent, Env, s , a , and r). Env provides a current state s as an input of the agent. Agent selects action a corresponding to s according to policy π . Env accepts and assesses a to calculate the reward r and then produces the next state ($state'$ in Figure 2). The value of policy π in the current Env is determined by accumulating r of all time steps in each epoch. The calculating formulas are shown as follows:

$$G_t = r_{t+1} + \gamma r_{t+2} + \gamma^2 r_{t+3} + \dots = \sum_{i=0}^T \gamma^i r_{t+i+1}, \quad (t < T),$$

$$V_\pi(S) = E_\pi[G_t | s_t = ns],$$

$$q_\pi(s, a) = E_\pi[G_t | s_t = nsq, ha_t = xa].$$

(6)

γ is the discounted factor for the reward of future time steps, whose range is $[0, 1]$. $V_\pi(S)$ is the value function of the state, and $q_\pi(s, a)$ is the value function of state-action.

The target of reinforcement learning is to seek the best policy π_* when facing different states in Env. Under the guidance of the best policy π_* , the accumulative reward G_t reaches the highest value. The corresponding value function

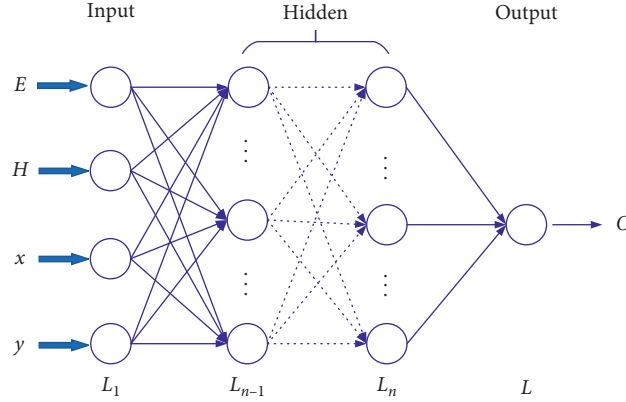


FIGURE 1: The structure of the DNN surrogate model.

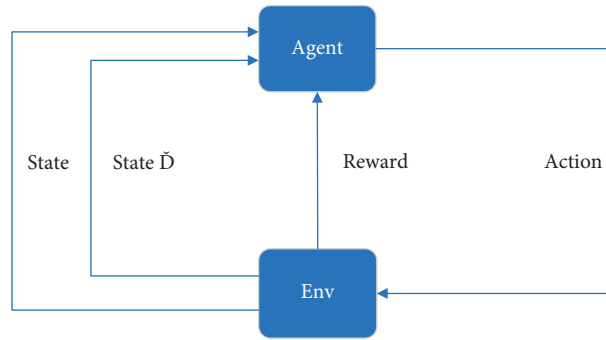


FIGURE 2: The framework of reinforcement learning.

of state-action is the optimal one $q_*(s, a)$. S is the collection of s , and A is the collection of a .

$$q_*(s, a) = \max_{\pi} q_{\pi}(s, a), \quad (s \in S, a \in A). \quad (7)$$

Q-learning is mainly adopted to work out $q_{\pi}(s, a)$, which was proved that the convergence can be guaranteed in theory by Watkins in 1992 [34]. It is a value-based method, upgrading $q_{\pi}(s, a)$ between different time steps with the time difference method in one epoch. The calculating method is shown in the following under a certain policy π :

$$q_t(s, a) = q_t(s, a) + \alpha(r + \gamma \max_{a'} q_{t+1}(s', a') - q_t(s, a)), \quad (8)$$

where $\max_{a'} q_{t+1}(s', a')$ means the value corresponding to a' , which maximizes the q value among the optional actions, under the state s' in $t+1$ th time step. α is the learning rate, which is used to control the update rate of each time step.

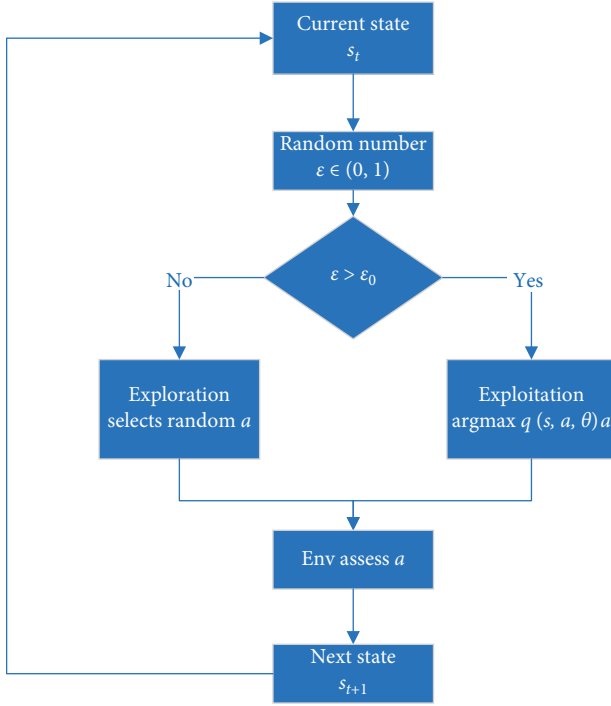
Agent selects a from A using two contradictory ways named exploitation and exploration. The former selects a by exploiting the past experience to solve the current state s , while the latter abandons the past experience and selects a at random to extend the action space A when facing the current state s . If RL only carries out the exploitation policy, the optimization would usually fall into local extremum because of the lack of full exploration in the action space. However, if RL gives up the exploitation policy, a thorough exploration process would make the algorithm lose the

definite objective and fail to search for a better policy π . Two search means are balanced by the ε -greedy method, whose flowchart is shown in Figure 3, where the range of the threshold ε_0 is $[0, 1]$.

The main idea of the ε -greedy method is that, in the initial period, exploring the action space A is the first choice because of short of experience. After being trained with suitable time steps, the model learned how to select better actions to accumulate experience when facing different states. The past memory is gradually used to promote the total reward. During this process, the model transits from the exploration stage to the exploitation stage by degrees, which means that the probability of random selection action shrinks correspondingly, shown with equation (9). t_{step} indicates the current time step.

$$\varepsilon = \max\left(0.01, \frac{(\varepsilon_0/2)}{t_{\text{step}}}\right). \quad (9)$$

The original reinforcement learning usually adopts linear transformation or look-up table method, which could not solve multidimension or nonlinear problems. DQN algorithm that combines deep learning algorithm and reinforcement learning not only obtains excellent characterization capability of deep learning to transform the data features into the state as the input of the Agent but also selects the proper action a by calculating all feasible state-action values $q_t(s, a)$. In the past, Env demanded relevance

FIGURE 3: The flowchart of ε -greedy.

between two successive time steps to a certain degree, which did not meet the demand for independence among samples when deep learning was applied. In 2013, Mnih proposed experience replay technology to deal with this obstacle, with another advantage that data could be used repeatedly to effectively increase the input samples. This method contained two main steps [23]:

- (1) Storage: store the past data $[s_t, a_t, r_t, s_{t+1}]$ in the memory zone as samples
- (2) Sample and replay: extract multiple samples $[s_t, a_t, r_t, s_{t+1}]$ from each batch as the input data of the deep network

During the iterative process of Q-learning, the parameters of the state-action value function operating in the t time step are the same as those operating in the $t+1$ time step, which results in synchronous ups and downs of the q value in two time steps, enhancing the probability of model divergence. So, the actor-critic framework was introduced. The actor is expressed as $q(s, a, \theta)$, and the critic is expressed as $q(s, a, \theta^-)$, which indicate that two models share the same structure with different network parameters. The former is used to assess value of the current state. The latter is applied in the next state to evaluate the result of the current network and guides the update of the actor network. The update mode of the q value is shown in equation (10). θ of actor is copied to θ^- of critic at a certain interval of time steps.

$$q_t(s, a, \theta) = q_t(s, a, \theta) + \alpha(r + \gamma \max_{a'} q(s', a', \theta^-) - q_t(s, a, \theta)). \quad (10)$$

2.4. Combination of the Improved DQN and Inversion Calculation. The target of mainstream RL is to develop the best policy to guide Agent to select proper a when facing different states from Env and obtain the highest accumulated reward, while the task of inversion calculation is to select an elastic modulus that is suitable for the deformation of the engineering structure and foundation. So, the interactive mode of information between Agent and Env is improved: after Agent selects a proper action a according to state s , Env assesses this a , and in the meantime, this a improves the parameters of the state to search the best material mechanical parameters.

2.4.1. Construction of the Inversion Agent. The DNN surrogate model, established according to Section 2.2, is used to calculate the agent displacement u_{cal} , as one part of Agent. Subtract u_{cal} from the displacement of target samples u_{true} , and the difference guides Agent to select a . After that, the corresponding state-action value would be evaluated. The flowchart is shown in Figure 4, where $p(a)$ means the probability of action a .

2.4.2. Improvement of the Interactive Mode between Agent and Env. How the reward r is produced by Env assessing the action a from Agent is shown in equations (11) and (12):

$$\text{error} = u_{\text{cal}} - u_{\text{true}}, \quad (11)$$

$$r = -|\text{error}|. \quad (12)$$

The target of DQN is to seek a proper elastic modulus E . The less the absolute value of reward r is, the closer the calculated elastic modulus is to the actual parameter in Env, which indicates that E in state s ceaselessly approaches the real value in Env during the iteration process.

The improvement of the interactive mode between Agent and Env in the DQN framework is that the action a selected by Agent adjusts the parameters in Env. The difference error has positive or negative states. Based on this, two kinds of action, 0 and 1, are adopted. The former indicates that E in state s is smaller than the actual one, so the positive increment ΔE could enlarge E in state s . The latter indicates that E in state s is bigger, so the negative increment ΔE could shrink E in state s . And there is a linear relation, to a certain extent, between the degree of shrinkage and expansion and the absolute value of reward r , so the mode that different actions adjust E in the state is shown with equations (13) and (14):

$$\Delta E = -r * E_{\text{step}} * (a - 0.5), \quad (13)$$

$$E = E + \Delta E, \quad (14)$$

where E_{step} is an adjustment factor, controlling the degree of adjusting E and ensuring the model could converge.

The overall process is presented as follows:

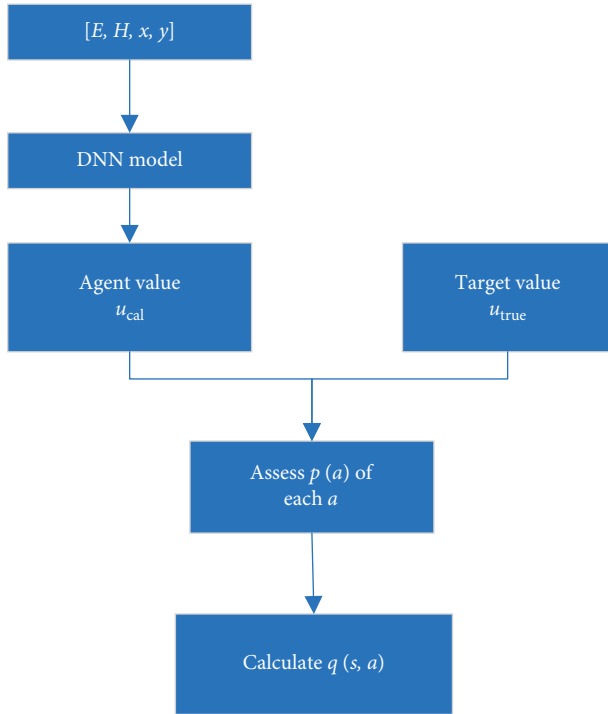


FIGURE 4: The structure of Agent.

Initialize memory zone D , the maximum epochs, discounted factor γ , adjustment factor E_{step} , and random probability ε_0

Initialize the actor network parameter θ , the critic network parameter $\theta^- = \theta$

for epoch = 1 to epochs:

initialize state s and the corresponding water pressure component disp_t

for $t = 1$ to T :

select action a_t from A randomly or actor network according to ε - greedy

update the random probability $\varepsilon = \max(0.01, (\varepsilon_0/2)/t)$

Env evaluate a_t and get r_t

update E in Env:

$$E = E - r_t * E_{\text{step}} * (a_t - 0.5)$$

get $s_{t+1}, \text{disp}_{t+1}$ from Env

store data $[s_t, \text{disp}_t, a_t, r_t, s_{t+1}, \text{disp}_{t+1}]$ in memory zone D as the sample

extract a batch of samples from memory zone D

Actor calculates $q(s_t, \text{disp}_t, a_t, \theta)$

Critic calculates

$$\max_{a_{t+1}} q(s_{t+1}, \text{disp}_{t+1}, a_{t+1}, \theta^-)$$

output = if $t \geq T - 1$ then r_t else $r_t + \gamma * \max_{a_{t+1}} q(s_{t+1}, \text{disp}_{t+1}, a_{t+1}, \theta^-)$

calculate

$$\text{loss} = (q(s_t, \text{disp}_t, a_t, \theta) - \text{output})^2$$

optimize actor network parameter θ with Adam algorithm

copy θ to θ^- every N time steps

output: the optimum E in Env

The DQN framework is shown in Figure 5.

In summary, this paper adopts the improved DQN algorithm embedded with the DNN surrogate model. Agent completes the task to adjust E in the state from Env to minimize the absolute error (maximize the reward) calculated by agent u_{cal} from Agent and actual displacement u_{true} from the target sample, which could evaluate the quality of the optimizing result.

2.4.3. Relation of Inversion in Multizones. In different zones in the dam section, relevance among the displacements of nodes, to a certain degree, exists without causality. So, it is unsuitable to adopt equation (16) to adjust parameters in all zones by identical adjustment extent, and it is also unreasonable to adjust the parameter only in one zone corresponding to the current sample, ignoring the relevance among deformation of all zones. With the action of upstream water pressure, the whole section of the dam body demands for the deformation coordination. For example, in Figure 6, the displacement of node P_A in the upper zone is related to not only the mechanical parameters in zone Ω_1 but also those in zone Ω_2 . The relevance is expressed with the following equation:

$$E_{\text{other}} = E_{\text{other}} - r_t * (a_t - 0.5) * (\text{randnum} * 0.1 * E_{\text{step}} + 0.01). \quad (15)$$

When a sample adjusts the mechanical parameters in other zones, the adjustment factor is $(\text{randnum} * 0.1 * E_{\text{step}} + 0.01)$, where randnum is a random number belonging to $(0, 1)$. The random number is used to control the adjustment amplitude. Besides, 0.01 is added into equation (18) to ensure that the relevance is positive. On the contrary, when the sample adjusts the parameter in its own zone, the adjustment increment is still calculated by equation (13).

3. Case Study

3.1. Inversion Calculation of the Single Dam Zone: Case A. This case A is to minimize the cumulative absolute error of the agent displacement u_{cal} and the sample displacement u_{true} to optimize the DQN model and search an elastic modulus suitable for the whole dam section. The target displacement u_{true} is the displacement of target node u_c calculated by the constitutive model.

Step 1: establish the finite element model. The finite element model is shown in Figure 7, containing two components, dam and foundation. The horizontal direction x is along the river, and the vertical direction y is the elevation. The dam height is 107.5 m, the length of dam bottom is 88 m, and the length and width of the dam foundation are 488 m and 300 m, respectively. All mechanical parameters of the model are listed in Table 1. E_A indicates the elastic modulus

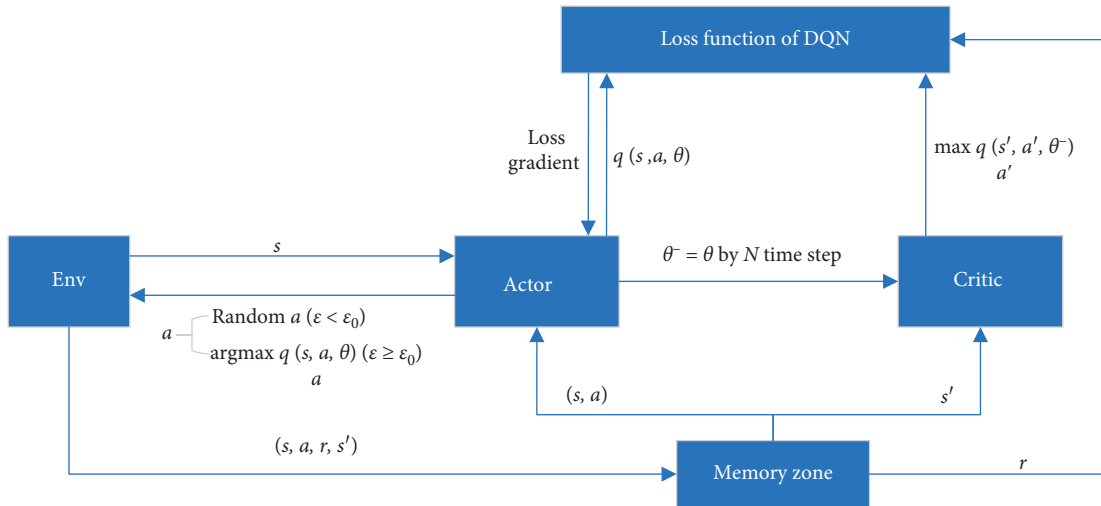


FIGURE 5: The framework of DQN.

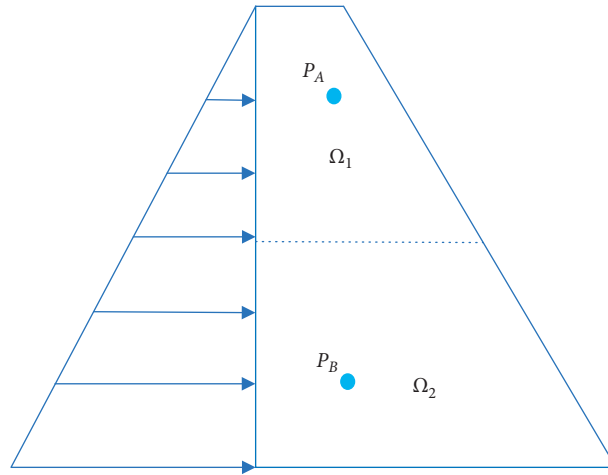


FIGURE 6: The diagram of multiple zones in the dam section.

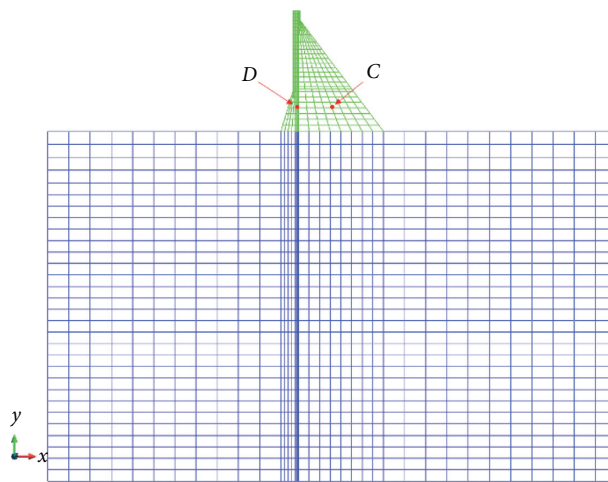


FIGURE 7: The finite element model of case A.

TABLE 1: The mechanical parameters of case A.

Component	Density (kg/m ³)	Elastic modulus (GPa)	Poisson's ratio
Dam body	2400	E_A	0.167
Foundation	2400	9	0.167

of the dam section. The nodes of foundation bottom are fixed in the horizontal and vertical direction, and the nodes at both sides of the foundation are fixed in the vertical direction.

Step 2: select the sample. 259 different water levels were extracted randomly from 86.5 m to 104.3 m, and 200 different elastic moduli E_A were randomly extracted from 5 GPa to 20 GPa evenly, not containing 10.3 GPa (the target parameter). There were 51,800 groups of combination states of mechanical parameter and water pressure. The model was calculated using software GeHoMadrid developed by Hohai University and Universidad Politécnic de Madrid to get the node displacement of all states. The result $[E, H, x, y, u_{\text{true}}]$ was stored as samples to train and verify the DNN model.

Step 3: construct the DNN surrogate model. The model had four layers, established by Keras. The first layer had four input nodes, named input-EHXY, and the form of the input vector is $[E_A, H, x, y]$. The second and third layers were fully connected layers, named Sec-layer and Third-layer, with 8 and 10 nodes, respectively. The fourth layer was the output layer named dispout with 1 node, and the calculating target was u_{true} . The specific structure is shown in Figure 8. The loss function was "mean_squared_error," optimized by Adam. The learning rate was 0.001, the maximum iterative epoch was 1000, and the activation function of all nodes adopted "relu."

The samples from step 2 were shuffled randomly, and all data were normalized to $[0, 1]$ according to the data features. Training samples occupied 80%, and the rest were verifying samples. The changing horizontal section and deformable foundation have an effect on the displacement in the dam. And the increase of altitude weakens the nonlinear effect. The location of node C is in the lower zone and near the foundation, so this zone could illustrate nonlinear deformation more clearly than those nodes in the higher area. Besides, the closer the node is to the foundation, the smaller the displacement is, so node C was selected. The predicting samples were the displacement along the river of node C in Figure 7 calculated under the state that the elastic modulus was 10.3 GPa with 259 water levels above.

The iterative process of the training error and verifying error is shown in Figure 9, where it indicated that, during the former 100 epochs, the two errors decreased sharply to the level close to 0. After 200 epochs, the network parameters were nearly stable. When the training stage was completed, the fixed DNN model was stored to replace the finite model in the later steps.

The displacement of different nodes is related to water level elevation and the elastic modulus of the dam body. According to the monitoring theory [32], u_{true} could be

calculated by the multivariable linear regression (MLR) model shown in the following equation:

$$u_{\text{true}} = \sum_{i=1}^3 \beta_i H^i + \beta_4 E + \beta_5 x + \beta_6 y + \tau. \quad (16)$$

Training samples and predicting samples are the same as those of the DNN model. The calculating results of predicting samples are shown in Table 2.

From Table 2, the mean relative errors of DNN and MLR were lower than 3%. Furthermore, the accuracy of the DNN model in both mean relative error and maximum relative error was an order of magnitude higher than that of the MLP model. The possible reason was that the MLP model constructed regression factors based on the plane cross-section assumption and complete elastomer assumption, but node C was near the dam foundation, which meant during the calculation, the deformation of the dam body and foundation did not meet the first assumption. The displacement of node C was not completely linear. DNN model was nonlinear, which represented that the neural network could map the relation between environmental load and displacement more efficiently. The maximum relative error was lower than 2%. From this, it was reasonable for the DNN, after being well trained, to replace the finite element model.

Step 4: construct Agent. The Agent included three parts. The first one was the DNN model stored in step 3, which received the state s , $[E_A, H, x, y]$ and produced agent displacement u_{cal} ; the second part was the target displacement u_{true} corresponding to the current state, named disp_value; the third part was two optional actions, named actions_input. u_{cal} minus u_{true} in the layer named subtrac_1 was the error, which was used to select action a , combining the layer actions_input to calculate the state-action value q . The specific structure is shown in Figure 10.

Step 5: calculation with the DQN algorithm. The predicting samples normalized in step 3 were target samples in this step. This maximum number of epoch was 100, and each epoch had 100 time steps. The initial value of probability ϵ_0 was determined as 0.2. With the increase of time step t , ϵ decreased with a linear trend and would be stable at 0.01 eventually. The sample volume of the memory zone was 512, the discounted factor γ was 0.5, the learning rate α was 0.5, the adjustment factor E_{step} was 0.01, and the replay size of samples in each time step was 32. The initial modulus could be selected randomly, whose range was from 5 GPa to 20 GPa. The target displacement was the value of node C calculated by FEM with 259 water levels when the elastic modulus was 10.3 GPa. The iterative process and result are shown in the following.

3.1.1. Process Analysis. Figures 11 and 12 show that, in the initial period, the model was in the exploration stage, selecting actions randomly, resulting in the fluctuation of the reward. Then, the DQN model moved into the exploitation stage, with the increase of epoch and selecting the right action when facing different states. The absolute value of the reward decreased smoothly, and the searching parameters

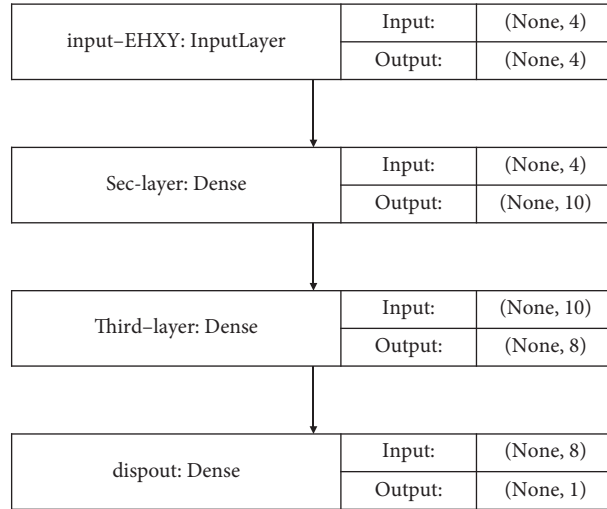


FIGURE 8: Structure of the DNN model in case A.

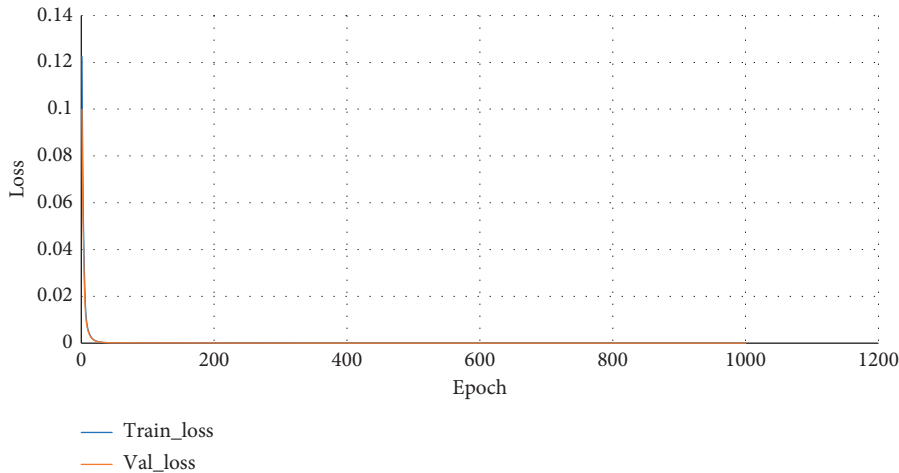


FIGURE 9: The iterative process of the model error in case A.

kept approaching the target value in the former 40 epochs before the model was generally stable. The result of inversion calculation reached the optimal status of the model.

3.1.2. Result Analysis. Figure 13 shows that the blue line that represented the agent displacement calculated by Agent almost coincided with the orange line that represented the actual displacement, which indicated that the values of two lines were very close in the same water level. Figure 14 shows the absolute error between two displacement lines, where the mean absolute error was 0.015 mm, and the standard deviation (SD) was 0.0085 mm. The error values were mainly concentrated in (0, 0.02) mm. Thus, the error value remained at a low level.

When the interactive process between Agent and Env was completed, the eventual elastic modulus E_A was 10.3187 GPa, and the actual target was 10.3 GPa. So, the absolute error was 0.0187 GPa, and the relative error was 0.18%. Two possible reasons of the error were as follows: the

first one was that the DNN surrogate model had a mean error of 0.372% relative to the finite element model, and its accuracy could determine the accuracy of DQN; the second reason was that the search method of DQN was not perfect. The error level indicated that the inversion consequence calculated by DQN algorithm was very close to the actual value in case A, which meant the method of this paper had a fine effect on the inversion analysis of the whole dam section.

3.2. Inversion Calculation of Double Dam Zones: Case B. This case B is to minimize the cumulative absolute error of the agent displacement u_{cal} and the sample displacement u_{true} to optimize the DQN model and search two elastic moduli suitable for the upper and lower dam zones. The target displacement u_{true} is the displacement of target node u_c calculated by the constitutive model.

Step 1: establish the finite element model. The finite element model is shown in Figure 15, containing three components: two zones in the dam section and foundation.

TABLE 2: Error of predicting samples in 10.3 GPa.

Relative error (%)	DNN	MLR
Mean	0.372	2.723
Maximum	1.833	16.212

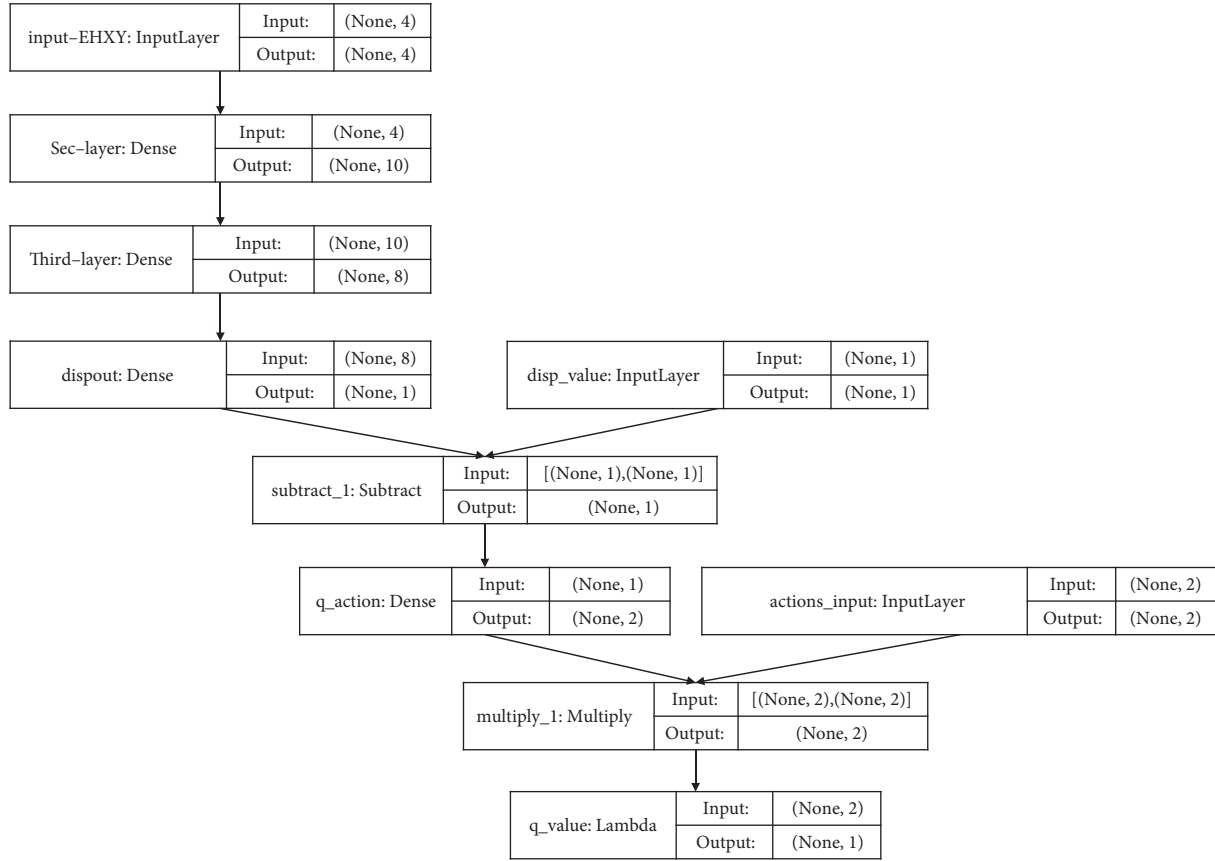


FIGURE 10: The structure of Agent in case A.

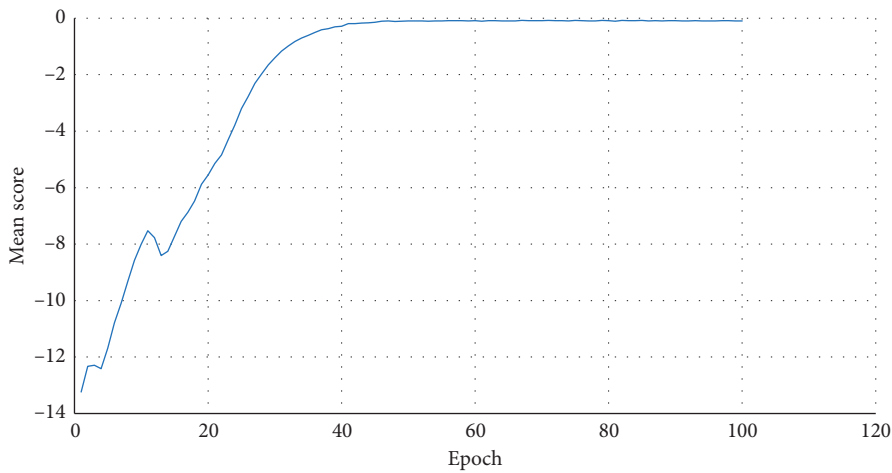


FIGURE 11: The iterative process of the reward in case A.

The horizontal direction x is along the river, and the vertical direction y is the elevation. The dam height is 50 m, the width of the dam crest is 5 m, the length of dam bottom is 5 m, and

the length and width of the dam foundation are 190 m and 100 m, respectively. All mechanical parameters of the model are listed in Table 3. E_{B1} indicates the elastic modulus of the

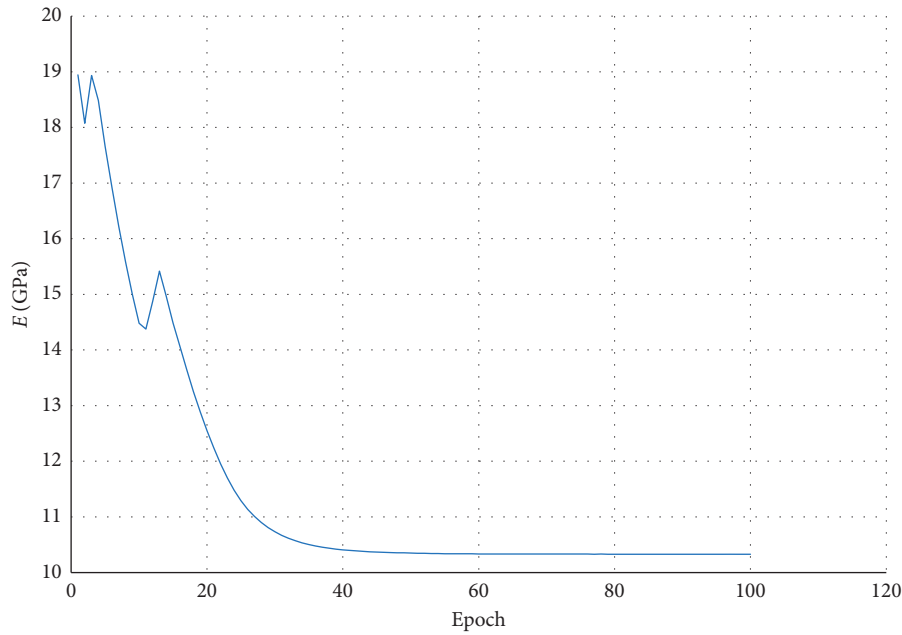


FIGURE 12: The iterative process of E of Env in case A.

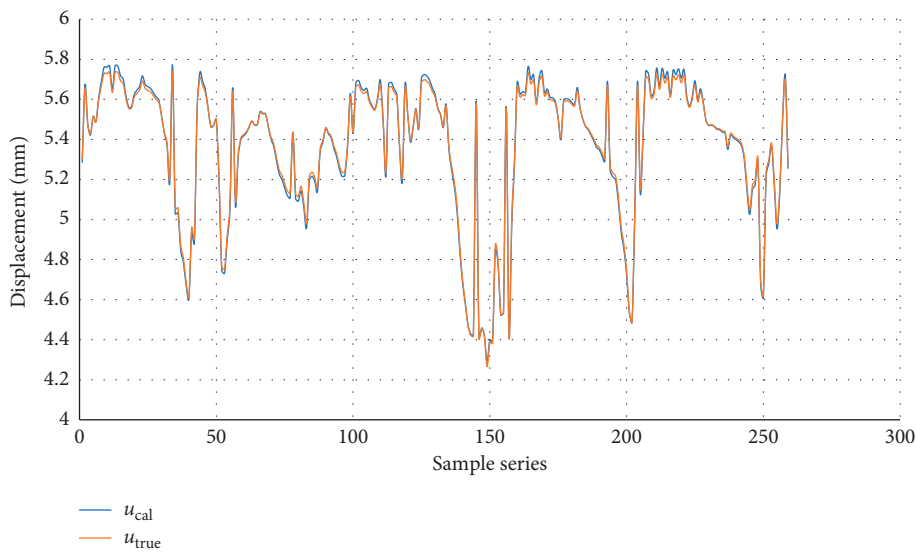


FIGURE 13: Contradiction of the calculating value and actual value.

upper zone, and E_{B2} indicates the elastic modulus of the lower zone. The nodes of foundation bottom are fixed in the horizontal and vertical direction, and the nodes at both sides of the foundation are fixed in the vertical direction.

Step 2: select the sample. 140 different water levels were extracted randomly from 36.0 m to 50.0 m, and 230 groups of different combinations of elastic moduli, E_{B1} and E_{B2} , were randomly extracted. The range of modulus in the upper zone, E_{B1} , was 9.5 GPa~22.5 GPa, not containing 18.0 GPa, while that in the lower zone, E_{B2} , was 15 GPa~25 GPa, not containing 22.0 GPa because the elastic module in the lower zone was larger than that in the upper zone in order to reduce the engineering cost. During the calculation of the finite element

model, the elastic modulus in the green zone including node A remained smaller than that in the yellow zone including node B. There were 32,200 groups of combination states of the mechanical parameter and water pressure. The model was calculated using software GeHoMadrid to get the node displacement of all states. The result $[E_{B1}, E_{B2}, H, x, y, u_{true}]$ was stored as samples to train and verify the DNN model.

Step 3: construct the DNN surrogate model. Different from case A, the input layer of the DNN surrogate model in case B had 5 nodes, and the input vector was $[E_{B1}, E_{B2}, H, x, y]$. The rest of the hyperparameters were identical to those of the DNN model in case A. The specific structure of the DNN model in case B is shown in Figure 16.

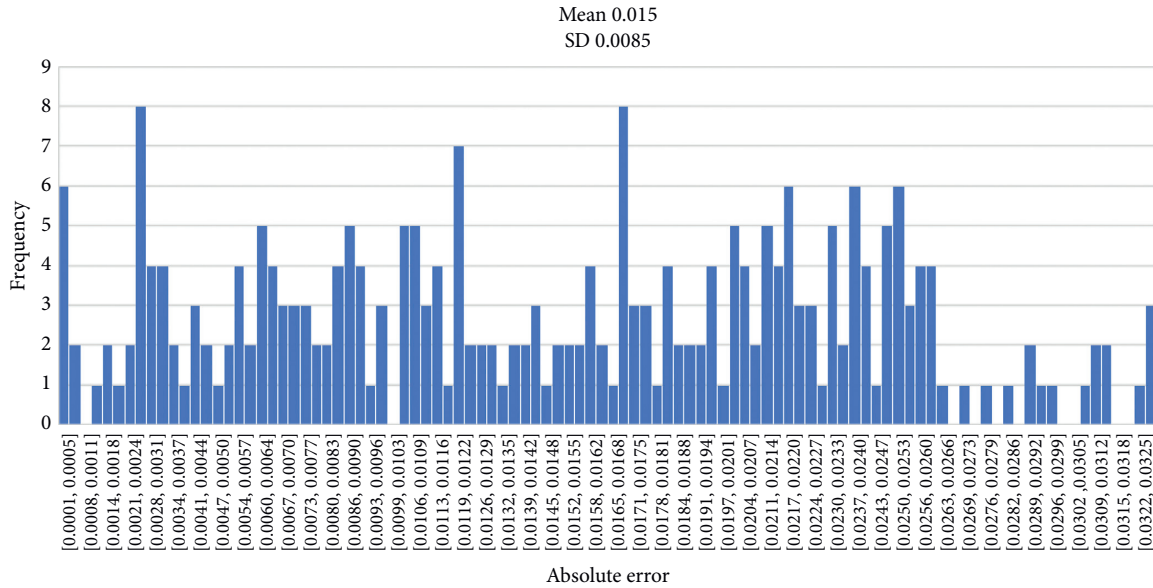


FIGURE 14: Histogram of the absolute error of distribution.

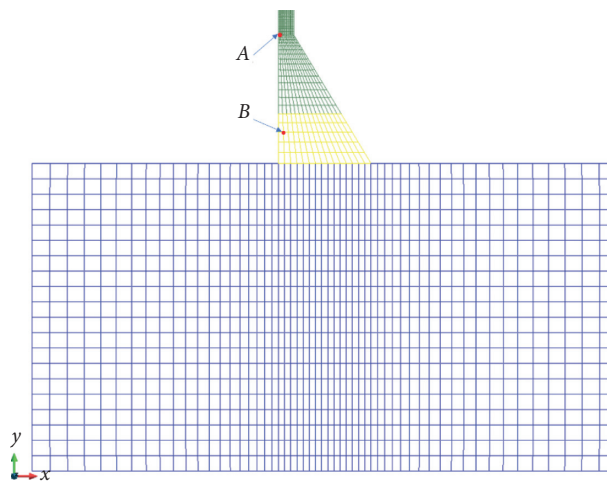


FIGURE 15: The finite element model of case B.

TABLE 3: The mechanical parameters of case B.

Component	Density (kg/m ³)	Elastic modulus (GPa)	Poisson's ratio
Upper zone	2400	E_{B1}	0.167
Lower zone	2400	E_{B2}	0.167
Foundation	2400	5	0.167

The samples from step 2 were shuffled randomly, and all data were normalized to [0, 1] according to the data features, where the first independent variable E_{B1} and the second one E_{B2} were normalized with the same scale. Training samples occupied 80%, and the rest were verifying samples. The predicting samples were the displacements along the river of nodes A and B in Figure 15 calculated under the state that the upper elastic modulus was 18.0 GPa and the lower one was 22.0 GPa with 140 water levels above.

The iterative process of the training error and verifying error is shown in Figure 17, where it indicated that, during the former 100 epochs, the two errors decreased sharply to the level close to 0. After the former 200 epochs, the network parameters were nearly stable. After the training stage, the DNN model was stored to replace the finite model in the later steps.

The maximum relative error was 3.56%, and the mean relative error was 0.59%, which indicated that the overall

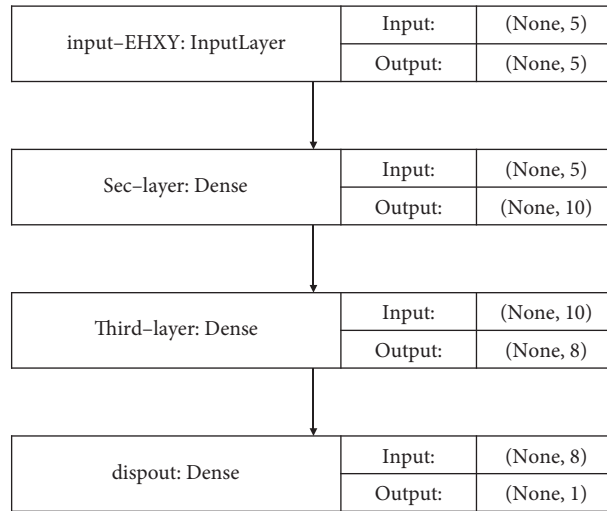


FIGURE 16: Structure of the DNN model in case B.

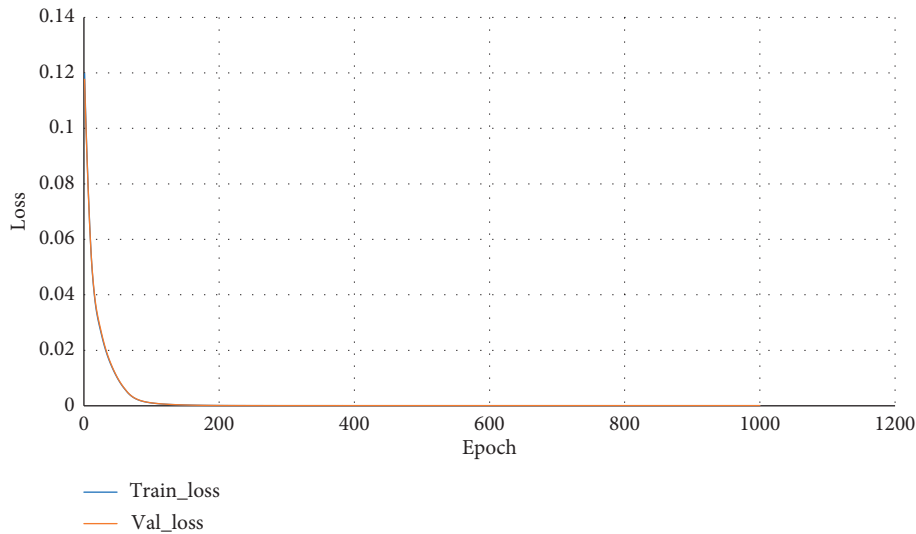


FIGURE 17: The iterative process of the model error in case B.

relative error was low. It was reasonable for DNN, after being well trained, to replace the finite element model according to the accuracy.

Step 4: construct Agent. The structure and parameters in Agent were the same as those in case A except that the input layer of the fixed DNN model had 5 nodes.

Step 5: calculation with DQN algorithm. The predicting samples normalized in step 3 were calculated as target samples in this step. This maximum number of epoch was 200, and each epoch had 100 time steps. The variation of random probability ϵ was identical to that in case A. The sample volume of the memory zone was 512, the discounted factor γ was 0.5, the learning rate α was 0.5, the adjustment factor E_{step} was 0.03, and the replay size of samples in each time step was 64. The initial modulus could be selected randomly in a reasonable range. In case B, the initial values in both the green zone and in the yellow part were determined to be 25 GPa. The target displacements

were the values of node C calculated by FEM with 140 water levels when the elastic moduli were 22.0 GPa and 18.0 GPa. The iterative process and result are shown in the following.

3.2.1. Process Analysis. Different from Figure 11, Figure 18 shows that the zoning reward had been increasing with constant fluctuation during the negative reinforcement stage and then was stable in $(-0.2 \sim 0)$, which indicated that the change of one zone would lead to the fluctuation of another zone. As a result, the agent displacement could not remain steady completely, but the overall trend was increasing, representing that the absolute value of the reward was decreasing, which meant that the penalty from Env was lower and lower and got stable in a certain range. Figure 19 shows the searching parameters kept approaching the target parameters and then tended to be stable. The result of

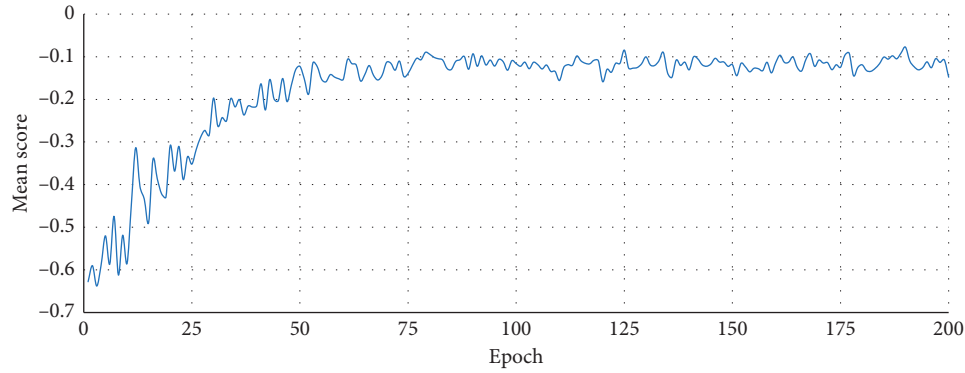


FIGURE 18: The iterative process of the reward in case B.

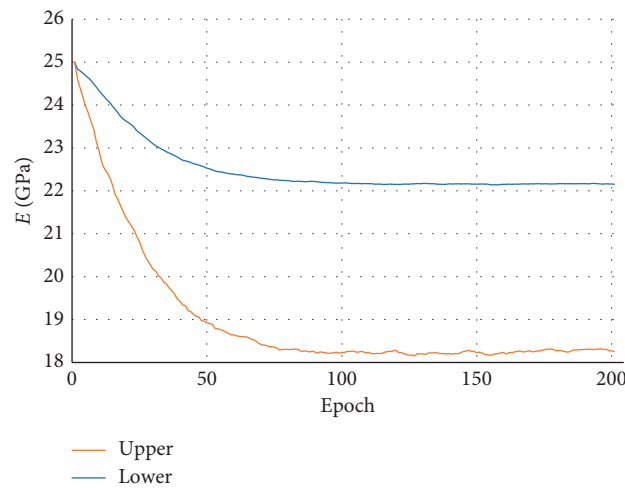


FIGURE 19: The iterative process of E in Env in case B.

inversion calculation reached the optimal status of the model.

3.2.2. Result Analysis. The results of the absolute error are shown in Figures 20 and 21. Both value and distribution of the error related to node A were better than those of node B . The possible reason was that node A was near the dam crest, so the water level elevation had a stronger effect on its displacement, and the foundation had a weaker influence on node A , which represented the deformation of node A had a better regularity.

The calculating result of DQN algorithm is listed in Table 4, which showed the relative error in the upper zone was 1.29%, and the other one in the lower zone was slightly smaller, 0.86%. The error level indicated that the inversion consequence calculated by DQN algorithm was very close to the actual parameter values in case B, meaning the method of this paper had a fine effect on the inversion analysis of the dam with multiple zones.

3.3. Verification with Actual Engineering: Case C. The engineering is a RCC dam on the main stream of a river in Cambodia, with 10 dam sections. The elevation of the dam crest is at 153.00 m, and the bottom surface is at 41.00 m, with a maximum dam height of 112.00 m. The width of the dam crest is 6.00 m. The top elevation of the upstream break slope is 84.0 m, and the slope is 1 : 0.3, and the downstream slope is 1 : 0.75. The mechanical parameters of the rock in the dam foundation are shown in Table 5. Under the long-term action of dam gravity and groundwater, the displacement along the river of the project showed a slow upward trend during the operating period, so the material parameters of the dam foundation should be paid attention to. The target of case C is the elastic modulus of the foundation of the project.

Step 1: establish the finite element model. This case selected one section of the dam, where the foundation was at 45.5 m, and the dam height was 107.5 m. The length of the dam foundation was 88.0 m, and the size of the dam foundation was 488 m * 300 m. Some scholars [35, 36]

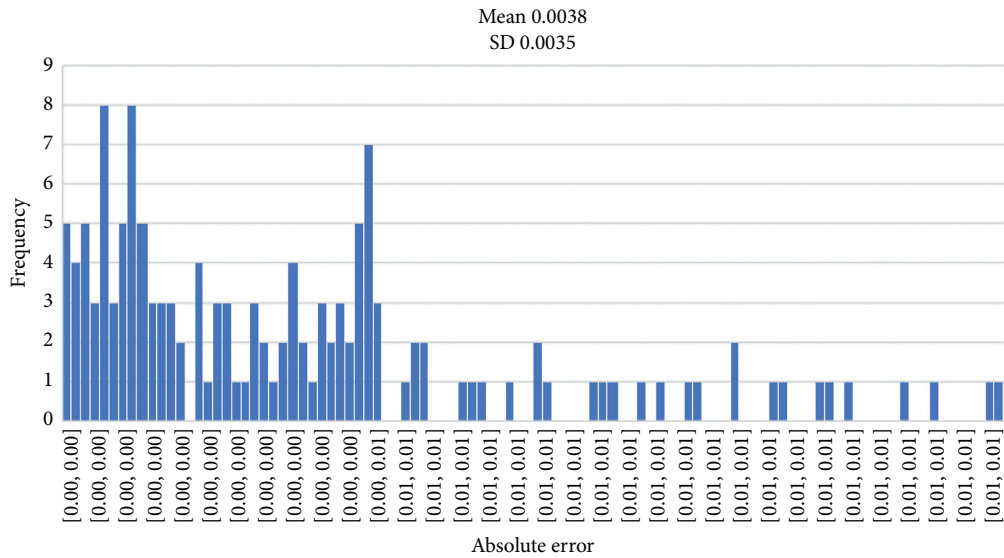


FIGURE 20: The distribution of the absolute error of node A.

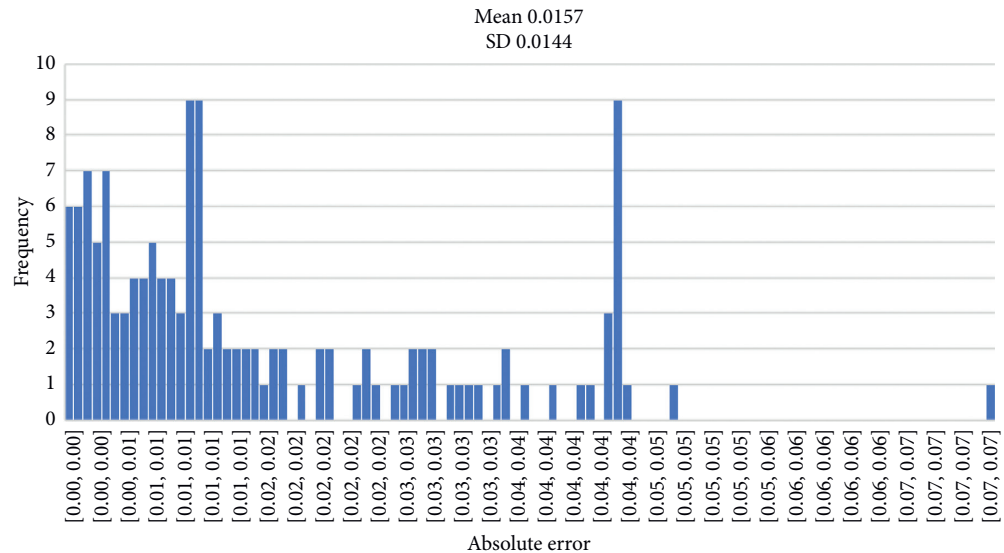


FIGURE 21: The distribution of the absolute error of node B.

TABLE 4: The result of inversion calculation in two zones.

Zone	Upper	Lower
Target (GPa)	18.0	22.0
Result (GPa)	18.2325	22.1893
Absolute error (GPa)	0.2325	0.1893
Relative error (%)	1.29	0.86

proposed that the mechanical parameters of the layer between structure and foundation were inferior to those of the surrounding rock mass because of the excavation technology or earthquake. However, the calculating model is based on the static load. Besides, the calculating depth of the foundation in this model is 300 m, so the weak layer is so thin to be ignored to reduce the complexity of this model. The finite element model was identical to the one in case A. The

monitoring displacement series, 221 data along the river from July 25, 2014, to Oct 31, 2019, came from the inverted plumb line, node *D* in Figure 7, located near the upstream side of the dam body. Mechanical parameters of the model are listed in Table 6. E_C indicated the elastic modulus of the foundation. Because the gravity dam is usually built on the fresh base rock, the main foundational material is quartz sandstone.

TABLE 5: The mechanical parameters of the rock in the dam foundation.

Rock type	Young's modulus (GPa)	Poisson's ratio	Shearing strength	Compressive strength (MPa)	Bulk density (kg/m ³)
Quartz sandstone	5~10	0.15~0.23	$C = 4.7\sim 8.4$ MPa $\varphi = 38.2^\circ\sim 45.5^\circ$	60~80	2520
Fine sandstone	7~8	0.18~0.25	$C = 3\sim 5$ MPa $\varphi = 35^\circ\sim 45^\circ$	45~55	2510
Silty mudstone	2~3	0.28~0.30	$C = 0.8\sim 1.0$ MPa $\varphi = 35^\circ\sim 38^\circ$	10~20	2530
Mudstone	1~2	0.30~0.35	$C = 0.6\sim 0.8$ MPa $\varphi = 30^\circ\sim 35^\circ$	1~3	2350

TABLE 6: The mechanical parameters of the actual project.

Component	Density (kg/m ³)	Elastic modulus (GPa)	Poisson's ratio
Dam body	2400	25	0.167
Foundation	2520	E_C	0.200

Step 2: select the sample. 221 water-level data, from 125.33 m to 145.96 m, were selected on the dates when the inverted plumb line measured displacement. Because of the unknown actual parameter in the dam foundation, in order

to make the training samples contain the possible target, 200 different elastic moduli E_C were selected from 3 GPa to 10 GPa according to the values in Table 5. There were 44,200 groups of combination states of the mechanical parameter and water pressure. The model was calculated using software GeHoMadrid to get the node displacement of all states. The result $[E_C, H, x, y, u_c]$ was stored as samples to train and verify the DNN model in step 4.

Step 3: withdraw the water pressure component. The multivariable linear regression model is shown in the following equation:

$$\text{disp} = \sum_{i=1}^3 \beta_i H^i + \sum_{j=1}^2 \left(\beta_{1j} \sin \frac{2\pi jt}{365} + \beta_{2j} \cos \frac{2\pi jt}{365} \right) + C_1 D + C_2 \ln(1 + D) + C_3 \frac{D}{D+1} + C_4 (1 - e^{-D}) + \tau, \quad (17)$$

$$D = \frac{(t - t_0)}{100}. \quad (18)$$

β and C are regression coefficients. H is the water level, while H_0 is the initial value. τ is the random error. t represents the current monitoring date, and t_0 represents the initial monitoring date. The water pressure component δ_H calculated by the MLP model above is the orange line in Figure 22. And it was used as the target displacement u_{true} in the samples calculated in DQN, $[E_C, H, x, y, \delta_H]$, where the initial value of E was determined randomly, H was the actual water level, and (x, y) was the coordinate of node D .

Step 4: construct the DNN surrogate model. The structure and parameters were the same as those of the DNN model in case A. The samples from step 2 were shuffled randomly, and all data were normalized to $[0, 1]$ according to the data features. After that, training samples occupied 70%, 15% of samples were used to verify the DNN model, and the rest were predicting samples.

The iterative process of the training error and verifying error is shown in Figure 23, where it indicated that, during the former 100 epochs, the two errors decreased sharply to the level close to 0. After the 200 epochs, the network parameters were nearly stable. After the training stage, the DNN model was stored to replace the finite element model in the later steps.

Step 5: construct Agent. The structure and parameters in Agent were the same as those in case A.

Step 6: the calculating target was searching the elastic modulus of the dam foundation to minimize the difference

between the inversion result and the actual water pressure component. This maximum number of epoch was 200, and each epoch had 100 time steps. The variation of random probability ε was identical to that in case A. The sample volume of the memory zone was 400, the discounted factor γ was 0.5, the learning rate α was 0.5, the adjustment factor E_{step} was 0.02, and the replay size of samples in each time step was 32. 10 GPa which was selected as the initial modulus. The iterative process and result are shown in the following.

3.3.1. Process Analysis. Figures 24 and 25 show that, in the initial period, the model was in the exploration stage, selecting actions randomly, resulting in the fluctuation of the reward. After that, the DQN model moved into the exploitation stage. With the increase of epoch and selecting the right action when facing different states, the absolute value of the reward was decreasing consistently, and the searching parameters kept approaching the target from the initial value 10 GPa in the former 50 epochs before the model was generally stable.

3.3.2. Result Analysis. After the interactive process between Agent and Env, the elastic modulus E_C of the dam foundation was 5.1549 GPa. All calculating results are shown in Figures 22 and 26. The former displayed that the blue line

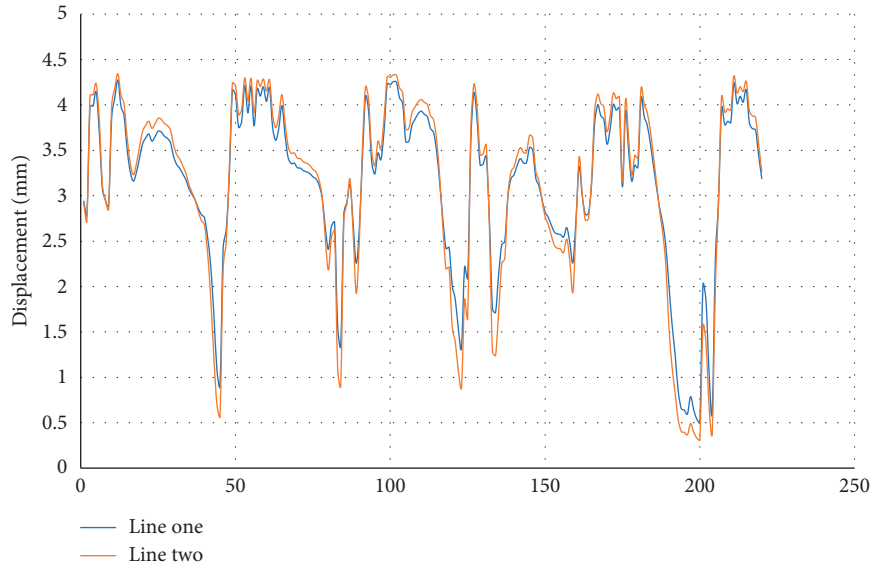


FIGURE 22: The contradiction between inversion displacement (blue) and water pressure component (orange).

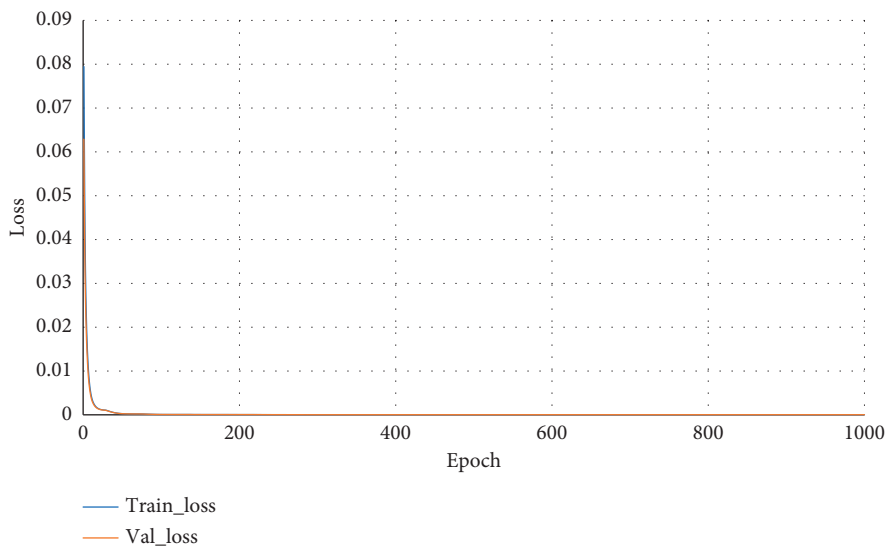


FIGURE 23: The iterative process of the model error of the engineering model.

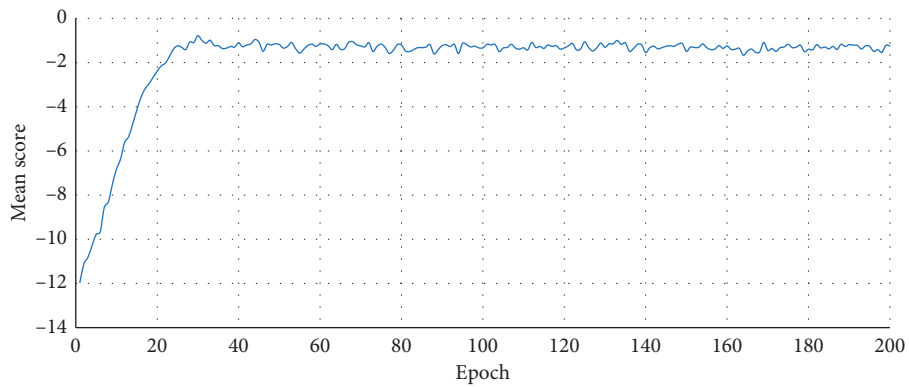


FIGURE 24: The iterative process of the reward in actual engineering.

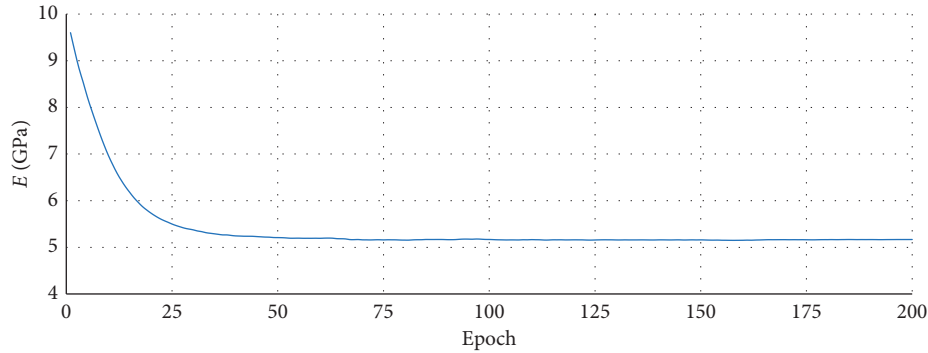


FIGURE 25: The iterative process of E in actual engineering.

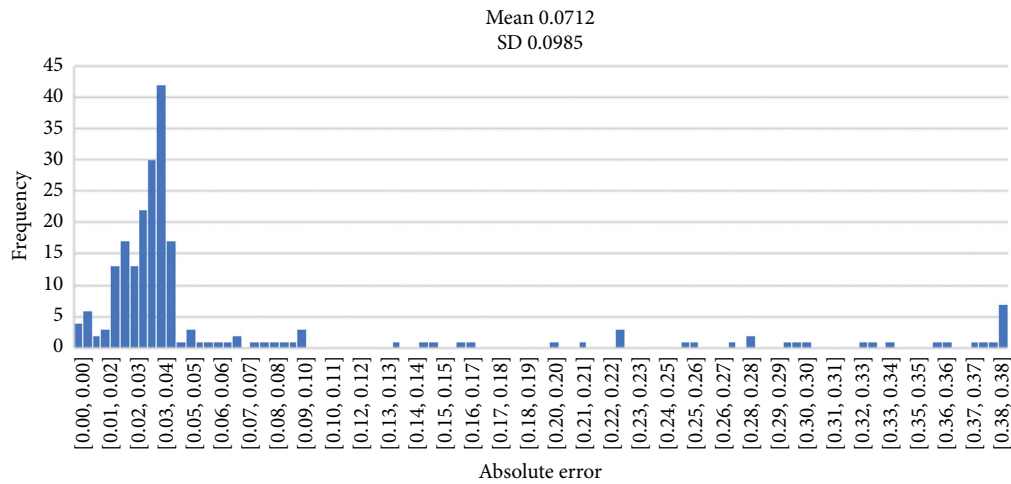


FIGURE 26: The distribution of the absolute error in the actual project.

indicating the inversion displacement series fitted well with the orange line representing the water pressure component, except a few points with obvious errors, which meant that the displacement values of two lines were close at the same water level on the whole. The latter was the distribution of the absolute error calculated by two displacement series, whose mean value was 0.0712 mm and standard deviation was 0.0985 mm. These errors were mainly concentrated on 0 mm~0.1 mm. A few values reached 0.3 mm~0.4 mm. The error level was low in the mass, which indicated that this method in the paper was suitable to be applied in actual engineering.

4. Conclusion

The accurate calculation of mechanical parameters in the engineering structure and foundation is dependent on detailed monitoring data of the structure and environment, reasonable constitutive model, and excellent searching algorithm. In this paper, the DNN model with a suitable structure replaced the finite element model and was embedded in the agent of the reinforcement algorithm to form the DQN, which was used to optimize the mechanical parameters in engineering in the global space. The conclusions are as follows:

- (1) According to the mechanical parameters and environmental loads of engineering, the corresponding DNN surrogate model was established to replace the finite element model. After the network model was verified, the mean relative error of predicting samples calculated by the DNN model with suitable hyperparameters and a regular training stage was lower than 1%, and the calculating efficiency of the DNN was much higher than that of the constitutive model, which indicated that it was advantageous for a reasonable DNN model to map the relation between the target displacement and the state of different mechanical parameters combining with variable environmental loads.
- (2) The DNQ algorithm improving the interactive mode between Env and Agent combined with the DNN surrogate model completed the inversion calculation of the structural mechanical parameter. After the improved framework calculated target values in examples, the maximum relative error and the minimum one of the elastic moduli after searching process were 1.29% and 0.18%, respectively. After the improved algorithm was used in actual engineering, the inversion displacement series fitted well with the water pressure component on the whole. Thus, the

DQN algorithm had a good effect in the inversion analysis of mechanical parameters in the hydraulic structure.

- (3) The method to express the displacement relation among different dam zones was introduced to ensure the relevance and coordination during the process of optimizing parameters from multizones. This improvement extended the FEM from a single region in case A to a double region in case B, providing a new path for inversion analysis in multiple structural zones.
- (4) The research focus is to combine the DNN surrogate model and the improved DQN algorithm and then apply the new model to the inversion calculation of mechanical parameters in the hydraulic structure and foundation with single or multiple zones. In future, the framework could be developed to improve the optimization method applied to inversion analysis in multiple monitoring points and several kinds of mechanical parameters.

Data Availability

The data used to support the findings of this study are available from the corresponding author upon request.

Conflicts of Interest

The authors declare no conflicts of interest.

Authors' Contributions

Wei Ji contributed to conceptualization, data curation, formal analysis, methodology, software, visualization, writing, reviewing, and editing. Xiaoqing Liu contributed to funding acquisition, investigation, project administration, supervision, writing, review, and editing. Huijun Qi contributed to conceptualization, methodology, software, visualization, writing, review, and editing. Chaoning Lin contributed to investigation and formal analysis. Xunnan Liu contributed to data curation and software. Tongchun Li contributed to resources and project administration.

Acknowledgments

This research was greatly supported by the National Key Research and Development Plan (no. 2018YFC0407102), the Fundamental Research Funds for the Central Universities (SN: B200202180), and the National Natural Science Foundation of China (SN: 52009035).

References

- [1] W. Ge, Z. Li, R. Y. Liang, W. Li, and Y. Cai, "Methodology for establishing risk criteria for dams in developing countries, case study of China," *Water Resources Management*, vol. 31, no. 13, pp. 4063–4074, 2017.
- [2] A. J. Wiley, "The St. Francis dam failure," *Journal-American Water Works Association*, vol. 20, no. 3, pp. 338–342, 1928.
- [3] P. Habib, "The Malpasset dam failure," *Engineering Geology*, vol. 24, pp. 295–329, 1987.
- [4] R. Ardito, G. Maier, and G. Massalongo, "Diagnostic analysis of concrete dams based on seasonal hydrostatic loading," *Engineering Structures*, vol. 30, no. 11, pp. 3176–3185, 2008.
- [5] R. Ardito, P. Bartalotta, L. Ceriani, and G. Maier, "Diagnostic inverse analysis of concrete dams with statical excitation," *Journal of the Mechanical Behavior of Materials*, vol. 15, no. 6, pp. 381–390, 2004.
- [6] C. Lin, T. Li, X. Liu et al., "A deformation separation method for gravity dam body and foundation based on the observed displacements," *Structural Control and Health Monitoring*, vol. 26, no. 2, Article ID e2304, 2019.
- [7] S. Chen, C. Gu, C. Lin et al., "Safety monitoring model of a super-high concrete dam by using RBF neural network coupled with kernel principal component analysis," *Mathematical Problems in Engineering*, vol. 2018, Article ID 1712653, 2018.
- [8] C. Lin, T. Li, S. Chen, X. Liu, C. Lin, and S. Liang, "Gaussian process regression-based forecasting model of dam deformation," *Neural Computing and Applications*, vol. 31, no. 12, pp. 8503–8518, 2019.
- [9] S. Chen, C. Gu, C. Lin et al., "Multi-kernel optimized relevance vector machine for probabilistic prediction of concrete dam displacement," *Engineering with Computers*, 2020.
- [10] C. Lin, T. Li, S. Chen et al., "Structural identification in long-term deformation characteristic of dam foundation using meta-heuristic optimization techniques," *Advances in Engineering Software*, vol. 148, Article ID 102870, 2020.
- [11] R. Perera, S.-E. Fang, and A. Ruiz, "Application of particle swarm optimization and genetic algorithms to multiobjective damage identification inverse problems with modelling errors," *Meccanica*, vol. 45, no. 5, pp. 723–734, 2010.
- [12] F. Kang, J. Li, and H. Li, "Artificial bee colony algorithm and pattern search hybridized for global optimization," *Applied Soft Computing*, vol. 13, no. 4, pp. 1781–1791, 2013.
- [13] F. Kang, J.-s. Li, and J.-j. Li, "System reliability analysis of slopes using least squares support vector machines with particle swarm optimization," *Neurocomputing*, vol. 209, pp. 46–56, 2016.
- [14] F. Kang, Q. Xu, and J. Li, "Slope reliability analysis using surrogate models via new support vector machines with swarm intelligence," *Applied Mathematical Modelling*, vol. 40, no. 11–12, pp. 6105–6120, 2016.
- [15] F. Kang and J. Li, "Artificial bee colony algorithm optimized support vector regression for system reliability analysis of slopes," *Journal of Computing in Civil Engineering*, vol. 30, no. 3, 2016.
- [16] S. Dou, J. Li, and F. Kang, "Parameter identification of concrete dams using swarm intelligence algorithm," *Engineering Computations*, vol. 34, no. 7, 2017.
- [17] R. Nian, J. Liu, and B. Huang, "A review on reinforcement learning: Introduction and applications in Industrial process control," *Computers & Chemical Engineering*, vol. 139, Article ID 106886, 2020.
- [18] R. Sutton and A. Barto, *Reinforcement Learning: An Introduction*, The MIT Press, Cambridge, Massachusetts, USA, 1998.
- [19] R. Sutton and A. Barto, *Reinforcement Learning: An Introduction*, The MIT Press, Cambridge, Massachusetts, USA, 2018.
- [20] R. Bellman, "A Markovian decision process," *Indiana University Mathematics Journal*, vol. 6, no. 4, pp. 679–684, 1957.

- [21] M. R. K. Mes and A. P. Rivera, "Approximate dynamic programming by practical examples," *Markov Decision Processes in Practice*, Springer, Cham, Switzerland, 2017, ISBN 978-3-319-47764-0.
- [22] D. Silver, G. Lever, N. Heess, T. Degris, D. Wierstra, and M. Riedmiller, "Deterministic policy gradient algorithms," in *Proceedings of the 31st International Conference on Machine Learning*, Beijing, China, 2014.
- [23] V. Mnih, "Playing atari with deep reinforcement learning," 2013, <http://arxiv.org/abs/1312.5602>.
- [24] V. Mnih, K. Kavukcuoglu, D. Silver et al., "Human-level control through deep reinforcement learning," *Nature*, vol. 518, pp. 529–533, 2015.
- [25] Z. Zhang, A. Chong, Y. Pan, C. Zhang, and K. P. Lam, "Whole building energy model for HVAC optimal control: a practical framework based on deep reinforcement learning," *Energy and Buildings*, vol. 199, pp. 472–490, 2019.
- [26] Z. Wang and T. Hong, "Reinforcement learning for building controls: the opportunities and challenges," *Applied Energy*, vol. 269, Article ID 115036, 2020.
- [27] Z. Bing, C. Lemke, and L. Cheng, "Energy-efficient and damage-recovery slithering gait design for a snake-like robot based on reinforcement learning and inverse reinforcement learning," *Neural Networks*, vol. 129, pp. 323–333, 2020.
- [28] I. Carlucho, M. De Paula, and G. Acosta, "An adaptive deep reinforcement learning approach for MIMO PID control of mobile robots," *ISA Transactions*, vol. 102, 2020.
- [29] J. García and D. Shafie, "Teaching a humanoid robot to walk faster through safe reinforcement learning," *Engineering Applications of Artificial Intelligence*, vol. 88, Article ID 103360, 2020.
- [30] F. Li, Q. Jiang, S. Zhang, M. Wei, and R. Song, "Robot skill acquisition in assembly process using deep reinforcement learning," *Neurocomputing*, vol. 345, pp. 92–102, 2019.
- [31] F. Chang, T. Chen, W. Su, and Q. Alsafasfeh, "Control of battery charging based on reinforcement learning and long short-term memory networks," *Computers & Electrical Engineering*, vol. 85, Article ID 106670, 2020.
- [32] Z. Wu, *Safety Monitoring Theory & its Application of Hydraulic Structures*, Higher Education Press, Beijing, China, 2003.
- [33] K. Hornik, M. Stinchcombe, H. White et al., "Multilayer feedforward networks are universal approximators," *Neural Networks*, vol. 2, no. 5, pp. 359–366, 1989.
- [34] C. J. C. H. Watkins and P. Dayan, "Q-learning," *Machine Learning*, vol. 8, no. 3-4, pp. 279–292, 1992.
- [35] J. Yang, J. Dai, C. Yao, S. Jiang, C. Zhou, and Q. Jiang, "Estimation of rock mass properties in excavation damage zones of rock slopes based on the Hoek-Brown criterion and acoustic testing," *International Journal of Rock Mechanics and Mining Sciences*, vol. 126, Article ID 104192, 2020.
- [36] Z. Z. Wang, Y. J. Jiang, and C. A. Zhu, "Seismic energy response and damage evolution of tunnel lining structures," *European Journal of Environmental and Civil Engineering*, vol. 23, no. 6, pp. 758–770, 2019.

Research Article

Evolution Laws for Frozen Wall Formation under Conditions of Sudden Seepage

Song Zhang ^{1,2,3}, Zurun Yue,^{1,2} Tiecheng Sun ^{1,2}, Yufu Han,³ Wei Gao,³ Tianfei Hu,^{1,2} and Yunxi Han^{1,2}

¹State Key Laboratory of Mechanical Behavior and System Safety of Traffic Engineering Structures, Shijiazhuang Tiedao University, Shijiazhuang, Hebei 050043, China

²School of Civil Engineering, Shijiazhuang Tiedao University, Shijiazhuang, Hebei 050043, China

³Beijing China Coal Mine Engineering Co Ltd., Beijing 100013, China

Correspondence should be addressed to Tiecheng Sun; sferetg@163.com

Received 11 September 2020; Revised 29 October 2020; Accepted 24 November 2020; Published 7 December 2020

Academic Editor: Yu-Sheng Shen

Copyright © 2020 Song Zhang et al. This is an open access article distributed under the Creative Commons Attribution License, which permits unrestricted use, distribution, and reproduction in any medium, provided the original work is properly cited.

Sudden seepage is a special working condition affecting artificial ground freezing (AGF) in many projects which results in significant differences within the temperature field. In order to study the characteristics of frozen walls influenced by water flow, a series of model tests were carried out at different seepage velocities. The model test results show that a frozen wall will change from symmetrical to eccentric as the cooling energy absorption of the soil and the brine return temperature increase. In model tests, when the seepage velocity was 0–30 m/d, the frozen wall was partially destroyed. When the seepage velocity exceeded 30 m/d, the frozen wall was completely destroyed. This study examines the expansion rate of the upstream and downstream freezing fronts, and the distribution law of the freezing temperature field, the average temperature change under different seepage speeds, and the bearing capacity of the freezing wall are analyzed. Research on these factors suggests that a frozen wall has a certain level of resistance to sudden seepage. When the flow velocity is small, the freezing effect will be strengthened. With an increase in the flow velocity, the freezing effect will gradually weaken. Based on these conclusions, the current study points out targeted solutions that should be adopted in cases of sudden seepage in a project.

1. Introduction

The artificial ground freezing (AGF) method is a soil reinforcement method applied in underground engineering. Initially, the method was used for subway construction in Swansea, South Wales, in 1862. Twenty years later, German mining engineering used the method in mine shaft construction [1]. Since then, AGF has also been applied for shaft sinking in coal mines [2]. In recent decades, the method has been widely used in the field of municipal engineering, especially in China.

AGF can enhance the strength of soils and reduce their permeability coefficients through the circulation of low-temperature liquid nitrogen or brine. Groundwater flow is one of the biggest threats to the AGF method [1, 2]. In response to this problem, a number of scholars have

conducted research on the best ways to mitigate the effects of groundwater [3–11]. Scholars have conducted numerical calculations, model tests, and other research methods to analyze the influence of seepage. The effect of conditions of seepage on the evolution of the freezing temperature field [3–5, 11] and the optimization of plans for freezing pipe layouts or freezing front analytical solutions [7, 10] have been successfully analyzed. While these aforementioned studies mainly analyze the working conditions of natural seepage in the soil, they pay less attention to groundwater seepage resulting from human activities which is present during the freezing process [9]. In particular, there is no groundwater flow before freezing, but seepage occurs during the freezing process.

In this paper, seepage is referred to as sudden seepage. In most working conditions, the groundwater velocity of

sudden seepage is basically constant. This study only discusses sudden seepage with a constant velocity, hereinafter referred to as sudden seepage. In the actual project, sudden seepage is mainly man-made. Various seepage causes are shown in Figure 1. Seepage 1 shows a freezing project for the shield arriving project. At the end of the active freezing period, the construction party began to dewater close to the project's frozen wall, causing sudden seepage (e.g., the first section of Zhengzhou Metro Line 2, China, and TBM arriving in a water diversion project in Hunan, China). Seepage 2 shows river water entering an annular space between a shield machine and the frozen wall along the soil fissure and causing sudden seepage in a TBM arriving project on Wuxi Metro Line 1, China [12]. Seepage 3 is caused by nearby engineering dewater during the freezing process of crossing passage [13, 14]. Seepage 4 is the space between the freezing pipe and tunnel segments which does not block in crossing passage and causes water leakage long-term. In the end, it caused a sudden seepage around the frozen wall (freezing project of the cross passage in Foshan Metro Line 2, China). Upon investigation of these cases, four of them can be seen to have occurred at the stage where the frozen wall was formed. Some projects were completed, and some projects caused engineering accidents. For the TBM arriving project of Wuxi Metro 2, sudden seepage which lasted 2~3 days destroyed the frozen wall. The work-well was submerged about 8.0 m. Therefore, sudden seepage cannot be ignored in an actual project as it might cause accidents or present safety risks.

2. Model Test

2.1. Similarity Laws. The effect of sudden seepage on the frozen wall is a problem characterized by the coupling of hydraulics and temperature. Therefore, a similarity law for the model test was determined before the model test was designed.

Based on dimensional analysis [15, 16], the temperature field governing equation in the dimensionless form is

$$F\left(\frac{at}{r^2}, \frac{L}{cT}, \frac{r_0}{r}, \frac{T_d}{T_0}, \frac{T_c}{T_0}\right) = 0, \quad (1)$$

where a is the thermal diffusivity of the soil, t denotes the time, r is the distance to the center of the freezing pipe, L is the latent heat of the soil, c is the specific heat of the soil, T denotes the temperature, r_0 is the outer radius of the freezing pipe, T_d is the freezing temperature of the soil, T_c is the temperature of the freezing pipe, and T_0 is the initial temperature of the soil.

The governing equation of water flow is [17]

$$F\left(R_e, \frac{vt}{d}\right) = 0, \quad (2)$$

$$R_e = \frac{\rho_w v d_s}{\mu_w}, \quad (3)$$

where v is the seepage velocity, d is the diameter of the freezing pipe, R_e is the Reynolds number, ρ_w is the density of water, d_s is the equivalent pore diameter of the soil, and μ_w is the dynamic viscosity of water.

Because model test sand was taken from a project in Guangzhou, the physical parameters of the soil were consistent with the prototype. Thus, the similarity ratio of the soil thermophysical parameters is

$$\frac{(C)_p}{(C)_m} = \frac{(L)_p}{(L)_m} = \frac{(T)_p}{(T)_m} = \frac{(\rho)_p}{(\rho)_m} = 1, \quad (4)$$

where subscripts m and p indicate the model and prototype, respectively.

The assumed geometric similarity ratio is C_l . The similarity ratio of temperature, time, and velocity of water can be expressed as

$$C_T \frac{(T)_p}{(T)_m} = \frac{(T_0)_p}{(T_0)_m} = \frac{(T_d)_p}{(T_d)_m} = \frac{(T_c)_p}{(T_c)_m} = 1, \quad (5)$$

$$C_t = \frac{(t)_p}{(t)_m} = C_l^2, \quad (6)$$

$$C_v = \frac{(v)_p}{(v)_m} = 1. \quad (7)$$

This model test defined the geometric similarity ratio to be 1/5. The key similarity ratios are listed in Table 1.

2.2. Model Soils. The soil used in the model test was collected from a construction site in Guangzhou, China. Its physical parameters are shown in Table 2. In this table, the density, moisture content, and porosity of the soil were obtained from a geological exploration engineering report. The remaining thermophysical parameters were measured using the remoulded soil made using special sample-making instruments. Soil was layered into a model tank, and a vibrating mechanism was then used to remould the soil and control compactness. Soil was collected using a ring knife for each layer (100 mm). Density and water content were made consistent with those of the undisturbed soil.

2.3. Model Test System. The model test apparatus consists of freezing, seepage, soil simulation, and measuring systems. Test system components are shown in Figure 2. In this figure, the blue dotted line represents the freezing system, while the green dotted line represents the seepage system, and the yellow dotted line represents the soil simulation system. Test equipment was installed inside a freezing station of a freezing project on Guangzhou Metro Line 11, as shown in Figure 3.

2.3.1. Freezing System. The freezing system was built over the refrigeration equipment of the freezing project. The project installed 38 YSLG16F refrigeration units (125 kW), 5

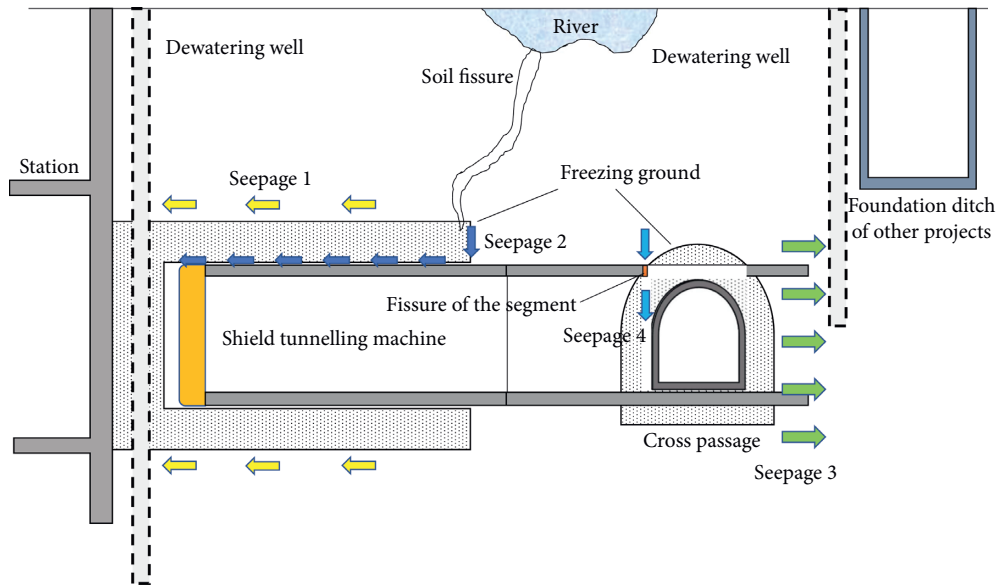


FIGURE 1: Types of sudden seepage.

TABLE 1: Similarity ratio of the model test.

Parameter	Geometric	Time	Temperature	Velocity of brine	Velocity of seepage
Similarity ratio	1/5	1/25	1	5/1	5/1

TABLE 2: Parameters of the soil.

Item	Density (kg·m ³)	Moisture content (%)	Porosity (%)	Thermal diffusivity (m ² /s)	Freezing temperature (°C)
Data	1.6 × 10 ³	25.3	31	0.77	-0.15

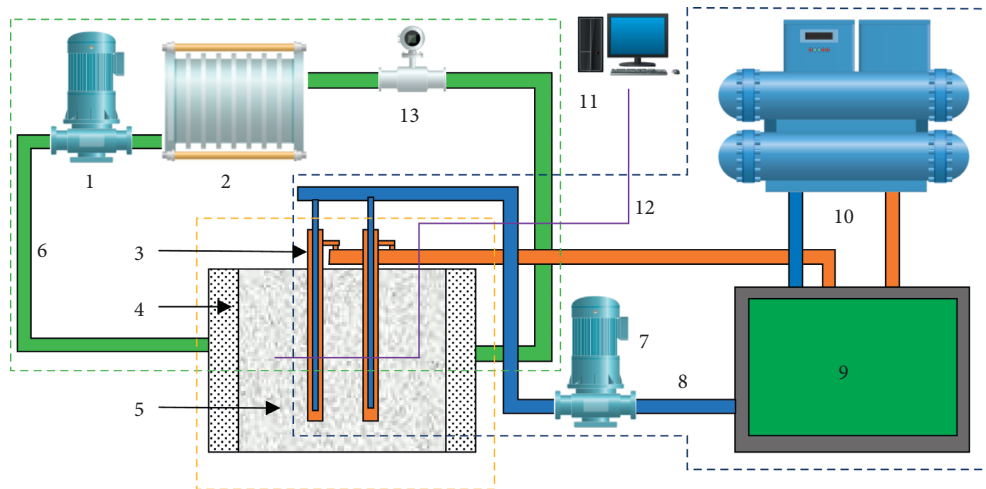


FIGURE 2: Model test system: 1, water circulation pump; 2, thermotank; 3, freezing pipe; 4, percolation filter layer; 5, soils; 6, water pipeline; 7, brine pump; 8, brine pipeline; 9, brine tank; 10, refrigerator; 11, data collection terminal; 12, temperature transmission cable; 13, electromagnetic flowmeter and mechanical flowmeter.

brine pumps (75 kW), and 2 brine tanks (10 m³). Test brine was channelled out using a separate pipeline from the main pipeline. An electromagnetic flowmeter was installed to measure the brine flow rate.

In this model test, the prototype freezing pipe was Φ108 × 8 mm, and the liquid supply pipe was Φ48 × 3 mm.

Based on the similarity ratio, the freezing pipe is Φ21.6 × 2 mm, and the liquid supply pipe is Φ9.6 × 1 mm. There were 8 freezing pipes in 2 rows in the model test system arranged. Every freezing pipe had a length of 1.2 m (1.0 m in the soils). Freezing tubes were arranged in a plum blossom shape at a distance of 140.0 mm to simulate the



FIGURE 3: Scene photo of the model test system: 1, soil simulation system; 2, water pump; 3, measuring system; 4, water pipeline.

actual engineering conditions of the 5.0 m field freezing pipes at an interval of 0.7 m. Each freezing pipe was equipped with an independent water inlet and return device to ensure that the brine inlet temperature was the same across the pipes.

2.3.2. Seepage System. The seepage system consists of a 400 W thermostatic tank of water, an 800 W clean water inline pump, an electromagnetic flowmeter (DN 40 mm), and mechanical flowmeter (DN40 mm). The two ends of each flowmeter were 20.0 cm long steel pipes to ensure the passage of water on either end of the flowmeter. A measuring cup was used for flow sampling in the open section near the thermostatic tank.

2.3.3. Soil Simulation System. The model test tank was $1.5 \times 1.5 \times 1.2$ m and made by an 8 mm steel plate. There were 5 water holes on the front and back of the tank. Each water hole's diameter was 50 mm, and they were spaced 20 cm apart. From bottom to top, the model test tank fillings were a 10.0 cm clay layer, an 80.0 cm test fine sand layer, another 10.0 cm clay layer, and a 5.0 cm cement mortar top layer. In order to buffer water flow and ensure the uniformity of seepage, 20 cm of medium-coarse gravel and sand were added to both sides of the seepage flow in and out of the model tank. 5 cm clay layers were set on the other sides to prevent seepage at the steel-soil interface. Details of the model tank are shown in Figure 4. In order to ensure the uniformity of leakage flow, three 1.5 inch diameter flow test tubes were set 10 cm below the temperature measurement plane with a spacing of 40 cm. The seepage system was run in a nonfreezing state, and the deviation of flow velocity in the 3 tubes was less than 5.6 %. Therefore, the seepage in the soils was considered uniform. In order to avoid heat exchange between the test soil and the outside air, a 5 cm insulation layer was placed around the model tank. A heat flux sensor was tied to the outside of the insulation layer. Throughout the test, the heat flux between the model tank and the outside air was less than 1 W/m^2 . Through infrared temperature measurement in the test process, the temperature difference between the test box and the surrounding environment was

found to be less than 1.0°C , indicating a good heat preservation effect.

2.3.4. Measuring System. In the model test, the DS18B20 sensor was chosen as a measuring point. The accuracy of the sensor was $\pm 0.06^\circ\text{C}$. All sensors used the CHL-RTU-V1 single-bus acquisition module to collect and transmit to an RS485/USB isolation converter before transmitting to a PC configuration system. The system connection is shown in Figure 5. All sensors were calibrated at four points of -20 , -10 , 0 , and 20°C before embedding. The calibration equipment was a JM222 handheld thermometer, as shown in Figure 6. The buried depth of temperature measurement points and the division of temperature measurement areas are shown in Figure 7. In the figure, area I is the upstream area, area II is the frozen central core area, area III is the single-row freezing area, and area IV is the downstream area. The location of T26 is the origin of the coordinates. X and Y coordinates are also shown.

2.4. Test Arrangement. The model test was divided into 5 sections listed in Table 3. In tests 2 to 5, seepage began after T18's temperature dropped to $-4.0 \sim -5.0^\circ\text{C}$. At that time, the frozen wall had formed, and the corresponding prototype was actively frozen in the late stages of the active freezing period. The frozen wall was approximated to meet design requirements. In this way, the working conditions of a formed frozen wall facing sudden seepage during the late stages of the active freezing period were simulated.

3. Results

3.1. Refrigeration Efficiency during the Freezing Period. The temperature of the return pipeline's outer surface during the active freezing period is shown in Figure 8. Data shown in this figure were tested using a DS18B20 temperature sensor attached to the return pipeline and covered with a thermal insulation layer. In all the tests, the inlet brine temperature was maintained at -28°C . In test 1, the return temperature was stable, while the return temperature rose obviously in the other 4 tests. The temperature increase in tests 2~5 occurred after seepage started 40~80 minutes in the test. The soil absorption cooling energy capacity was measured as

$$Q = q \cdot c \cdot \rho_b \cdot \Delta t, \quad (8)$$

where Q is the absorption cooling energy, kJ/h; q is the flux of brine, m^3/h ; Δt is the temperature difference, $^\circ\text{C}$, of brine between the inlet and the outlet; and ρ_b is the density of brine, kg/m^3 .

In tests 1~5, the brine inlet temperature and the length of the freezing pipe were the same. In Figure 8, soil absorption cooling capacity can be seen to have a linear relationship with the temperature. This indicates that, after seepage occurs, soil absorption cooling capacity will increase significantly, and brine return temperature will increase rapidly.

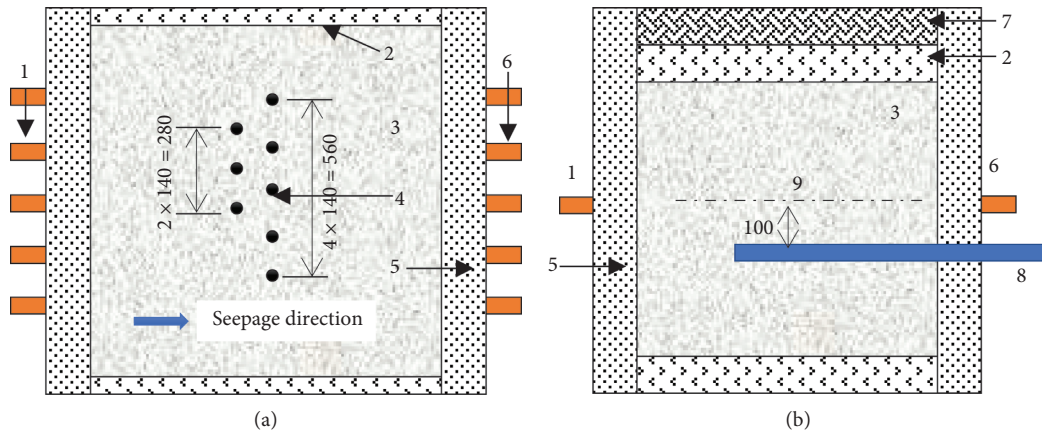


FIGURE 4: Design of the model tank. (a) Top view of the model tank. (b) Side view of the model tank. 1, seepage entrance; 2, clay layer; 3, soils; 4, freezing pipe; 5, percolation filter layer; 6, export of seepage; 7, cement mortar; 8, seepage velocity tube; 9, temperature measurement plane.

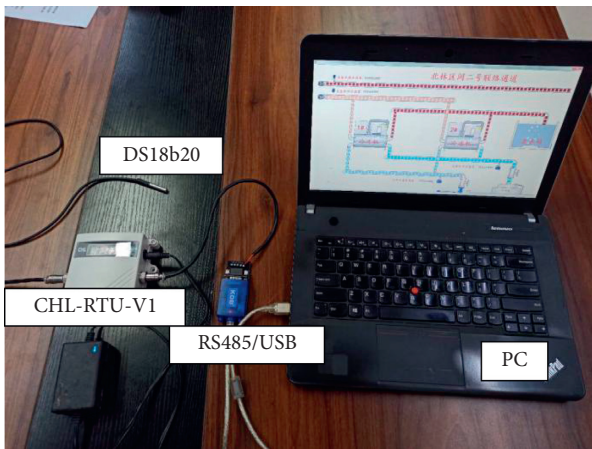


FIGURE 5: Schematic diagram of the temperature test system.



FIGURE 6: Sensor temperature calibration.

3.2. The Evolution Law of the Temperature Field. In the model test, every test took more than 600 minutes. The sudden seepage starting time was roughly between 170 and 190 min. Figure 9 shows the temperature field for tests 1, 3, and 5 at the 100th, 300th, and 600th minute. In this figure, the black dotted line is the reference line of the upstream and downstream frozen front. As shown in Figure 9, the frozen wall for each test was uniform before seepage ($t = 100$ min). Though the upstream frozen wall was still uniform, test 3's downstream frozen wall was thicker than tests 1 and 5 at $t = 300$ min. At the end of the tests ($t = 600$ min), the upstream frozen wall in test 1 was thicker than that of tests 3 and 5, while the downstream frozen wall in test 3 was obviously thicker than tests 1 and 5.

At $t = 300$ min during the active freezing period, the unfrozen zone in area III was 48 mm in test 1, 45 mm in test 3, and 64 mm in test 5. At $t = 600$ min during the active freezing period, there was no unfrozen zone in tests 1 and 3. However, the thickness of the unfrozen zone in test 5 was 13 mm.

Above all, the results of all the tests show that when the velocity of seepage is low, it does not affect the integrity of the frozen wall. With the increase of seepage velocity, this promoting effect will gradually disappear. The double-row pipe layout obviously outperformed the single-row pipe layout in terms of seepage conditions. It can quickly complete the freezing wall closure and maintain the expansion of the frozen wall under a certain seepage velocity.

Figure 10 is the time history curve of the main temperature measurement points for each test. As shown in the figure, upstream area I demonstrated a significant temperature drop under the influence of seepage. Area II showed a certain degree of freezing effect enhancement. The enhancement effect of test 2 was the most obvious. Area III showed similarity to area I in that the temperature drop slowed. Area IV showed significant acceleration in the temperature drop.

Comparing the temperature of each main measuring point, the temperature drop degree of T34 was about 6~10°C

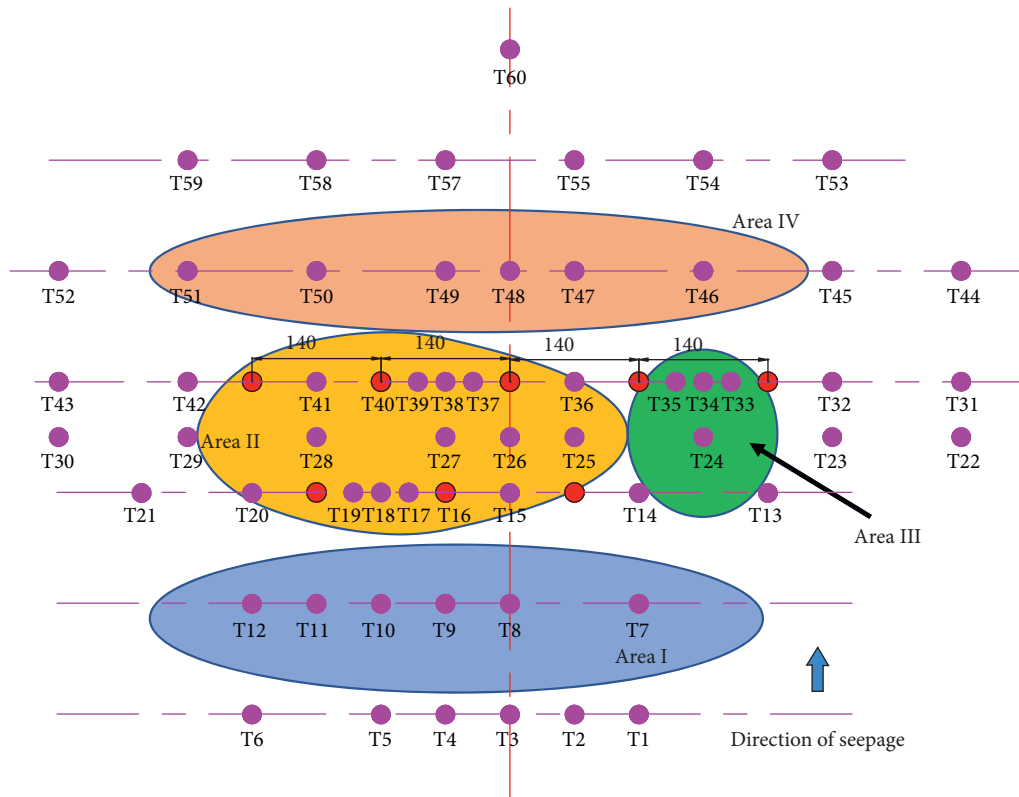


FIGURE 7: Layout of temperature measurement points.

TABLE 3: Velocity of the model test.

No.	Velocity of seepage (m/d)
1	0
2	8
3	16
4	20
5	30

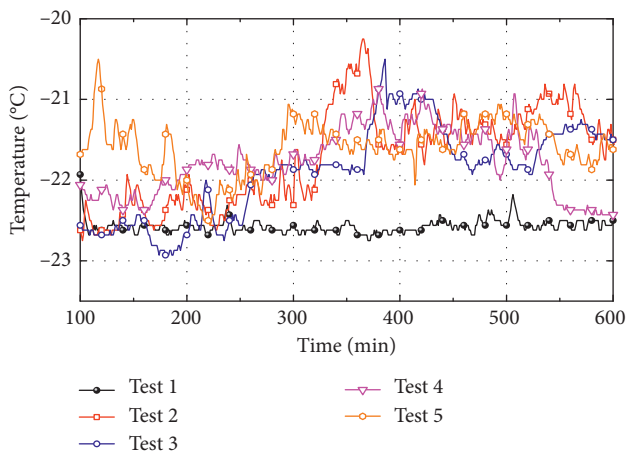


FIGURE 8: Temperature of the return pipeline's outer surface.

(from seepage start to 600 min), and T26 was about 12~14°C. This means that the double-rowed freezing pipes had a better cooling effect.

Figure 11 shows data extracted from each measuring point of the $X = 0$ mm section of tests 2~4, used to obtain the temperature distribution curve along the seepage direction. The cyan column is the projection position of the freezing pipes, and the black dashed line is the temperature distribution curve at the same time as the purple solid line under no seepage conditions.

Based on these data, the negative effects of seepage seem to exist mainly in area I, while the promotion effect is mainly concentrated in areas II and IV. When the flow velocity reaches 30 m/d, the freezing effect of each area was found to be weaker than or equal to the nonseepage test.

4. Discussion

According to the test results, under certain seepage velocity conditions, the frozen wall exhibits a state of weakening in the upstream and strengthening in the middle and downstream. However, the freezing curtain should be regarded as a whole in order to evaluate its carrying capacity. Therefore, it is necessary to further analyze the freezing effect through the macroindicators of freezing curtain thickness and average temperature.

4.1. The Thickness and Expansion Rate of the Frozen Wall.

As the result shows, the soil between the two rows of freezing pipes is in a frozen state, so the thickness of the freezing wall mainly depends on the position of the upstream and downstream freezing fronts.

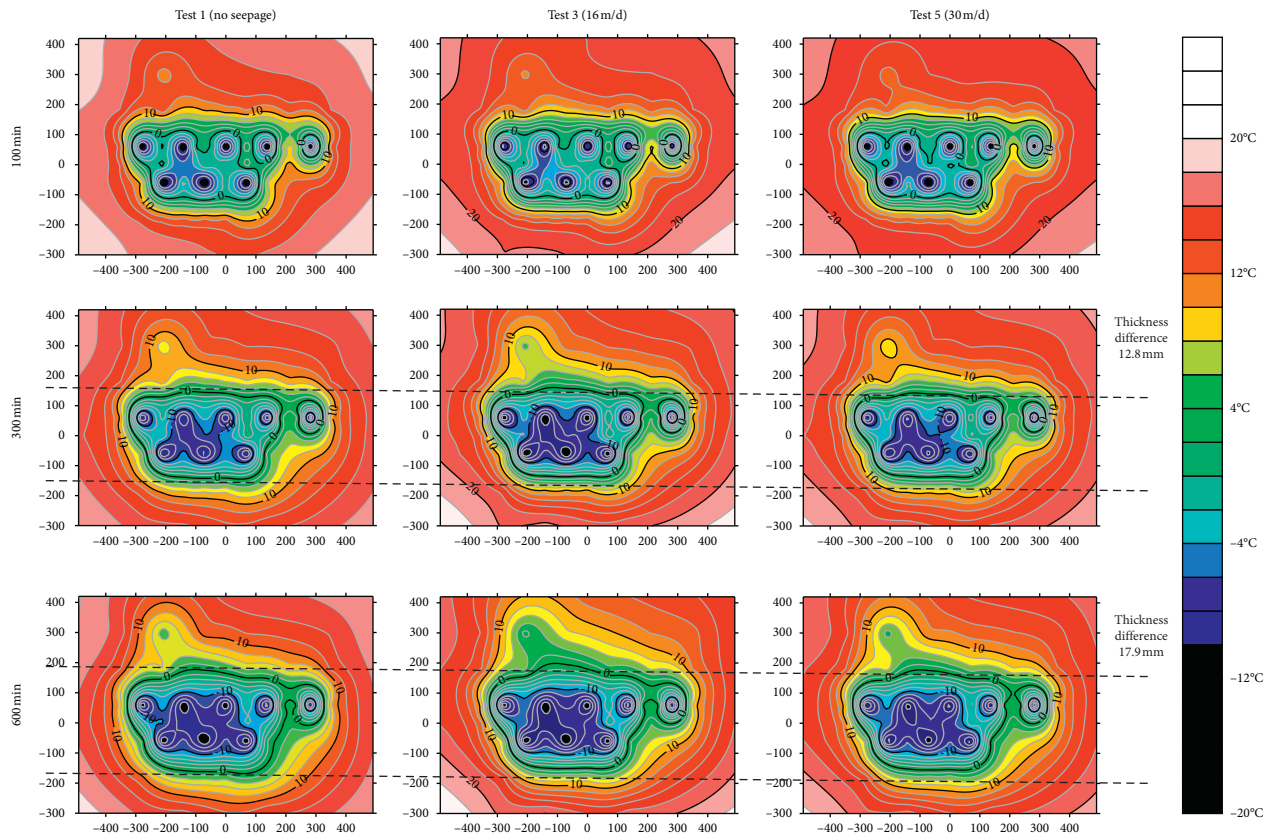


FIGURE 9: Temperature field at different times.

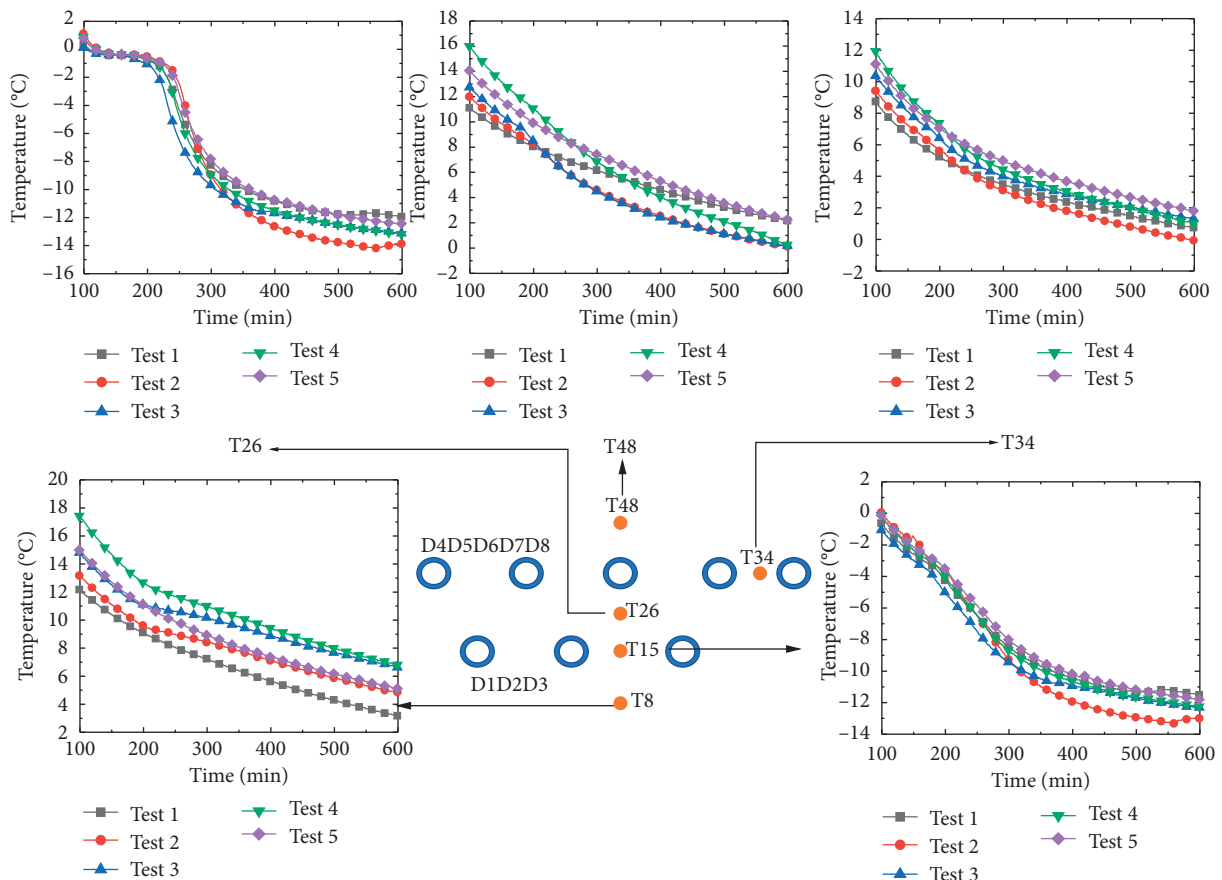


FIGURE 10: Time history curve for the main temperature measurement points.

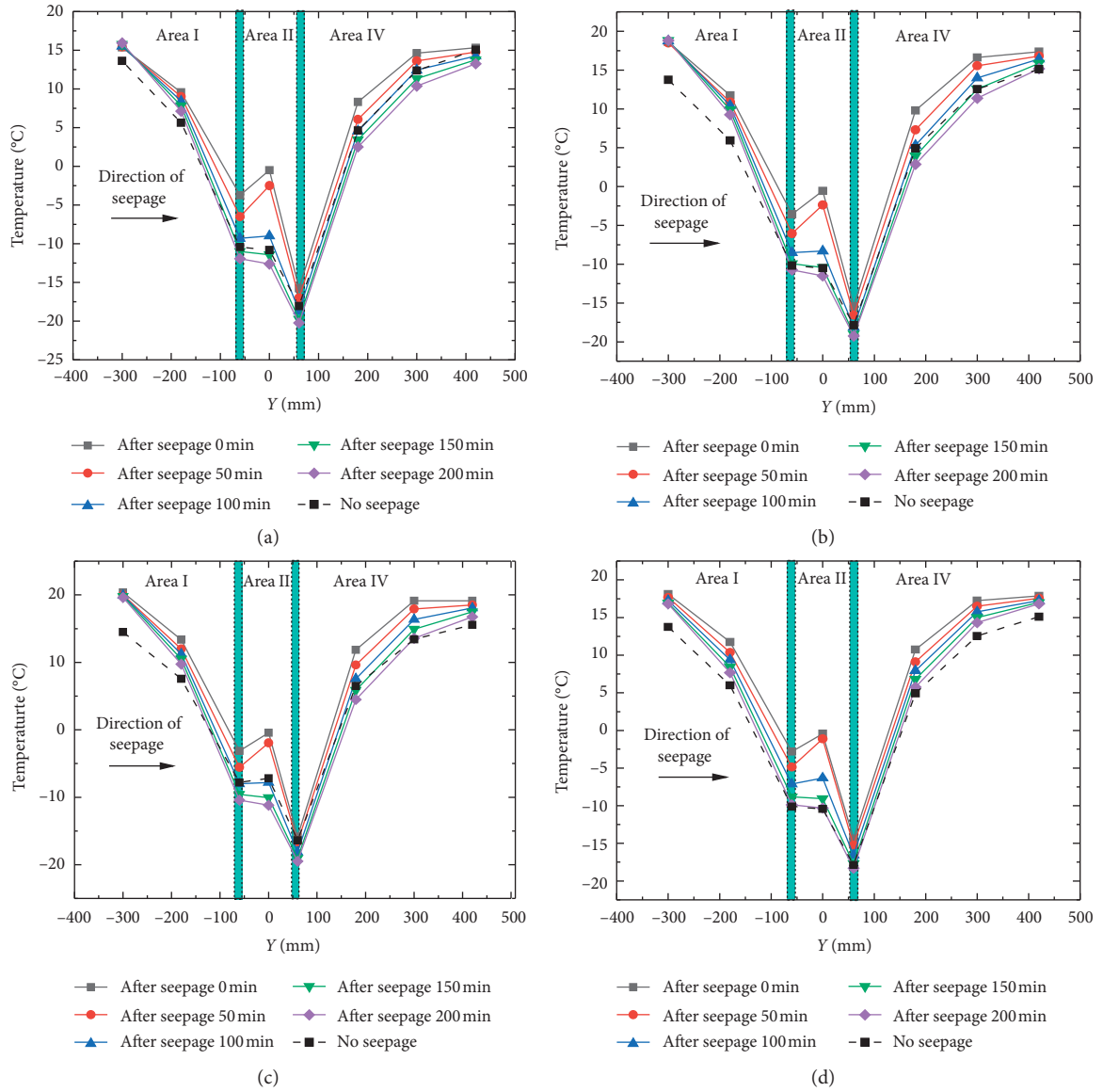


FIGURE 11: Temperature distribution in the $X=0$ mm section. (a) Test 2. (b) Test 3. (c) Test 4. (d) Test 5.

The upstream freezing front position was calculated using T9 and D2 temperature data. The downstream freezing front position was calculated using data from T48 and D6. The calculation formula uses Bahorkin's analytical solution [2]:

$$m_1(x, y) = \frac{1}{2} \ln \left[2 \left(ch \frac{2\pi}{l} y - \cos \frac{2\pi}{l} x \right) \right], \quad (9)$$

$$\xi = \frac{l}{\pi} \frac{t(x, y) \ln(l/2\pi r_0) + t_{CT} m_1(x, y)}{t_{CT} - t(x, y)}, \quad (10)$$

where x and y are the location of the local coordinate system where the temperature measurement point is used in the calculation. The coordinate system takes the center of the freezing pipe closest to the temperature measurement point as the coordinate origin. The freezing axis is the x -direction, and the unit is m . l is the freezing hole spacing in meters,

$t(x, y)$ is the temperature at the temperature measurement point in $^{\circ}\text{C}$, and t_{ct} is the out surface temperature of the freezing pipe in $^{\circ}\text{C}$.

Since Bahorkin's solution is a calculation scheme, it can be used after closure of the freezing curtain. The thickness of the frozen wall was only calculated from the 100th to 700th minute of the test. The results are shown in Figure 12. As shown in the figure, in the states of no flow velocity and 8 m/d flow velocity, the thickness of the upstream and downstream frozen walls both increased logarithmically, and the growth pattern was basically the same. When the flow velocity reached 16 m/d, the growth trend of the upstream and downstream frozen wall thickness developed and differentiated. The upstream frozen wall's growth slowed down slightly, while the downstream frozen wall's thickness increased rapidly. When the flow velocity reached 20 m/d, the growth effect of the downstream freezing wall began to

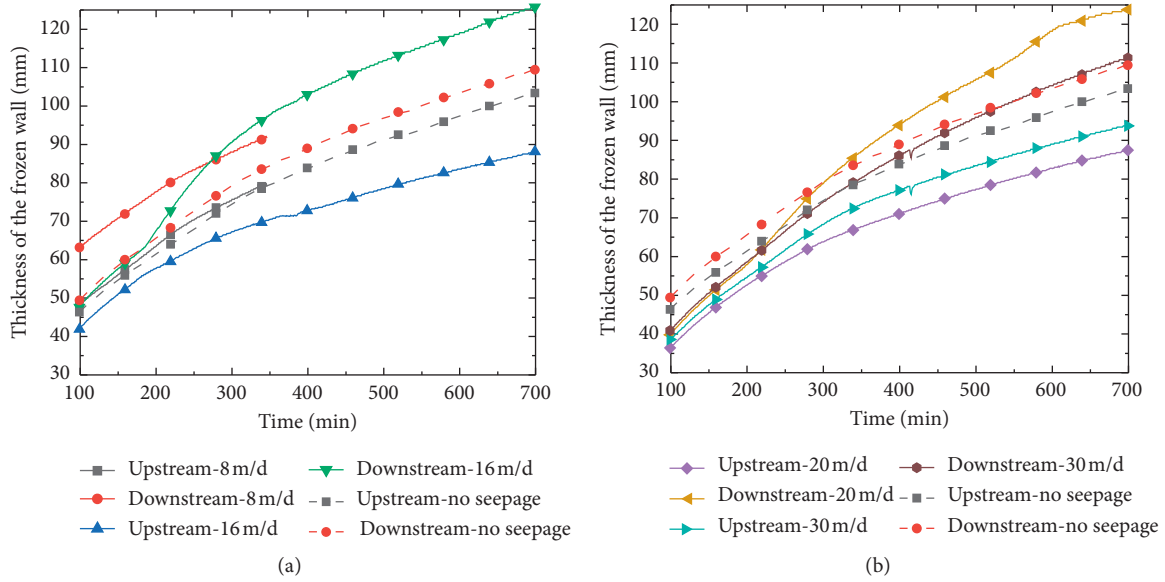


FIGURE 12: Thickness of the frozen wall in upstream and downstream. (a) Tests 1, 2, and 3. (b) Tests 1, 4, and 5.

weaken, but that of the upstream wall was basically the same. When the flow velocity reached 30 m/d, the thickness increase effect of the downstream frozen wall caused by seepage had basically disappeared, while that of the upstream remained basically the same.

Derivation of the position curve for the freezing front in each test with respect to time and the expansion rate of the frozen curtain in the upstream and downstream directions are shown in Figure 13. After seepage occurred, the expansion rate of the upstream freezing wall decreased, but the decrease was not large, and the difference was more or less negligible in the later stages of the test. The expansion rate of the downstream frozen wall demonstrated a rapid growth stage (cyan in Figure 13) under seepage rate conditions of 16 m/d and 20 m/d. The peak appearance time of the growth stage slowed down with the increase of seepage velocity. Following the growth stage, the expansion rate under seepage was the same as it was under nonseepage conditions. This indicates seepage from upstream to downstream will transfer a lot of cooling energy. Thus, a rapid change stage is formed in the period of time after seepage. After this stage, the expansion rate of the frozen wall will slow down to match that of the wall when no seepage conditions are present.

4.2. The Average Temperature of the Frozen Wall. In order to analyze the distribution of the temperature field under different seepage conditions, the freezing wall temperature is divided into four temperature ranges: 0~−5°C, −5~−10°C, −10~−15°C, and below −15°C. The area of each temperature range was then calculated under different conditions. The area calculation method was used to refine measurement point data to 1000 × 560 by the kriging method [18]. These refined data were then used to draw an isotherm map to calculate the area of each temperature interval. The calculation results are shown in Figure 14. As shown in the

figure, when the flow rate was low (8 m/d), the area of 0~−5°C remained basically unchanged, the area of below −15°C increased rapidly, and the area of −5~−15°C weakened. Therefore, the whole frozen wall increased to a certain extent. When the flow rate reached the range of 16~20 m/d, the area within 0~−5°C and the area below −15°C obviously decreased, while the area within the −5~−15°C temperature range decreased slightly. When the flow rate reached 30 m/d, the area within the 0~−5°C temperature range continued to decrease slightly, while the area within the −5~−15°C range rose slightly, and the area below −15°C dropped rapidly.

Since the temperature points obtained by the kriging interpolation method were evenly distributed, the average temperature of the freezing wall was obtained by calculating the average temperature of all the points lower than 0°C. The average temperature and the area of the frozen wall are shown in Figure 15. Assuming that the area of the frozen wall under nonseepage conditions was 100%, the area of the frozen wall under different conditions for tests 1–5 was calculated to be 110.4%, 101.7%, 101.5%, and 97.1%, respectively. These data indicate how low-velocity seepage can promote frozen wall expansion.

4.3. Frozen Wall Bearing Capacity under Seepage. The frozen wall was defined as a line elastomer in accordance with the construction design code in China [19]. The bending modulus EI is generally used to evaluate its bearing capacity. It can be calculated as

$$EI = a \cdot \bar{T} \cdot \frac{bh^3}{12}, \quad (11)$$

where a is the empirical coefficient, which is the ratio of elastic modulus to average temperature, mainly related to parameters such as soil quality, moisture content, and porosity; \bar{T} is the average temperature of the frozen wall in °C; b

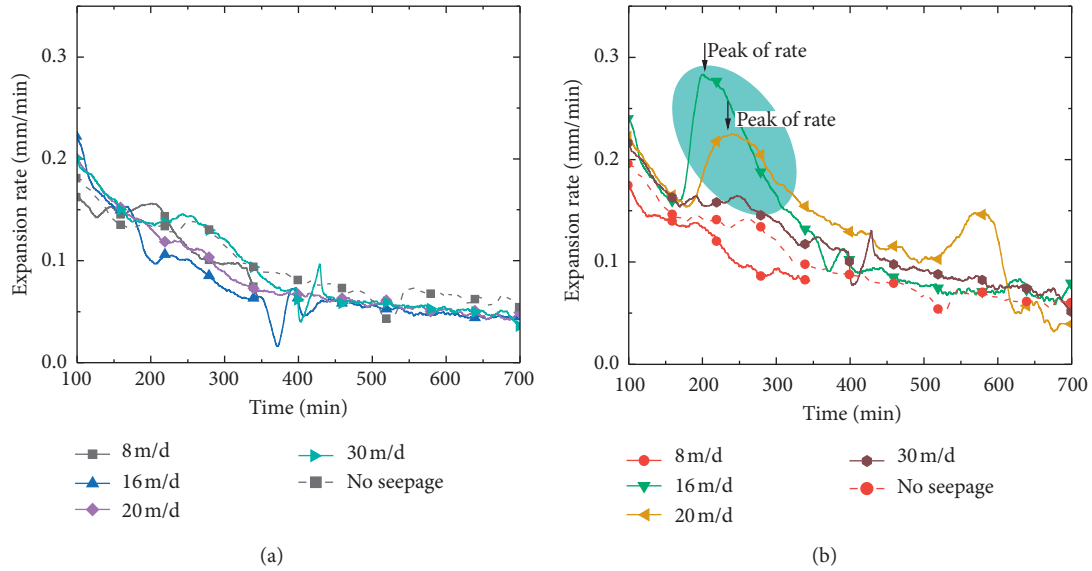


FIGURE 13: Expansion of the frozen wall in (a) upstream and (b) downstream.

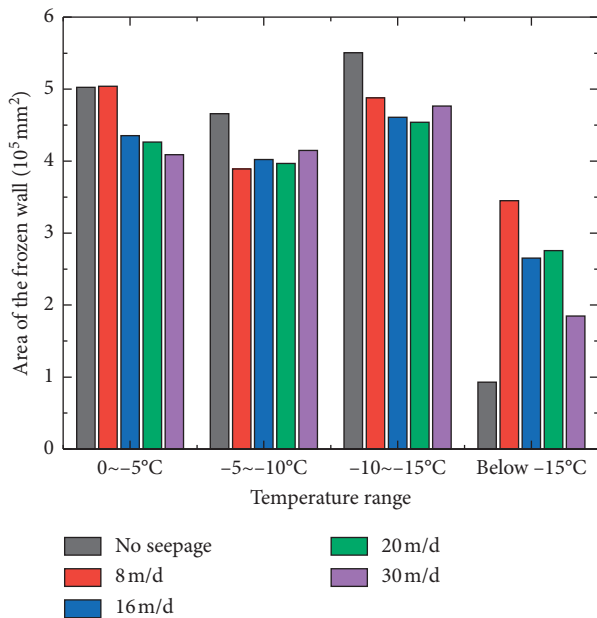


FIGURE 14: Area of the temperature stage.

is the width of the frozen wall, generally taken to be 1.0 m in conventional calculations; and h is the thickness of the frozen wall in meters. The positional relationship of each parameter is shown in Figure 16.

Because the elastic modulus of the frozen soil has a linear relationship with the average temperature [20], a is a fixed value, and b is also taken as a fixed value in the calculation. The damage evaluation coefficient of the frozen wall under the action of the flow field at any time can be written as

$$\eta = \frac{EI|_{\text{seepage}}}{EI|_{\text{no seepage}}} = \frac{\bar{T}h^3|_{\text{seepage}}}{\bar{T}h^3|_{\text{no seepage}}}, \quad (12)$$

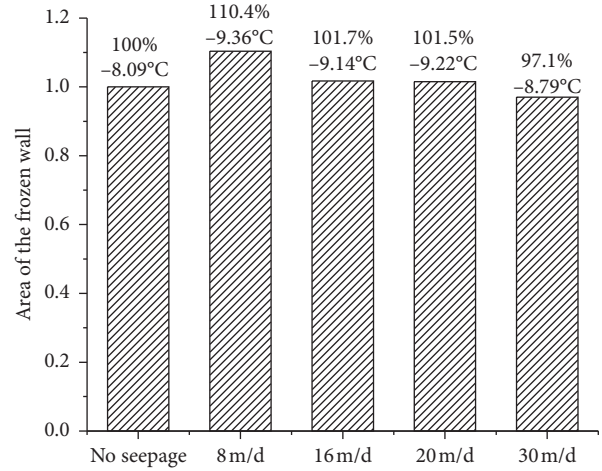


FIGURE 15: Average temperature in different tests.

where η is the freezing damage coefficient, and its unit is 1. When the unit is less than 1, the soil is in a damage stage. When it is greater than 1, the soil is in a strengthening state.

The damage coefficient of the bearing capacity at different seepage rates during active freezing at $t = 400$ min, $t = 500$ min, and $t = 600$ min was calculated. The thickness of the frozen wall was selected as the section thickness of $x = 0$ mm. The calculation results are listed in Table 4. The damage coefficient curve is plotted in Figure 17.

When the flow rate is low, the seepage has a certain enhancement effect on the bearing capacity of the frozen wall, but with the increase of the seepage velocity, the enhancement effect gradually weakens and enters the stage of damage. Under similar seepage rate conditions, the damage evaluation coefficient showed an increasing trend with the extension of freezing time, indicating that the damage caused by the flow field to the frozen wall was most obvious in the early stages of freezing and that, with the

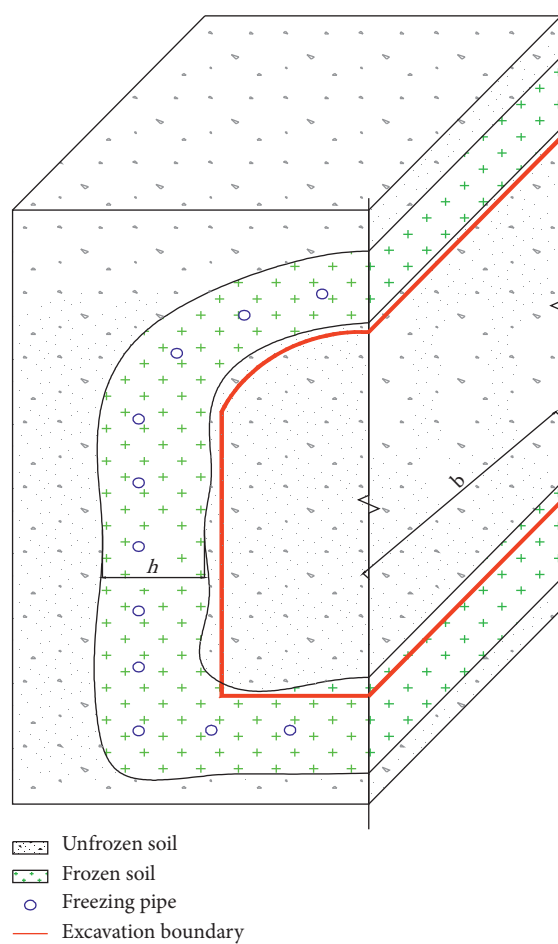


FIGURE 16: Schematic diagram of bending modulus calculation parameters.

TABLE 4: Damage coefficient.

Seepage velocity (m/d)	0	8	16	20	30	Time (min)
h (mm)	295.89	295.89	286	276.2	276.2	400
T (°C)	-8.51	-10	-9.4	-8.8	-8.8	
EI	2.20×10^8	2.59×10^8	2.2×10^8	1.85×10^8	1.85×10^8	
η	1	1.175088	0.997483	0.841072	0.841072	500
h (mm)	295.89	315.6	305.8	295.9	286	
T (°C)	-9.4	-10.4	-9.6	-9.8	-9.5	
EI	2.43×10^8	3.27×10^8	2.75×10^8	2.54×10^8	2.22×10^8	600
η	1	1.342535	1.127366	1.042659	0.912647	
h (mm)	325	337	328	326	319	
T (°C)	-9.17	-10.72	-10.3	-10.3	-9.59	600
EI	3.14×10^8	4.1×10^8	3.63×10^8	3.57×10^8	3.11×10^8	
η	1	1.303362	1.154621	1.133628	0.988943	

extension of freezing time, such damage could be repaired to a certain extent.

All in all, it can be seen that low-rate seepage can promote the bearing capacity of the frozen wall. In the actual project, if sudden seepage occurs, it must take a series of

measures to reduce or remove the seepage such as grouting, reducing the temperature of brine, or increasing the brine flow. However, such treatments would greatly increase the cost of a project. Therefore, identifying a critical flow rate (30 m/d in this test) through model testing to distinguish

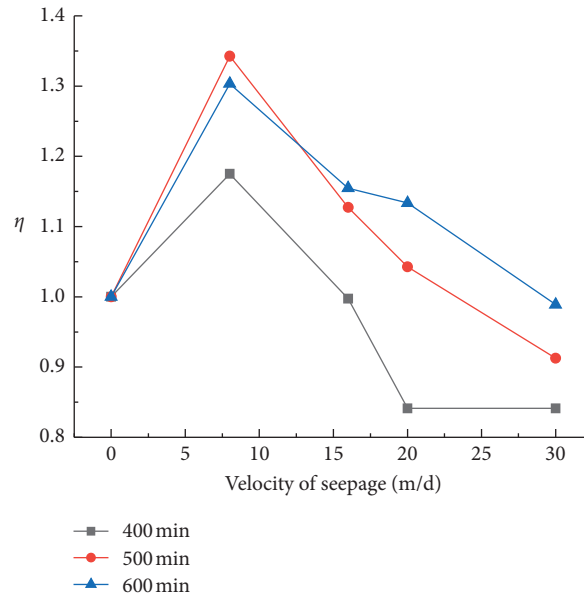


FIGURE 17: The relation curve between the damage coefficient and the seepage velocity.

seepage conditions can effectively reduce engineering treatment time and cost.

5. Conclusion

In this paper, the evolution laws of frozen wall formation under the influence of sudden seepage are analyzed through a series of model tests. The spatial-temporal variation characteristics of the thickness and average temperature of the frozen wall in relation to the flow field and the bearing capacity damage after the occurrence of seepage are analyzed. Based on the results, the following conclusions can be drawn:

- (1) The frozen wall changed rapidly when seepage occurred. When the velocity of flow was not enough to destroy the frozen wall, a thin upstream and thick downstream eccentric frozen wall was formed. Moreover, the antiseepage properties of double-rowed pipes obviously outperformed those of the single-rowed pipes during freezing.
- (2) According to the brine return temperature, the cold efficiency of all of the project's five tests was found to be consistent in the nonseepage stage. Following the start of seepage, brine return temperature increased rapidly.
- (3) When the seepage velocity was 0~30 m/d, the seepage caused obvious damage to the upper reaches of the frozen wall, while the wall was strengthened in the middle and lower reaches to a small extent. When the flow velocity was more than 30 m/d, the frozen wall was completely damaged.
- (4) After seepage occurred, the downstream frozen wall demonstrated a rapid expansion stage before the expansion rate of the frozen wall gradually

approached a normal state. This stage was the most important stage for conversion from a symmetrically frozen wall to an eccentrically frozen wall. After the rapid expansion stage, the eccentrically frozen wall will take shape, and this time period thus presents the riskiest stage in the excavation process.

- (5) After seepage occurred, the temperature field of the frozen wall indicated that the high-temperature permafrost area (0~-15°C) relatively reduced, while the low-temperature permafrost area (-15~-30°C) relatively increased. The average temperature of the frozen wall first increased and then decreased with the increase of the seepage velocity.
- (6) Based on the analysis of the damage coefficient, it can be concluded that the bearing capacity of the frozen wall increases first and then decreases. At a seepage rate of 8 m/d, the bearing capacity of the frozen wall can thus be expected to increase significantly. It is proposed that if low-flow velocity seepage occurs during construction, it does not need to extend the freezing time.

Data Availability

The data used to support the findings of this study are included within the article.

Conflicts of Interest

The authors declare no conflicts of interest.

Acknowledgments

The scientific research program was supported by the State Key Laboratory of Mechanical Behavior and System Safety of Traffic Engineering Structures, Shijiazhuang Tiedao

University (ZZ2020-07) and the Special Funds for Scientific and Technological Innovation of Tiandi Science & Technology Co., Ltd. (2019-TD-QN009 and 2019-TD-MS007).

References

- [1] M. A. Alzoubi, M. Xu, F. P. Hassani et al., "Artificial ground freezing: a review of thermal and hydraulic aspects," *Tunnelling and Underground Space Technology*, vol. 104, Article ID 103534, 2016.
- [2] X.-D. Hu, T. Fang, and Y.-G. Han, "Mathematical solution of steady-state temperature field of circular frozen wall by single-circle-piped freezing," *Cold Regions Science and Technology*, vol. 148, pp. 96–103, 2018.
- [3] P. Erich, S. Anton, and G. Anagnostou, "Modelling of ground freezing in tunnelling," ITA and World Tunnel Congress, Prague, 2007.
- [4] P. Erich, S. Anton, and G. Anagnostou, "Large-scale laboratory tests on artificial ground freezing under seepage-flow conditions," *Geotechnique*, vol. 3, no. 62, pp. 227–241, 2012.
- [5] P. Erich, S. Papakonstantinou, and G. Anagnostou, "Numerical interpretation of temperature distributions from three ground freezing applications in urban tunnelling," *Tunnelling and Underground Space Technology*, vol. 28, pp. 57–69, 2012.
- [6] M. Vitel, A. Rouabhi, M. Tijani, and F. Guérin, "Modeling heat and mass transfer during ground freezing subjected to high seepage velocities," *Computers and Geotechnics*, vol. 73, pp. 1–15, 2016.
- [7] S. Huang, Y. Guo, Y. Liu, L. Ke, G. Liu, and C. chen, "Study on the influence of water flow on temperature around freeze pipes and its distribution optimization during artificial ground freezing," *Applied Thermal Engineering*, vol. 135, pp. 435–445, 2018.
- [8] M. A. Alzoubi and A. P. Sasmito, "Development and validation of enthalpy-porosity method for artificial ground freezing under seepage conditions," *Fluids Engineering Division Summer Meeting*, vol. 51562, 2018.
- [9] S. Zhang, Z. R. Yue, T. C. Sun et al., "Evolution of ground freezing temperature field under sudden seepage with stable flow rate and discriminate method of seepage," *Journal of China Coal Society*, vol. 51, 2018.
- [10] R. L. Shan, J. W. Liu, G. J. Chai et al., "Experimental study on the expansion law of local horizontal frozen body under seepage," *Journal of China Coal Society*, vol. 44, pp. 526–534, 2019.
- [11] W. J. Liu, J. J. Zhang, R. L. Shan et al., "Experiments on temperature field of multi-row-pipe partial horizontal freezing body in Beijing sand-gravel stratum under seepage," *Rock and Soil Mechanics*, vol. 44, no. 9, pp. 3425–3434, 2019.
- [12] J. Y. Yu, "Coping with water gushing in shield arrival," *Tunnel Construction*, vol. 33, no. 4, pp. 315–318, 2013.
- [13] F. Z. Li, F. R. Luo, Y. F. Han et al., "Cause analysis and countermeasure research for unclosed freezing wall of subway contact passage under complex conditions," *Industrial Construction*, vol. 45, no. 11, pp. 187–190, 2015.
- [14] S. Ao, "Longitudinal temperature measuring Technology applied to ground freezing construction of Metro connecting passage," *Mine Construction Technology*, vol. 38, no. 3, pp. 54–58, 2017.
- [15] H. Cai, S. Li, Z. Yao, and H. Cheng, "Model test and numerical simulation of frost heave during twin-tunnel construction using artificial ground-freezing technique," *Computers and Geotechnics*, vol. 115, 2019.
- [16] J. Liu, B. Ma, and Y. Cheng, "Design of the Gongbei tunnel using a very large cross-section pipe-roof and soil freezing method," *Tunnelling and Underground Space Technology*, vol. 72, pp. 28–40, 2018.
- [17] F. Z. Li, H. Ding, and X. Z. Zhang, "Model test research of formation law of double-row-pipe freezing wall in water rich sand layer under seepage," *Chinese Journal of Rock Mechanics and Engineering*, vol. 38, no. 2, pp. 386–395, 1975.
- [18] S. B. Bai, H. Chen, and J. Wang, "An introduction to nine gridding methods and their application in surfer version 7.0," *Computing Techniques for Geophysical and Geochemical Exploration*, vol. 24, no. 2, pp. 157–163, 2002.
- [19] F. Z. Li, "Application and prospect of freezing Technology in municipal engineering," *Mine Construction Technology*, vol. 38, no. 4, pp. 55–60, 2017.
- [20] Y. Q. Zhang, P. Yang, and J. Y. Wang, "Effect of water content and strain rate on the strength characteristics of frozen silty clay," *Journal of Zhengzhou University(Engineering Science)*, vol. 41, no. 3, pp. 79–84, 2020.

Research Article

Application of PS-INSAR Technique on Health Diagnosis of the Deformable Body on Front Slope beside Mountain Tunnel Portal

Jiixin Jia 

Survey and Design Company of Sichuan Road & Bridge (Group) Co.,Ltd., Chengdu, China

Correspondence should be addressed to Jiixin Jia; 157432187@qq.com

Received 18 September 2020; Revised 10 October 2020; Accepted 4 November 2020; Published 29 November 2020

Academic Editor: Zheng-zheng Wang

Copyright © 2020 Jiixin Jia. This is an open access article distributed under the Creative Commons Attribution License, which permits unrestricted use, distribution, and reproduction in any medium, provided the original work is properly cited.

When tunnel construction develops to surrounding mountainous areas, tunnel portal presents the topographic characteristics of “high, steep, and slant” and geological characteristics of kinds of hugely thick colluvial or residual slope, and the health condition of the deformable body on front slope beside tunnel portal has a great influence on tunnel construction and operation. Tunnel portal has suffered from many disasters, and it is urgent to study and solve the engineering problem on how to diagnose the health condition of front slope beside tunnel portal quickly and accurately. Based on the tunnel of Jianquan village, this paper uses PS-INSAR technique for the first time to analyze and diagnose the health condition of the deformable body on front slope beside mountain tunnel portal at the construction stage and operation stage, so as to provide early warnings to unstable deformable body at tunnel portal and provide strong bases for the treatment of unstable deformable body. Therefore, PS-INSAR technique promotes the health monitoring method for deformable body on front slope beside mountain tunnel portal to a higher level.

1. Introduction

Geological problems of tunnel portal primarily include weak foundation of tunnel portal, severe bias of tunnel portal, hugely thick overburden of tunnel portal, and instability of front slope beside tunnel portal [1]. Early detection and early treatment are basic principles for the treatment of surface deformation and even landslide on front slope beside mountain tunnel portal [2]. There are two main types of health monitoring method for deformable body on front slope beside mountain tunnel portal: the first type is adopting a variety of sensor monitoring means on the ground, e.g., vertical slant monitoring hole [3], external vertical monitoring pier, vertical displacement monitoring, multipoint displacement meter, and GNSS, to monitor internal deformation, external deformation, and seepage pressure of cracking body and stress of supporting body, etc. [4, 5]. These means have advantages of high precision and reliable results, and their disadvantages are spending too much manpower and material resources, high cost, sparse measuring points, long interval before repetition measuring, cannot effectively guaranteeing the safety of monitoring

personnel, small monitoring scope, and severe environment influence [6]. Besides, most side slopes of highways locate in remote mountains and canyons, employees have large fluidity and uneven professional quality, and they are prone to have strong thinking inertia and fluky mind. Their safety awareness is weak, and then the accuracy and timeliness of monitoring data cannot be guaranteed due to measurement difficulty and serious influence of human factors [7]. The second type is adopting traditional surface deformation monitoring means such as GPS which have high precision, but they have low spatial density and cannot provide surface deformation information of the whole area [8, 9].

Differential interferometric synthetic aperture radar technique (INSAR technique) is a kind of space-to-earth observation technique [10]. In recent years, INSAR technique is in wide application stage of business, such as surface settlement observation and analysis of the southwest of Tianjin based on PS-INSAR technique, landslide seismic damage observation and analysis of Zhangmu Port of Tibet based on INSAR technique, geological disaster monitoring based on applying INSAR technique in Beidou satellite [11], and the application of INSAR technique in research of

western coal mine goaf of Guizhou [12]. At present, INSAR technique has also made great progress in the field of surface deformation monitoring on highways. For example, PS-INSAR technique was used to extract the settlement speed figure and settlement profile along Beijing-Shanghai highway and successfully identified 9 settlement centers along the highway [13]. And the section of Kunmo highway in Yunnan from Kunming to Yuxi was selected, and a “general survey” of disasters along the highway was conducted and then put forward suggestions for reasonable monitoring of the highway according to test results. However, the application of INSAR technique was still lacking in the field of tunnel and underground engineering construction. SBAS-INSAR technique was used to select scene 10 sentinel-1A data covering the engineering scope to conduct time sequence settlement monitoring on the tunnel engineering site [14], and settlement monitoring results of the engineering site was obtained. Then, the monitoring accuracy was evaluated and verified by actual leveling data [15]. Time sequence INSAR technique was adopted to monitor surface settlement along Beijing subway network. And taking Taoping tunnel of Houyue line as an example, INSAR technique was adopted for surface deformation monitoring investigation research of deep coal mine goaf in railway tunnel damage [16]. Above research studies primarily applied INSAR technique in the deformation monitoring of railway tunnel site [17], but as a millimeter level technique having higher reliability than traditional INSAR technique, PS-INSAR technique has not been applied in health diagnosis of the deformable body on front slope beside mountain tunnel portal [18, 19].

Based on the tunnel of Jianquan village, this paper uses PS-INSAR technique for the first time to analyze and diagnose the health condition of the deformable body on front slope beside mountain tunnel portal [20, 21]. Through the inversion and long-term dynamic tracking of historical deformation of the deformable body on front slope beside tunnel portal, understanding and awareness of the slope deformation law in monitoring area are improved [22], thus providing a more scientific basis and reference for the early warning and treatment of the deformation of the deformable body on front slope beside tunnel portal.

2. General Situation

2.1. Characteristics of INSAR Technique. PS-INSAR technique is to use two synthetic aperture radar antennas with interference imaging ability (or use an antenna to repeat observation), to obtain two coherent single-view complex images from the same area with a certain angle of view [23], obtain surface elevation information by interference phase information, and then reconstruct the digital surface elevation model [24]. It is characterized by all-day and all-weather Earth observation without restrictions of light and climate conditions, and even the information covered by it can be obtained through the surface or vegetation [25]. The primary applications of this technique are to produce digital elevation models and to monitor the vertical direction of small displacements or deformations [26].

2.2. Basic Information of Front Slope beside the Portal of Jianquan Village Tunnel. The tunnel is located on the right bank of Hanyuan Lake in Hanyuan County, Ya'an. The highest elevation is over 1200 m, the lowest elevation is about 800 m above the river bed of Dadu River, and the relative height difference is up to 400m. It belongs to Zhongshan landform. The tunnel is laid out in SE~NW direction, the numbers of starting pile and ending pile are K118 + 222~K119 + 664, and the length is 1442 m.

The surrounding rock at the entrance of tunnel is primarily composed of colluvial deposits and silty mudstones, and the colluvial deposits are primarily composed of granular structure. The rock mass at the exit of tunnel is primarily silty mudstone, carbonaceous shale, and sandstone, which is soft rock and medium soft rock. The exit section (K119 + 700) develops a toppling deformable body, and the surface occurrence of the deformable body is $143^{\circ}\angle 32^{\circ}$. Because of the steep dip angle of surface rock mass, it is pulled by gravity to topple outwards. The distribution elevation of the deformable body is 914~1050 m, and the lowest point is 23 m away from the tunnel roof.

3. The Application of PS-INSAR Technique in Diagnosing Deformable Body on Front Slope beside Tunnel Portal

3.1. Technical Parameter Selection

3.1.1. SAR Data Selection. Sentinel-1 is a two-satellite Earth observation satellite operated by the European Space Agency's Copernicus Project (GMES) [27]. It consists of two satellites, c-band synthetic aperture radar (frequency: 5.4 GHz), with a 12-day revisit cycle. Sentinel-1 satellite SAR data is used to obtain the distribution map in the operation area (shown in Figure 1). Inside it, IW shooting mode can obtain SAR image data with a resolution of $5\text{ m} \times 20\text{ m}$ and a width of 250 km. Here, scene 68 data from 2018 to 2020 were selected.

3.1.2. SAR Data Processing. Key steps of INSAR interferometric data processing process were (1) selection of public primary image, (2) image registration, (3) differential interference processing, (4) target extraction of point CS, (5) INSAR phase unwrapping, (6) linear deformation phase and residual elevation phase calculation, and (7) estimation and removal of error and atmospheric effect.

Among them, the basic principle of differential interference processing was that, after scene 68 image registration, all auxiliary images were resampled to primary images space. In frequency domain, public frequency band of primary and auxiliary images was prefiltered to generate the filtered primary and auxiliary images. After resampling, all auxiliary images were multiplied by the conjugate of the main image to generate interference phase diagram of images. Obtained phase information included the information of surface deformation, surface terrain phase, and so on. Meanwhile, the data of external digital elevation model (DEM) was used to simulate terrain phase, and the terrain phase of interference graph generated in this step was

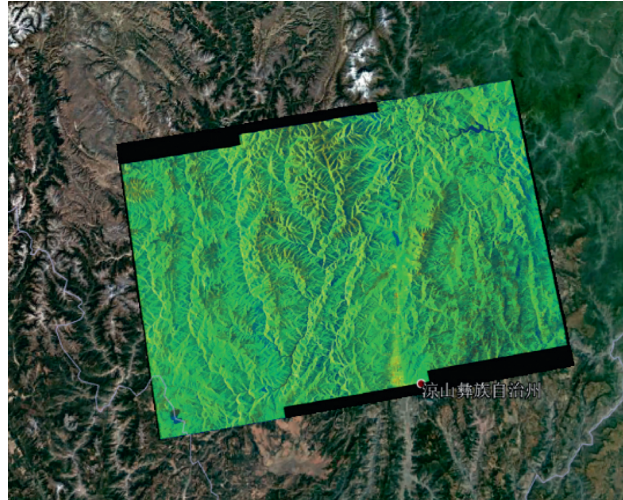


FIGURE 1: Distribution of SAR data operation area.

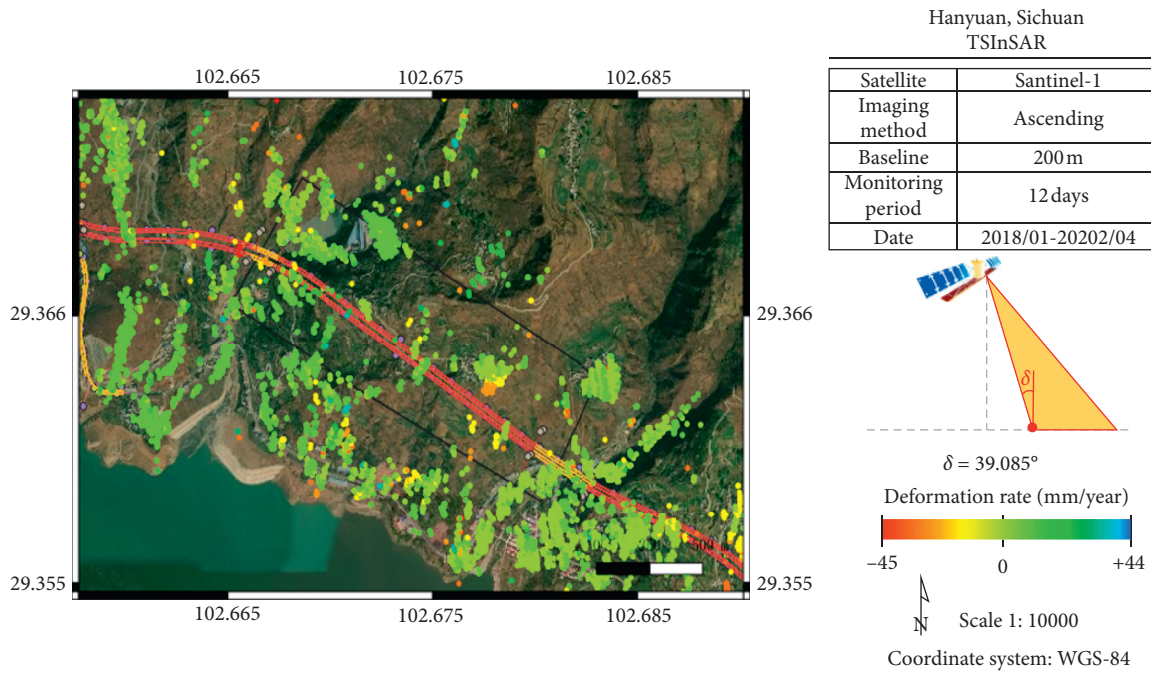


FIGURE 2: Distribution of deformation speeds of front slope beside tunnel portal.

removed to generate differential interference graph. At this point, the phase of the X-th scatterer point (PS) of the i th differential interference graph was obtained as follows:

$$\phi_{x,i} = \phi_{D,x,i} + \phi_{A,x,i} + \phi_{S,x,i} + \phi_{\theta,x,i} + \phi_{N,x,i}, \quad (1)$$

where $\phi_{D,x,i}$ is the deformation phase in view direction; $\phi_{A,x,i}$ is the atmospheric influence phase; $\phi_{S,x,i}$ is the orbit error phase; $\phi_{\theta,x,i}$ is the residual terrain phase due to DEM error; and $\phi_{N,x,i}$ is the noise phase.

3.2. Deformation Monitoring Calculation Results

3.2.1. Deformation Monitoring Calculation Results of Front Slope beside Tunnel Portal. Deformation speeds distribution

in the whole research area is shown in Figure 2. 70% of them were between -10 and $+10$ mm/year. Overall, the deformation speeds ranged from -26.277 to $+15.42$ mm/year.

3.2.2. Deformation Monitoring Calculation Results of the Entrance Section of Jianquan Village Tunnel.

According to deformation monitoring results of the entrance section of Jianquan village tunnel shown in Figure 3, the location was 29.3603388°N and $102.67806388^\circ\text{E}$. The deformation value of point TS1 continued to decrease from October 2018 to October 2019 and is relatively stable recently. Its accumulative settlement maximum in two years was about 30 mm, and the annual settlement speed was 12.628 mm/year. Point TS2 continued to settle from April 2018 to April 2020

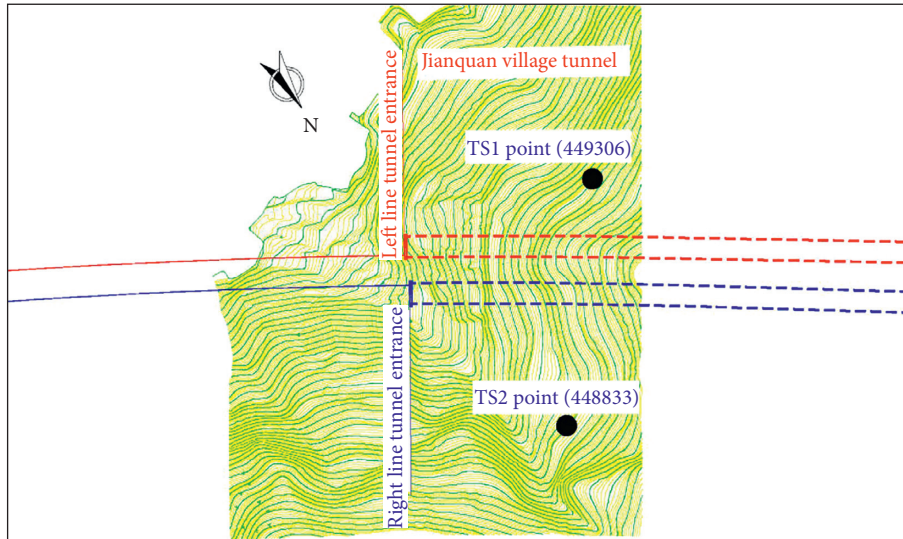
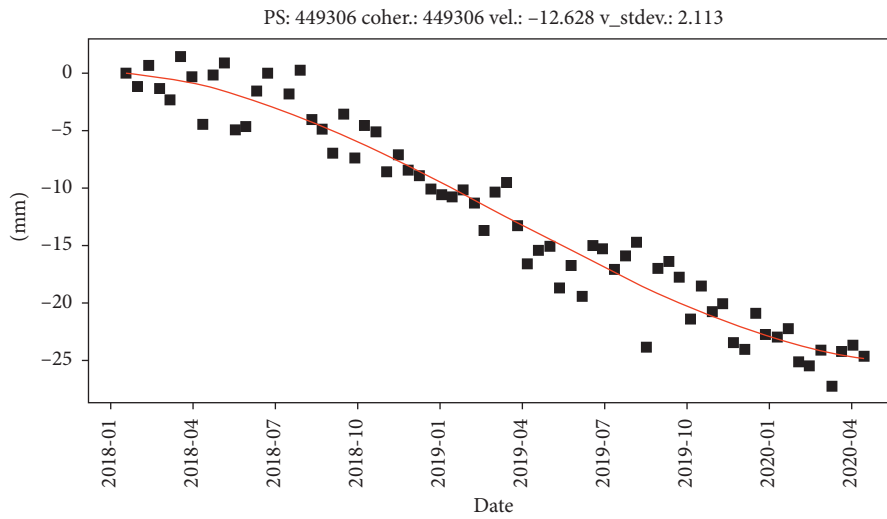
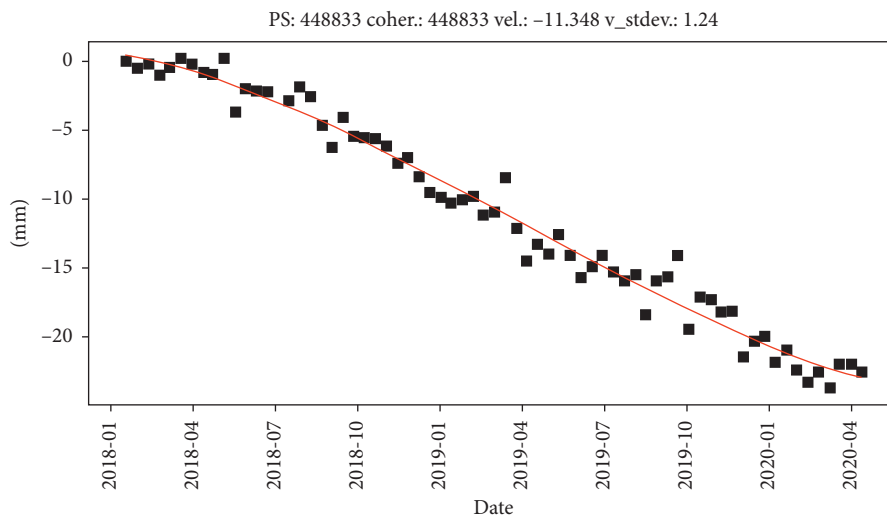


FIGURE 3: Deformation monitoring results of the entrance section of Jianquan village tunnel.



(a)



(b)

FIGURE 4: Time sequence deformation curves: (a) TS1 point (449306) and (b) TS2 point (448833).

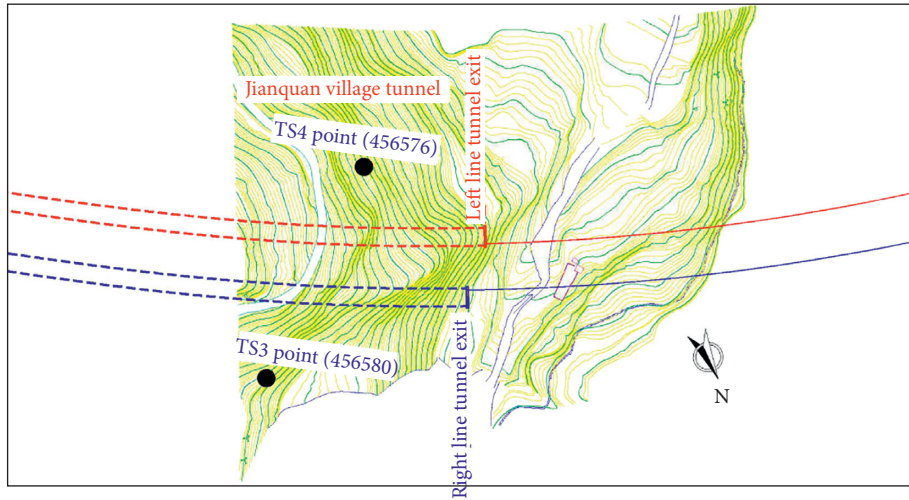
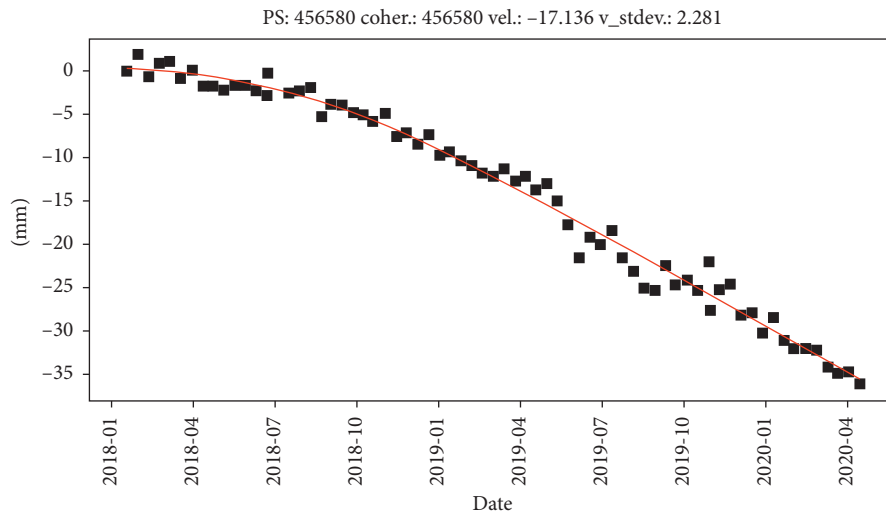
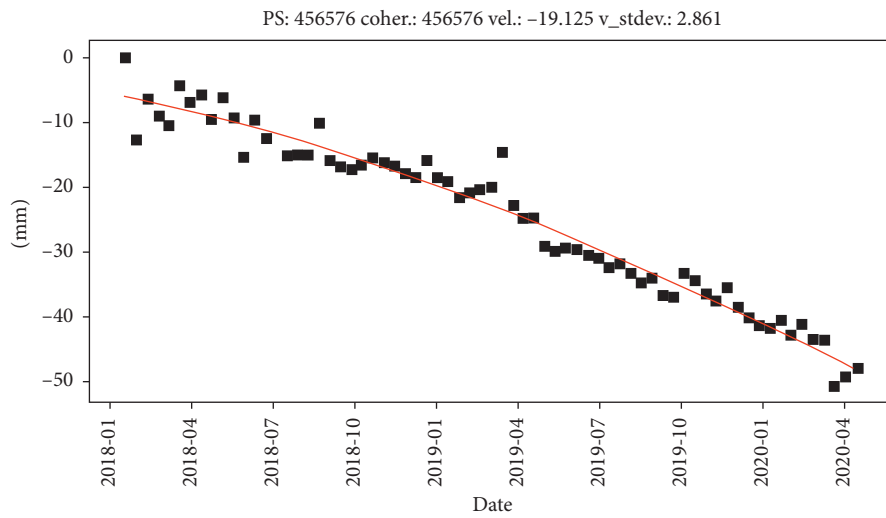


FIGURE 5: Deformation monitoring results of the exit section of Jianquan village tunnel.



(a)



(b)

FIGURE 6: Time sequence deformation curves: (a) TS3 point (456580) and (b) TS4 point (456576).

(Figure 4). The cumulative settlement maximum in two years was about 25 mm, and the annual settlement speed was 11.348 mm/year.

3.2.3. Deformation Monitoring Calculation Results of the Exit Section of Jianquan Village Tunnel. According to deformation monitoring results of the exit section of Jianquan village tunnel shown in Figure 5, the location was 29.362805°N and 102.677111°E. The deformation values continued to decrease from October 2018 to April 2020. The cumulative settlement maximum of point TS3 in two years was more than 35 mm, and the annual settlement speed was 17.136 mm/year. The cumulative settlement maximum of point TS4 in two years was about 50 mm, and the annual settlement speed was 19.125 mm/year.

3.3. Analysis of Deformation Monitoring Results. By using PS-INSAR technique to conduct quantitative analysis on the surface deformation of front slope beside Jianquan village tunnel portal in Emeishan-Hanyuan highway, the following results are obtained: through precise analysis on the surface deformation speed of Jianquan village tunnel in Emeishan-Hanyuan highway from January 2018 to April 2020, as exhibited in Figure 6, it is found that the exit section (K119 + 700) of Jianquan village develops a deformable body, which is consistent with original investigation results. The annual deformation speed maximum of this deformable body is 19.125 mm/year, the annual deformation speed of section K118 + 400 is 11.348 mm/year, and this quantitative analysis of the change of the deformable body has important value to guide the treatment of the deformable body on front slope beside tunnel portal.

4. Conclusions

By using PS-INSAR technique to conduct research and analysis on the surface deformation law of front slope beside tunnel portal, the development state of the deformable body is quantitatively grasped, and the parameters (position, deformation speed, accumulative deformation, etc.) of the deformable body on front slope beside tunnel portal are obtained. Therefore, health condition of the bad deformable body is diagnosed. Then, the “bull’s-eye” advantage is taken to detect early and treat early, which can attain the effect of rapid warning and precise management, reduce the safety risk during periods of tunnel construction and operation, and reduce deformation treatment cost.

Data Availability

The data are mainly composed of graphs and tables in the paper and can be referenced.

Conflicts of Interest

The author declares no conflicts of interest.

Acknowledgments

This research was supported by the Miaozi Engineering Key Project of the Science and Technology Department of Sichuan Province (grant no. 2020JDRC0078) and the State Key Laboratory of Geohazard Prevention and Geo-environment Protection (China) Open Fund (grant no. SKLGP2020K018).

References

- [1] W.-F. Chen, H.-L. Gong, B.-B. Chen, K.-S. Liu, M. Gao, and C.-F. Zhou, “Spatiotemporal evolution of land subsidence around a subway using InSAR time-series and the entropy method,” *GIScience & Remote Sensing*, vol. 54, no. 1, pp. 78–94, 2016.
- [2] B. Bayer, A. Simoni, D. Schmidt, and L. Bertello, “Using advanced InSAR techniques to monitor landslide deformations induced by tunneling in the Northern Apennines, Italy,” *Engineering Geology*, vol. 226, pp. 20–32, 2017.
- [3] K. Teshebaeva, H. Echtler, and B. Bookhagen, “Deep-seated gravitational slope deformation (DSGSD) and slow-moving landslides in the southern Tien Shan Mountains: new insights from InSAR, tectonic and geomorphic analysis,” *Earth Surface Processes and Landforms*, vol. 44, no. 12, pp. 2333–2348, 2019.
- [4] J. Scoular, R. Ghail, P. Mason et al., “Retrospective InSAR analysis of east london during the construction of the lee tunnel,” *Remote Sensing*, vol. 12, p. 5, 2020.
- [5] Y. Chen, K. Tan, S. Y. Yan et al., “Monitoring land surface displacement over Xuzhou (China) in 2015–2018 through PCA-based correction applied to SAR interferometry,” *Remote Sensing*, vol. 11, p. 12, 2019.
- [6] C. Noviello, S. Verde, V. Zamparelli et al., “Buildings at landslide risk with SAR: a methodology based on the use of multipass interferometric data,” *IEEE Geoscience and Remote Sensing Magazine*, vol. 8, no. 1, pp. 91–119, 2019.
- [7] J. Zhou, P. Ezquerro, J. A. Fernández-Merodo et al., “Analysis of an open-pit slope failure: las cruces case study, Spain,” *Landslides*, vol. 17, no. 9, pp. 2173–2188, 2020.
- [8] Ł. Rudziński, K. Mirek, and J. Mirek, “Rapid ground deformation corresponding to a mining-induced seismic event followed by a massive collapse,” *Natural Hazards*, vol. 96, no. 1, pp. 461–471, 2018.
- [9] A. J. García, M. Marchamalo, R. Martínez, B. González-Rodrigo, and C. González, “Integrating geotechnical and SAR data for the monitoring of underground works in the Madrid urban area: application of the persistent scatterer interferometry technique,” *International Journal of Applied Earth Observation and Geoinformation*, vol. 74, pp. 27–36, 2018.
- [10] M. González, I. Armaş, P. Dumitru, and M. Necsoiu, “Subway construction using Sentinel-1 data: a case study in Bucharest, Romania,” *International Journal of Remote Sensing*, vol. 41, no. 7, pp. 2644–2663, 2019.
- [11] R. Guo, S. M. Li, Y. N. Chen, X. Li, and L. Yuan, “Identification and monitoring landslides in longitudinal range-gorge region with InSAR fusion integrated visibility analysis,” *Landslides*, vol. 15, 2020.
- [12] G. Giardina, P. Milillo, M. J. DeJong et al., “Evaluation of InSAR monitoring data for post-tunnelling settlement damage assessment,” *Structural Control and Health Monitoring*, vol. 26, no. 2, Article ID e2285, 2018.
- [13] X. G. Shi, Q. Xu, and L. Zhang, “Surface displacements of the heifangtai terrace in Northwest China measured by X and

- C-band InSAR observations,” *Engineering Geology*, vol. 259, 2019.
- [14] P. Milillo, G. Giardina, and M. DeJong, “Multi-temporal InSAR structural damage assessment: the london crossrail case study,” *Remote Sensing*, vol. 10, p. 2, 2018.
- [15] X. Hu, R. Burgmann, W. H. Schulz, and F. J. Fielding, “Four-dimensional surface motions of the Slumgullion landslide and quantification of hydrometeorological forcing,” *Nature Communications*, vol. 11, no. 1, p. 2792, 2020.
- [16] L. Zhou, J. Guo, J. Hu, J. Maau, F. Weiau, and X. Xue, “Analysis of ELH Bridge through ground-based interferometric radar during the crossing of a subway shield tunnel underneath the bridge,” *International Journal of Remote Sensing*, vol. 39, no. 6, pp. 1911–1928, 2017.
- [17] M. Pauciuillo, D. Piacentini, and E. Tirincanti, “Detection and monitoring of tunneling induced ground movements using sentinel-1 SAR interferometry,” *Remote Sensing*, vol. 11, p. 6, 2019.
- [18] A. A. Malinowska, W. T. Witkowski, and R. Hejmanowski, “Sinkhole occurrence monitoring over shallow abandoned coal mines with satellite-based persistent scatterer interferometry,” *Engineering Geology*, vol. 262, 2019.
- [19] G. Strecker, M. Komac, and M. Jemec, “PS-InSAR displacements related to soil creep and rainfall intensities in the Alpine foreland of western Slovenia,” *Geomorphology*, vol. 175, p. 176, 2012.
- [20] C. Crippa, F. Franzosi, M. Zonca et al., “Unraveling spatial and temporal heterogeneities of very slow rock-slope deformations with targeted DInSAR analyses,” *Remote Sensing*, vol. 12, p. 8, 2020.
- [21] M. Khorrami, B. Alizadeh, and T. E. Ghasemi, “How groundwater level fluctuations and geotechnical properties lead to asymmetric subsidence: a PSInSAR analysis of land deformation over a transit corridor in the los angeles metropolitan area,” *Remote Sensing*, vol. 11, p. 4, 2019.
- [22] B. W. Lowry, S. Baker, and W. Zhou, “A case study of novel landslide activity recognition using ALOS-1 InSAR within the ragged mountain western hillslope in gunnison county, Colorado, USA,” *Remote Sensing*, vol. 12, p. 12, 2020.
- [23] X. T. Chen, X. F. He, and X. L. Yang, “Terrain point cloud assisted GB-InSAR slope and pavement deformation differentiate method in an open-pit mine,” *Sensors (Basel)*, vol. 20, p. 8, 2020.
- [24] M. Bădescu, A. Gaber, F. Abdalla et al., “Use of optical and radar remote sensing satellites for identifying and monitoring active/inactive landforms in the driest desert in Saudi Arabia,” *Geomorphology*, vol. 362, 2020.
- [25] D. Marsh, G. Wang, T. Yang, and F. Zhang, “Remote sensing-based detection of the deformation of a reservoir bank slope in Laxiwa hydropower station, China,” *Landslides*, vol. 10, no. 2, pp. 231–238, 2015.
- [26] A. Hu, M. T. Hendry, and R. Macciotta, “GB-InSAR monitoring of vegetated and snow-covered slopes in remote mountainous environments,” *Landslides*, vol. 17, no. 7, pp. 1713–1726, 2017.
- [27] Y. Tian, J. Liu-Zeng, Y. Luo et al., “Deformation during the Milashan Tunnel construction in northern sangri-cuona rift, Southern Tibet, China observed by Sentinel-1 satellites,” *Science Bulletin*, vol. 63, no. 21, pp. 1439–1447, 2018.

Research Article

Research on Design Parameters and Fatigue Life of Tunnel Bottom Structure of Single-Track Ballasted Heavy-Haul Railway Tunnel with 40-Ton Axle Load

W. B. Ma,^{1,2} J. F. Chai^{1,2},, Z. L. Han,^{1,2} Z. G. Ma,^{1,2} X. X. Guo,^{1,2} W. H. Zou,^{1,2} Z. L. An,^{1,2} T. F. Li,^{1,2} and Y. B. Niu^{1,2}

¹Railway Engineering Research Institute, China Academy of Railway Sciences Corporation Limited, Beijing 100081, China

²State Key Laboratory for Track Technology of High-speed Railway, Beijing 100081, China

Correspondence should be addressed to J. F. Chai; chaijinfei@rails.cn

Received 23 August 2020; Revised 5 October 2020; Accepted 7 November 2020; Published 21 November 2020

Academic Editor: Zheng-zheng Wang

Copyright © 2020 W. B. Ma et al. This is an open access article distributed under the Creative Commons Attribution License, which permits unrestricted use, distribution, and reproduction in any medium, provided the original work is properly cited.

The coupling calculation model of tunnel and surrounding rock is established by the finite difference method, and the main design parameters of lining structure of single-track ballasted tunnel under 40-ton axle load, heavy train load, are studied in combination with cumulative damage mechanism of surrounding rock at tunnel bottom and the fatigue life characteristics of concrete structure at tunnel bottom. The results show that (1) inverted arch shall be set in sections of III-grade and above. Whether an invert is set in sections of II-grade and below shall be determined according to lithology and groundwater conditions. When the surrounding rock condition is good and the tunnel bottom structure (without invert structure) is adopted, the thickness is recommended to be more than 20 cm, and the concrete strength grade should not be lower than C35. (2) Connection mode: the inverted arch and side wall of the tunnel should be connected in sequence to reduce the stress concentration and improve the stress state of the connection part between the inverted arch and the side wall. (3) It is suggested that the rise-span ratio of invert of single-track tunnel should be $1/6 \sim 1/8$; the larger value should be taken when the surrounding rock condition is poor and the small value should be taken when the surrounding rock condition is good. (4) The thickness of inverted arch is recommended to be no less than 20 cm under the condition of V-grade surrounding rock, to be no less than 15 cm under IV-grade surrounding rock, and to be no less than 10 cm under the condition of III-grade surrounding rock and II-grade surrounding rock sections requiring inverted arch. (5) The recommended value of bedding thickness meeting the design service life is 20 cm under the condition of II-grade surrounding rock.

1. Introduction

Heavy-haul railway has become the best choice for transporting bulk goods in the world because of its advantages of large volume, high speed, low energy consumption, and low cost. A lot of researchers have studied the heavy-haul railway and achieved a series of results.

Jakobsen obtained the relationship between ground vibration level and relevant track parameters through field test of ground vibration caused by train load [1]. Dawn et al. tested the vibration response of British railway subgrade and

studied the relationship between train speed, excitation frequency, and track parameters [2]. Based on a heavy-haul railway tunnel project, Zou et al. studied the stress distribution and dynamic response of the foundation structure of heavy-haul railway tunnel under the action of train load of 30-ton axle load combined with field vehicle test and numerical simulation [3]. Li et al. clarified the dynamic characteristics of ballasted and ballastless double-track heavy-haul railway tunnel structure under the conditions of 27 t ~ 30 t axle load and III ~ V surrounding rock through field measurement [4]. Chang studied the influence of key

parameters on the dynamic response of heavy-haul track structure with 30-ton axle load and provided suggestions for the selection of structural parameters by analyzing the static and dynamic characteristics of heavy-haul track structure [5]. Huo simulated and analyzed the fatigue damage of heavy-haul lines and concluded that the track bed, invert filling layer, and invert of tunnel bottom structure all showed damage in turn [6]. Liu et al. carried out wave fatigue test of double-side high limit static load and low dynamic load according to the mechanical characteristics of key fatigue parts at the bottom of heavy-haul railway tunnel and obtained the evolution law of maximum tensile strain and electrical conductivity of structural specimens at the bottom of heavy-haul railway tunnel [7]. Song analyzed and obtained the influence rules of parameters such as train speed, width of track bed slab, thickness of track bed slab, stiffness of tunnel foundation, and other parameters on dynamic performance of heavy-haul vehicle ballastless track system and proposed reasonable value selection suggestions for structural parameters of ballastless track in heavy-haul railway tunnel [8]. Li researched the energy evolution characteristics of hard rock during triaxial failure with different loading and unloading paths and the Brazilian disc test for rock mechanics applications [9–11]. Wang researched the shaking table tests of tunnel linings in progressive states of damage and analyzed the seismic damage classification and risk assessment of mountain tunnels [12–16]. Chai studied the internal fracture mechanism of simulated rock acoustic emission events using T-k diagram method and P-T graph method [17–19]. Cheng researched the element-free Galerkin method based on the nonsingular weight functions [20–23].

At present, the “Heavy-Haul Railway Design Code” (TB10625-2017) of China is usually applicable to heavy-haul railway with axle loads less than 30 tons. There is still insufficient understanding of the stress distribution characteristics and dynamic response of railway tunnel structure with 40-ton axle load. Therefore, it is inevitable that railway tunnels with 40-ton axle load under construction and completed will inevitably have greater hidden dangers due to the bearing of heavy train load on the foundation structure.

In this paper, the coupling calculation model of tunnel and surrounding rock is established by the finite difference method, and the main design parameters of lining structure of single-track ballasted tunnel under 40-ton axle load heavy train load are studied in combination with cumulative damage mechanism of surrounding rock at tunnel bottom and the fatigue life characteristics of concrete structure at tunnel bottom. This study has important reference significance for the design parameters of heavy-haul railway tunnel lining with 40-ton axle load.

2. Dynamic Performance Analysis of Tunnel Bottom Structure

The finite difference method is used to establish a dynamic numerical analysis model to calculate the dynamic response characteristics of the foundation structure of heavy-haul railway tunnel under the action of train load.

2.1. Numerical Calculation Model

2.1.1. Numerical Computation Grid. The numerical model grid under typical working conditions is shown in Figure 1. The model size is 60 m * 12 m * 60 m. The unit thickness is taken along the tunnel axis direction, the width is taken as 30 m from the tunnel axis to both sides, and the distance between the upper and lower boundaries in the height direction and the tunnel axis is 30 m.

2.1.2. Calculation Condition. The tunnel section in BFS stage is taken as the typical calculation section. The influence of different design parameters on dynamic response and damage characteristics of tunnel foundation structure is mainly aimed at. The calculation conditions are shown in Table 1.

The benchmark example of the above conditions is as follows: the axle load of the train is 40 tons, the surrounding rock grade is grade IV, the invert thickness is 20 cm, and the rise-span ratio is 1/6. Other conditions only need to change the corresponding parameters.

2.1.3. Calculation Parameters. The physical and mechanical parameters of surrounding rock are selected according to the survey and design data of typical tunnels and referring to similar strata. The basic mechanical parameters of invert, filling layer, primary support, secondary lining, and other tunnel structural materials are selected according to the code for “Design of Railway Tunnel” (TB 10003-2005), and equivalent treatment is conducted for anchor bolt and reinforcement. See Table 2 for specific parameters.

2.1.4. Simulation Method of Train Dynamic Load. The factors that should be considered in the simulation of train dynamic load include axle load, suspension mass, running speed, and line smoothness. The commonly used simulation methods are field test method, artificial simulation excitation method, and train track coupling model method. The field test method is affected by the load, speed, track state, and other factors, so the test results obtained by the field test method are more discrete, and it is difficult to accurately describe with the expression and can only analyze the specific working conditions; the train track coupling model connects the train model and the track model through the assumed wheel rail contact relationship, which is more comprehensive, but the model and parameters are too complex, and the wheel rail contact relationship is not. The artificial simulation excitation method uses an excitation function fitted by empirical formula to simulate train load, which can fully consider the influence of axle load, speed, and other factors, and its form is relatively simple and widely used at present.

In this paper, the excitation force function is used to simulate the heavy-haul train load. The excitation force function includes the static load and the vibration load reflecting the factors such as irregularity and rail surface waveform wear effect. The superposition combination of train wheel set force and the scattered transmission of rail and sleeper is considered.

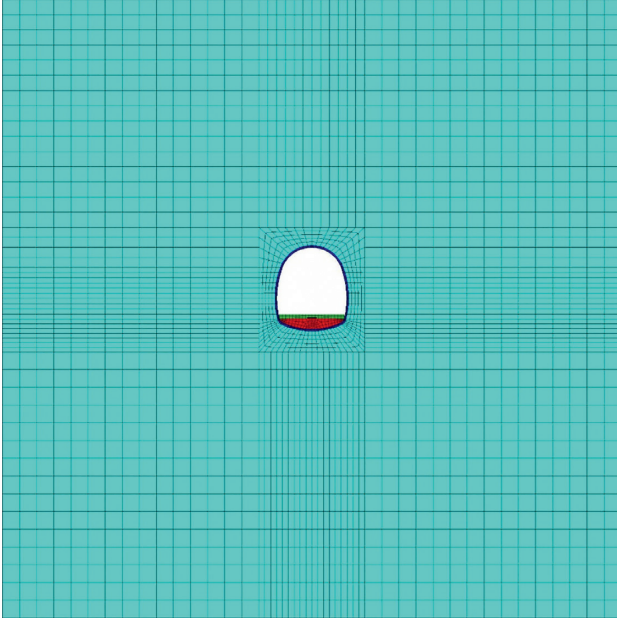


FIGURE 1: Numerical calculation model.

TABLE 1: Calculation conditions under different design parameters of tunnel foundation structure.

Influence factor	Grade of surrounding rock	Invert/floor thickness (cm)	Invert rise-span ratio
Specific parameters	II	10	1/5
	III	15	1/6
	IV	20	1/7
	V	30	1/8

$$F(t) = k_1 k_2 (P_0 + P_1 \sin \omega_1 t + P_2 \sin \omega_2 t + P_3 \sin \omega_3 t), \quad (1)$$

where P_0 is the static load of the wheel; P_1, P_2, P_3 are the typical vibration load values related to the ride irregularity, dynamic additional load, and waveform wear, respectively, corresponding to a typical value in the control conditions ①–③ in Table 3; k_1 is the wheel rail force superposition coefficient; and k_2 is the rail dispersion transmission coefficient.

The amplitude of vibration load is

$$P_i = m a_i \omega_i, \quad i = 1, 2, 3, \quad (2)$$

where m is the unsprung mass of the train; a_i is the typical rise height, corresponding to the situations of ①, ②, and ③ in Table 3; ω_i is the vibration circumference ratio under the condition of irregularity control, and the expression is $\omega_i = 2\pi v/L_i$, v is the running speed, and L_i is the wavelength management value of track geometric irregularity, corresponding to ①, ②, and ③ in Table 3.

2.1.5. Boundary Conditions of Dynamic Analysis and Material Damping Model

1. Artificial Boundary Conditions. The setting of artificial boundary conditions and the input of vibration wave are the

key links to realize the dynamic numerical analysis, which directly affects the accuracy and credibility of the calculation results. In the engineering rock mass of semi-infinite space, when the vibration wave propagates around, it will transmit and refract when it meets the structure or rock structure plane and will interfere with the incident wave to form a complex wave field. In the near-field dynamic numerical analysis, in order to effectively simulate the scattering wave passing through the truncated boundary of the model and make the vibration wave energy dissipate to infinity, it is necessary to introduce artificial boundary conditions to eliminate the reflection and oscillation of the vibration wave on the artificially cut boundary in the calculation area. In the FLAC3D dynamic analysis of this chapter, the free field boundary is used as the dynamic analysis boundary condition.

In the numerical simulation of vibration response of near-surface structures such as slopes and shallow underground structures, the lateral boundary of the numerical model must consider the free field motion without structures. In the numerical simulation, the free field motion is applied to the model boundary to keep the artificial boundary non-reflective. The lateral boundary of the discrete model is coupled with the free field to simulate the viscous boundary. The unbalanced force on a surface parallel to the axis in the normal direction can be expressed as follows:

$$\begin{cases} F_x = -\rho C_p (v_x^m - v_x^{ff}) A + F_x^{ff}, \\ F_y = -\rho C_s (v_y^m - v_y^{ff}) A + F_y^{ff}, \\ F_z = -\rho C_s (v_z^m - v_z^{ff}) A + F_z^{ff}, \end{cases} \quad (3)$$

where ρ is the density of material medium; C_p and C_s are the wave velocity of P-wave and S-wave in the material medium; A is the influence area of free field node; $v_x^m, v_y^m, v_z^m, v_x^{ff}, v_y^{ff}, v_z^{ff}$ represent the three components of particle vibration velocity along the coordinate axis on the main node and corresponding free field node on the artificial boundary, respectively; and $F_x^{ff}, F_y^{ff}, F_z^{ff}$ are the contribution of normal stress and tangential stress of node influence element in free field.

If the calculation model is a homogeneous medium without near-surface structure, the motion law of the calculation area is consistent with that of the free field, and the lateral damper does not work; when the two move relatively, the damper absorbs the energy of the traveling wave. In FLAC3D, the free field boundary conditions require that the bottom of the model is horizontal, and the normal direction is the axis; the side must be vertical, and the normal direction is x -axis or y -axis.

2. Material Damping Model. Material damping is a professional term to describe the energy dissipation mode of structural materials in the process of vibration. It means the energy dissipation of materials under the action of external dynamic load due to the friction between molecules in the medium, the sliding between structural planes, and the plastic response of materials. According to the different mechanism of damping, the damping forms in dynamic

TABLE 2: The physical and mechanical parameters of materials.

Structure	Elastic modulus (GPa)	Poisson's ratio	Density (kN·m ⁻³)	Cohesion (kPa)	Friction angle (°)
Ballast	32.0	0.18	25.0		
Filling layer	29.0	0.18	25.0		
Invert	30.0	0.18	25.0		
Second lining	30.0	0.18	25.0		
Primary lining	27.5	0.18	25.0		
Surrounding rock	1.5	0.36	19.5	200	42

TABLE 3: Simulation analysis parameters of track geometric irregularity.

Control conditions	Wavelength (m)	Sagittal (mm)
According to ride comfort①	50.00	16.00
	20.00	9.00
	10.00	5.00
According to the dynamic additional load acting on the line②	5.00	2.50
	2.00	0.60
	1.00	0.30
Waveform wear③	0.50	0.10
	0.05	0.005

analysis are divided into internal damping, external friction damping, sliding friction damping, plastic damping, and spatial dissipation damping. Different damping forms have different calculation methods. Rayleigh damping is used as material damping model in FLAC3D dynamic analysis in this chapter.

Rayleigh damping was first applied to the dynamic analysis of structures and elastic medium systems under natural vibration modes.

$$C = \alpha M + \beta K, \quad (4)$$

where α is the proportional damping constant of the mass matrix M and β is the proportional damping constant of the stiffness matrix K . For a multi-degree-of-freedom system, the relationship between the damping constant and the damping ratio ξ_i and the system frequency ω_i of the corresponding mode is as follows:

$$\xi_i = \frac{((\alpha/\omega_i) + \beta\omega_i)}{2}. \quad (5)$$

It can be seen from equation (5) that the damping ratio tends to increase rapidly when the frequency is very high or low. In contrast, the mass proportional damping has a greater contribution to the damping of the system in the low frequency band, while the stiffness proportional damping has a dominant contribution in the high frequency band. In the fundamental frequency band, the damping effect of mass term is equivalent to that of stiffness term:

$$\begin{aligned} \alpha &= \xi_{\min} \omega_{\min}, \\ \beta &= \frac{\xi_{\min}}{\omega_{\min}}, \end{aligned} \quad (6)$$

where ξ_{\min} is the minimum damping ratio and ω_{\min} is the system reference frequency. The center frequency f_{\min} is defined as

$$f_{\min} = \frac{\omega_{\min}}{2\pi}, \quad (7)$$

and when the damping ratio ξ_{\min} and center frequency f_{\min} are known, the Rayleigh damping constants can be obtained. In FLAC3D explicit time domain dynamic calculation, the stiffness damping term in Rayleigh damping model often reduces the critical time step. For geotechnical materials, the damping ratio is usually desirable; for structural systems, the damping ratio is usually desirable; when the material in the stress system adopts the inelastic constitutive model, the plastic deformation will dissipate most of the energy, so for large deformation dynamic analysis, the damping ratio is usually smaller.

2.1.6. Numerical Simulation Steps. The specific steps of numerical simulation are as follows:

- (1) The model grid is established, the rock mass parameters are given, the static boundary conditions are applied, and then the initial in situ stress field is generated.
- (2) Simulation of excavation process. After the full face excavation, the in situ stress will be released by 10% and 20% after the initial support. The remaining in situ stress will be released after the secondary lining construction, and then the filling layer and ballast bed will be constructed.
- (3) The dynamic response of the tunnel structure is obtained by applying normal and tangential dynamic boundary conditions to the boundary and applying heavy load train load in the form of artificial excitation force.

2.2. Analysis of Simulation Results. The dynamic response of the foundation structure of heavy-haul railway tunnel under the conditions of different surrounding rock grade, different invert thickness, and different invert rise-span ratio is analyzed. The stress and dynamic response analysis is carried out at the top of filling layer, the top and bottom of inverted arch, the bottom of side wall arch foot, and the bottom of 1/4 position of inverted arch. See Figure 2.

The vertical dynamic stress of measuring points 1, 2, and 3 under different working conditions is monitored to master the influence of design parameters of tunnel foundation structure on the vertical transmission law of train load.

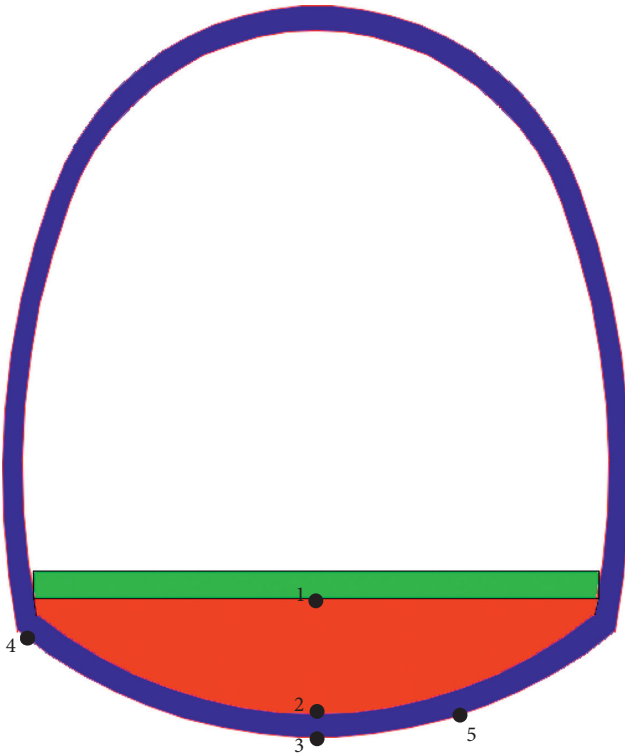


FIGURE 2: Layout of measuring points.

2.2.1. *Influence of Surrounding Rock Grade.* The vertical dynamic stress amplitude of measuring points 1, 2, and 3 under different surrounding rock levels can be seen in Table 4. The vertical dynamic stress amplitudes of point 1 are close to each other under different surrounding rock grades; the vertical dynamic stress amplitudes of measuring points 2 and 3 decrease with the increase of surrounding rock grade, and the amplitude of measuring point 3 decreases more.

2.2.2. *Influence of Invert Thickness.* The vertical dynamic stress time history amplitudes of measuring points 1, 2, and 3 with different invert thickness are shown in Table 5. The results show that the vertical dynamic stress amplitude of measuring point 1 is close to that of measuring point 1 under different invert thickness conditions; the vertical dynamic stress amplitude of measuring point 2 increases with the increase of invert thickness; the vertical dynamic stress amplitude of measuring point 3 decreases with the increase of invert thickness.

2.2.3. *Influence of Invert Rise-Span Ratio.* The vertical dynamic stress amplitude of measuring points 1, 2, and 3 under different rise-span ratio can be seen in Table 6. The vertical dynamic stress amplitudes of point 1 are close to each other under different invert rise-span ratios, while the vertical dynamic stress amplitudes of measuring point 2 and measuring point 3 decrease with the increase of invert rise-span ratio. The dynamic response of heavy-haul railway tunnel foundation structure under different base structure design

TABLE 4: The vertical dynamic stress amplitude of measuring points 1, 2, and 3 under different surrounding rock grades.

Measuring point	The vertical dynamic stress amplitude of different surrounding rock grades (kPa)			
	II	III	IV	V
1	163.324	161.196	162.393	161.728
2	113.449	96.558	88.844	79.667
3	93.765	66.899	52.402	35.777

TABLE 5: The vertical dynamic stress amplitude of measuring points 1, 2, and 3 under different invert thickness conditions.

Measuring point	Vertical dynamic stress amplitude of different invert thickness conditions (kPa)			
	10 cm	15 cm	20 cm	30 cm
1	162.127	162.393	162.393	161.595
2	80.864	86.317	88.844	92.036
3	59.584	56.126	52.402	48.545

TABLE 6: The vertical dynamic stress amplitude of measuring points 1, 2, and 3 under different invert rise-span ratios.

Measuring point	Vertical dynamic stress amplitude of different invert rise-span ratios (kPa)			
	1/8	1/7	1/6	1/5
1	161.994	161.861	162.393	161.196
2	96.691	92.834	88.844	82.593
3	58.387	56.392	52.402	45.885

parameters is analyzed numerically. The main conclusions are as follows.

- (1) The thicker invert is helpful to improve the stress state of the tunnel base structure. The larger the thickness of the invert, the smaller the vertical dynamic stress at the bottom of the invert, but the range of the dynamic stress changes with it, and the less the influence of train dynamic load on the surrounding rock, which indicates that the thicker inverted arch is beneficial to the long-term stress stability of the tunnel bottom stratum.
- (2) Under the condition of large invert span ratio (1/5), the smaller the vertical dynamic stress at the bottom of tunnel invert is (45.885 kPa), the better improved the internal force of inverted arch structure can be, which can reduce the requirements of structural thickness and reinforcement to a certain extent and improve the stability and safety of the structure. But on the other hand, a large rise-span ratio, corresponding to thick invert filling, will increase the project cost to a certain extent.
- (3) The worse the surrounding rock grade is, the more obvious the vertical dynamic stress attenuation along the base structure is; the greater the invert thickness is, the lower the load transfer rate at the bottom of inverted arch is; and the greater the invert rise-span ratio is, the lower the load transfer rate at the bottom of inverted arch is.

3. Design Parameters of Heavy-Haul Railway Tunnel Bottom with 40-Ton Axle Load

3.1. Fatigue Life Prediction Method of Tunnel Bottom Structure. In the range of random fatigue load and high cycle fatigue zone, the Miner linear fatigue cumulative damage criterion can accurately meet the engineering requirements. So, Miner linear fatigue cumulative damage theory is generally used to analyze the fatigue life of the bottom structure of heavy-haul railway tunnel.

In the calculation of structural fatigue life, it is necessary to define the S-N curve of materials. Here, S-N curve refers to the relationship curve between stress amplitude and fatigue life. The calculation formula of stress amplitude is as follows:

$$\sigma_a = \frac{\sigma_{\max} + \sigma_{\min}}{2}, \quad (8)$$

where σ_a is the stress amplitude; σ_{\max} is the maximum stress value in the cycle; and σ_{\min} is the minimum stress value in the cycle.

Considering the maximum stress level and the minimum stress level, the S-N fatigue life curve of concrete material is expressed as follows.

$$\begin{cases} \lg N = 16.67 - 16.67S_{f\max} + 5.17S_{f\min}, \\ S_{\max} = \frac{\sigma_{\max}}{f}, \\ S_{\min} = \frac{\sigma_{\min}}{f}, \end{cases} \quad (9)$$

where S_{\max} is the maximum stress level; S_{\min} is the minimum stress level; and f is the ultimate strength of the material.

The corresponding relationship between different stress amplitude and fatigue life can be obtained by formula (9). In addition, the influence of average stress on fatigue life is considered. The greater the average stress is, the smaller the fatigue life of the structure under each stress amplitude is. The average stress is expressed as follows:

$$\sigma_m = \frac{\sigma_{\max} - \sigma_{\min}}{2}, \quad (10)$$

where σ_m is the average stress.

According to the above formulas, the fatigue life of the tunnel bottom structure under various working conditions can be obtained. In the fatigue calculation, if the single intersection of a pair of unit 10000-ton trains in the tunnel is considered, the service life of the structure is

$$T = \frac{N}{365 \times a}, \quad (11)$$

where T is the service life of the structure; N is the fatigue life, which is generally used to express $\lg N$; and a is the number of 10000-ton trains per day, with the empirical value of 135.

The fatigue life distribution law of tunnel bottom structure under different structural types and the minimum

logarithmic fatigue life of tunnel bottom structure under various working conditions are obtained by calculation, and the load cycle times of tunnel bottom structure under fatigue failure can be obtained. Combined with the operation parameters of heavy-haul railway, the calculation results of minimum fatigue logarithmic life under different invert rise-span ratios are obtained, that is, the service life of tunnel structure.

Taking different invert rise-span ratios as examples, the service life of tunnel lining structure is calculated. According to the life calculation method, when the rise-span ratio is 1/8, 1/10, 1/12, and 1/14, the minimum logarithmic fatigue life of the tunnel is 6.879, 6.728, 6.631, and 6.550, respectively. It can be seen that the load cycles of the tunnel lining structure when the fatigue failure occurs are 106.879, 106.728, 106.631, and 106.550, because a pair of unit 10000-ton train tunnels are considered in the fatigue calculation. In the case of single intersection, the service life is as follows:

$$\begin{aligned} 1/8: T &= \frac{10^{6.879}}{365 \times 135} = 153 \text{ (years)}, \\ 1/10: T &= \frac{10^{6.728}}{365 \times 135} = 108 \text{ (years)}, \\ 1/12: T &= \frac{10^{6.631}}{365 \times 135} = 86 \text{ (years)}, \\ 1/14: T &= \frac{10^{6.550}}{365 \times 135} = 72 \text{ (years)}. \end{aligned} \quad (12)$$

Similarly, the service life of tunnel lining structure under other different working conditions can be calculated in this way.

3.2. Transport Conditions. Consider that the total weight of the train is 32400 tons and the average daily operation number is 10 pairs. The fatigue life distribution law of tunnel bottom structure under different surrounding rock grade, invert (bedding) thickness, and rise-span ratio is obtained by calculation, and the minimum fatigue life of tunnel bottom structure under various working conditions, that is, the number of load cycles that the tunnel bottom structure bears when fatigue failure occurs, can be calculated by combining with the operation parameters of heavy-haul railway, and the reasonable value range of design parameters meets the service life.

3.3. Design Parameters of Tunnel Invert. Taking V-grade surrounding rock as an example, the service life of tunnel lining structure under different invert rise-span ratio conditions (the thickness of tunnel inverts is 20 cm and 30 cm) can be calculated as in Table 7. The variation curve of service life with invert rise-span ratio is shown in Figure 3.

The following can be seen from Figure 3 and Table 7:

- (1) Under the condition of grade V surrounding rock, when the invert thickness is 30 cm, when the rise-span ratio of tunnel invert is 1/5, the fatigue life of

TABLE 7: Tunnel service life (years) under different rise-span ratios.

Invert thickness	Rise-span ratio			
	1/8	1/7	1/6	1/5
30 cm	48	61	75	92
20 cm	36	43	53	65

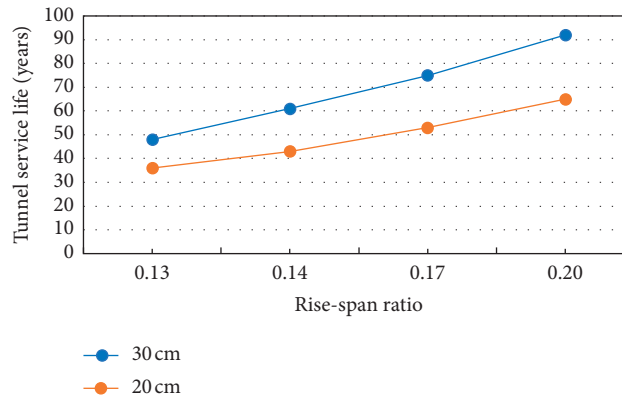


FIGURE 3: Relationship between tunnel structure life and invert rise-span ratio.

heavy-haul railway tunnel structure is 92 years; when the rise-span ratio is 1/6, the fatigue life of tunnel structure is 75 years; when the rise-span ratio is 1/7, the fatigue life of tunnel structure is 61 years, which meets the design service life (50 years); when the rise-span ratio is 1/8, the tunnel structure fatigue life is poor. The service life is 48 years, which is less than the design service life (50 years), which cannot meet the requirements of structural anti-fatigue.

- (2) Under the condition of V-grade surrounding rock and the invert thickness of 20 cm, when the rise-span ratio of tunnel invert is 1/5, the fatigue life of heavy-haul railway tunnel structure is 65 years. And when the rise-span ratio is 1/6, the fatigue life of tunnel structure is 53 years, which meets the design service life (50 years); when the rise-span ratio is 1/7 and 1/8, the fatigue life of tunnel structure is 43 and 36 years, respectively. It is less than the design service life (50 years), which cannot meet the requirements of structural fatigue resistance.
- (3) From the perspective of the relationship between the fatigue life of tunnel structure and the rise-span ratio of invert, the fatigue life also has a corresponding increasing trend with the increase of invert rise-span ratio. It shows that the fatigue resistance of heavy-haul railway tunnel structure can be significantly improved by optimizing the rise-span ratio of tunnel invert.
- (4) According to the relationship curve between the fatigue life of tunnel structure and the rise-span ratio of invert, and based on the design service life of 50 years, it can be estimated that the thickness value of invert should be greater than or equal to 20 cm; and

the rise-span ratio value should be greater than or equal to 1/6.

- (5) Under the condition of IV-grade surrounding rock, it is suggested that the thickness value of invert should be greater than or equal to 15 cm; and the rise-span ratio should be greater than or equal to 1/7. Under the condition of III-grade surrounding rock, it is suggested that the thickness of invert should be greater than or equal to 10 cm; and the rise-span ratio should be greater than or equal to 1/8.

3.4. *The Thickness of Tunnel Bottom.* The service life of tunnel bottom structure with different thickness can be calculated as shown in Table 8. The variation curve of service life with bedding thickness can be calculated as shown in Figure 4.

- (1) When the thickness of tunnel bottom is 30 cm, the service life of tunnel bottom structure is 89 years; and when the thickness of tunnel bottom is 20 cm, the service life of tunnel bottom structure is 58 years, which can meet the design service life (50 years) of the 40-ton axle load heavy-haul railway tunnel; when the thickness of tunnel bottom is 10 cm and 15 cm, the service life of tunnel bottom structure is 32 years and 47 years, respectively. It is less than the design service life (50 years), which cannot meet the requirements of structural anti-fatigue.
- (2) According to the relationship curve between the fatigue life of tunnel structure and the thickness of pavement, and based on the design service life of a 40-ton heavy-haul railway tunnel for 50 years, it can be estimated that the recommended bottom

TABLE 8: Service life of tunnel bottom structure with different bottom thickness.

Thickness of bedding (cm)	10	15	20	30
Service life (years)	32	47	58	89

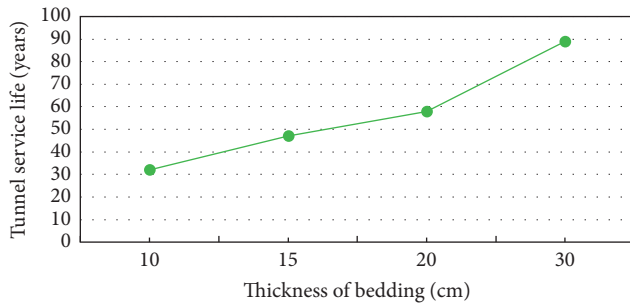


FIGURE 4: Relationship between service life of tunnel bottom structure and bottom thickness.

thickness should be no less than 20 cm under the condition of III-grade surrounding rock.

4. Conclusion

4.1. Dynamic Performance Analysis of Tunnel Bottom Structure. The dynamic response of heavy-haul railway tunnel foundation structure under different base structure design parameters is analyzed numerically. The main conclusions are as follows.

- (1) The thicker invert is helpful to improve the stress state of the tunnel base structure. The larger the thickness of the invert, the smaller the vertical dynamic stress at the bottom of the invert, but the range of the dynamic stress changes with it, and the less the influence of train dynamic load on the surrounding rock, which indicates that the thicker inverted arch is beneficial to the long-term stress stability of the tunnel bottom stratum.
- (2) Under the condition of large invert span ratio (1/5), the smaller the vertical dynamic stress at the bottom of tunnel invert is (45.885 kPa), the better improved the internal force of inverted arch structure can be, which can reduce the requirements of structural thickness and reinforcement to a certain extent and improve the stability and safety of the structure. But on the other hand, a large rise-span ratio, corresponding to thick invert filling, will increase the project cost to a certain extent.
- (3) The worse the surrounding rock grade is, the more obvious the vertical dynamic stress attenuation along the base structure is; the greater the invert thickness is, the lower the load transfer rate at the bottom of inverted arch is; and the greater the invert rise-span ratio is, the lower the load transfer rate at the bottom of inverted arch is.

4.2. Design Parameters of Heavy-Haul Railway Tunnel Bottom with 40-Ton Axle Load. According to the calculation and analysis of the dynamic response and fatigue life of the tunnel bottom structure under the above different tunnel design parameters, taking the tunnel design service life of 50 years as the benchmark, the tunnel bottom structure type and design parameters under different conditions can be determined as follows:

- (1) Structural type: inverted arch shall be set in sections of III-grade and above. Whether an invert is set in sections of II-grade and below shall be determined according to lithology and groundwater conditions. When the surrounding rock condition is good and the tunnel bottom structure (without invert structure) is adopted, the thickness is recommended to be more than 20 cm, and the concrete strength grade should not be lower than C35.
- (2) Connection mode: the inverted arch and side wall of the tunnel should be connected in sequence to reduce the stress concentration and improve the stress state of the connection part between the inverted arch and the side wall.
- (3) Rise-span ratio: when invert structure is adopted, considering the angle of ensuring the filling thickness and service life of the tunnel bottom, it is suggested that the rise-span ratio of invert of single-track tunnel should be 1/6 ~ 1/8; the larger value should be taken when the surrounding rock condition is poor and the small value should be taken when the surrounding rock condition is good.
- (4) Invert thickness: when inverted arch structure is adopted, the thickness of inverted arch is recommended to be no less than 20 cm under the condition of V-grade surrounding rock, to be no less than 15 cm under IV-grade surrounding rock, and to be no less than 10 cm under the condition of III-grade surrounding rock and II-grade surrounding rock sections requiring inverted arch.
- (5) Bottom thickness: according to the relationship curve between the service life of tunnel bottom structure and the thickness of pavement, taking the tunnel design service life of 50 years as the benchmark, it can be calculated that the recommended value of bedding thickness meeting the design service life is 20 cm under the condition of II-grade surrounding rock.

Data Availability

The data used to support the findings of this study are available within the article.

Conflicts of Interest

The authors declare that there are no conflicts of interest regarding the publication of this paper.

Acknowledgments

Thanks are due to the support of the Scientific Research Fund of China Academy of Railway Sciences Group Co., Ltd. (no. 2018YJ030).

References

- [1] J. Jakobsen, "Ground vibration from rail traffic," *Journal of Low Frequency Noise, Vibration and Active Control*, vol. 6, no. 3, pp. 96–103, 1987.
- [2] T. M. Dawn and C. G. Stanworth, "Ground vibrations from passing trains," *Journal of Sound and Vibration*, vol. 66, no. 3, pp. 355–362, 1979.
- [3] W. H. Zou, M. Zhang, Y. Q. Liu, and W. B. Ma, "Stress distribution and dynamic response of foundation structure of heavy haul railway tunnel under 30t axle load," *China Railway Science*, vol. 37, no. 5, pp. 50–57, 2016.
- [4] Z. Q. Li, Q. Wu, and Y. M. Cheng, *Study on Dynamic Characteristics and Design Method of Heavy Haul Railway Tunnel Structure*, Southwest Jiaotong University, Changsha, China, 2018.
- [5] W. H. Chang, *Study on Mechanical Characteristics of Heavy Haul Railway Track Structure with 30t Axle Load*, Beijing Jiaotong University, Beijing, China, 2009.
- [6] J. X. Huo, "Disease characteristics and fatigue damage mechanism of heavy haul railway tunnel bottom structure," *Railway Construction*, vol. 59, no. 7, pp. 61–64, 2019.
- [7] C. Li, L. M. Peng, M. F. Lei, and N. Liu, "Experimental study on fatigue performance and cumulative damage of sub-structure of heavy haul railway tunnel," *China Railway Science*, vol. 40, no. 4, pp. 77–85, 2019.
- [8] H. R. Song, *Structural Parameter Dynamic Analysis of Ballastless Track in Heavy Haul Railway Tunnel Section*, Southwest Jiaotong University, Changsha, China, 2015.
- [9] D. Y. Li and L. N. Y. Wong, "The Brazilian disc test for rock mechanics applications: review and new insights," *Rock Mechanics And Rock Engineering*, vol. 46, no. 2, pp. 269–287, 2018.
- [10] D. Y. Li, Q. Q. Zhu, Z. L. Zhou, X. B. Li, and P. G. Ranjith, "Fracture analysis of marble specimens with a hole under uniaxial compression by digital image correlation," *Engineering Fracture Mechanics*, vol. 183, pp. 109–124, 2017.
- [11] D. Li, Z. Sun, T. Xie, X. Li, and P. G. Ranjith, "Energy evolution characteristics of hard rock during triaxial failure with different loading and unloading paths," *Engineering Geology*, vol. 228, pp. 270–281, 2017.
- [12] Z. Z. Wang and Z. Zhang, "Seismic damage classification and risk assessment of mountain tunnels with a validation for the 2008 Wenchuan earthquake," *Soil Dynamics and Earthquake Engineering*, vol. 45, pp. 45–55, 2013.
- [13] J. F. Chai, A. B. Jin, Y. T. Gao et al., "Water inrush inoculation process in mines based on moment tensor inversion," *Chinese Journal of Engineering*, vol. 37, no. 3, p. 267, 2015.
- [14] Z. Z. Wang, L. Jiang, and Y. Gao, "Shaking table test of seismic response of immersed tunnels under effect of water," *Soil Dynamics and Earthquake Engineering*, vol. 116, pp. 436–445, 2019.
- [15] Z. Z. Wang and C. Chen, "Fuzzy comprehensive Bayesian network-based safety risk assessment for metro construction projects," *Tunnelling and Underground Space Technology*, vol. 70, pp. 330–342, 2017.
- [16] Z. Z. Wang, Y.-J. Jiang, C. A. Zhu, and T. C. Sun, "Shaking table tests of tunnel linings in progressive states of damage," *Tunnelling and Underground Space Technology*, vol. 50, pp. 109–117, 2015.
- [17] J. F. Chai, A. B. Jin, and S. C. Wu, "Rock fracture mechanism and its evolution law of triaxial compression test based on P-T distribution diagram method," *Electronic Journal of Geotechnical Engineering*, vol. 20, no. 28, pp. 13451–13464, 2015.
- [18] J. F. Chai, A. B. Jin, and S. C. Wu, "Mechanism and evolution law of rock failure based on moment tensor inversion," *Electronic Journal of Geotechnical Engineering*, vol. 20, no. 15, pp. 6659–6672, 2015.
- [19] J. F. Chai, Y. T. Gao, S. C. Wu et al., "Research on single jointed rock failure mechanism based on mesoscopic characteristics analysis," *Journal of Mining and Safety Engineering*, vol. 33, no. 3, pp. 528–534, 2016.
- [20] F. Liu and Y. Cheng, "The improved element-free Galerkin method based on the nonsingular weight functions for inhomogeneous swelling of polymer gels," *International Journal of Applied Mechanics*, vol. 10, no. 04, p. 1850047, 2018.
- [21] F. Liu, Q. Wu, and Y. Cheng, "A meshless method based on the nonsingular weight functions for elastoplastic large deformation problems," *International Journal of Applied Mechanics*, vol. 11, no. 01, Article ID 1950006, 2019.
- [22] Q. Wu, F. B. Liu, and Y. M. Cheng, "The interpolating element-free Galerkin method for three-dimensional elastoplasticity problems," *Engineering Analysis with Boundary Elements*, vol. 115, pp. 156–167, 2020.
- [23] S. Y. Yu, M. J. Peng, H. Cheng, and Y. M. Cheng, "The improved element-free Galerkin method for three-dimensional elastoplasticity problems," *Engineering Analysis with Boundary Elements*, vol. 104, pp. 215–224, 2019.

Research Article

Intelligent Classification Method for Tunnel Lining Cracks Based on PFC-BP Neural Network

Hao Ding ¹, Xinghong Jiang ², Ke Li ³, Hongyan Guo ², and Wenfeng Li ⁴

¹National Engineering Laboratory for Highway Tunnel Construction Technology, Chongqing 400067, China

²Chongqing University, Chongqing 400044, China

³China Merchants Chongqing Communications Research & Design Institute Co. Ltd., Chongqing 400067, China

⁴Xi'an Jiaotong University, Xi'an 710049, China

Correspondence should be addressed to Xinghong Jiang; jxh_cq@163.com and Ke Li; nick.88@163.com

Received 15 September 2020; Revised 11 October 2020; Accepted 6 November 2020; Published 18 November 2020

Academic Editor: Zheng-zheng Wang

Copyright © 2020 Hao Ding et al. This is an open access article distributed under the Creative Commons Attribution License, which permits unrestricted use, distribution, and reproduction in any medium, provided the original work is properly cited.

Tunnel lining crack is the most common disease and also the manifestation of other diseases, which widely exists in plain concrete lining structure. Proper evaluation and classification of engineering conditions directly relate to operation safety. Particle flow code (PFC) calculation software is applied in this study, and the simulation reliability is verified by using the laboratory axial compression test and 1 : 10 model experiment to calibrate the calculation parameters. Parameter analysis is carried out focusing on the load parameters, structural parameters, dimension, and direction which affect the crack diseases. Based on that, an evaluation index system represented by tunnel buried depth (H), crack position (P), crack length (L), crack width (W), crack depth (D), and crack direction (A) is put forward. The training data of the back propagation (BP) neural network which takes load-bearing safety and crack stability as the evaluation criteria are obtained. An expert system is introduced into the BP neural network for correction of prediction results, realizing classified dynamic optimization of complex engineering conditions. The results of this study can be used to judge the safety state of cracked lining structure and provide guidance to the prevention and control of crack diseases, which is significant to ensure the safety of tunnel operation.

1. Introduction

Tunnels are key nodes of road network, so the safety and stability of tunnel structure is the important foundation to guarantee the overall traffic capacity. However, due to the discontinuity, heterogeneity, anisotropy, and other complex characteristics of underground rock mass, it is difficult to meet all requirements in design and construction. Given the plain concrete lining structure lacks reinforcement skeleton and its bending strength is inadequate, it is a commonplace that “90% of the tunnels will have leakage and 100% of the tunnels may have cracks,” and diseases such as cracking and water seepage are very prominent [1–3] with the weakening of material performance and the change of external environment during operation. However, as the most common disease and the manifestation of other disease problems, the results of existing evaluation systems targeted to cracks such

as specifications, guidelines, and monographs are flawed such as simplex indexes and insufficient consideration of load-bearing characteristics. So, it is imperative to carry out the research on cracked lining under multiple indexes and extract the evaluation indexes and standards based on mechanical principles so as to map out tunnel maintenance plans and transition from an apparent state-determined way to a load-bearing characteristic-determined way [4,5].

In the research of load-bearing capacity characteristics of tunnel cracked lining structure, the causes of tunnel structural diseases are various, presenting complex phenomena and causing different degrees of consequences. Model experiment and monitoring measurement are mainly aimed at specific working conditions, and parameter regularity analysis mainly focuses on finite element calculation. By establishing the physical crack model or setting the contact relationship pattern at the crack position, the load-

bearing capacity characteristics of cracked lining structure under different load conditions such as plastic ground pressure, loose ground pressure, and unsymmetrical pressure, and the space scale conditions of different crack length, width, depth, and location have been calculated and obtained [5–7]. However, the finite element method has insufficient mechanism in crack tip treatment and crack propagation characteristics, which fails to reflect the crack stability state of the cracked lining structure. The development of algorithms such as extended finite element, boundary element, and discrete element can provide more powerful tools for the detailed study of the mechanical characteristics of cracked lining. Particle flow is a kind of discrete element, which identifies the contact state between particles to calibrate the basic characteristics of a medium. From the perspective of basic particle microstructure, it has prominent advantages of direct-viewing and high efficiency in the analysis and research of crack propagation [8–10].

In the classification evaluation of cracked lining structure, the most commonly used qualitative methods currently are expert scoring method and fault tree analysis, while the quantitative methods are fuzzy comprehensive evaluation method, analytic classification method, and neural network method [11–13]. Methods such as expert scoring and analytic hierarchy process are simple, easy-to-operate, and are the most commonly used. However, these methods are based on the structural damage performance index, which is greatly influenced by the subjectivity of experts and not directly related to structural load conditions and load-bearing safety, so the evaluation results fail to distinguish structural damage from nonstructural damage of lining and thus the methods mentioned above are unable to provide guidance in disease treatment. The BP neural network has the ability of self-adaptation, self-learning, nonlinear generalization, etc. which is widely used in tunnel construction control, rock-soil deformation prediction, operation disease evaluation, etc. [14–16]. Model experiment and numerical simulation are carried out to obtain initial training data, and the system associating the disease phenomena, load conditions, and stability characteristics through the BP neural network algorithm is established, which proves to be an effective plan combined with the advantages of focused calculation and generalized analysis.

This paper, in response to the problem of lining crack evaluation, uses a PFC particle flow calculation tool to calibrate the calculation parameters through uniaxial compression test and 1:10 large-scale model experiment of cracked lining first. On this basis, parameter analysis is carried out to calculate the bearing stability state and development trend of cracked lining structure under different external effects such as different surrounding rock grades and loading conditions, different design conditions such as lining structure thickness, and different damage states such as crack length, width, and depth, combined with the crack indexes as well as the crack bearing stability and propagation characteristics revealed by calculation results. The BP neural network training data are obtained by the expert scoring method; the tunnel lining crack classification software based on the BP neural network kernel is developed by virtue of

Python programming. The project research combines the advantages of the qualitative macro, detailed, and reliable quantitative calculation of expert evaluation, which provides a new way and idea for tunnel crack classification research.

2. Bearing Capacity Calculation Method for Cracked Lining

2.1. Calibration Parameters of Axial Compression Test. The key to numerical simulation of particle flow depends on whether the microparameters of interparticle are reasonably determined. However, given the uncertainty and complexity of interparticle microparameters, there is still no uniform formula to establish the corresponding relationship between the interparticle microparameters and actual macroparameters of materials. The common method at present is to change the micromechanical properties of particle units and their aggregate fabrics, so as to approximate the macromechanical response of materials. In this paper, according to the parameter calibration process proposed by Cundall [17,18], the uniaxial compression numerical simulation experiment is applied and multiple adjustments are made for the microparameters of the model so as to align with the macroproperties of the materials.

The specific process of calibrating the microparameters of C30 concrete material is as follows. In PFC, the contact bond strength model is selected for the numerical uniaxial test. The loaded specimens selected are the standard model specimens adopted by the European Concrete Association (CEB). The diameter of the cylinders is 152 mm and the height is 305 mm. The calculation model is shown in Figure 1. Through trial calculation and calibration, the calculation parameters are shown in Table 1. Under this condition, the stress-strain curve of concrete is shown in Figure 2. The peak strain of concrete obtained by the simulation test is about 0.0024, the ultimate strain is about 0.0035, and the compressive strength is about 23.7 MPa, which are consistent with the stress-strain curve of C30 concrete material. In the PFC parameter analysis of mechanical characteristics of cracked lining structure, C30 concrete calculation parameters adopt the values listed in the table.

2.2. Model Experiment Verification. Loading structure method is applied in PFC to calculate the load-bearing capacity characteristics of cracked lining. To ensure the reliability of the calculation results and verify the accuracy of calculation, the load-bearing capacity characteristics of cracked lining are studied in combination with the multifunctional engineering test system for traffic tunnels. According to the system dimensions, the dimensional similarity ratio is taken as 1:10, the lining section adopts the section shape of a two-lane highway tunnel, with the lining thickness taken as 40 mm; the rock mass around the lining is filled with grease to lessen the influence of boundary effect and realizes vertical and horizontal uniform loading, with applying load in steps to arrive at the thickness of 27 m of equivalent soil mass.

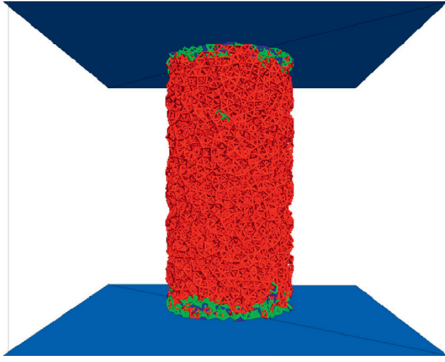


FIGURE 1: PFC uniaxial compression model.

TABLE 1: Model parameters.

Parameter	Value
Particle radius (rad/m)	0.03~0.05
Density (des/kg/m ³)	2040
Equivalent elastic modulus of particles (GPa)	30
Coefficient of friction, fric	0.577
Stiffness ratio, kratio	2
Parallel bond tensile strength, pb_ten (Pa/m)	$2.01e^7$
Parallel bond cohesion, pb_coh (Pa/m)	$15e^6$

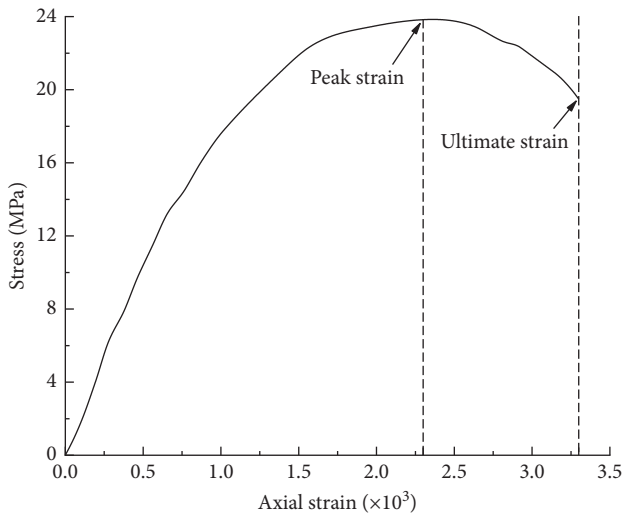


FIGURE 2: Stress-strain curve of C30 concrete.

The calculation results of the model experiment and the PFC simulation during the loading process are shown in Figure 3. The monitoring results of vault settlement and vault crack depth development are shown in Figures 4 and 5, respectively. In the loading process, the displacement growth trends of the model experiment and the numerical simulation remain the same, and the numerical values are similar. In addition, the error between the test results and the simulated structure is within 10%, which can be considered that the values taken for the PFC parameters and the simulation calculation can reflect the overall bearing stability of the cracked lining structure in a real scenario. In the loading process, the increasing trends of

crack depth at the top arch of the model experiment and the numerical simulation maintain the same; the distribution position and form of structural cracks under simulation conditions are consistent with the results of the model experiment, and the process of equivalent crack depth propagation is similar to the final form. In the loading process, the overall error between the model experiment and the numerical simulation of vault crack depth monitoring position is less than 18%, and the model experiment results are relatively smaller. The main reason is that the crack depth acquisition mainly depends on manual measurement, which is limited by the accuracy and difference of measuring instruments, and there are detailed differences in the specific measurement points under different loads. The measurement results of lining structure cracks are smaller than the actual situation. To sum up, it can be considered that the PFC parameter values are consistent with the simulation calculation and the actual situation, which can reflect the crack propagation law of lining structure under real conditions.

3. Mechanical Characteristics of Cracked Lining

3.1. Index Parameter Selection. The load-bearing capacity characteristics of cracked lining structure are related to external loads, structural parameters, and cracking conditions.

Tunnel rock mass environment is complex, and external load modes are various. For ease of calculation and analysis, the surrounding rock grades are used during PFC parameter analysis to comprehensively reflect the load conditions, and the standard method is applied to calculate the load size. Following the experience in tunnel design, the thickness of plain concrete lining structure is normally 30 cm, 35 cm, and 40 cm, and in some old tunnels, the thickness may also be 45 cm or 50 cm, so the simulation parameters of lining thickness are taken according to the gradient of 5 cm.

According to the investigation data of nearly 7000 cracks in nearly 50 tunnels on the Shanghai-Chongqing Riverside Expressway, more than 95% of the lining cracks are less than 10 m as shown in Figure 6. Therefore, in the PFC calculation, the cracked length parameters taken are 2.0 m, 4.0 m, 6.0 m, 8.0 m, and 10.0 m. The distribution of lining cracks is extremely uneven, with more cracks in vault, followed by hance, and then side wall in Figure 7. Therefore, five different crack distribution forms, including vault, hance, side wall, vault + hance, and vault + side wall, are taken in the PFC simulation calculation. It is hard to set the initial crack width in the PFC crack simulation calculation. Considering that the crack width is the main manifestation index of crack depth, so it is characterized by different crack depth ratios in the calculation process. In terms of crack direction, given the tunnel structure is dominated by bearing capacity and protection in the circumferential direction, and the influence of longitudinal crack-damage bearing is far greater than that in the circumferential direction, so four angles are set in the simulation calculation in Table 2.

In the table, H represents the width of the tunnel.

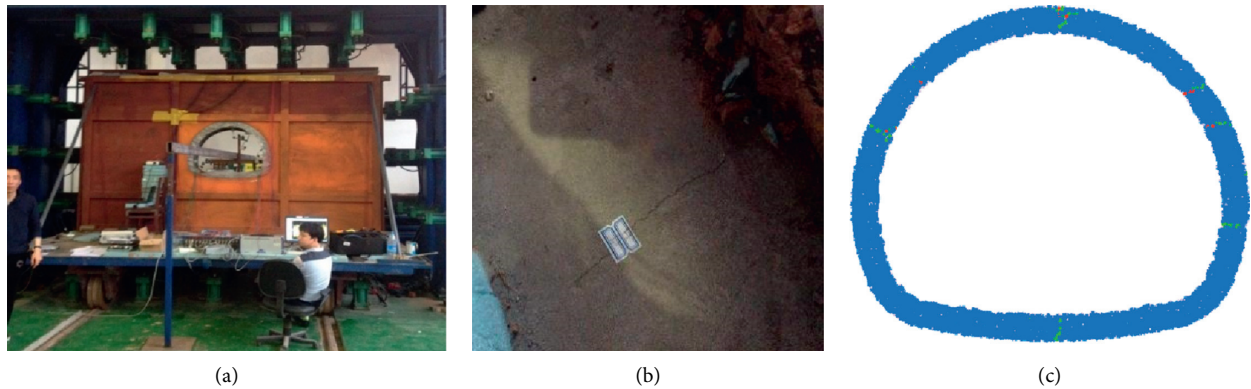


FIGURE 3: Schematic diagram of model experiment and numerical simulation.

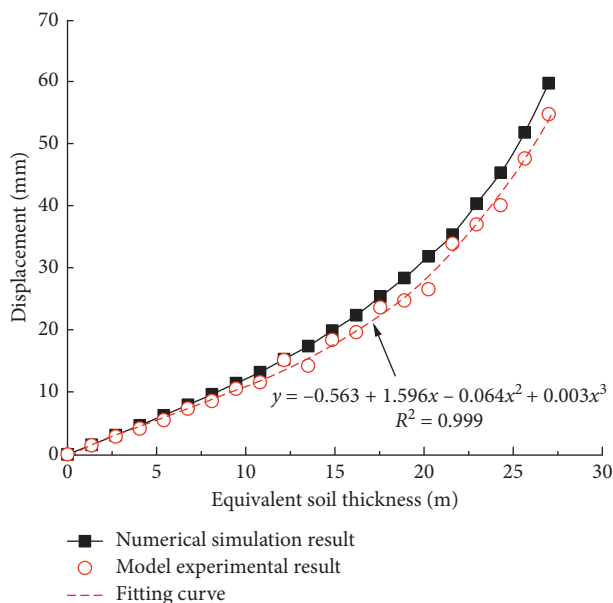


FIGURE 4: Monitoring diagram of lining displacement during loading.

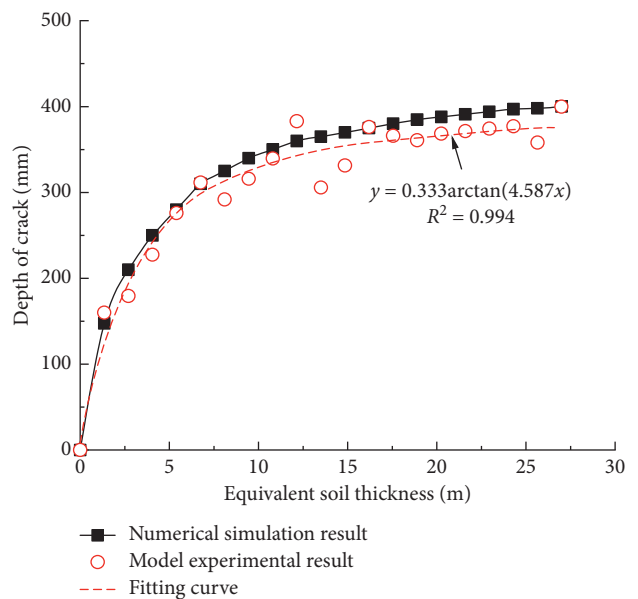


FIGURE 5: Curve of lining vault depth propagation during loading.

3.2. Parameter Analysis on Load Condition (Lining Thickness).

The crack depth in the hance is 250 mm, and PFC2D is used to calculate the crack propagation characteristics of the lining structure under deep-buried load condition of different surrounding rock grades (the grade of surrounding rock is determined according to the “Specifications for Design of Highway Tunnels, Section 1, Civil Engineering” (JTG 3370.1-2018), Grade III surrounding rock with a soil column height of 2.7 m, Grade IV surrounding rock with a soil column height of 6.8 m and Grade V surrounding rock with a soil column height of 13.5 m, Grade III surrounding rock lining with a thickness of 30 cm, Grade IV surrounding rock lining with a thickness of 40 cm and, Grade V surrounding rock lining with a thickness of 50 cm). The simulation results are shown in Figure 8. Under the action of different surrounding rock loads, when the structure cracked, the derivative cracks are similar in position and degree. Slight cracks appear in the vault, side wall, and the

middle of invert, and the inner and outer sides of cracks have not been connected, or regional large-scale cracks have not been formed, causing the overall instability or collapse of the structure. It can be preliminarily judged that when the surrounding rock condition is poor, the strengthening of the lining structure design can partially offset the structural adverse effects caused by the increased load, and the surrounding rock grade exerts less influence on the mechanical characteristics of the cracked lining in this type of supporting structure.

Green represents intact lining structures, blue for tensile cracks, red for shear cracks, and yellow for preset cracks. The calculation results remain the same for all subsequent PFC2D.

3.3. Parameter Analysis on Cracked Position. For Grade V surrounding rock with the lining thickness of 50 cm and the crack depth of $3/4 h$, when there exist different cracks in the

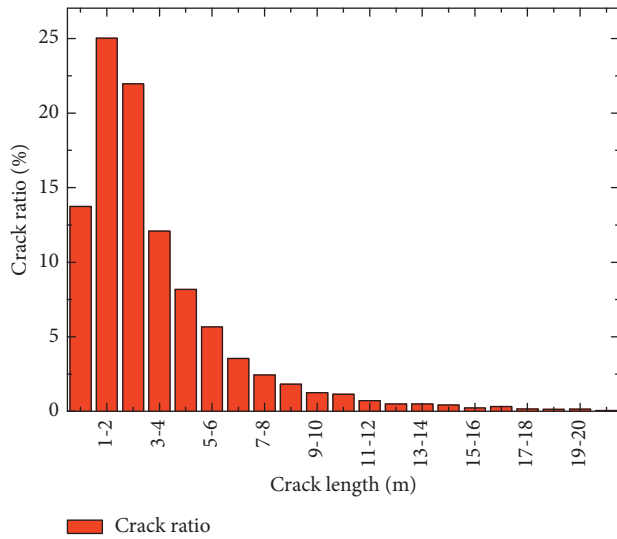


FIGURE 6: Investigation results of crack length.

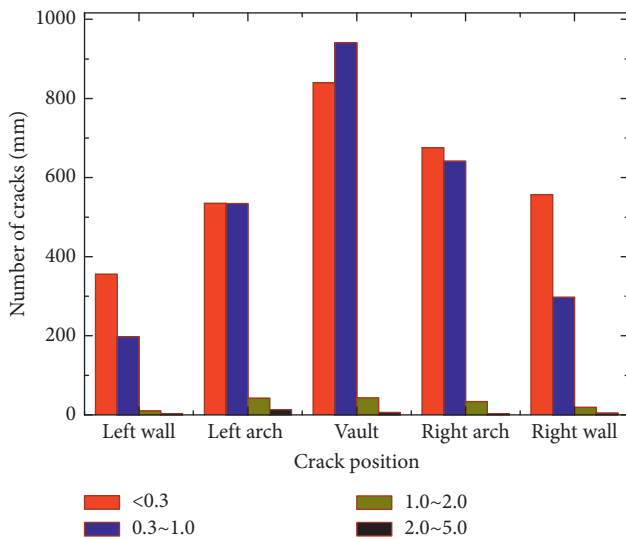


FIGURE 7: Investigation results of crack position.

vault, hance, and side wall, the final PFC2D calculation results of structural damage distribution are shown in Figure 9. Under the action of vault cracks, the derivative cracks are mainly tensile cracks, and there are secondary cracks on both sides of the vault, the hance, the bottom of the side walls, and the invert, forming a cluster of cracks in the arch with a small number of shear cracks on the outside, and the arch structure is likely to slide and fall. Under the action of hance cracks, derivative cracks appear in the vault, the hance, and the middle of the invert. The cracks are mainly shear cracks, which are distributed both inside and outside the vault and hance, and the structural risk is mainly the collapse and falling of the lateral blocks where the cracks are close to the arch. Under the action of side wall cracks, when secondary tensile cracks appear in the arch and the opposite side wall, shear cracks appear in the opposite side wall. The structural risk lies in the damage to the arch wall on the opposite side by cracks.

3.4. *Parameter Analysis on Crack Depth.* For Grade V surrounding rock with the lining thickness of 50 cm, the PFC2D calculation results of lining structure crack derivative state under the action of different crack depths are shown in Figure 10. Under the action of cracks at $1/4H$ of the vault, there are secondary cracks in the vault, hance, and invert, and the main types of cracks belong to tension crack. When the crack depth increases to $2/4H$, cracks occur at the bottom of the side wall, and the type of the new cracks belongs to tension crack. When the crack depth increases to $3/4H$, the number of cracks in the vault increases, and new cracks occur in the left and right vaults. The main types of the new cracks are attributed to tension crack, with shear cracks existing in some areas outside the structure. The difference in tunnel crack depth may lead to the increase of the number and distribution of secondary cracks in the structure, especially in the arch, where the risk of peeling, chip off-falling, and even collapse is greatly increased.

3.5. *Parameter Analysis on Crack Length.* For Grade V surrounding rock with the lining thickness of 50 cm, when the crack depth is $3/4h$, PFC3D is used to calculate the influence of different crack lengths on the load-bearing characteristics of the lining structure. In the calculation process, the longitudinal length of the structure is 10 m, which is the length of the lining structure of Model-1 tunnel. The simulation results are shown in Figure 11. When the crack length is 5 m, a small number of tensile cracks appear in the arch of lining structure under the action of load. A large number of arch tensile cracks appear when the crack length increases to 6 m. When the crack length increases to 7 m, shear cracks begin to occur in the hance on the opposite side. When the crack length increases to 8 m, the cracks in the hance on the opposite side penetrated. It can be concluded that, if the tunnel Model-1 is taken as a load-bearing unit and the crack depth is large, the structural stress is closely related to the length.

Red represents the intact lining structure, green for tensile cracks, blue for the shear cracks, and yellow for preset cracks. The calculation results are the same for all subsequent PFC3D.

3.6. *Parameter Analysis on Crack Direction.* For Grade V surrounding rock with the lining thickness of 50 cm, when the crack depth is $3/4h$, the PFC3D calculation results of lining structure crack derivative state under the action of different crack directions (longitudinal and 45° oblique) are shown in Figure 12. It can be seen that longitudinal cracks have a greater impact on the load-bearing safety of the structure by comparison and analysis of the distribution and number of cracks. Under the action of longitudinal cracks, structural damage occurs in the arch and arch walls on both sides of the structure, and there exist both tensile and shear cracks of derivative cracks, so the structural integrity is relatively poor. Under the action of oblique cracks, the structural derivative cracks are mainly distributed in the envelope area of vault longitudinal direction and crack

TABLE 2: Table for selection of influencing factors and calculation level of bearing capacity of cracked lining structure.

Level	Surrounding rock grade, R	Tunnel buried depth, H_t	Factor		Length, L (m)	Width, W (mm)	Depth, D	Direction, A (°)
			Lining thickness, T (cm)	Cracked position, P				
1	III	$0.5H$	30	Vault	2.0	1.0	0	0
2	IV	$1.0H$	35	Hance	4.0	2.0	$1/4 h$	22.5
3	V	$1.5H$	40	Side wall	6.0	3.0	$2/4 h$	45
4	VI	$2.0H$	45	Vault + hance	8.0	4.0	$3/4 h$	67.5
5	—	$2.5H$	50	Vault + side wall	10.0	5.0	$4/4 h$	90

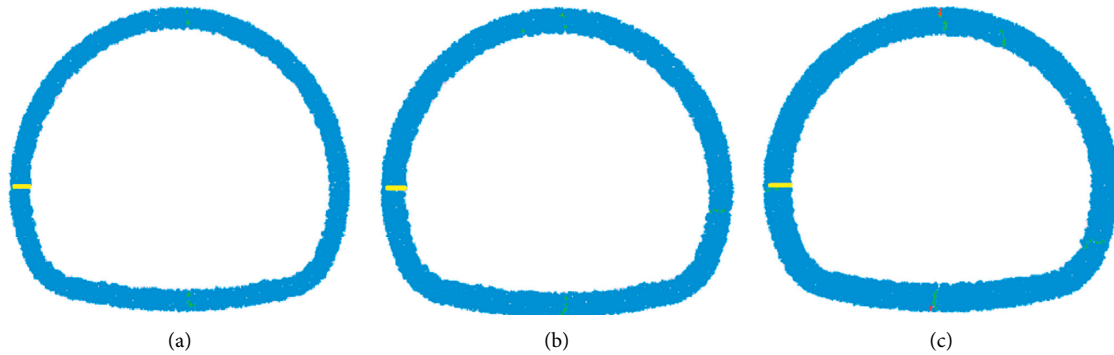


FIGURE 8: Crack-damage propagation characteristics of lining structure under different loads (thicknesses). (a) Grade III surrounding rock (30 cm thick). (b) Grade IV surrounding rock (40 cm thick). (c) Grade V surrounding rock (50 cm thick).

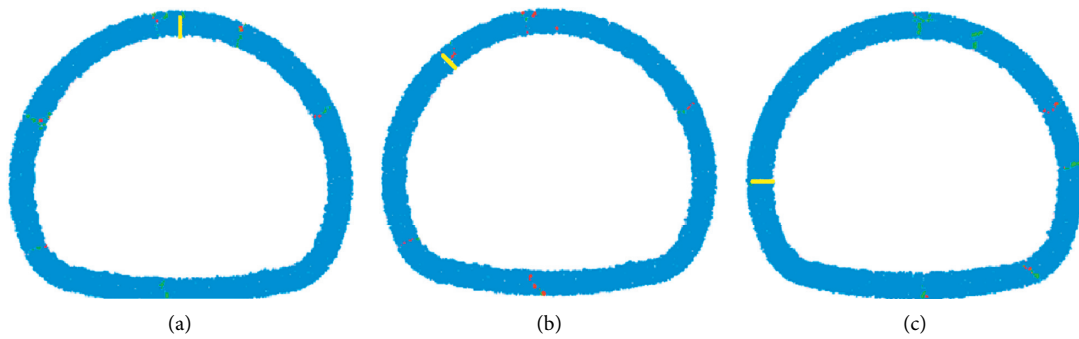


FIGURE 9: Crack-damage propagation characteristics of lining structure at different crack positions. (a) Vault crack action. (b) Hance crack action. (d) Side wall crack action.

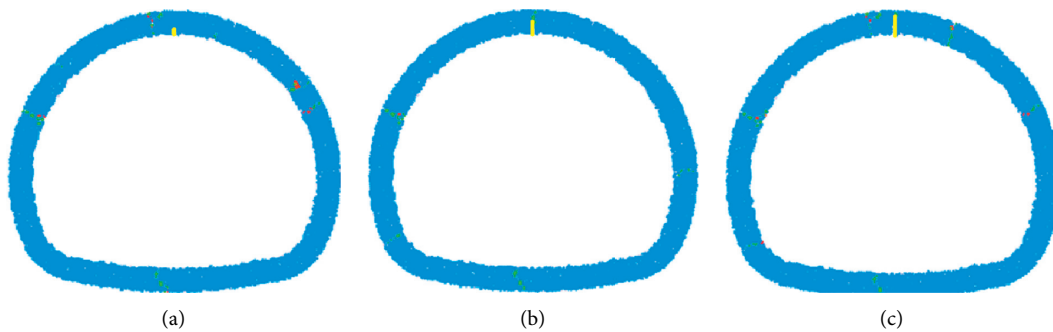


FIGURE 10: Crack-damage propagation characteristics of lining structure under different crack depths. (a) Crack depth: $1/4H$. (b) Crack depth: $2/4H$. (c) Crack depth: $3/4H$.

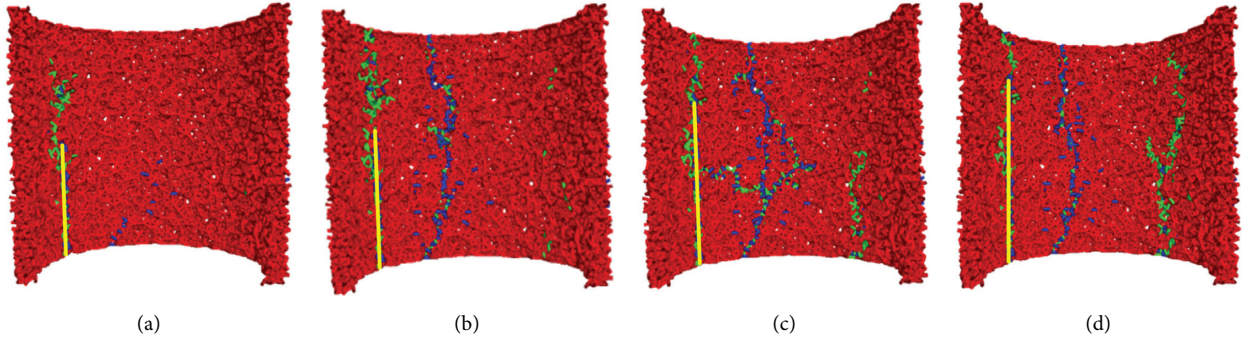


FIGURE 11: Crack-damage propagation characteristics of lining structure under different crack lengths. (a) 5 m long crack. (b) 6 m long crack. (c) 7 m long crack. (d) 8 m long crack.

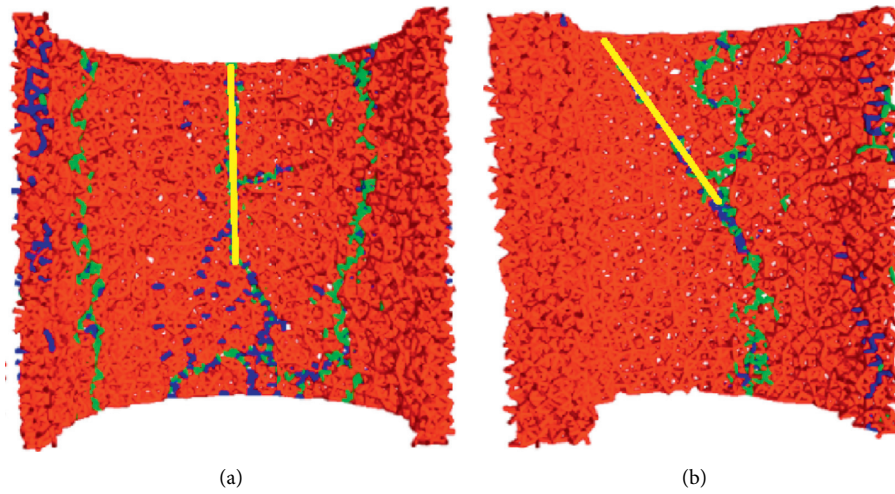


FIGURE 12: Crack-damage propagation characteristics of lining structure in different crack directions.

direction, and the influence of structural integrity is relatively small.

4. Classification of Tunnel Cracks

4.1. BP Neural Network. BP neural network is one of the most commonly used neural networks, whose full name is the artificial neural network based on the error back propagation algorithm [18]. The BP neural network is composed of input layer, hidden layer, and output layer. When the number of neurons in hidden layer is enough, the BP neural network with a three-layer structure can well approximate a discontinuous function with limited parameters. When there are i inputs, j hidden layer neurons, and k outputs, the output of the hidden layer is

$$P_j = f\left(\sum_i w_{ij}x_i - b_j\right), \quad (1)$$

where w_{ij} is the connection weight between the input layer and the hidden layer, the input variable, the threshold of the hidden layer, and also the activation function of the hidden layer. The S-shaped function is often used as the activation

function for the hidden layer, which is mainly divided into log-sigmoid function and tan-sigmoid function. Although both of them encounter the gradient disappearance, compared with log-sigmoid function, tan-sigmoid output is centered on 0 and converges fast. At the same time, tan-sigmoid function has been successfully applied in the nonlinear prediction [19]. Therefore, this paper chooses tan-sigmoid function as the activation function of the hidden layer, and its expression is

$$f_{\tan\text{-sig}} = \frac{2}{1 + e^{-2t}} - 1, \quad (2)$$

where t is the input variable of the hidden layer. The output of the output layer is

$$S_k = g\left(\sum_j w_{jk}P_j - b_k\right), \quad (3)$$

where w_{jk} is the connection weight of the hidden layer and output layer, b_k is the threshold of the output layer, and g is the transfer function of the output layer. In this paper, the linear function, purelin function, is selected as the transfer function of the output layer, and its expression is

$$g_p = a, \quad (4)$$

where a is the input variable of the output layer.

4.2. Parameters of BP Neural Network Variables. The load-bearing characteristics of cracked plain concrete lining structure mainly include two surrounding rock parameters (surrounding rock grade R and tunnel buried depth H_t), and one lining structural dimension parameter (lining thickness), and five crack information parameters (crack position P , crack length L , crack width W , crack depth D , and crack direction A). Due to the strong correlation between the design thickness of lining structure and the surrounding rock grade, the worse the surrounding rock condition is, the thicker the structure is. According to the calculation and analysis, the enhancement of corresponding structure thickness design under different surrounding rock grade conditions makes it able to resist the load increased by the change of surrounding rock, and the ultimate crack-damage bearing characteristics are similar. Therefore, in BP neural network training, the surrounding rock grade and lining structure thickness are not considered as the amount of training.

To sum up, the comprehensive evaluation of crack lining performance is characterized as follows:

$$P_x = f(H_t, P, L, W, D, A). \quad (5)$$

4.3. Crack Classification Sample. The training data of the BP neural network are mainly calculated from crack bearing characteristics. Through modeling and calculation, the load-bearing characteristics data of cracked lining under 471 sets of working conditions are obtained. For each set of calculation results, they are divided into four grades according to the degrees of influence, which are denoted as 1, 2, 3, and 4, respectively. The crack meanings are the same as I, II, III, and IV in Table 3. Combined with PFC numerical calculation results and the expert scoring system, the initial data of the 471 lining crack conditions and the comprehensive rating are determined. When the training data of the BP neural network are sorted out, different tunnel depths are characterized by 0.5, 1.0, 1.5, 2.0, and 2.5, respectively, vault, hance, side wall, vault+hance, and vault+side wall are characterized by 1, 2, 3, 4 and 5, respectively, and the relative depths of cracks are characterized by 0, 0.25, 0.5, 0.75, and 1.0, respectively. Due to the limits of textual length, some parts of the training data are extracted after, as shown in Table 4.

4.4. Data Set Division and Effect Evaluation

4.4.1. Data Division. In this paper, a BP neural network model is established by using 471 sets of data samples. Through the stratified sampling method, the data are divided into 10 parts according to the attributes of data source. Then, Kennard-Stone algorithm is used to divide each part of data into two parts according to the ratio of 4:1. 80% of the

samples in each part are combined as the training set and 20% as the test set.

When using the model for training and testing, the parameters are normalized to the interval of [0, 1], and the final output value of the model is transformed into the actual order of magnitude value through antinormalization. In the setting of the network parameter, the number of iterations is 2000, the target accuracy is 1×10^{-5} , and the maximum number of failures in the verification set is 200 (this parameter does not exist in the Bayesian regularization algorithm).

4.4.2. Evaluation Indexes. Mean square error (E^2) and determination coefficient (R^2) are used as evaluation indexes:

$$E^2 = \frac{1}{n} \sum_{i=1}^n (p_i - \hat{p}_i)^2, \quad (6)$$

$$R^2 = 1 - \frac{\sum_{i=1}^n (p_i - \hat{p}_i)^2}{\sum_{i=1}^n (p_i - \bar{p})^2},$$

where n is the number of data samples; p_i is the measured value; \hat{p}_i is the predicted value; and \bar{p} is the average value of measured data.

4.4.3. Number of Neurons. To compare the influence of different neuron numbers and training algorithms on the prediction performance of the BP neural network, L-M algorithm, quasi-Newton algorithm, and Bayesian regularization algorithm are used to compare the prediction performance, and each training algorithm is used to predict the hidden layer neurons at three levels (6, 7, and 8), respectively. Among them, the middle level selection with 7 neurons in the hidden layer is based on the empirical formula $2m + 1$, where m is the number of neurons in the input layer. In order to avoid the influence of network initial weight and threshold randomness, each combination of BP neural networks continuously runs for 10 times, and the 10-time mean value of evaluation indexes is selected for evaluation. The predicted E^2 mean values of the training set and test set are shown in Figure 2.

It can be seen that, under the same training algorithm, different numbers of hidden-layer neurons have an impact on the prediction accuracy of the training set and the test set. According to the comparison, the E^2 of each training algorithm is greater when the number of hidden layer neurons is 6 and 8 than when the number of hidden layer neurons is 7. Therefore, 7 is the optimal number of neurons in the hidden layer, L-M algorithm, quasi-Newton algorithm, and Bayesian regularization algorithm [20–22] shown in Figure 13, and it is used to carry out fitting process, having achieved more optimal prediction performance. The E^2 predicted for the training set is 2.021×10^{-10} , 2.378×10^{-10} , and 2.132×10^{-10} , respectively, and the E^2 predicted for the test set is 1.512×10^{-10} , 1.994×10^{-10} , and 1.257×10^{-10} , respectively.

TABLE 3: Judgment of fitting result grade of the BP neural network.

Crack grade	Fitting result	Engineering significance
I	0.8~1.2	The cracks are stable without growth
II	1.8~2.2	The degree of crack damage is deepening, but the cracks have not yet penetrated along the vertical and horizontal directions. New cracks form in different positions
III	2.8~3.2	New cracks form in different positions. Some cracks have penetrated, but there is no concentrative penetration of multiple cracks.
IV	3.8~4.2	Multiple cracks penetrate concentratively.

TABLE 4: BP neural network training sample data.

Simulation number	Buried depth, H_t	Cracked position, P	Length, L (m)	Width, W (mm)	Depth, D	Direction, A (°)	Crack grade
1	0.5	1	6.0	3.0	0.5	0	2
2	2.5	1	6.0	3.0	0.5	0	4
3	1.5	3	6.0	3.0	0.5	0	1
4	1.5	5	6.0	3.0	0.5	0	4
5	1.5	1	2.0	3.0	0.5	0	1
6	1.5	1	10.0	3.0	0.5	0	3
7	1.5	1	6.0	1.0	0.5	0	2
8	1.5	1	6.0	5.0	0.5	0	4
9	1.5	1	6.0	3.0	0	0	1
10	1.5	1	6.0	3.0	1	0	4
11	1.5	1	6.0	3.0	0.5	45	2
12	1.5	1	6.0	3.0	0.5	90	1
...
471	1.5	1	6.0	3.0	0.5	0	3

4.4.4. *Training Algorithm.* When the number of neurons in the hidden layer is 7, it can be seen from Table 5 that the R^2 predicted by the three training algorithms for both the training set and the test set is greater than 0.95, showing good accuracy of prediction. The R^2 for the training set and the test set by the L-M algorithm is 0.958 and 0.982, respectively. The prediction accuracy is higher than that by the quasi-Newton algorithm and is slightly lower than that by Bayesian regularization algorithm. Among them, the Bayesian regularization algorithm shows the best prediction performance, and the R^2 for the training set and the test set was 0.976 and 0.989, respectively. The Bayesian regularization algorithm which has adaptive regularization parameters can better avoid the underfitting and overfitting issues in network training, and then guarantee the robustness and generalization performance of the BP neural network. In this paper, the Bayesian regularization algorithm-based BP neural network with the hidden layer neuron being 7 is established.

4.5. *Crack Classification System.* Through data training, the BP neural network has been able to fit the classification characteristics of cracked lining perfectly. During engineering application, in order to facilitate practical operation within the range of reliability requirements, the calculation result grade of the BP neural network is judged according to Table 3, and the bearing capacity and stability of cracked structure gradually weaken from Grade I to Grade IV. If the fitting result is within the table range, the expert system can be introduced for comprehensive judgment. The judgment data as the training data are updating continuously, thus

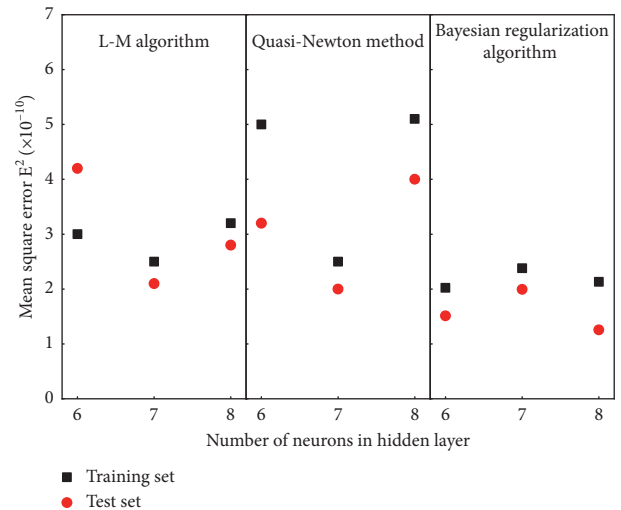


FIGURE 13: Comparison of E2 among different BP neural network models (E2 is the average of 10 prediction results).

making the trained BP neural network dynamically optimal so as to enable them to have both mechanical calculation reliability and practicability of experience judgment.

The training of the BP neural network requires professionals to program, adjust, and update, and the demand for professional knowledge is high, so there is difficulty in wide application and popularization. In order to reduce the learning difficulty and ensure the universality and feasibility, a software for classifying cracked lining structure is developed on the basis of numerical calculation and BP neural network training, as well as the features (such as light weight,

TABLE 5: Average value of R^2 predicted by different training data functions for 10 times.

Training algorithm	Number of neurons in hidden layer	Training set R^2	Test set R^2
L-M algorithm	7	0.958	0.982
Quasi-Newton method	7	0.947	0.953
Bayesian regularization algorithm	7	0.976	0.989

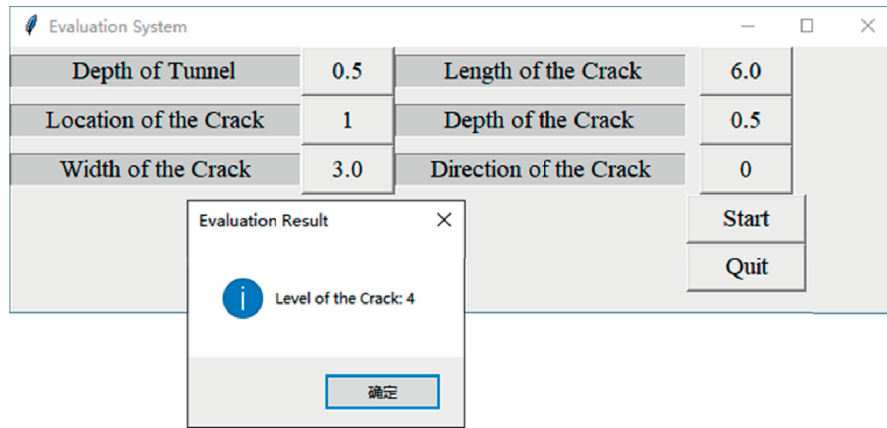


FIGURE 14: Crack classification system based on Python programming and neural network kernel.

high efficiency, and safety) of Python language. Users only need to input crack detection data, and the classification results can be output automatically. The system interface is shown in Figure 14. Through continuous application, update, and optimization, the classification software has already demonstrates good accuracy.

5. Discussion

This study aims at crack classification and achieves the accuracy and efficiency of lining crack classification by taking PFC particle flow mechanics calculation as the basis and making use of the BP neural network for training and prediction, supplemented by the expert system to dynamically optimize and adjust the high deviation results. However, due to the following factors, which include the reliability guarantee of using PFC particle flow to calculate and analyze the cracked lining structure, the cause index when calculating the cracked lining and the mechanical characteristics of cracks in the reinforced concrete lining structure is complicated, and further discussion and explanation are elaborated separately as follows:

- (1) Reliability guarantee of PFC calculation: compared with traditional finite element analysis or extended finite difference analysis, the selection of PFC calculation parameters involves complex dynamic calibration and optimization, which requires a long adjustment process and a high use cost, so it is relatively less applied. However, as a major challenge affecting engineering safety, it is urgent to seek new analysis ideas and obtain intuitive calculation results to guide engineering disease prevention and control. In addition, the significance far exceeds the cost

itself. Based on the existing mechanical test of concrete specimen and the model experiment of bearing characteristics of cracked lining, this project conducts macrosimulation effect controls from both aspects of material characteristics and structural characteristics, thus ensuring the validity and reliability of calculation parameters and calculation results.

- (2) Consideration of lining crack causes: the causes of cracks in lining structure are the key external causes that affect the crack state. However, due to the characteristics of tunnel structure, most of the genetic parameters, such as structural bias, stratum dislocation, and hydrostatic pressure, cannot be directly obtained by testing, which need to be refined and judged by combining expert analysis. Too many parameters may lead to extremely complex calculation and make it difficult to realize and control. In this paper, taking the tunnel buried depth, surrounding rock grade, and lining thickness as representatives of external action and structural strength, the crack length, width, depth, and direction as phenomenon indexes, the corresponding relationship between the external action and the internal response is established on mechanics. Due to the strong correlation between the causes and phenomena of diseases, the crack phenomena are very different under different causes of diseases. If the input parameters are contrary to the model assumptions, the fitting results of the BP neural system will deviate greatly from the training data, so expert system intervention is adopted for constantly improving and optimizing the neural network

parameters, so as to dynamically consider the complex conditions eventually.

- (3) Consideration of cracks in reinforced concrete lining: tunnel lining structure is mainly divided into plain concrete and reinforced concrete. In early tunnel construction, due to the inadequate economic development, plain concrete is widely used. However, due to the weak tensile capacity of concrete materials, when the surrounding rock condition is poor, the tunnel lining is prone to bending failure and shear failure under the action of load, thus leads to a lot of cracks in the early plain concrete structure. That is the reason why this study mainly focuses on plain concrete structure. For reinforced concrete structure, the PFC particle flow method in the study of lining cracks is still not mature, the numerical modeling and reduction of the cooperative bearing capacity with different materials of steel and concrete are relatively complex and involve more indexes and parameters. Therefore, the research on the mechanical characteristics and classification of cracks in reinforced concrete structure is included in the next stage of work, and the follow-up research will be carried out continually upon the maturity of conditions.

6. Conclusion

This study focuses on the difficult problem of tunnel crack classification, taking plain concrete structure as the object, using the PFC particle flow calculation method to calculate the bearing capacity and crack propagation characteristics of cracked structure under different load conditions, structural conditions, and crack phenomena. The BP neural network system based on mechanical calculation results has been obtained through training. In this study, expert dynamic errata mechanism is introduced and the software is programmed to achieve accurate and efficient fracture classification.

The specific research achievements are as follows:

- (1) In this study, the axial compression test of C30 plain concrete structure and the bearing capacity test of cracked tunnel have been carried out. Through the analysis and comparison of bearing capacity and deformation characteristics, the calculation parameters of PFC are dynamically investigated. The errors between the final simulation results of structural displacement, crack depth, and the test results are less than 10% and 18%, respectively, which proves the feasibility of PFC in tunnel crack calculation and the accuracy of parameter values taken.
- (2) Based on the statistical analysis of diseases, practical operation feasibility, and numerical simulation analysis, a classification index system is proposed, which takes the tunnel buried depth H as the load characterization quantity, and the crack position P , crack length L , crack width W , crack depth D , and crack direction A as the disease characterization quantities. Combined with the state of load-bearing safety, crack stability, and expert system, the basic data of lining crack classification based on mechanical characteristics are obtained.
- (3) A neural network system using seven hidden layer neurons and the Bayesian regularization algorithm is obtained through the BP neural network artificial intelligence prediction tool as well as the training and verification of the basic data of mechanical calculation results. An expert system errata mechanism is introduced to target the high deviation prediction results, which realizes the dynamic optimization, stability, and reliability of complex disease evaluation.

Data Availability

The (BP neural network training sample) data used to support the findings of this study are currently under embargo while the research findings are commercialized. Requests for data, (6/12 months) after publication of this article, will be considered by the corresponding author.

Conflicts of Interest

The authors declare that they have no conflicts of interest.

Authors' Contributions

Hao Ding and Xinghong Jiang contributed equally.

Acknowledgments

This work was financially supported by the National Key Research and Development Program of China (2017YFC08060010), the Science and Technology Project of Department of Transportation of Yunnan Province (grant no. YJKJ (2018) 22), and The Key Technology Innovation Special of Key Industries of the Chongqing Science and Technology Bureau (grant nos. cstc2019jscx-fxydX0017, cstc2019jscx-gksbX0071, and cstc2019jscx-gksbX0008).

References

- [1] K. Yau, C. Paraskevopoulou, and S. Konstantis, "Spatial variability of karst and effect on tunnel lining and water inflow. A probabilistic approach," *Tunnelling and Underground Space Technology*, vol. 97, Article ID 103248, 2020.
- [2] "Structural health monitoring of a road tunnel intersecting a large and active landslide," *Applied Sciences*, vol. 7, no. 12, p. 1271, 2017.
- [3] D. L. N. d. F. Amorim, S. P. B. Proença, and J. Flórez-López, "Simplified modeling of cracking in concrete: application in tunnel linings," *Engineering Structures*, vol. 70, pp. 23–35, 2014.
- [4] G. Xu, C. He, Z. Chen, C. Liu, B. Wang, and Y. Zou, "Mechanical behavior of secondary tunnel lining with longitudinal crack," *Engineering Failure Analysis*, vol. 113, Article ID 104543, 2020.
- [5] Y.-C. Chiu, C.-H. Lee, and T.-T. Wang, "Lining crack evolution of an operational tunnel influenced by slope instability," *Tunnelling and Underground Space Technology*, vol. 65, pp. 167–178, 2017.

- [6] J. Z. Xiao, F. C. Dai, Y. Q. Wei et al., "Cracking mechanism of secondary lining for a shallow and asymmetrically-loaded tunnel in loose deposits," *Tunnelling and Underground Space Technology*, vol. 43, pp. 232–240, 2014.
- [7] Y. Kim and A. Bruland, "Analysis and evaluation of tunnel contour quality index," *Automation in Construction*, vol. 99, pp. 223–237, 2019.
- [8] H. Ding, K. Li, Y. Xiayang et al., "Study on the grade evaluation of highway tunnel cracks based on PFC simulation and BP neural network," in *Tunnelling and Underground Construction. GSIC 2018*, D. Zhang and X. Huang, Eds., Springer, Singapore, pp. 605–611, 2018.
- [9] Y. Zhang, Z. Shao, W. Wei, and R. Qiao, "PFC simulation of crack evolution and energy conversion during basalt failure process," *Journal of Geophysics and Engineering*, vol. 16, no. 3, pp. 639–651, 2019.
- [10] H. Haeri, V. Sarfarazi, and Z. Zhu, "Effect of normal load on the crack propagation from pre-existing joints using Particle Flow Code (PFC)," *Computers and Concrete*, vol. 19, no. 1, pp. 99–110, 2017.
- [11] C. Xu, G. Wang, and Q. Zhang, "A new multi-step backward cloud transformation algorithm based on normal cloud model," *Fundamenta Informaticae*, vol. 133, no. 1, pp. 55–85, 2014.
- [12] R. Jiang, F. Dai, Y. Liu, and M. Wei, "An automatic classification method for microseismic events and blasts during rock excavation of underground caverns," *Tunnelling and Underground Space Technology*, vol. 101, p. 103425, 2020.
- [13] S.-C. Lau, M. Lu, and S. T. Ariaratnam, "Applying radial basis function neural networks to estimate next-cycle production rates in tunnelling construction," *Tunnelling and Underground Space Technology*, vol. 25, no. 4, pp. 357–365, 2010.
- [14] B. Liu, R. Wang, G. Zhao et al., "Prediction of rock mass parameters in the TBM tunnel based on BP neural network integrated simulated annealing algorithm," *Tunnelling and Underground Space Technology*, vol. 95, Article ID 103103, 2020.
- [15] J. Ninić and G. Meschke, "Model update and real-time steering of tunnel boring machines using simulation-based meta models," *Tunnelling and Underground Space Technology*, vol. 45, pp. 138–152, 2015.
- [16] X. Zhang, H. Nguyen, X.-N. Bui et al., "Evaluating and predicting the stability of roadways in tunnelling and underground space using artificial neural network-based particle swarm optimization," *Tunnelling and Underground Space Technology*, vol. 103, Article ID 103517, 2020.
- [17] P. A. Cundall and O. D. L. Strack, "Discussion: a discrete numerical model for granular assemblies," *Géotechnique*, vol. 30, no. 3, pp. 331–336, 2008.
- [18] D. E. Rumelhart, G. E. Hinton, and R. J. Williams, "Learning representations by back-propagating errors," *Nature*, vol. 323, no. 6088, pp. 533–536, 1986.
- [19] J. L. Ticknor, H. Hsu-Kim, and M. A. Deshusses, "A robust framework to predict mercury speciation in combustion flue gases," *Journal of Hazardous Materials*, vol. 264, pp. 380–385, 2014.
- [20] A. Antoniou and W. S. Lu, *Practical Optimization: Algorithms and Engineering Applications*, Springer Publishing Company, Incorporated, New York, NY, USA, 2010.
- [21] M. T. Hagan and M. B. Menhaj, "Training feedforward networks with the Marquardt algorithm," *IEEE Transactions on Neural Networks*, vol. 5, no. 6, pp. 989–993, 2002.
- [22] F. D. Foresee and M. T. Hagan, "Gauss-Newton approximation to Bayesian learning," in *Proceedings of International Conference on Neural Networks (ICNN'97)*, Houston, TX, USA, June 1997.

Research Article

An Improved Nondestructive Semantic Segmentation Method for Concrete Dam Surface Crack Images with High Resolution

Jun Zhang ¹ and Jia Zhang ²

¹State Grid Hunan Electric Power Company Limited Research Institute, Changsha, Hunan, China

²Changsha Jinfengtan High-Tech Company Limited, Changsha, Hunan, China

Correspondence should be addressed to Jun Zhang; sghnzj1988@163.com

Received 8 June 2020; Revised 16 September 2020; Accepted 28 October 2020; Published 17 November 2020

Academic Editor: Yu-Sheng Shen

Copyright © 2020 Jun Zhang and Jia Zhang. This is an open access article distributed under the Creative Commons Attribution License, which permits unrestricted use, distribution, and reproduction in any medium, provided the original work is properly cited.

To nondestructive semantic segment the crack pixels in the image with high resolution, previous methods often use sliding window and the crack patches to train the FCNs, and then use the trained FCNs for crack recognition. However, the FCNs will produce a higher proportion of false crack predictions with messy distributions in the high-resolution image. A CNN-to-FCN method is proposed to solve this problem. The CNN is trained by all the patches for large-scale crack and background recognition, and the screened crack predictions are then segmented by the FCN. A real-world concrete dam surface crack image database is firstly established to verify the improved method. The results indicated that (1) the improved method can extremely avoid the higher proportion of false crack predictions and their messy distributions in the high-resolution image through the full utilization of background patches and large-scale background recognition; (2) the ResNetv2 backbone and DeepLabv3 architecture recommended by the improved method can be further modified by reducing the bottleneck channels and adding a DUC module to achieve better performance; (3) the improved method can also reduce the prediction time when the image has low proportion of crack patches, which becomes more practicable for the engineering applications.

1. Introduction

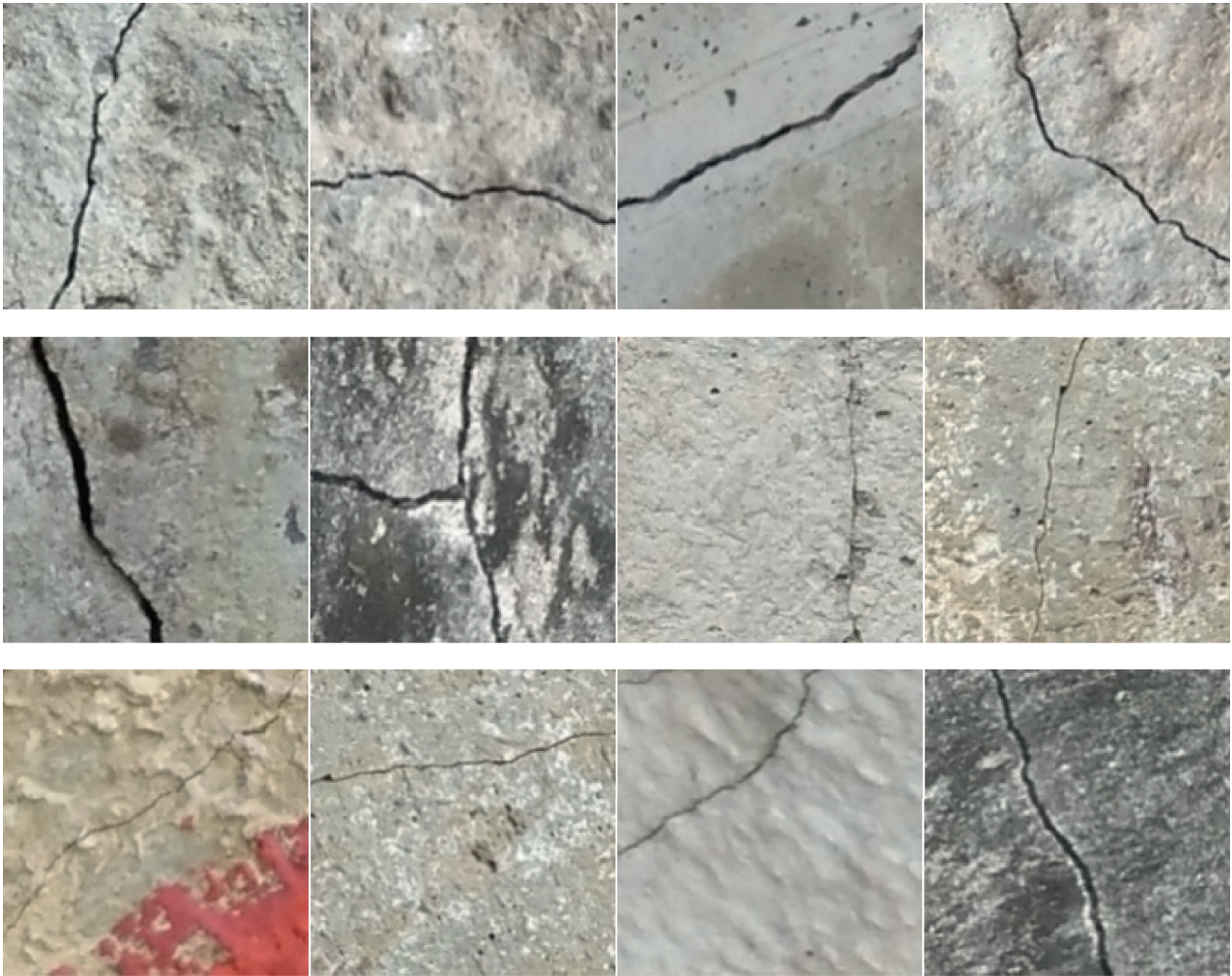
Dam safety monitoring is one of the most important tasks in reservoir project management. The “monitoring” includes not only the instrument observation and analysis of the fixed measuring points [1, 2] but also the visual inspection and instrument exploration on the dam. Through monitoring, the abnormal state of the dam can be discovered and dealt with in time to avoid serious consequences.

Crack detection plays a vital role in dam safety monitoring. The crack occurs on the concrete dam since the construction stage. Some cracks are beneficial, such as the artificial crack which is used to prevent the hydration heat temperature crack. Some cracks are harmful, which can decline the dam concrete strength or format leakage passage. Manual inspection is a traditional way to detect cracks. However, the vast space of the dam will limit the inspection scope and lead to time-consuming and inefficient.

Moreover, the crack detail and developing process are difficult to track and evaluate.

Automated crack detection with computer vision method is an effective way to replace manual inspection. In the past, researchers often adopted image processing, edge detection, and morphological operations to detect crack [3–9]. For dam concrete, Fan Xinnan et al. [10] uses local-global clustering analysis and the image processing method to identify the visual detection of underwater dam surface cracks. These methods have been proved to be useful in some situations, such as bright characteristics, high contrast, less noise, and strong continuity of crack. However, they may not be applicable to the dam concrete surface with diverse background texture, various types of noise, and irregular crack distribution (Figure 1(b)).

In recent years, a more powerful image recognition and detection technology based on the convolutional neural network (CNN) has been proposed by Lecun et al. [11], and



(a)

FIGURE 1: Continued.



(b)

FIGURE 1: The crack patches from high-resolution images of dam surface: (a) simple cracks; (b) intricate cracks.

then shows excellent potential in dealing with these complex scenarios above. To further classify the image in pixel level, Long et al. [12] proposed a specific CNN named the fully convolutional network (FCN). The basic FCN model is then developed by some optimized backbones and algorithms, including decoder variants and integrating context knowledge, such as the SG-net, U-net, and DeepLab [13]. Meanwhile, the crack detection techniques based on CNN or FCN have already applied in various civil structures such as

the bridges, roads, buildings, highways, and tunnel, and proved to be a more efficient way than the previous methods.

For classification tasks, Dorafshan et al. [14] compare the performance of common edge detectors and deep convolutional neural networks (AlexNet DCNN) for image-based crack detection in concrete panels. Hongyan Xu et al. [15] use the techniques of atrous convolution, atrous spatial pyramid pooling (ASPP) module, and depthwise separable convolution to improve the traditional CNN, and the bridge

crack dataset is established to verify the proposed model. Umme Hafsa Billah et al. [16] propose the ResNet to detect cracks of various roads, highways, and bridge decks at different times of the day and for different light orientation conditions. With the ResNet-based classifier, Chen Feng et al. [17] use AL to reduce the number of civil infrastructure surface images required for annotation and thus reduce the effort and cost of annotation by domain experts. Meanwhile, the backbones of VGG and GoogLeNet are also used to detect concrete crack [18–20].

For pixel-level classification tasks, Jianming Zhang et al. [21] use FCN and dilated convolution to detect cracks from various campus buildings. Zhenqing Liu et al. [22] propose U-Net to detect the concrete cracks of campus buildings. Allen Zhang et al. [23] developed a CNN architecture without pooling layers named CrackNet for automated pavement crack detection on 3D asphalt surfaces. Weidong Song et al. [24] used multiscale dilated convolutional module for automated pavement crack detection. Yupeng Ren et al. [25] used techniques of dilated convolution, spatial pyramid pooling, skip connections, and an optimized loss function for concrete crack detection in tunnels. For backbones, the VGG, DenseNet, and ResNet are frequently used to detect pixel-wise concrete crack [26–28].

In this study, we establish a crack image database of dam concrete surface for the first time. A high-resolution camera acquires these images. However, the high-resolution image is inappropriate as the FCN input directly due to the limited calculating conditions such as GPU memory. To pursuit the speed, a destructive way is to shrink the image size, but it will reduce the accuracy, especially for the small pixel width of cracks, as shown in Figure 1(b). A nondestructive solution is to apply the sliding window to divide the high-resolution image into small patches to fit the input size of FCN. However, previous FCNs only adopt the crack patches to alleviate the category imbalance and extensive computation, which has a small percentage of all the patches. Frustratingly, it will produce a higher proportion of false crack predictions with messy distributions in the high-resolution image prediction.

Therefore, we provide a CNN-to-FCN nondestructive semantic segmentation method to solve the problem above. The method firstly adopts sliding window and CNN to locate the crack approximately and then uses FCN to segment the crack predictions. CNN and FCN are trained separately by different datasets. The CNN trains the crack and background patches to ensure the background information is fully utilized, while the FCN trains only the crack patches.

The contributions of this paper mainly include five aspects, as follows:

- (1) Propose a CNN-to-FCN nondestructive semantic segmentation method for dam crack detection
- (2) Apply the ResNetv2 backbone and the DeepLabv3 architecture for dam crack semantic segmentation
- (3) Crop the ResNetv2 backbone bottleneck channels to accelerate networks and improve their performance

- (4) Propose the dense upsampling convolution (DUC) in the upsampling stage of DeepLabv3
- (5) Establish a concrete dam crack dataset (Dam-CrackDataset) for the first time

The content of this paper is described as follows: Section 2 demonstrates the basic CNN and FCN, the mainstream backbone ResNet and the DeepLab architecture, and the DUC module. Section 3 introduces our improved nondestructive semantic segmentation method and improved model for concrete dam crack detection. The Dam-CrackDataset is established to verify the performance of different methods and models in Section 4. Finally, Section 5 concludes this article.

2. CNN and FCN

2.1. Basic CNN and FCN. The basic CNN consists of three parts: the input layer, convolution layers, and pooling layers, and a fully connected multilayer perceptron classifier. Convolution and pooling operations can greatly simplify model complexity and reduce model parameters. The basic CNN is a feature extractor with the advantage that human engineers do not need to design multiple layers of features. Compared to the standard feedforward neural networks, CNN has better learning and adaptive ability due to its unique designs.

The main function of the convolution layer is to convolve the convolution kernel with the input data of the upper layer, in which the convolution kernel in the convolutional layer is applied to feature extraction. It can also reduce the connection between different layers to prevent overfitting and too many parameters. The next layer output can be expressed as follows:

$$y(i, j) = \sum_{m=1}^M \sum_{n=1}^N x(i+m-1, j+n-1)k(m, n), \quad (1)$$

$$i = 1, 2, \dots, p, j = 1, 2, \dots, q,$$

where $y(i, j)$ is the element of the output matrix \mathbf{y} with order $p \times q$; $x(i+m-1, j+n-1)$ is the element of the input matrix \mathbf{x} with order $p \times q$; and $k(m, n)$ is the element of the convolution kernel \mathbf{k} with order $M \times N$.

The pooling layer divides the input data into multiple nonoverlapping regions, and take the maximum value (maximum pooling) or average value (average pooling) of each region. It can eliminate noncritical feature samples, thus improving the training efficiency and estimation accuracy, and the pooling formula is

$$y' = \max_R(y) \text{ or } \text{mean}_R(y), \quad (2)$$

where R is the pooling region.

The fully connected layer expands the two-dimensional data passing through the convolution layer and pooling layer into one-dimensional data. It can be expressed as follows:

$$o = f(\mathbf{w}^T \mathbf{c} + b), \quad (3)$$

where \mathbf{w} is the connection weight vector; c is the expanded one-dimensional data; b is the bias; o is the output; and f is an activation function which can enhance the network's nonlinear characteristics. For example, rectified linear unit (ReLU) is a popular activation function which can activate the neurons of the neural network sparsely and can be expressed as follows:

$$\text{ReLU}(y(i, j)) = \begin{cases} y(i, j), & y(i, j) > 0, \\ 0, & y(i, j) \leq 0. \end{cases} \quad (4)$$

The difference between FCN and CNN is that FCN converts the fully connected layer of CNN to the convolution layer. The converted convolution layer adopts upsampling to make the output to be the same size as the input image, which can achieve pixel-level prediction and retaining the original input space information of images.

2.2. ResNet Backbone. The ResNet backbone [29, 30] is put forward to solve the problem that deeper networks are more challenging to train. This kind of network is equivalent to add a new channel of the input so that the input can reach the output directly. Then, the optimization objective changes from the original output $H(x)$ to the residual between the $H(x)$ and input x . The ResNet backbone shows excellent characteristics in precision and convergence by using an extremely deep network. The ResNet series have two versions named ResNetv1 and ResNetv2 (Figure 2). ResNetv2 adopts the identity after-addition activation to make information propagation smoother. The asymmetric after-addition activation is equivalent to constructing a preactivation residual unit. In this study, the ResNetv2 model is adopted.

2.3. DeepLab Architecture. DeepLab series [31–34] are semantic segmentation deep learning models developed from FCN model. There are two technical hurdles in the application of basic FCN model: downsampling and spatial invariance. The downsampling method will reduce the resolution, especially at the high-level layers. The spatial invariance means that obtaining object-centric decisions from a classifier requires invariance to spatial transformations, inherently limiting the spatial accuracy. DeepLabv1 employs the atrous convolution algorithm and conditional random field (CRF) to address the downsampling and the spatial invariance, respectively. DeepLabv2 uses atrous spatial pyramid pooling (ASPP) to robustly segment objects at multiple scales. To encode multiscale information, DeepLabv3 proposes a cascaded module and an improved ASPP module. The cascaded module gradually doubles the atrous rates, and the improved ASPP module augmented with image-level features probes the features with filters at multiple sampling rates and effective field-of-views. DeepLabv3+ extends DeepLabv3 by adding a simple yet effective decoder module to refine the segmentation results, especially along object boundaries. For backbone, DeepLabv1 is constructed by VGG-16. DeepLabv2 and DeepLabv3 use the ResNet. DeepLabv3+ adopts the ResNet and Xception.

3. Improved Method and Model

3.1. CNN-to-FCN Method. The flowchart of our CNN-to-FCN nondestructive semantic segmentation method is shown in Figure 3 and demonstrated as follows:

- (i) Step 1: get high-resolution images of dam concrete surface. The images are then manual labelled by pixel level.
- (ii) Step 2: use the sliding window to get the image patches and their annotations. Meanwhile, the patches can be augmented, but the annotations should be nondestructive for FCN. For CNN, annotation of each patch should be further used to generate a new global crack dichotomy annotation. For FCN, the pixel-level annotations are used directly.
- (iii) Step 3: split the patches into training, validation, and test patches. The training patches are applied to train the model, while the validation patches are to choose the best parameters. The test patches are used to estimate the performance of the model.
- (iv) Step 4: train and optimize CNN using the training and validation patches, including crack and background patches.
- (v) Step 5: train and optimize FCN using the training and validation patches, including only the crack patches.
- (vi) Step 6: predict the test patches and judge whether each patch is crack by using the trained CNN.
- (vii) Step 7: classify the crack predictions according to Step 6 on pixel level by using the trained FCN.

Significantly, previous methods only train and test the crack patches, while the improved method trains the crack and background patches to fully utilize the background information. The large-scale background recognition by the improved method can make us focus on the fewer crack patches of the high-resolution image, thus avoiding the messy distributions of false crack predictions.

3.2. Improved Model. In this study, we use the ResNetv2-50 backbone and integrate a dense upsampling convolution (DUC Figure 4) module proposed by Wang et al. [35] into DeepLabv3 architecture (Figure 5) because the DUC operation can be naturally integrated into the DeepLabv3, makes the whole encoding and decoding process end-to-end trainable, and only increases the FLOPs by a small amount.

At the stage of upsampling, the DeepLab series models often used the bilinear interpolation method. As most of the width pixels of cracks are fewer than 4 pixels in our DamCrackDatabase, the bilinear interpolation will more likely miss the fine-detailed information of crack when the downsampling rate is less than 1/4. DUC is more effective than the bilinear interpolation method, and the deconvolution method used by the basic FCN model. The key idea of DUC is to transform the whole label map into a smaller label map with multiple channels. At the upsampling stage, DUC

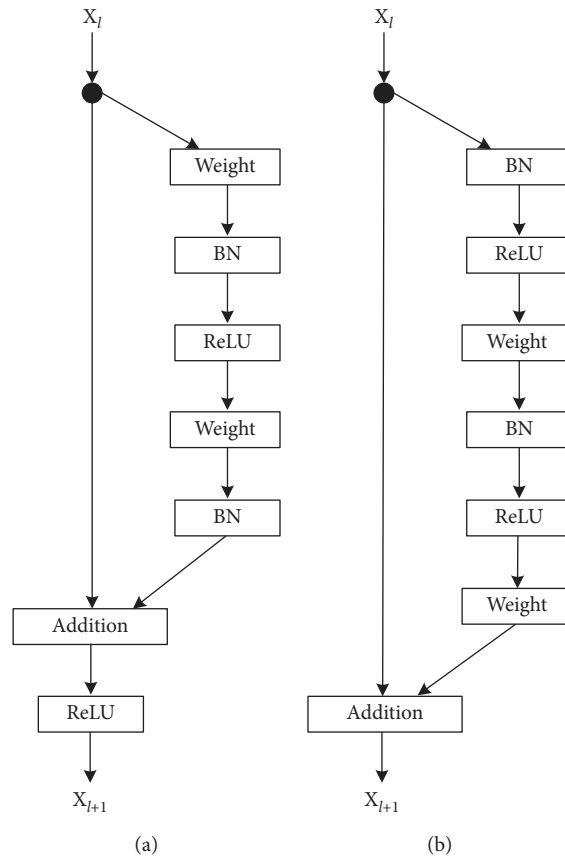


FIGURE 2: ResNetv1 and ResNetv2 units. The units consist of the same components, while the orders are different. (a) ResNetv1. (b) ResNetv2.

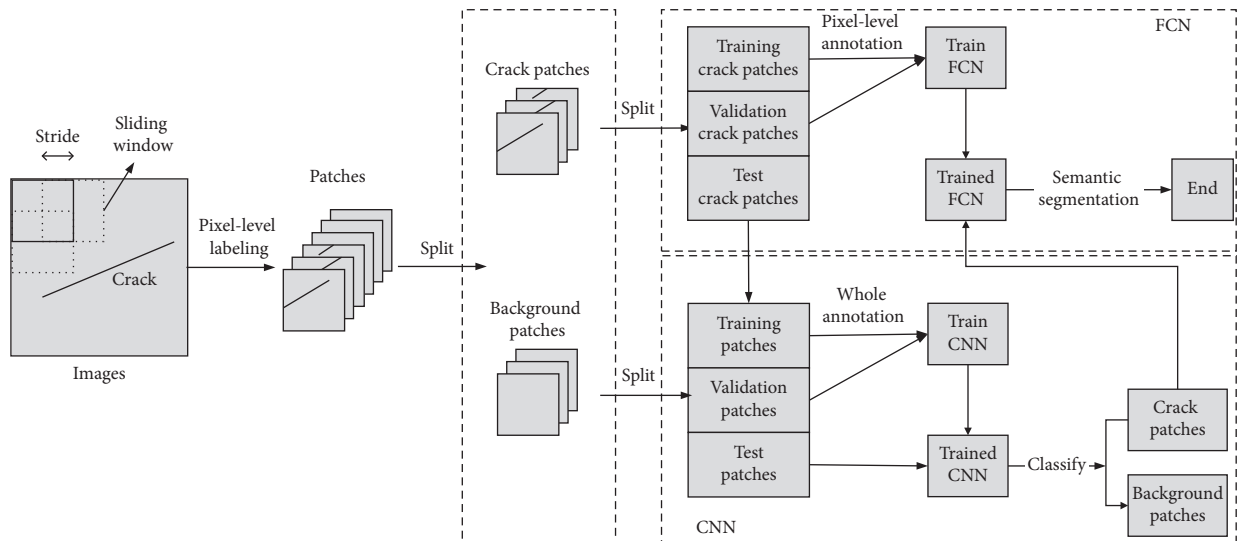


FIGURE 3: The CNN-to-FCN method for dam crack detection.

only needs to reshape the output feature map into the whole label map.

ResNet is invented to deal with the large datasets, such as the ImageNet [36]. However, our DamCrackDatabase is a relatively smaller dataset which may not need many

parameters to learn. Therefore, we cut the bottleneck channels of ResNetv2-50 in half (named ResNetv2-50 s) to reduce the learning parameters and accelerate the computing speed. As shown in Table 1, the FLOPs of ResNetv2-50 and DeepLabv3-DUC are shortened about three times as

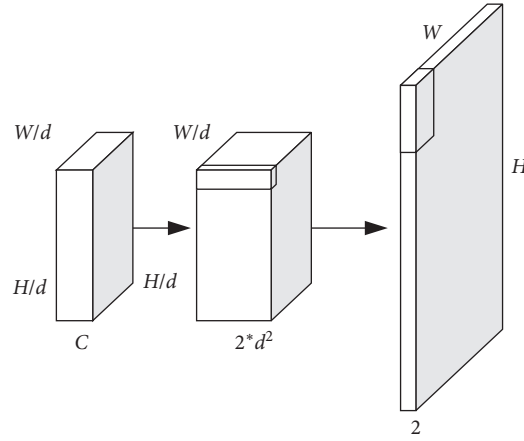


FIGURE 4: Dense upsampling convolution (DUC) module.

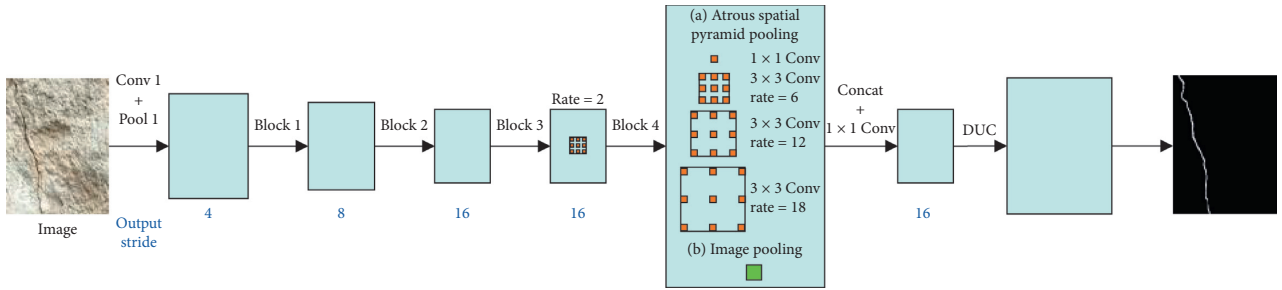


FIGURE 5: Illustration of the DeepLabv3 with the DUC layer. DUC is applied on top of the network for decoding purpose.

TABLE 1: Different backbones and architectures and their FLOPs.

Layer name	Output size	ResNet v2-50	ResNet v2-50 s	DeepLabv3-DUC ResNetv2-50	DeepLabv3-DUC+ ResNetv2-50 s
conv1	112 × 112		7 × 7, 64, stride 2 3 × 3 max pool, stride 2		
conv2_x	56 × 56	$\begin{bmatrix} 1 \times 1, 64 \\ 3 \times 3, 64 \\ 1 \times 1, 256 \end{bmatrix} \times 3$	$\begin{bmatrix} 1 \times 1, 32 \\ 3 \times 3, 32 \\ 1 \times 1, 128 \end{bmatrix} \times 3$	$\begin{bmatrix} 1 \times 1, 64 \\ 3 \times 3, 64 \\ 1 \times 1, 256 \end{bmatrix} \times 3$	$\begin{bmatrix} 1 \times 1, 32 \\ 3 \times 3, 32 \\ 1 \times 1, 128 \end{bmatrix} \times 3$
conv3_x	28 × 28	$\begin{bmatrix} 1 \times 1, 128 \\ 3 \times 3, 128 \\ 1 \times 1, 512 \end{bmatrix} \times 4$	$\begin{bmatrix} 1 \times 1, 64 \\ 3 \times 3, 64 \\ 1 \times 1, 256 \end{bmatrix} \times 4$	$\begin{bmatrix} 1 \times 1, 128 \\ 3 \times 3, 128 \\ 1 \times 1, 512 \end{bmatrix} \times 4$	$\begin{bmatrix} 1 \times 1, 64 \\ 3 \times 3, 64 \\ 1 \times 1, 256 \end{bmatrix} \times 4$
conv4_x	14 × 14	$\begin{bmatrix} 1 \times 1, 256 \\ 3 \times 3, 256 \\ 1 \times 1, 1024 \end{bmatrix} \times 6$	$\begin{bmatrix} 1 \times 1, 128 \\ 3 \times 3, 128 \\ 1 \times 1, 512 \end{bmatrix} \times 6$	$\begin{bmatrix} 1 \times 1, 256 \\ 3 \times 3, 256 \\ 1 \times 1, 1024 \end{bmatrix} \times 6$	$\begin{bmatrix} 1 \times 1, 128 \\ 3 \times 3, 128 \\ 1 \times 1, 512 \end{bmatrix} \times 6$
conv5_x	7 × 7 1 × 1	$\begin{bmatrix} 1 \times 1, 512 \\ 3 \times 3, 512 \\ 1 \times 1, 2048 \end{bmatrix} \times 3$ Average pool, 2-d fc, softmax	$\begin{bmatrix} 1 \times 1, 256 \\ 3 \times 3, 256 \\ 1 \times 1, 1024 \end{bmatrix} \times 3$		
conv5_d	14 × 14			$\begin{bmatrix} 1 \times 1, 512 \\ 3 \times 3, 512 \\ 1 \times 1, 2048 \end{bmatrix} \times 3$	$\begin{bmatrix} 1 \times 1, 256 \\ 3 \times 3, 256 \\ 1 \times 1, 1024 \end{bmatrix} \times 3$
conv6_d	14 × 14 1 × 1			$\begin{bmatrix} 1 \times 1, 256 \\ 3 \times 3, 256 \\ 1 \times 1, 256 \end{bmatrix} \times 3$	$\begin{bmatrix} 1 \times 1, 256 \\ 3 \times 3, 256 \\ 1 \times 1, 256 \end{bmatrix} \times 3$

TABLE 1: Continued.

Layer name	Output size	ResNet v2-50	ResNet v2-50 s	DeepLabv3-DUC ResNetv2-50	DeepLabv3-DUC+ ResNetv2-50 s
conv7_d	14 × 14 14 × 14			[1 × 1, 256] [1 × 1, 512]	[1 × 1, 256] [1 × 1, 512]
DUC	224 × 224			Reshape, 14 × 14 × 512 to 224 × 224 × 2, softmax	
FLOPs		3.87 × 10 ⁹ [33]	1.04 × 10 ⁹	8.72 × 10 ⁹	3.08 × 10 ⁹

TABLE 2: mIoU index of FCNs on validation crack set.

Model name	FCN architecture	Backbone	Bath size	Max mIoU	Total epoch	Relative/absolute training time
A	DeepLabv3	ResNetv2-50s	30	0.27	400	1.00x/59 h
B	DeepLabv3-DUC	ResNetv2-50s	30	0.57 + 111.1%	400	1.04x/61 h
C	DeepLabv3+	ResNetv2-50s	30	0.56 + 107.4%	400	1.73x/102 h

before when using the ResNetv2-50 s backbone. Furthermore, our experiments will demonstrate that the improved backbone and architecture can achieve better performance.

We have also considered the U-Net and DeepLabv3+ architectures. The U-Net is proved to be an effective way to detect concrete crack [22]. However, its training set is less than 1×10^2 , and the VGG-16 backbone has the FLOPs of 1.54×10^{10} , which is about 15 times more than our proposed model's FLOPs (1.04×10^9) by adopting the same input size. That is time-consuming and unacceptable to train our data over 5×10^4 . The DeepLabv3+ with ResNetv2-50 s backbone is used for comparison in Table 2.

4. Experiments and Results

We collected 344 images of cracks from a concrete arch dam surface at different elevations. These images with the resolution of 3456×4608 are labelled on pixel level by domain experts and then cut into 224×224 resolution patches using the sliding window with a stride of 112. We assign each patch a crack label if its centring 200×200 region contains at least one pixel. Otherwise, patches are labelled as background. Meanwhile, the crack patches are augmented by rotating the angle to 90, 180, and 270 degrees. Finally, we get 484092 patches including 402796 background patches and 81296 crack patches with the ratio about 5:1. For CNN, all the patches are divided into training, validation, and test data with the ratio of 4:1:1, respectively. For FCN, we only use the crack patches in the training, validation, and test data, and these data are also set as the ratio of 4:1:1, respectively.

For the two networks, the initial learning rates are both set as 0.001 and the Adam updater which designs an independent adaptive learning rate for different parameters by calculating the first-order moment estimation and the second-order moment estimation of the gradient is used. It is very robust and usually converges quickly and gives pretty good performance and the hyperparameters $\beta_1 = 0.9$, $\beta_2 = 0.999$, and $\epsilon = 10e - 8$ [37]. The weight decay to use for regularizing the model is set $10e - 5$ to prevent overfitting.

The batch normalization (BN) parameter is set $\epsilon = 10e - 6$ [38], which is a small constant to prevent division by zero when normalizing activations by their variance in BN.

All these algorithms are implemented using TensorFlow (v1.14.1), and used in their original version and performed via a laptop (CPU: Intel i9 9900K @ 3.6 GHz, RAM: 32 GB, GPU: Nvidia GeForce RTX 2080). The class-balanced cross-entropy loss function is used in equation (5) to alleviate the category imbalance:

$$\text{Loss} = -\alpha y \log y' - (1 - \alpha)(1 - y) \log(1 - y'), \quad (5)$$

where $\alpha = (Y_+/Y)$ and $1 - \alpha = (Y_-/Y)$; Y_+ and Y_- denote the crack and background label sets, respectively; y denotes the positive and negative label; and y' denotes the output probability.

The performance indexes are as follows:

$$\begin{aligned} \text{Precision} &= \frac{\text{TP}}{\text{TP} + \text{FP}}, \\ \text{Recall} &= \frac{\text{TP}}{\text{TP} + \text{FN}}, \\ F &= \frac{(1 + \beta^2) * \text{Recall} * \text{Precision}}{\text{Recall} + \beta^2 * \text{Precision}}, \end{aligned} \quad (6)$$

where TP denotes the true positive predictions; FP means the false positive predictions; FN denotes the false negative predictions; F score measures the weighted harmonic mean of Precision and Recall; and β is a weighted factor.

When focusing on the Recall, the β is set larger than 1, while focusing on the Precision, the β should be smaller than 1. We increase the Recall to obtain the TP predictions from the true positive labels as many as possible at the CNN stage. So, the β is set as 2. For CNN, we use the indexes to value all the patches. For FCN, we use the above indexes to estimate each patch, and their mean indexes to value all the patches. If each patch's Precision or Recall is

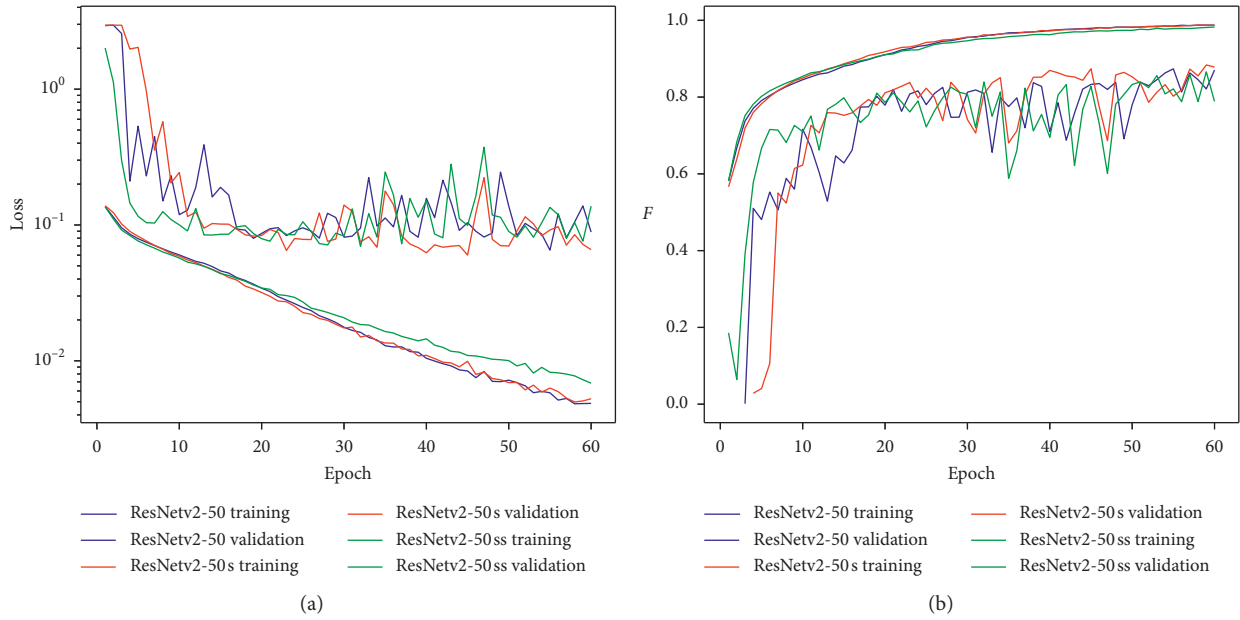


FIGURE 6: CNN loss and F during training and validation: (a) loss; (b) F .

TABLE 3: F index of different CNN backbones on validation set.

Model name	CNN backbone	Bath size	Max F	Total epoch	Relative/absolute training time
I	ResNetv2-50	50	0.87	60	1.00x/49 h
II	ResNetv2-50s	50	0.88 + 1.1%	60	0.43x/21 h
III	ResNetv2-50s	50	0.86 - 1.1%	60	0.29x/14 h

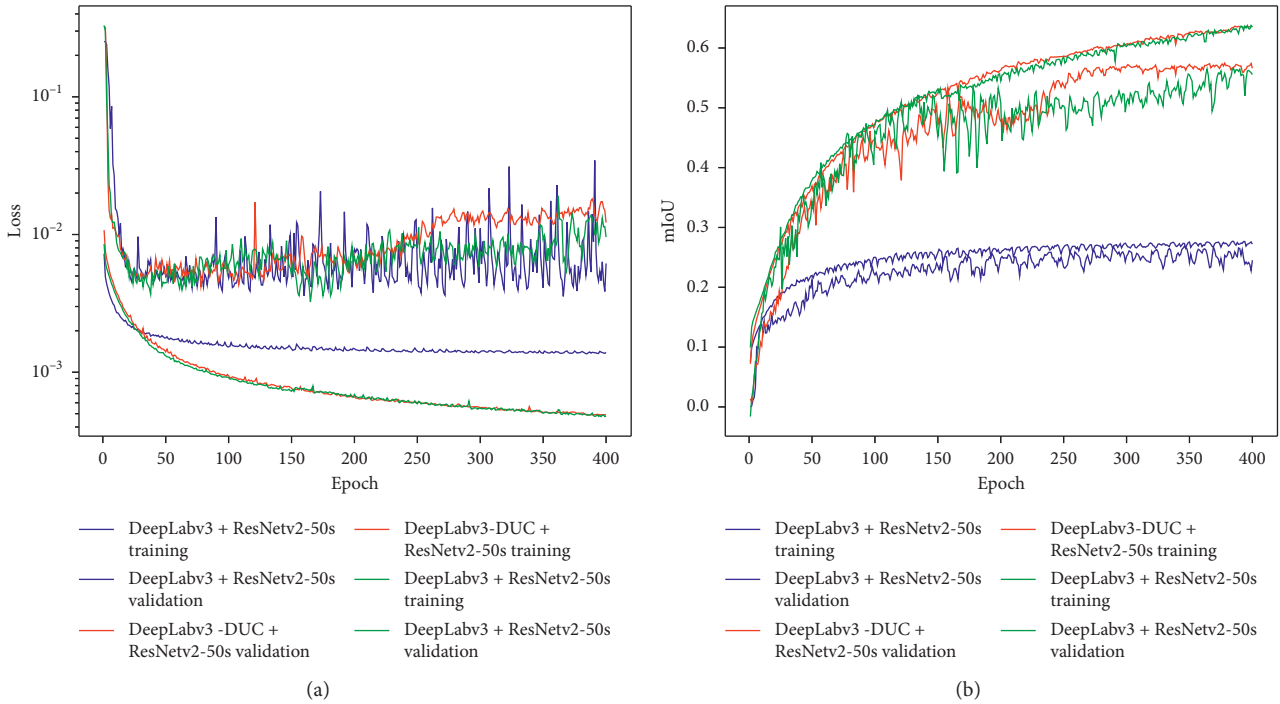


FIGURE 7: FCN loss and mIoU during training and validation: (a) loss; (b) mIoU.

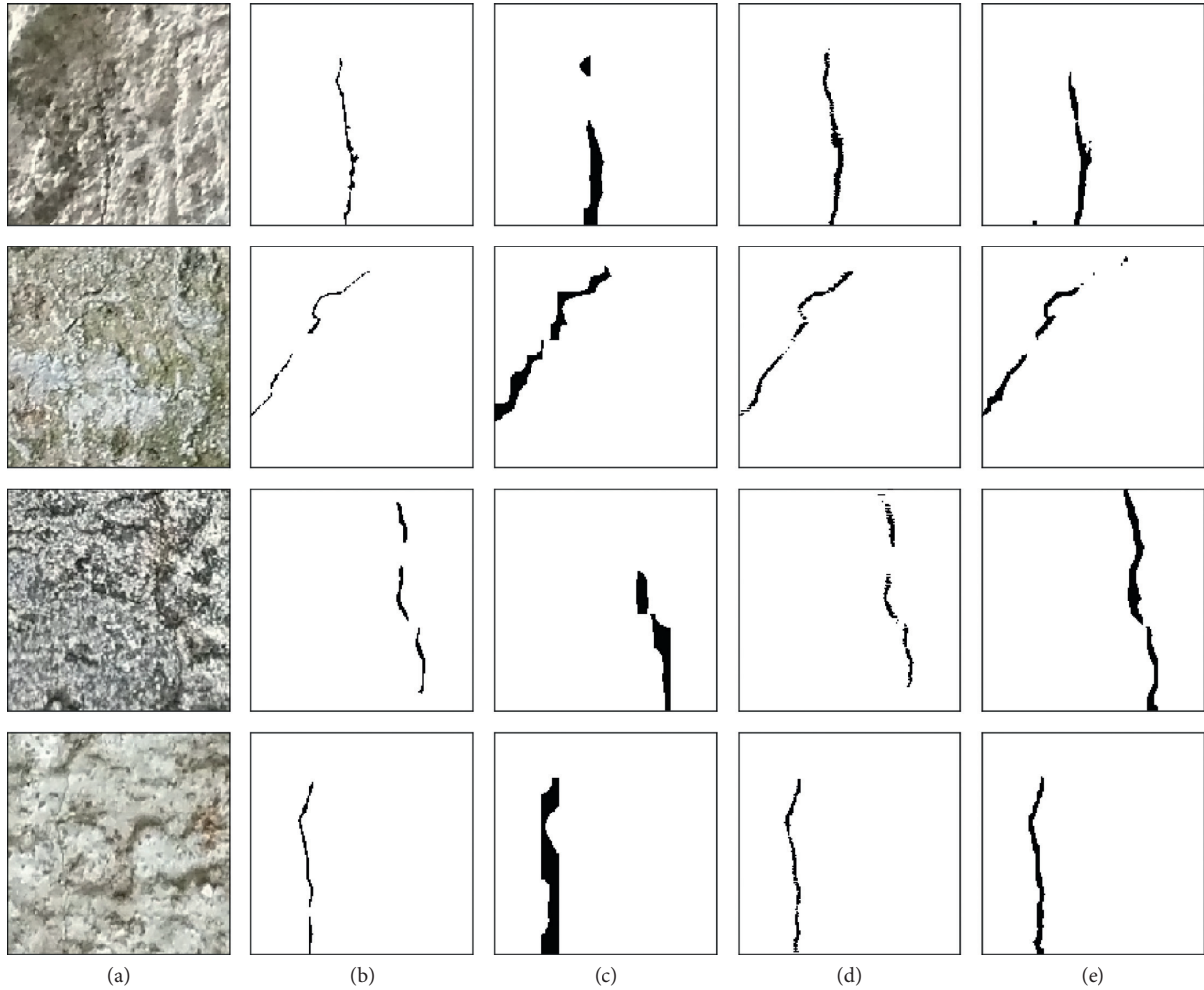


FIGURE 8: Different models' prediction results on test crack set: (a) original patch, (b) labelled patch, (c) model A, (d) model B, and (e) model C.

TABLE 4: Indexes of ONLY-FCN and CNN-FCN by different thresholds on test set.

Method name	Model II threshold	Model B threshold	Model II				Model B			Relative/absolute prediction time per patch
			TP	FP	TN	FN	mR	mP	mIoU	
ONLY-FCN	—	0.999	—	29227	—	—	0.188	0.865	0.182	1.00x/7.9 ms
	—	0.99	—	40719	—	—	-76.4%	+33.5%	-66.7%	
	—	0.9	—	54502	—	—	0.408	0.806	0.370	
	—	0.9	—	54502	—	—	-48.7%	+24.4%	-32.4%	
	—	0.5	—	69316	—	—	0.645	0.729	0.514	
CNN-FCN	0.001	0.5	13496	56779	10364	43	0.795	0.648	0.547	1.42x/11.2 ms
	0.01	0.5	13410	41299	25844	129	+0.0%	+0.0%	+0.0%	
	0.1	0.5	12885	10988	56155	654	0.795	0.648	0.548	
	0.1	0.5	12885	10988	56155	654	+0.0%	+0.0%	+0.2%	
	0.5	0.5	12151	2851	64292	1388	0.798	0.649	0.550	
CNN	—	—	—	—	—	—	—	—	—	0.84x/6.6 ms
										0.73x/5.8 ms
										0.53x/4.2 ms

TN denotes the true background predictions.

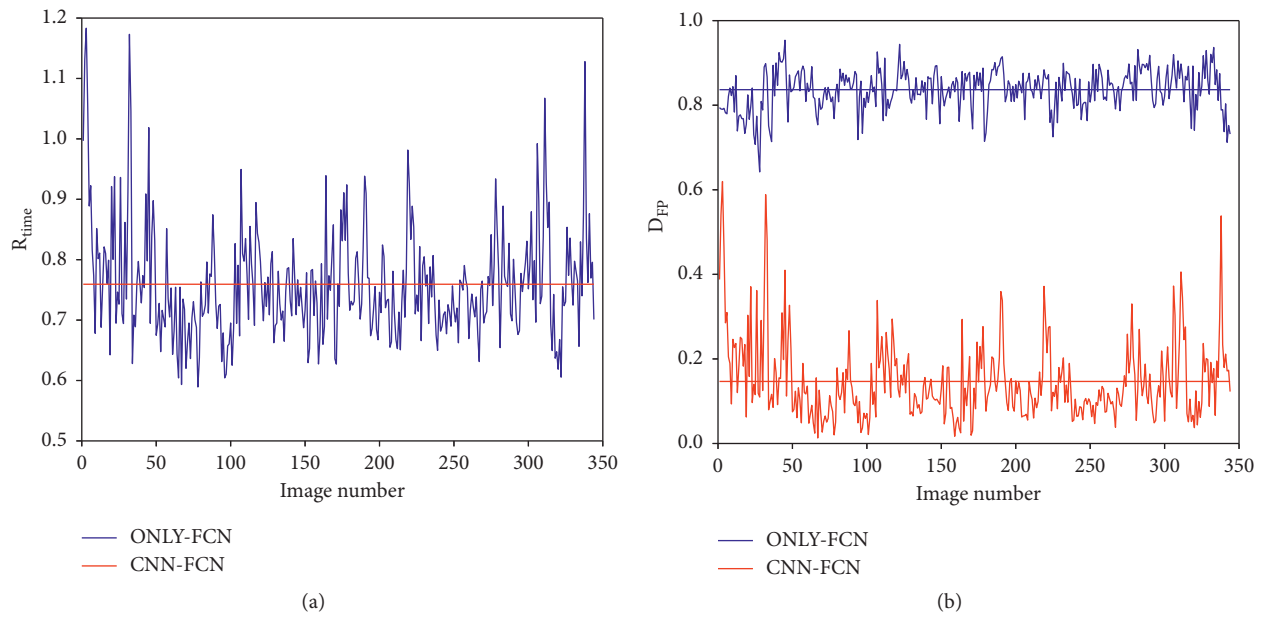


FIGURE 9: R_{time} and D_{FP} of all the image: (a) R_{time} ; (b) D_{FP} .

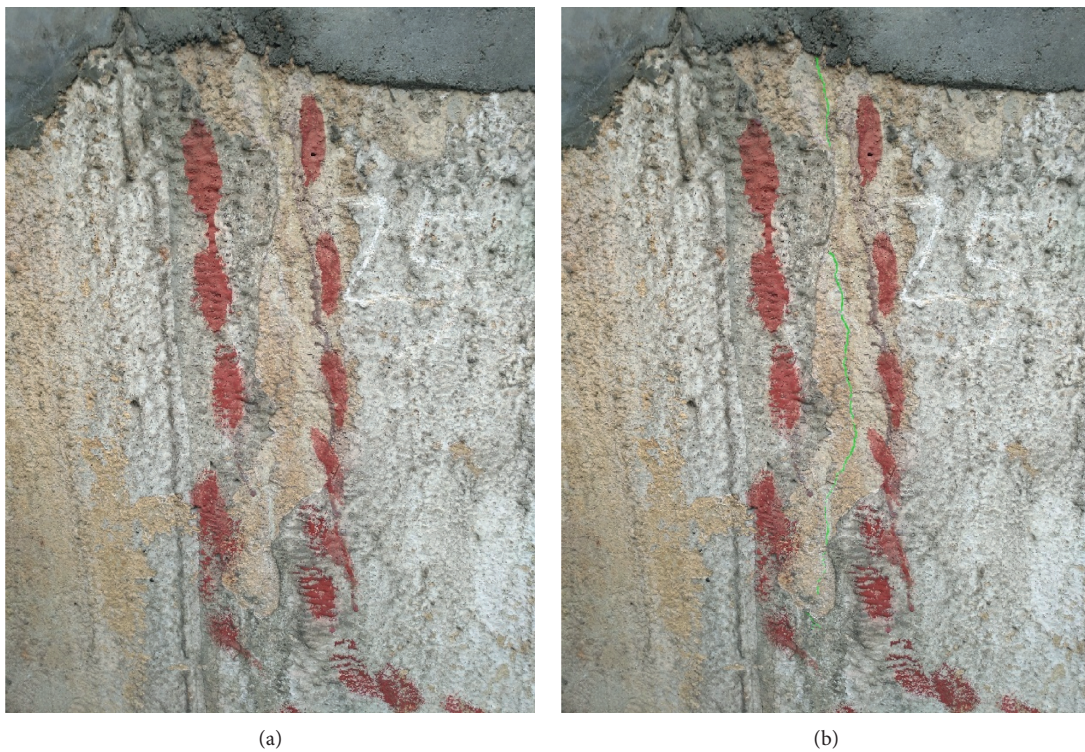


FIGURE 10: Continued.

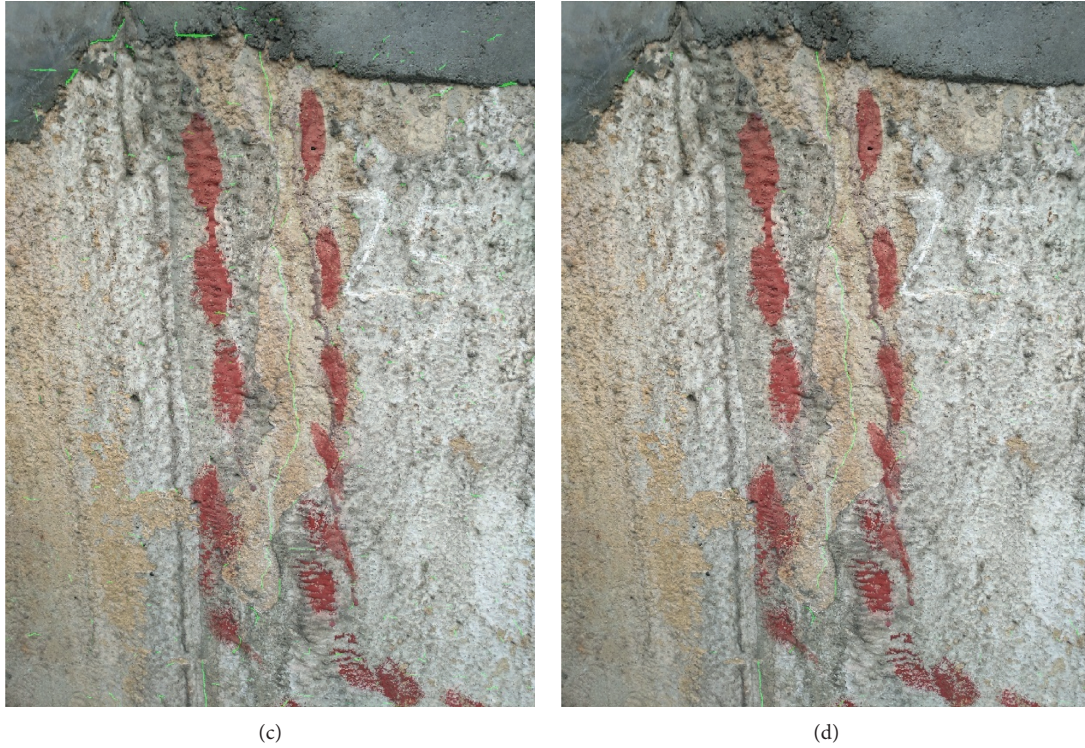


FIGURE 10: Different methods for high-resolution image nondestructive semantic segmentation: (a) original image, (b) labelled image, (c) ONLY-FCN, and (d) CNN-FCN.

incomputable, then the patch is not taken into account, respectively.

For FCN, we also add the common index as follows:

$$mIoU = \frac{1}{M} \sum_{m=1}^M \frac{TP}{TP + FP + FN}, \quad (7)$$

where M denotes the number of patches which are computable.

The CNNs are trained for 60 epochs. Observing the curves in Figure 6(a), the loss decreases gradually on the training set, while the validation set converges after about the 20th epoch. As shown in Table 3 and Figure 6(b), model II changes the backbone of model I to ResNetv2-50s, and obtain the best F and saves more than half of the training time. Model III cut the bottleneck channels of ResNetv2-50 to a quarter (named ResNetv2-50s) and obtain the worst F , which shows that the bottleneck channels cannot be cut too much. Therefore, we finally choose the ResNetv2-50s as the backbone for the next FCNs.

The FCNs are trained for 400 epochs because we found that model B and model C need more time to obtain a better mIoU (Table 2 and Figure 7(b)). As can be seen from Figure 7, the loss and mIoU of model A converge the most quickly than model B and model C on both the training and validation sets. Model B substantial increases the mIoU more than 110% by adding the DUC module, and shows the best prediction performance on the test crack set (Table 2

and Figure 8). Model C is the most time-consuming over 100 hours, and its mIoU is worse than model B.

Significantly, the loss in model B has the poorest convergence performance than model A and model C after about the 250th epoch, which shows that the loss function may not be the best training way to achieve a better mIoU.

Thresholds are vital parameters to tune the models' indexes. To compare the distributions of false crack (FP) predictions by using the methods ONLY-FCN and CNN-FCN (our improved method), we assign each patch predicted by model B and model II FP if its region contains at least one FP pixel. As shown in Table 4, the threshold of model B can be applied to reduce the FP and increase the mean Precision (mP) for method ONLY-FCN. However, it will reduce the mean Recall (mR) and mIoU at the same time. The threshold of model II can be applied to reduce the FP more efficiently than the threshold of model B. As the FN growth rate is much less than the rate of FP decline, and the mR and mIoU rise by the increase of the model II threshold without loss of mean Precision (mP). Therefore, we can coordinate the FP and FN by tuning the threshold of model II to adapt to different requirement on recognition. Meanwhile, we use the index as follows to evaluate model II FP distribution:

$$DFP = \frac{FP}{TP + FP + TN + FN} \quad (8)$$

For prediction time-consuming, we can conclude the function as follows:

$$\begin{aligned}
 T_{\text{FCN}} &= t_{\text{FCN}}N, \\
 T_{\text{CNN-FCN}} &= t_{\text{CNN}}N + t_{\text{FCN}}N_{\text{cp}}, \\
 R_{\text{time}} &= \frac{T_{\text{CNN-FCN}}}{T_{\text{FCN}}} = \frac{t_{\text{CNN}}}{t_{\text{FCN}}} + \frac{N_{\text{cp}}}{N},
 \end{aligned} \tag{9}$$

where $T_{\text{CNN-FCN}}$ and T_{FCN} denote the time-consuming on all the patches using the methods CNN-FCN and ONLY-FCN, respectively; t_{CNN} and t_{FCN} denote the time-consuming on each patch using CNN and FCN, respectively; N represents the number of all the patches; N_{cp} represents the number of crack predictions from model II; and R_{time} denotes the ratio of $T_{\text{CNN-FCN}}$ to T_{FCN} .

For our proposed model, the $(t_{\text{CNN}}/t_{\text{FCN}})$ is 0.53 (Table 4), so if the (N_{cp}/N) is smaller than 0.47, our CNN-FCN method can reduce the prediction time-consuming. Note that the test set has a low proportion of crack patches (about 15%) and the crack predictions (TP + FP) can be controlled in a close range. As we have augmented the crack patches, for the real-world dam surface, the crack patches will have a lower proportion. Therefore, our improved method will reduce the prediction time, which becomes more practicable for the engineering applications.

The R_{time} and D_{FP} are used to estimate all the 344 images. The thresholds of model II and model B are set 0.1 and 0.5, respectively. As shown in Figures 9 and 10, our proposed method CNN-FCN can reduce the prediction time to 76% as before and extremely eliminate the messy distribution of FP from 84% to 15%.

5. Conclusions

Image with high resolution can acquire more information and ensure clarity when the camera frame is enlarged. It is beneficial for the dam with wide spaces and small width of cracks which are hard to discover.

To nondestructive segment the dam surface crack pixels of the image with high resolution, this study proposed a CNN-to-FCN method. Comparing with the previous FCNs, our method can extremely avoid the higher proportion of false crack predictions and their messy distributions in the high-resolution image through the large-scale background information recognition by CNN. The improved method also makes the computer easy to get the primary information of dam surface crack and achieve better mIoU than previous FCNs. A few true crack patches are missed at the CNN prediction stage, which should be controlled in a reasonable range by tuning the threshold. Meanwhile, the improved method can also reduce the prediction time when the image has a low proportion of crack patches, which becomes more practicable for the engineering applications.

To obtain better results, we also modify the ResNetv2 backbone and DeepLabv3 architecture by reducing the bottleneck channels and adding a DUC module. The results indicated that the modified model is efficient and dramatically increases the mIoU on dam crack recognition.

Note that our proposed method is universal. However, for a deep learning model, both data and model selection affect the final performance. We have augmented the data from the 344 images to improve the deep learning model's generalization ability. Meanwhile, we proposed an improved model for nondestructive semantic segmentation. However, more data from different dam scenarios will be more representative. We need to collect more representative data to verify and further improve our proposed model in the future.

Finally, the DamCrackDataset is established for the first time and can be found in https://figshare.com/articles/DamCrackDataset_crack_encrypted_zip/12362159 for further study on concrete dam surface crack detection.

Data Availability

The DamCrackDataset used to support the findings of this study is currently under embargo while the research findings are commercialized. Requests for data, 6 months after publication of this article, will be considered by the corresponding author.

Conflicts of Interest

The authors declare that they have no conflicts of interest.

Acknowledgments

This work was supported by the State Grid Hunan Electric Power Company Limited Science Project (no. 5216A518000N). The authors would like to thank Yan Zhaohui, Chen Shiqiao, and Zhang Zhichao of the State Grid Hunan Hydropower Company for providing the verification data.

References

- [1] F. Kang, J. Li, and J. Dai, "Prediction of long-term temperature effect in structural health monitoring of concrete dams using support vector machines with jaya optimizer and salp swarm algorithms," *Advances in Engineering Software*, vol. 131, no. 5, pp. 60–76, 2019.
- [2] F. Kang, J. Li, S. Zhao, and Y. Wang, "Structural health monitoring of concrete dams using long-term air temperature for thermal effect simulation," *Engineering Structures*, vol. 180, no. 2, pp. 642–653, 2019.
- [3] A. Mohan and S. Poobal, "Crack detection using image processing: a critical review and analysis," *Alexandria Engineering Journal*, vol. 57, no. 2, pp. 787–798, 2017.
- [4] H.-B. Yun, S. Mokhtari, and L. Wu, "Crack recognition and segmentation using morphological image-processing techniques for flexible pavements," *Transportation Research Record: Journal of the Transportation Research Board*, vol. 2523, no. 1, pp. 115–124, 2015.
- [5] Y. Fujita, Y. Mitani, and Y. Hamamoto, "A method for crack detection on a concrete structure," in *Proceedings of the 18th International Conference on Pattern Recognition*, Hong Kong, China, August 2006.
- [6] I. Abdel-Qader, O. Abudayyeh, and M. E. Kelly, "Analysis of edge-detection techniques for crack identification in bridges,"

- Journal of Computing in Civil Engineering*, vol. 17, no. 4, pp. 255–263, 2003.
- [7] P. Prasanna, K. J. Dana, N. Gucunski et al., “Automated crack detection on concrete bridges,” *IEEE Transactions on Automation Science and Engineering*, vol. 13, no. 2, pp. 591–599, 2016.
 - [8] T. Nishikawa, J. Yoshida, T. Sugiyama, and Y. Fujino, “Concrete crack detection by multiple sequential image filtering,” *Computer-Aided Civil and Infrastructure Engineering*, vol. 27, no. 1, pp. 29–47, 2012.
 - [9] H. Kim, E. Ahn, M. Shin, and S.-H. Sim, “Crack and noncrack classification from concrete surface images using machine learning,” *Structural Health Monitoring*, vol. 18, no. 3, pp. 725–738, 2019.
 - [10] X. Fan, J. Wu, P. Shi, X. Zhang, and Y. Xie, “A novel automatic dam crack detection algorithm based on local-global clustering,” *Multimedia Tools and Applications*, vol. 77, no. 20, pp. 26581–26599, 2018.
 - [11] Y. Lecun, L. Bottou, Y. Bengio, and P. Haffner, “Gradient-based learning applied to document recognition,” *Proceedings of the IEEE*, vol. 86, no. 11, pp. 2278–2324, 1998.
 - [12] J. Long, E. Shelhamer, and T. Darrell, “Fully convolutional networks for semantic segmentation,” in *Proceedings of the Computer Vision and Pattern Recognition*, pp. 3431–3440, Boston, MA, USA, June 2015.
 - [13] A. Garcia, S. Ortsescolano, S. Oprea, V. Villenamartinez, and J. Garcia, “A review on deep learning techniques applied to semantic segmentation,” 2017, <https://arxiv.org/abs/1704.06857>.
 - [14] S. Dorafshan, R. J. Thomas, and M. Maguire, “Comparison of deep convolutional neural networks and edge detectors for image-based crack detection in concrete,” *Construction and Building Materials*, vol. 186, pp. 1031–1045, 2018.
 - [15] H. Xu, X. Su, Y. Wang, H. Cai, K. Cui, and X. Chen, “Automatic bridge crack detection using a convolutional neural network,” *Applied Sciences*, vol. 9, no. 14, p. 2867, 2019.
 - [16] U. H. Billah, H. La, N. Gucunski, and A. Tavakkoli, “Classification of concrete crack using deep residual network,” in *Proceedings of the 9th International Conference on Structural Health Monitoring of Intelligent Infrastructure*, St Louis, MO, USA, August 2019.
 - [17] C. Feng, M.-Y. Liu, C.-C. Kao, and T.-Y. Lee, “Deep active learning for civil infrastructure defect detection and classification,” in *Proceedings of the ASCE International Workshop on Computing in Civil Engineering*, June 2017.
 - [18] W. Ricardo Leal Da Silva and D. S. D. Lucena, “Concrete cracks detection based on deep learning image classification,” in *Proceedings of the Eighteenth International Conference of Experimental Mechanics*, Brussels, Belgium, July 2018.
 - [19] K. Gopalakrishnan, S. K. Khaitan, A. Choudhary, and A. Agrawal, “Deep convolutional neural networks with transfer learning for computer vision-based data-driven pavement distress detection,” *Construction and Building Materials*, vol. 157, pp. 322–330, 2017.
 - [20] K. Jang, N. Kim, and Y.-K. An, “Deep learning-based autonomous concrete crack evaluation through hybrid image scanning,” *Structural Health Monitoring*, vol. 18, no. 5–6, pp. 1722–1737, 2019.
 - [21] J. Zhang, C. Lu, J. Wang, L. Wang, and X.-G. Yue, “Concrete cracks detection based on FCN with dilated convolution,” *Applied Sciences*, vol. 9, no. 13, p. 2686, 2019.
 - [22] Z. Liu, Y. Cao, Y. Wang, and W. Wang, “Computer vision-based concrete crack detection using U-net fully convolutional networks,” *Automation in Construction*, vol. 104, pp. 129–139, 2019.
 - [23] A. Zhang, K. C. P. Wang, B. Li et al., “Automated pixel-level pavement crack detection on 3D asphalt surfaces using a deep-learning network,” *Computer-aided Civil and Infrastructure Engineering*, vol. 32, no. 10, pp. 805–819, 2017.
 - [24] W. Song, G. Jia, H. Zhu, D. Jia, and L. Gao, “Automated pavement crack damage detection using deep multiscale convolutional features,” *Journal of Advanced Transportation*, vol. 2020, Article ID 6412562, 11 pages, 2020.
 - [25] Y. Ren, J. Huang, Z. Hong et al., “Image-based concrete crack detection in tunnels using deep fully convolutional networks,” *Construction and Building Materials*, vol. 234, Article ID 117367, 2020.
 - [26] S. Li, X. Zhao, and G. Zhou, “Automatic pixel-level multiple damage detection of concrete structure using fully convolutional network,” *Computer-aided Civil and Infrastructure Engineering*, vol. 34, no. 7, pp. 616–634, 2019.
 - [27] C. V. Dung and L. D. Anh, “Autonomous concrete crack detection using deep fully convolutional neural network,” *Automation in Construction*, vol. 99, pp. 52–58, 2019.
 - [28] M. M. Islam and J. Kim, “Vision-based autonomous crack detection of concrete structures using a fully convolutional encoder–decoder network,” *Sensors*, vol. 19, no. 19, p. 4251, 2019.
 - [29] K. He, X. Zhang, S. Ren, and J. Sun, “Deep residual learning for image recognition,” in *Proceedings of the Computer Vision and Pattern Recognition*, Las Vegas, NV, USA, June 2016.
 - [30] K. He, X. Zhang, S. Ren, and J. Sun, “Identity mappings in deep residual networks,” 2016, <https://arxiv.org/abs/1603.05027>.
 - [31] L. Chen, G. Papandreou, I. Kokkinos, K. Murphy, and A. L. Yuille, “Semantic image segmentation with deep convolutional nets and fully connected CRFs,” 2014, <https://arxiv.org/abs/1412.7062>.
 - [32] L.-C. Chen, G. Papandreou, I. Kokkinos, K. Murphy, and A. L. Yuille, “DeepLab: semantic image segmentation with deep convolutional nets, atrous convolution, and fully connected CRFs,” *IEEE Transactions on Pattern Analysis and Machine Intelligence*, vol. 40, no. 4, pp. 834–848, 2018.
 - [33] L. Chen, G. Papandreou, F. Schroff, and H. Adam, “Rethinking atrous convolution for semantic image segmentation,” 2017, <https://arxiv.org/abs/1706.05587>.
 - [34] L. Chen, Y. Zhu, G. Papandreou, F. Schroff, and H. Adam, “Encoder-decoder with atrous separable convolution for semantic image segmentation,” in *Proceedings of the European Conference on Computer Vision*, Munich, Germany, September 2018.
 - [35] P. Wang, P. Chen, Y. Yuan et al., “Understanding convolution for semantic segmentation,” in *Proceedings of the 2018 IEEE Winter Conference on Applications of Computer Vision (WACV)*, pp. 1451–1460, Lake Tahoe, NV, USA, March 2018.
 - [36] J. Deng, W. Dong, R. Socher, L. Li, K. Li, and L. Feifei, “ImageNet: a large-scale hierarchical image database,” in *Proceedings of the Computer Vision and Pattern Recognition*, pp. 248–255, Miami, FL, USA, June 2009.
 - [37] D. P. Kingma and J. B. Adam, “A method for stochastic optimization,” in *Proceedings of the International Conference on Learning Representations*, San Diego, CA, USA, May 2015.
 - [38] S. Ioffe and C. Szegedy, “Batch normalization: accelerating deep network training by reducing internal covariate shift,” in *Proceedings of the International Conference on Machine Learning*, Lille, France, July 2015.

Research Article

Experimental Study on Structural Mechanics of Asphalt Pavement by Digital Speckle Correlation Methods

Hailiang Xu , Hehuan Ren , Jining Qin , and Xu Guo 

School of Civil Engineering, North China University of Technology, Beijing 100144, China

Correspondence should be addressed to Hailiang Xu; hailiang_xu@126.com and Hehuan Ren; 13552701671@163.com

Received 7 September 2020; Revised 9 October 2020; Accepted 21 October 2020; Published 5 November 2020

Academic Editor: Zheng-Zheng Wang

Copyright © 2020 Hailiang Xu et al. This is an open access article distributed under the Creative Commons Attribution License, which permits unrestricted use, distribution, and reproduction in any medium, provided the original work is properly cited.

The experiments on the structural mechanics of asphalt pavement were carried out by the digital speckle correlation method (DSCM). The digital speckle correlation method is used to collect experimental data. The displacement and strain values of each layer of the asphalt pavement structure are analyzed. The research showed that (1) the digital speckle correlation methods could accurately observe the displacement value and the strain value of the pavement structure. (2) The stress state of the pavement structure was greatly influenced by the interlayer effect. The vertical displacement changed suddenly between layers. The concentration phenomenon of the tension-compression strain and the shear strain appeared between layers. (3) The overloading situation seriously worsened the overall stress state of the pavement structure, especially at the bottom of the asphalt top layer and lower layer and at the top of the cement-stabilized crushed stone. The research results are of great significance to the structural design of heavy-duty roads.

1. Introduction

Vehicle load is the main factor affecting the service life of asphalt pavement and causing damage to pavement structure. The research on the mechanical properties of asphalt pavement structure under different load conditions mainly includes numerical simulation, theoretical calculation, and experimental research.

In terms of finite element numerical simulation, Liu et al. [1] used the BISAR3.0 numerical calculation software to calculate the stress and displacement under the contact of different base and surface layers of the asphalt pavement structure. Gao [2] established a dynamic finite element calculation model under traffic load to explore the relationship between subgrade dynamic response and influencing factors. In terms of theory, Xu [3, 4] and Zhang [5] established a vertical-coupled dynamic model of heavy-duty vehicle-road-subgrade. They studied the dynamic interaction of moving heavy-duty vehicles, road structure, and subgrade under the excitation of road roughness. Mao et al. [6] established a theoretical model of mechanical friction strength between asphalt pavement layers based on fractal

theory and analyzed the mechanical friction strength characteristics of the asphalt pavement with different grading structure layers. In the aspect of experimental research, Zhou et al. [7] obtained the change of strain between layers of the same material and different materials through the experiment of small-size interlayer bonding and analyzed the influencing factors of the interlayer strain conduction of the asphalt pavement. Wang [8] designed a full-scale pavement loop test to study the structural design and verification direction of more than ten kinds of typical pavement structures and explored the relationship between the mechanical properties of asphalt pavement and different materials. Wu [9] conducted a four-point fatigue bending test of the trabecular beam of the asphalt mixture. Xu et al. [10] used shear test and pull-out test to evaluate and rank the performance of five adhesive layer materials in terms of temperature change, freeze-thaw cycles, and adhesive layer oil aging. Chen et al. [11] used shear stress and pull-out stress testing equipment to test the maximum stress of the test samples and compared the asphalt pavement formed after the pits were treated on the semirigid cement-stabilized gravel base with the traditional interlayer treatment

methods. Safavizadeh et al. [12–14] verified the reliability of DIC technology in the fatigue and fracture testing of asphalt concrete.

Limited by the means of measurement and testing, the test mainly uses buried pressure box, asphalt strain gauge, and axis gauge. Although these test methods can reflect the overall stress status of the pavement structure, there are some unfavorable factors such as the limited number of layout points, the inconvenience of the test originals, and the high accuracy of the test quality.

Aiming at the above problems in the experimental research, this paper uses the new digital speckle observation correlation method (DSCM) to test the mechanical properties of asphalt pavement structure under different loading conditions.

2. Basic Principles of Digital Speckle Correlation Methods

The digital speckle correlation method (DSCM) was independently proposed by Yamaguchi [15] in Japan and Peter

and Ranson et al. [16] in the United States in the early 1980s. It mainly uses optical observation and postimage processing. This method has the advantages of global observation, adjustable range accuracy, noncontact mode, easy operation, and reliable data.

2.1. Correlation Function of Digital Speckle. In graphics processing, grayscale is the carrier of graphics data (grayscale is the speckle field formed by black-white spots or white-spotted black spots). DSCM establishes the correlation function between the gray level of the image before deformation and the gray level of the image after deformation and uses the calculation software to convert the graphic data into digital data. The general standardized correlation function [17–20] commonly used in DSCM is shown as follows:

$$C(u, v) = \frac{\sum_{x=-M}^M \sum_{y=-M}^M [f(x, y)g(x+u, y+v)]}{\sqrt{\sum_{x=-M}^M \sum_{y=-M}^M f^2(x, y)} \sqrt{\sum_{x=-M}^M \sum_{y=-M}^M g^2(x+u, y+v)}} \quad (1)$$

where $f(x, y)$ is the grayscale function of the reference image at a certain point (x, y) before deformation and $g(x+u, y+v)$ is the gradation function of the target image at the point $(x+u, y+v)$ after deformation, and the correlation coefficient $C(u, v)$ ranges from $[0, 1]$. The existing research [14] normalizes the correlation function by the mean square error of gray and can highlight the mutation value of the correlation function in the coefficient matrix (that is, the normalized covariance correlation function).

2.2. Digital Speckle Correlation Search Method. In the grayscale pictures taken by the camera, the grayscale search algorithm is also crucial. The classical gray search methods include the thickness search method, the cross search method, the mountain climbing search method, the neighborhood search method, and the Newton–Raphason partial differential correction method.

As for the cross search method used in this experiment, since it reduces the two-dimensional search method to the one-dimensional search method, the search time is reduced, and the search efficiency is improved. The specific search process is as follows: starting from the reference image point A, several points equidistant from point A are made on the x and y axes, and the correlation $C(u, v)$ coefficients of these points are calculated to find point B of the maximum value in the direction of the single coordinate axis. Then, starting from point B, point C where the correlation coefficient $C(u, v)$ is the largest is found on the x -axis, and then point C is the peak point at which the final correlation coefficient is

the largest. A schematic diagram of the cross search method is shown in Figure 1.

3. Production of Test Model for the Pavement Structure

The structural test piece is prepared by a layer of asphalt (top, middle, and lower layers) and a layer of cement-stabilized macadam (top and lower base layers). The parameter settings of each layer are shown in Table 1. After each layer was prepared for bonding, an artificial speckle field was sprayed on the observation surface.

Cement-stabilized macadam layer was prepared according to 5% cement-stabilized macadam mixture ratio. It was prepared according to the mass ratio of cement: coarse aggregate: fine aggregate: sand: water = 113:906:566:793:112, and three sets of test pieces were prepared. For the preparation of the asphalt structural layer material, the commercial asphalt concrete materials AC-13, AC-20, and AC-25 are, respectively, poured into the asphalt mold and then compacted, allowed to stand, demoulded, and maintained.

For the pavement of each layer of the structure, firstly the cement mortar is equipped with a cement: sand ratio of 1:3 to connect the cement-stabilized layer, the cement mortar is used to smooth the top surface of the water-stable base and the upper and lower water-stable bases are connected. To connect the asphalt layers, first water-based bitumen permeable layer oil is used to wet the bottom layer, and then oily 70# bituminous layer oil is evenly applied, and the two bitumen layers are combined and statically pressed for 12 h.

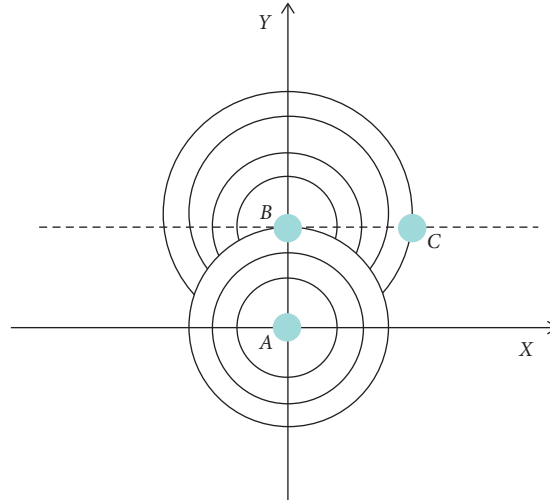


FIGURE 1: Rood pattern search.

TABLE 1: Structure layer parameters.

Position	Material	Length (m)	Width (m)	Thickness (m)
Top layer of asphalt	AC-13	0.8	0.3	0.04
Middle layer of asphalt	AC-20	0.8	0.3	0.05
Lower layer of asphalt	AC-25	0.8	0.3	0.07
Upper base layer of cement-stabilized macadam	Cement-stabilized macadam	0.8	0.3	0.2
Lower base layer of cement-stabilized layer	Cement-stabilized macadam	0.8	0.3	0.2

The artificial speckle field was sprayed at a center area of the test piece of 20×56 cm. First black lacquer is used to make a primer. After the black lacquer is dried, white spots are evenly sprayed with white lacquer. The speckle field is the analysis range. The overall structure is shown in Figure 2.

The testing system consisted of the WAW-600 electro-hydraulic servo universal testing machine and two CCD cameras, as shown in Figure 3. Three-stage loading (static load) was used during the test, which were standard load (0.7 MPa), 50% overload (1.05 MPa), and 100% overload (1.4 MPa). The load was symmetrically loaded on both sides of the center line of the test piece, and the loading range was 20×56 cm.

4. Mechanical Analysis of the Pavement Structure

According to the existing research results [17], the failure forms of pavement structure corresponding to the mechanical indexes are shown in Table 2.

According to the contents in the table, the analysis indexes of the pavement structure, including vertical displacement (deflection value), vertical strain, and vertical shear strain, are selected as the main analysis indexes for the main forms of structural failure.

4.1. Vertical Displacement Analysis of Structural Floor. Vertical displacement (deflection value) of the pavement structural layer is an important reference value in pavement structural design. In the test process, the vertical

displacement cloud maps of some pavement structural layers under different loads are shown in Figures 4~6.

The displacement cloud diagram data are read, and the representative vertical displacement value on the center line in the diagram is selected for specific analysis, as shown in Figure 7.

As can be seen from Figure 7,

- (1) The displacement between layers of pavement structure is discontinuous, and there is a sudden change in the displacement value at the junction between layers, which is greatly different from the assumed displacement continuity condition in most current numerical calculation models. Taking 100% overload as an example, the mutation values of the upper, middle, and lower surface layers of asphalt are 9.2 (unit: the same as below 0.01 mm) and 3 (0.01 mm) respectively, and the mutation amplitude reaches 23.3% and 10.3%. The same rule is also observed under other loads, as shown in Table 3.
- (2) The vertical displacement value within the asphalt surface layer decreases gradually with the increase of the structure depth, but the displacement value between the asphalt layer and the water-stable layer increases abruptly. Similarly, taking 100% overload as an example, the displacement value of the bottom of the asphalt layer is 25.1 (0.01 mm), while the displacement value of the top layer above the water-stable layer is 33.5 (0.01 mm), and the added value of displacement is 8.4 (0.01 mm), with an increase of 33.27%.

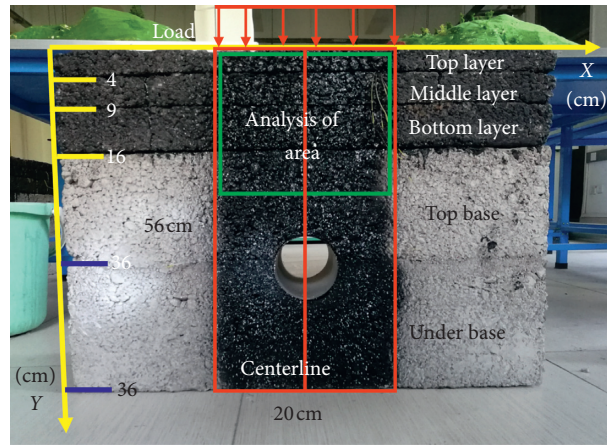


FIGURE 2: The whole structure.

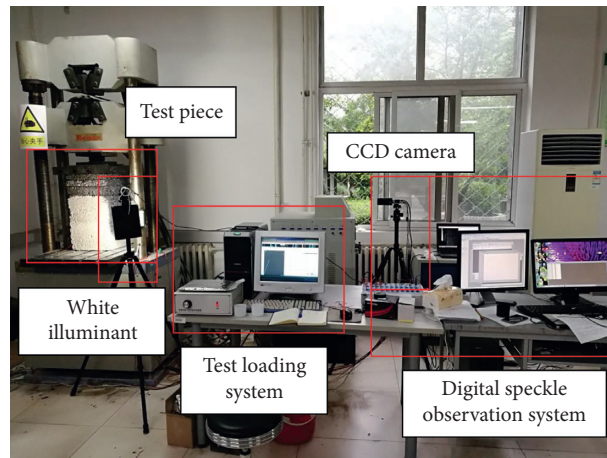


FIGURE 3: Arrangement of the site experiment.

TABLE 2: The form of structure collapse.

Mechanics index	Mechanical symbol	Pavement structure failure mode
Vertical displacement	U_y	Vertical deformation
Transverse stress	σ_x	Cracks in the bottom layer caused by cracking
Vertical stress	σ_y	The bottom of a U-shaped crack
Transverse shear stress	τ_{xz}	Both sides of the U-shaped dehiscence
Vertical shear stress	τ_{xy}	Lateral slip, rutting, side cracking
Longitudinal shear stress	τ_{yz}	Longitudinal slip

- (3) It can be seen from Figure 7 that the abrupt change amplitude of displacement value between layers of pavement structure increases with the increase of load. That is to say, the greater the load is, the greater the influence of the interlayer effect will be.
- (4) With the increase of load, the displacement value of each layer of the pavement shows an increasing trend, but the influence degree is the largest on the asphalt layer, followed by the base layer on the water-stabilized gravel. Therefore, for some heavy load roads, the thickness and strength of the asphalt layer above the pavement structure and the base layer on

the water-stabilized gravel should be appropriately increased.

4.2. *Pavement Structure Layer Strain Analysis.* The strain index of the pavement structure layer is an important research content of pavement structure stress. Figures 8–10 show the strain cloud diagram of pavement structure under different loads obtained during the test.

The strain data observed in Figures 8–10 are arranged, and the strain data at the center line are selected for analysis, as shown in Figure 11.

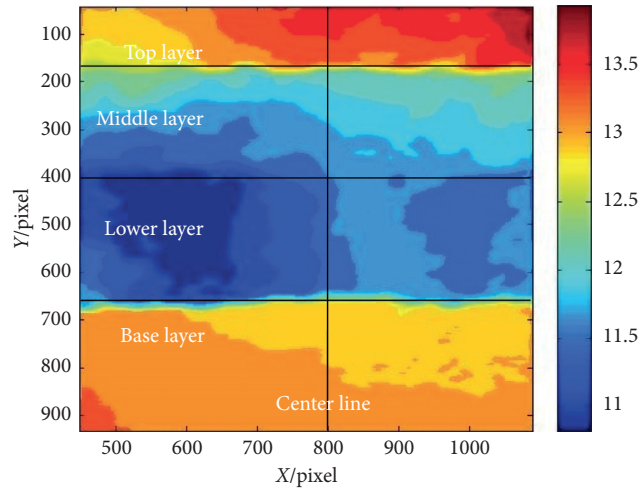


FIGURE 4: Vertical displacement cloud chart under standard load.

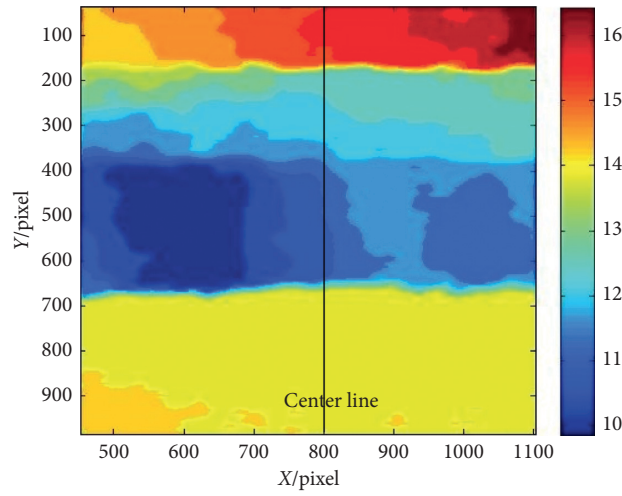


FIGURE 5: Vertical displacement under 50% overload.

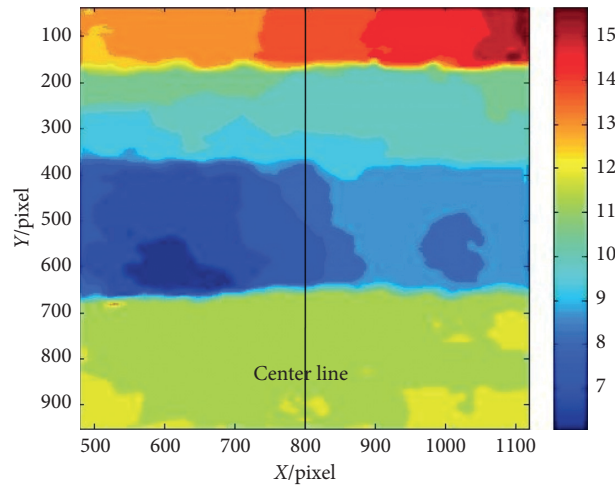


FIGURE 6: Vertical displacement under 100% overload.

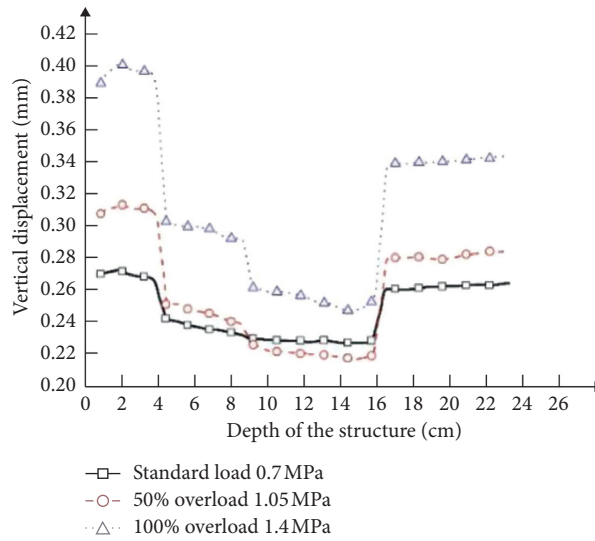


FIGURE 7: Vertical displacement line of the center line.

TABLE 3: Vertical displacement of structure interlayer.

Working condition	Bottom of the upper layer		Bottom of the middle layer		Bottom of the lower layer	
	Top of the middle layer		Top of the lower layer		Top of the cement-stabilized layer	
Standard load	0.2670	0.2420	0.2319	0.2293	0.2274	0.2607
		-9.36%		-1.12%		14.65%
50% overload	0.309	0.251	0.238	0.226	0.218	0.279
		-18.85%		-5.40%		27.87%
100% overload	0.395	0.303	0.291	0.261	0.251	0.335
		-23.30%		-10.35%		33.27%

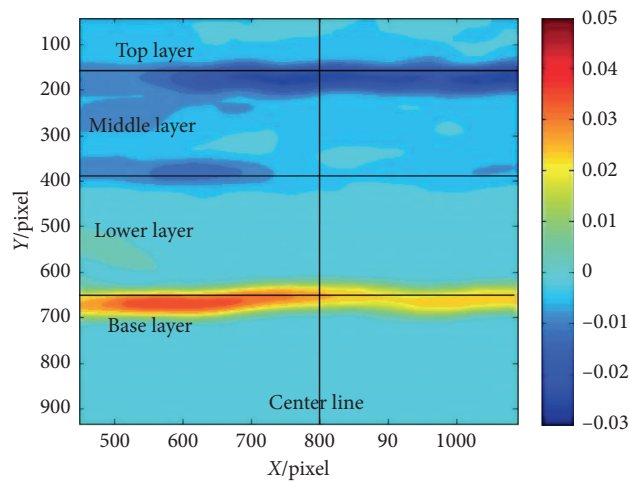


FIGURE 8: Vertical strain under standard load.

From Figures 8 to 11, it can be intuitively seen that the overall stress of the pavement structure is dominated by compression, but the bottom of the asphalt underlayer is under tension. Meanwhile, it can be seen from Figure 11 that (1) the phenomenon of strain concentration appears at the bottom of each layer of pavement structure, that is, the

maximum strain of each layer appears at the bottom of the layer; (2) under different load conditions, the maximum compressive strain appears at the bottom of the layer above the asphalt, and the maximum tensile strain appears at the bottom layer below the asphalt. This is due to the upward bending of the pavement structure. Moreover, the variation

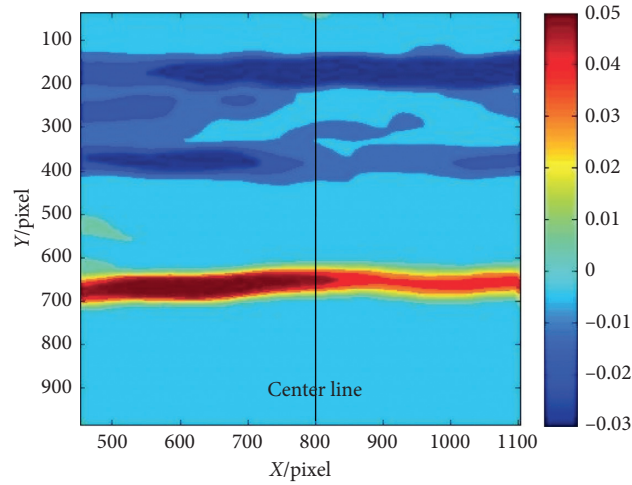


FIGURE 9: Vertical strain under 50% overload.

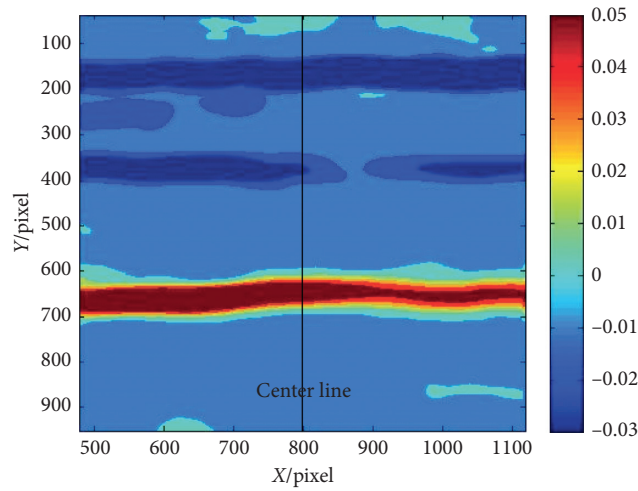


FIGURE 10: Vertical strain under 100% overload.

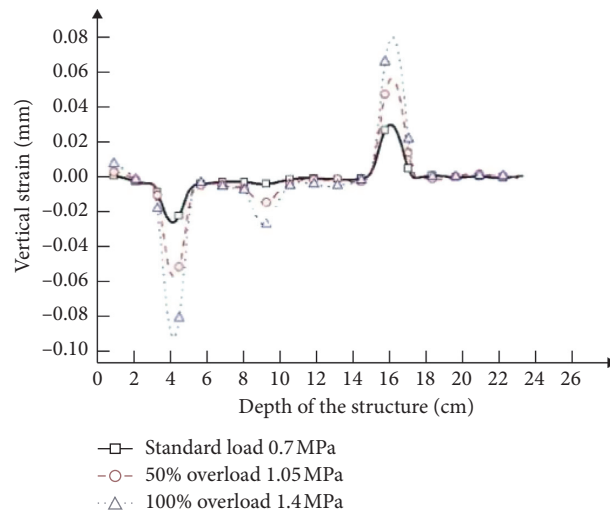


FIGURE 11: Vertical strain line of the center line.

TABLE 4: Maximum vertical strain value of the asphalt layer bottom.

Working condition	Bottom of the upper layer/ ε	Bottom of the middle layer/ ε	Bottom of the lower layer/ ε
Standard load	-0.0251	-0.0033	0.0303
50% overload	-0.0559 122.71%	-0.0139 321.21%	0.0570 88.12%
100% overload	-0.0907 261.35%	-0.0263 696.97%	0.0807 166.33%

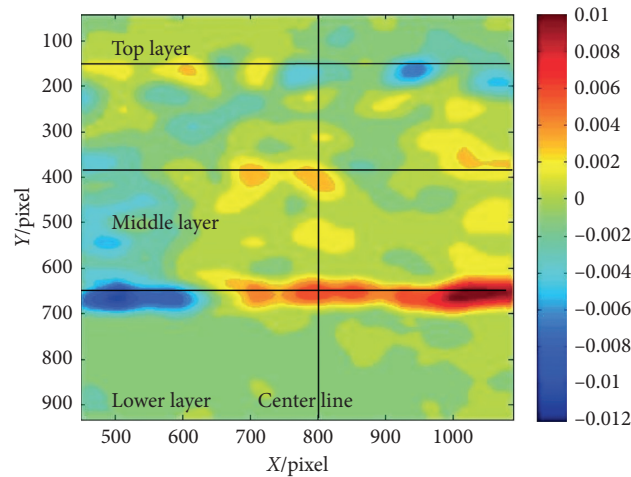


FIGURE 12: Shear strain under standard load.

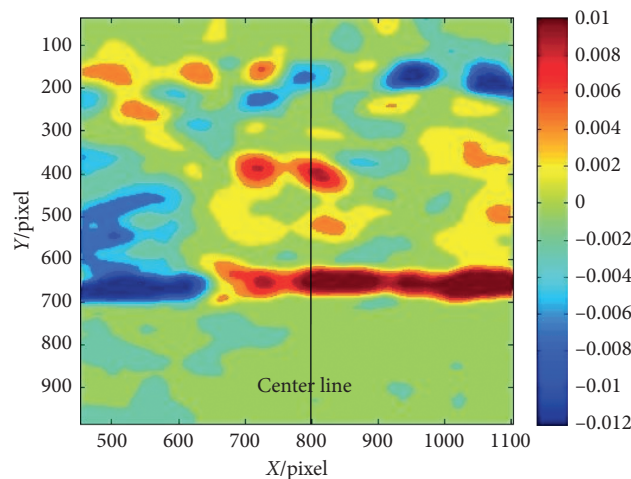


FIGURE 13: Shear strain under 50% overload.

amplitude of the strain value in the above two locations is the most obvious with the increase of load. Taking 100% overload as an example, the vertical compressive strain at the bottom of the upper layer of asphalt is 3.6 times of the standard load, and the tensile strain at the bottom of the lower layer of asphalt is 2.7 times of the standard load. Under different load conditions, the strain values and variation amplitude of each layer bottom are shown in Table 4. As can be seen from Table 4, the influence of overload on the stress state of pavement structure cannot be ignored.

4.3. Pavement Structure Shear Strain Analysis. Shear stress can lead to surface cracking, rutting, and sliding. Figures 12~14 show the distribution of shear stress of the pavement structure under different load conditions.

The shear strain data observed in Figures 12~14 are arranged, and the shear strain at the center line is selected for analysis, as shown in Figure 15.

From Figures 12 to 15, it can be seen that (1) the phenomenon of shear strain concentration appears at the bottom of each layer of pavement structure, that is, the

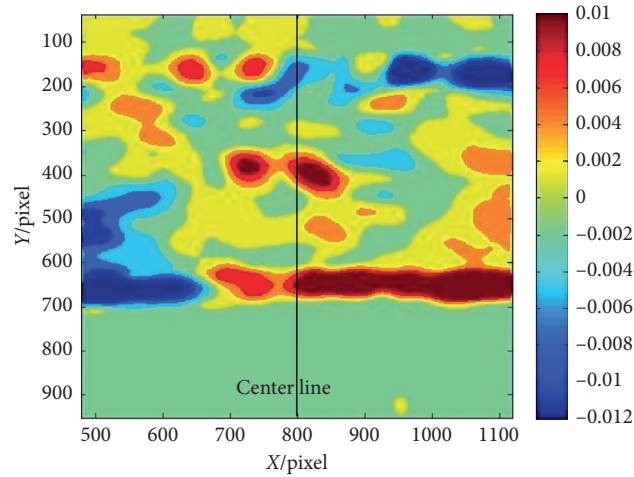


FIGURE 14: Shear strain under 100% overload.

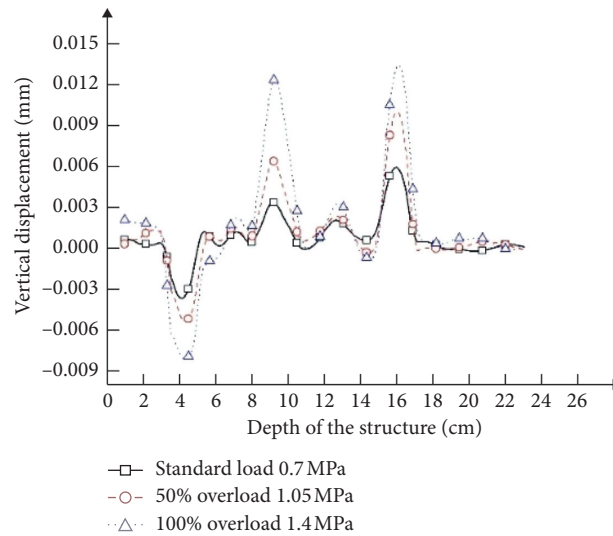


FIGURE 15: Shear strain line of the center line.

TABLE 5: Center line shear strain of the asphalt layer bottom.

Working condition	Bottom of the upper layer/ ϵ	Bottom of the middle layer/ ϵ	Bottom of the lower layer/ ϵ
Standard load	-0.003768	0.003234	0.005789
50% overload	-0.005441 44.40%	0.006221 92.37%	0.009878 70.63%
100% overload	-0.008164 116.67%	0.012155 275.83%	0.013278 129.36%

maximum shear strain of each layer appears at the bottom of the layer; (2) under the same load, the maximum shear strain occurs at the bottom of asphalt. This is caused by discontinuity between layers; (3) with the increase of load, the internal shear strain value of the pavement structure increases, and the most significant increase value of each layer bottom is between 44.40% and 275.83%, as shown in Table 5.

5. Conclusion

- (1) Digital speckle observation test method can accurately obtain the displacement value and stress-strain value of each layer of the pavement structure, and the application effect is good.
- (2) The stress state of each layer of the pavement structure is greatly affected by the interlayer effect,

and its influence cannot be ignored. The vertical displacement of each layer will be abrupt, and the strain concentration of tensile strain and shear strain will occur between layers.

- (3) Overload seriously worsens the overall stress state of the pavement structure, among which the bottom of the asphalt upper layer, the bottom of the asphalt lower layer, and the top of the water-stabilized gravel layer are the most significant. Therefore, the structural design of heavy-duty road requires targeted research on the above parts.

Data Availability

The data used to support the findings of this study are included within the article.

Conflicts of Interest

The authors declare that they have no conflicts of interest.

References

- [1] H. Liu, Y. Q. Tan, X. H. Song, and L. D. Zhao, "Influence of bonding condition between base and surface courses of asphalt pavement on pavement stress response," *Journal of Highway and Transportation Research and Development*, vol. 26, no. 3, pp. 1–6, 2009.
- [2] U. Zhan, D. C. Fend, X. Z. Linu, and Q. L. Li, "Vertical coupling dynamics model of heavy truck-pavement-subgrade," *China Journal of Highway and Transport*, vol. 28, no. 4, pp. 1–12, 2015.
- [3] H. L. Xu, Y. Yuan, T. J. Qu, and J. R. Tang, "Dynamic model for a vehicle-pavement coupled system considering pavement roughness," *Journal of Vibration and Shock*, vol. 19, no. 33, pp. 152–156, 2014.
- [4] H. L. Xu, Z. C. He, and L. He, "Analysis on asphalt concrete pavement deformation characteristics time-domain considering vehicle-pavement coupling effect," *Journal of Highway and Transportation Research and Development*, vol. 34, no. 12, pp. 16–22, 2017.
- [5] H. J. Gao, "Analysis of roadbed under traffic load based on dynamic finite element," *Journal of Lanzhou Institute of Technology*, vol. 20, no. 6, pp. 39–41, 2013.
- [6] Y. Mao, P. Li, T. F. Nian, M. Lin, and X. Y. Wei, "Mechanical friction intensity behavior of asphalt pavement based on fractal theory," *Journal of Jilin University: Engineering and Technology Edition*, vol. 50, no. 2, pp. 594–605, 2020.
- [7] X. Y. Zhou, J. T. Shi, and X. D. Wang, "Experimental study on interlayer strain transfer of semi-rigid base asphalt pavement and analysis on influencing factors," *Journal of Highway and Transportation Research and Development*, vol. 34, no. 6, pp. 1–6, 2017.
- [8] X. D. Wang, "Design of pavement structure and material for full-scale test track," *Journal of Highway and Transportation Research and Development*, vol. 34, no. 6, pp. 30–37, 2017.
- [9] Z. Y. Wu, *Research on Cumulative Fatigue Damage of Asphalt Mixture and Asphalt Layer Based on Multi-Level Amplitude Loading*, South China University of Technology, Guangzhou, China, 2014.
- [10] S. B. Chen, Y. Q. Yuan, and Y. S. Yao, "Test on strengthening interlayer cohesion of semi-rigid base asphalt pavement by interlayer treatment," *Journal of Chang'an University: Natural Science Edition*, vol. 39, no. 4, pp. 44–51, 2019.
- [11] S. F. Xu, D. Z. Zhu, and Z. Y. Wang, "Analysis on the influence of interlayer bonding conditions on cracking of heavy duty asphalt pavement," *Highway*, vol. 64, no. 8, pp. 1–7, 2019.
- [12] S. Safavizadeh, A. D. Wargo, and Y. R. Kim, "Utilizing digital image correlation (DIC) in asphalt pavement testing," *Journal of Testing and Evaluation*, vol. 46, no. 3, 2017.
- [13] E. Romeo and A. Montepara, "Characterization of reinforced asphalt pavement cracking behavior using flexural analysis," *Procedia-Social and Behavioral Sciences*, vol. 53, pp. 356–365, 2012.
- [14] M. Bueno, J. Andrés, A. Treuholz, M. Arraigada, and M. N. Partl, "Digital image correlation to monitor cracking and induction healing of asphalt roads," in *Proceedings of the 8th RILEM International Conference on Mechanisms of Cracking and Debonding in Pavements*, Springer, Delft, Netherlands, May 2016.
- [15] I. Yamaguchi, "A laser-speckle strain gauge," *Journal of Physics E: Scientific Instruments*, vol. 14, no. 11, pp. 1270–1273, 1981.
- [16] W. H. Peters and W. F. Ranson, "Digital imaging techniques in experimental stress analysis," *Optical Engineering*, vol. 21, no. 3, pp. 427–431, 1982.
- [17] J. Zhao, *Research on Digital Speckle Correlation Method and its Applications in Mechanical Engineering Measurement*, Beijing Forestry University, Beijing, China, 2014.
- [18] Y. H. Wang, H. Liang, S. H. Wang, H. Zhang, and L. X. Yang, "Advance in digital speckle correlation method and its applications," *Chinese Optics*, vol. 6, no. 4, pp. 470–480, 2013.
- [19] D. Q. Chen, *Digital Speckle Correlation Technique and its Application in Monitoring Structure*, Suzhou University, Suzhou, China, 2005.
- [20] X. H. Li, *Merchanical Response of Asphalt Pavement Under Different Contact Condition Among Interfacials*, Chang'an University, Xi'an, China, 2012.

Research Article

Evaluating Construction Risks of Modified Shield Machine Applicable to Soft Soils Based on Fuzzy Comprehensive Evaluation Method

Qingfei Luo ¹, Wei Li ², Honglin Su ³, and Xinru Chen ⁴

¹School of Railway Transportation, Shanghai Institute of Technology, Shanghai 201499, China

²School of Civil Engineering, Putian University, Putian 351100, Fujian, China

³Sinohydro Engineering Bureau 7 Co., Ltd., Chengdu 610500, Sichuan, China

⁴Shanghai Baoye Group Corp. Ltd., Shanghai 201100, China

Correspondence should be addressed to Wei Li; weiliyy@126.com

Received 15 September 2020; Revised 26 September 2020; Accepted 30 September 2020; Published 28 October 2020

Academic Editor: Zheng-zheng Wang

Copyright © 2020 Qingfei Luo et al. This is an open access article distributed under the Creative Commons Attribution License, which permits unrestricted use, distribution, and reproduction in any medium, provided the original work is properly cited.

Metro tunnel sections in China can generally be divided into two types, those in granite formations ($D = 6.0$ m) and those in soft soils ($D = 6.2$ m), to which the same shield tunnel machine cannot be applied. The consequent low rate of machine utilization needs to be addressed. One solution is to modify shield machines which tend to tunnel granite strata with varying degrees of weathering ($D = 6.0$ m) into those applicable in soft soils ($D = 6.2$ m). Shield tunneling is a complex operation accompanied by potential risks, and accordingly it is demanded in risk evaluation and management. Hence, according to the construction features of modified shield machines in soft soil areas, this paper identifies relevant risks before establishing a specific model of risk evaluation by virtue of a fuzzy comprehensive evaluation method. This model weighs risk factors by triangular fuzzy numbers, and the membership function included is of L-R type that is frequently used in engineering. This risk evaluation model is applied to one section tunnel (Binhai New Town-Lianhua) of Metro Line 6 in Fuzhou City. Tunneling tests in the field uncover problems of the modified shield machine, including inappropriate tunneling parameters, segment dislocation, segment damage, and inadequate grouting. The result conforms to that produced by the risk evaluation model, which in turn proves the reliability of this model. Field data are also analyzed to address existing problems and to determine the appropriate tunneling parameters. The validity of these tunneling parameters is verified when surface settlement is measured.

1. Introduction

Metro tunnels hold different geology and operation speeds, thereby different cross-sections. Tunnel sections in China have two different boundary lines of construction: one is those located in soft soil areas ($D = 6.2$ m), as represented by Shanghai; the other is those in granite strata with varying degrees of weathering ($D = 6.0$ m), and a typical example is Shenzhen. The construction of tunnel sections with varying geology and diameters cannot utilize the same shield machine. This would pose a great challenge to the budget control of companies which are to construct both types. To enable a single shield machine to operate in geologically different strata, there are two methods. The first is to add

materials to change the nature of soil, so that a single machine can be consistently employed [1, 2]. The second is that the machine can be conditioned to the strata under construction by adjusting its cutterhead and screw conveyor [3–8]. With respect to the second method, Li and Yuan [9] transformed the cutterhead and other components of a slurry pressure balanced shield machine three times to enable it to tunnel various soil layers. Another example is that Zhang et al. [10] aimed to design a new type of shield machine which can successfully tunnel water-rich mylonite faults. This machine was designed to operate like an EPB in strata which were not full of water, and in water-rich layers, it was equipped with a specific system to remove slurry. The researches cited above focus on what adjustments can be

made to ensure that a single shield machine can handle geologically different strata within the same tunnel section, while the machine's diameter remains unchanged. Few studies have been conducted to find out how to modify a shield machine so that it can be employed in tunnels which vary in geology and diameter. Research of this kind, however, is of vital importance, as it can further reduce the budget cost of construction and increase the rate of machine utilization.

Shield tunneling is complicated in operation and has many potential risks in which risk factors are of high degrees of fuzziness [11]. The adaptive modification adds new construction risks to the existing ones a shield machine has to face. Metros tend to be built in populous areas, implying that an accident can bring about heavy losses. Risk evaluation of shield tunneling construction usually adopts methods like machine learning [12, 13], neural network [14, 15], and fuzzy comprehensive evaluation [16–18]. The third method, by virtue of its high accuracy, practicality, and easiness, is widely used in most industries including finance [19, 20], materials [21], environmental protection [22], and electricity [23]. The fuzzy comprehensive evaluation method is employed to evaluate the risk of shield tunneling, as well as other aspects of engineering [24–26], for example, assessing road conditions [27, 28], calculating the durability of reinforced concrete structures [29], and evaluating the safety of deep foundation pits of metro stations [30]. The paper mentioned before mainly used AHP to weigh risk factors. AHP utilizes the traditional scale table, of which the scales of values are derived from pairwise comparisons and are integrated into a risk matrix. After the consistency check, the maximum eigenvalue of the matrix is regarded as the weight vector of the risk. Yet, this method is too subjective, for the consistency check depends on the researcher's experience, and the lack of theoretical foundation cannot guarantee its precision [31, 32]. The weight of each risk represents its own significance, so the weighting process must be scientific; if not, the final assessment will be affected. To avoid subjectivity, the matrix is optimized by triangular fuzzy numbers [33]. Compared with traditional risk weighting, triangular fuzzy numbers can give the upper and lower limits of a risk, which can lower the researcher's subjectivity to some extent.

During the risk evaluation of shield tunneling construction, the fuzzy comprehensive evaluation is mainly used to monitor tunnel conditions [34], decide the type of shield machines [35, 36], and assess the risk of water inrush during tunnel construction [37, 38], among others. Less consideration is given to the construction risk of modified shield machines applicable to soft soils, its identification, and the corresponding evaluation model. This should not be the case, however. The identification and evaluation model of this kind of risk should be emphasized. Apart from that, tunneling tests on site are needed to examine if the modified shield machine can reach the original expectation, especially when it is applied to a tunnel section which is diametrically different from the previous one in geology. Problems need to be identified directly in the process. After the test, relevant solutions and the resetting of tunneling parameters should be considered.

Based on one section (Binhai New Town-Lianhua) of Metro Line 6 in Fuzhou City, this paper discusses how composite EPB shield machines which tend to tunnel granite strata ($D=6\text{ m}$) can be modified and applied to soft soils ($D=6.2\text{ m}$). After identifying the construction risk of the modified shield machine in soft soils, this paper weighs risk factors by triangular fuzzy numbers and calculates the membership grades of risk events by L-R membership function, so as to provide a fuzzy comprehensive evaluation model which is tailored to the application of the modified shield machine. This model is used to rate the risk of this project. Tunneling tests on-site show that problems like inappropriate tunneling parameters segment dislocation and damage can occur when the modified shield machine is working at soft soils. This result is in line with that produced by the evaluation model, proving the reliability of this model. These problems are carefully considered before figuring out appropriate tunneling parameters and possible solutions. With the assistance of surface settlement measurement, these new parameters are certified as right.

2. Risk Identification

Shield tunneling in soft soils often faces risks from the following five aspects: shield launching and receiving, shield tunneling, segment assembly, grouting, and the working environment [39]. Shield machines modified to soft soils are likely to be at risk in shield tunneling, segment assembly, and grouting, for the reason that they might not undergo an overall modification. Risks of the three aspects will be further introduced.

2.1. Risks of Shield Tunneling. Shield construction in soft soils might be risky because of excessive rotation of the shield machine, deviation from the designed tunneling axis, inappropriate tunneling parameters, blockage in earth conveying, and leakage in the shield sealing system. The latter three problems can easily happen when the modified shield machine is tunneling soft soils.

Tunneling parameters include total shield thrust, cutterhead torque and rotation speed, tunneling speed, earth pressure, and excavation volume. These parameters vary with the geological conditions of strata; for example, earth pressure is decided by soil bulk density, and the torque and rotation speed of cutterhead vary from stratum to stratum. If a shield machine is modified and applied to a stratum different from the previous one, problems caused by inappropriate tunneling parameters are likely to occur during construction.

The shield machine's internal structure needs to be modified before it can be applied to soft soils. Modification in the internal structure can cause misalignment between the screw and the shell. Tunneling in soft soils requires screw conveyors of higher power than in solid rocks; hence the previous screw machine may not be powerful enough to convey earth smoothly in soft soils.

Leakage in the shield sealing system is caused when the shield tail gap is so large that sealing devices fail to function

well. This excessively large gap occurs if the sealing connection is not elastic enough or the shield tail is not aligned with the segment. The shield tail gap can also be enlarged when the machine has been used for a long time, which is usually the case of the modified shield machine. All these are possible reasons for the reduced tightness.

2.2. Risks of Segment Assembly. Segment-related risks during the tunneling construction in soft soils include segment dislocation, damage, and attitude deviation. Dislocation of segments has three main causes: (1) nonstandard segment assembly and the consequent loose bolted connection can make segments dislocated; (2) changes of shield tail gap in shield deviation correction can dislocate segments; (3) when a shield is tunneling through the shallow-covered soil section in silt strata, its attitude is difficult to be controlled and it tends to advance at a high speed. Under such circumstances, the axes of the shield and the segment are prone to diverge, leading to the dislocation of segments.

Segment damage might happen for the following three reasons: (1) if the center of the segment is not in line with that of the shield machine, there will be an uneven force on the segment. The lateral pressure on it will exceed its designed value of tensile or compressive strength and cause damage; (2) when the segment is transported and stacked, some bumps would result in cracks on it; (3) the segment might be broken by the uneven force exerted during the process of axis deviation correction.

Segment attitude deviation can be caused (1) if the initial setting time of synchronous grouting is too long and the grouting materials surrounding the segment cannot bind them immediately and (2) if, in a shallow tunnel, the pressure of the abundant groundwater is more than the segment can bear and results in segment uplifting.

Briefly, the above risks mainly occur in the procedures of segment transportation, segment assembly, shield deviation correction, and grouting. If a shield machine is to be conditioned to the tunneling construction in soft soils, its thrust system, cutterhead and cutting tool, and shield need to be modified considerably. If the modification is incomplete, the safety during construction cannot be guaranteed, particularly in the steps mentioned before. This is why segment assembly is of high risk for the modified shield machines applicable to soft soils.

2.3. Risks of Grouting. Grouting-related problems in soft soils tunneling can occur if the grout is not injected in a timely and consistent way, the pipes are blocked, or the grout is poor in quality.

Like shield tunneling and segment assembling, grouting-related factors also vary with the geology of strata. The modified shield machine requires different grouting material, grouting volume, and grouting pressure when the strata under construction are shifted from rocks to soft soils. If these factors are not thoroughly considered, grouting-related risks might be brought about. These risks can be intensified if the new grout is mixed with the residue accumulated in grouting pipes. The residue is grouting

materials which had been applied to a stratum of totally different geological conditions. Such a mixture will give rise to more blockages in the grouting pipes. Therefore grouting-related risks are of significance during the operation of the modified shield machine applicable to soft soils.

3. Fuzzy Comprehensive Evaluation Model

3.1. Establishing the Risk Evaluation System. The risk index system for modified shield construction applicable to soft soils is set up by the analytic hierarchy process (AHP) according to the identification results of the above construction risk factors. The risk index system can be roughly divided into three layers, which are, respectively, the target layer, the first-level index layer, and the second-level index layer, among which the target layer is the first layer that represents the final evaluation targets and is recorded as U , namely, the safety risk evaluation for modified shield machine construction applicable to soft soils. The second and third layers are, respectively, the first-level index layer (risk accidents) and the second-level index layer (potential risk factors), among which the first-level index layer should be denoted as U_i ($i = 1, 2, 3, 4, 5$), while the second-level index layer is denoted as U_{ij} . Please see Figure 1.

The risks of modified shield machine construction suitable for soft soils are divided into 5 levels: “extremely low risk,” “low risk,” “medium risk,” “high risk,” and “extremely high risk,” which are denoted as V :

$$V = \{v_1, v_2, v_3, v_4, v_5\}. \quad (1)$$

3.2. Determining Risk Weights

3.2.1. Building up Triangular Fuzzy Number Complementary Judgment Matrix. Experts conduct paired comparison on the importance of risks at the same level by referring to the fuzzy scale table (see Table 1) and the risk evaluation system, to obtain the triangular fuzzy number complementary matrix A :

$$\begin{cases} A = (\tilde{a}_{ij})_{m \times n}, \\ \tilde{a}_{ij} = (l_{ij}, m_{ij}, u_{ij}), \end{cases} \quad (2)$$

where \tilde{a}_{ij} refers to the ratio of the relative importance of the No. i factor to No. j factor, and l_{ij} , m_{ij} , and u_{ij} , respectively, refer to the lower bound value, most probable value, and upper bound value in experts' judgment on risks. Meanwhile, these three also satisfy the conditions $l_{ij} < m_{ij} < u_{ij}$, $l_{ij} + u_{ij} = 1$, and $u_{ij} + l_{ij} = 1$. And the value of $|u_{ij} - l_{ij}|$ indicates the fuzzy degree of this judgment interval. When the value is 0, it means that the judgment is not fuzzy; instead, it is an accurate judgment.

3.2.2. Determining Initial Fuzzy Weights. The initial weight of risk represents the relative importance ranking of risk events at the same level to the superior level. Supposing that there are a total of n indices in a certain second-level index

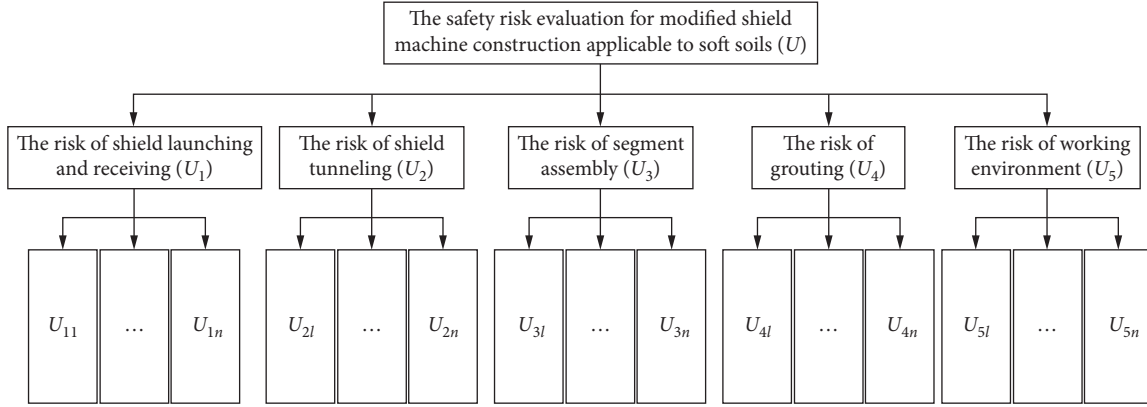


FIGURE 1: Risk evaluation system.

TABLE 1: Fuzzy scale table.

Scale	Meaning
0.1	Risk i is absolutely not as important as risk j
0.3	Risk i is obviously not as important as risk j
0.5	Risk i has the same importance as risk j
0.7	Risk i is obviously more important than risk j
0.9	Risk i is absolutely more important than risk j

where 0.2, 0.4, 0.6, and 0.8 are the median of adjacent judgment intervals.

layer, the corresponding initial fuzzy weight \tilde{w}_i of No. i index could be obtained by the following calculation:

$$\left\{ \begin{array}{l} \tilde{w}_i = \frac{\sum_{j=1}^n a_{ij}}{\sum_{i=1}^n \sum_{j=1}^n a_{ij}}, \quad i = 1, 2, \dots, n, \\ \frac{\sum_{j=1}^n a_{ij}}{\sum_{i=1}^n \sum_{j=1}^n a_{ij}} = \left(\frac{\sum_{j=1}^n l_{ij}}{\sum_{i=1}^n \sum_{j=1}^n l_{ij}}, \frac{\sum_{j=1}^n m_{ij}}{\sum_{i=1}^n \sum_{j=1}^n m_{ij}}, \frac{\sum_{j=1}^n u_{ij}}{\sum_{i=1}^n \sum_{j=1}^n u_{ij}} \right). \end{array} \right. \quad (3)$$

3.2.3. Calculating Weight Vectors. First, the possibility that the vectors of the initial fuzzy weights at the same level are $\tilde{w}_1 > \tilde{w}_2$ should be calculated, namely, $P(\tilde{w}_1 > \tilde{w}_2)$. It can be calculated by the following formula:

$$P(\tilde{w}_1 \geq \tilde{w}_2) = \begin{cases} 1, & m_1 \geq m_2, \\ \frac{l_2 - u_1}{(m_1 - u_1) - (m_2 - l_2)}, & m_1 < m_2, u_1 \geq l_2, \\ 0, & \text{otherwise.} \end{cases} \quad (4)$$

Next, the possibility that \tilde{w}_1 is greater than or equal to the vector of the other fuzzy weight at the same level should be considered, namely, $P(\tilde{w}_1 \geq \tilde{w}_2, \tilde{w}_3, \dots, \tilde{w}_n)$. It can be calculated by the following formula:

$$P(\tilde{w}_1 \geq \tilde{w}_2, \tilde{w}_3, \dots, \tilde{w}_n) = \min P(\tilde{w}_1 \geq \tilde{w}_i), \quad i = 2, \dots, n. \quad (5)$$

Set $d'(A_i) = \min P(\tilde{w}_i \geq \tilde{w}_k)$, $k = 1, 2, \dots, n$, and $k \neq i$. Then, the weight vector W' of this hierarchy should be

$$W' = (d'(A_1), d'(A_2), \dots, d'(A_n)). \quad (6)$$

After being normalized, the final weight vector W could be obtained as follows:

$$W = \left(\frac{d'(A_1)}{\sum_{i=1}^n d'(A_i)}, \frac{d'(A_2)}{\sum_{i=1}^n d'(A_i)}, \dots, \frac{d'(A_n)}{\sum_{i=1}^n d'(A_i)} \right). \quad (7)$$

3.3. Calculating Membership Degree. First, the consequence valuation of risk events (C) and the probability valuation of risk occurrence (P) are conducted by scoring of experts. And the valuing methods for the above two are as shown in Tables 2 and 3.

After that, the specific form of the membership function is determined. The membership function is calculated by L-R function; see the following formula:

$$r_{ij}(x) = \begin{cases} 0, & x \leq a \text{ or } x \geq b, \\ L(x), & a < x < m, \\ R(x), & m \leq x < b, \end{cases} \quad (8)$$

where a and b are both positive numbers. For specific details, please see (9)~(13).

$$\text{Extremely low risk : } r_{i1} = \begin{cases} 1, & 0 < x \leq 3, \\ 4 - x, & 3 < x \leq 4, \\ 0, & x > 4, \end{cases} \quad (9)$$

$$\text{low risk : } r_{i2} = \begin{cases} x - 3, & 3 \leq x < 4, \\ 1, & 4 \leq x \leq 7, \\ 8 - x, & 7 < x \leq 8, \\ 0, & x < 3 \text{ or } x > 8, \end{cases} \quad (10)$$

$$\text{medium risk : } r_{i3} = \begin{cases} x - 7, & 7 \leq x < 8, \\ 1, & 8 \leq x \leq 15, \\ 16 - x, & 15 < x \leq 16, \\ 0, & x < 7 \text{ or } x > 16, \end{cases} \quad (11)$$

TABLE 2: Consequence of valuation of risk events.

Degree	Valuation	Description
Slight	1	Does not result in significant loss
Medium	2	Results in a few losses
Severe	3	Results in compensable losses
Material	4	Results in significant but compensable losses
Disastrous	5	Results in uncompensable losses

where 1.5, 2.5, 3.5, and 4.5 indicate that the severity of the risk event is between the adjacent degrees.

TABLE 3: Probability valuation of risk occurrence.

Degree	Valuation	Description
Rare	1	The risk is rarely seen
Occasional	2	The risk is unlikely to happen
Possible	3	The risk may happen
Anticipated	4	The risk may happen repeatedly
Frequent	5	The risk may happen frequently

where 1.5, 2.5, 3.5, and 4.5 indicate that the probability of occurrence of the risk event is between the adjacent levels.

$$\text{high risk : } r_{i4} = \begin{cases} x - 15, & 15 \leq x < 16, \\ 1, & 16 \leq x \leq 20, \\ 16 - x, & 20 < x \leq 21, \\ 0, & x < 15 \text{ or } x > 21, \end{cases} \quad (12)$$

$$\text{extremely high risk : } r_{i5} = \begin{cases} x - 20, & 20 \leq x < 21, \\ 1, & 21 \leq x \leq 25, \\ 0, & x < 20. \end{cases} \quad (13)$$

Finally, the product of the consequence valuation of the risk event and the probability valuation of the risk occurrence is, respectively, brought into the above five membership functions, and then the membership degrees of the risk events to the five risk levels can be obtained. The membership degrees of the risk events at the same level are then composed into judgment matrix $R_i (i = 1, 2, \dots, 5)$:

$$R_i = \begin{pmatrix} r_{11} & \cdots & r_{51} \\ \vdots & \ddots & \vdots \\ r_{n1} & \cdots & r_{5n} \end{pmatrix}_{n \times 5}, \quad (14)$$

where n refers to the specific number of indices of a certain second-level index layer.

3.4. Fuzzy Comprehensive Judgment. First, calculate the comprehensive judgment matrix of the first-level index layer B_i :

$$B_i = W_i \circ R_i = [b_{i1}, b_{i2}, b_{i3}, b_{i4}, b_{i5}], \quad i = 1, 2, \dots, 5, \quad (15)$$

where W_i refers to the weight of risk event in the first-level index layer and \circ refers to the fuzzy operator.

After that, the comprehensive judgment matrices of all first-level index layers are compounded into the judgment matrix R of the target index layer:

$$R = [B_1, B_2, B_3, B_4, B_5]^T. \quad (16)$$

Finally, calculate the comprehensive judgment matrix B of the target layer as follows:

$$B = W \circ R = [b_1, b_2, b_3, b_4, b_5], \quad (17)$$

where W refers to the weight vector of the target layer.

According to the maximum membership principle, evaluation index v_i that the maximum element of B corresponds to is taken, namely, the construction risk level of the modified shield machine suitable for soft soil.

4. Case Study

4.1. Project Overview

4.1.1. Hydrological and Geological Conditions. The metro section between Binhai New Town Station and Lianhua Station is 1190 m long, and the right tunnel is 14 m away from the left one. The longitudinal profile of this tunnel section is a V-shaped slope. This section has a connection passage and pumping station at XK27 + 800.933. The minimum thickness of overburden layer along the line is 6.81 m at Lianhua Station, and the maximum depth is 14.51 m at the connection passage. The thickness of Binhai New Town Station is 7.36 m. The surface in this section is mainly covered by farms and ponds, and there are no large buildings and underground utilities within the construction area. This tunnel section largely passes through strata with soft soils (silt or mucky soil), fine-medium sand with mud, and sandy clay, as shown in Figure 2.

The surface is scattered with a few small rivers which are 10–30 m wide and 1.00–4.00 m deep. These rivers are not equipped with impervious facilities and are not sensitive to tides. The groundwater level is around 0.00–1.89 m, with an annual change between 1.0 and 1.5 m. This section is tunneled by the modified shield machine applicable in soft soils. The shield machine ($D = 6.28$ m) is originally applied to the upper-soft lower-hard ground between Taoyuancun Station and Shenyun Station in Shenzhen Metro Line 7. After modification, its diameter is now 6.48 m and can be utilized to tunnel soft ground. In this project, the shield machine is launched at Binhai New Town Station and received at Lianhua Station, and the construction organization is illustrated in Figure 3.

4.1.2. Modifications of Shield Machines Conditioned to Soft Soils. Considering the tunnel diameter and the geology of the soft ground between Binhai New Town Station and Lianhua Station in Fuzhou Metro Line 6, the shield machine has undergone the following modifications:

- (1) **Enlarging Shield Outer Diameter.** The outer diameter of the shield is enlarged by 0.2 m, from 6.28 m to 6.48 m. This enlargement will increase the perimeter of the shield (front shield, middle shield, and shield tail). The shield is easy to be worn out in the upper-soft lower-hard ground Figure 4(a), so a new one is applied to the modified machine Figure 4(b). Yet, the internal system remains unchanged, including the articulation seal, emergency airbag, tail brush, grout

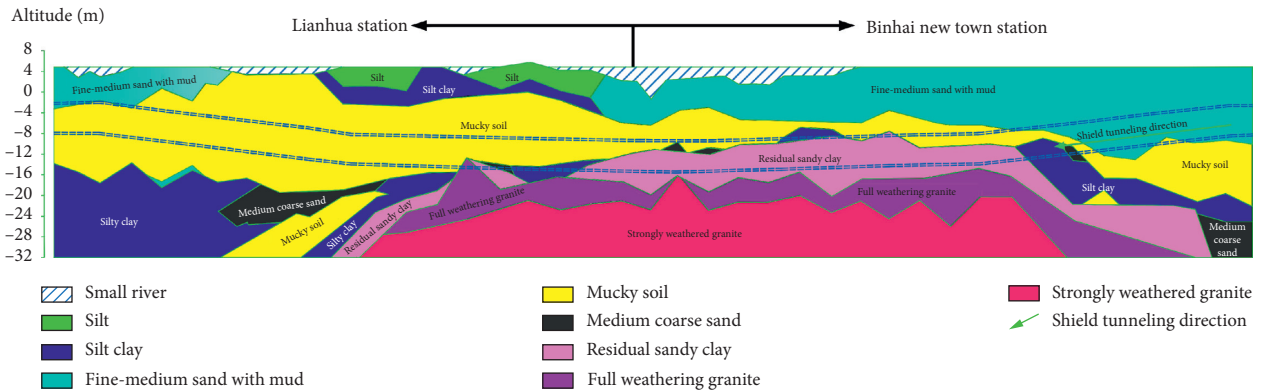


FIGURE 2: Longitudinal geological profile of Binhai New Town-Lianhua.

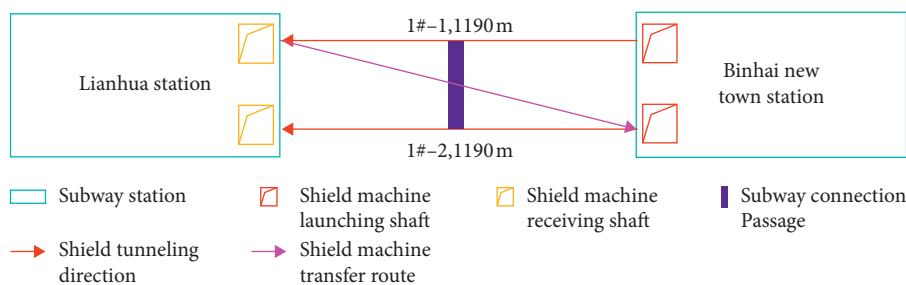


FIGURE 3: Construction organization diagram of Binhai New Town-Lianhua.

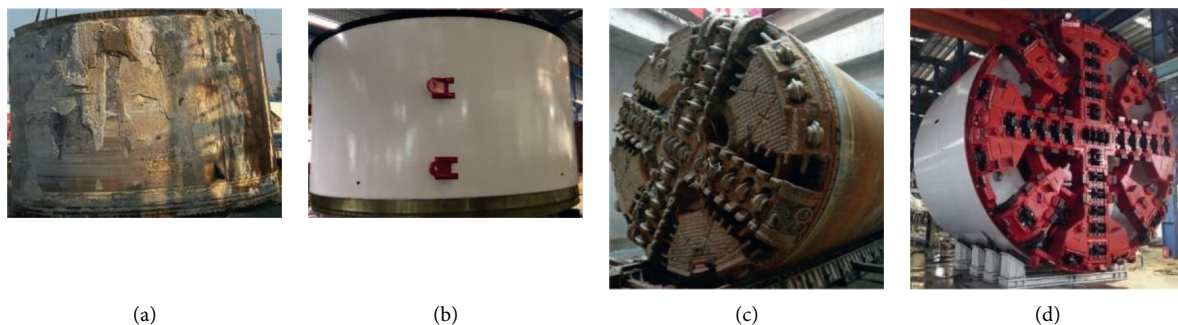


FIGURE 4: Unmodified and modified shield machines. (a) Unmodified shield. (b) Modified shield with enlarged diameter. (c) Cutterhead in upper-soft lower-hard ground. (d) Cutterhead in soft soil.

cover, clamping pad, trailer pad, screw conveyor, segment erector, belt conveyor, circulating water system, guiding system, hydraulic system, display screen, boring control box, internal control line of the machine, and two articulation cylinders.

- (2) *Changing Cutterhead and Tools.* In the upper-soft lower-hard ground where the strength of rock is very high, the cutterhead is easy to be worn, and the cutter tools are generally hobs. The machine in the beginning is equipped with 4 central double-edge hobs and 31 single-edge hobs Figure 4(c), together with 52 scrapers, 8 edge blades, and 1 super digging knife. The aperture of the cutterhead is 30%. In contrast, the soft soil between Binhai New Town Station and Lianhua Station requires that the main cutter tool is the tearing knife, including 8 main tearing knives in

reserve, 32 ordinary tearing knives, and 23 welding tearing knives. Apart from that, the modified shield machine has 16 side scrapers, 36 cutters, 1 super digging knife, 16 big ring protection knives, and 8 gauge knives. The cutter-head aperture is increased to 40% Figure 4(d). The cutterhead is driven by a hydraulic system with a power of 945 kW. The rated torque of the cutterhead is 6228 kN·m, and its maximum release torque stands at 7440 kN·m. The maximum rotating speed can reach 4.4 rpm and it contains 6 foam injection holes.

- (3) *Modifying the Thrust System.* The thrust system of the unmodified shield machine has 30 thrust oil cylinders. The modified shield machine has a larger outer diameter, and accordingly it is equipped with 2 more oil cylinders, 32 in total. The previous thrust

cylinders consist of 10 sets of double cylinders and 10 sets of single cylinders, with 5 sets at the left, the right, the top, and the bottom, respectively. The modified thrust system holds 16 sets of double cylinders, with 3 sets at the top, 5 at the bottom, 4 at the right, and 4 at the left. The model of the oil cylinder is $\varnothing 220/180 \times 2200$ mm, and the thrust power it can provide is 1330 kN. The total thrust power of the unmodified machine reaches 39900 kN, and that of the modified machine 42560 kN. The thrust stroke of the cylinder is 2200 mm, and its speed arrives at 80 mm/min. There are 4 cylinders which wear stroke sensors.

4.2. *Setting up the Risk Evaluation System.* The risk evaluation system (see Table 4) for this project is set up by the expert group based on discussion and review of a large

number of references, combined with the actual situation of the project. This system is composed of 5 first-level indices and 20 second-level indices.

Besides, the above-mentioned evaluation set is taken for this project, including “extremely low risk,” “low risk,” “medium risk,” “high risk,” and “extremely high risk,” which are denoted as $V = \{v_1, v_2, v_3, v_4, v_5\}$.

4.3. *Application of the Fuzzy Comprehensive Evaluation Model.* By taking the shield launching and receiving risk U_1 for instance, it is hereby to introduce how to use this model.

4.3.1. *Determining Risk Weight Vector.* First of all, the complementary matrix A_{U_1} of triangular fuzzy numbers on shield launching and receiving risks is obtained by expert scoring:

$$A_{U_1} = \begin{pmatrix} (0.50, 0.50, 0.50) & (0.20, 0.32, 0.44) & (0.28, 0.43, 0.48) & (0.25, 0.36, 0.46) & (0.31, 0.45, 0.49) \\ (0.56, 0.68, 0.80) & (0.50, 0.50, 0.50) & (0.53, 0.59, 0.74) & (0.51, 0.55, 0.69) & (0.54, 0.64, 0.79) \\ (0.52, 0.57, 0.72) & (0.26, 0.41, 0.47) & (0.50, 0.50, 0.50) & (0.27, 0.45, 0.48) & (0.51, 0.55, 0.71) \\ (0.54, 0.64, 0.75) & (0.31, 0.45, 0.49) & (0.52, 0.55, 0.73) & (0.50, 0.50, 0.50) & (0.53, 0.58, 0.74) \\ (0.51, 0.55, 0.69) & (0.21, 0.36, 0.46) & (0.29, 0.45, 0.49) & (0.26, 0.42, 0.47) & (0.50, 0.50, 0.50) \end{pmatrix}. \quad (18)$$

Calculate the initial fuzzy weight of each factor under the risk of shield launching and receiving according to (3) as follows:

$$\begin{cases} \tilde{w}_{U_{11}} = (0.106 \ 0.165 \ 0.228), \\ \tilde{w}_{U_{12}} = (0.181 \ 0.237 \ 0.338), \\ \tilde{w}_{U_{13}} = (0.141 \ 0.198 \ 0.277), \\ \tilde{w}_{U_{14}} = (0.165 \ 0.218 \ 0.308), \\ \tilde{w}_{U_{15}} = (0.121 \ 0.182 \ 0.251). \end{cases} \quad (19)$$

The weight vector W_{U_1}' of each factor under the shield launching and receiving risk can be calculated by (4)~(5) as follows:

$$W_{U_1}' = (0.394 \ 1 \ 0.714 \ 0.869 \ 0.562). \quad (20)$$

The final weight vector W_{U_1} under the risk of shield launching and receiving can be obtained by normalization by (7) as follows:

$$W_{U_1} = (0.111 \ 0.283 \ 0.201 \ 0.246 \ 0.159). \quad (21)$$

The final weight vectors $W_{U_2} \sim W_{U_5}$ of the remaining first-level index layers are as follows:

$$\begin{cases} W_{U_2} = (0.281 \ 0.150 \ 0.209 \ 0.258 \ 0.102), \\ W_{U_3} = (0.442 \ 0.219 \ 0.339), \\ W_{U_4} = (0.358 \ 0.291 \ 0.132 \ 0.219), \\ W_{U_5} = (0.345 \ 0.440 \ 0.215). \end{cases} \quad (22)$$

Final weight vector W of the target layer is as follows:

$$W = (0.211 \ 0.274 \ 0.122 \ 0.240 \ 0.153). \quad (23)$$

4.3.2. *Determining Risk Membership.* According to the valuing methods of Tables 2 and 3, the product of the consequence valuation (C) and the occurrence probability valuation (P) of risks under U_1 is determined by expert scoring, as shown in Table 5.

The judgment matrix R_{U_1} for the shield launching and receiving risks can be obtained by bringing the aforementioned product into the membership function:

$$R_{U_1} = \begin{pmatrix} 0.25 & 0.75 & 0 & 0 & 0 \\ 0 & 0 & 1 & 0 & 0 \\ 0 & 1 & 0 & 0 & 0 \\ 0 & 1 & 0 & 0 & 0 \\ 0.25 & 0.75 & 0 & 0 & 0 \end{pmatrix}. \quad (24)$$

The results of the judgment matrix of the remaining first-level index layers $R_{U_2} \sim R_{U_5}$ are as follows:

$$R_{U_2} = \begin{pmatrix} 0 & 0 & 0 & 0.75 & 0.25 \\ 0 & 0 & 1 & 0 & 0 \\ 0 & 0 & 0 & 1 & 0 \\ 0 & 0 & 0 & 1 & 0 \\ 0 & 0 & 1 & 0 & 0 \end{pmatrix},$$

TABLE 4: The risk evaluation system of Binhai New Town station-Lianhua station of Metro Line 6 in Fuzhou City.

The target layer	The first-level index layer	The second-level index layer
The safety risk evaluation for modified shield machine construction applicable to soft soils (U)	The risk of shield launching and receiving (U_1)	Deformation of the base (U_{11})
		Deviation from the axis during launching (U_{12})
	The risk of shield tunneling (U_2)	Soil influx into receiving shaft after dismantling portal (U_{13})
		Deviation from the axis during receiving (U_{14})
	The risk of segment assembly (U_3)	Deformation of support during receiving (U_{15})
Inappropriate tunneling parameters (U_{21})		
Excessive rotation of the shield machine (U_{22})		
The risk of grouting (U_4)	Blockage in earth conveying (U_{23})	
	Deviation from the designed tunneling (U_{24})	
	Leakage in the shield sealing system (U_{25})	
	Segment dislocation (U_{31})	
The risk of working environment (U_5)	Segment deviation (U_{32})	
	Segment damage (U_{33})	
	Not grouting in time (U_{41})	
	Inadequate grouting (U_{42})	
	Clogging of the grouting pipe (U_{43})	
		Low quality of the grouting material (U_{44})
		Effect of groundwater (U_{51})
		The effect of tunnel underneath the river (U_{52})
		Tunneling through unfavorable geology (U_{53})

TABLE 5: Products of the consequence valuation and the occurrence probability valuation of risks under U_1 .

Risk index	U_{11}	U_{12}	U_{13}	U_{14}	U_{15}
C	2.50	3.00	2.50	2.75	2.50
P	1.50	2.75	2.00	2.50	1.50
$C \times P$	3.75	8.25	5.00	6.88	3.75

$$\begin{aligned}
 R_{U_3} &= \begin{pmatrix} 0 & 0 & 0 & 1 & 0 \\ 0 & 0 & 1 & 0 & 0 \\ 0 & 0 & 0 & 1 & 0 \end{pmatrix}, \\
 R_{U_4} &= \begin{pmatrix} 0 & 0 & 0 & 1 & 0 \\ 0 & 0 & 0 & 1 & 0 \\ 0 & 0 & 1 & 0 & 0 \\ 0 & 0 & 1 & 0 & 0 \end{pmatrix}, \\
 R_{U_5} &= \begin{pmatrix} 0 & 1 & 0 & 0 & 0 \\ 0 & 0.56 & 0.44 & 0 & 0 \\ 0.25 & 0.75 & 0 & 0 & 0 \end{pmatrix}.
 \end{aligned} \tag{25}$$

4.3.3. *Fuzzy Comprehensive Judgment.* Calculate the comprehensive judgment matrix B_{U_1} of the shield launching and receiving risks by (15) as follows:

$$B_{U_1} = (0.07 \ 0.65 \ 0.28 \ 0 \ 0). \tag{26}$$

The comprehensive judgment matrices $B_{U_2} \sim B_{U_5}$ of the remaining first-level index layers are as follows:

$$\begin{cases} B_{U_2} = (0 \ 0 \ 0.25 \ 0.68 \ 0.07), \\ B_{U_3} = (0 \ 0 \ 0.22 \ 0.78 \ 0), \\ B_{U_4} = (0 \ 0 \ 0.35 \ 0.65 \ 0), \\ B_{U_5} = (0.05 \ 0.75 \ 0.19 \ 0 \ 0). \end{cases} \tag{27}$$

The judgment matrix R of the target layer can be obtained by (16) as follows:

$$R = \begin{pmatrix} 0.07 & 0.65 & 0.28 & 0 & 0 \\ 0 & 0 & 0.25 & 0.68 & 0.07 \\ 0 & 0 & 0.22 & 0.78 & 0 \\ 0 & 0 & 0.35 & 0.65 & 0 \\ 0.05 & 0.75 & 0.19 & 0 & 0 \end{pmatrix}. \tag{28}$$

The comprehensive judgment matrix B of the target layer can be obtained by (17) as follows:

$$B = (0.02 \ 0.25 \ 0.27 \ 0.44 \ 0.02). \tag{29}$$

4.4. *Risk Evaluation Results.* According to the maximum membership principle, the project is finally evaluated as having high risk, among which the shield launching and receiving risk U_1 is evaluated as low risk, shield tunneling risk U_2 as high risk, segment assembly risk U_3 as high risk, grouting risk U_4 as high risk, and environmental risk U_5 as low risk.

It can be known from the above risk evaluation results that the risks of shield tunneling, segment assembly, and grouting should be paid great attention during the construction process of the modified shield machine applicable to soft soils.

4.5. Verifying the Effectiveness of the Risk Evaluation. In the above case, the level that the maximum membership corresponds to is taken as the final grade of the evaluated object. Though it is easy to operate, it may lead to irrational conclusions in circumstances of similar membership degrees.

Therefore, it is necessary to verify the effectiveness of the final grade of the evaluated object. Set α as the effectiveness index; then, the calculation formula and the corresponding effectiveness interval are as follows [40]:

$$\alpha = \frac{m\beta - 1}{2\gamma(m - 1)}, \quad (30)$$

where β refers to the maximum membership value in judgment matrix B of the target layer, m refers to the number of risk evaluation grades, and γ refers to the second-highest membership value in judgment matrix B of the target layer.

The relationship between the α value and the effectiveness of the maximum membership principle is shown in Table 6.

According to (30), the effective index α of this project is as follows:

$$\alpha = \frac{5 \times 0.44 - 1}{2 \times 0.27 \times (5 - 1)} = 0.56. \quad (31)$$

It can be seen from Table 6 that, since the effective index is ($0.5 \leq \alpha = 0.56 < 1$), the above-mentioned maximum membership principle is effective and can be used as the basis for the final risk evaluation.

5. Countermeasures to Cope with Risks

By analyzing the situation after the 100-ring tunneling test, the main problems figured out therefrom include inappropriate tunneling parameters, segment dislocation, segment damage, inadequate grouting, etc. This is in line with the above risk evaluation results. In addition, the setting range of the tunneling parameters and the treatment measures for related problems are proposed by analyzing the above-mentioned test data.

5.1. Test for Shield Tunneling Parameters. During the tunneling process of the test section, the shield tunneling parameters are tracked, including earth pressure, cutterhead torque and rotation speed, total thrust, tunneling speed, and excavation volume. Then, by analyzing the data of the aforementioned tunneling test, proper parameters are summarized to provide relevant experience for follow-up projects.

5.1.1. Total Thrust of Shield Machine. The total thrust changes of the shield machine are as shown in Figure 5. For the first 10 rings, it tunnels in the reinforced zone with the thrust controlled within 9000 kN. For the 11th~60th rings, the tunneling thrust in fine-medium sand with mud is controlled within a range of 8000~15000 kN. For the 61st~73rd rings, it tunnels in the zone that is composed of 1 m thick mucky soil at the bottom and fine-medium sand with

TABLE 6: The relationship between α value and the effectiveness of the maximum membership principle.

Interval	Effectiveness of maximum membership principle
$\alpha \rightarrow +\infty$	Absolutely effective
$\alpha \in [1, +\infty)$	Very effective
$\alpha \in [0.5, 1)$	Effective
$\alpha \in [0, 0.5)$	Slightly effective
$\alpha \rightarrow 0$	Ineffective

mud at the top, with the thrust controlled between 11000 and 14000 kN. For 74th~100th rings, the shield machine tunnels in fine-medium sand with mud containing silt with thrust controlled between 10000 and 15000 kN. It shows comparatively stable thrust changes in general. But the attitude adjustment of the shield machine fluctuates a little bit during the tunneling process.

5.1.2. Torque and Rotation Speed of Cutterhead. The rotation speed of cutterhead runs at around 1 rpm in the initial stage but is adjusted gradually to 0.9~1.3 rpm when entering normal tunneling stage according to the tunneling speed. The torque is maintained steadily during the process. For the tunneling of the first 100 rings in the zone with a whole section of fine-medium sand with mud, the torque of the cutterhead is maintained between 500 and 1600 kN·m. For the changing process, please see Figure 6.

5.1.3. Tunneling Speed. The process of tunneling speed changes of the shield machine is as shown in Figure 7. It stands in stratum with whole section fine-medium sand with mud when the shield machine launches. For the first 1~5 rings, the speed is controlled within 40 mm/min. Then, the zone of the 6th~90th rings still lies in stratum with whole section fine-medium sand with mud, so the speed is controlled between 30 and 60 mm/min. For the 80th~100th rings, exceptional rolling angle parameter occurs, and the tunneling speed is reduced to below 30 mm/min to correct the rolling angle.

5.1.4. Earth Pressure. For the tunnel interval after the shield machine finishes tunneling and moves out from the reinforced zone, the embedded depth is 9.74~13.24 m, indicating that this interval is a shallow tunnel section. And its static earth pressure P is as follows:

$$\begin{aligned} P &= k_0 \gamma h \\ &= 0.493 \times 18.9 \times (9.74 \sim 13.24) \\ &= 90.8 \sim 123.4 \text{ kPa}, \end{aligned} \quad (32)$$

where k_0 refers to the coefficient of static earth pressure, h refers to the buried depth of tunnel (m), and γ refers to bulk density of soil (kN/m^3).

During the initial tunneling, the earth pressure is set strictly according to the theoretical earth pressure value but is adjusted and optimized according to the monitoring data of the surface settlement during the construction process.

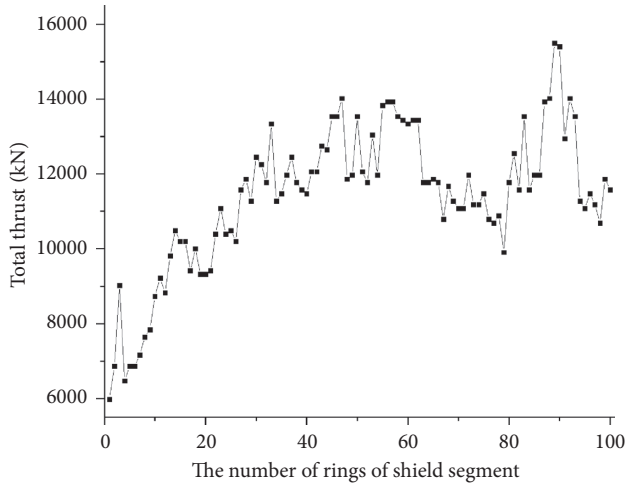


FIGURE 5: Variation law of total thrust of shield machine.

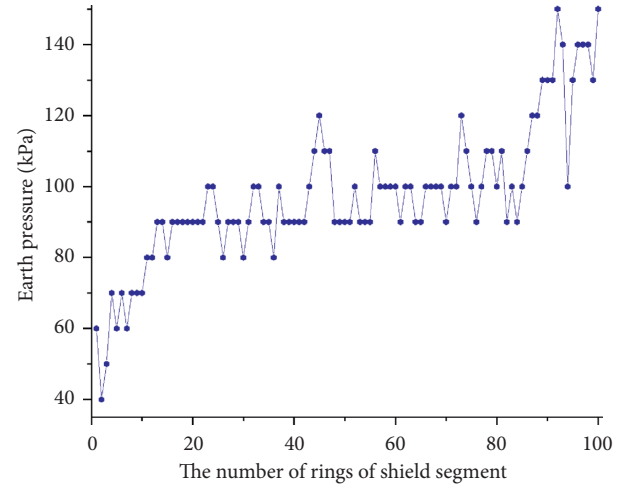


FIGURE 8: Variation law of earth pressure.

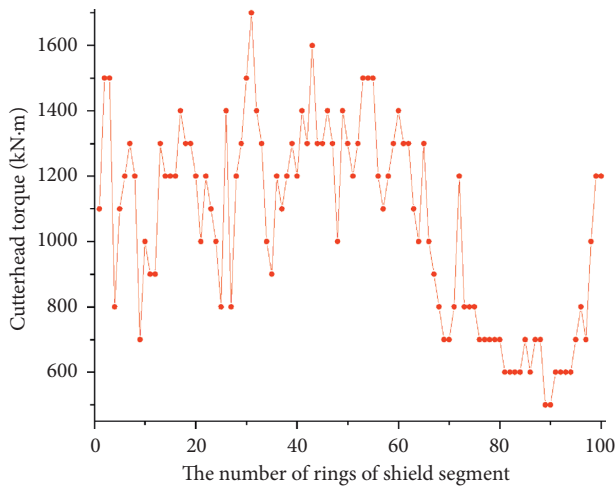


FIGURE 6: Variation law of torque of cutterhead.

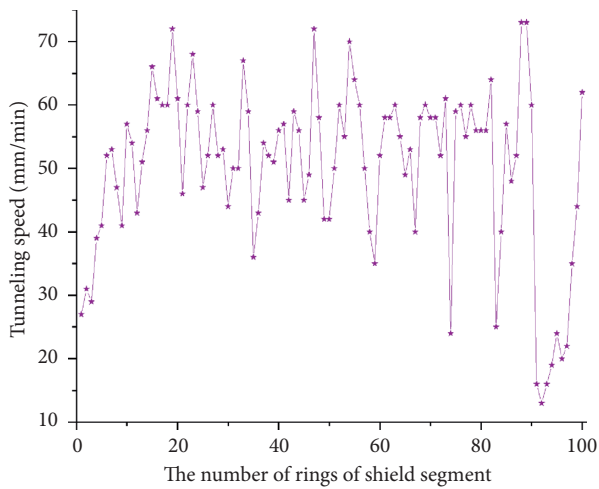


FIGURE 7: Variation law of tunneling speed.

Due to the significant settlement volume, the earth pressure slightly higher than the theoretical value is adopted in practical tunneling process, as shown in Figure 8.

5.1.5. *Excavation Volume.* The theoretical excavation volume of each ring of segments is as follows:

$$\begin{aligned} Q_1 &= \frac{n_0 \pi D'^2 L}{4} \\ &= \frac{1.2 \times \pi \times 6.48^2 \times 1.2}{4} \\ &= 47.5 \text{ m}^3, \end{aligned} \quad (33)$$

where n_0 refers to the loose coefficient (1.2), D' refers to the cutterhead diameter (6.48 m), and L refers to the segment width (1.2 m).

Therefore, the excavation volume of each ring of segment is about 47.5 m^3 . The amount of excavation produced by shield tunneling is controlled within 98%~102%, namely, within $46.5 \text{ m}^3 \sim 48.3 \text{ m}^3$. According to the statistical analysis on the first 100 rings' excavation volumes (see Figure 9), it can be known that the mean value of the excavation volume of each ring is 45 m^3 , which is slightly lower than the theoretical value.

5.2. *Synchronous Grouting Test of Shield Machine.* Synchronous grouting is an important work step of shield construction. Full and even grouting can help to control surface settlement effectively.

The theoretical grouting quantity Q is as follows:

$$\begin{aligned} Q &= V \cdot \lambda = \frac{(D'^2 - d^2) \cdot \pi \cdot L}{4} \\ &= \frac{(6.48^2 - 6.2^2) \times \pi \times 1.2}{4} \times (150\% \sim 200\%) \\ &= 5.17 \sim 6.69 \text{ m}^3, \end{aligned} \quad (34)$$

where V refers to the void caused by shield construction, d refers to the outer diameter of the segment (6.2 m), and λ is the grouting rate, which is taken as 150%~200% herein.

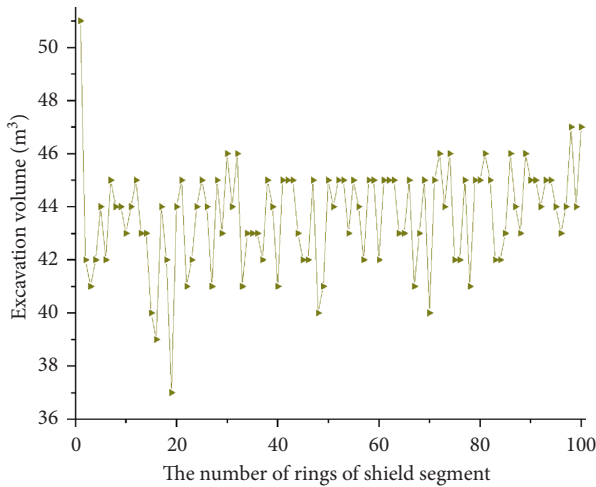


FIGURE 9: Variation law of excavation volume.

The synchronous grouting changes are as shown in Figure 10. The total grouting quantity is controlled between 4 and 7 m³.

5.3. Segment Assembly Test

5.3.1. Measures to Cope with Segment Dislocation. The changes of segment dislocation are as shown in Figures 11 and 12. The segments have both circumferential and longitudinal dislocations in almost the same amounts. Most of the dislocations are 5 mm. The largest circumferential dislocation happens in place between the 82nd ring and the 83rd ring, reaching a 9 mm dislocation quantity but smaller than the control quantity of 15 mm. The largest longitudinal dislocation occurs in place between the L2 block and the K block of 86th ring, showing an 18 mm dislocation quantity, which is greater than 10 mm. Among the above, segments of a total of 4 rings (83/84/85/86) have longitudinal dislocation quantities exceeding the control quantity of 10 mm and need to be corrected and carried out with anti-crack and waterproof measures.

The measures to cope with the segment dislocation include the following:

- (1) If possible, use the middle and upper grouting pipeline to conduct synchronous grouting.
- (2) The sludge and sewage at the assembling part of the shield tail must be cleaned up before assembling the segments, and the sundries in the gap between the upstream surface of the segment of the previous ring and the shield tail must be cleaned up as well, thus to guarantee assembling the segments in a condition with no sundries or residual water.
- (3) Bolt re-tightening must reach the design requirement, and the re-tightening measures shall be conducted at least three times (after assembling, during tunneling, and after moving out from the shield tail).
- (4) The assembly of segments must follow the requirements of bottom-to-top sequence, left-and-right

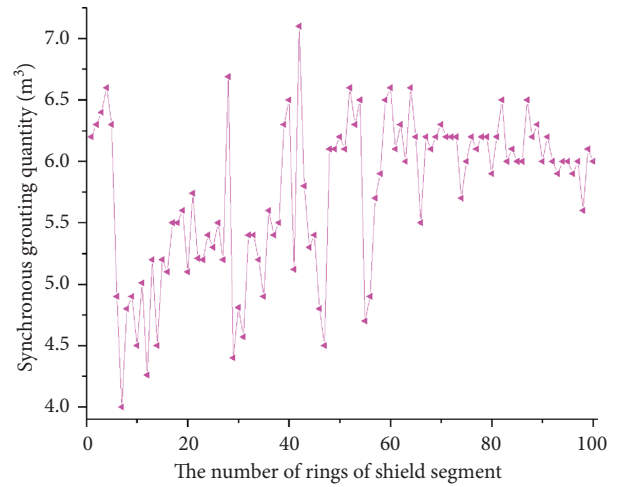


FIGURE 10: Variation law of synchronous grouting quantity.

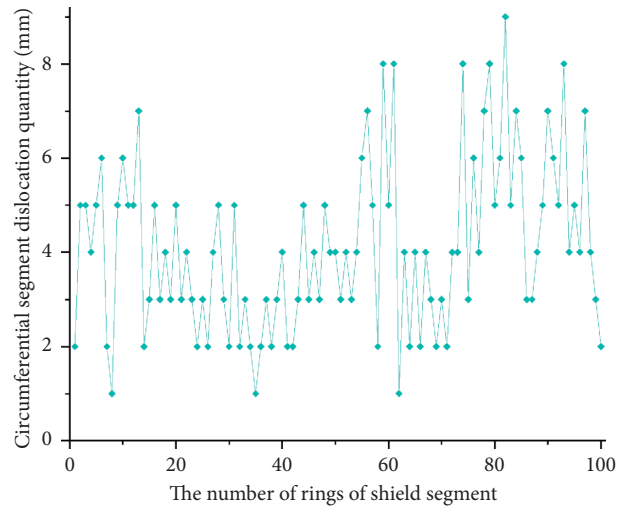


FIGURE 11: Variation law of circumferential segment dislocation quantity.

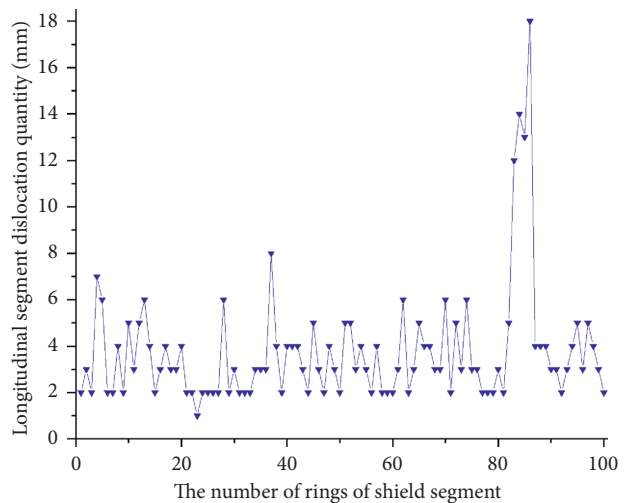


FIGURE 12: Variation law of longitudinal segment dislocation quantity.

crossed arrangement, and sealing the top finally. Meanwhile, the fine-tuning device for segment installation must be used to adjust the inner arc between the to-be-installed segment and the installed segment into smooth connection status. The bolt holes shall be well aligned to make bolt insertion easy.

- (5) Reasonably inject the shield tail grease to reduce the friction brought by the shield tail brush to the segment.
- (6) Reasonably optimize the slurry proportion to reduce the uplifting volume of the segment.

5.3.2. Measures to Deal with Damaged Segment. On-site segment damage is shown in Figure 13. The obviously damaged segments include point 8 of block B2 of the 58th ring, point 2 and point 12 of block B2 of the 56th ring, point 12 of block B1 of the 52nd ring, and point 11 of block K of the 53rd ring.

The fixed segment is as shown in Figure 14. The measures to deal with damaged segment are as follows:

- (1) Strengthen the acceptance inspection of segments. It is strictly forbidden to transport segments with uneven surfaces, missing edges or corners, excessive air bubbles, pitted surfaces, and exposed rebar to the construction site.
- (2) Strengthen the training to the assembly workers, make clear assembly identification for each ring, and assign special personnel to take charge of it.
- (3) During the assembling of the segments, in any case that the uneven local ring surface is found, the assembly shall be paused to adjust the force transmission liner timely, to guarantee the flatness of the ring surface.
- (4) Conduct grouting strictly according to the designed synchronous grouting quantity.
- (5) Strictly implement the bolt tightening regulations during the tunneling process, thus to prevent the segment floating that may result in segment dislocation and damage.
- (6) Fix the segments strictly according to the segment fixation plan, and adjust the color difference properly.
- (7) Maintain the shield posture and the clearance between the shield tails, and clean up the mud in the shield tails in time.

5.3.3. Measures to Deal with Segment Attitude Deviation. The changes of on-site segment attitude deviation are as shown in Figures 15 and 16. The segment suffers not only the horizontal deviation but also the vertical deviation. And the vertical deviation is greater than the horizontal deviation. The segments deviate upward in the fine-medium sand with mud. The largest vertical deviation happens at the 45th ring, which is 78.1mm deviation quantity. At the horizontal



FIGURE 13: On-site segment damage.

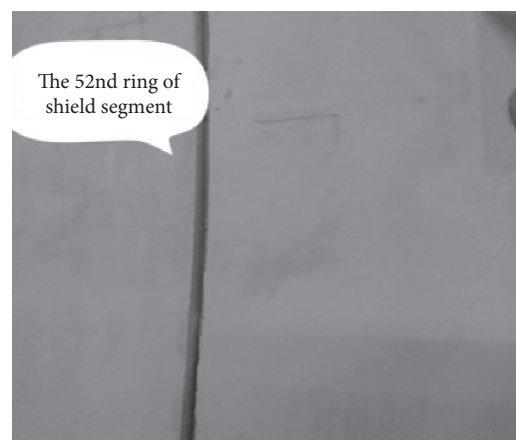


FIGURE 14: Segment repair.

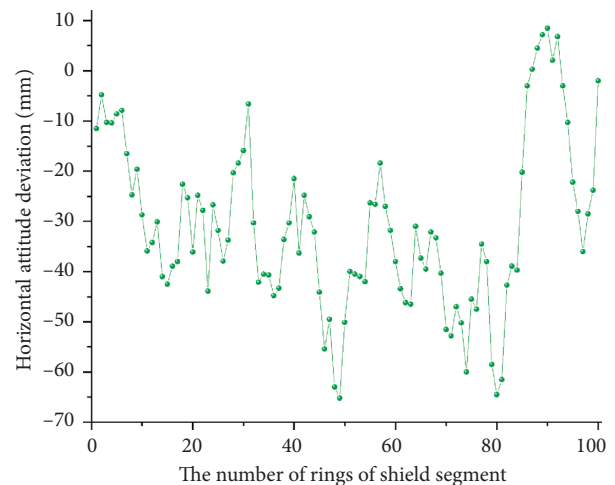


FIGURE 15: Variation law of horizontal attitude deviation of segments.

direction, rightward deviation of segments happens, for which the largest deviation occurs at the 49th ring, reaching 65.2 mm.

The measures to control segment deviation include the following:

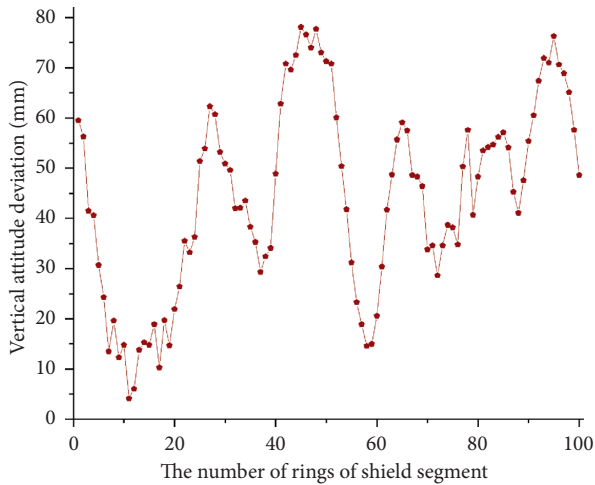


FIGURE 16: Variation law of horizontal attitude deviation of segments.

- (1) For the tunneling in the fine-medium sand with mud, the measure of controlling tunneling speed should be taken. Each work shift shall tunnel for 6-7 rings in their shift and follow up the secondary double liquid grouting timely. Currently, the method of grouting once every two rings is applied on-site.
- (2) Targeting the problems of insufficient shield machine thrust and hard-to-control attitude, the method of enlarging soil pressure properly is adopted to control the uplifting problem.
- (3) Adjust the proportion of synchronous grouting to shorten the initial setting time. The initial setting time of the current synchronous grouting is 6-7 hours, and the problem of segment uplifting has been improved to a certain extent.
- (4) When the shield machine tunneling attitude is well controlled, it shall adjust the vertical trend of the shield machine slowly, to guarantee that the formed segments meet the design requirements.

6. In Situ Monitoring

Figure 17 shows how surface settlement changes, by 7 April 2018, as the right tunneling line of the metro section between Binhai New Town Station and Lianhua Station is under construction.

As the shield machine is processing, the surface settlement is on the rise. The cumulative subsidence is -104.04 mm at the most, exceeding the maximum subsidence control of urban road, -30 mm. Additionally, daily subsidence peaks at -26.12 mm. The large settlement will not give rise to safety problems during the construction of this metro section which is mainly covered by farms and fishponds, whereas it can bring about heavy economic losses. Therefore, surface settlement needs to be controlled by modifying tunneling parameters.

After relevant tests, the tunneling parameters are modified. Total thrust power is $8000\text{--}16000$ kN. The

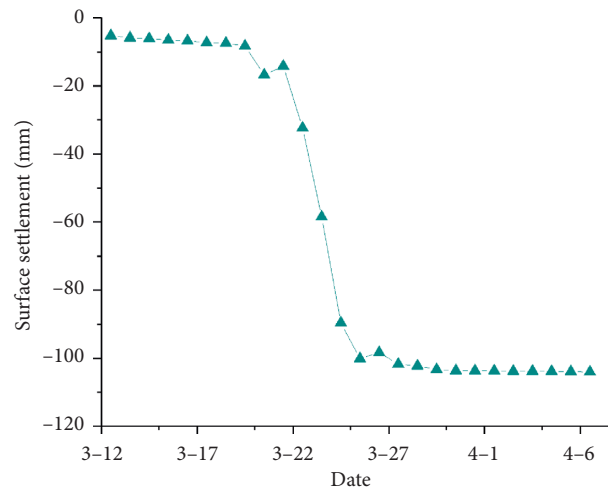


FIGURE 17: Changes in surface settlement.

cutterhead torque is $1000\text{--}1600$ kN·m, and its rotating speed is around 1.0 rpm. The thrust speed is about 50 mm/min. Earth pressure lies between 120 and 140 kPa, and the volume of excavation is tested as 45 m^3 . The amount of synchronous grouting is $5\text{--}7\text{ m}^3$. When these modified tunneling parameters are applied, the surface settlement is developing in a steady way.

7. Conclusions

- (1) After analyzing the construction features of modified shield machines applicable in soft soils, it is concluded that relevant risks exist in operating steps including shield launching, receiving, and tunneling, segment assembly, and grouting, as well as in the surroundings. The risks of shield tunneling, segment assembly, and grouting rank high indicate that preparations are needed to counteract emergencies during construction.
- (2) A risk evaluation model is specifically established for the modified shield tunneling in soft soils. This model weighs risk factors through triangular fuzzy numbers, which helps avoid subjectivity and better reflects the fuzziness of risk factors, without the consistency check as analytic hierarchy process (AHP) does. Furthermore, efficacy indices are used to ensure the reliability of maximum membership principle, rendering the fuzzy comprehensive evaluation method more accurate.
- (3) This specific model is applied to the construction of one section tunnel (Binhai New Town-Lianhua) of Metro Line 6 in Fuzhou City. The model rates this project as high-risk. High risks exist in shield tunneling, segment assembly, and grouting. The same assessment is shown by data obtained from tunneling tests on-site and surface settlement measurement, which again certifies the reliability of this model.
- (4) Recommended tunneling parameters and countermeasures against segment dislocation, damage, and

attitude deviation can be derived from data collected from field tests of 100-ring tunneling. It is hoped that these findings will serve as a reference for future application of modified shield tunneling in soft soils.

Data Availability

The data used to support the findings of this study are included within the article.

Conflicts of Interest

The authors declare that there are no conflicts of interest regarding the publication of this paper.

Acknowledgments

This work was funded by the China Power Construction Major Project (DJ-ZDXM-2017-23).

References

- [1] R. Zumsteg and L. Langmaack, "Mechanized tunneling in soft soils: choice of excavation mode and application of soil-conditioning additives in glacial deposits," *Engineering*, vol. 3, no. 6, pp. 863–870, 2017.
- [2] K. Cui and W. Lin, "Muck problems in subway shield tunneling in sandy cobble stratum," *Polish Maritime Research*, vol. 23, no. s1, pp. 175–179, 2016.
- [3] N. Bilgin, H. Copur, and C. Balci, "Effect of replacing disc cutters with chisel tools on performance of a TBM in difficult ground conditions," *Tunnelling and Underground Space Technology*, vol. 27, no. 1, pp. 41–51, 2012.
- [4] S. Cao, J. Cui, Y. Fang, and R. Deng, "Performance of slurry tbm tunnelling in sandy cobble ground—a case study in Lanzhou," *KSCE Journal of Civil Engineering*, vol. 23, no. 7, pp. 3207–3217, 2019.
- [5] Q. M. Gong, L. J. Yin, and Q. R. She, "TBM tunneling in marble rock masses with high in situ stress and large groundwater inflow: a case study in China," *Bulletin of Engineering Geology and the Environment*, vol. 72, no. 2, pp. 163–172, 2013.
- [6] J. Zhao, Q. M. Gong, and Z. Eisensten, "Tunnelling through a frequently changing and mixed ground: a case history in Singapore," *Tunnelling and Underground Space Technology*, vol. 22, no. 4, pp. 388–400, 2007.
- [7] J. Tebar and N. Alonso, "Quejigares tunnels. Excavation in soft ground and rock with a mixed shield EPB," in *Proceedings of the World Tunnel Congress: Underground—the Way to the Future, WTC 2013*, Taylor and Francis—Balkema, Geneva, Switzerland, pp. 2046–2053, May 2013.
- [8] K. Rafie, S. Skelhorn, and A. Mitchell, "EPB tunnelling at high pressures: customization of tunnelling systems for Port Mann tunnel," in *Proceedings of the 2013 Rapid Excavation and Tunneling Conference, RETC 2013*, Society for Mining, Metallurgy and Exploration, Washington, DC, USA, pp. 967–986, June 2013.
- [9] X. Li and D. Yuan, "Creating a working space for modifying and maintaining the cutterhead of a large-diameter slurry shield: a case study of Beijing railway tunnel construction," *Tunnelling and Underground Space Technology*, vol. 72, pp. 73–83, 2018.
- [10] N. Zhang, J. S. Shen, A. Zhou, and A. Arulrajah, "Tunneling induced geohazards in mylonitic rock faults with rich groundwater: a case study in Guangzhou," *Tunnelling and Underground Space Technology*, vol. 74, pp. 262–272, 2018.
- [11] H. Pan, J. Gou, Z. Wan et al., "Research on coupling degree model of safety risk system for tunnel construction in subway shield zone," *Mathematical Problems in Engineering*, vol. 2019, Article ID 5783938, 19 pages, 2019.
- [12] R. L. Sousa and H. H. Einstein, "Risk analysis during tunnel construction using Bayesian networks: Porto Metro case study," *Tunnelling and Underground Space Technology*, vol. 27, no. 1, pp. 86–100, 2012.
- [13] X. L. Jia, Q. M. Dai, and H. Z. Yang, "Susceptibility zoning of karst geological hazards using machine learning and cloud model," *Cluster Computing*, vol. 22, pp. S8051–S8058, 2019.
- [14] X. H. Deng, T. Xu, and R. Wang, "Risk evaluation model of highway tunnel portal construction based on BP fuzzy neural network," *Computational Intelligence and Neuroscience*, vol. 2018, Article ID 8547313, 16 pages, 2018.
- [15] A. Pourtaghi and M. A. Lotfollahi-Yaghin, "Wavenet ability assessment in comparison to ANN for predicting the maximum surface settlement caused by tunneling," *Tunnelling and Underground Space Technology*, vol. 28, pp. 257–271, 2012.
- [16] W. Zhang, K. Sun, C. Lei, Y. Zhang, H. Li, and B. F. Spencer, "Fuzzy analytic hierarchy process synthetic evaluation models for the health monitoring of shield tunnels," *Computer-Aided Civil and Infrastructure Engineering*, vol. 29, no. 9, pp. 676–688, 2014.
- [17] F. Barpi and D. Peila, "Influence of the tunnel shape on shotcrete lining stresses," *Computer-Aided Civil and Infrastructure Engineering*, vol. 27, no. 4, pp. 260–275, 2012.
- [18] K.-C. Hyun, S. Min, H. Choi, J. Park, and I.-M. Lee, "Risk analysis using fault-tree analysis (FTA) and analytic hierarchy process (AHP) applicable to shield TBM tunnels," *Tunnelling and Underground Space Technology*, vol. 49, pp. 121–129, 2015.
- [19] Y. Cao and S. Xiong, "A sustainable financing credit rating model for China's small- and medium-sized enterprises," *Mathematical Problems in Engineering*, vol. 2014, Article ID 861085, 5 pages, 2014.
- [20] M. Jakšić, S. Moljević, A. Aleksić et al., "Fuzzy approach in ranking of banks according to financial performances," *Mathematical Problems in Engineering*, vol. 2016, Article ID 6169586, 11 pages, 2016.
- [21] F.-Y. Hsiao, S.-H. Wang, W.-C. Wang, C.-P. Wen, and W.-D. Yu, "Neuro-fuzzy cost estimation model enhanced by fast messy genetic algorithms for semiconductor hookup construction," *Computer-Aided Civil and Infrastructure Engineering*, vol. 27, no. 10, pp. 764–781, 2012.
- [22] W.-C. Huang, C.-H. Jhong, and J.-F. Ding, "Key factors influencing sustainable development of a green energy industry in Taiwan," *Mathematical Problems in Engineering*, vol. 2013, Article ID 791896, 10 pages, 2013.
- [23] Y. Li, Y. Li, Z. Han, G. Li, K. Gao, and Z. Wang, "Determination of optimal opening scheme for electromagnetic loop networks based on fuzzy analytic hierarchy process," *Mathematical Problems in Engineering*, vol. 2016, Article ID 3965608, 11 pages, 2016.
- [24] W. Graf, S. Freitag, J.-U. Sickert, and M. Kaliske, "Structural analysis with fuzzy data and neural network based material description," *Computer-Aided Civil and Infrastructure Engineering*, vol. 27, no. 9, pp. 640–654, 2012.
- [25] H. Li, W.-J. Yi, and X.-X. Yuan, "Fuzzy-valued intensity measures for near-fault pulse-like ground motions," *Computer-Aided Civil and Infrastructure Engineering*, vol. 28, no. 10, pp. 780–795, 2013.

- [26] W. B. Tagherouit, S. Bennis, and J. Bengassem, "A fuzzy expert system for prioritizing rehabilitation of sewer networks," *Computer-Aided Civil and Infrastructure Engineering*, vol. 26, no. 2, pp. 146–152, 2011.
- [27] A. Bianchini, "Fuzzy representation of pavement condition for efficient pavement management," *Computer-Aided Civil and Infrastructure Engineering*, vol. 27, no. 8, pp. 608–619, 2012.
- [28] M. Dell'Orco and M. Mellano, "A new user-oriented index, based on a fuzzy inference system, for quality evaluation of rural roads," *Computer-Aided Civil and Infrastructure Engineering*, vol. 28, no. 8, pp. 635–647, 2013.
- [29] M. B. Anoop, B. K. Raghuprasad, and K. Balaji Rao, "A refined methodology for durability-based service life estimation of reinforced concrete structural elements considering fuzzy and random uncertainties," *Computer-Aided Civil and Infrastructure Engineering*, vol. 27, no. 3, pp. 170–186, 2012.
- [30] G. Zhang, C. Wang, Y. Jiao et al., "Collapse risk analysis of deep foundation pits in metro stations using a fuzzy Bayesian network and a fuzzy AHP," *Mathematical Problems in Engineering*, vol. 2020, Article ID 4214379, 18 pages, 2020.
- [31] H. M. Lyu, W. J. Sun, S. L. Shen et al., "Risk assessment using a new consulting process in fuzzy AHP," *Journal of Construction Engineering and Management*, vol. 146, no. 3, p. 12, 2020.
- [32] Y. Wang, B. Liu, and Y. Qi, "A risk evaluation method with an improved scale for tunnel engineering," *Arabian Journal for Science and Engineering*, vol. 43, no. 4, pp. 2053–2067, 2017.
- [33] T. L. Saaty, "How to make a decision: the analytic hierarchy process," *European Journal of Operational Research*, vol. 48, no. 1, pp. 9–26, 1990.
- [34] B. Wang, C. Mo, C. He et al., "Fuzzy synthetic evaluation of the long-term health of tunnel structures," *Applied Sciences*, vol. 7, no. 2, 2017.
- [35] J. Khademi Hamidi, K. Shahriar, B. Rezai, J. Rostami, and H. Bejari, "Risk assessment based selection of rock TBM for adverse geological conditions using fuzzy-AHP," *Bulletin of Engineering Geology and the Environment*, vol. 69, no. 4, pp. 523–532, 2010.
- [36] A. Yazdani-Chamzini and S. H. Yakhchali, "Tunnel boring machine (TBM) selection using fuzzy multicriteria decision making methods," *Tunnelling and Underground Space Technology*, vol. 30, pp. 194–204, 2012.
- [37] X. Wang, K. Shi, Q. Shi et al., "A normal cloud model-based method for risk assessment of water inrush and its application in a super-long tunnel constructed by a tunnel boring machine in the arid area of northwest China," *Water*, vol. 12, no. 3, p. 644, 2020.
- [38] A. Aalianvari, H. Katibeh, and M. Sharifzadeh, "Application of fuzzy Delphi AHP method for the estimation and classification of Ghomrud tunnel from groundwater flow hazard," *Arabian Journal of Geosciences*, vol. 5, no. 2, pp. 275–284, 2012.
- [39] H. Yao, H.-B. Zhou, L.-B. Cai, and Y.-F. Zhang, "Fuzzy synthetic evaluation on construction risk of EPBS during tunnelling in soft soil area," *Yantu Lixue/Rock and Soil Mechanics*, vol. 28, no. 8, pp. 1753–1756, 2007.
- [40] L. Han, Q. Mei, Y.-m. Lu et al., "Analysis and study on AHP-fuzzy comprehensive evaluation," *China Safety Science Journal*, vol. 14, no. 7, pp. 89–92, 2004.

Research Article

Concrete Cracks Detection Using Convolutional Neural Network Based on Transfer Learning

Chao Su and Wenjun Wang 

College of Water Conservancy and Hydropower Engineering, Hohai University, Nanjing 210098, China

Correspondence should be addressed to Wenjun Wang; wenjunwang@hhu.edu.cn

Received 5 August 2020; Revised 21 September 2020; Accepted 26 September 2020; Published 17 October 2020

Academic Editor: Zheng-zheng Wang

Copyright © 2020 Chao Su and Wenjun Wang. This is an open access article distributed under the Creative Commons Attribution License, which permits unrestricted use, distribution, and reproduction in any medium, provided the original work is properly cited.

Crack plays a critical role in the field of evaluating the quality of concrete structures, which affects the safety, applicability, and durability of the structure. Due to its excellent performance in image processing, the convolutional neural network is becoming the mainstream choice to replace manual crack detection. In this paper, we improve the EfficientNetB0 to realize the detection of concrete surface cracks using the transfer learning method. The model is designed by neural architecture search technology. The weights are pretrained on the ImageNet. Supervised learning uses Adam optimizer to update network parameters. In the testing process, crack images from different locations were used to further test the generalization capability of the model. By comparing the detection results with the MobileNetV2, DenseNet201, and InceptionV3 models, the results show that our model greatly reduces the number of parameters while achieving high accuracy (0.9911) and has good generalization capability. Our model is an efficient detection model, which provides a new option for crack detection in areas with limited computing resources.

1. Introduction

In the current infrastructure, the concrete structure accounts for the largest proportion. For the concrete structure, cracks are a frequently encountered disease. With the increase in service time, the number and width of cracks show a gradual increasing trend, which seriously affects the safety, applicability, and durability of the structure. Therefore, it is of great significance to detect cracks regularly and takes corresponding maintenance measures for the safety of the concrete structures [1–3]. The traditional crack detection method is mainly based on the direct detection of professionals with related instruments. This detection method is not only labor-consuming but also time wasting. In addition, it also brings great hidden dangers to the safety of people.

In order to find an efficient and safe crack detection method and overcome various shortcomings of manual detection, people turned their attention to image processing technologies (IPTs) [4]. In the past decades, the computer vision community has been working on the automated detection of images and proposed a series of image

processing techniques, including thresholding [5, 6], edge detection [7], wavelet transforms [8, 9], and machine learning [10] and so on. Image thresholding divides the crack in the image at the pixel level according to the features of different pixel values, which makes the image simple and facilitates further processing. Differential operators used for edge detection mainly contain Roberts operator, Sobel operator, and Laplace operator [11]. The basic idea of wavelet transform is using a set of wavelet functions or basis functions to represent a function or signal, such as an image signal. Machine learning extracts feature vectors of crack from the training dataset and combines certain algorithms to make prediction. These methods solve the problem of crack detection in engineering effectively. However, due to the unevenness of cracks, the diversity of surface textures, and the complexity of the background, this field of research is still active.

As a new technology in the research of machine learning algorithms, deep learning is motivated by the establishment and simulation of a neural network for analyzing problems and learning like the human brain. Through typical feature

learning [12], each layer of the network takes the output of the previous layer as its own input, learns a deep nonlinear network structure, and transforms the specific raw data into a more abstract expression model. The rapid expansion of effective datasets, the realization of high-performance computing hardware, and the continuous improvement of training methods are driving the rapid development of deep learning. In 2012, AlexNet [13] won the championship with an overwhelming advantage in ImageNet Large-Scale Visual Recognition Challenge (ILSVRC). Convolutional neural network (CNN) begins to attract the attention of many researchers since then. CNN is a feed-forward neural network, and the connection between neurons is inspired by the animal visual cortex. It has the characteristics of local connectivity and parameter sharing and has excellent performance in large-scale image processing [14]. In recent years, researchers have begun to use convolutional neural networks to detect road defects automatically. The following is a brief overview of the application of CNN in crack detection.

Zhang et al. [15] proposed a crack detection method based on deep learning, which seems to be one of the earliest works applying CNN to road crack detection. The pavement pictures are taken by smartphones, and the network model is built on the Caffe DeepLearning (DL) framework. By comparing with traditional machine learning classifiers such as support vector machine (SVM) and boosting methods, the author proved the effectiveness of deep learning methods. Pauly et al. [16] studied the influence of CNN depth and the position change between training dataset and test dataset on pavement crack detection accuracy. The results show that increasing the network depth can improve the network performance, but when the image position changes, the detection accuracy will be greatly reduced. Maeda et al. [17] created a large-scale road damage dataset and marked the location and type of road damage in each picture. Finally, an end-to-end object detection method based on deep learning was used to train the damage detection model. Maeda et al. also transplanted their model into a mobile phone application to facilitate road damage detection in areas lacking experts and financial resources. Xu et al. [18] established an end-to-end bridge crack detection model to realize automatic bridge crack detection. The use of depthwise separable convolution reduces the number of parameters effectively. The atrous spatial pyramid pooling (ASPP) module extracts information at multiple scales. The model achieves a detection accuracy of 96.37% without pretraining. Li et al. [19] proposed the YOLOv3-Lite method, which greatly improves the crack detection speed without reducing the detection accuracy. Tong et al. [20] used convolutional neural networks (CNNs) to detect, locate, and measure ground penetrating radar images automatically and finally reconstruct concealed cracks in three dimensions, realizing a low-cost damage characterization method. Yang et al. [21] realized the pixel-level detection of cracks based on a fully convolutional neural network. The fully convolutional neural network is composed of upsampling and downsampling and can detect objects at different scales. In terms of crack segmentation, the accuracy, precision, recall, and F1-score

are 97.96%, 81.73%, 78.97%, and 79.95%, respectively. Zhu and Song [22] used the transfer learning method to improve VGG16 and realized the accurate classification of surface defects on concrete bridges. The training of convolutional neural networks usually requires a large number of data, but in many cases, it is more expensive to obtain large-scale data. The pretrained model can be transferred to the task of crack detection by means of transfer learning. The results show that the model can effectively extract defect features and provide a new idea for surface defect detection. Deng et al. [23] added a region-based deformable module to Faster R-CNN [24], R-FCN [25], and FPN-based Faster R-CNN [26] to improve the evaluation accuracy of crack detection.

In this paper, we use the transfer learning method to build a model for concrete surface crack detection. Compared with existing models, our model achieves a good balance among accuracy, model size, and training speed. Due to the use of transfer learning, the model becomes easier to train and faster to converge and has better generalization capability.

The remaining of this paper is structured as follows: Section 2 describes the dataset and image preprocessing method; Section 3 presents the overall model architecture and training details; Section 4 shows our experimental results; and Section 5 delivers the conclusion of this paper.

2. Dataset and Data Augmentation

2.1. Building Dataset. In this study, we use the dataset collected by Li and Zhao [27]. The photos in this dataset were obtained by a smartphone with a resolution of 4160×3120 pixels from the surface of a pylon and anchor room of a suspension bridge in Dalian, Liaoning, China. Then, images are cropped to 256×256 pixel resolutions. After cropping, the images are manually divided into two categories: with cracks and without cracks. In this study, we only use 12,000 photos of the dataset, and the number of crack and noncrack images are set to equal. These images include crack features and background features under various conditions. The 12,000 selected images are divided into the training set, validation set, and test set at the ratio of 6 : 2 : 2. The number of crack and noncrack images in the three datasets are set to equal. In addition, we also select 1,000 concrete bridge images with cracks and 1,000 images without cracks from the SDNET2018 [28] dataset. This will introduce various changes, such as changes in lighting conditions and the features of cracks and crack surface texture to further test the generalization capability of the model and make a more comprehensive evaluation of the model. Figure 1 shows several crack and noncrack images in the two datasets.

2.2. Data Augmentation. The generalization capability of the neural network model is closely related to the number of training datasets. But in reality, the amount of data is limited. One way to solve this problem is to create fake data and add it to the training set—data augmentation [29]. By allowing limited data to generate more equivalent data to artificially expand the training dataset, data augmentation can also

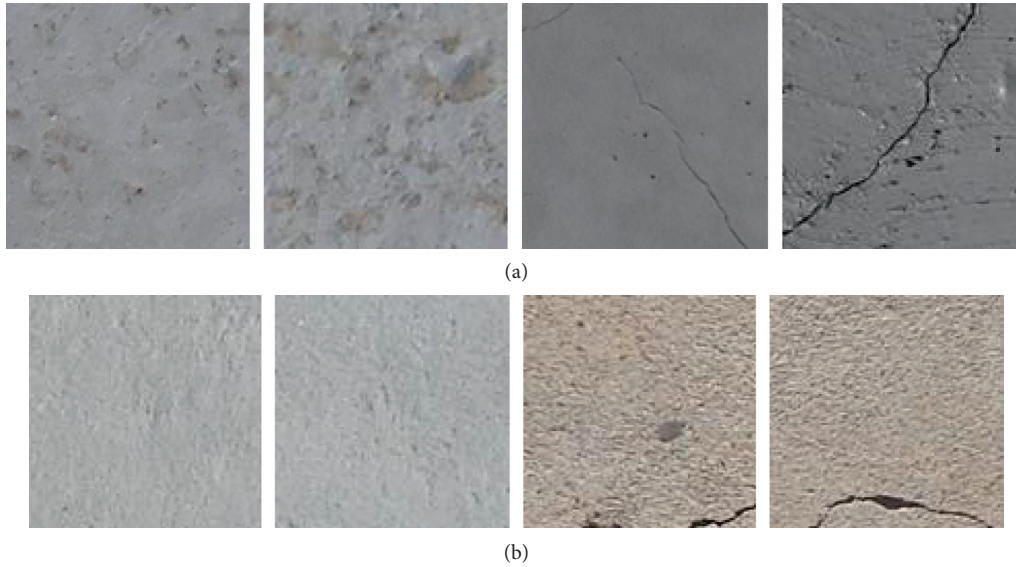


FIGURE 1: (a) Sample noncrack and crack images from the original dataset; (b) sample noncrack and crack images from the SDNET2018 dataset.

effectively overcome the overfitting phenomenon. Currently, it is widely used in various fields of deep learning. At present, the commonly used methods of data augmentation in the field of computer vision mainly include data augmentation based on image processing techniques and data augmentation based on deep learning.

In this paper, we use the built-in ImageDataGenerator interface of Tensorflow2.0 to enhance the input image data, including image flip, rotation, shift, and other operations. Figure 2 shows several crack images after data augmentation.

3. Model Construction and Training

3.1. The CNN. Convolutional neural network is a special kind of neural network. Its main feature is convolution operation, which has excellent performance for large-scale image processing. Generally speaking, a convolutional neural network is a hierarchical model that extracts the original data (such as RGB images) from the input layer through a series of operations such as convolution, pooling, and nonlinear activation function mapping. Abstract layer by layer, extract feature information, and finally make predictions. Deep convolutional neural networks have become popular since 2012, and now, they have become a pivotal research topic in the field of artificial intelligence. Classical convolutional neural network includes AlexNet [13], VGG [30], GoogLeNet [31], and ResNet [32]. A layer is the basic calculation unit of a CNN. CNN is mainly composed of input layer, convolution layer, activation function, pooling layer, fully connected layer, and Softmax layer.

3.2. Swish Activation Function. Ramachandran et al. [33] proposed a Swish activation function using a combination of exhaustive and reinforcement learning-based search. The effectiveness of this activation function has been verified in some large neural networks. The EfficientNet model used in

this article uses the Swish activation function. The definition of Swish is defined as follows:

$$f(x) = x \cdot \sigma(\beta x), \quad (1)$$

where $\sigma(t) = (1 + \exp(-t))^{-1}$ and β is either a constant or a trainable parameter.

Figure 3 shows the graph of Swish for different values of β .

3.3. Architecture Description. EfficientNet [34] was proposed by Google in 2019 which has great capability of feature extraction. Compared with other classic convolutional neural networks, it has fewer parameters and higher accuracy. The baseline network of EfficientNet is designed using multiobjective neural architecture search, and then, the baseline network is scaled in terms of depth, width, and resolution to achieve a balance among them. The compound scaling method is defined as follows:

$$\text{depth} = \alpha^\phi, \quad (2)$$

$$\text{width} = \beta^\phi, \quad (3)$$

$$\text{resolution} = \gamma^\phi, \quad (4)$$

$$\alpha \cdot \beta^2 \cdot \gamma^2 \approx 2, \quad (5)$$

$$\begin{aligned} \alpha &\gg 1, \\ \beta &\gg 1, \\ \gamma &\gg 1, \end{aligned} \quad (6)$$

where α , β , and γ can be calculated by a small grid search.

Firstly, EfficientNetB0 performs a 3×3 convolution operation on the input image, and then, the next 16 mobile

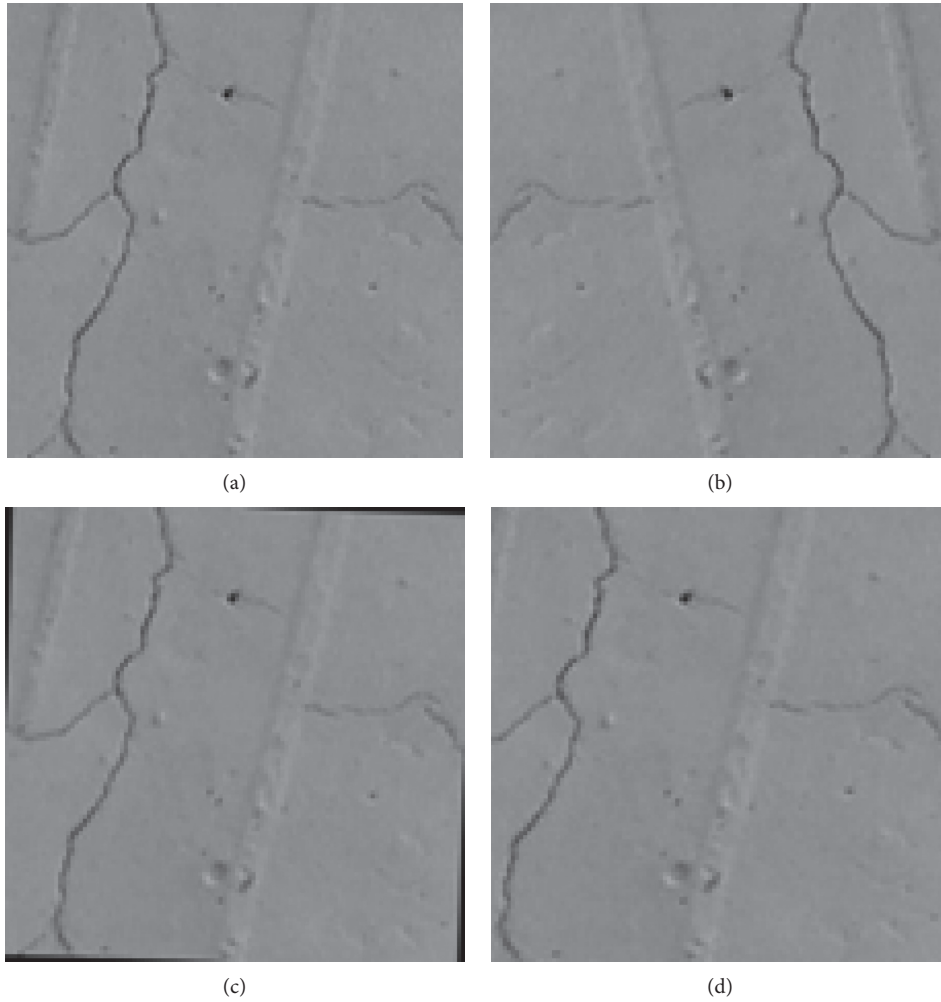


FIGURE 2: Images after data augmentation: (a) original image; (b) horizontal flip; (c) rotation; (d) horizontal shift.

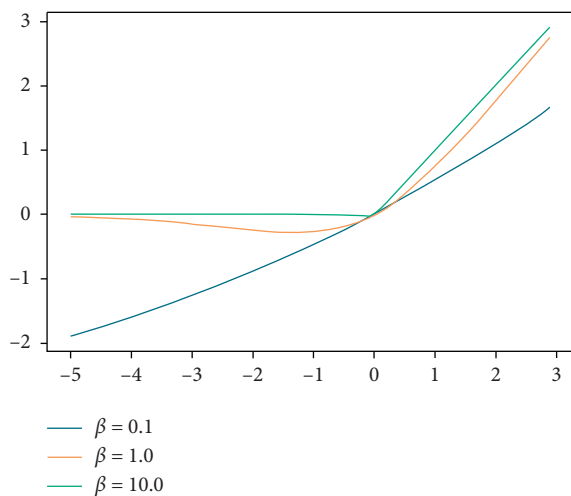


FIGURE 3: The Swish activation function.

inverted bottleneck convolution modules are used to further extract image features. Finally, after 1×1 convolution and global average pooling operations, the classification results

can be obtained in the fully connected layer. After each convolution operation in the network, batch normalization is performed. The activation function used in this network is Swish. The overall architecture of EfficientNetB0 is shown in Figure 4.

The core component of the network is a mobile inverted bottleneck convolution module (MBConv). Figure 5 shows the framework of this module. The design of this module is inspired by inverted residual and residual structure. Before performing on 3×3 or 5×5 convolution, the dimension of images is increased via 1×1 convolution in order to extract more feature information. The Squeeze-and-Excitation (SE) [35] model is added after 3×3 or 5×5 convolution operation to further improve performance. Finally, 1×1 convolution operation is used to reduce the dimension, and a residual connection is added.

The Squeeze-and-Excitation block compresses the feature map, performs a global average pooling operation in the direction of the channel dimension, and performs an excitation operation on the global feature to learn the relationship in each channel. Then, it obtains the weights of different channels through the sigmoid activation function. Finally, the weights multiply the original feature map to get

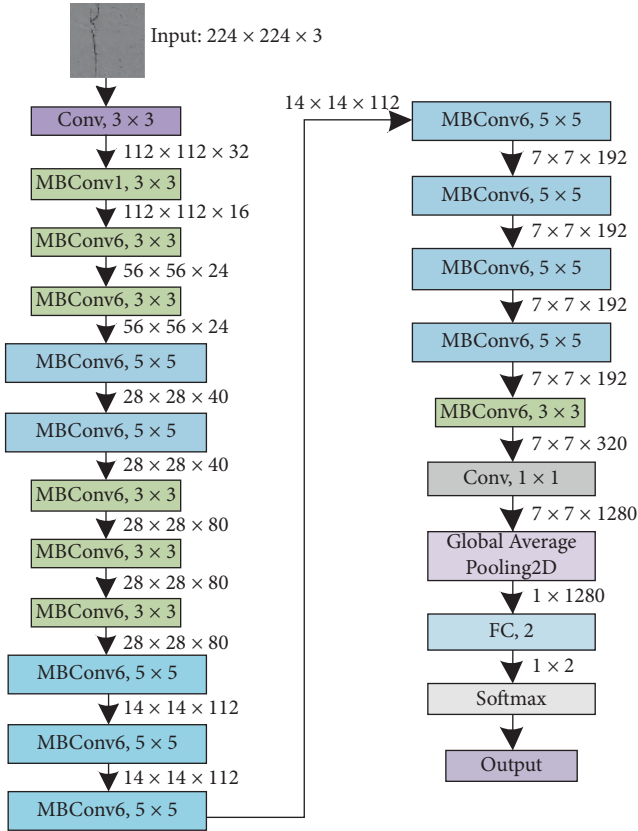


FIGURE 4: The EfficientNetB0 network architecture.

the final feature. The block allows the model to pay more attention to the channel features which has the most information, while suppressing those that are not important. Figure 6 illustrates the detail of the Squeeze-and-Excitation block.

3.4. Loss Function and Adam

3.4.1. *Loss Function.* The loss function is mainly used to evaluate the effect of the model. For a large amount of information, the machine discovers the laws through autonomous learning and makes predictions. The loss function is used to measure the degree of deviation between the predicted result and the actual value. During the network training process, the function is continuously updated until the best fitting result is found to reduce the error.

The cross-entropy loss function, also known as the Softmax function, is widely used to measure the gap between the predicted value and the actual value when the convolutional neural network deals with classification problems. The Softmax function is defined as follows:

$$L_{\text{softmax loss}} = -\frac{1}{N} \sum_{i=1}^N \log\left(\frac{e^{a_k}}{\sum_j e^{a_j}}\right), \quad (7)$$

where N represents the number of neurons in the output layer. a_k is the input signal.

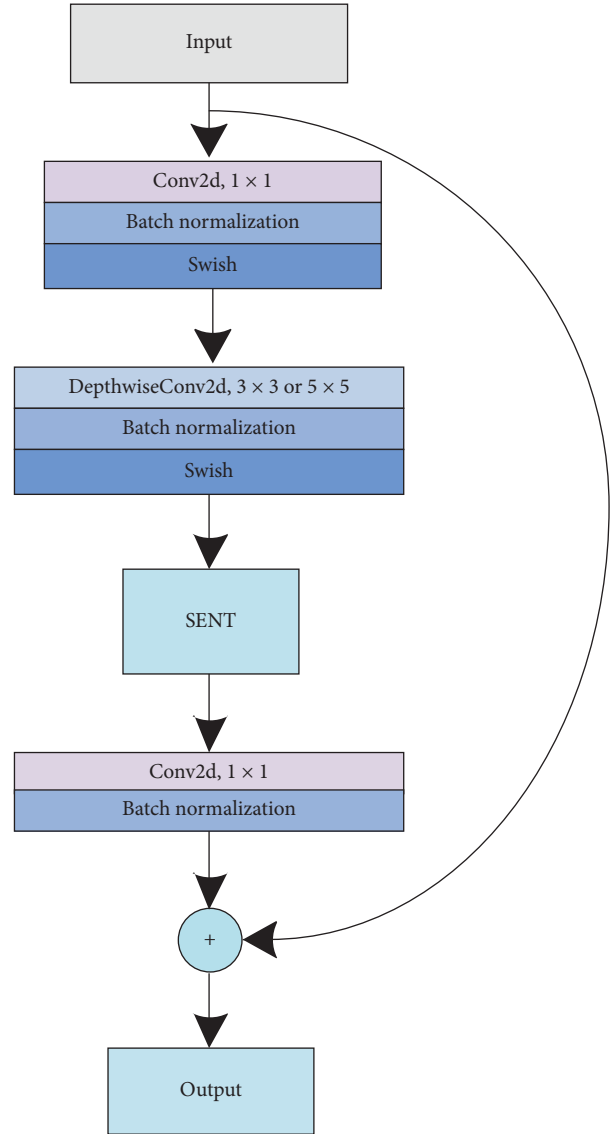


FIGURE 5: Illustration of MBConv's framework.

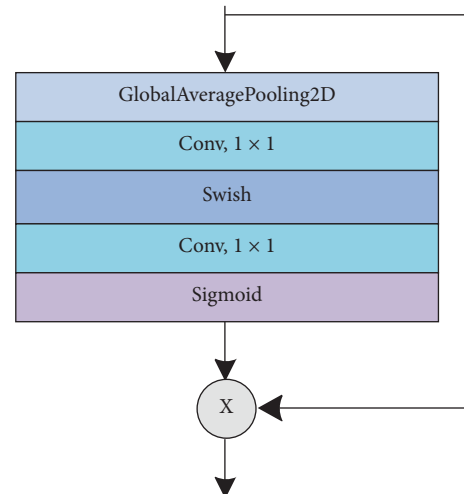


FIGURE 6: Squeeze-and-excitation block.

3.4.2. *Adam*. When training the model effectively and making accurate predictions, the internal parameters of the model play a significant role. This is why we ought to choose a suitable optimizer to update network parameters to approximate or reach the optimal value. The optimization algorithm helps to minimize the loss function, update the model parameters, and finally reach converge. In this article, the Adam algorithm is utilized to update weights.

Kingma [36] utilizes exponentially moving averages to estimate the moments:

$$m_t = \beta_1 m_{t-1} + (1 - \beta_1) \cdot g_t, \quad (8)$$

$$v_t = \beta_2 v_{t-1} + (1 - \beta_2) \cdot g_t^2, \quad (9)$$

where m and v are moving averages, g_t is gradient, and β_1 and β_2 are the decay rates of moment estimate (setting to 0.9 and 0.999, respectively).

Then, we do bias correction:

$$\widehat{m}_t = \frac{m_t}{1 - \beta_1^t}, \quad (10)$$

$$\widehat{v}_t = \frac{v_t}{1 - \beta_2^t}. \quad (11)$$

The final formula for weight update is

$$\omega_{t+1} = \omega_t - lr \cdot \frac{\widehat{m}_t}{\sqrt{\widehat{v}_t + \epsilon}}, \quad (12)$$

where lr is the learning rate and ϵ is the hyperparameter (setting to $1e - 3$).

3.5. *Training*. The convolutional neural network models used in this article use transfer learning methods to detect concrete surface crack. Specifically, the weight of the model is trained on the ImageNet and saved and then transferred to our model. Therefore, our model has a higher starting point, which greatly saves training time and obtains better performance.

All the experiments in this paper are performed on TensorFlow in Windows system: hardware settings: CPU: Intel (R) Core (TM) i7CPU@3.20 GHz, RAM: 16G, and GPU: NVIDIA GTX1080Ti.

Pretrained model is a model that has been trained and saved in advance on a large dataset. In order to realize the detection of concrete surface cracks, we need to retrain the pretrained convolutional neural network model. In addition, the last fully connected layer of the original model is replaced by a new fully connected layer. The specific experimental steps are as follows:

Step 1: data loading

Importing concrete surface crack images. A batch of data is randomly loaded from the training set (batch size: 16) for subsequent data processing.

Step 2: image preprocessing

We use built-in function in TensorFlow to adjust the size of input image to the fixed size of the model. Then,

do data augmentation via image flip, translation, rotation, and other operations. It is worth noting that, due to the use of TensorFlow's built-in function, a large number of pictures generated by data augmentation will not be saved to the local computer. All pictures are online.

Step 3: define the structure of the crack detection model

The pretrained model (such as EfficientNetB0) is loaded and fine-tuned. We remove the last fully connected layer and replace it with a custom layer. In this article, the number of classifications in the custom layer is set to 2. The value of weights in other layers will not change.

Step 4: compile the model and start training

Before training the model, it is necessary to specify the hyperparameters related to the network structure and select the appropriate optimization strategy. In this experiment, a random batch training method is used to train the neural network. The dataset is randomly shuffled before each epoch of training to ensure that the same batch of data in each epoch of model training is different, which can increase the rate of model convergence. The learning rate plays a significant role in the training of model. Choosing an appropriate learning rate can speed up the model's convergence speed; on the contrary, it may cause the loss value of objective function to explode. Since the transfer learning method is used, the network has converged on the original dataset, so the initial learning rate in this experiment is set to $5e - 7$. When the validation loss does not decrease for two consecutive times, the model learning rate will be reduced to half. We select the adaptive learning rate optimization algorithm Adam and use the cross-entropy loss function to guide the model training. The initialization method of weights is as follows: initialize the weights of newly added fully connected layer randomly and initialize the remaining weights with the pretrained weights. Figure 7 shows the process of model adjustment and weights initialization.

In order to solve the problem of how long to train the model, we adopt an early stopping strategy to avoid overtraining the network. During the training process, we monitor the validation loss. Once the validation loss drops less than $1e - 3$ for 30 epochs, the model will stop training.

Step 5: test the performance of the model.

Test the performance of the model on the test dataset. In addition, we also select 1000 crack and 1000 no crack images of concrete bridge decks from the SDNET2018 dataset to construct a completely different dataset so that we can further evaluate the detection performance of the model.

4. Experimental Results and Analyses

4.1. *Experimental Results and Evaluation Index*. When doing image classification tasks, in order to evaluate the

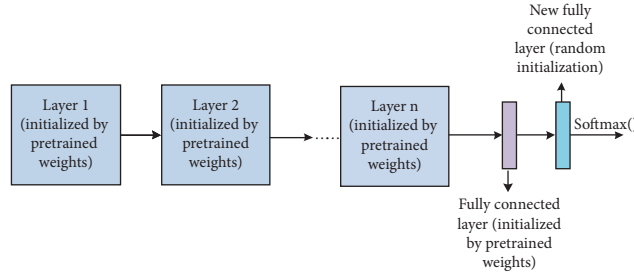


FIGURE 7: Transfer learning.

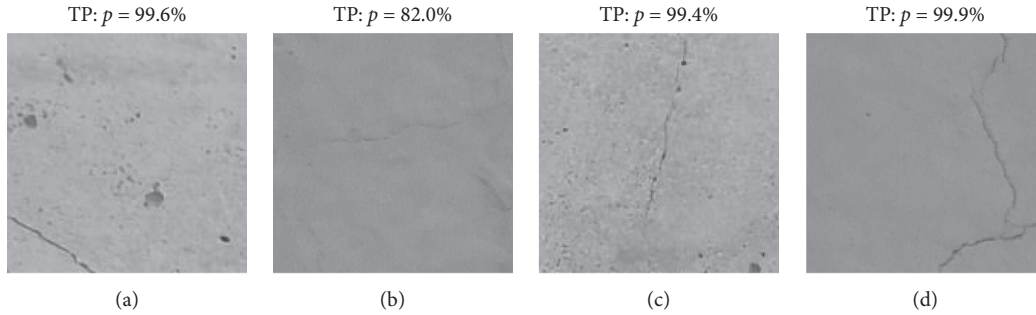


FIGURE 8: Detection of crack. TP denotes true positive.

performance of different algorithms, some evaluation metrics need to be selected. Accuracy refers to the ratio of number of correctly predicted crack and noncrack images to the total number of input images. Precision can be understood as the number of correctly predicted crack images divided by the number of crack images predicted by the classifier. Recall is the percentage of the number of correctly predicted crack images to the total number of cracked images. $F_{1\text{-score}}$ is the harmonic mean of precision and recall. Accuracy, Precision, Recall, and $F_{1\text{-score}}$ are defined as follows:

$$\text{Accuracy} = \frac{\text{TP} + \text{TN}}{\text{TP} + \text{FP} + \text{TN} + \text{FN}}, \quad (13)$$

$$\text{Precision} = \frac{\text{TP}}{\text{TP} + \text{FP}}, \quad (14)$$

$$\text{Recall} = \frac{\text{TP}}{\text{TP} + \text{FN}}, \quad (15)$$

$$F_{1\text{-score}} = 2 \cdot \frac{\text{Precision} \cdot \text{Recall}}{\text{Precision} + \text{Recall}}, \quad (16)$$

where TP and TN mean images with crack and without crack, which are correctly classified. FP and FN mean images with crack and without crack which are wrongly classified.

Figures 8 and 9 show the images, together with the respective probability of correct classification.

4.2. Comparative Experiments. In order to verify the performance of the model, we compare the proposed model with other classic convolutional neural networks on the

same dataset. Figure 10 shows the change in loss and accuracy during the training and validation process. The number of parameters of each model can be seen in Table 1. The results of different methods are compared in Table 2. Table 3 compares the training time of four models. Table 4 shows the size of four models. We can see that, in contrast to the other three models, MobileNetV2 [37] has the smallest number of parameters in the task of detecting concrete surface cracks, but its test accuracy is obviously lower than the other three models. Although the accuracy of EfficientNetB0 on the test dataset is slightly lower than DenseNet201 [38] (0.21%), its model size is 3.5x smaller and 2.5x faster (average training time of each epoch). Its parameters are reduced by 77.89% at the same time. EfficientNetB0 achieves a good balance among accuracy, model size, and training speed. In terms of crack detection task, the model is quite efficient. It can also be seen from Table 2 that when tested on a dataset which is quite different from the training dataset, the performance of the network drops a little. This drop is mainly caused by the changes in background conditions of the images in the dataset, and some image features have not been well learned by the network.

It is worth noting that, in Figure 10, the accuracy of validation during the training and the validation process is slightly higher than that of the training. Two reasons can account for this phenomenon. On the one hand, we use the transfer learning method to train the model. The network was initialized with pretrained weights (pretrained on ImageNet). Therefore, the model has a better feature extraction ability and features are more effective. On the other hand, this phenomenon results from the use of dropout since its behavior during training and validation is different. Dropout forces the neural network to become a very large set

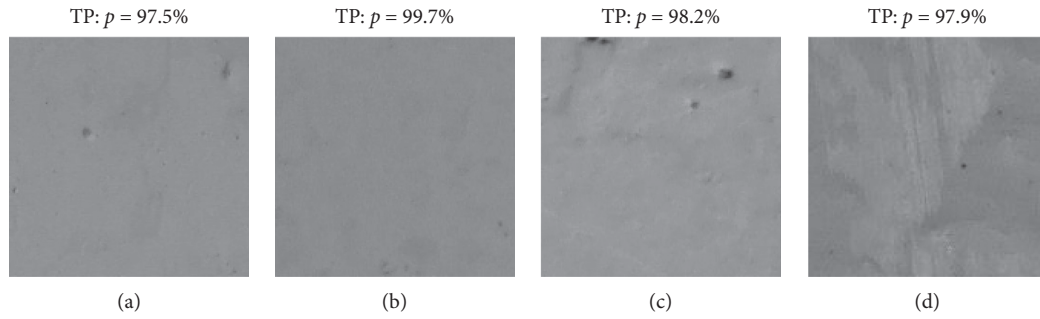


FIGURE 9: Detection of noncrack. TN denotes true negative.

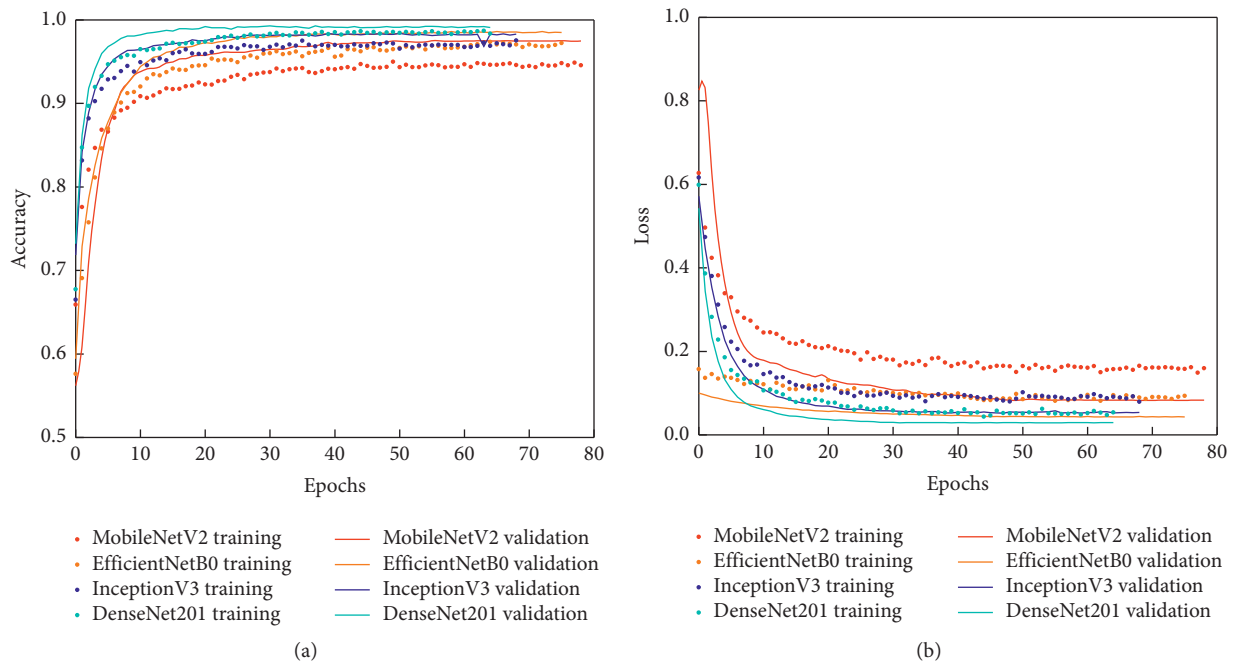


FIGURE 10: Accuracy (a) and loss (b) during training and validation.

TABLE 1: Parameters of different models.

Recognition model	Number of parameters
MobileNetV2	2,260,546
EfficientNetB0	4,052,126
DenseNet201	18,325,826
InceptionV3	21,806,882

TABLE 2: Comparison of four models' crack detection results.

Recognition model	Accuracy	Precision	Recall	F_1 score	Accuracy (tested on different datasets)
MobileNetV2	0.9782	0.9821	0.9740	0.9781	0.9655
EfficientNetB0	0.9911	0.9878	0.9945	0.9912	0.9737
DenseNet201	0.9932	0.9892	0.9973	0.9932	0.9749
InceptionV3	0.9898	0.9891	0.9904	0.9898	0.9715

of weak classifiers, which means that a single classifier does not have too high classification accuracy, and only when we connect them together will they become more powerful.

During training, dropout cuts off the random set of these classifiers, so the training accuracy will be affected. During validation, dropout will automatically turn off and allow all

TABLE 3: Comparison of four models' training time.

Model	Training epochs	Total training time	Average training time of each epoch (s)
MobileNetV2	79	2 h 1 m 47 s	92.49
EfficientNetB0	76	3 h 14 m 32 s	153.58
DenseNet201	65	9 h 47 m 8 s	541.97
InceptionV3	69	3 h 46 m 14 s	196.72

TABLE 4: Size of four models.

Model	Size (M)
MobileNetV2	8.8
EfficientNetB0	15.7
DenseNet201	70.6
InceptionV3	83.5

weak classifiers in the neural network to be used, so the validation accuracy is improved.

5. Conclusions

In this paper, a concrete surface crack detection model based on transfer learning and convolutional neural network is proposed. EfficientNetB0 is a highly effective convolutional neural network. The last fully connected layer is replaced by a new fully connected layer with a classification number of 2. The newly added fully connected layer is initialized randomly, and the remaining weights are initialized with pretrained weights. Finally, by comparing with other models, the results show that our model achieves a good balance among accuracy, model size, and training speed. In addition, when tested on crack images taken from other places, our model also shows good performance and generalization capability. Our model is an efficient crack detection model, which is a good choice for areas with limited computing resources. Traditional crack detection mostly pays attention to how to identify the cracks in the image. In addition, it is also important to characterize the severity of the cracks, which is an area that is often overlooked. We will be devoted to this work in future research.

Data Availability

The codes used in this paper are available from the author upon request.

Conflicts of Interest

The authors declare that there are no conflicts of interest regarding the publication of this paper.

Acknowledgments

This study was funded by the National Natural Science Foundation of China (grant no. 51579089).

References

- [1] D. G. Aggelis, N. Alver, and H. K. Chai, "Health monitoring of civil infrastructure and materials," *Scientific World Journal*, vol. 2014, Article ID 435238, 2 pages, 2014.
- [2] I.-H. Kim, H. Jeon, S.-C. Baek, W.-H. Hong, and H.-J. Jung, "Application of crack identification techniques for an aging concrete bridge inspection using an unmanned aerial vehicle," *Sensors*, vol. 18, no. 6, p. 1881, 2018.
- [3] T. Liu, H. Huang, and Y. Yang, "Crack detection of reinforced concrete member using rayleigh-based distributed optic fiber strain sensing system," *Advances in Civil Engineering*, vol. 2020, Article ID 8312487, 11 pages, 2020.
- [4] T. Yamaguchi, S. Nakamura, R. Saegusa, and S. Hashimoto, "Image-based crack detection for real concrete surfaces," *IEEJ Transactions on Electrical and Electronic Engineering*, vol. 3, no. 1, pp. 128–135, 2008.
- [5] Y.-C. Tsai, V. Kaul, and R. M. Mersereau, "Critical assessment of pavement distress segmentation methods," *Journal of Transportation Engineering*, vol. 136, no. 1, pp. 11–19, 2010.
- [6] D. Zhang, Q. Li, Y. Chen, M. Cao, L. He, and B. Zhang, "An efficient and reliable coarse-to-fine approach for asphalt pavement crack detection," *Image and Vision Computing*, vol. 57, pp. 130–146, 2017.
- [7] A. Ayenu-Prah and N. Attoh-Okine, "Evaluating pavement cracks with bidimensional empirical mode decomposition," *EURASIP Journal on Advances in Signal Processing*, vol. 2008, pp. 1–7, 2008.
- [8] P. Subirats, J. Dumoulin, V. Legeay, and D. Barba, "Automation of pavement surface crack detection using the continuous wavelet transform," in *Proceedings of the International Conference on Image Processing*, pp. 3037–3040, IEEE, Atlanta, GA, USA, October 2006.
- [9] L. Ying and E. Salari, "Beamlet transform-based technique for pavement crack detection and classification," *Computer-Aided Civil and Infrastructure Engineering*, vol. 25, no. 8, pp. 572–580, 2010.
- [10] A. Hizukuri and T. Nagata, "Development of a classification method for a crack on a pavement surface images using machine learning," in *Proceedings of the Thirteenth International Conference on Quality Control by Artificial Vision*, Tokyo, Japan, May 2017.
- [11] P. P. Acharjya, R. Das, and D. Ghoshal, "Study and comparison of different edge detectors for image segmentation," *Global Journal of Computer Science and Technology*, vol. 12, no. 13, 2012.
- [12] Y. LeCun, Y. Bengio, and G. Hinton, "Deep learning," *Nature*, vol. 521, no. 7553, pp. 436–444, 2015.
- [13] A. Krizhevsky, I. Sutskever, and G. E. Hinton, "Imagenet classification with deep convolutional neural networks," in *Proceedings of the Advances in Neural Information Processing Systems*, pp. 1097–1105, Lake Tahoe, NV, USA, December 2012.
- [14] M. Valueva, N. Nagornov, P. Lyakhov, G. Valuev, and N. Chervyakov, "Application of the residue number system to reduce hardware costs of the convolutional neural network implementation," *Mathematics and Computers in Simulation*, vol. 177, 2020.
- [15] L. Zhang, F. Yang, Y. D. Zhang, and Y. J. Zhu, "Road crack detection using deep convolutional neural network," in

- Proceedings of the IEEE International Conference on Image Processing (ICIP)*, pp. 3708–3712, IEEE, Phoenix, AZ, USA, September 2016.
- [16] L. Pauly, D. Hogg, R. Fuentes, and H. Peel, “Deeper networks for pavement crack detection,” in *Proceedings of the 34th ISARC*, IAARC, Taipei, Taiwan, pp. 479–485, June 2017.
- [17] H. Maeda, Y. Sekimoto, T. Seto, T. Kashiyama, and H. Omata, “Road damage detection using deep neural networks with images captured through a smartphone,” 2018, <https://arxiv.org/abs/1801.09454>.
- [18] H. Xu, X. Su, Y. Wang, H. Cai, K. Cui, and X. Chen, “Automatic bridge crack detection using a convolutional neural network,” *Applied Sciences*, vol. 9, no. 14, p. 2867, 2019.
- [19] Y. Li, Z. Han, H. Xu, L. Liu, X. Li, and K. Zhang, “YOLOv3-lite: a lightweight crack detection network for aircraft structure based on depthwise separable convolutions,” *Applied Sciences*, vol. 9, no. 18, p. 3781, 2019.
- [20] Z. Tong, J. Gao, and H. Zhang, “Recognition, location, measurement, and 3D reconstruction of concealed cracks using convolutional neural networks,” *Construction and Building Materials*, vol. 146, pp. 775–787, 2017.
- [21] X. Yang, H. Li, Y. Yu, X. Luo, T. Huang, and X. Yang, “Automatic pixel-level crack detection and measurement using fully convolutional network,” *Computer-Aided Civil and Infrastructure Engineering*, vol. 33, no. 12, pp. 1090–1109, 2018.
- [22] J. Zhu and J. Song, “An intelligent classification model for surface defects on cement concrete bridges,” *Applied Sciences*, vol. 10, no. 3, p. 972, 2020.
- [23] L. Deng, H.-H. Chu, P. Shi, W. Wang, and X. Kong, “Region-based CNN method with deformable modules for visually classifying concrete cracks,” *Applied Sciences*, vol. 10, no. 7, p. 2528, 2020.
- [24] S. Ren, K. He, R. Girshick, and J. Sun, “Faster r-cnn: towards real-time object detection with region proposal networks,” *IEEE Transactions on Pattern Analysis and Machine Intelligence*, vol. 39, pp. 91–99, 2015.
- [25] J. Dai, Y. Li, K. He, and J. Sun, “R-fcn: object detection via region-based fully convolutional networks,” in *Proceedings of the Advances in Neural Information Processing Systems*, pp. 379–387, Barcelona, Spain, December 2016.
- [26] T.-Y. Lin, P. Dollár, R. Girshick, K. He, B. Hariharan, and S. Belongie, “Feature pyramid networks for object detection,” in *Proceedings of the IEEE Conference on Computer Vision and Pattern Recognition*, pp. 2117–2125, Honolulu, HI, USA, July 2017.
- [27] S. Li and X. Zhao, “Image-based concrete crack detection using convolutional neural network and exhaustive search technique,” *Advances in Civil Engineering*, vol. 2019, 12 pages, 2019.
- [28] S. Dorafshan, R. J. Thomas, and M. Maguire, “SDNET2018: an annotated image dataset for non-contact concrete crack detection using deep convolutional neural networks,” *Data in Brief*, vol. 21, pp. 1664–1668, 2018.
- [29] L. Perez and J. Wang, “The effectiveness of data augmentation in image classification using deep learning,” 2017, <https://arxiv.org/abs/1712.04621>.
- [30] K. Simonyan and A. Zisserman, “Very deep convolutional networks for large-scale image recognition,” 2014, <https://arxiv.org/abs/1409.1556>.
- [31] C. Szegedy, “Going deeper with convolutions,” in *Proceedings of the IEEE Conference on Computer Vision and Pattern Recognition*, pp. 1–9, Boston, MA, USA, June 2015.
- [32] K. He, X. Zhang, S. Ren, and J. Sun, “Deep residual learning for image recognition,” in *Proceedings of the IEEE Conference on Computer Vision and Pattern Recognition*, pp. 770–778, Boston, MA, USA, June 2016.
- [33] P. Ramachandran, B. Zoph, and Q. V. Le, “Searching for activation functions,” 2017, <https://arxiv.org/abs/1710.05941>.
- [34] M. Tan and Q. V. Le, “Efficientnet: rethinking model scaling for convolutional neural networks,” 2019, <https://arxiv.org/abs/1905.11946>.
- [35] J. Hu, L. Shen, and G. Sun, “Squeeze-and-excitation networks,” in *Proceedings of the IEEE Conference on Computer Vision and Pattern Recognition*, pp. 7132–7141, Salt Lake City, UT, USA, June 2018.
- [36] D. P. Kingma and J. Ba, “Adam: a method for stochastic optimization,” 2014, <https://arxiv.org/pdf/1412.6980.pdf>.
- [37] M. Sandler, A. Howard, M. Zhu, A. Zhmoginov, and L.-C. Chen, “Mobilenetv2: inverted residuals and linear bottlenecks,” in *Proceedings of the IEEE Conference on Computer Vision and Pattern Recognition*, pp. 4510–4520, Salt Lake City, UT, USA, June 2018.
- [38] G. Huang, Z. Liu, L. Van Der Maaten, and K. Q. Weinberger, “Densely connected convolutional networks,” in *Proceedings of the IEEE Conference on Computer Vision and Pattern Recognition*, pp. 4700–4708, Honolulu, HI, USA, July 2017.

Research Article

Projection of Future Hydropower Generation in Samanalawewa Power Plant, Sri Lanka

Bhabishya Khaniya , **Chamaka Karunanayake** , **Miyuru B. Gunathilake** ,
and Upaka Rathnayake 

Department of Civil Engineering, Faculty of Engineering, Sri Lanka Institute of Information Technology, Malabe, Sri Lanka

Correspondence should be addressed to Upaka Rathnayake; upakasanjeewa@gmail.com

Received 3 September 2020; Revised 6 October 2020; Accepted 8 October 2020; Published 17 October 2020

Academic Editor: Danial Armaghani

Copyright © 2020 Bhabishya Khaniya et al. This is an open access article distributed under the Creative Commons Attribution License, which permits unrestricted use, distribution, and reproduction in any medium, provided the original work is properly cited.

The projection of future hydropower generation is extremely important for the sustainable development of any country, which utilizes hydropower as one of the major sources of energy to plan the country's power management system. Hydropower generation, on the other hand, is mostly dependent on the weather and climate dynamics of the local area. In this paper, we aim to study the impact of climate change on the future performance of the Samanalawewa hydropower plant located in Sri Lanka using artificial neural networks (ANNs). ANNs are one of the most effective machine learning tools for examining nonlinear relationships between the variables to understand complex hydrological processes. Validated ANN model is used to project the future power generation from 2020 to 2050 using future projected rainfall data extracted from regional climate models. Results showcased that the forecasted hydropower would increase in significant percentages (7.29% and 10.22%) for the two tested climatic scenarios (RCP4.5 and RCP8.5). Therefore, this analysis showcases the capability of ANN in projecting nonstationary patterns of power generation from hydropower plants. The projected results are of utmost importance to stakeholders to manage reservoir operations while maximizing the productivity of the impounded water and thus, maximizing economic growth as well as social benefits.

1. Introduction

Hydropower spines almost 16% of the total electricity generation, which is far more than the contribution from any other renewable resources all over the world [1]. Hydropower plants supply as much as 40% of the energy required to satisfy Sri Lanka's power demand [2]. Harnessing electricity from hydropower is still considered one of the most sustainable methods of power generation around the world. Therefore, a 75–100% upsurge in production capacity is expected in the near future [1]. Developing countries have just explored 23% of its economically feasible hydropower projects relative to developed countries, which have exploited 70% of their potential [3]. Many developing countries are now rapidly investing significant capital in developing hydropower plants as it is regarded to be a secure and affordable form of sustainable energy, limiting carbon

emissions [4]. However, the output from the hydropower plant is highly variable as the production largely depends on climatic factors and weather conditions. Apart from this, global warming is likely to alter water cycle phenomena, frequency of rainfall events, and temperature rise causing disruptions to smooth operation of hydropower plants. For example, the temperature in Sri Lanka is increasing at the rate of 0.0164°C/year, influencing intensifications in evaporation [5]. Even though the seasonal rainfall is expected to increase in the coastal areas, rainfall patterns in mountainous areas of Sri Lanka, where most of the hydropower plants are located, are very dynamic and rapidly fluctuating [6].

The hydropower industry stands a high chance to get splintered into the most vulnerable industry if confronted by detrimental impacts of climate change either due to the unavailability of water in the basin area for a long period of

time or due to excess water resulting in landslide or soil erosion in the catchment area. On the other hand, developing hydropower systems is very costly and causes significant threats to aquatic ecosystem preservation and social concerns [7]. Therefore, forecasting energy production from hydropower plants is crucial, not only to optimize the demand of renewable energy needed for growing demand but also to manage the operations within the hydropower plant (e.g., routing excess water for other beneficial purposes) aiming for the environmental sustainability. Nevertheless, the future prediction of hydropower production is very complex due to the nonlinear nature of the input functions along with spatial and temporal variations of the meteorological datasets such as rainfall, temperature, and evaporation [8]. The output from prediction models may have high economic value in regulating sustainable energy development projects such as hydropower [9].

Many researchers have studied the impact of climatic variation on hydropower generation mostly using Global/Regional Climate Models (GCMs/RCMs), trend analysis, and statistical downscaling methods (e.g., [10–12]). Few studies have focused on the economic impact of climate change on hydropower (e.g., [13]), while some researchers have used an assessment and comparison approach to quantify the effects of climate change on hydropower generation [14]. For example, [15] interestingly used a distributed hydrological model together with an optimal operational reservoir model to predict future hydropower generation of large-scale reservoir groups in the upper Yangtze River basin, China.

Currently, intelligent machine learning techniques such as Artificial Neural Network (ANN), Genetic Algorithms, fuzzy logic, Multilayer Perceptron (MLP), Support Vector Regression (SVR), and Random Forest (RF) approaches are dominantly being used in hydrological prediction to understand the role of climate change on water-energy nexus [16] including the hydropower generation. To the present date, the majority of past research in the hydropower engineering sector is focused on the study of overall risk management of the hydropower industry (almost 35%), while only 16% of research is focused on studying the impact of climate change on hydropower generation [17]. The authors reckon a substantial number of studies are needed to monitor the impact of climate change on the hydropower industry, especially in countries, which are heavily dependent on hydropower for stabilizing power requirements. ANNs showcase a potential solution paradigm for these issues.

ANNs are “data-driven” models having mathematical computation capability analogous to the human nervous system and brain functions utilizing statistical techniques to recognize patterns between input variables and output variables [18]. ANNs have been efficiently used to predict and classify future operations of hydropower plants through past data observations. The study in [19] concluded that ANN is a versatile tool to predict storage of water in hydropower reservoirs while conducting a case study in Nigeria at Jebba and Kainji reservoirs using independent input parameters such as reservoir inflow, reservoir storage,

reservoir elevation, plant use coefficient, tail race level, release from a turbine, and evaporation losses. A similar study was conducted by [20], where the authors discovered an upward trend in hydropower generation at Jebba, Kainji, and Shiroro hydropower reservoirs. The study in [21] used ANN to predict future hydroelectric generation using the artificial bee colony algorithm in Turkey using input variables such as electricity demand, energy use, population, and temperature and found that electricity generation in Turkey is not in line with the country’s vision to produce 30% of its electricity from renewable resources by 2023. In addition, the study in [22] analyzed future streamflow up to 2040 for the Ranganadi river in India to project hydropower generation using 3 GCM models along with ANN. Patil has shown the catchment area would face flooding issues; however, there would also be an increase in hydroelectricity production due to abundant water.

The study in [8] suggested that characteristics of input parameters play a dominant role in predicting future power generation when using feed-forward backpropagation algorithms in the ANN platform. They used the conclusions from their work on predicting the future performance of the Himreen Lake Hydropower Plant located in Iraq. The power production, flow rate of water, and turbine head were the input parameters for their study. In addition, [23] recommended ANN-ARIMA hybrid model instead of ANN for predicting future data of renewable energy resources (e.g., hydroelectricity, solar, and wind) while forecasting electricity generation from various energy resources in the USA. The study in [24] has further supported this argument to couple ANN with supervised or unsupervised learning algorithm to enhance reservoir outflow prediction after reviewing 66 papers, which employed ANN for optimizing reservoir operations. Furthermore, the study in [17] has suggested conducting future research, which is related to risk management on hydropower, using a fuzzy model combined with ANN and genetic algorithm.

Several researchers have highlighted the benefit of ANNs in hydropower prediction. The study in [25] revealed hidden neurons have a greater impact on the performance of the ANN model while predicting water discharge at a hydropower reservoir located in Malaysia. In addition, [26] revealed that ANN models are the most accurate in predicting short-term and long-term hydropower generation after conducting case studies in run-of-the-river (ROR) type of hydropower located in France, Portugal, and Spain using historical meteorological data such as precipitation, snowfall, and temperature.

However, to the authors’ knowledge, there was only one study in Sri Lanka to forecast the power generation using ANN. The study in [27] has forecasted solar power using ANN. In addition, the study in [28] has forecasted the daily electricity demand; however, forecasting power generation was not carried out. Nevertheless, as it was stated earlier, there are not any studies conducted in Sri Lankan watersheds linked with hydropower plants to forecast the future power generation using ANNs. Therefore, for the first time in the context of Sri Lanka, a hydropower forecasting model is presented herein using the ANN. In this paper, we

examine the capability of ANNs to forecast the future hydropower generation by using historical rainfall data for training as well as validating the forecasting model and future rainfall data extracted from the regional climate model (Coordinated Regional Downscaling Experiment-CORDEX) for forecasting the future power generation through a feed-forward with backpropagation algorithm.

The main objective of this study is to check the performance of the Samanawala hydropower plant, which is a reservoir type of plant in the perspective of climate variability. Due to the lack of other meteorological variables such as air temperature, humidity, which could be used as input variables to the model, we only used rainfall data for training and validating the ANN model. The authors reckon this research would be beneficial in optimizing the usage of water collected in the reservoir for various uses such as hydropower production and irrigation. This research may be important to water resource planners and government authorities to manage water resource projects by monitoring the trend in hydropower production.

2. Sri Lanka and Its Hydropower Generation

Sri Lanka has an installed capacity of 1,719 Megawatts (MW) of hydroelectric power and current commitments on hydropower development would add around 247 MW to the national grid in the coming years [2]. Most of the hydropower stations in Sri Lanka are aged over 25 years of their total lifespan [29]. Though hydropower plants have a long life of around 50 years, if any of the older hydropower plants stops functioning, either due to consequences of climate change or mechanical failure, then Sri Lanka would have to face power shortage issues as it would be difficult for the country to substitute the botched hydropower plants in a short period. Hence, the assessment of the power generation capacity of hydropower plants is essential in the Sri Lankan context. This is to manage the power needs for a growing economy and then to regulate water resource development projects in the context of climate variability. However, there are limited studies conducted in Sri Lanka to analyze future power generation from running or planned hydropower plants. The study in [30] studied ways to increase power generation in hydropower plants by controlling soil erosion, reservoir siltation in Uma Oya basin, which is regarded to be one of the most important catchments in Sri Lanka. The study in [31] studied inflows in the Kotmale reservoir using El Nino Southern Oscillation (ENSO) phase index for the period of 1960 to 2005 and found that the inflows to the reservoir have decreased, altering hydropower production and irrigation plan. The study in [32] using GCMs based studies (mainly rainfall) projected that the future production capacity of the hydropower plants in the Mahaweli basin would increase as a result of an increase in consecutive wet days, decrease in consecutive dry days, and increase in annual total precipitation. In addition, [11] used a multiyear rainfall trend analysis where they found climate change would not influence the power generation of Denawaka Ganga minihydropower located in the Rathnapura district. The study in [33] has also put efforts to study the impact of

climate change on the Erathna minihydropower plant located in the Rathnapura district. They have concluded that there would be a decrease in power generation in future years. The study in [34] further performed a similar study considering the newly functioned Uma Oya basin, where the authors clarified there would be no major threats to hydropower production in the coming years due to scarcity of water in the basin area. However, as it was stated in the introduction section, there is no comprehensive study on forecasting hydropower in Sri Lanka for future years. Therefore, this research work has a greater potential in attracting the authorities' attention for better planning and control processes in hydropower stations in Sri Lanka.

3. Future Climate Data Extraction

Global climatic models (GCMs) provide climatic information on large scales covering vastly differing landscapes, whereas regional climatic models (RCMs) are applied over much smaller scales (typical horizontal resolution 10–50 km), which may provide much detailed information for adaptation assessment and planning [35]. GCMs forecast the climate variation of the Earth in the future as a forecasted tool. However, they should be studied under regional or even national scales to reveal effective adaptation strategies.

The four RCMs used in this research for extracting future climatic data are ACCESS_CCAM, MPI_ESM_CCAM, CNRM_CCAM, and REMO2009. These RCMs were developed by the Commonwealth Scientific and Industrial Research Organization (CSIRO) from CORDEX. The corresponding GCMs of the RCMs used are ACCESS 1.0, MPI_ESM_LR, CNRM_CM5, and ECHAM-4 GCM [36–40].

The future climate data can be extracted for different scenarios. Representative Concentration Pathways (RCP) are such scenarios from which the climate data can be extracted. RCPs are trajectories, which are based upon greenhouse gas concentrations adopted by the Intergovernmental Panel on Climate Change [41]. Four RCPs are widely used in the literature and they are RCP2.6, RCP4.5, RCP6.0, and RCP8.5 [41]). RCP4.5 can be described as the intermediate emission scenario, where the emissions will start declining by approximately 2045, whereas RCP8.5 is defined as the higher emission scenario, where emissions continue to increase throughout the 21st century. For further details on RCP, states can be found in [42, 43].

It is a well-known fact that RCMs suffer from varying levels of systematic biases [44, 45]. The reasons for such biases may be due to systematic model errors caused by imperfect conceptualization, discretization, and spatial averaging within grid cells. To deal with these biases, several bias correction methods such as linear scaling, local intensity scaling, power transformation, variance scaling, distribution transfer, and delta change approach are used in the literature [46].

Due to the simplicity and fast application, Linear Scaling (LS) method [47] has been widely used in many studies. LS is capable of adjusting all climatic factors to an acceptable level, where errors in precipitation are adjusted with the use of a

multiplier [48–51]. Linear scaling bias correction method can be applied using the two equations given below (equations (1) & (2)) where cor, his, obs, sim, P and d stand for bias-corrected data, raw RCM data, observed data, raw RCM corrected data, precipitation and daily, respectively, and μ_m stands for a long-term monthly mean of precipitation data:

$$P_{\text{his},d}^{\text{cor}} = P_{\text{his},d} * \frac{\mu_m(P_{\text{obs},d})}{\mu_m(P_{\text{his},d})}, \quad (1)$$

$$P_{\text{sim},d}^{\text{cor}} = P_{\text{sim},d} * \frac{\mu_m(P_{\text{obs},d})}{\mu_m(P_{\text{his},d})}. \quad (2)$$

4. Study Area

The Samanalawewa Hydropower Project area is in the Belihul Oya area, Rathnapura district, Sabaragamuwa province, in the central region of Sri Lanka. The project was completed in 1992, just downstream of the convergence point of the Walawe River and Belihul Oya. The catchment area (359 km²) can be physiographically categorized as midland, consisting of marbles, quartz with an average altitude of about 530 m [52]. The area lies in the wet zone of the country, which receives an average annual rainfall of around 2500 mm [53]. The project area receives most of the rainfall from the southwest monsoon, while small influences are experienced from northeast monsoon and intermonsoon cyclones. Samanalawewa Hydropower Project consists of a u -shaped reservoir (as it is shown in Figure 1), a waterway system, a small irrigation canal, a minihydropower plant, and a 120 (2*60) Megawatts (MW) power plant for hydroelectricity generation. A detailed catchment map is shown in Figure 1.

The study area has many agricultural lands with significant forest cover. The irrigated water from the dam is essential to downstream villages like Kaltota, Madabadda (left & right), Welipotayaya, and Koongahamankada for agricultural purposes. Paddy yield reduction by 11.5% has been reported in the regions located downstream of the study area because of the scarcity of water in the reservoir [54].

Samanalawewa hydropower is one of the largest and the oldest reservoir-type power plants in Sri Lanka, and over the years, it has been playing a dominant role in stabilizing power supply at peak hours. It contributes to 8.69% out of all large hydropower systems in generating power to meet electricity demand in Sri Lanka. This project, starting from its construction, has gained significant attraction due to the water leakage problem encountered from the right bank of the dam because of the poor geologic condition [55]. In addition, there were several environmental concerns during the project planning phase; however, no greater attention was given as there were no strict environmental regulation obligatory in major development works [56]. Though the provision for Environmental Impact Assessment (EIA) was established in Sri Lanka in 1988, EIA during the planning of

Samanalawewa was conducted partially focused on vegetation replantation and ecosystem preservation.

Due to the leakage, phase II construction of hydropower plant (120 MW capacity) was suspended; instead, a mini-hydropower plant was built, which operates using the leaked water. Even after a tremendous effort from Ceylon Electricity Board (CEB) to stop the leakage, impounded water is leaking approximately at the rate of 2.1–2.8 m³/s [57]. Analysis of future water availability in the Samanalawewa reservoir in terms of power generation is essential as a portion of seized water is directly supplied to irrigation without passing the power station and another portion (leaked portion) goes to minihydropower plants producing comparatively lesser energy. Additionally, with the increasing requirement of water from downstream areas for irrigation, water management at the Samanalawewa reservoir needs to be more engineered. Moreover, climate variability might influence negatively or positively on water resource management objectives led out by CEB at Samanalawewa hydropower plant. Hence, the presented research herein would be interested in the many stakeholders of the Samanalawewa Hydropower Project.

5. ANN Model Development

To identify the impact of climatic variation (in terms of precipitation) on hydropower generation at Samanalawewa hydropower station, monthly rainfall data of four gauging stations at Alupola (annual mean rainfall-4272 mm), Detangalla (annual mean rainfall-2843 mm), Balangoda (annual mean rainfall-2170 mm), and Belihul Oya (annual mean rainfall-2704 mm) were used. The catchment is one of the data scarcity catchments in the country and only some of the rainfall data are available even at the gauging stations. Therefore, the model development has to rely on the available data. The annual rainfall distributions over the 30 years are given in Figure 2 for more information.

The numerical computing software MATLAB (version 9.4.0.813654–R2018a) was used to develop the ANN model. The ANN model is composed of an input layer, an output layer, and a hidden layer with neurons linking each layer to the other by interconnecting weights. In a feed-forward neural network, the hidden layer performs all the computations and the output layer does the prediction. Training the neural network generally refers to discovering the weights for links between neurons. In this study, the monthly rainfall data of the four stations from 1996 to 2016 was used as the input parameter and the power generation at Samanalawewa power station was used as the target parameter while training the ANN model. The historical rainfall data was collected from the Department of Meteorology, Sri Lanka, while power generation data were collected from the Ceylon Electricity Board, Sri Lanka. The nonlinear relationship between rainfall and power generation can be expressed as in the following equation:

$$\text{power generation} = \phi(\text{rainfall}_i), \quad (3)$$

where ϕ represents the nonlinear function between the power generation and the rainfall, while i represents the rain

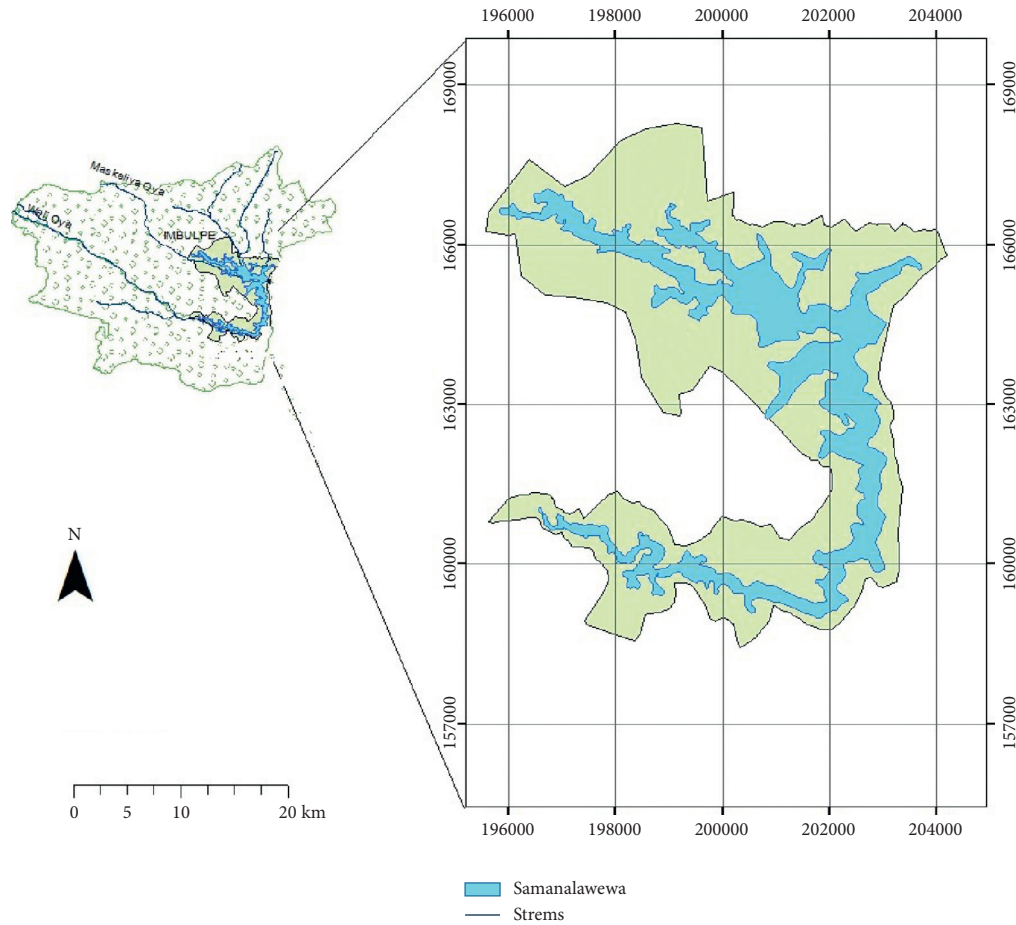


FIGURE 1: Samanalawewa catchment.

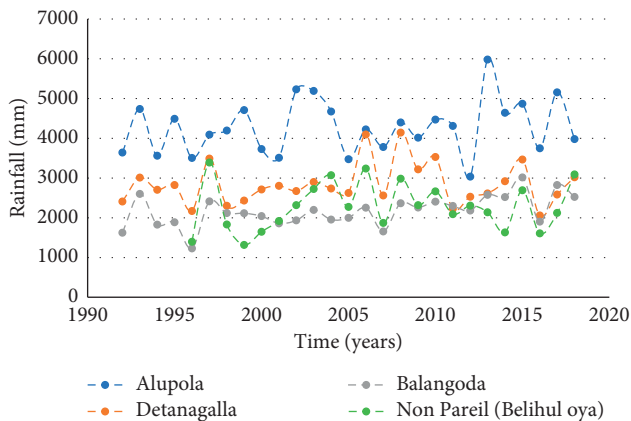


FIGURE 2: Annual rainfall distribution in Samanalawewa catchment.

gauges. Out of the overall input data, 70% of data were used to train the neural network, whereas 15% of data were used for validation and the other 15% were used to test the network.

Though most of the past literature supports ANN models to be one of the powerful soft computing tools in predicting future hydropower generation either from minihydropower

type or reservoir type hydropower plant, still deep understanding is required on the selection of independent input parameters and the type of algorithm to be used in ANN model, which would best resemble real-time climate change scenarios to give best estimates for future hydropower generation. However, there are not any specific rules to organize ANN configuration [58]. The range of hyper-parameters was determined based on the authors knowledge and experience and the availability of the data. Two hidden layers were used with 10 hidden neurons and LEARNGDM was used as the adaptation learning function. Optimum neuron number in the hidden layer was determined using a trial and error procedure by varying the hidden neuron number from 5 to 30, with increments of five. The linear transfer function (purelin) and hyperbolic tangent sigmoid transfer function (tansig) were applied to the hidden and output layers of the network as the simulation function. The number of iterations varied between 5 and 10. The conceptual diagram of the developed ANN model is shown in Figure 3.

The developed ANN model was trained using seven training algorithms, namely, BFGS, Quasi Newton (BFG), Polak-Ribière conjugate gradient (CGP), Conjugate gradient with Powell/Beale Restarts (CGB), Fletcher-Reeves conjugate gradient algorithm (CGF), Levenberg-Marquadt (LM),

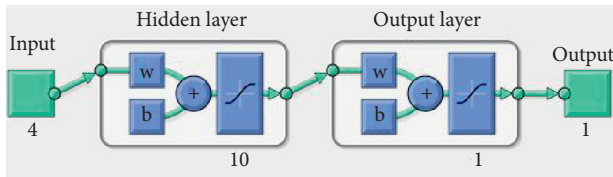


FIGURE 3: Conceptual diagram of the ANN model.

Resilient Backpropagation (RP), and scaled conjugate gradient (SCG) algorithms. These algorithms have outperformed many other algorithms and are widely used in engineering applications [59–63].

The best performing network was chosen based upon the coefficient of correlation (R), mean squared error (MSE), and the computational efficiency in terms of the number of epochs. Many researchers used either R and MSE [64–66] or the coefficient of determination (R^2) and root mean square error (RMSE) [67–70] to check the performance of the ANN models. It was found that the BFGS Quasi Newton (BFG) vanquished all other algorithms. Therefore, the ANN trained with the BFG algorithm was selected to be used for the future projection process. The saved ANN model was validated by using monthly rainfall data of the years 2017–2018. The use of independent validation sets is very vital in ANN development to avoid overfitting of the training data as well as to verify the quality of the trained model [71].

The future climate data were extracted from RCMs using CORDEX for the period between the years 2021–2050. However, out of the four RCPs, only RCP4.5 and RCP8.5 were used for the forecasting stage. The linear scaling technique was then used to correct the bias on the rainfall data. The forecasted but bias-corrected rainfall data were used as the input of the developed ANN model to project the power generation of the Samanalawewa Hydropower plant.

6. Results

Table 1 depicts the correlation coefficients (R value) and performances for different algorithms for different cases. With R value greater than 0.6, BFG and CGB algorithms have produced proficient training results. Though R values of 0.5–0.6 obtained during training cannot be considered promising for prediction purposes in the normal condition, they are acceptable especially based on input characteristics used in training. The spatial variation of rain gauges along with the spatiotemporal variation of precipitation, which is the chief input in this ANN model, could have negatively impacted on R values. On the other hand, R values might have got lowered due to a nonlinear relationship between input and output variables along with a scattering of data in a broad scale. However, the values obtained are adequate for forecast future hydropower generation. Based on the lower MSE value out of 2 algorithms, the BFG algorithm was selected for validation and prediction purposes.

Figure 4 presents the results from the ANN model under the BFG training algorithm for different stages, including training, validation, test, and everything together. Even though the model was developed for a significant number of

data set, the overall acceptability is not the highest ($R > 0.9$). This can be understood from the coefficient of correlation between the observed and predicted power generations. Nevertheless, the validation process has a good correlation ($R > 0.8$); therefore, the selection of using the BFG training algorithm can be justified.

Figure 5 presents the validation results conducted after the culminating training ANN model. The developed projected model was validated to the years 2017 and 2018. Therefore, Figure 5 shows the relationship between the forecasted power generation from the ANN model to the observed power generation in the Samanalawewa reservoir. The determination coefficient ($R^2 = 0.83$) is high and therefore, the validation process for forecasting can be accepted.

Figure 6 illustrates the forecast of hydropower generation from 2020 to 2050 for two different emission scenarios, RCP4.5 and RCP8.5. The comparison of power generation for two scenarios is given in Figure 6. Until 2039, power generation under the RCP4.5 scenario is higher than for RCP8.5. However, from 2040 the power generation trend follows reverse order, where lesser power is generated under RCP8.5. Under the RCP4.5 condition, a decreasing trend of power production is discovered in future years, which would get lowered to as much as 173 GWh in 2036, while peak production is observed in 2031, generating 446 GWh energy. On the other hand, slightly increasing drift on power generation is observed under the RCP8.5 scenario, where peak production is in 2045 engineering 406 GWh, while the lowest production is in 2037 generating 211 GWh energy.

Figure 7 shows the historical power generation at the Samanalawewa hydropower plant. The historical plot of power generation shows an increasing trend of power production (visible trend from the trend-line drawn) from hydropower plants starting from 1992 to 2019 with maximum power generated in 2015 producing 425 GWh of energy. Comparing historical power generation and projected future power generation, it is certain Samanalawewa hydropower plant would continue to produce energy equivalent or slightly higher than the amount it has been generating in the past years. However, the generation has to be limited to the capacity of the power turbines. Moreover, close monitoring of historical and future power generation to illuminate RCP8.5 scenario is much favorable rather than RCP4.5 in terms of power generation at Samanalawewa hydropower plant.

7. Discussion

Samanalawewa reservoir is currently functioning as a multipurpose reservoir, which sustains various objectives, though it was initially designed as a single-purpose project. The main target of this study was to project the future power generation at Samanalawewa hydropower in the perspective of climate variability. The annual power generation after partially resolving the leakage problem was premeditated at 403 GWh/year. However, the actual average annual power generation during the period of 1993–2005 was 274 GWh/year. A considerable difference of 129 GWh has been

TABLE 1: Correlation coefficients for ANN results.

Algorithm	Correlation coefficients				Performance
	Training	Validation	Test	All	MSE
BFG	0.62	0.82	0.64	0.67	86
CGB	0.59	0.67	0.60	0.61	90
RP	0.53	0.58	0.70	0.56	84
LM	0.55	0.55	0.57	0.55	86
SCG	0.57	0.65	0.17	0.52	114
CGF	0.42	0.74	0.53	0.49	99
CGP	0.52	0.41	0.35	0.49	102

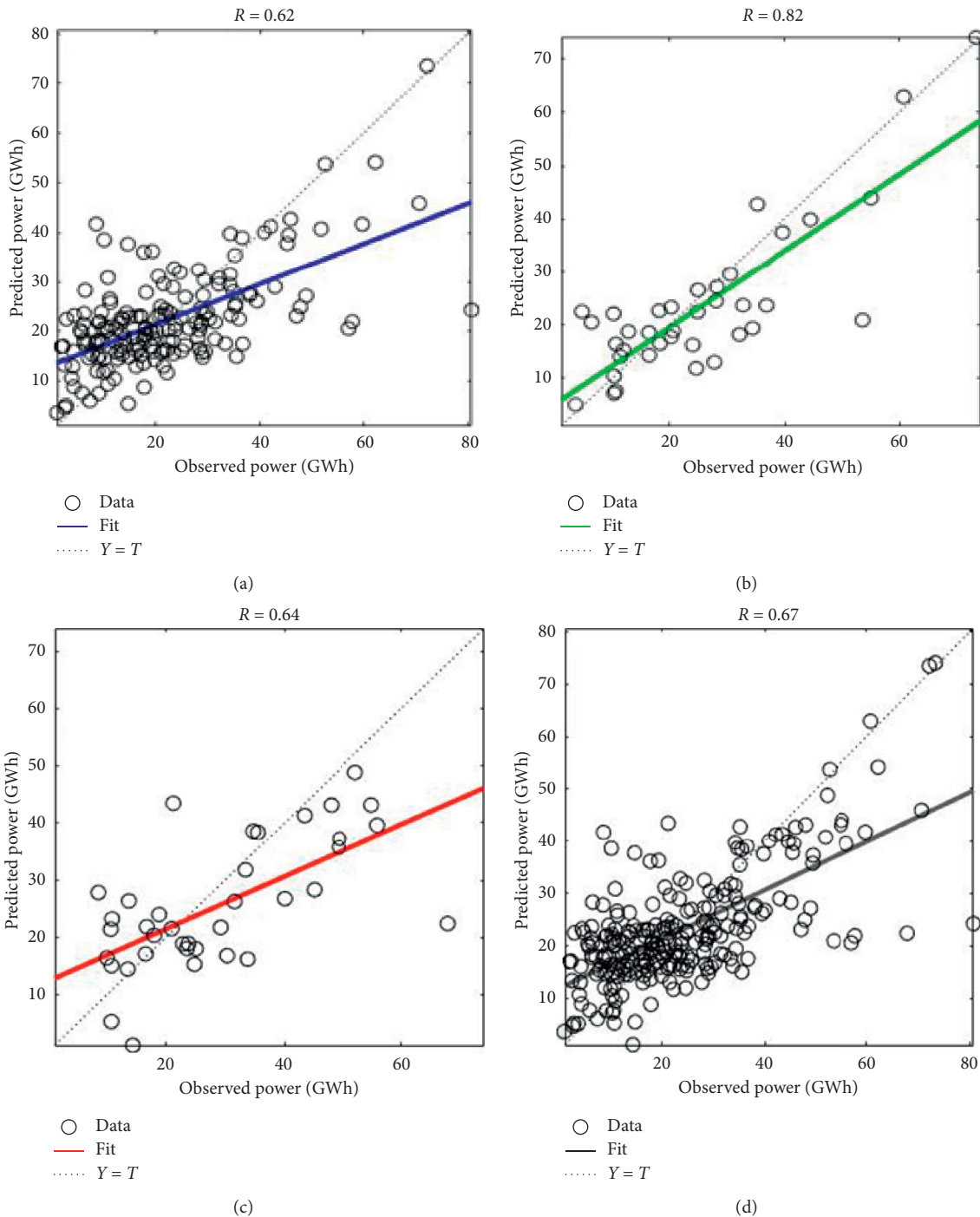


FIGURE 4: ANN results under the BFG training algorithm. (a) For training, (b) for validation, (c) for test, and (d) for all.

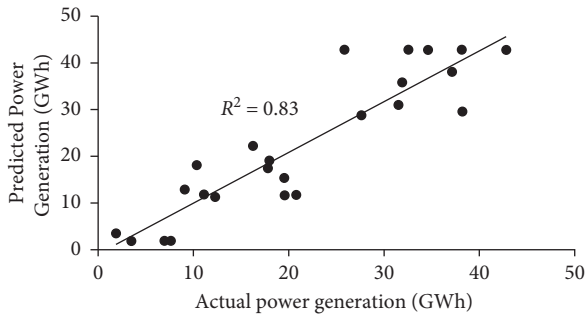


FIGURE 5: Validation results of the developed ANN model.

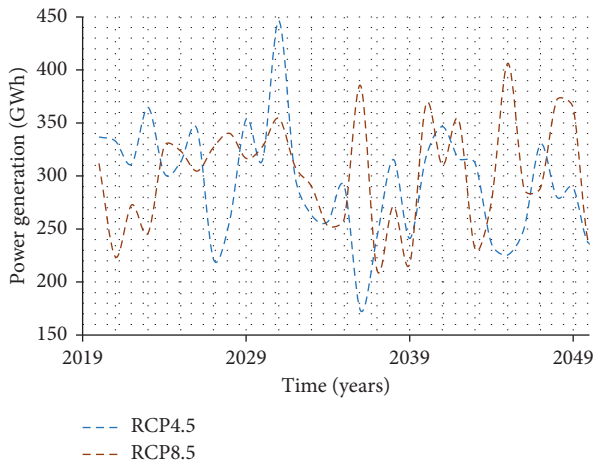


FIGURE 6: Power generation forecast for RCP4.5 & RCP8.5 scenarios.

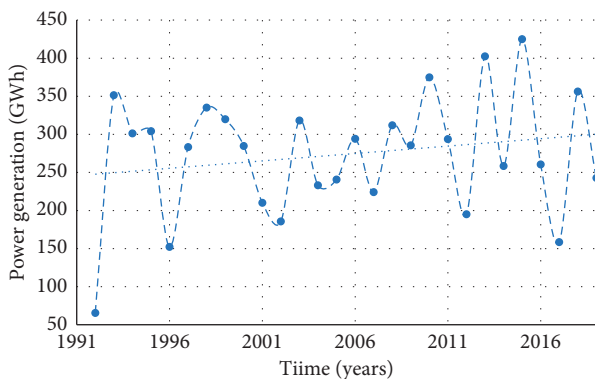


FIGURE 7: Historic power generation with time.

observed between planned and actual power production in past years. Therefore, other than the reduction of runoff received to the reservoir, increasing demand for agricultural purposes can be a reason for the power generation reduction.

Initially, it was decided to release 50 million- m^3 for the year for agricultural purposes from the Samanalawewa reservoir; however, due to the various pressures and stresses from the local people and authorities, the agricultural release was increased to 80 million- m^3 per year. Therefore, a

reduction of 35 GWh of power can be expected from the hydropower plant [72].

However, it was found out that Samanalawewa hydropower generation may not be wedged by climate variability until 2050. Hydropower generation was found to increase in future years until 2050 because of the abundant water in the reservoir under both tested RCP scenarios. The annual average forecasted power generations under tested RCP scenarios (RCP4.5 and RCP8.5) for years 2020 to 2050 are 294 GWh/year and 302 GWh/year, respectively. Therefore, the forecasted increases in power production under RCP4.5 and RCP8.5 scenarios are 7.29% and 10.22%, respectively. If water release from Samanalawewa is controlled to a limit, where it harvests electricity as it used to generate in the past, there will be some excess water in the reservoir, which can perhaps be diverted to other demanding sectors such as agriculture.

However, the forecasted increase in power generation is not uniform (refer to Figure 6). Nonuniformity is also a likely effect of climate variation, where the wet season would continue to get more rainfall, whereas the dry season would get drier due to less precipitation. This adds major challenges in developing a concrete strategy for the overall management of reservoir operations. Low power generation in a particular year specifies Samanalawewa catchment receiving less rainfall in that particular year and vice versa. This indicates the management of water can get complicated in certain years due to prolonged drought or excessive rainfall, resulting in natural disasters.

Hence, this study is of paramount importance to the representatives from various agencies to plan resources based on the forecasts. Water release from hydropower plants for electricity generation and irrigation at Samanalawewa is controlled by representatives from the Ceylon Electricity Board, Water Management Secretariat, Mahaweli Authority, and National Water Supply and Drainage Board. Therefore, the meetings which are held weekly [73] would be much fruitful from the results presented herein.

Nevertheless, the accurate projection of power generation from any hydropower plant is challenging as well as uncertain due to its dynamics. In addition, forecasts from ANN models are reliant on the quality and availability of the input and output parameters. In this study, rainfall and power generation data of the past 21 years were used with only 1 type of input climatic variable. This could be the probable reason to have obtained high MSE values during the training of the ANN model. The authors, therefore, reckon more accurate projections can be made by incorporating comprehensive input parameters, which play an influencing role in hydropower generation provided that relevant data are available. Furthermore, the authors suggest performing seasonal and monthly projections to visualize the supply of water in deeper scales.

8. Conclusions

An ANN model was efficaciously implemented to forecast the future power generation at the Samanalawewa hydropower plant. As it was already stated, this is novel research

work in the Sri Lankan context, which also can be used in forecasting the hydropower generation. BFG algorithm was found to be the best training algorithm among the tested other training algorithms for the developed ANN model to predict the hydropower generation. Results revealed that the power generation would increase by 7.29% and 10.22% under RCP4.5 and RCP8.5 scenarios, respectively, until 2050. This is a significant contribution to the energy demand in Sri Lanka, and more importantly, the forecasted increase is from renewable energy. This highlights that there are not any significant intimidations of climate variability in the Samanalawewa catchment area. This is an advantageous finding for the energy authorities in Sri Lanka due to the scarcities of power generations. However, the authors realize that representatives from various agencies have a vital role to play, as the forecasted increase in hydropower generation is not uniform. Hence, this study provides some clues to stakeholders to preplan natural disasters such as drought and flooding to minimize associated risks.

However, the developed forecasting model is only formulated using the rainfall to the catchment. The other climate variables, such as temperature, evapotranspiration, wind speed and direction, relative humidity, and soil infiltration, would be useful in a comprehensive forecasting model development. Nevertheless, the developed forecasting model can be effectively used in a climatic data scarcity environment. Most of the developed countries do not have an improved network of meteorological stations; even the available stations only record the rainfall. Therefore, the developed model is extremely important, at least to have some clues for the future.

In addition, the presented ANN model can be used to forecast the future power generation from hydropower plants located elsewhere. Therefore, the authors suggest carrying out similar projection studies using ANN for all the major hydropower plants located in Sri Lanka and to have a common management plan of water resources to generate hydropower for the future. However, it is always important to plan for the uncertainty in the neural network models due to the forecasted future climates rather than the observed climatic parameters.

Data Availability

The climatic data and the analysis data are available from the corresponding author upon request.

Disclosure

The research was carried out in the Sri Lanka Institute of Information Technology Environment.

Conflicts of Interest

The authors declare that there are no conflicts of interest.

Acknowledgments

The authors would like to appreciate Dr. Kamal Laksiri, Project Director, Broadlands Hydropower Project, Ceylon

Electricity Board, Sri Lanka, for support which is given in obtaining hydropower generation data from Samanalawewa Hydropower Project.

References








- [1] WEC (World Energy Council), *Energy Resources: Hydropower*, WEC (World Energy Council), London, UK, 2019.
- [2] Asian Development Bank (ADB), *Sri Lanka Energy Sector Assessment, Strategy, and Road Map*, Asian Development Bank (ADB), Mandaluyong, Philippines, 2019.
- [3] The World Bank, "Directions in hydropower: scaling up for development," in *Water Working Notes* The World Bank, Washington, DC, USA, 2009.
- [4] International Hydropower Association (IHA), *Hydropower Status Report*, IHA Central Office, London, UK, 2019.
- [5] G. Chen and G. D. Costa, "Climate change impacts on water resources case of Sri Lanka," *Environment and Ecology Research*, vol. 5, no. 5, pp. 347–356, 2017.
- [6] G. Naveendrakumar, M. Vithanage, H.-H. Kwon, M. C. M. Iqbal, S. Pathmarajah, and J. Obeysekera, "Five decadal trends in averages and extremes of rainfall and temperature in Sri Lanka," *Advances in Meteorology*, vol. 2018, Article ID 4217917, 13 pages, 2018.
- [7] X. Zhang, H.-Y. Li, Z. D. Deng et al., "Impacts of climate change, policy and water-energy-food nexus on hydropower development," *Renewable Energy*, vol. 116, pp. 827–834, 2018.
- [8] A. Hammid, M. Sulaiman, and A. Abdalla, "Prediction of small hydropower plant power production in Himreen Lake dam (HLD) using artificial neural network," *Alexandria Engineering Journal*, vol. 57, no. 1, pp. 211–221, 2017.
- [9] D. Yadav and N. Veena Sharma, "Artificial neural network based hydro electric generation modelling," *International Journal of Applied Engineering Research*, vol. 2, no. 1, pp. 56–72, 2010.
- [10] M. S. Khan, P. Coulibaly, and Y. Dibike, "Uncertainty analysis of statistical downscaling methods," *Journal of Hydrology*, vol. 319, no. 1–4, pp. 357–382, 2006.
- [11] B. Khaniya, H. Priyantha, N. Baduge, H. Azamathulla, and U. Rathnayake, "Impact of climate variability on hydropower generation: a case study from Sri Lanka," *ISH Journal of Hydraulic Engineering*, pp. 1–9, 2018.
- [12] P. Qin, H. Xu, M. Liu et al., "Climate change impacts on three Gorges reservoir impoundment and hydropower generation," *Journal of Hydrology*, vol. 580, Article ID 123922, 2020.
- [13] S. Mishra, T. Veselka, A. Prusevich et al., "Differential impact of climate change on the hydropower economics of two river basins in high mountain Asia," *Frontiers in Environmental Science*, vol. 8, no. 26, 2020.
- [14] S. K. Mishra, J. Hayse, T. Veselka et al., "An integrated assessment approach for estimating the economic impacts of climate change on river systems: an application to hydropower and fisheries in a Himalayan river, Trishuli," *Environmental Science & Policy*, vol. 87, pp. 102–111, 2018.
- [15] W. Zhong, J. Guo, L. Chen, J. Zhou, J. Zhang, and D. Wang, "Future hydropower generation prediction of large-scale reservoirs in the upper Yangtze river basin under climate change," *Journal of Hydrology*, vol. 588, Article ID 125013, 2020.
- [16] S. Zaidi, V. Chandola, M. Allen et al., "Machine learning for energy-water nexus: challenges and opportunities," *Big Earth Data*, vol. 2, no. 3, pp. 228–267, 2018.

- [17] A. Shaktawat and S. Vadhera, "Risk management of hydro-power projects for sustainable development: a review," *Environment, Development and Sustainability*, 2020.
- [18] H. I. Mohamed, "Design of alluvial Egyptian irrigation canals using artificial neural networks method," *Ain Shams Engineering Journal*, vol. 4, no. 2, pp. 163–171, 2013.
- [19] T. S. Abdulkadir, A. W. Salami, A. R. Anwar, and A. G. Kareem, "Modelling of hydropower reservoir variables for energy generation: neural network approach," *Ethiopian Journal of Environmental Studies and Management*, vol. 6, no. 3, pp. 310–316, 2013.
- [20] A. Salami, A. Mohammed, J. Adeyemo, and O. Olanlokun, "Modeling of reservoir inflow for hydropower dams using artificial neural network," *Nigerian journal of Technology*, vol. 34, no. 1, pp. 28–36, 2015.
- [21] E. Uzlu, A. Akpınar, H. T. Özturk, S. Nacar, and M. Kankal, "Estimates of hydroelectric generation using neural networks with the artificial bee colony algorithm for Turkey," *Energy*, vol. 69, pp. 638–647, 2014.
- [22] M. Patil, "Stream flow modeling for Ranganadi hydropower project in India considering climate change," *Current World Environment*, vol. 11, no. 3, pp. 834–845, 2016.
- [23] M. Khodaverdi, "Forecasting future energy production using hybrid artificial neural network and arima model," vol. 4004 Graduate Theses, Dissertations, and Problem Reports, Morgantown, West Virginia, 2018.
- [24] A. Ladanu, S. Akanmu, and J. Adeyemo, "Enhancing artificial neural network with multi-objective evolutionary algorithm for optimizing real time reservoir operations: a review," *American Journal of Water Resources*, vol. 8, no. 3, pp. 118–127, 2020.
- [25] N. Anuar, M. Khan, J. Pasupuleti, and A. Ramli, "Flood risk prediction for a hydropower system using artificial neural network," *International Journal of Recent Technology and Engineering*, vol. 8, no. 4, pp. 6177–6181, 2019.
- [26] V. Sessa, E. Assoumou, and M. Bossy, "Modeling the climate dependency of the run-of-river based hydro power generation using machine learning techniques: an application to French, Portuguese and Spanish cases." hal-02520128, 2020.
- [27] P. Amarasinghe, N. Abeygunawardana, T. Jayasekara, E. Edirisinghe, and S. Abeygunawardane, "Ensemble models for solar power forecasting—a weather classification approach," *AIMS Energy*, vol. 8, no. 2, pp. 252–271, 2020.
- [28] S. Karunathilake and H. Nagahamulla, "Artificial neural networks for daily electricity demand prediction of Sri Lanka," in *Proceedings of the International Conference on Advances in ICT for Emerging Regions (ICTer)*, pp. 128–133, IEEE, Colombo, Sri Lanka, September 2017.
- [29] C. Gunasekara, "Modelling and simulation of temperature variations of bearings in a hydropower generation unit," M.S. thesis, Sweden: Department of Energy Technology, Royal Institute of Technology, Stockholm, Sweden, 2011.
- [30] E. Udayakumara and U. Gunawardana, "Reducinng siltation and Increasing hydropower generation from the rantambe reservoir, Sri Lanka. Kathmandu," *South Asian Network for Development and Environmental Economics (SANDEE)*, vol. 113, no. 16, pp. 1–20, 2016.
- [31] S. Chandrasekara, V. Prasanna, and H.-H. Kwon, "Monitoring water resources over the Kotmale reservoir in Sri Lanka using ENSO phases," *Advances in Meteorology*, vol. 2017, Article ID 4025964, 9 pages, 2017.
- [32] N. Imbulana, S. Gunawardana, S. Shrestha, and A. Datta, "Projections of extreme precipitation events under climate change scenarios in Mahaweli river basin of Sri Lanka," *Current Science*, vol. 114, no. 7, pp. 1495–1509, 2018.
- [33] A. Perera and U. Rathnayake, "Impact of climate variability on hydropower generation in an un-gauged catchment: Erathna run-of-the-river hydropower plant, Sri Lanka," *Applied Water Science*, vol. 9, no. 57, 2019.
- [34] B. Khaniya, I. Jayanayaka, P. Jayasanka, and U. Rathnayake, "Rainfall trend analysis in Uma Oya basin, Sri Lanka, and future water scarcity problems in perspective of climate variability," *Advances in Meteorology*, vol. 2019, Article ID 3636158, 10 pages, 2019.
- [35] M. Jakob Themeßl, A. Gobiet, and A. Leuprecht, "Empirical-statistical downscaling and error correction of daily precipitation from regional climate models," *International Journal of Climatology*, vol. 31, no. 10, pp. 1530–1544, 2010.
- [36] W. Cabos, D. V. Sein, A. Durán-Quesada et al., "Dynamical downscaling of historical climate over CORDEX central America domain with a regionally coupled atmosphere–ocean model," *Climate Dynamics*, vol. 52, no. 7–8, pp. 4305–4328, 2019.
- [37] S. K. Dubey and D. Sharma, "Assessment of climate change impact on yield of major crops in the Banas River Basin, India," *Science of The Total Environment*, vol. 635, pp. 10–19, 2018.
- [38] D. Jacob, B. J. J. M. Van Den Hurk, U. Andrae et al., "A comprehensive model inter-comparison study investigating the water budget during the BALTEX-PIDCAP period," *Meteorology and Atmospheric Physics*, vol. 77, no. 1–4, pp. 19–43, 2001.
- [39] V. P. Pandey, S. Dhaubanjari, L. Bharati, and B. R. Thapa, "Hydrological response of Chamelia watershed in Mahakali basin to climate change," *Science of the Total Environment*, vol. 650, pp. 365–383, 2019.
- [40] S. A. Thasneem, N. Chithra, and S. Thampi, "Analysis of extreme precipitation and its variability under climate change in a river basin," *Natural Hazards*, vol. 98, no. 2, pp. 1169–1190, 2019.
- [41] IPCC Climate Change, "Synthesis report. 2014. fifth assessment report of the intergovernmental panel on climate change," in *Intergovernmental Panel on Climate Change*, R. K. Pachauri and L. A. Meyer, Eds., pp. 1–151, Geneva, Switzerland, 2014.
- [42] H. Kawase, T. Nagashima, K. Sudo, and T. Nozawa, "Future changes in tropospheric ozone under representative concentration pathways (RCPs)," *Geophysical Research Letters*, vol. 38, no. 5, 2011.
- [43] D. P. V. Vuuren, J. Edmonds, M. Kainuma et al., "The representative concentration pathways: an overview," *Climatic Change*, vol. 109, no. 1–2, p. 5, 2011.
- [44] J. H. Christensen, F. Boberg, O. B. Christensen, and P. Lucas-Picher, "On the need for bias correction of regional climate change projections of temperature and precipitation," *Geophysical Research Letters*, vol. 35, no. 20, 2008.
- [45] C. Piani, J. O. Haerter, and E. Coppola, "Statistical bias correction for daily precipitation in regional climate models over Europe," *Theoretical and Applied Climatology*, vol. 99, no. 1–2, pp. 187–192, 2010.
- [46] C. Teutschbein and J. Seibert, "Bias correction of regional climate model simulations for hydrological climate-change impact studies: review and evaluation of different methods," *Journal of Hydrology*, vol. 456–457, pp. 12–29, 2012.
- [47] G. Lenderink, A. Buishand, and W. Van Deursen, "Estimates of future discharges of the river Rhine using two scenario

- methodologies: direct versus delta approach,” *Hydrology and Earth System Sciences*, vol. 11, no. 3, pp. 1145–1159, 2007.
- [48] U. Ghimire, G. Srinivasan, and A. Agarwal, “Assessment of rainfall bias correction techniques for improved hydrological simulation,” *International Journal of Climatology*, vol. 39, no. 4, pp. 2386–2399, 2018.
- [49] T. Lafon, S. Dadson, G. Buys, and C. Prudhomme, “Bias correction of daily precipitation simulated by a regional climate model: a comparison of methods,” *International Journal of Climatology*, vol. 33, no. 6, pp. 1367–1381, 2013.
- [50] M. Luo, T. Liu, F. Meng et al., “Comparing bias correction methods used in downscaling precipitation and temperature from regional climate models: a case study from the Kaidu river basin in Western China,” *Water*, vol. 10, no. 8, p. 1046, 2018.
- [51] R. Mahmood, S. Jia, N. K. Tripathi, and S. Shrestha, “Precipitation extended linear scaling method for correcting GCM precipitation and its evaluation and implication in the transboundary Jhelum river basin,” *Atmosphere*, vol. 9, no. 5, p. 160, 2018.
- [52] E. P. N. Udayakumara, R. P. Shrestha, L. Samarakoon, and D. Schmidt-Vogt, “Mitigating soil erosion through farm-level adoption of soil and water conservation measures in Samanalawewa Watershed, Sri Lanka,” *Acta Agriculturae Scandinavica, Section B-Soil & Plant Science*, vol. 62, no. 3, pp. 273–285, 2012.
- [53] D. T. Udagedara, C. T. Oguchi, and J. K. Gunatilake, “Evaluation of geomechanical and geochemical properties in weathered metamorphic rocks in tropical environment: a case study from Samanalawewa hydropower project, Sri Lanka,” *Geosciences Journal*, vol. 21, no. 3, pp. 441–452, 2017.
- [54] E. P. N. Udayakumara and U. A. D. P. Gunawardena, “Cost-benefit analysis of Samanalawewa hydroelectric project in Sri Lanka: an ex post analysis,” *Earth Systems and Environment*, vol. 2, no. 2, pp. 401–412, 2018.
- [55] K. Laksiri, J. Gunathilake, and Y. Iwao, “A case study of the Samanalawewa reservoir in the Walawe river in an area of Karst in Sri Lanka,” in *Proceedings of Tenth Multidisciplinary Conference Sinkholes and the Engineering and Environmental Impacts of Karst (GSP 144)*, San Antonio, TX, USA, September 2005.
- [56] D. Wijesinghe, “Optimization of hydro-power potential of Samanalawewa project,” *Engineer: Journal of the Institution of Engineers, Sri Lanka*, vol. 39, no. 1, p. 27, 2006.
- [57] M. Pathiraja and W. Wijayapala, “Optimization of the usage of Samanalawewa water resource for power generation,” in *Proceedings of the 2016 Electrical Engineering Conference (EECon)*, Colombo, Sri Lanka, December 2016.
- [58] B. D. Kristen and W. L. Lee, “Artificial neural networks for the management researcher: the state of the art, department of organizational leadership and strategy, Marriott school of management Brigham Young University Provo,” UT 84602, 2003.
- [59] U. R. Alo, S. I. Ele, and H. F. Nweke, “A conceptual framework for network traffic control and monitoring using artificial neural networks,” *Journal of Theoretical and Applied Information Technology*, vol. 97, no. 22, pp. 3396–3412, 2019.
- [60] T. Chaipimonplin, “Comparison learning algorithms for artificial neural network model for flood forecasting, Chiang Mai, Thailand,” in *Proceedings of the 22nd International Congress on Modelling and Simulation (MODSIM 2017)*, pp. 472–479, Hobart, Australia, December 2017.
- [61] P. Chopra, R. K. Sharma, and M. Kumar, “Artificial neural networks for the prediction of compressive strength of concrete,” *International Journal of Applied Sciences & Engineering*, vol. 13, no. 3, pp. 187–204, 2015.
- [62] A. Perera, U. S. Rathnayake, and H. M. Azamathulla, “Comparison of different artificial neural network (ANN) training algorithms to predict atmospheric temperature in Tabuk, Saudi Arabia, MAUSAM,” *Quarterly Journal of Meteorology, Hydrology, and Geophysics*, vol. 71, no. 2, pp. 233–244, 2020.
- [63] L. Zhou and X. Yang, “Training algorithm performance for image classification by neural networks,” *Photogrammetric Engineering & Remote Sensing*, vol. 76, no. 8, pp. 945–951, 2010.
- [64] D. Baskaran, A. Sinharoy, T. Paul, K. Pakshirajan, and R. Rajamanickam, “Performance evaluation and neural network modeling of trichloroethylene removal using a continuously operated two-phase partitioning bioreactor,” *Environmental Technology & Innovation*, vol. 17, Article ID 100568, 2020.
- [65] R. Celikel, “ANN based angle tracking technique for shaft resolver,” *Measurement*, vol. 148, Article ID 106910, 2019.
- [66] W. Han, L. Nan, M. Su, Y. Chen, R. Li, and X. Zhang, “Research on the prediction method of centrifugal pump performance based on a double hidden layer BP neural network,” *Energies*, vol. 12, no. 14, p. 2709, 2019.
- [67] M. Cai, M. Koopialipoor, D. Armaghani, and B. Thai Pham, “Evaluating slope deformation of earth dams due to earthquake shaking using MARS and GMDH techniques,” *Applied Sciences*, vol. 10, no. 4, p. 1486, 2020.
- [68] M. Koopialipoor, E. Ghaleini, H. Tootoonchi, D. Armaghani, M. Haghighi, and A. Hedayat, “Developing a new intelligent technique to predict overbreak in tunnels using an artificial bee colony-based ANN,” *Environmental Earth Sciences*, vol. 78, no. 5, 2019.
- [69] L. Sun, M. Koopialipoor, D. Armaghani, R. Tarinejad, and M. Tahir, “Applying a meta-heuristic algorithm to predict and optimize compressive strength of concrete samples,” *Engineering with Computers*, 2019.
- [70] D. Tang, B. Gordan, M. Koopialipoor et al., “Seepage analysis in short embankments using developing a metaheuristic method based on governing equations,” *Applied Sciences*, vol. 10, no. 5, p. 1761, 2020.
- [71] G. Foody, “Impacts of sample design for validation data on the accuracy of feedforward neural network classification,” *Applied Sciences*, vol. 7, no. 9, p. 888, 2017.
- [72] Japan International Cooperation Agency (JICA), *Samanalawewa Hydroelectric Power Project (I) (II) (III) and Samanalawewa Hydroelectric Project (Reservoir Remedial Works)*, Japan Water Agency, Colombo, Sri Lanka, 2006.
- [73] H. S. Somatilake, K. A. U. S. Imbulana, P. Droogers, and I. W. Makin, “Water for energy,” in *Proceedings of the World Water Assessment Programme Sri Lanka Case Study, Ruhuna basins: Proceedings of a Workshop Held at Koggala Beach Hotel, Sri Lanka*, International Water Management Institute, Colombo, Sri Lanka, pp. 129–141, April 2002.

Research Article

Improving Voting Feature Intervals for Spatial Prediction of Landslides

Binh Thai Pham ¹, **Tran Van Phong** ², **Mohammadtaghi Avand** ³,
Nadhir Al-Ansari ⁴, **Sushant K. Singh** ⁵, **Hiep Van Le** ⁶, and **Indra Prakash** ⁷

¹University of Transport Technology, Hanoi 100000, Vietnam

²Institute of Geological Sciences, Vietnam Academy of Sciences and Technology, 84 Chua Lang Street, Dong da, Hanoi 100000, Vietnam

³Department of Watershed Management Engineering, College of Natural Resources, TarbiatModares University, Tehran 14115-111, Iran

⁴Department of Civil, Environmental and Natural Resources Engineering, Lulea University of Technology, Lulea 971 87, Sweden

⁵Artificial Intelligence and Analytics, Health Care and Life Sciences, Virtusa Corporation, New York, NY, USA

⁶Institute of Research and Development, Duy Tan University, Da Nang 550000, Vietnam

⁷DDG(R) Geological Survey of India, Gandhinagar 382010, India

Correspondence should be addressed to Binh Thai Pham; binhpt@utt.edu.vn, Nadhir Al-Ansari; nadhir.alansari@ltu.se, and Hiep Van Le; levanhiep2@duytan.edu.vn

Received 4 June 2020; Revised 25 August 2020; Accepted 25 September 2020; Published 12 October 2020

Academic Editor: Zheng-zheng Wang

Copyright © 2020 Binh Thai Pham et al. This is an open access article distributed under the Creative Commons Attribution License, which permits unrestricted use, distribution, and reproduction in any medium, provided the original work is properly cited.

In this study, the main aim is to improve performance of the voting feature intervals (VFIs), which is one of the most effective machine learning models, using two robust ensemble techniques, namely, AdaBoost and MultiBoost for landslide susceptibility assessment and prediction. For this, two hybrid models, namely, AdaBoost-based Voting Feature Intervals (ABVFIs) and MultiBoost-based Voting Feature Intervals (MBVFIs) were developed and validated using landslide data collected from one of the landslide affected districts of Vietnam, namely, Muong Lay. Quantitative validation methods including area under the ROC curve (AUC) were used to evaluate model performance. The results indicated that both the newly developed ensemble models ABVFI (AUC = 0.859) and MBVFI (AUC = 0.839) outperformed the single VFI (AUC = 0.824) model. Thus, ensemble framework-based VFI algorithms can be used for the accurate spatial prediction of landslides, which can also be applied in other landslide prone regions of the world. Landslide susceptibility maps developed by ensemble VFI models can be used for better landslide prevention and risk management of the area.

1. Introduction

In recent years, population growth and development in unstable hilly areas have led to an increase in natural disasters such as landslides [1]. Based on 100 years of data analysis of natural hazards, after floods and earthquakes, landslides are the most frequent and important natural disaster causing casualties, financial losses, and adverse environmental impacts all over the world [2]. Landslides can cause destruction of infrastructure facilities, land use

changes, erosion, and a high volume of sediment production in watersheds [3–5]. Mostly landslides occur due to gravity action on groundmass as a result of rainfall, earthquakes, soil saturation, and excavation of slopes [6, 7]. Landslide influencing factors include topography (slope, aspect, curvature, altitude, and elevation), geology (lithology, fault, and weathering crust), hydrology (rainfall and drainage), and land use [8–11]. Understanding the features and elements of landslide development and expansion helps in risk prediction and prevention of landslide damages [12].

In landslide study, it is important to identify and demarcate landslide susceptible zones [13, 14]. Landslide zoning mapping requires an assessment of the relationship between the prevailing conditions of the basin situation and the factors affecting the occurrence of the landslides [15]. In general, there are several methods of landslide susceptibility mapping and zoning [16, 17] which include mathematical/statistical and machine learning techniques [18, 19]. Mathematical modeling approach for delineating landslide hazards in watersheds was discussed in detail by Simons and Ward (<http://andrewsforest.oregonstate.edu/pubs/pdf/pub2055.pdf>) and Simons and Ward [20]. Corominas et al. [21] reviewed the literature and recommended methodologies for the quantitative analysis of landslide hazard, vulnerability, and risk at different spatial scales. They have also used this method for the verification and validation of the results [21].

However, it is difficult to demarcate natural boundary of transitional/gradational geological units and also continuous topographic features and factors such as elevation, slope, and topographic indices by traditional and statistical models [22, 23]. Simplification of major landslide parameters, their classes, and interactions between them can lead to incorrect results in the final map [24, 25]. These concerns led to the use of machine learning (ML) and data mining techniques in landslide studies [1, 26]. Nowadays, these methods are being used more widely for landslide susceptibility mapping due to their accuracy and speed [13, 14, 27]. Some of the prominent models used for mapping include artificial neural network (ANN) [28, 29], boosted regression trees (BRTs) [30, 31], random forest (RF) [32, 33], rotation forest (ROF) [34, 35], particle swarm optimization (PSO) [36, 37], support vector machine (SVM) [28, 38], binary logistic regression (BLR) [22], bagging [39, 40], logistic regression (LR) [33, 41], and canonical correlation forest (CCF) [42]. ML models have proven their relative superiority over bivariate and multivariate statistical models in several studies [43, 44]. In addition, to increase accuracy in dealing with complex problems and uncertainties, these models also lead to the development of new approaches to various problems [45, 46]. Although a number of ML models have been used in the landslide study, no model is perfect to be applied in all geoenvironmental conditions. Therefore, there is always scope of improvement in methodology by using different combinations of algorithms.

With this objective, a new ensemble framework-based ML models, namely, ABVFI and MBVFI, which are combination of a popular single ML model voting feature intervals (VFIs), and two effective ensemble techniques, namely, AdaBoost and MultiBoost algorithms, were proposed for the development of landslide susceptibility maps. Muong Lay district, which is one of the most landslide affected areas of Vietnam, was selected as the study area. The main contribution of this study is in the development and application of a novel hybrid approach for accurate landslide susceptibility mapping. Validation of these models was carried out using different quantitative statistical indices including area under the ROC curve and accuracy. Weka and ArcGIS software were implemented for processing the data, modeling, and mapping of landslide susceptibility.

2. Methods Used

2.1. Voting Feature Intervals. Voting feature intervals (VFIs) is one of the classification methods that is based on feature separation and works on nonincremental classification [47]. In the VFI method, the features are considered independently [48]. This method has been used successfully in various medical, computer, and natural sciences studies [49, 50]. The primary purpose of this approach is to deal with very imbalanced datasets [51].

VFI methodology involves two main steps: [1] training and [2] classification. First, in the training phase, the feature intervals are constructed around each class by calculating the lowest and highest values of each feature. In the classification stage, a feature vote is computed for each category based on each interval from each element, and then, the votes for each feature interval are united to produce one output [47]. One of the most important advantages of this algorithm is that it ignores the missing feature values at both the training and classification stages [47].

2.2. AdaBoost. AdaBoost or Adaptive Boosting is a ML algorithm devised by Yoav Freund and Robert Schapire [52]. AdaBoost is a hybrid learning technique and most well-known method of the algorithm's family. In this algorithm, models learned sequentially so that a model is trained at any one time. At the end of each time, incorrectly classified examples are identified, and their emphasis is on a new training set which can be used for the next training session for training a new model [53]. The idea is that new models should be able to compensate for errors created by previous models. In fact, AdaBoost is a meta-algorithm used to enhance performance along with other learning algorithms. Purpose of the AdaBoost algorithm is to increase learning rate of the classifiers. This algorithm combines several weak clusters to obtain a suitable boundary between two classes of data. The AdaBoost algorithm is sensitive to noise and outliers, but it is better suited to the overfitting problem in comparison to other learning algorithms [52].

If the base classifier used is better than the random classifier (50%), the algorithm's performance improves with more iteration. Even classifiers with higher error than random classifiers enhance overall performance by taking the negative coefficient [54]. In the AdaBoost algorithm, a weak classification is added at each round. At each call, weights are assigned based on the importance of the samples. With each round, the weight of misclassified samples increases, and the weight of correctly classified samples decreases, so the new classifier will focus on the more difficult-to-learn samples [55].

2.3. MultiBoost. MultiBoost is one of the ensemble learning methods developed by combining two ensemble learning algorithms, namely, AdaBoost and Wagging [56–58]. Wagging uses training samples with deferring weight, which could significantly reduce the high bias of the AdaBoost algorithm [59]. Combination of the two AdaBoost and Wagging techniques improves weak

classifications learning and transforms them into a robust classifier [56]. In case of MultiBoost technique, training of data is done in three main stages: (i) randomly, a subset is separated from the training data and used for models based on initial classification; (ii) sample weight is adjusted according to the predictive ability of the model; and (iii) the new subset is selected according to the weighted sample and is used to train the new model [60].

2.4. Validation Methods. Performance of the models was evaluated using statistical measures such as positive predictive value (PPV), area under receiver operating characteristic (ROC) curve (AUC), specificity (SPF), accuracy (ACC), negative predictive value (NPV), sensitivity (SST), root mean square error (RSME), and Kappa index (k) [61, 62]. Detail description of these indices is presented in relevant studies [4, 63–70]. Formulas of these indices are presented in Table 1.

3. Study Area

The study area of Muong Lay district is located in the northwest of Vietnam between $22^{\circ}0'N$ and $22^{\circ}5'N$ and $103^{\circ}5'E$ and $103^{\circ}10'E$, covering 11403 km^2 is highly prone to landslides (Figure 1). The area is located, at the confluence of Da, Nam Na, and Nam Lay Rivers in a narrow and long valley [3, 4]. The elevation varies between 125 and 1778 m. The hill slopes are connected with sheered cliffs and marked by rapids. The area is tectonically active, structurally disturbed, and traversed by several faults including Chay River fault, Red River fault, and Dien Bien-Lai Chau fault zones, within the Lai Chau-Dien Bien fault zone, thus vulnerable to natural disasters such as floods and landslides. This area experiences annual average temperature ranging between $21^{\circ}C$ and $23^{\circ}C$, humidity up to 84% and average number of sunshine hours ranging from 1820 to 2035 hours per year [3, 4].

4. Geospatial Database

Geospatial data of landslide inventory were obtained from the Vietnam Academy of Geosciences and Minerals official web portal (<http://canhbaotruotlo.vn>) and updated from Google Earth images and field surveys. In total, 271 landslide events were recorded and studied for the development of models. Landslides in the area are of rotational, translational, debris, rock falls, and mixed types. Most of the landslides occur along and adjacent to the main connecting road to the Muong Lay district, on the Highways 6 and 12 [3, 4]. For developing landslides prediction models, landslide conditioning or affecting factors such as topographical factors (aspect, slope, and curvature) were generated from digital elevation model (DEM) of 12.5 m available online (<https://vertex.daac.asf.alaska.edu>). Geological and topographical factors (distance to faults, distance to rivers, geology/lithology, focal flow, weathering rocks, and distance to roads) were generated and extracted from geology and topography maps (1:50000) collected from General Department of Geology and Minerals of Vietnam. Maps of these

conditioning factors are presented in Figure 2, while the spatial analysis of past and present landslides carried out on these conditioning maps is presented in Figure 3 [3, 4]. More detailed analysis of the individual influencing factors and mechanism of landslides is presented in the published works carried out in the same area [3, 4].

5. Modeling Methodology

Major steps of the methodological framework include [1] data collection and preparation, [2] model development, [3] model validation, and [4] generation and validation of landslide susceptibility maps (Figure 4).

5.1. Data Collection and Preparation. Landslide data of 271 past landslide events were generated by identifying landslides on Google Earth images in conjunction with available landslide records. Out of these, 70% of landslide (152 locations) and nonlandslide (152 locations) data were used to generate the training dataset for building the models, whereas 30% remaining (65 landslide locations and 65 nonlandslide locations) data were used to create testing dataset for model validation. Training and testing data in the ratio of 70/30 were selected based on the experience of authors and other published work on the similar studies [72–75]. Correlation-based feature selection method [76], which is known as one of the most effective feature selection methods for landslide susceptibility modeling [77, 78], was used to select the suitable factors for landslide modeling.

5.2. Landslide Susceptibility Model Development. For the developments of models, the training dataset was used to construct the models (VFI, ABVFI, and MBVFI). In ABVFI, AdaBoost was used as an optimization technique to optimize the training dataset, which was then used as inputs for classification of landslide and nonlandslide classes using a base classifier of VFI. Similarly, in MBVFI, MultiBoost was used as an optimization technique to optimize the training dataset which was then used as inputs for classification of landslide and nonlandslide classes using a base classifier of VFI.

5.3. Landslide Susceptibility Model Validation. Validation of the models (VFI, ABVFI, and MBVFI) was carried out using the testing dataset and quantitative statistical indices, namely, AUC, ACC, SST, SPE, PPV, NPV, RMSE, and Kappa index.

5.4. Landslide Susceptibility Map Generation and Validation. Landslide susceptibility indices scores generated by the models were classified into very low, low, moderate, high, and very high susceptibility areas based on Jenks' natural break classification method [79] for map generation. Thereafter, performance of the generated maps was validated by frequency ratio analysis [80].

TABLE 1: Formulas of quantitative indices used for validation of the models.

No.	Quantitative indices	Formulas	
1	Positive predictive value (%)	$PPV = TP / (TP + FP)$	[1]
2	Negative predictive value (%)	$NPV = TN / (TN + FN)$	[2]
3	Sensitivity (%)	$SST = TP / (TP + FN)$	[3]
4	Specificity (%)	$SPE = TN / (TN + FP)$	[4]
5	Accuracy (%)	$ACC = (TP + TN) / (TP + TN + FP + FN)$	[5]
6	Kappa	$k = (R_a - R_{ept}) / (1 - R_{ept})$	[6]
7	Root mean square error	$RMSE = \sqrt{(1/m) \sum_{i=1}^m (V_p - V_a)^2}$	[7]
8	Area under the ROC curve	$AUC = \sum TP + \sum (TN/P) + N$	[8]

TP, TN, FP, and FN are considered the percentage of pixels classified correctly and incorrectly as landslide and nonlandslide classes; m is the total number of instances in the datasets; V_p and V_a are predicted and actual values of outputs; R_{ept} and R_a are expected agreements and the percentage of samples predicted correctly for landslide or nonlandslide classes; N and P are the total number of landslide and nonlandslide classes, respectively [71].

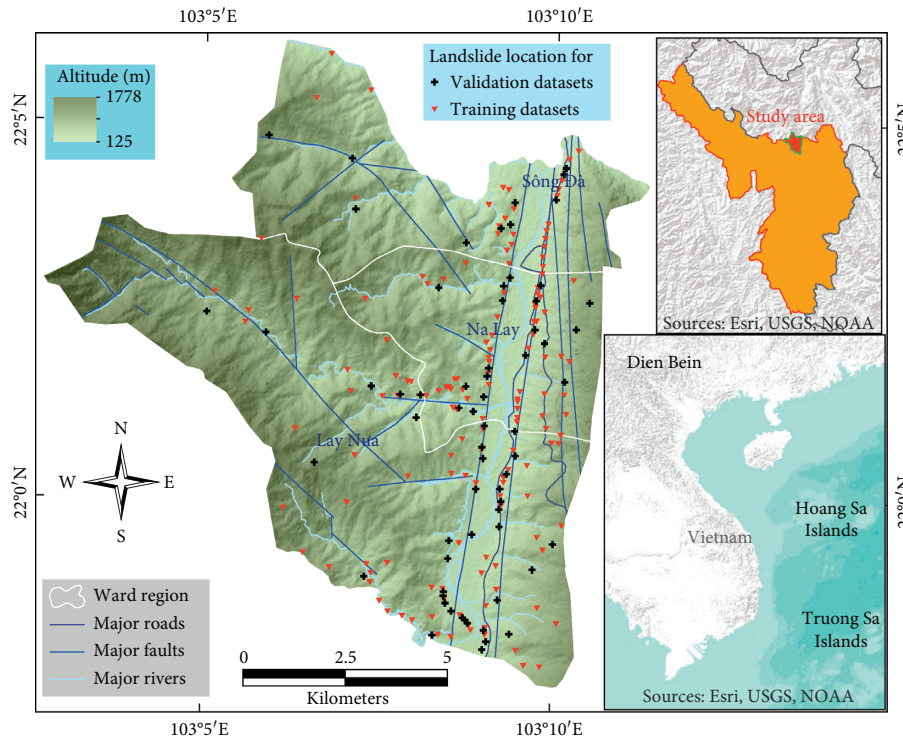


FIGURE 1: Spatial distribution of the landslide events in the study area.

6. Results and Analysis

6.1. Validation and Selection of Important Factors.

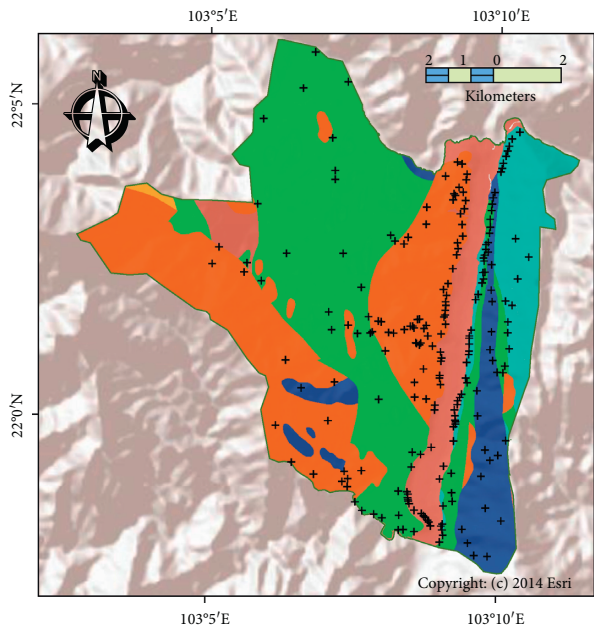
Validation and selection of important factors was done using correlation-based feature selection [3, 77], and the results are presented in Table 2. It can be observed that distance from rivers ($AM = 0.437$) is the most important factor, followed by distance from roads ($AM = 0.404$) and distance from faults ($AM = 0.336$) aspect ($AM = 0.226$), weathering crust ($AM = 0.126$), geology ($AM = 0.115$), slope ($AM = 0.076$), focal flow ($AM = 0.054$), and curvature ($AM = 0.029$), respectively (Table 2).

6.2. Validation and Comparison of Landslide Susceptibility Models.

Validation and comparison of landslide susceptibility models were done using PPV, NPV, SST, SPF, ACC, Kappa, and RMSE scores. The ABVFI model achieved the

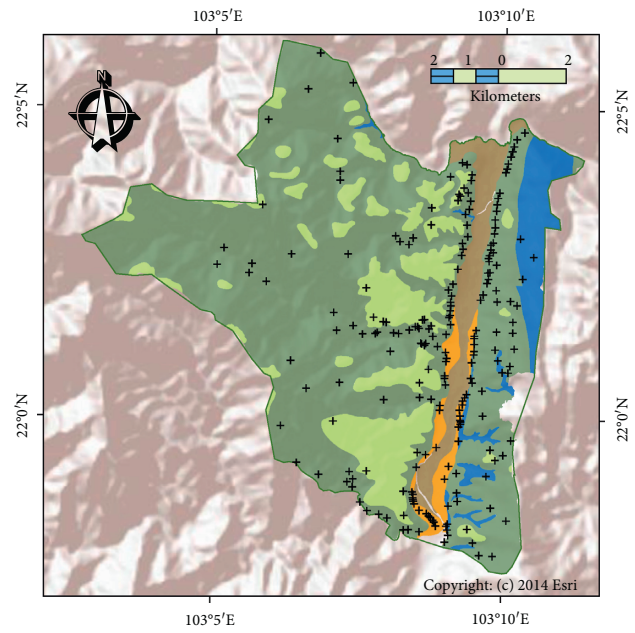
highest accuracy on both training ($ACC = 82.12\%$) and testing datasets ($ACC = 81.54\%$) compared with other models (VFI and MBVFI). This model also achieved the highest PPV (83.08%) on test data, the highest NPV on training (86.75%) and testing (80.0%) datasets. ABVFI was highly sensitive towards correctly predicting landslides in this area on both training ($SST = 85.40\%$) and testing ($SST = 80.60\%$) datasets. It achieved the highest SPF on the test (82.54%) dataset. ABVFI scored the highest kappa value on both training (0.624) and testing ($k = 0.631$) datasets. In contrast, ABVFI achieved the smallest RMSE on both training (0.367) and testing (0.390) datasets (Table 3 and Figure 5).

ABVFI model achieved the highest AUC on training ($AUC = 0.897$) and testing data ($AUC = 0.859$), followed by MBVFI on training and ($AUC = 0.895$) testing data ($AUC = 0.839$) and VFI on training ($AUC = 0.845$) and testing data ($AUC = 0.814$), respectively (Figure 6).



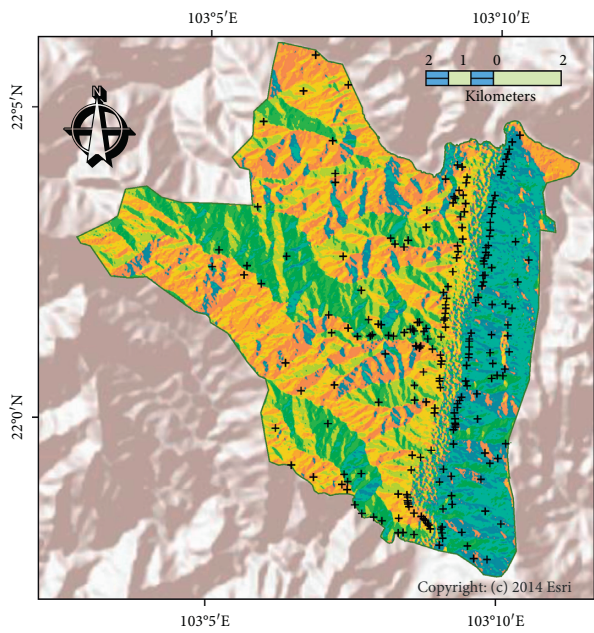
- Geological map**
- Neoproterozoic system
 - Devonian system
 - Permian system
 - Triassic system
 - Cretaceous system
 - Quaternary system
- + Landslide locations

(a)



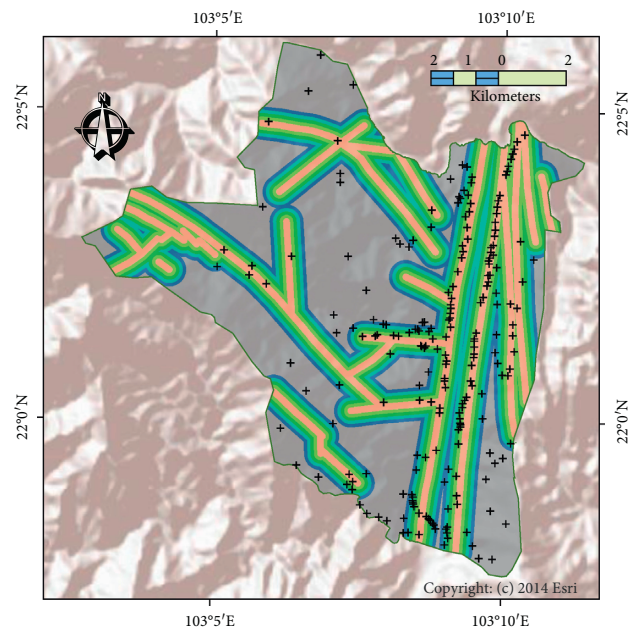
- Weathering crust**
- Rough saprolite
 - Smooth saprolite
 - Maculose silicate
 - Silicate nodule
 - Concretionary silicate
- + Landslide locations

(b)



- Aspect**
- Flat
 - N
 - NE
 - E
 - SE
 - S
 - SW
 - W
 - NW
- + Landslide locations

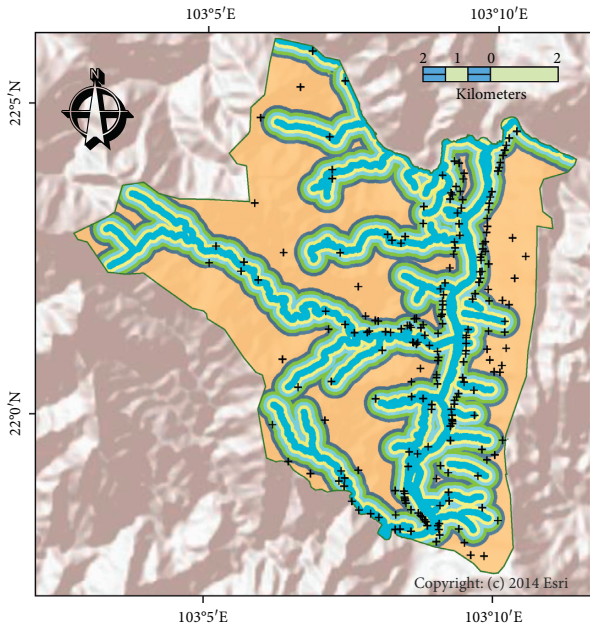
(c)



- Distance from faults (m)**
- 0 - 100
 - 100 - 200
 - 200 - 300
 - 300 - 400
 - 400 - 500
 - >500
- + Landslide locations

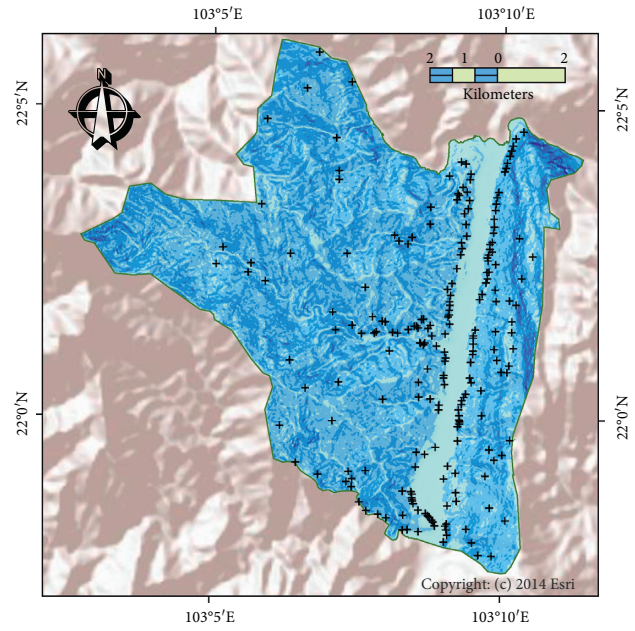
(d)

FIGURE 2: Continued.



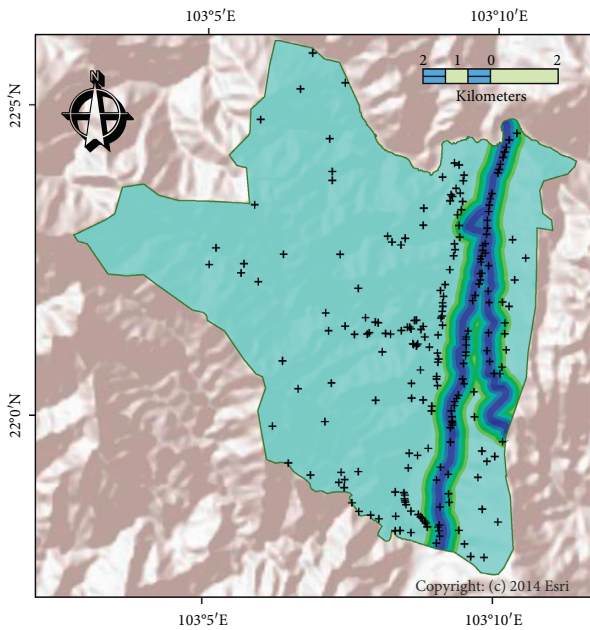
- Distance from rivers (m)
- 0 - 100
 - 100 - 200
 - 200 - 300
 - 300 - 400
 - 400 - 500
 - >500
- + Landslide locations

(e)



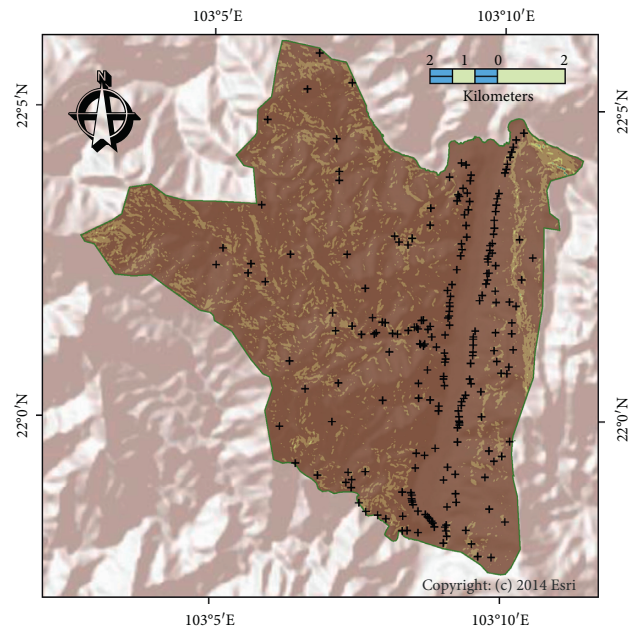
- Slope (degree)
- 0 - 14.54
 - 14.54 - 29.09
 - 29.09 - 43.63
 - 43.63 - 58.18
 - 58.18 - 72.72
- + Landslide locations

(f)



- Distance from roads (m)
- 0 - 100
 - 100 - 200
 - 200 - 300
 - 300 - 400
 - 400 - 500
 - >500
- + Landslide locations

(g)



- Focal flow 1/1406.25 m²
- 0 - 22.2
 - 22.2 - 44.4
 - 44.4 - 66.8
 - 66.8 - 88.8
 - 88.8 - 111
- + Landslide locations

(h)

FIGURE 2: Continued.

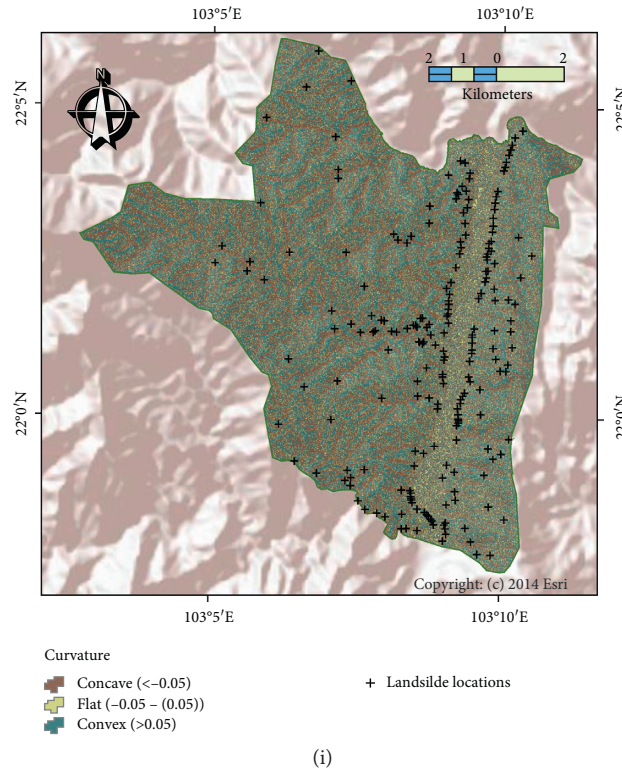


FIGURE 2: Thematic maps: (a) geology; (b) weathering crust; (c) aspect; (d) distance from faults; (e) distance from rivers; (f) slope; (g) distance from road; (h) focal flow; (i) curvature.

In general, it is apparent that ABVFI scored the highest AUC, ACC, and kappa values and the lowest RMSE on both the train and test data; therefore, this model can be selected as the best model in terms of predictability as well as robustness. MBVFI was the second-best model followed by the VFI model.

6.3. Construction of Landslide Susceptibility Maps. Landslide susceptibility maps based on the model's study were generated into five classes: very low, low, moderate, high, and very high susceptibility areas (Figure 7). Based on the frequency analysis of each class of landslide susceptibility for each model, we found that VFI algorithm was able to predict more correctly very high and high landslide susceptible areas than the moderate and low landslide classes (Table 4). Very low landslide areas could not be predicted by VFI. MBVFI was able to predict more correctly very high landslide susceptible areas. MBVFI could equally predict high and moderate landslide susceptible areas (Table 4). Like MBVFI, ABVFI was also found to be good at predicting very high landslide-sensitive areas. Overall, ABVFI could correctly predict most of the landslide susceptible classes (Table 4).

7. Discussion

In this study, we have developed improved hybrid VFI models ensemble with AdaBoost and MultiBoost algorithms and applied them at the Muong Lay district, Dien Bien province, Vietnam, for landslide susceptibility mapping and

prediction. To develop the ML models, it is important to validate and select the most suitable conditioning factors for better landslide susceptibility assessment and mapping [81]. In this study, correlation-based feature selection was applied to validate importance of the conditioning factors and accordingly select the best factors for landslide susceptibility modeling. The main principle of this method is based on the correlation analysis between the input and output variables and among input variables [3, 82]. It is a well-known feature selection method for ML applications [82]. The results indicated that distance from rivers ($AM=0.437$), distance from roads ($AM=0.404$), and the distance from faults ($AM=0.336$) had the highest impact in the landslide susceptibility prediction in the models (Table 1), which corroborated the study of earlier workers in this region [3, 4]. Reason for greater impact of rivers on the landslide occurrences is that slope close to rivers is generally saturated with water; moreover, erosion of toe support is likely at the bottom of valleys through which river flows thus causing more landslides in river valleys. Similarly, removal of toe support while construction of roads on hilly and mountainous areas also creates instability of groundmass. Road construction also disturbs slope and surrounding rock/ground mass, which cause landslides unless protected adequately. Faults are one of the prominent slopes affecting factors, which may itself cause landslides depending on its location, orientation, and nature of infilling material. Landslides generally occur in the fault affected areas due to ongoing tectonic activities.

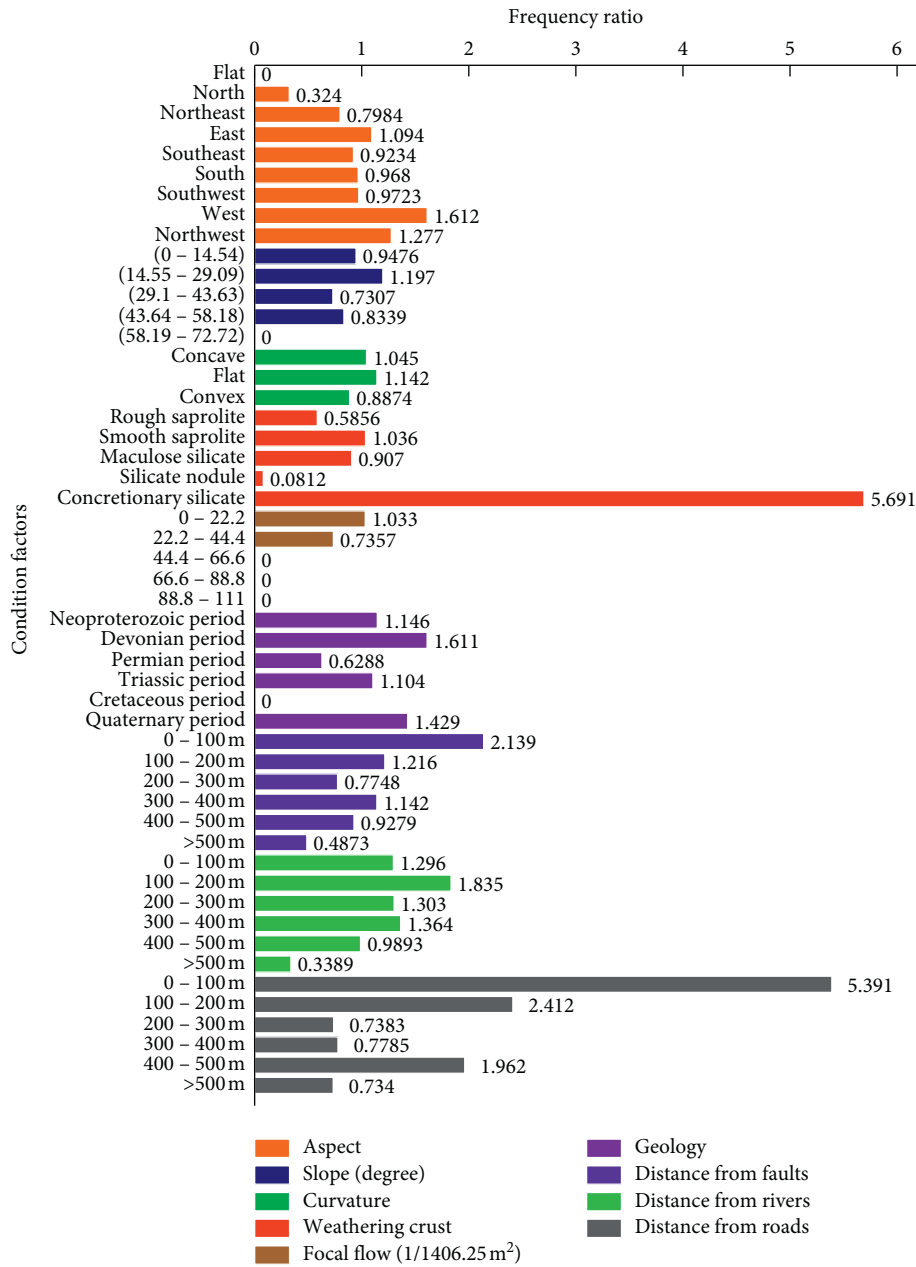


FIGURE 3: Frequency analysis histograms of landslide condition factors.

Validation and comparison results of the models showed that ABVFI is the most accurate and robust model on both the training and testing datasets (Table 2 and Figures 5 and 6). One of the advantages of this is that it is neither overtrained nor undertrained when compared to specifically VFI. Kappa statistics are used to evaluate the robustness of machine learning models. ABVFI and MBVFI both scored “K” greater than 0.61 on test data that makes both the models substantially robust [83, 84]. However, VFI shows a moderate kappa value of 0.446 on testing data [83, 84]. Although the RMSE value of all the three models relatively increased on testing data, it was the lowest for the ABVFI model (increase of 0.023) on training data. MBVFI scored the second lowest RMSE

on testing data with an increase of 0.026 when compared to the RMSE value on training data. With the highest AUC on testing data, ABVFI scored 0.038 which is lower than it achieved on training data. On the contrary, the second-best AUC scorer MBVFI achieved 0.056, which is less AUC score on testing data than it achieved on training data. VFI achieved 0.021 which is less AUC score on the test data than it achieved on training data. In addition, it can be seen from Table 4 that the frequency ratio values of high and very high classes of the map produced by ABVFI are higher than those produced by other models (MBVFI and VFI), which proves that prediction probability of landslides of the ABVFI is higher than other models. Main reason for the better

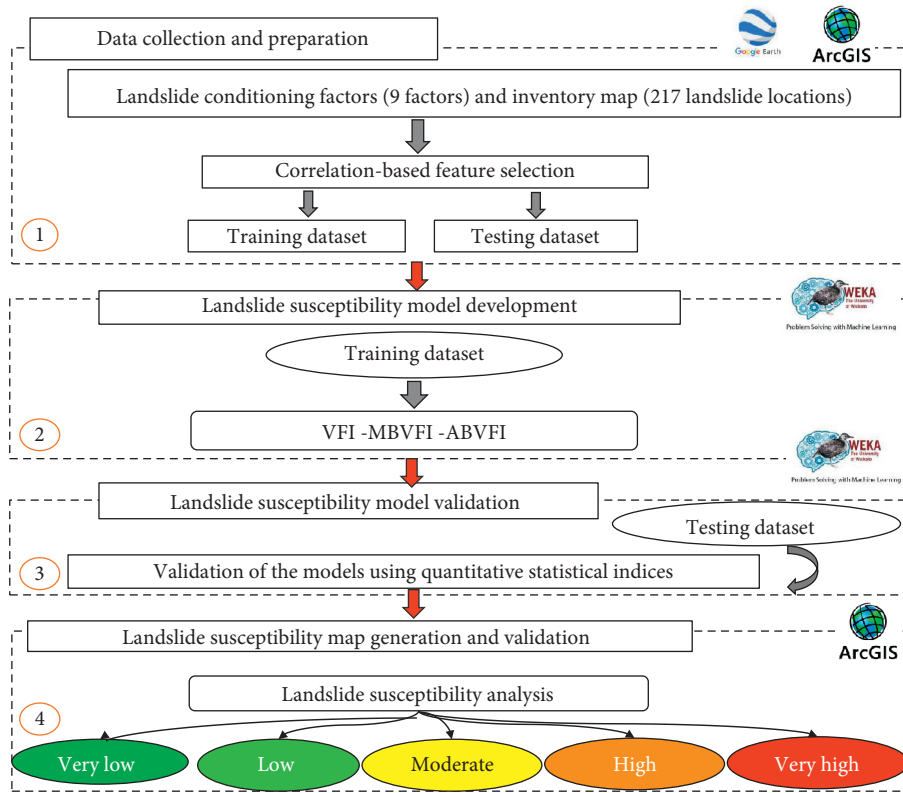


FIGURE 4: Methodological framework of this study.

TABLE 2: Importance of factors using correlation-based feature selection.

Average merit (AM)	Average rank	Landslide conditioning factors
0.437	1	Distance from rivers
0.404	2	Distance from roads
0.336	3	Distance from faults
0.226	4	Aspect
0.126	5.3	Weathering crust
0.115	5.7	Geology
0.076	7.2	Slope
0.054	8.2	Focal flow
0.029	8.6	Curvature

TABLE 3: Model performance using various quantitative indices.

No.	Parameters	Training model			Validation model		
		VFI	MBVFI	ABVFI	VFI	MBVFI	ABVFI
1	TP	101	120	117	47	53	54
2	TN	124	127	131	47	52	52
3	FP	50	31	34	18	12	11
4	FN	27	24	20	18	13	13
5	PPV (%)	66.89	79.47	77.48	72.31	81.54	83.08
6	NPV (%)	82.12	84.11	86.75	72.31	80.00	80.00
7	SST (%)	78.91	83.33	85.40	72.31	80.30	80.60
8	SPF (%)	71.26	80.38	79.39	72.31	81.25	82.54
9	ACC (%)	74.50	81.79	82.12	72.31	80.77	81.54
10	Kappa	0.490	0.636	0.642	0.446	0.615	0.631
11	RMSE	0.463	0.395	0.367	0.473	0.421	0.390

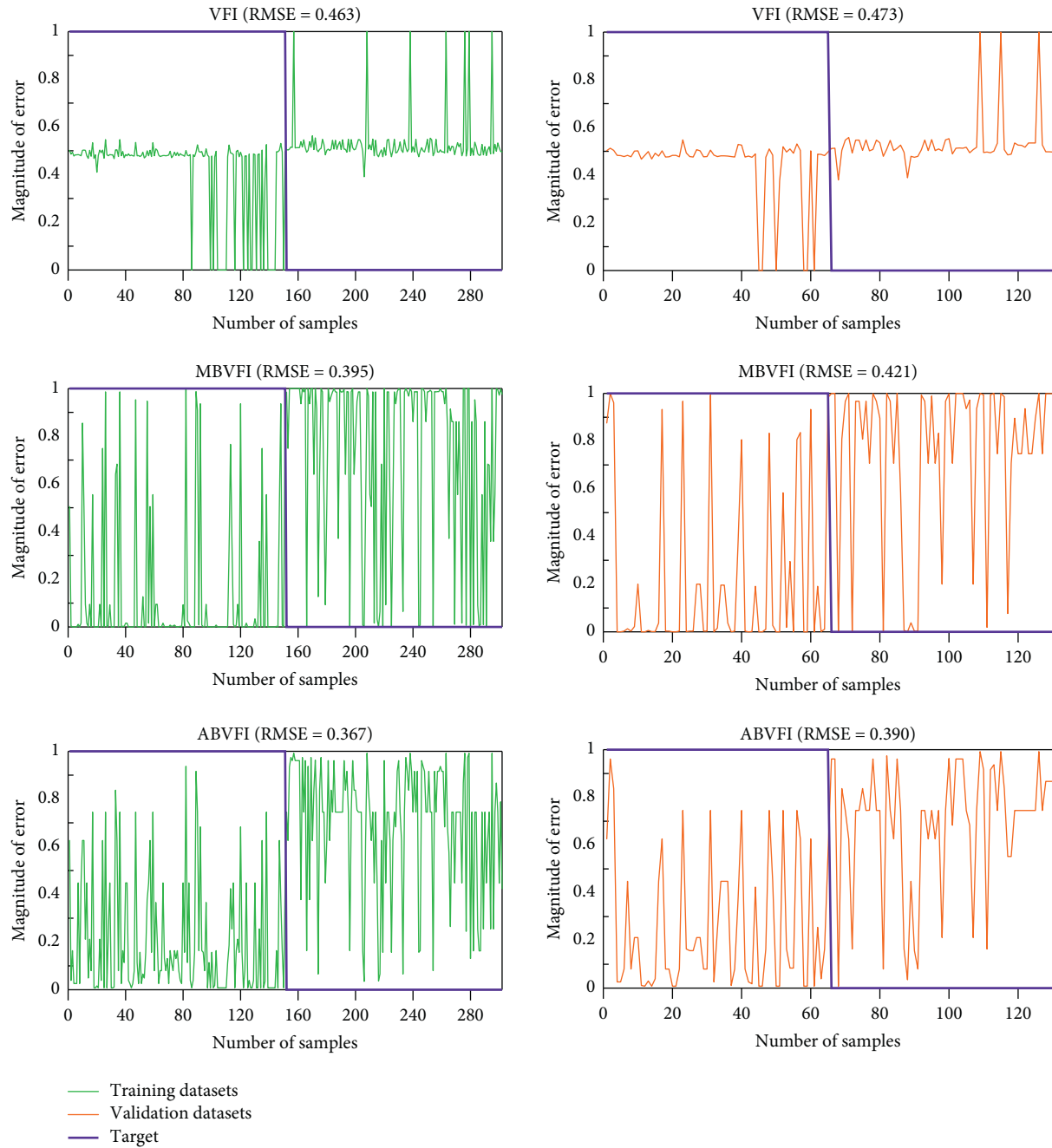


FIGURE 5: RMSE analysis of the models.

performance of ABVFI in comparison to other two models (MBVFI and VFI) is that it uses the AdaBoost ensemble technique, which has many advantages such as (i) it analyses large amount of data efficiently; (ii) it handles uncertainties and performs error analysis in better way; (iii) it optimizes the training dataset, selects the informative features, and provides appropriate weights to features for better data interpretation; and (iv) it is mathematically insensitive to overtraining and training error diverges to zero exponentially [85].

In general, ABVFI achieved the best performance in this study, while comparing to other models. It is noticed that this is the first time AdaBoost and MultiBoost ensemble with VFI as base classifier and were developed as hybrid models (ABVFI and MBVFI) and evaluated for the prediction of landslide susceptibility. Limitation of the study is that we have used data of available 271 landslide events for the development of models. Therefore, we suggest a larger sample size of data in future study to check and refine performance of the models.

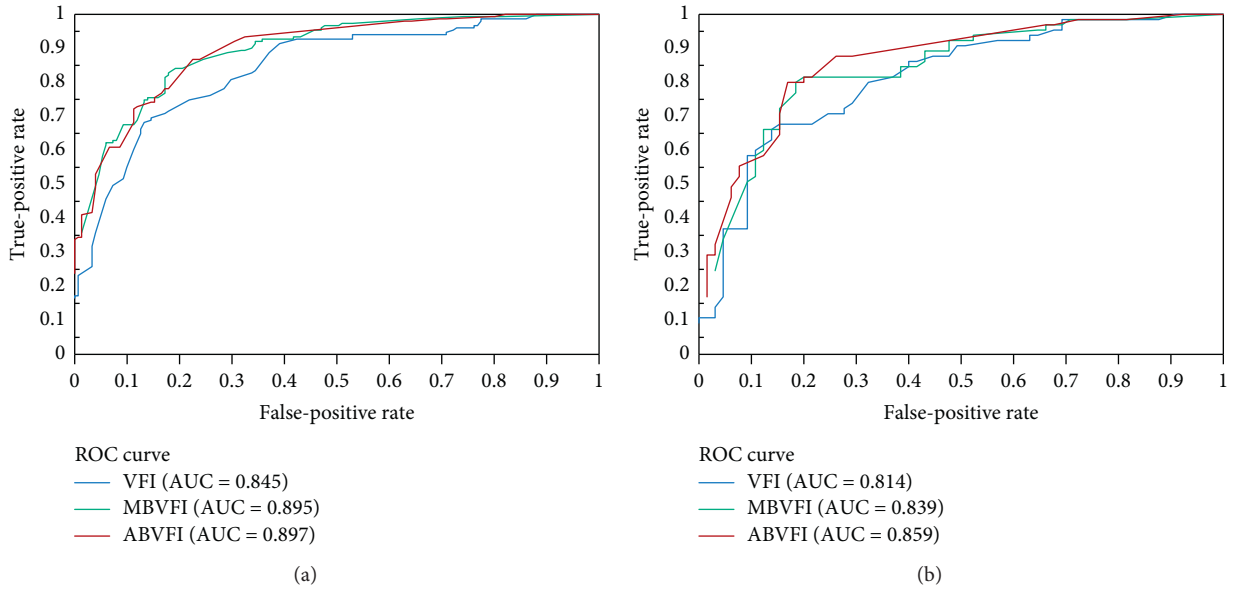


FIGURE 6: Validation and comparison of the models using the ROC curve: (a) training dataset; (b) validating dataset.

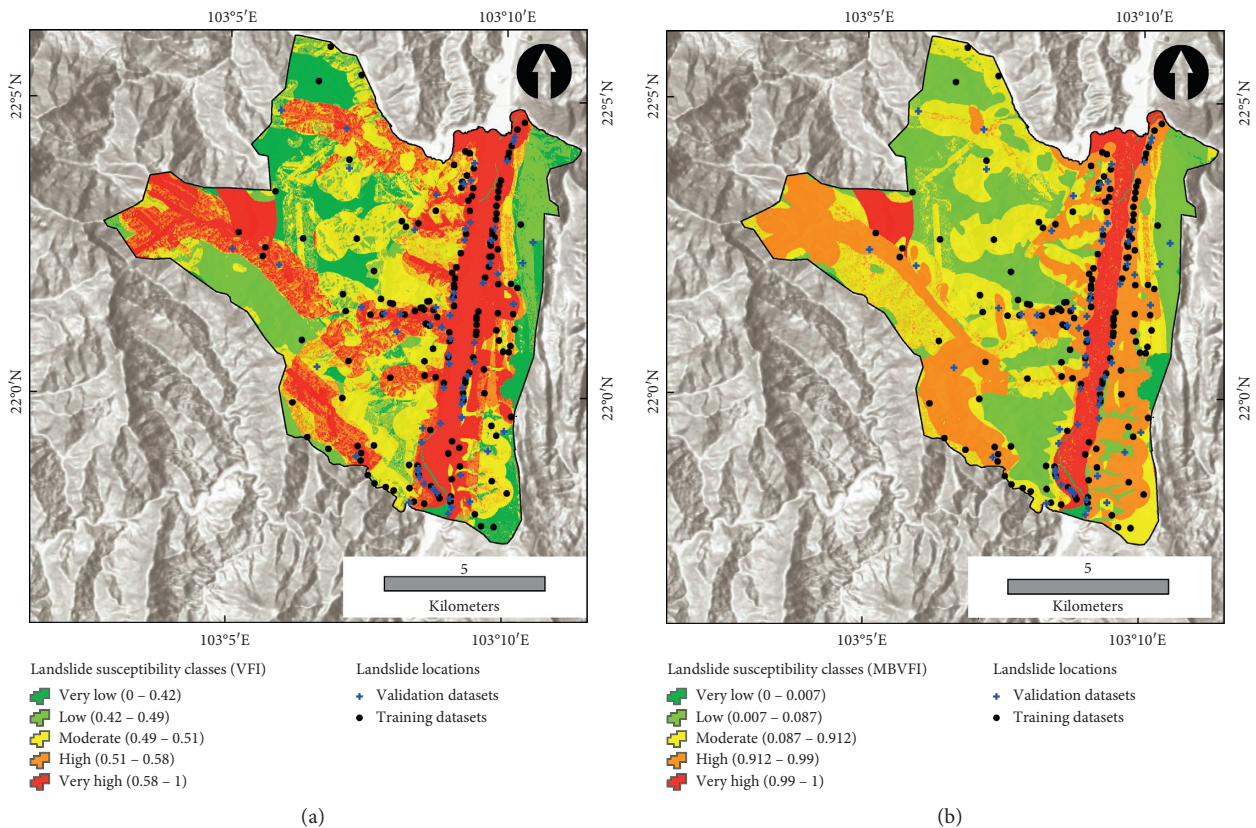


FIGURE 7: Continued.

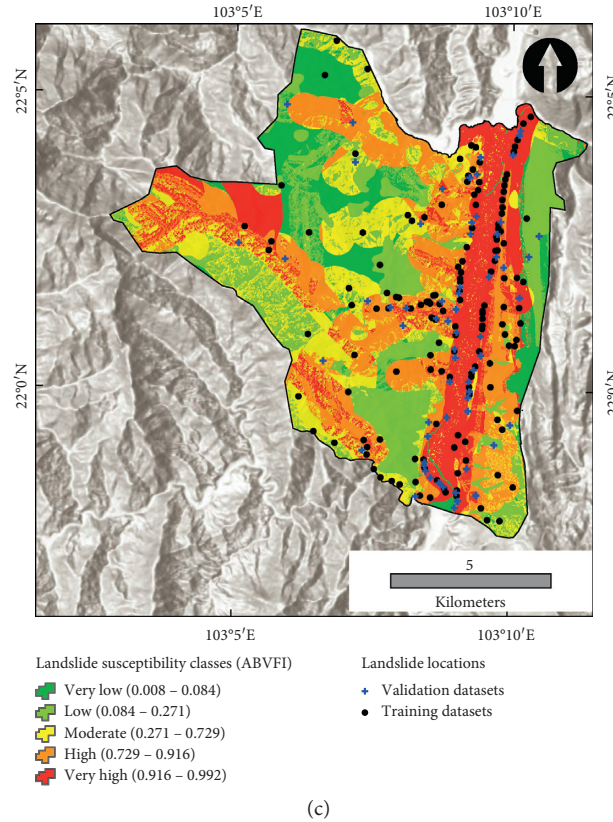


FIGURE 7: Landslide susceptibility maps using different models: (a) VFI; (b) MBVFI; (c) ABVFI.

TABLE 4: Validation of landslide susceptibility maps.

Model	Class	Class pixels	Landslide pixels	% class pixels	% landslide pixels	Frequency ratio
VFI	Very low	11751	0	1.618646	0	0
	Low	196916	6	27.12428	9.230769	0.340314
	Moderate	220244	9	30.3376	13.84615	0.456402
	High	226270	35	31.16765	53.84615	1.727629
	Very high	70796	15	9.751824	23.07692	2.366421
MBVFI	Very low	99237	2	13.66944	3.076923	0.225095
	Low	108692	1	14.97182	1.538462	0.102757
	Moderate	201878	10	27.80777	15.38462	0.553249
	High	82944	5	11.42516	7.692308	0.673278
	Very high	233226	47	32.12581	72.30769	2.250766
ABVFI	Very low	79710	1	10.97969	1.538462	0.140119
	Low	167322	4	23.04784	6.153846	0.267003
	Moderate	146596	9	20.19293	13.84615	0.685693
	High	169770	14	23.38504	21.53846	0.921036
	Very high	162579	37	22.39451	56.92308	2.541832

8. Concluding Remarks

In the present study, spatial landslide susceptibility prediction models, namely, ABVFI and MBVFI with VFI as a base classifier were developed as ensemble or hybrid models, which have emerged as better decision-making tools. The hybrid novel model ABVFI ($AUC = 0.897$) is the best model in comparison to single VFI ($AUC = 0.845$) and other developed hybrid model MBVFI (0.895). Validation and

statistical analysis results show that ABVFI is the most accurate and robust model on both the training and testing datasets. Accurate susceptibility maps generated by this model can be used for safe and economic construction of roads, powerhouses, and other infrastructures. Thus, the ABVFI model can be used for the proper management of landslides in the hilly areas not only in Vietnam but also other areas of the world. In future study, it is proposed to consider excessive rains and drought factors due to climate

change effects for further improvement in prediction capability of landslide susceptibility models.

Data Availability

Some or all data, models, or code that support the findings of this study are available from the corresponding author upon reasonable request.

Conflicts of Interest

The authors declare that they have no conflicts of interest.

Acknowledgments

This research was funded by the Vietnam National Foundation for Science and Technology Development (NAFOSTED) under grant no. 105.08–2019.03.

References

- [1] F. Guzzetti, A. Carrara, M. Cardinali et al., "Landslide hazard evaluation: a review of current techniques and their application in a multi-scale study, Central Italy," *Geomorphology*, vol. 31, no. 1–4, pp. 181–216, 1999.
- [2] O. Kjekstad, "The challenges of landslide hazard mitigation in developing countries," in *Proceedings of the First North American Landslide Conference*, Vail, CO, USA, June 2007.
- [3] T. V. Phong, T. T. Phan, I. Prakash et al., "Landslide susceptibility modeling using different artificial intelligence methods: a case study at Muong lay district, Vietnam," *Geocarto International*, pp. 1–24, 2019.
- [4] D. V. Dao, A. Jaafari, M. Bayat et al., "A spatially explicit deep learning neural network model for the prediction of landslide susceptibility," *Catena*, vol. 188, Article ID 104451, 2020.
- [5] D. T. Mafi-Gholami, B. Pradhan, O. Lofman et al., "Spatial prediction of landslide hazards in Hoa Binh province (Vietnam): a comparative assessment of the efficacy of evidential belief functions and fuzzy logic models," *Catena*, vol. 96, pp. 28–40, 2012.
- [6] T. Can, H. A. Nefeslioglu, C. Gokceoglu et al., "Susceptibility assessments of shallow earthflows triggered by heavy rainfall at three catchments by logistic regression analyses," *Geomorphology*, vol. 72, no. 1–4, pp. 250–271, 2005.
- [7] H. R. Pourghasemi and N. Kerle, "Random forests and evidential belief function-based landslide susceptibility assessment in Western Mazandaran province, Iran," *Environmental Earth Sciences*, vol. 75, no. 3, p. 185, 2016.
- [8] P. M. Atkinson and R. Massari, "Autologistic modelling of susceptibility to landsliding in the Central Apennines, Italy," *Geomorphology*, vol. 130, no. 1–2, pp. 55–64, 2011.
- [9] K. C. Devkota, A. D. Regmi, H. R. Pourghasemi et al., "Landslide susceptibility mapping using certainty factor, index of entropy and logistic regression models in GIS and their comparison at Mugling-Narayanghat road section in Nepal Himalaya," *Natural Hazards*, vol. 65, no. 1, pp. 135–165, 2013.
- [10] D. Q. Yoshida, D. H. Nguyen, I. Prakash et al., "GIS based frequency ratio method for landslide susceptibility mapping at Da Lat city, Lam Dong province, Vietnam," *Vietnam Journal of Earth Sciences*, vol. 42, no. 1, pp. 55–66, 2020.
- [11] B. T. Jaafari, I. Prakash, J. Dou et al., "A novel hybrid approach of landslide susceptibility modelling using rotation forest ensemble and different base classifiers," *Geocarto International*, vol. 35, no. 12, pp. 1267–1292, 2020.
- [12] H. R. Singh, H. R. Moradi, S. M. Fatemi Aghda, C. Gokceoglu, and B. Pradhan, "GIS-based landslide susceptibility mapping with probabilistic likelihood ratio and spatial multi-criteria evaluation models (North of Tehran, Iran)," *Arabian Journal of Geosciences*, vol. 7, no. 5, pp. 1857–1878, 2014.
- [13] T. Gokceoglu, H.-B. Ly, P. T. Trinh et al., "Landslide susceptibility mapping using forest by penalizing attributes (FPA) algorithm based machine learning approach," *Vietnam Journal of Earth Sciences*, vol. 42, no. 3, 2020.
- [14] B. Ghasemian, D. T. Asl, B. T. Pham et al., "Shallow landslide susceptibility mapping: a comparison between classification and regression tree and reduced error pruning tree algorithms," *Vietnam Journal of Earth Sciences*, vol. 42, no. 3, 2020.
- [15] N. Micheletti, L. Foresti, S. Robert et al., "Machine learning feature selection methods for landslide susceptibility mapping," *Mathematical Geosciences*, vol. 46, no. 1, pp. 33–57, 2014.
- [16] M. Leuenberger, "A landslide susceptibility model using the analytical hierarchy process method and multivariate statistics in perialpine slovenia," *Geomorphology*, vol. 74, no. 1–4, pp. 17–28, 2006.
- [17] N. R. Regmi, J. R. Giardino, and J. D. Vitek, "Modeling susceptibility to landslides using the weight of evidence approach: western Colorado, USA," *Geomorphology*, vol. 115, no. 1–2, pp. 172–187, 2010.
- [18] A. Ávila, F. Justino, A. Wilson, and M. Amorim, "Recent precipitation trends, flash floods and landslides in southern Brazil," *Environmental Research Letters*, vol. 11, no. 11, Article ID 114029, 2016.
- [19] H. A. Bromwich, T. Y. Duman, and S. Durmaz, "Landslide susceptibility mapping for a part of tectonic kelkit valley (eastern black sea region of Turkey)," *Geomorphology*, vol. 94, no. 3–4, pp. 401–418, 2008.
- [20] D. B. Simons and T. J. Ward, *Landslide Potential Delineation*, prepared for Colorado State University Experiment Station, Fort Collins, CO, USA, 1979.
- [21] J. Corominas, C. van Westen, P. Frattini et al., "Recommendations for the quantitative analysis of landslide risk," *Bulletin of Engineering Geology and the Environment*, vol. 73, no. 2, pp. 209–263, 2014.
- [22] H. R. Pourghasemi, H. R. Moradi, and S. M. Fatemi Aghda, "Landslide susceptibility mapping by binary logistic regression, analytical hierarchy process, and statistical index models and assessment of their performances," *Natural Hazards*, vol. 69, no. 1, pp. 749–779, 2013.
- [23] D. G. Toll, "Artificial intelligence applications in geotechnical engineering," *Electronic Journal of Geotechnical Engineering*, vol. 1, pp. 767–773, 1996.
- [24] A. Kornejady, M. Ownegh, and A. Bahremand, "Landslide susceptibility assessment using maximum entropy model with two different data sampling methods," *Catena*, vol. 152, pp. 144–162, 2017.
- [25] B. Pradhan, "A comparative study on the predictive ability of the decision tree, support vector machine and neuro-fuzzy models in landslide susceptibility mapping using GIS," *Computers & Geosciences*, vol. 51, pp. 350–365, 2013.
- [26] H. Hong, J. Liu, and A.-X. Zhu, "Modeling landslide susceptibility using logit boost alternating decision trees and forest by penalizing attributes with the bagging ensemble," *Science of the Total Environment*, vol. 718, Article ID 137231, 2020.

- [27] B. T. Pham, T. Nguyen-Thoi, C. Qi et al., "Coupling RBF neural network with ensemble learning techniques for landslide susceptibility mapping," *Catena*, vol. 195, Article ID 104805, 2020.
- [28] W. Phong, H. R. Pourghasemi, A. Kornejady, and N. Zhang, "Landslide spatial modeling: introducing new ensembles of ANN, MaxEnt, and SVM machine learning techniques," *Geoderma*, vol. 305, pp. 314–327, 2017.
- [29] X. Zhang, F. Lin, S. Zhu et al., "Mine landslide susceptibility assessment using IVM, ANN and SVM models considering the contribution of affecting factors," *PloS One*, vol. 14, no. 4, 2019.
- [30] S. A. Naghibi, H. R. Pourghasemi, and K. Abbaspour, "A comparison between ten advanced and soft computing models for groundwater qanat potential assessment in Iran using R and GIS," *Theoretical and Applied Climatology*, vol. 131, no. 3-4, pp. 967–984, 2018.
- [31] P. Vorpahl, H. Elsenbeer, M. Märker, and B. Schröder, "How can statistical models help to determine driving factors of landslides?" *Ecological Modelling*, vol. 239, pp. 27–39, 2012.
- [32] A. Schröder, B. Pradhan, and K. Rezaei, "Assessment of landslide susceptibility using statistical and artificial intelligence-based FR-RF integrated model and multiresolution DEMs," *Remote Sensing*, vol. 11, no. 9, p. 999, 2019.
- [33] W. Lee, X. Xie, J. Wang et al., "A comparative study of logistic model tree, random forest, and classification and regression tree models for spatial prediction of landslide susceptibility," *Catena*, vol. 151, pp. 147–160, 2017.
- [34] Q. Pradhan, Z. Xu, S. Li et al., "Novel entropy and rotation forest-based credal decision tree classifier for landslide susceptibility modeling," *Entropy*, vol. 21, no. 2, 106 pages, 2019.
- [35] H. Hong, J. Liu, D. T. Bui et al., "Landslide susceptibility mapping using J48 decision tree with adaboost, bagging and rotation forest ensembles in the guangchang area (China)," *Catena*, vol. 163, pp. 399–413, 2018.
- [36] W. Pradhan, M. Panahi, and H. R. Pourghasemi, "Performance evaluation of GIS-based new ensemble data mining techniques of adaptive neuro-fuzzy inference system (ANFIS) with genetic algorithm (GA), differential evolution (DE), and particle swarm optimization (PSO) for landslide spatial modelling," *Catena*, vol. 157, pp. 310–324, 2017.
- [37] H. Moayedi, M. Mehrabi, M. Mosallanezhad, A. S. A. Rashid, and B. Pradhan, "Modification of landslide susceptibility mapping using optimized PSO-ANN technique," *Engineering with Computers*, vol. 35, no. 3, pp. 967–984, 2019.
- [38] C. Rashid, F. Dai, X. Xu, and Y. H. Lee, "GIS-based support vector machine modeling of earthquake-triggered landslide susceptibility in the Jianjiang river watershed, China," *Geomorphology*, vol. 145-146, pp. 70–80, 2012.
- [39] W. Lee, H. Shahabi, S. Zhang et al., "Landslide susceptibility modeling based on gis and novel bagging-based kernel logistic regression," *Applied Sciences*, vol. 8, no. 12, p. 2540, 2018.
- [40] B. T. Khosravi and I. Prakash, "A novel hybrid model of bagging-based naïve bayes trees for landslide susceptibility assessment," *Bulletin of Engineering Geology and the Environment*, vol. 78, no. 3, pp. 1911–1925, 2019.
- [41] S. Lee, "Application of logistic regression model and its validation for landslide susceptibility mapping using GIS and remote sensing data," *International Journal of Remote Sensing*, vol. 26, no. 7, pp. 1477–1491, 2005.
- [42] E. K. Sahin, I. Colkesen, and T. Kavzoglu, "A comparative assessment of canonical correlation forest, random forest, rotation forest and logistic regression methods for landslide susceptibility mapping," *Geocarto International*, vol. 35, no. 4, pp. 341–363, 2020.
- [43] W. Chen, X. Xie, J. Peng, J. Wang, Z. Duan, and H. Hong, "GIS-based landslide susceptibility modelling: a comparative assessment of kernel logistic regression, naïve-bayes tree, and alternating decision tree models," *Geomatics, Natural Hazards and Risk*, vol. 8, no. 2, pp. 950–973, 2017.
- [44] H. Wang, H. Shahabi, A. Shirzadi et al., "Landslide susceptibility assessment at the wuning area, China: a comparison between multi-criteria decision making, bivariate statistical and machine learning methods," *Natural Hazards*, vol. 96, no. 1, pp. 173–212, 2019.
- [45] J.-C. Chen, S. Lee, and H.-S. Jung, "Landslide susceptibility mapping using random forest and boosted tree models in Pyeong-Chang, Korea," *Geocarto International*, vol. 33, no. 9, pp. 1000–1015, 2018.
- [46] S. Lee and J. Choi, "Landslide susceptibility mapping using GIS and the weight-of-evidence model," *International Journal of Geographical Information Science*, vol. 18, no. 8, pp. 789–814, 2004.
- [47] G. Demiröz and H. A. Güvenir, "Classification by voting feature intervals," in *Proceedings of the European Conference on Machine Learning*, Springer, Berlin, Germany, pp. 85–92, April 1997.
- [48] K. Marsolo, M. Twa, and M. A. Bullimore, "Spatial modeling and classification of corneal shape," *IEEE Transactions on Information Technology in Biomedicine*, vol. 11, no. 2, pp. 203–212, 2007.
- [49] H. A. Parthasarathy, G. Demiröz, and N. İlter, "Learning differential diagnosis of erythematous-squamous diseases using voting feature intervals," *Artificial Intelligence in Medicine*, vol. 13, no. 3, pp. 147–165, 1998.
- [50] B. T. Pham, D. T. Bui, I. Prakash et al., "A comparative study of sequential minimal optimization-based support vector machines, vote feature intervals, and logistic regression in landslide susceptibility assessment using GIS," vol. 76, no. 10, p. 371, 2017.
- [51] R. Del Gaudio, G. Batista, and A. Branco, "Coping with highly imbalanced datasets: a case study with definition extraction in a multilingual setting," *Natural Language Engineering*, vol. 20, no. 3, pp. 327–359, 2014.
- [52] Y. Freund and L. Mason, "The alternating decision tree learning algorithm," in *ICML '99: Proceedings of the Sixteenth International Conference on Machine Learning*, pp. 124–133, Bled, Slovenia, June 1999.
- [53] H. Schwenk and Y. Bengio, "Boosting neural networks," *Neural Computation*, vol. 12, no. 8, pp. 1869–1887, 2000.
- [54] Y. Freund, R. E. Schapire, and R. Schapire, "Experiments with a new boosting algorithm," in *Thirteenth International Conference on ML*, pp. 3–6, Bari, Italy, July 1996.
- [55] S.-J. Wang, A. Mathew, Y. Chen et al., "Empirical analysis of support vector machine ensemble classifiers," *Expert Systems with Applications*, vol. 36, no. 3, pp. 6466–6476, 2009.
- [56] G. I. Xi, "Multiboosting: a technique for combining boosting and wagging," *Machine Learning*, vol. 40, no. 2, pp. 159–196, 2000.
- [57] V.-T. Nguyen, T. H. Tran, N. A. Ha et al., "GIS based novel hybrid computational intelligence models for mapping landslide susceptibility: a case study at da lat city, Vietnam," *Sustainability*, vol. 11, no. 24, p. 7118, 2019.
- [58] P. T. Ngo, D. H. Ha, H. D. Nguyen et al., "Improvement of credal decision trees using ensemble frameworks for groundwater potential modeling," *Sustainability*, vol. 12, no. 7, p. 2622, 2020.

- [59] M. Van Phong, E. Benetos, C. Kotropoulos et al., "A neural network approach to audio-assisted movie dialogue detection," *Neurocomputing*, vol. 71, no. 1-3, pp. 157–166, 2007.
- [60] D. Tien Bui, B. T. Pham, and Q. P. Nguyen, "Spatial prediction of rainfall-induced shallow landslides using hybrid integration approach of least-squares support vector machines and differential evolution optimization: a case study in central Vietnam," *International Journal of Digital Earth*, vol. 9, no. 11, pp. 1077–1097, 2016.
- [61] M. Hoang, S. Janizadeh, D. Tien Bui et al., "A tree-based intelligence ensemble approach for spatial prediction of potential groundwater," *International Journal of Digital Earth*, pp. 1–22, 2020.
- [62] H. Pham, B. Jarihani, S. Tavakkoli Piralilou, M. Avand, and O. Ghorbanzadeh, "A semi-automated object-based gully networks detection using different machine learning models: a case study of bowen catchment, queensland, Australia," *Sensors*, vol. 19, no. 22, p. 4893, 2019.
- [63] B. T. Chittleborough, T. V. Phong, T. Nguyen-Thoi et al., "Ensemble modeling of landslide susceptibility using random subspace learner and different decision tree classifiers," *Geocarto International*, pp. 1–23, 2020.
- [64] B. T. Parial, M. Avand, S. Janizadeh et al., "GIS based hybrid computational approaches for flash flood susceptibility assessment," *Water*, vol. 12, no. 3, p. 683, 2020.
- [65] H.-B. Ly, P. G. Asteris, and B. Pham, "Accuracy assessment of extreme learning machine in predicting soil compression coefficient," *Vietnam Journal of Earth Sciences*, vol. 42, no. 1, 2020.
- [66] B. T. Pham, S. K. Singh, and H.-B. Ly, "Using artificial neural network (ann) for prediction of soil coefficient of consolidation," *Vietnam Journal of Earth Sciences*, vol. 42, no. 1, 2020.
- [67] B. T. Pham, T. Van Phong, T. Nguyen-Thoi et al., "GIS-based ensemble soft computing models for landslide susceptibility mapping," *Estudios Geológicos*, vol. 65, no. 1, pp. 49–65.
- [68] B. T. Pham, A. Jaafari, M. Avand et al., "Performance evaluation of machine learning methods for forest fire modeling and prediction," *Symmetry*, vol. 12, no. 6, p. 1022, 2020.
- [69] P. T. Al-Ansari, D. H. Ha, M. Avand et al., "Soft computing ensemble models based on logistic regression for groundwater potential mapping," *Applied Sciences*, vol. 10, no. 7, p. 2469, 2020.
- [70] A. Jaafari, A. P. Yunus, J. Dou et al., "Machine learning methods for landslide susceptibility studies: a comparative overview of algorithm performance," *Earth-Science Reviews*, vol. 207, Article ID 103225, 2020.
- [71] P. Yariyan, S. Janizadeh, T. Van Phong et al., "Improvement of best first decision trees using bagging and dagging ensembles for flood probability mapping," *Water Resources Management*, vol. 34, no. 9, pp. 3037–3053, 2020.
- [72] B. T. Nguyen, I. Prakash, and A. Jaafari, "Spatial prediction of rainfall-induced landslides using aggregating one-dependence estimators classifier," *Journal of the Indian Society of Remote Sensing*, vol. 46, no. 9, pp. 1457–1470, 2018.
- [73] A. Bui, K. Solaimani, M. H. Roshan et al., "Uncertainties of prediction accuracy in shallow landslide modeling: sample size and raster resolution," *Catena*, vol. 178, pp. 172–188, 2019.
- [74] B. Pham, A. Shirzadi, H. Shahabi et al., "Landslide susceptibility assessment by novel hybrid machine learning algorithms," *Sustainability*, vol. 11, no. 16, p. 4386, 2019.
- [75] W. Omidvar, H. R. Pourghasemi, S. A. Naghibi et al., "Prioritization of landslide conditioning factors and its spatial modeling in Shangnan ccounty, China using GIS-based data mining algorithms," *Bulletin of Engineering Geology and the Environment*, vol. 77, no. 2, pp. 611–629, 2018.
- [76] M. A. Hall, *Correlation-based Feature Selection for Machine Learning*, University of Waikato, Hamilton, NewZealand, 1999.
- [77] B. Thai Pham, D. Tien Bui, I. J. C. E. Prakash et al., "Landslide susceptibility modelling using different advanced decision trees methods," vol. 35, no. 1–4, pp. 139–157, 2018.
- [78] B. T. Pham, B. Pradhan, D. Tien Bui, and M. B. Dholakia, "A comparative study of different machine learning methods for landslide susceptibility assessment: a case study of Uttarakhand area (India)," *Environmental Modelling & Software*, vol. 84, pp. 240–250, 2016.
- [79] G. Prakash, "The data model concept in statistical mapping," *International Yearbook of Cartography*, vol. 7, pp. 186–190, 1967.
- [80] A. Yalcin, S. Reis, and A. C. Aydinoglu, "A GIS-based comparative study of frequency ratio, analytical hierarchy process, bivariate statistics and logistics regression methods for landslide susceptibility mapping in Trabzon, NE Turkey," *Catena*, vol. 85, no. 3, pp. 274–287, 2011.
- [81] S. Park, S. Son, J. Han et al., "Effects of variable selection on the landslide susceptibility assessment using machine learning techniques," in *Proceedings of Earth Resources and Environmental Remote Sensing/GIS Applications X*, Febuary 2019, Article ID 111560M.
- [82] M. Mokarram, H. R. Pourghasemi, and J. P. Tiefenbacher, "Comparison analytic network and analytical hierarchical process approaches with feature selection algorithm to predict groundwater quality," *Environmental Earth Sciences*, vol. 78, no. 21, p. 625, 2019.
- [83] J. L. Fleiss and J. Cohen, "The equivalence of weighted kappa and the intraclass correlation coefficient as measures of reliability," *Educational and Psychological Measurement*, vol. 33, no. 3, pp. 613–619, 1973.
- [84] S. K. Singh, R. W. Taylor, and M. M. Rahman, "Developing robust arsenic awareness prediction models using machine learning algorithms," *Journal of Environmental Management*, vol. 211, no. 1, pp. 25–137, 2018.
- [85] M. Pradhan, M. A. Sadeghi, S. Nourizadeh et al., "Power system security assessment using adaboost algorithm," in *Proceedings of the North American Power Symposium (NAPS)*, Starkville, MS, USA, October 2009.

Research Article

The Optimization Research of Diesel Cylinder Gasket Parameters Based on Hybrid Neural Network and Improved Grey Wolf Algorithm

Yi Dong,¹ Jianmin Liu,¹ Yanbin Liu ,¹ Xinyong Qiao ,¹ Xiaoming Zhang,¹ Qi Kang,² and Tianqi Wang¹

¹Vehicle Engineering Department, Army Academy of Armored Forces, Beijing 100072, China

²China Satellite Maritime Tracking and Controlling Department, Jiangyin 214431, China

Correspondence should be addressed to Yanbin Liu; aafelyb@163.com

Received 6 July 2020; Revised 18 September 2020; Accepted 28 September 2020; Published 10 October 2020

Academic Editor: Diyuan Li

Copyright © 2020 Yi Dong et al. This is an open access article distributed under the Creative Commons Attribution License, which permits unrestricted use, distribution, and reproduction in any medium, provided the original work is properly cited.

In order to improve reliability and fatigue life of cylinder gaskets in heavy duty diesel engine, several methods and algorithms are applied to optimize operating factors of gaskets. Finite element method is utilized to figure out and analyze the temperature fields, thermal-mechanical coupling stress fields, and deformations of gasket. After determining the maximum values of three state parameters, the orthogonal experimental design method is adopted to analyze the influence rules of five operating factors on three state parameters of the gaskets and four factors which most significantly affect these state parameters are determined. Then, the method which uses operating factors to predict state parameters is established on the application of hybrid neuron network based on partial least squares regression and deep neural network. The comparison results between the predicted values and real values verified the accuracy of the hybrid neuron network method. Based on artificial bee colony algorithm, improvement is attached to the way three kinds of grey wolves locate preys in grey wolf algorithm and the way how using different hierarchy wolves in grey wolf algorithm to determine three weight coefficients and the location of prey is put forward with. The method using artificial bee colony algorithm to optimize the grey wolf algorithm is called ABC and GWO. The proposed HNN and the ABC and GWO method are applied to work out operating factors values which correspond to optimal state parameters of gasket, and the gaskets are optimized according to the optimal values. It has been demonstrated by finite element analysis results that maximum temperature, maximum coupling stress, and the maximum deformation decrease to 6 K, 12.57 MPa, and 0.0925 mm compared to the original values, respectively, which proves the accuracy of the algorithm and the validity of the improvement.

1. Introduction

Cylinder gaskets are critical to reliable sealing and stable operating of diesel engine. However, they are not only subjected to the scour from high-temperature gas, but also subjected to the pressure of cylinder heads, bodies, and the bolt preload forces during operation, the operating environment of which is very harsh. The area between the coolant flow channel and the combustor especially should bear not only the heat transfer from high-temperature gas and the heat dissipation of coolant, but also the explosive pressure and the bolt preload. In consequence, it is much

likely for the gaskets to suffer fatigue damage failure. Thus, the detailed research on the temperature, stress, and deformation of the area mentioned is significant for ensuring the safe and reliable work of gaskets so as to improve the reliability and the performance index of diesel engine.

There are many researches which focus on the diesel engine and its high-temperature components, the research subject including combustion [1], engine performance [2], injection [3], fault diagnosis [4], mixture fuel [5], and waste heat recovery [6]. Kumar et al. [7] investigated the performance (emission and quality of the fuel) of engine using the diesel alcohol blend as the fuel. To compare the

difference of the fuel, they conducted a series of experiment in different situations to observe the performance of engine, including different operating load, different fuel component, and different operating speed. Results show that the diesel alcohol blend fuel has a better performance than other fuels and that methanol has a better emission performance than other fuels. Wei et al. [8] researched the problem about soot properties and its generating process. They investigated the macroscopic shape, nanostructure, and thermophysical properties of the soot. Results show that dimethyl carbonate diesel blends can generate smaller soot than other fuels and that macroscopic shape has less influence than nanostructure on the soot generation process. Subramaniam et al. [9] studied the properties of algae blend fuel and used the single cylinder diesel engine to do the experiment about the fuel. The experimental condition includes various algae volume, and the output parameters to be compared are thermal efficiency of engine, fuel consumption per unit output power, temperature of exhaust, and some properties of combustion. Results show that A20 has the better properties than the other blend fuels. Jabbr et al. [10] researched the performance of dual fuel engine. In order to figure out the influence rule of parameters and the balance of the state factors, they used the method of analysis of variance and genetic algorithm and neuron network. Results show that increasing the ratio of hydrogenated oil can reduce the soot generation and improve the performance of combustion. Allam et al. [11] studied the economic efficiency and air filter of the diesel engine. Zhang [12] studied the influence rule of boiling heat transfer on the performance of diesel engine. They verified the simulation results of boiling heat transfer and the general heat transfer. They also used the perturbation method to investigate parameters of diesel engine.

As for the high temperature in the engine, the researches focused on the cylinder liner [13], piston [14], cylinder head [15], cylinders [16], crank [17], shaft [18], and so on. Zhaoju et al. [19] studied the thermal-mechanical coupling stress of the piston. Based on the calculated results, they optimized the piston about its top height and its pin bore using the response surface method. Results show that the geometry of piston does not have obvious effect on the temperature and stress of the piston. At last, to decrease the maximum stress and mass of piston, they used the multiobjective optimization method to optimize the piston. Wang et al. [20] studied the fatigue rule of the piston alloy and come up with a life prediction method to evaluate the working state and left life of the piston. They studied the properties of piston among high and low temperature. Based on the model and the calculation results, they provided the optimal strategy to guarantee the reliability and working life of piston alloy. Wang et al. [21] researched the seal of cone using the method of finite element method. They established the model of cone combing with gasket, considering the effect of relaxation and long time working, and studied the leakage rule of the cone at the different conditions. This study can contribute to the reliability of satellite and its seal performance. Liu et al. [22] studied the experimental method to measure the heat transfer coefficient of refrigerator gasket. They used the

reverse heat loss method to specify the heat flow through the gasket. To guarantee the experimental results, they used three gaskets and divided the heat transfer area small enough to measure the heat transfer condition. By experiment and analysis, they find some methods which could enhance the seal ability and could decrease the heat transfer coefficients. Rashnoo et al. [23] used two methods to optimize the alloy used in cylinder gasket, which is different displacement rates and reinforcement. To figure out the influence of these two factors, they used the method of sensitivity analysis and regression analysis. Results show that the reinforcement has more influence on the alloy strength and that the alloy microstructure will be better after the reinforcement.

The orthogonal experiment method is applied in the research widely; the related subject and issues are composite material [24], road construction [25], plasma spray [26], batteries [27], alloy powder [28], and concrete properties [29]. Subramani et al. [30] explored the method to improve the quality of exhaust and minimize the variation of performance of engine. They selected a single cylinder engine and its eight factors to perform the study. The target objective of the research is the quality of the exhaust and engine performance and the method used in this study are taguchi design, analysis of variance, and the response surface methodology. Nagasankar et al. [31] researched the welding process of the exhaust value of engine. They used the orthogonal experiment to investigate the influence rule of pressure, time, and other factors on the welding quality. Based on the calculation results, they conducted the multiple liner regression and variance analysis.

The applied fields of hybrid neural network are more and more wide with the development of the algorithm. The related research areas are stock market [32], language identification [33], property prediction [34], life prediction of component [35], emotion recognition [36], and so on. Baklacioglu et al. [37] used a new method to establish the mathematical model of engine; the method is hybrid genetic algorithm artificial neuron network strategy. In the calculation process, five state parameters of engine are set as input factors and the condition of the main components as output. Results show that the method has a good prediction accuracy. Jiang et al. [38] conducted the output prediction of the engine using artificial neuron network. They established two improved artificial neuron networks for two engines and used the extended database to train the model. Results show that two improved networks have more prediction accuracy than the original network and that the improved networks have better robustness when facing different datasets. Fagundez et al. [39] established the model of engine with the methods of artificial neuron network and particle swarm optimization artificial neuron network, respectively. Results show that both algorithms are applicable for the prediction of performance of engine. It can be concluded that the particle swarm optimization artificial neuron network method has more prediction accuracy in emissions compared to artificial neuron network. Chen et al. [40] studied the effectiveness of fault diagnosis using hybrid neuron network based on the extensive experiment data. During the process of training and diagnosis, they captured the feature

of data by method of convolutional and recurrent computing and trained the network by method of convolutional and recurrent backpropagation algorithm. Results show that the method is verified to do the diagnosis. Cui et al. [41] studied the predictive method of fuel saving on the washing engine; the method they used was singular value decomposition, convolutional neural network, and empirical mode decomposition. To improve the prediction accuracy, they replaced the continuous flight data by discrete data to train the model which would be used to predict the quantity of fuel savings.

There are many researches that focus on grey wolf optimization, which are related to grid [42], fuel cell [43], robot controlling [44], blend fuel [45], engines [46], forecasting of investment [47], and so on. Gujarathi et al. [46] optimized the engine with grey wolf algorithm for its performance and emissions. In the optimization process, a wide range of parameters are considered, including specific fuel consumption, hydrocarbon, carbon monoxide, nitrogen oxide, and particulate matters. Results show that grey wolf algorithm can find the optimal values with least costs. Ileri et al. [45] studied the optimization problem of cetane concentration in blend fuel used in diesel engine. They conducted a series of experiment under different conditions and using the grey wolf algorithm to find the optimal results of the blend. At the optimization process, they took the performance of engine and emission of combustion into consideration. At last they find the optimal fuel composition under different conditions and calculate the performance results. Luo et al. [48] come up with an improved grey wolf algorithm by improving the weight of leader wolf location. Considering the convergence speed and the optimization accuracy, the new algorithm is better than the original one. The new algorithm has a low cost when calculating the actual engineering problems. Vijay and Nanda [49] optimized the grey wolf algorithm with three strategies which are prey weight, control level, and both of them. They compared the new algorithm's performance with other five algorithms and the compared parameters are data scalability, noise, and algorithm parameter. Results show that the new algorithm has advantage in solving engineering problems.

The paper mainly optimizes the operating factors of cylinder gaskets based on their maximum temperature, maximum stress, and maximum deformation. The methods involved in the process mainly contain finite element method, orthogonal experimental design, a hybrid neural network model based on partial least squares regression and deep neural network, and grey wolf optimization algorithm based on an artificial bee colony algorithm. In different parts, the corresponding research contents are described below. In Part 1, FEM is utilized to figure out and analyze temperature fields, thermal-mechanical coupling stress fields, and deformations of cylinder gaskets and to analyze areas where operating conditions are comparatively poor. In Part 2, orthogonal experimental design method is adopted to calculate and analyze the influence rules of five operating factors (i.e., the diameter of the combustion chamber circle, the diameter of coolant channel, the length of thermal insulation area between the 3rd and 4th cylinders, the

thickness of cylinder gasket, and bolt preload force) on three state parameters of the cylinder gaskets (i.e., the maximum temperature, maximum stress, and maximum deformation of the gasket), and the four operating factors which most significantly affect these state parameters are determined. In Part 3, a hybrid neural network based on partial least squares regression and deep neural network is applied to establish the corresponding relationship between 4 operating factors and 3 state parameters. In Part 4, on the foundation of grey wolf algorithm, three different weight coefficients are introduced to weigh the locations of three kinds of grey wolves so as to figure out the preys' location in a more accurate way. In addition, artificial bee colony algorithm is also adopted to calculate three weight coefficients. In Part 5, the optimal operating factors of the gaskets can be determined by the calculation in combination with the hybrid neural network and the improved grey wolf algorithm.

1.1. Analysis of Cylinder Gasket Working Condition. As the most important sealing component in diesel engine [50], cylinder gaskets function with the primary goals of reliable combustor and coolant channel sealing by virtue of material elasticity. In practice, not only are cylinder gaskets subjected to bolt preload forces and scour from high-temperature and high-pressure gases inside the cylinder, but some areas in them exposed to the coolant may be corroded. In this consideration, cylinder gaskets should meet the following requirements [51]. With certain flexibility and elasticity, they are capable of compensating for roughness and deformation on the interface; with sufficient mechanical strength, they have the ability to support bolt preload forces and the subsidiary loads generated by interface deformation, and under actions of high-pressure gases, it is less likely for gasket to be damaged; with heat and corrosion resistance, they cannot be easily eroded by cooling liquid and no ablation takes under actions of high-temperature gases; at last, with convenient assembly and disassembly, they can be capable of recycling and have a long service life.

According to the proposed working process model of diesel engine and data achieved by experiments, boundary conditions are figured out for temperature fields and thermal-mechanical coupling stress fields of cylinder gaskets. As measured through experiment, bolt preload force of gaskets on the diesel engine turns out to be 153.8 kN. To calculate the temperature of gasket accurately, a coupling heat transfer model is established specific to high-temperature parts inside the diesel including cylinder head, cylinder gasket, cylinder body, and cylinder sleeve. In this manner, temperature field of the cylinder gasket is acquired.

Temperature fields of the cylinder gasket have been presented in Figure 1. To validate accuracy of these results, the real temperature of the cylinder gasket in engine is measured. Considering that the gasket is located between cylinder body and head, only its exterior area can be measured under the circumstance that the diesel engine is not dismantled. The location of measuring points is shown in Figure 2. Comparison between experimental values and

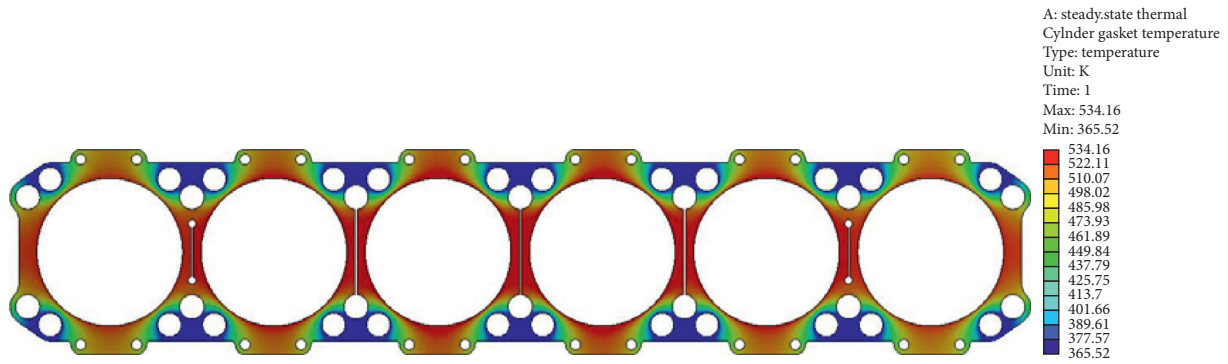


FIGURE 1: The results of gasket temperature field.

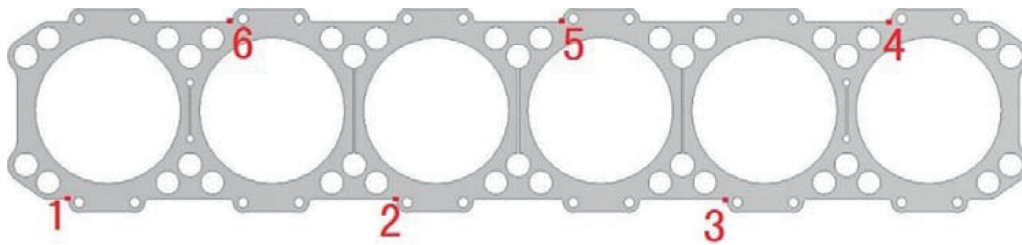


FIGURE 2: The schematic diagram of experimental measuring point arrangement for gasket temperature fields.

the calculated values is listed in Table 1. As can be observed from Table 1, the maximum error between the calculated value and the experimental value is 7.1%, which satisfies the accuracy requirement of engineering calculation.

As shown in Figure 1, maximum temperature (534.16 K) of the gasket is achieved at the middle position between the 3rd and the 4th cylinders, and such a position is in contact with the combustor. Moreover, the minimum temperature is 365.52 K, found nearby the coolant channel. Overall, cylinder gaskets with moderate temperature values are faced with a high-temperature gradient; with the conditions that materials are soft and flexible, great importance should be attached to their temperature and stress conditions.

The thermal-mechanical coupling stress field of the cylinder gasket at the moment of maximum explosion pressure of first cylinder is presented in Figure 3. Clearly, it is revealed by this figure that maximum thermal-mechanical coupling stress of the gasket is 246.17 MPa, found in the position next to the coolant channel of first cylinder. Besides the action of scour generated by the explosion pressure within the cylinder, such an area is also under the influence of heat transfer from high-temperature gas, heat dissipation to the coolant, and heavy mechanical and thermal loads. Therefore, its thermal-mechanical coupling stress is comparatively high. Additionally, this figure also reflects that the influence of the maximum explosion pressure on cylinder gaskets is only limited to areas close to the first cylinder. This signifies that bold preload force, together with interaction of cylinder body and head, plays a favorable role in fixing and supporting the cylinder gasket.

As for deformation of cylinder gasket, it is presented in Figure 4. Here, maximum deformation of the cylinder gasket

is 0.3771 mm, which principally takes place in exterior areas of 1st and 6th cylinders. Moreover, the deformation is appeared to gradually increase from the center towards both sides of the gasket.

Through analysis on temperature fields, thermal-mechanical coupling stress fields, and the deformation condition of cylinder gaskets, it is found that thermal-mechanical coupling stress is rather high at the area near the coolant channel. In addition, deformation condition of both sides is still considerable. Considering that materials are soft, it is much likely for cylinder gaskets to suffer fatigue failure and damage. Hence, research on operating factors optimization is carried out in the following parts.

2. Analysis of Cylinder Gasket Operating Factors based on Orthogonal Experiment

2.1. Experimental Design. As can be known from the above analysis, coupling stress and deformations of cylinder gaskets are comparatively high in the process of their operation. For this reason, orthogonal experimental design was conducted to realize optimal design of such gaskets and further identify the optimal operating factors. It is shown by calculation result that gasket temperature reaches its maximum value in the area nearby the “combustion chamber circle,” and the maximum stress is found in the area between the “combustion chamber circle” and the “coolant channel circle.” The most serious condition of gasket occurred at the area between 3rd and 4th cylinders. In this context, the following five factors are selected to be optimized, including “radius of combustion chamber circle, A,” “radius of coolant

TABLE 1: The comparison between experimental and calculated temperature values of the gasket.

Measuring points	1	2	3	4	5	6
Experimental values	414.73	417.59	412.711	420.054	417.4528	422.839
Calculated values	391.81	414.75	432.88	446.83	447.10	440.32
Errors (%)	5.53	0.68	-4.89	-6.37	-7.10	-4.13

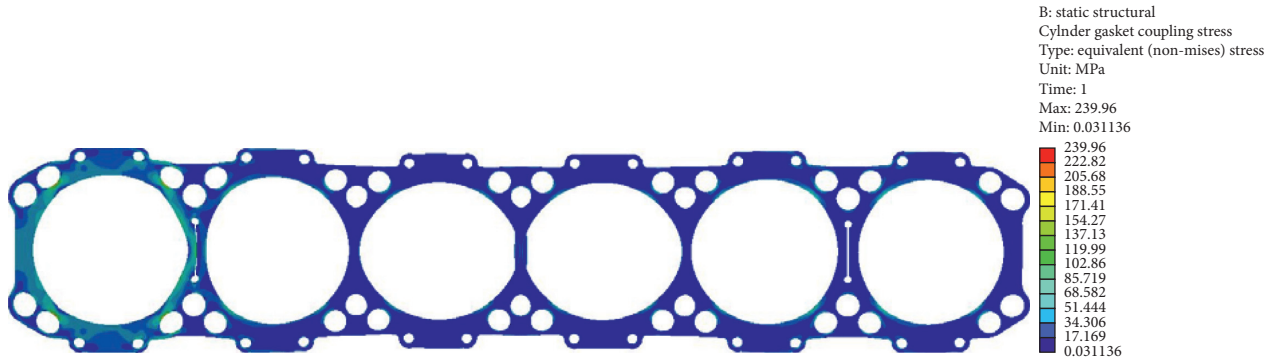


FIGURE 3: The schematic diagram of thermal-mechanical coupling stress distribution of cylinder gasket.

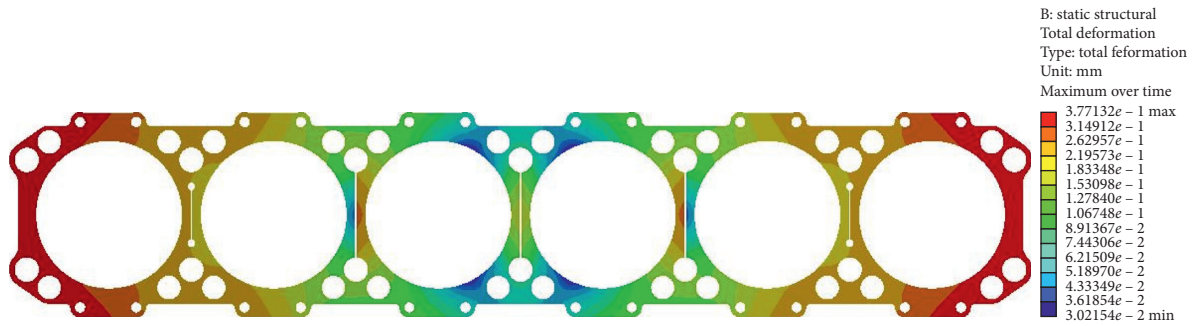


FIGURE 4: The schematic diagram of cylinder gasket deformations.

channel, B,” “length of insulation area between 3rd and 4th cylinder, C,” “thickness of cylinder gasket, D,” and “bolt preload force, E.”

The experiment is concerned with 5 levels in total, which means, for each factor, 5 values were selected for computational analysis. The corresponding levels of different factors are listed in Table 2. Here, the table of $L_{25}(5^6)$ was adopted to fulfill the experimental design. $L_{25}(5^6)$ means that this table totally consists of 25 experiments, 6 factors in each experiment and 5 values corresponding to each factor. For details, please refer to the left section of Table 3.

2.2. Statistical Analysis of Experimental Results. As orthogonal experimental design is performed for cylinder gaskets, corresponding maximum temperature T_{max} , maximum coupling stress S_{max} , and maximum deformation D_{max} of gasket were, respectively, figured out. The computing results have been listed in Table 3.

It is clear in Table 4 that the minimum value of T_{max} is 524.16K, obtained from the experimental group 3, while

TABLE 2: The levels of different factors.

Factors	A	B	C	D	E
1	153	23	1	2	133.8
2	154	24	1.25	2.5	143.8
3	155	25	1.5	3	153.8
4	156	26	1.75	3.5	163.8
5	157	27	2	4	173.8

minimum values of S_{max} and D_{max} , respectively, 225.18 MPa and 0.2075 mm, are found in experimental groups 22 and 14, respectively. Additionally, relevant results should be further analyzed, which is shown in Table, because optimal values of three state parameters are acquired from different groups of experiments and it is impossible to evaluate influence rules of various factors merely dependent on their optimal values.

Tables 1 to 5 represent sums of state parameters’ values corresponding to levels 1–5 of various factors; Max and Min stand for maximum and minimum values of 5 data in the corresponding columns, and R is the difference between

TABLE 3: The arrangement and computing results of experiment.

Number	A	B	C	D	E	F	T_{\max}	S_{\max}	D_{\max}
1	1	1	1	1	1	1	536.24	243.51	0.4844
2	1	2	2	2	2	2	534.47	242.7	0.285
3	1	3	3	3	3	3	524.16	230.02	0.3095
4	1	4	4	4	4	4	534.99	237.63	0.3509
5	1	5	5	5	5	5	536.12	250.01	0.4496
6	2	1	2	3	4	5	531.18	253.76	0.3629
7	2	2	3	4	5	1	536.85	226.73	0.4253
8	2	3	4	5	1	2	533.37	251.56	0.4963
9	2	4	5	1	2	3	536.45	225.64	0.3836
10	2	5	1	2	3	4	535.8	229.66	0.3501
11	3	1	3	5	2	4	531.38	256.49	0.3825
12	3	2	4	1	3	5	533.18	233.61	0.3853
13	3	3	5	2	4	1	531.62	243.36	0.2488
14	3	4	1	3	5	2	531.3	235.74	0.2075
15	3	5	2	4	1	3	534.81	245.86	0.4761
16	4	1	4	2	5	3	536.38	247.56	0.3223
17	4	2	5	3	1	4	531.18	244.87	0.4411
18	4	3	1	4	2	5	535.67	247.27	0.3581
19	4	4	2	5	3	1	535.87	232.76	0.3543
20	4	5	3	1	4	2	533.99	242.24	0.3447
21	5	1	5	4	3	2	536.4	261.49	0.2194
22	5	2	1	5	4	3	532.73	225.18	0.2978
23	5	3	2	1	5	4	531.76	233.14	0.3444
24	5	4	3	2	1	5	532.71	238.26	0.3775
25	5	5	4	3	2	1	533.86	243.55	0.3265

Max and Min. “Tem,” “Str,” and “Def” are temperature, stress, and deformation of the gasket, respectively.

As observed from the table, factors A and D have great influence on deformations of gasket; coupling stress of gasket is dramatically affected by factor B, and temperature of gasket is under high influence of factor D. Considering that three parameters (i.e., temperature, stress, and deformation) are associated with factors A, B, and D, it is difficult to comprehensively confirm gasket’s optimization conditions simply depending on the table. For this reason, experimental results are further analyzed by a variance analysis method.

2.3. Variance Analysis of Experimental Results. During variance analysis on experimental results, mathematical statistics method is used to be sure whether differences in experimental results are incurred by differences in levels corresponding to factors or by experimental errors [52]. In this way, influence of various factors on experimental results may be analyzed in a more intuitive manner.

Firstly, the sum of squares of deviations can be expressed in the following equation as far as various factors are concerned:

$$S_i^2 = \frac{I_i^2 + II_i^2 + III_i^2 + IV_i^2 + V_i^2}{n_{sp}} - \frac{T^2}{n_z} \quad (1)$$

In the above equation, i is the number of column and is equal to 1–5; n_{sp} is level repeat number and is 5 in this article; T and n_z , respectively, refer to summation and the total

number of data, where $n_z = 25$. In this case, factors’ degree of freedom that corresponds to the sum of squares of deviations can be written into the following equation:

$$f_i = n_{sp} - 1. \quad (2)$$

After sums of squares of deviations of all factors have been worked out, error sums of squares of experimental results can be obtained based on the following equation:

$$S_e^2 = S_T^2 - S_1^2 - S_2^2 - S_3^2 - S_4^2 - S_5^2. \quad (3)$$

In line with the following formula:

$$S_T^2 = \sum S_i^2. \quad (4)$$

The error sum of squares here can be expressed as follows:

$$S_e^2 = S_6^2. \quad (5)$$

Afterwards, mean square values are obtained in accordance with the following equation:

$$F_i = \frac{S_i^2/f_i}{S_e^2/f_e}. \quad (6)$$

If the critical value of F is close to 1, it indicates that influence of level variations on state parameters is similar to that of experimental errors on them. Therefore, it is deemed that this factor has no significant influences on state parameters. Otherwise, it is believed that the factors enormously affect state parameters. In this study, probability

TABLE 4: Further analysis of computing results.

Factor	I	II	III	IV	V	Max	Min	R	
A	Temp	2665.98	2673.65	2662.29	2673.09	2667.46	2673.65	2662.29	11.36
	Str	1203.87	1187.35	1215.06	1214.7	1201.62	1215.06	1187.35	27.71
	Def	1.88	2.02	1.7	1.82	1.565	2.02	1.565	0.455
B	Temp	2671.58	2668.41	2656.58	2671.32	2674.58	2674.58	2656.58	18
	Str	1262.81	1173.09	1205.35	1170.03	1211.32	1262.81	1170.03	92.78
	Def	1.77	1.835	1.755	1.675	1.945	1.945	1.675	0.27
C	Temp	2671.74	2668.09	2659.09	2671.78	2671.77	2671.78	2659.09	12.69
	Str	1181.36	1208.22	1193.74	1213.91	1225.37	1225.37	1181.36	44.01
	Def	1.7	1.825	1.84	1.88	1.74	1.88	1.7	0.18
D	Temp	2671.62	2670.98	2651.68	2678.72	2669.47	2678.72	2651.68	27.04
	Str	1178.14	1201.54	1207.94	1218.98	1216	1218.98	1178.14	40.84
	Def	1.94	1.585	1.65	1.83	1.98	1.98	1.585	0.395
E	Temp	2668.31	2671.83	2665.41	2664.51	2672.41	2672.41	2664.51	7.9
	Str	1224.06	1215.65	1187.54	1201.79	1222.91	1224.06	1187.54	36.52
	Def	2.275	1.735	1.62	1.605	1.75	2.275	1.605	0.67

TABLE 5: The variance analysis of results.

State parameters	Factor	S_i^2	S_i^2/f_i	F value	Critical value of F			Significance
					0.10	0.05	0.01	
T_{max}	A	18.717	4.679	0.540	2.250	2.870	4.430	
	B	39.300	9.825	1.133	2.250	2.870	4.430	
	C	24.133	6.033	0.696	2.250	2.870	4.430	
	D	80.837	20.209	2.331	2.250	2.870	4.430	※
	E	10.376	2.594	0.299	2.250	2.870	4.430	
S_{max}	A	103.673	32.818	0.278	2.250	2.870	4.430	
	B	1124.412	126.088	3.018	2.250	2.870	4.430	※※
	C	237.836	42.609	0.638	2.250	2.870	4.430	
	D	211.473	42.408	0.568	2.250	2.870	4.430	
	E	185.625	67.386	0.498	2.250	2.870	4.430	
D_{max}	A	0.024	0.006	0.984	2.250	2.870	4.430	
	B	0.008	0.002	0.328	2.250	2.870	4.430	
	C	0.004	0.001	0.164	2.250	2.870	4.430	
	D	0.061	0.01525	1.025	2.250	2.870	4.430	
	E	0.12	0.03	2.500	2.250	2.870	4.430	※

distribution of factor F is selected to evaluate influence of factors on state parameters. The computing results are presented in Table 5.

It is embodied by analysis results in the table that temperature of cylinder gaskets suffers great influence of factor D (thickness of cylinder gasket), and the corresponding F value is 2.331. In terms of stress of cylinder gaskets, factor B (radius of coolant channel) has a tremendous influence on it and the corresponding F value reaches 3.018. As for the cylinder gasket deformation, it is under a significant influence of factor E (bolt preload force) and the F value in this case turns out to be 2.5. As proven by the results in Tables 4 and 5, three state parameters are considerably affected by factors A, B, D, and E. On this account, only the influence of such four factors on state parameters of cylinder gaskets is taken into consideration during subsequent computational analysis. The above calculations and analyzation can only obtain cylinder gasket optimization situations in several discrete and limited conditions. Based on these situations, we

cannot optimize cylinder gaskets to find its optimal operating factors accurately. Therefore, an approach based on hybrid neural network is put forward so that the existing optimization research on cylinder gaskets can be extended from a limited point working condition to an unlimited surface working condition.

3. Operating State Prediction for Cylinder Gaskets Based on Hybrid Neural Network

Depending on the above analysis and calculations, an operating state prediction method is proposed for cylinder gaskets according to relatedness of 4 operating factors to be optimized and 3 state parameters of diesel cylinder gaskets, and the prediction method mainly based on partial least squares regression (PLSR) and Deep Neuron Network (DNN).

3.1. Hybrid Neural Network Based on PLSR and DNN.

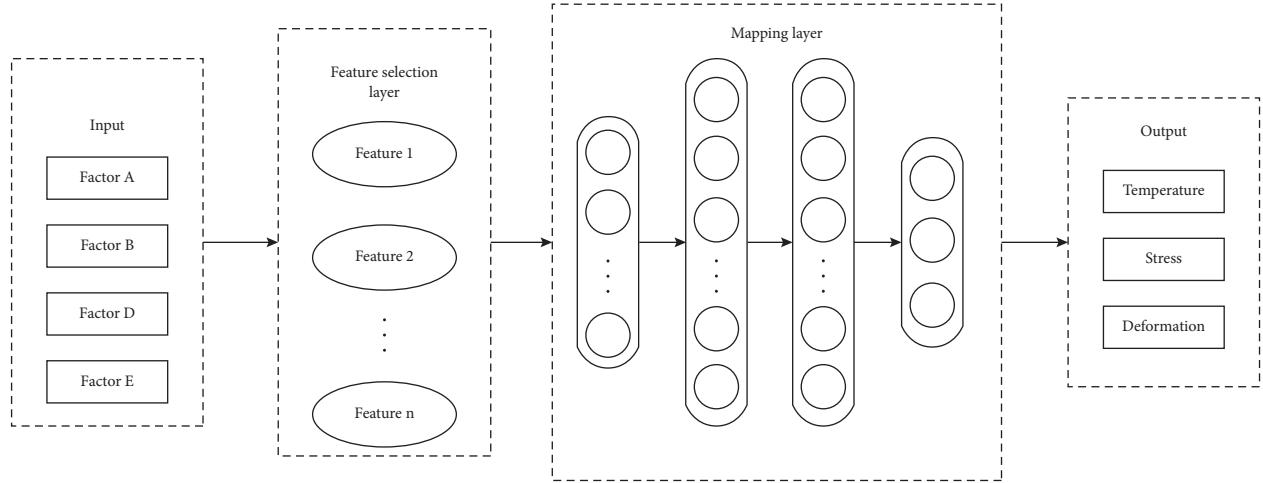


FIGURE 5: The main process of hybrid neural network.

The neural network selected for this study is mainly divided into two layers. While one layer is known as a feature selection layer, the other layer is a mapping layer. In terms of the former, a PLSR algorithm [53] is utilized to perform feature selection for cylinder gasket operating factors to be optimized; as for the latter, a DNN [54] is used to establish mapping between features of operating factors to be optimized and state parameters of cylinder gaskets. Through joint actions of such two layers, an operating state prediction model is built for cylinder gaskets according to the hybrid neural network based on PLSR and DNN. Additionally, basic working process of the hybrid neural network based on PLSR and DNN is shown in Figure 5 [55].

Next, both the feature selection layer and the mapping layer are briefly described.

3.2. Feature Selection Layer. Four normalized operating factors, to be optimized, of the cylinder gasket are selected as input of the feature selection layer, and the purpose of regression is to acquire extrema of state parameters related to the cylinder gasket. Moreover, corresponding output result can be seen as linear approximation of state parameters [56]. Respectively, input parameters and output targets can be expressed as follows:

$$P_{\text{in}} = [p_1^T, p_2^T, \dots, p_n^T], \quad (7)$$

$$G_{\text{out}} = [g_1^T, g_2^T, \dots, g_m^T], \quad (8)$$

where P_{in} stands for the input data matrix, G_{out} for a feature selection data matrix, p_1^T for input sample vectors, and g_1^T for a matrix of selected features.

Using these two equations to do the space projection of the previous two data matrixes,

$$P_{\text{in}}\omega_1 = p_1\omega_{11} + p_2\omega_{12} + \dots + p_n\omega_{1n} = t_1, \quad (9)$$

$$G_{\text{out}}v_1 = g_1v_{11} + g_2v_{12} + \dots + g_mv_{1m} = u_1, \quad (10)$$

where ω_1 is eigenvector of $P_{\text{in}}^T G_{\text{out}} G_{\text{out}}^T P_{\text{in}}$ and v_1 represents eigenvector of $G_{\text{out}}^T P_{\text{in}} P_{\text{in}}^T G_{\text{out}}$.

Here, correlation of t_1 and u_1 is primarily investigated. Once the spatial correlation reaches its maximum level, a regression model is established as follows:

$$P_{\text{in}} = t_1\alpha_1 + E_1, \quad (11)$$

$$G_{\text{out}} = t_1\beta_1 + F_1, \quad (12)$$

where α_1 and β_1 are parameter vectors and E_1 and F_1 are residuals matrixes.

Furthermore, the following formulas can be acquired:

$$P_{\text{in}} = t_1\alpha_1 + t_2\alpha_2 + \dots + t_r\alpha_r + E_r, \quad (13)$$

$$G_{\text{out}} = t_1\beta_1 + t_2\beta_2 + \dots + t_r\beta_r + F_r, \quad (14)$$

$$\alpha_i = \frac{P_{\text{in}}^T t_i}{t_i^2}, \quad (15)$$

$$\beta_i = \frac{G_{\text{out}}^T t_i}{t_i^2}, \quad (16)$$

$$t_i = P_{\text{in}}\omega_i, \quad (17)$$

where r represents a rank of matrix P_{in} and both E_r and F_r are least-residuals matrixes.

By combining the above formulas simultaneously, the PLSR equation is achieved as follows:

$$G_{\text{out}} = P_{\text{in}}\omega_1\beta_1 + P_{\text{in}}\omega_2\beta_2 + \dots + P_{\text{in}}\omega_r\beta_r + F_r. \quad (18)$$

By virtue of the above equation, dimensionality reduction and feature selection can be fulfilled for data at the minimum cost (i.e., the least residuals).

3.3. Mapping Layer. Here, output of the feature selection layer acts as the input of the mapping layer. Through the

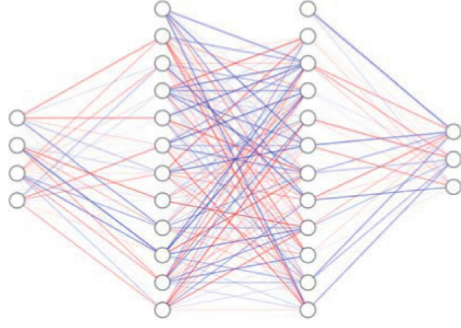


FIGURE 6: DNN framework.

weighting operation which is based on DNN containing two hidden layers, the data is eventually mapped on three state parameters of cylinder gaskets. The core of the mapping layer is DNN which includes the multihidden layer. Comparing with other mapping structures, DNN is capable of adapting to the nonlinear mapping process more accurately [57].

The proposed DNN framework is shown in Figure 6.

In the figure above, the output matrix of the first hidden layer is expressed as follows:

$$a_1 = g_1(W_1^T x + b_1). \quad (19)$$

The output matrix of the second hidden layer is expressed in another equation:

$$a_2 = g_2(W_2^T a_1 + b_2). \quad (20)$$

The matrix of output values is denoted by the following equation:

$$\hat{y} = g_0(W_3^T a_2 + b_3). \quad (21)$$

In the previous equation, $g_1(X)$, $g_2(X)$ and $g_0(X)$ are activation functions; W_1 , W_2 , and W_3 are corresponding weight matrixes; and, b_1 , b_2 , and b_3 represent deviation matrixes.

When training using DNN, a loss function is introduced to evaluate training effects so that optimal weight matrixes and deviation matrixes can be achieved. For the purpose of avoiding overfitting, regularization is performed for the loss function. In this way, the final loss function can be written into the following equation:

$$J(W, b) = \frac{1}{m} \sum_{i=1}^m (\hat{y}^i - y^i)^2 + \frac{\lambda}{2m} \sum_{j=1}^n W^T W. \quad (22)$$

In this equation, m refers to the number of sample sets, \hat{y}^i to predicted values of data in group i , y^i to calculated values of data in group i , and λ to regularization parameters.

3.4. The Processing of Training Samples. Correspondence of state parameters and operating factors was figured out. Totally, 241 sets of data were obtained, among which 226 sets (group A) serve as training samples to train the PLSR and DNN based hybrid neural network model. As for the

TABLE 6: Part of training samples for hybrid neural network.

Number	A	B	D	E	T_{\max}	S_{\max}	D_{\max}
1	153	23.1	2.05	134.8	532.3381	241.4961	0.46534
2	153	24.2	2.6	145.8	534.0272	240.6686	0.28951
3	153	25.5	3.25	158.8	529.6143	235.9869	0.329427
4	153	26.8	3.9	171.8	532.3895	246.3937	0.427519
5	154	23.1	3.05	164.8	528.7039	252.5735	0.366654
6	154	24.4	3.7	157.8	530.7526	238.5101	0.454281
7	154	25.7	2.6	140.8	530.554	235.3738	0.416173
8	154	27	2.5	153.8	535.8	229.66	0.3501
9	155	23.3	3.4	146.8	534.3776	251.1415	0.383875
10	155	24.6	2.3	159.8	534.8501	238.6299	0.302998
11	155	25.9	2.95	172.8	533.9187	237.7446	0.210332
12	155.2	26.2	3.3	141.8	532.5061	248.4274	0.44481
13	156	23.5	2.75	153.8	537.0808	244.8637	0.385204
14	156	24.8	3.4	141.8	536.8542	248.0838	0.371042
15	156	26.1	3.8	154.8	534.3468	232.0513	0.353681
16	156.4	25.4	2.6	159.8	530.9911	247.8942	0.291781
17	157	23.7	3.85	160.8	535.0463	237.8009	0.272666
18	157	25	2	173.8	531.76	233.14	0.3444
19	157	26.3	2.65	136.8	529.1457	242.2156	0.364453
20	157	27	3	143.8	533.86	243.55	0.3265

remaining 15 sets (group B), they were used to check the neural network. Some of these training samples are presented in Table 6.

To prevent data differences from affecting training results, the following equation was utilized to normalize samples before training.

$$x_l = \frac{|x - x_{\min}|}{x_{\max} - x_{\min}}. \quad (23)$$

In the above equation, x_l refers to the processed data, x to raw data, x_m to the mean value of data, and x_{\max} and x_{\min} to maximum and minimum values of data, respectively.

3.5. Validation of Training Results. Data of group B were adopted to check prediction results which were generated from the model of hybrid neural network based on PLSR and DNN. Comparison between calculated and predicted values is shown in Table 7.

As revealed from the table, all errors between the predicted and the calculated values are within 4.72%, which satisfies engineering calculation requirements. Therefore, this hybrid neural network is applicable to subsequent calculations and analysis.

Next, this article will use this neural network to search the operating factors corresponding optimal state parameters combined with a new algorithm named artificial bee colony based grey wolf optimizer (ABC and GWO).

4. ABC and GWO Algorithm

On account of the above analysis, a grey wolf optimization (GWO) algorithm [58] was put forward based on artificial bee colony (ABC) method [59] so as to perform computational analysis on optimal operating factors. The proposed algorithm aims to locate prey locations (optimal solutions)

TABLE 7: The comparison between calculated and predicted values.

Num	T_{\max}			S_{\max}			D_{\max}		
	Cal	Pre	Error (%)	Cal	Pre	Error (%)	Cal	Pre	Error (%)
1	534.47	518.88	2.92	242.70	244.30	-0.66	0.28500	0.28448	0.18
2	530.30	549.12	-3.55	230.07	238.88	-3.83	0.30835	0.30637	0.64
3	527.60	515.45	2.30	234.42	228.21	2.65	0.34017	0.34077	-0.18
4	536.12	550.72	-2.72	250.01	251.31	-0.52	0.44960	0.46605	-3.66
5	534.01	529.07	0.92	252.55	264.47	-4.72	0.41185	0.41937	-1.83
6	537.03	528.73	1.54	224.76	233.98	-4.10	0.37450	0.36216	3.29
7	537.19	529.54	1.42	231.43	230.75	0.29	0.35352	0.36466	-3.15
8	533.76	548.69	-2.80	256.38	266.05	-3.77	0.38435	0.40143	-4.44
9	534.85	513.51	3.99	238.63	227.39	4.71	0.30300	0.30813	-1.69
10	533.26	517.57	2.94	248.15	247.10	0.42	0.38401	0.40146	-4.55
11	539.84	536.30	0.66	248.46	259.93	-4.62	0.35915	0.37588	-4.66
12	537.53	536.07	0.27	237.79	228.44	3.93	0.34507	0.34217	0.84
13	537.21	519.08	3.37	232.47	229.89	1.11	0.28220	0.27699	1.85
14	536.81	528.71	1.51	230.70	221.02	4.19	0.33111	0.32097	3.06
15	528.34	509.59	3.55	237.52	240.49	-1.25	0.37087	0.36707	1.02

by combining GWO with ABC. Here, this algorithm is named ABC and GWO.

4.1. Grey Wolf Optimization Algorithm. Grey wolf is a kind of social predators. Based on its methods of surrounding, attacking, and hunting, Mirjalili raised GWO algorithm. According to different command hierarchies, grey wolves are divided into three major categories by the algorithm. In line with hierarchical levels, such three categories are α wolf, β wolf, and δ wolf. Among them, grey wolves in the middle hierarchy are primarily in charge of assisting grey wolves at higher levels and directing grey wolves at lower levels [60].

During calculation, the population size of grey wolves is denoted as N , the search space is set to be d -dimensional, spatial position of grey wolf i is designed as $X_i = (x_{i1}, x_{i2}, \dots, x_{id})$, and spatial position of preys is set as $X_p = (x_{p1}^*, x_{p2}^*, \dots, x_{pd}^*)$. Moreover, the spatial position of preys is where grey wolves get together for hunting and it is also a global optimal solution of GWO.

In the process of hunting, position of grey wolves is updated by the following equations:

$$X(t+1) = X_i(t) - A * |C * X_i(t) - X(t)|, \quad (24)$$

$$A = 2(r_1 - E) * a, \quad (25)$$

$$C = 2r_2 * a, \quad (26)$$

where both r_1 and r_2 are random vectors, E refers to column vectors with all elements equal to 1, and a represents a convergence factor vector. As for the relational expression of a and E , it can be written as follows:

$$a = 2 \left(\frac{(1-t)}{t_{\max}} \right) * E^T. \quad (27)$$

For the convenience of subsequent representation, $|C * X_i(t) - X(t)|$ is denoted by D . Regarding wolves

α, β and δ , their positions can be updated according to the following equations:

$$X_1 = X_\alpha - A_1 * D_\alpha, \quad (28)$$

$$D_\alpha = |C_1 * X_\alpha - X|, \quad (29)$$

$$X_2 = X_\beta - A_2 * D_\beta, \quad (30)$$

$$D_\beta = |C_2 * X_\beta - X|, \quad (31)$$

$$X_3 = X_\delta - A_3 * D_\delta, \quad (32)$$

$$D_\delta = |C_3 * X_\delta - X|, \quad (33)$$

where X_1, X_2 , and X_3 are the latest positions of α, β and δ wolves after present iterative computations. In this case, position of preys can be figured out by the following formula:

$$X(t+1) = \frac{X_1 + X_2 + X_3}{3}. \quad (34)$$

GWO has the capability to sufficiently utilize information of wolves α, β and δ to carry out global search of optimal solutions. In this way, occurrence of local optimal solutions can be avoided to the greatest extent. However, influence of different types of wolves on optimal solutions is left out of consideration. Consequently, it is likely for excessive iterations or overfitting to take place. On this basis, a modified GWO based on ABC is proposed to calculate and analyze optimal operating factors of cylinder gaskets.

4.2. Calculation of Prey Positions. Considering that GWO fails to consider the influence of wolves α, β , and δ on prey positions, weight coefficients were introduced for such wolves in order to solve this defect; on this basis, the prey position can be figured out.

The modified prey position calculation formula is given in the following:

$$\widehat{X}(t) = \frac{\eta_1 X_1 + \eta_2 X_2 + \eta_3 X_3}{3} \quad (35)$$

In the previous equation, η_1 , η_2 , and η_3 represent the weight coefficients related to three types of grey wolves.

The operating factors that correspond to optimal conditions of three state parameters of cylinder gaskets were obtained based on the results of orthogonal experiment. In specific calculation procedures, these operating factors were included into an optimal dataset DS; subsequently, data in DS were adopted to solve values of η_1 , η_2 , and η_3 . After that, data in DS were updated in conformity with these values and corresponding cyclical iteration does not stop until data in DS remain unchanged.

During cyclical iteration described above, ABC was utilized to optimize values of η_1 , η_2 , and η_3 . In the ABC algorithm, a bee colony is randomly produced using the equation

$$x_{ij} = x_j^{\min} + R^* (x_j^{\max} - x_j^{\min}), \quad (36)$$

$$R^* = \text{rand}(0, 1), \quad (37)$$

where x_{ij} represents i th bee in the bee colony, j is the number of solutions to the optimized problems, and x_j^{\max} and x_j^{\min} are maximum and minimum extrema of the optimization range.

The bee colony begins to look for nectar sources:

$$v_{ij} = x_{ij} + R^* (x_{ij} - x_{kj}), \quad (38)$$

where v_{ij} is a new nectar source (a new solution) nearby the current nectar source and x_{ij} and x_{kj} , respectively, stand for the current solution and a random solution next to the current solution. Once quality of the new nectar source is higher than that of the previous nectar source, the former can be reserved. In the entire process, an observing bee may identify where a new nectar source is at a certain probability according to quality of nectar sources. In order to figure out such a probability, the following equation should be followed:

$$P = \frac{\text{fit}_i(v_{ij})}{\sum_{n=1}^N \text{fit}_n(v_{ij})}, \quad (39)$$

where fit_i is a fitness function corresponding to a position of the i th nectar source.

4.3. Fitness Function. During practical calculations, a fitness function for the above ABCBGWO algorithm is defined as follows:

$$\text{fit}_i(v_{ij}) = \left(T_\alpha(v_{ij}) \right)^2 + \left(S_\alpha(v_{ij}) \right)^2 + \left(D_\alpha(v_{ij}) \right)^2. \quad (40)$$

In the previous equation, α represents serial numbers of arrays for η_1 , η_2 , and η_3 ; $T_\alpha(v_{ij})$, $S_\alpha(v_{ij})$, and $D_\alpha(v_{ij})$, respectively, refer to normalized temperature, stress, and deformations of cylinder gaskets under the circumstance that α set data are taken from η_1 , η_2 , and η_3 .

4.4. The Main Procedure of ABC and GWO Algorithm. In essence, the ABC and GWO algorithm is a process during which three corresponding weight coefficients are introduced when prey positions are working based on wolves α , β and δ of the GWO, and then such three coefficients are further optimized by means of ABC. To be specific, major steps of this algorithm are described as follows.

Step 1: control variables of the grey wolf population are initialized, including the population size, the number of iterations, and the convergence factor vector.

Step 2: grey wolves are randomly generated, and the number of which is N . They are used to figure out prey positions which correspond to wolves α , β and δ .

Step 3: the number of iterations is set as $t = 1$ and iteration starts.

Step 4: the convergence factor vector a is updated.

Step 5: parameters of ABC are initialized, and the initial nectar source is randomly generated.

Step 6: the bee is directed to search for a new nectar source, and if the nectar source is better than all of the others, its position should be labelled as a potential one.

Step 7: the onlooker bee searches for and changes the labelled nectar source.

Step 8: a scout bee is determined to be present or not; if not, skip to Step 10.

Step 9: a new position is generated by the scout bee and replaces the current nectar source; in this case, the labelled nectar is changed.

Step 10: it is judged whether termination conditions are satisfied; if not, skip to Step 7.

Step 11: position of the grey wolf is updated and prey position is obtained by the combination of coefficients and grey wolf position.

Step 12: the value of the fitness function is figured out in this scenario.

Step 13: it is judged whether to continue the algorithm or not; if yes, please go back to Step 3.

Step 14: iteration is terminated and relevant results are output.

In this process, ABC is utilized in Steps 5–10 to calculate and analyze three weight coefficients; as for other steps, they represent an iteration framework of GWA.

Figure 7 presents a flow chart of the ABC and GWO algorithm.

5. Multiobjective Optimization of Cylinder Gasket Parameters

5.1. The Main Process. Regarding maximum temperature, maximum stress, and maximum deformation of the cylinder gasket, their least values are set as objects of multiobjective optimization. As far as the proposed algorithm is concerned, that described above is embodied in searching for the minimum value of the corresponding fitness function. As for

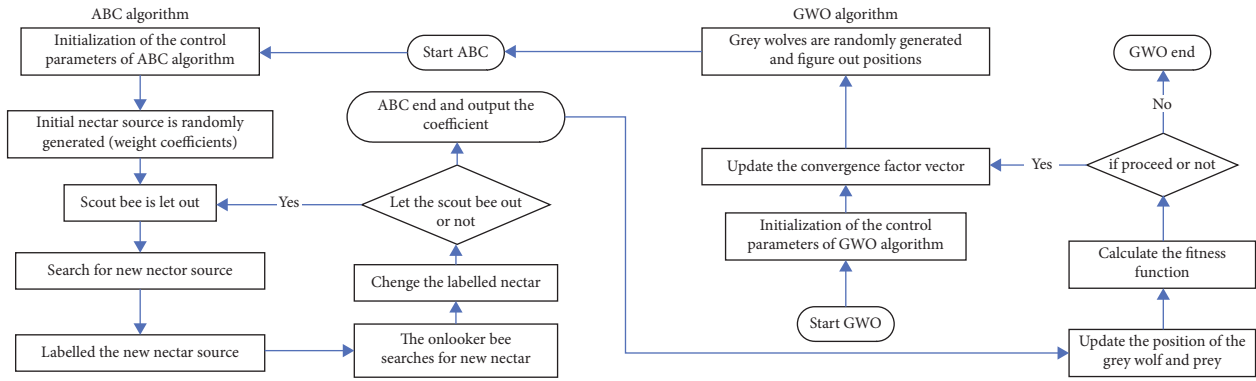


FIGURE 7: The flow chart of ABC and GWO algorithm.

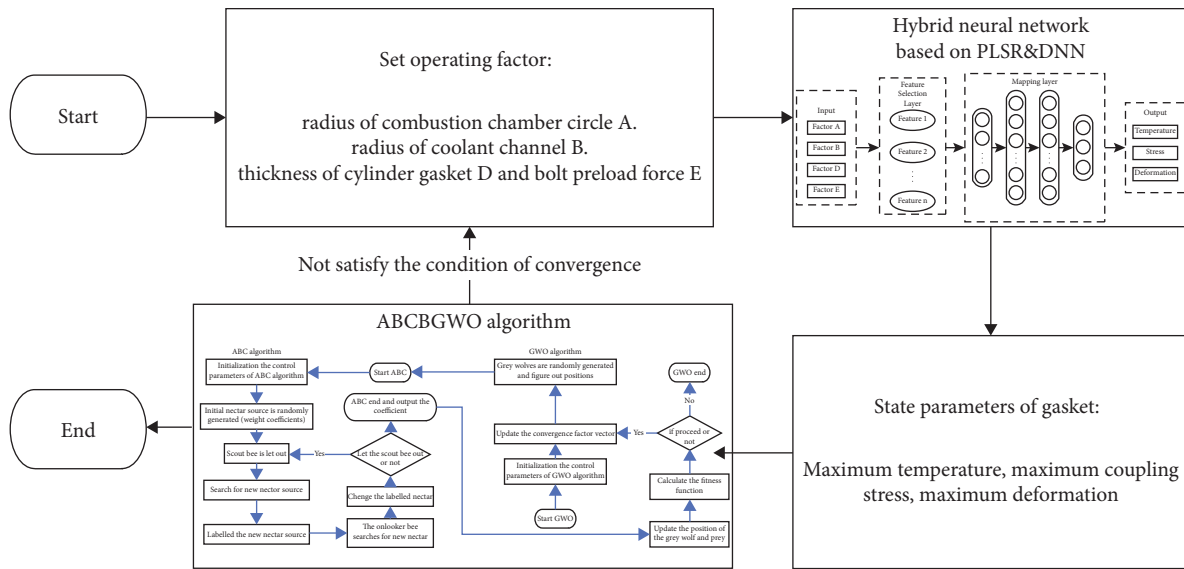


FIGURE 8: The main process of optimization.

TABLE 8: Initial values of different factors selected for multiobjective optimization.

Factors	A	B	C	D	E
Initial values	154	24	1.75	2.5	143.8

TABLE 9: The RMSE and NRMSE of different algorithms.

	RMSE		NRMSE	
	Training	Evaluation	Training	Evaluation
HNN and ABCBGWO	2.5134	2.3674	0.0720	0.0740
Genetic algorithm	5.5476	5.7400	0.1578	0.1795
Support vector machine	3.4239	4.2288	0.0977	0.1322

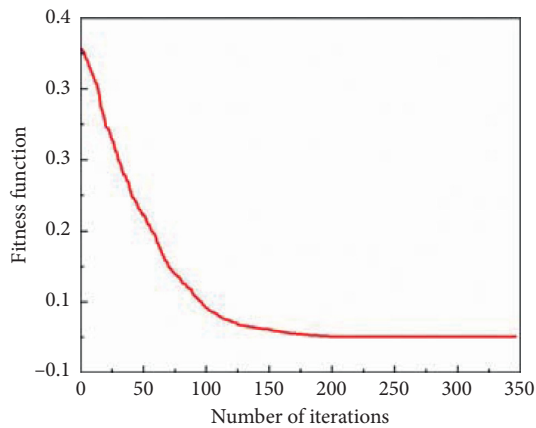


FIGURE 9: Variation rules of fitness function values.

TABLE 10: Optimal factors of cylinder gaskets calculated from the optimization algorithm.

Factors	A	B	C	D	E
Initial values	155	25	1.5	3	153.8
Optimal values	154	24.2	1.75	2.53	144.2

three state parameters of the cylinder gaskets, they are optimized in line with hybrid neural network based on PLSR and DNN as well as the ABC and GWO algorithm. Major procedures of the algorithm have been shown in Figure 8.

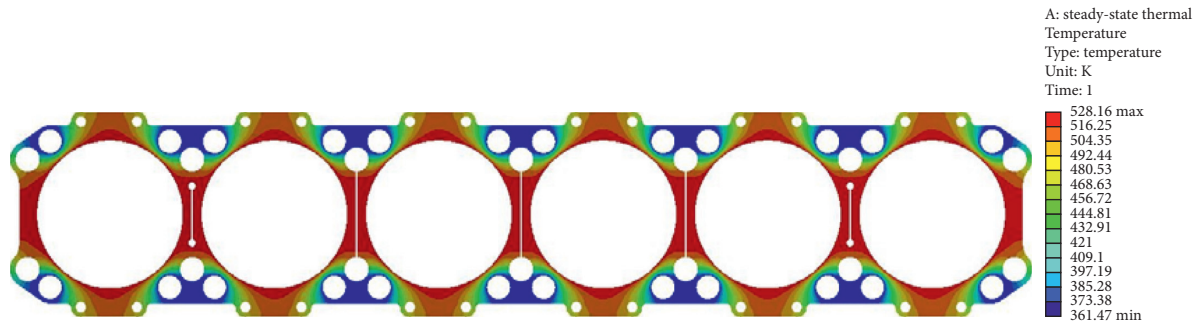


FIGURE 10: The schematic diagram of temperature field distribution of cylinder gaskets after optimization.

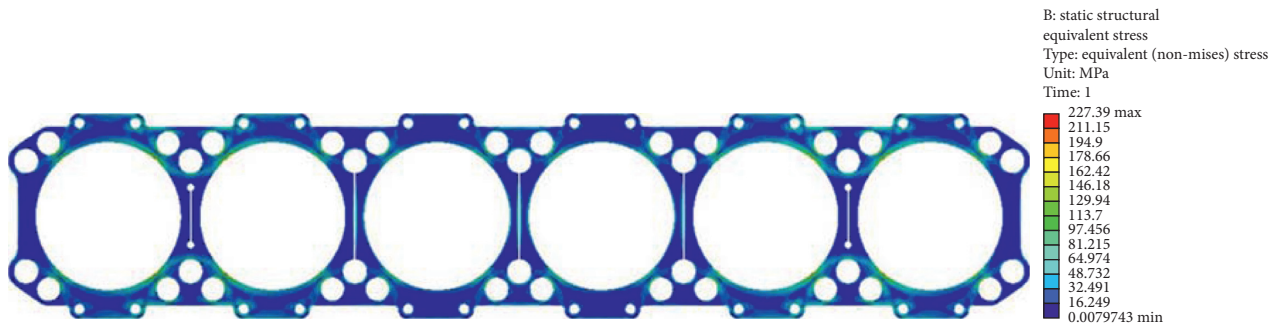


FIGURE 11: The schematic diagram of thermal-mechanical coupling stress field of gaskets after optimization.

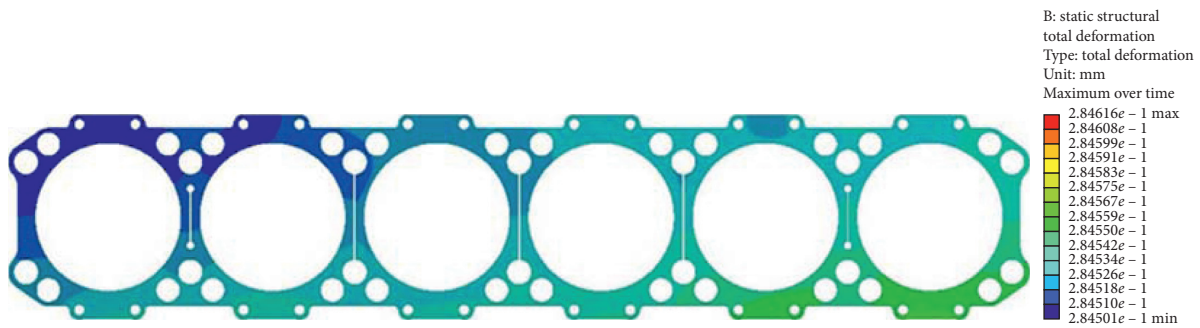


FIGURE 12: The schematic diagram of cylinder gasket deformation after optimization.

TABLE 11: The state parameters comparison before and after optimization.

Parameters	T_{\max} (K)	S_{\max} (MPa)	D_{\max} (mm)
Before optimization	534.16	239.96	0.3771
After optimization	528.16	227.39	0.2846
Difference	6	12.57	0.0925
Percent of difference	1.12%	5.23%	24.52%

5.2. *The Computing Process.* Depending on Figure 8, three operating factors of the cylinder gaskets were optimized. Then, initial values of operating factors were eventually confirmed based on results of the orthogonal experiment; see Table 8.

In the course of calculation, values of the fitness function vary as the number of iterations changes. Corresponding variation rules have been shown in Figure 9.

To validate the performance of the hybrid neural network and ABCBGWO algorithm, the genetic algorithm and support vector machine are adopted to compare the RMSE and NRMSE of the predicted data with our algorithm. The detailed results are shown in Table 9.

From Table 9, we can conclude that, compared with genetic algorithm and support vector machine, the hybrid neural network and ABCBGWO can perform better in RMSE and NRMSE which proves the performance of the algorithm. In the next section, accuracy and effectiveness of the algorithm are examined.

5.3. *Computing Results.* In the light of hybrid neural network based on PLSR and DNN and the ABCBGWO algorithm, the optimal operating factors are figured out for diesel cylinder gaskets (as shown in Table 10).

Cylinder gasket is optimized using the values in Table 9. Afterwards, corresponding boundary conditions are utilized to establish FEM model of the gasket. Through computing, results of temperature fields, thermal-mechanical coupling stress fields, and deformations of the cylinder gasket are worked out, as shown in Figures 10–12.

Additionally, maximum temperatures, maximum thermal-mechanical coupling stresses, and maximum deformation of cylinder gaskets subsequent and prior to optimization are compared in Table 11.

Through the calculation results we can conclude that the maximum temperature, maximum coupling stress, and the maximum deformation of gasket are improved obviously. The maximum temperature, maximum coupling stress, and the maximum deformation decrease 6 K, 12.57 MPa, and 0.0925 mm compared to the original values, respectively. The thermal stress load and the deformation are relieved after the optimization, which proved the effectiveness of the algorithm.

6. Conclusion

The paper applies FEM, orthogonal experimental design, HNN, and GWO to optimize the operating factors in conjunction with state parameters of cylinder gaskets. The main tasks are described as follows:

- (1) The FEM model is adopted to perform computational analysis on temperature fields, thermal-mechanical coupling stress fields, and deformations of cylinder gaskets; temperature field experiment is also conducted to validate accuracy of the computing model, and areas with comparatively high temperature and stress as well as obvious deformations are analyzed in line with computing results.
- (2) Orthogonal experimental design is selected to investigate and analyze how operating factors of cylinder gaskets affect state parameters. Totally, there are 5 operating factors and 3 state parameters. In detail, the former includes the radius of combustion chamber circle, radius of coolant channel, length of insulation area between 3rd and 4th cylinder, thickness of cylinder gasket, and bolt preload force, while the latter consists of maximum temperature, maximum stress, and maximum deformation of the cylinder gasket. It is found that temperature, stress, and deformation of cylinder gaskets are under significant influences of the radius of combustion chamber circle, radius of coolant channel, thickness of cylinder gasket, and the bolt preload force. For this reason, subsequent analysis is made only specific to such four operating parameters.
- (3) In order to overcome the problem of correspondence discontinuity between operating factors and state parameters of the cylinder gasket, a method is proposed to predict such a relation by virtue of a hybrid neural network model. To be specific, the hybrid neural network model consists of two layers in total. On the first layer, features of 4 operating

factors are selected based on PLSR, and, on the second layer, the correspondence of feature of operating factors and state parameters is established according to DNN. As demonstrated by validation results, such prediction model of hybrid neural network is provided with accuracy that is high enough to meet engineering calculation requirements.

- (4) When GWO is adopted to identify the prey's positions, differences in different grey wolves are neglected. With the goal of settling such a defect, three weight coefficients corresponding to three kinds of grey wolves are introduced to figure out prey positions, and ABC is also used to calculate and analyze values of such three weight coefficients. Not only is the defect of traditional GWA overcome, but final result can be obtained through rapid and accurate calculations by the proposed method. That is, such a method gives consideration to both computational efficiency and computing result accuracy.
- (5) Orthogonal experimental design results, the proposed "the hybrid neural network model based on PLSR and DNN," and "ABCBGWO algorithm" are applied to figure out values of operating factors in the case where optimal state parameters are achieved for the cylinder gasket. Furthermore, operating factors of the cylinder gasket are optimized by virtue of computing results. Besides, the FEM model is utilized again to calculate and analyze corresponding temperature, stress, and deformations of the optimized gasket. It is revealed by results that state parameters of the optimized cylinder gasket are all improved, which proves good optimization effects and validity of the proposed algorithm.

Next, optimized cylinder gaskets will be subjected to experimental verification, and the proposed algorithm will be applied in optimization research on other high-temperature components inside the diesel cylinder. With respect to load reduction and reliability/service life improvement for high-temperature components and even the complete machine, such a study is of great significance.

Data Availability

The raw/processed data required to reproduce these findings can be accessed through the table in the article.

Conflicts of Interest

The authors declare that there are no conflicts of interest regarding the publication of this paper.

Acknowledgments

The research has received no fund by any institute or person.

References

- [1] D. Khatri and R. Goyal, "Performance, emission and combustion characteristics of water diesel emulsified fuel for diesel engine: a review," *Materials Today: Proceedings*, vol. 28, no. 4, pp. 2275–2278, 2020.
- [2] S. Uslu and M. Aydın, "Effect of operating parameters on performance and emissions of a diesel engine fueled with ternary blends of palm oil biodiesel/diethyl ether/diesel by Taguchi method," *Fuel*, vol. 275, Article ID 117978, 2020.
- [3] S. Gopinath, P. K. Devan, C. Mohan, L. R. Krishna rao, P. Lokesh kumar, and S. Vara Prasad, "A review on influence of injection timing and injection pressure on DI diesel engine fuelled with low viscous fuel," *Materials Today: Proceedings*, In press, 2020.
- [4] X. Xu, Z. Zhao, X. Xu et al., "Machine learning-based wear fault diagnosis for marine diesel engine by fusing multiple data-driven models," *Knowledge-Based Systems*, vol. 190, Article ID 105324, 2020.
- [5] H. Sevinc and H. Hazar, "Investigation of performance and exhaust emissions of a chromium oxide coated diesel engine fueled with dibutyl maleate mixtures by experimental and ANN technique," *Fuel*, vol. 278, Article ID 118338, 2020.
- [6] J. Jannatkah, B. Najafi, and H. Ghaebi, "Energy and exergy analysis of combined ORC–ERC system for biodiesel-fed diesel engine waste heat recovery," *Energy Conversion and Management*, vol. 209, Article ID 112658, 2020.
- [7] V. Kumar, A. P. Singh, and A. K. Agarwal, "Gaseous emissions (regulated and unregulated) and particulate characteristics of a medium-duty CRDI transportation diesel engine fueled with diesel-alcohol blends," *Fuel*, vol. 278, Article ID 118269, 2020.
- [8] J. Wei, W. Lu, M. Pan, Y. Liu, X. Cheng, and C. Wang, "Physical properties of exhaust soot from dimethyl carbonate-diesel blends: characterizations and impact on soot oxidation behavior," *Fuel*, vol. 279, Article ID 118441, 2020.
- [9] M. Subramaniam, J. M. Solomon, V. Nadanakumar, S. Anaimuthu, and R. Sathyamurthy, "Experimental investigation on performance, combustion and emission characteristics of DI diesel engine using algae as a biodiesel," *Energy Reports*, vol. 6, pp. 1382–1392, 2020.
- [10] A. I. Jabbar, H. Gaja, and U. O. Koşlu, "Multi-objective optimization of operating parameters for a H₂/Diesel dual-fuel compression-ignition engine," *International Journal of Hydrogen Energy*, vol. 45, no. 38, pp. 19965–19975, 2020.
- [11] S. Allam and A. M. Elsaid, "Parametric study on vehicle fuel economy and optimization criteria of the pleated air filter designs to improve the performance of an I.C diesel engine: experimental and CFD approaches," *Separation and Purification Technology*, vol. 241, Article ID 116680, 2020.
- [12] Z. Zhang, J. E. J. Chen et al., "Effects of boiling heat transfer on the performance enhancement of a medium speed diesel engine fueled with diesel and rapeseed methyl ester," *Applied Thermal Engineering*, vol. 169, Article ID 114984, 2020.
- [13] X. Peiyu, G. Daojing, H. Guannan et al., "Influence of piston pin hole offset on cavity erosion of diesel engine cylinder liner," *Engineering Failure Analysis*, vol. 103, pp. 217–225, 2019.
- [14] E. Mancaruso and L. Sequino, "Measurements and modeling of piston temperature in a research compression ignition engine during transient conditions," *Results in Engineering*, vol. 2, Article ID 100007, 2019.
- [15] E. Natesan, S. Eriksson, J. Ahlström, and C. Persson, "Effect of temperature on deformation and fatigue behaviour of A356–T7 cast aluminium alloys used in high specific power IC engine cylinder heads," *Materials*, vol. 13, no. 5, 2020.
- [16] A. E. Segall, C. C. Schoof, and D. E. Yastishock, "Thermal solutions for a plate with an arbitrary temperature transient on one surface and convection on the other: direct and inverse formulations," *Journal of Pressure Vessel Technology Transactions of the ASME*, vol. 142, no. 5, 2020.
- [17] M. Kota, N. Kyotaro, T. Yuichiro, and U. Kenko, "Control device for compression ignition type engine, and cylinder temperature determining method," US Patent-9719441B2, 2020.
- [18] N. P. Starostin and M. A. Vasileva, "Determination of load-speed modes for fluoroplastic seals of rotary shaft by temperature limitation," vol. 459, 2020.
- [19] Q. Zhaoju, L. Yingsong, Y. Zhenzhong, D. Junfa, and W. Lijun, "Diesel engine piston thermo-mechanical coupling simulation and multidisciplinary design optimization," *Case Studies in Thermal Engineering*, vol. 15, Article ID 100527, 2019.
- [20] M. Wang, J. C. Pang, H. Q. Liu, S. X. Li, and Z. F. Zhang, "Property optimization of low-cycle fatigue in Al-Si piston alloy at elevated temperatures by ultrasonic melt treatment," *Journal of Materials Research and Technology*, vol. 8, no. 5, pp. 4556–4568, 2019.
- [21] L.-N. Wang, H.-C. Sun, L. Qi et al., "Effect of stress relaxation on globe-cone seal performance with a gasket," *Vacuum*, vol. 168, Article ID 108827, 2019.
- [22] G. Liu, G. Yan, and J. Yu, "Research on test method of heat transfer coefficient for refrigerator gasket," *International Journal of Refrigeration*, vol. 110, pp. 106–120, 2020.
- [23] K. Rashnoo, M. J. Sharifi, M. Azadi, and M. Azadi, "Influences of reinforcement and displacement rate on microstructure, mechanical properties and fracture behaviors of cylinder-head aluminum alloy," *Materials Chemistry and Physics*, vol. 255, Article ID 123441, 2020.
- [24] D. Wang, J. Wang, S. Ding, and H. Chu, "Study on evaporation heat transfer performance of composite porous wicks with spherical-dendritic powders based on orthogonal experiment," *International Journal of Heat and Mass Transfer*, vol. 156, 2020.
- [25] R. T. Steinbakk, P. Ulleberg, F. Sagberg, and K. I. Fostervold, "Analysing the influence of visible roadwork activity on drivers' speed choice at work zones using a video-based experiment," *Transportation Research Part F: Traffic Psychology and Behaviour*, vol. 44, pp. 53–62, 2017.
- [26] H. Ni, J. Zhang, S. Lv, X. Wang, Y. Zhu, and T. Gu, "Preparation and performance optimization of original aluminum ash coating based on plasma spraying," *The Coatings*, vol. 9, no. 11, 2019.
- [27] K. Li, W. Yao, Y. Xie et al., "A strongly hydrophobic and serum-repelling surface composed of CrN films deposited on laser-patterned microstructures that was optimized with an orthogonal experiment," *Surface & Coatings Technology*, vol. 391, 2020.
- [28] L. Shu, B. Wang, and Y. He, "Optimization of process parameters of laser cladding 304L alloy powder based on orthogonal experiment," vol. 1, no. 9, 2020.
- [29] F. Tao, P. Gu, and Y. Yang, "Study on influencing factors of mechanical properties of ceramsite foam concrete based on orthogonal test," *Mechanical Engineering Science*, vol. 768, 2020.
- [30] S. Subramani, R. Govindasamy, and G. L. N. Rao, "Predictive correlations for NO_x and smoke emission of DI CI engine fuelled with diesel-biodiesel-higher alcohol blends-response

- surface methodology approach,” *Fuel*, vol. 269, Article ID 117304, 2020.
- [31] P. Nagasankar, P. Gurusamy, S. Gopinath, K. Gnanaprakash, and G. Pradeep, “Optimization of process parameters on engine exhaust valves using Taguchi method in friction welding process,” *Materials Today: Proceedings*, 2020.
- [32] P. V. de Campos Souza, “Fuzzy neural networks and neuro-fuzzy networks: a review the main techniques and applications used in the literature,” *Applied Soft Computing*, vol. 92, Article ID 106275, 2020.
- [33] D. Deshwal, P. Sangwan, and D. Kumar, “A language identification system using hybrid features and back-propagation neural network,” *Applied Acoustics*, vol. 164, Article ID 107289, 2020.
- [34] H. Wang, Z. Zhang, and L. Liu, “Prediction and fitting of weld morphology of Al alloy-CFRP welding-rivet hybrid bonding joint based on GA-BP neural network,” *Journal of Manufacturing Processes*, 2020, In press.
- [35] G. Ma, Y. Zhang, C. Cheng, B. Zhou, P. Hu, and Y. Yuan, “Remaining useful life prediction of lithium-ion batteries based on false nearest neighbors and a hybrid neural network,” *Applied Energy*, vol. 253, Article ID 113626, 2019.
- [36] J. Chen, D. Jiang, Y. Zhang, and P. Zhang, “Emotion recognition from spatiotemporal EEG representations with hybrid convolutional recurrent neural networks via wearable multi-channel headset,” *Computer Communications*, vol. 154, pp. 58–65, 2020.
- [37] T. Baklacioglu, O. Turan, and H. Aydin, “Dynamic modeling of exergy efficiency of turboprop engine components using hybrid genetic algorithm-artificial neural networks,” *Energy*, vol. 86, pp. 709–721, 2015.
- [38] H. Jiang, Z. Xi, A. Rahman, and X. Zhang, “Prediction of output power with artificial neural network using extended datasets for Stirling engines,” *Applied Energy*, vol. 271, Article ID 115123, 2020.
- [39] J. L. S. Fagundes, T. D. M. Lanza, M. E. S. Martins, and N. P. G. Salau, “Joint use of artificial neural networks and particle swarm optimization to determine optimal performance of an ethanol SI engine operating with negative valve overlap strategy,” *Energy*, vol. 204, Article ID 117892, 2020.
- [40] Z. Chen, X. Yuan, M. Sun, J. Gao, and P. Li, “A hybrid deep computation model for feature learning on aero-engine data: applications to fault detection,” *Applied Mathematical Modelling*, vol. 83, pp. 487–496, 2020.
- [41] Z. Cui, S. Zhong, and Z. Yan, “Fuel savings model after aero-engine washing based on convolutional neural network prediction,” *Measurement*, vol. 151, Article ID 107180, 2020.
- [42] D. Miao and S. Hossain, “Improved gray wolf optimization algorithm for solving placement and sizing of electrical energy storage system in micro-grids,” *ISA Transactions*, vol. 102, pp. 376–387, 2020.
- [43] D. Miao, W. Chen, W. Zhao, and T. Domsas, “Parameter estimation of PEM fuel cells employing the hybrid grey wolf optimization method,” *Energy*, vol. 193, Article ID 116616, 2020.
- [44] Y. Dong, J. Liu, Y. Liu et al., “A RBFNN & GACMOO-based working state optimization control study on heavy-duty diesel engine working in plateau environment,” *Energies*, vol. 13, no. 1, p. 279, 2020.
- [45] E. Ileri, A. D. Karaoglan, and S. Akpınar, “Optimizing cetane improver concentration in biodiesel-diesel blend via grey wolf optimizer algorithm,” *Fuel*, vol. 273, 2020.
- [46] P. K. Gujarathi, V. A. Shah, and M. M. Lokhande, “Grey wolf algorithm for multidimensional engine optimization of converted plug-in hybrid electric vehicle,” *Transportation Research Part D: Transport and Environment*, vol. 63, pp. 632–648, 2018.
- [47] S. Dai, D. Niu, and Y. Han, “Forecasting of power grid investment in China based on support vector machine optimized by differential evolution algorithm and grey wolf optimization algorithm,” *Applied Science*, vol. 8, no. 4, 2018.
- [48] K. Luo, “Enhanced grey wolf optimizer with a model for dynamically estimating the location of the prey,” *Applied Soft Computing*, vol. 77, pp. 225–235, 2019.
- [49] R. K. Vijay and S. J. Nanda, “A quantum grey wolf optimizer based clustering model for analysis of earthquake catalogs in an ergodic framework,” *Journal of Computational Science*, vol. 36, Article ID 101019, 2019.
- [50] J. Xudong, W. Qingchun, and R. Weiping, “High-wer diesel engine’s alletal cylinder gasket,” 2016.
- [51] W. Lei, X. Yang, X. Fang et al., “High-ressure oil pump for heavyuty diesel engine,” 2014.
- [52] A. P. Singh, N. Sharma, D. P. Satsangi, and A. K. Agarwal, “Effect of fuel injection pressure and premixed ratio on mineral diesel-methanol fueled reactivity controlled compression ignition mode combustion engine,” *Journal of Energy Resources Technology Transactions of the ASME*, vol. 142, no. 12, 2020.
- [53] J. F. Hair, G. T. M. Hult, C. M. Ringle, and M. Sarstedt, “Aprimer on partial least squares structural equation modeling(PLS-SEM),” 2014.
- [54] J. Shen, M. D. Petkova, F. Liu, and C. Tang, “Toward deciphering developmental patterning with deep neural network,” 2018.
- [55] L. Xiao, Z. Liu, Y. Zhang, Y. Zheng, and C. Cheng, “Degradation assessment of bearings with trend-reconstruct-based features selection and gated recurrent unit network,” *Measurement*, vol. 165, Article ID 108064, 2020.
- [56] G. E. Hinton and R. R. Salakhutdinov, “Reducing the dimensionality of data with neural networks,” *Science*, vol. 313, no. 5786, pp. 504–507, 2006.
- [57] C. H. Tong, P. Furgale, and T. D. Barfoot, “Gaussian Process Gauss-Newton for non-parametric simultaneous localization and mapping,” *The International Journal of Robotics Research*, vol. 32, no. 5, pp. 507–525, 2013.
- [58] E. Emary, H. M. Zawbaa, and A. E. Hassanien, “Binary grey wolf optimization approaches for feature selection,” *Neurocomputing*, vol. 172, no. 8, pp. 371–381, 2016.
- [59] D. Karaboga and B. Basturk, “A powerful and efficient algorithm for numerical function optimization: artificial bee colony (ABC) algorithm,” *Journal of Global Optimization*, vol. 39, no. 3, pp. 459–471, 2007.
- [60] Z. Xue, Y. Zhang, C. Cheng, and G. Ma, “Remaining useful life prediction of lithium-ion batteries with adaptive unscented kalman filter and optimized support vector regression,” *Neurocomputing*, vol. 376, pp. 95–102, 2020.

Research Article

Study on the Intelligent Evaluation System of Tunnel Frost Damage in Cold Regions Based on the Fuzzy Comprehensive Evaluation Model

Dao-yuan Wang ^{1,2}, Yong-quan Zhu,² Guang-yao Cui ³, Yong-jun Luan,⁴ Hai-long Cui,⁴ Liang Sun,⁵ Yong-jie Sun,⁴ Yue Wang,⁴ and Jin-xiu Yuan ¹

¹Department of Civil Engineering, Hebei Jiaotong Vocational and Technical College, Shijiazhuang, Hebei 050091, China

²School of Civil Engineering, Shijiazhuang Tiedao University, Shijiazhuang, Hebei 050043, China

³School of Civil Engineering, North China University of Technology, Beijing 100144, China

⁴Hebei Construction Group Corporation Limited, Baoding, Hebei 071052, China

⁵Hebei Provincial Communications Planning and Design Institute, Shijiazhuang, Hebei 050000, China

Correspondence should be addressed to Dao-yuan Wang; wtg-888@163.com

Received 12 June 2020; Accepted 21 July 2020; Published 21 August 2020

Guest Editor: Yu-Sheng Shen

Copyright © 2020 Dao-yuan Wang et al. This is an open access article distributed under the Creative Commons Attribution License, which permits unrestricted use, distribution, and reproduction in any medium, provided the original work is properly cited.

At present, the tunnel design specifications in China do not provide a clear and systematic intelligent evaluation system of tunnel frost damage in cold regions. Based on the research results of 122 seasonal frozen soil tunnels in high-latitude areas of China, four key influencing factors of geohydrology, temperature, surrounding rock, and engineering measures were determined, the intelligent fuzzy comprehensive evaluation model was established, the weights of all factors were considered, and the intelligent evaluation technology system of tunnel frost damage in cold areas had been put forward. Meanwhile, the rationality of the intelligent model was verified by a specific engineering case. The research suggests that the intelligent evaluation model of tunnel frost damage proposed in this paper can accurately describe the relationship of influencing factors of tunnel frost damage in cold areas, the weight of each influencing factor is calculated by using analytic hierarchy process, and the main risk sources of tunnel frost damage in cold areas are found out. The intelligent evaluation model is an efficient and practical method for Intelligent prediction of frost damage. By using the subordinate function method, the improvement from qualitative analysis to quantitative index calculation is realized. The blindness of engineering analogy construction is avoided, and the scientificity and accuracy of renovation measures for frost damage have been improved. At the same time, the research results provide a theoretical basis for the improvement of the intelligent evaluation system of tunnel frost damage in cold regions.

1. Introduction

With the implementation of the Belt and Road Initiative and the promotion of basic construction of the Beijing Winter Olympic Games, more and more tunnels are built in cold regions of seasonal frozen soil. The problems of frost damage of tunnels have been gradually highlighted, such as leakage of lining, ice hanging, water pouring from tunnel bottom, frost heaving of icing, cracking, crumbling and peeling of lining, freezing of the drainage system, thermal melting, and sliding of the tunnel portal.

In view of the problems of tunnel frost damage in cold areas, the tunnellers have carried out the research work on the temporal and spatial variation law of temperature field [1–9], thermal insulation, and prevention measures of frost damage [10–16]. However, the research on the intelligent evaluation system of tunnel frost damage in cold regions is rarely reported, mainly including as follows: according to the average temperature and freezing depth of the coldest month, the Qinghai-Tibet Plateau, Inner Mongolia, and Northeast China are divided into three cold regions, and the characteristics of frost damage are analyzed according to different cold regions

[17]. The causes of tunnel frost damage in cold areas can be divided into three categories: external force, material cracking, and other reasons. The characteristics of tunnel frost damage in the cold area are qualitatively explained [18]. The frost damage of tunnels in cold areas is considered to be caused by vertical load, plastic load, and creep of the inclined slope, and corresponding preventive measures are put forward according to different classifications [19]. Based on the event tree theory, the frost damage level of tunnels in the cold region has been established, and the scientific and effective measures to control frost damage of tunnels in the cold region have been improved [20]. According to the fatigue strength of concrete frost damage, the durability of the concrete structure under freeze-thaw environment, and the action level of lining frost heaving force, the frost damage level of the tunnel in cold areas is divided, and corresponding preventive measures are put forward according to different classifications [21].

Based on the investigation results of 122 tunnels in high-latitude areas of China, four key influencing factors (geological hydrology, temperature, surrounding rock, and engineering measures) are determined, an intelligent fuzzy comprehensive evaluation model is established, and an intelligent evaluation system of tunnel frost damage in cold areas is proposed considering the weight relationship of key factors.

2. Investigation of Tunnel Frost Damage in Cold Areas

The data of 122 tunnels in cold regions in Northeast China and Inner Mongolia were collected. The frost damage of 12 tunnels is caused by unreasonable design, which accounts for 23% of the total number of tunnels. The frost damage of 27 tunnels is caused by the wrong construction method, which accounts for 53% of the total number of tunnels. The frost damage of 9 tunnels is due to improper operation and maintenance, which accounts for 18% of the total number of tunnels. The frost damage of 3 tunnels is caused by unreasonable remedial measures, which accounts for 6% of the total number of tunnels. The percentage of each influencing factor of tunnel frost damage is shown in Figure 1.

3. Establishment of the Intelligent Evaluation System of Tunnel Frost Damage in Cold Regions

3.1. Establishment of the Intelligent Evaluation Model. Considering the four basic influencing factors of temperature condition, hydrological condition, surrounding rock condition, and engineering measures, an intelligent evaluation model is established by the fuzzy comprehensive evaluation method, and the intelligent evaluation model of tunnel frost damage in cold regions is shown in Figure 2.

3.2. Establishment of Comment Collection. According to the degree of frost damage, the comments on the intelligent

evaluation system of tunnel frost damage in cold areas are as follows:

$$V = \{V_1, V_2, V_3, V_4\} = \{I, II, III, IV\}. \quad (1)$$

In this formula, class I is no frost damage or slight frost damage, class II is moderate frost damage, class III is relatively serious frost damage, and class IV is serious frost damage.

The classification of tunnel frost damage in cold regions is shown in Table 1.

3.3. Determination of the Membership Function. The intelligent evaluation system of tunnel frost damage in cold areas includes 10 quantitative indexes (air temperature outside the tunnel, ground temperature of the surrounding rock, driving density, wind speed inside the tunnel, void area length between surrounding rock and lining, annual precipitation, blockage rate of the drainage pipe, buried depth of the tunnel, fracture rate of the surrounding rock, and lining strength) and 6 qualitative indexes (waterproof design of three joints, solubility of the surrounding rock, design problems, construction problems, operation and maintenance problems, and remedial measures). Among them, the quantitative indexes can be divided into 7 positive quantitative indexes (air temperature outside the tunnel, traffic density, wind speed inside the tunnel, void area length between surrounding rock and lining, annual precipitation, blockage rate of the drainage pipe, and fracture rate of the surrounding rock) and 3 negative quantitative indexes (ground temperature of the surrounding rock, buried depth of the tunnel and lining strength).

3.3.1. Determine the Membership Function of the Quantitative Index. The reduced half trapezoid distribution function is selected as the membership function of the positive-type quantitative index. The membership function is shown in formulae (2) ~ (5). The parameters of the membership function of the positive-type quantitative index are shown in Table 2.

$$\mu_1 = \begin{cases} 1, & x < S_1, \\ \frac{S_2 - x}{S_2 - S_1}, & S_1 \leq x \leq S_2, \\ 0, & x > S_2, \end{cases} \quad (2)$$

$$\mu_2 = \begin{cases} 0, & x \leq S_1, x > S_3, \\ \frac{x - S_1}{S_2 - S_1}, & S_1 < x \leq S_2, \\ \frac{S_3 - x}{S_3 - S_2}, & S_2 < x \leq S_3, \end{cases} \quad (3)$$

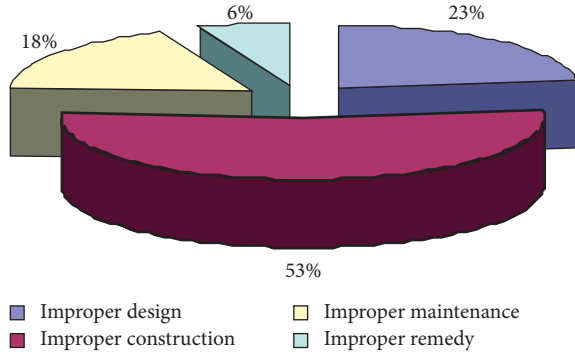


FIGURE 1: Proportion of influencing factors of tunnel frost damage.

$$\mu_3 = \begin{cases} 0, & x \leq S_2, x > S_4, \\ \frac{x - S_2}{S_3 - S_2}, & S_2 < x \leq S_3, \\ \frac{S_4 - x}{S_4 - S_3}, & S_3 < x \leq S_4, \end{cases} \quad (4)$$

$$\mu_4 = \begin{cases} 0, & x \leq S_3, \\ \frac{x - S_3}{S_4 - S_3}, & S_3 < x \leq S_4, \\ 1, & x > S_4, \end{cases} \quad (5)$$

where $S_1, S_2, S_3,$ and S_4 are determined by each critical state index in the evaluation benchmark.

The reduced half trapezoid distribution function is also selected as the membership function of the negative-type quantitative index. The membership function is shown in formulae (6) ~ (9). The parameters of the membership function of the negative quantitative index are shown in Table 3.

$$\mu_1 = \begin{cases} 1, & x > S_1, \\ \frac{S_2 - x}{S_2 - S_1}, & S_1 \geq x \geq S_2, \\ 0, & x < S_2, \end{cases} \quad (6)$$

$$\mu_2 = \begin{cases} 0, & x \geq S_1, x < S_3, \\ \frac{x - S_1}{S_2 - S_1}, & S_1 > x \geq S_2, \\ \frac{S_3 - x}{S_3 - S_2}, & S_2 > x \geq S_3, \end{cases} \quad (7)$$

$$\mu_3 = \mu_2 = \begin{cases} 0, & x \geq S_2, x < S_4, \\ \frac{x - S_2}{S_3 - S_2}, & S_2 > x \geq S_3, \\ \frac{S_4 - x}{S_4 - S_3}, & S_3 > x \geq S_4, \end{cases} \quad (8)$$

$$\mu_4 = \begin{cases} 0, & x \geq S_3, \\ \frac{x - S_3}{S_4 - S_3}, & S_3 > x \geq S_4, \\ 1, & x < S_4. \end{cases} \quad (9)$$

3.3.2. Determine the Membership Function of the Qualitative Index. Trapezoidal distribution function is selected as the membership function of the qualitative index, and its membership function is shown in formulae (10) ~ (13):

$$\mu_1 = \begin{cases} 0, & x < 0.75, \\ 10x - 7.5 & 0.75 \leq x < 0.85, \\ 1, & x \geq 0.85, \end{cases} \quad (10)$$

$$\mu_2 = \begin{cases} 0, & x < 0.55, \\ 10x - 05.5 & 0.55 \leq x < 0.65, \\ 1, & 0.65 \leq x < 0.75, \\ 8.5 - 10x & 0.75 \leq x < 0.85, \\ 0, & x \geq 0.85, \end{cases} \quad (11)$$

$$\mu_3 = \begin{cases} 0, & x < 0.35, \\ 10x - 3.5 & 0.35 \leq x < 0.65, \\ 1, & 0.45 \leq x < 0.55, \\ 6.5 - 10x & 0.55 \leq x < 0.65, \\ 0, & x \geq 0.65, \end{cases} \quad (12)$$

$$\mu_4 = \begin{cases} 1, & x < 0.35, \\ 4.5 - 10x & 0.35 \leq x < 0.45, \\ 0, & x \geq 0.45. \end{cases} \quad (13)$$

3.4. Determination of the Weighted Set. Analytic hierarchy process is used to determine the weighted set of the intelligent evaluation system of tunnel frost damage in cold regions. The steps are as follows: establish the evaluation model (Figure 2), build two judgment matrices, and calculate the relative weight of each index and consistency test.

The sensitivity of each index of temperature conditions is ground temperature of the surrounding rock, driving density, wind speed inside the tunnel, and air temperature outside the tunnel. The judgment matrix of temperature conditions is shown in Table 4.

The calculation results of the relative weight of four indexes under temperature conditions are as follows: $W_{U_1} = (W_{U_{11}}, W_{U_{12}}, W_{U_{13}}, W_{U_{14}}) = (0.10, 0.40, 0.30, 0.20)$, $\lambda_{\max} = 4, CI = 0, CR = 0 < 0.1$, and the conformance test meets the requirements.

The sensitivity of each index of the hydrological condition is void area length of the surrounding rock between lining, blockage rate of the drainage pipe,

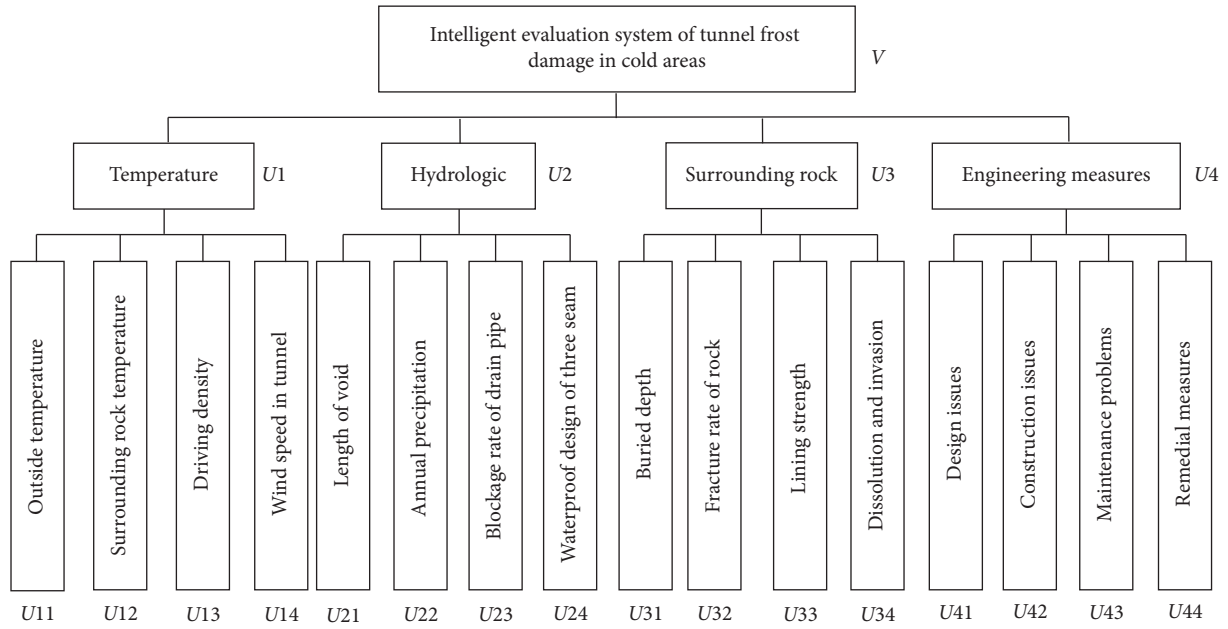


FIGURE 2: Frost damage intelligent evaluation model of the tunnel in cold areas.

TABLE 1: Classification of tunnel frost damage in cold regions.

Frost damage classification	Judgment basis	Average temperature in the coldest month/°C
I	Icing at the portal section, leakage and icing of the partial lining surface, slight frost damage, no impact on traffic	-5~-10
II	Moderate serious icing at the portal section, moderate severe leakage and freezing damage of the lining surface, affecting traffic	-10~-15
III	Relatively serious icing at the portal section, relatively severe leakage and freezing damage of the lining surface, serious impact on traffic	-15~-25
IV	Serious crack of the lining surface, serious ice hanging in the tunnel, ice plug of the drain system, traffic disruption	<-25

TABLE 2: Membership function parameters of the positive quantitative index.

Positive quantitative index	I	II	III	IV
Air temperature outside the tunnel/°C	-5	-10	-15	-25
Driving density/(对/h)	2	4	6	8
Wind speed inside the tunnel/(m/s)	1	2	3	5
Void area length between surrounding rock and lining/m	3	5	10	20
Annual precipitation/mm	200	600	1600	2500
Blockage rate of the drainage pipe	0.2	0.5	0.8	0.9
Fracture rate of the surrounding rock	0.001	0.5	10	15

waterproof design of three joints, and annual precipitation. The judgment matrix of hydrological conditions is shown in Table 5.

The calculation results of the relative weight of four indexes under hydrological conditions are as follows: $W_{U_2} = (W_{U_{21}}, W_{U_{22}}, W_{U_{23}}, W_{U_{24}}) = (0.49, 0.10, 0.25, 0.16)$, $\lambda_{\max} = 4, CI = 0, CR = 0 < 0.1$, and the conformance test meets the requirements.

The sensitivity of each index of the surrounding rock condition is fracture rate of the surrounding rock, dissolution and invasion of the surrounding rock, lining strength,

and tunnel buried depth. The judgment matrix of surrounding rock conditions is shown in Table 6.

The calculation results of the relative weight of the four indexes under surrounding rock conditions are as follows: $W_{U_3} = (W_{U_{31}}, W_{U_{32}}, W_{U_{33}}, W_{U_{34}}) = (0.08, 0.38, 0.23, 0.31)$, $\lambda_{\max} = 4, CI = 0, CR = 0 < 0.1$, and the conformance test meets the requirements.

According to the investigation on frost damage of 122 tunnels in seasonally cold regions in China (Figure 1), the sensitivity of each index of engineering measures is the design problem, the construction problem, the operation

TABLE 3: Membership function parameters of the negative quantitative index.

Negative quantitative index	I	II	III	IV
Ground temperature of the surrounding rock/ $^{\circ}\text{C}$	25	15	10	5
Buried depth of the tunnel/m	600	500	300	100
Lining strength	0.66	0.5	0.33	0

TABLE 4: Judgment matrix of temperature conditions.

U_1	U_{11}	U_{12}	U_{13}	U_{14}
U_{11}	1.000	0.250	0.333	0.500
U_{12}	4.000	1.000	1.333	2.000
U_{13}	3.000	0.750	1.000	1.500
U_{14}	2.000	0.500	0.667	1.000

TABLE 5: Judgment matrix of hydrological conditions.

U_2	U_{21}	U_{22}	U_{23}	U_{24}
U_{21}	1.000	5.000	2.000	3.000
U_{22}	0.200	1.000	0.400	0.600
U_{23}	0.500	2.500	1.000	1.500
U_{24}	0.333	1.667	0.667	1.000

TABLE 6: Judgment matrix of surrounding rock conditions.

U_3	U_{31}	U_{32}	U_{33}	U_{34}
U_{31}	1.000	0.200	0.333	0.25
U_{32}	5.000	1.000	1.667	1.250
U_{33}	3.000	0.600	1.000	0.750
U_{34}	4.000	0.800	1.333	1.000

and maintenance problem, and the unreasonable remedial measures. Among the four factors, temperature and hydrological conditions are the most important followed by engineering measures and surrounding rock conditions. The calculation results of the relative weight of four indexes under engineering measure conditions are as follows: $W_{U_4} = (W_{U_{41}}, W_{U_{42}}, W_{U_{43}}, W_{U_{44}}) = (0.23, 0.53, 0.18, 0.06)$. The judgment matrix of engineering measures is shown in Table 7.

The calculation results of the relative weights of four basic influencing factors in the criteria layer are as follows: $W_{U_V} = (W_{U_1}, W_{U_2}, W_{U_3}, W_{U_4}) = (0.29, 0.29, 0.13, 0.29)$, $\lambda_{\max} = 4$, $CI = 0$, $CR = 0 < 0.1$, and the conformance test meets the requirements. The weight relationship between criterion level and index level is shown in Table 8.

3.5. *Calculation Method of the Intelligent Fuzzy Comprehensive Evaluation Model.* The weighted average evaluation model is used in the first-level and the second-level

TABLE 7: Judgment matrix of engineering measure conditions.

U_4	U_{41}	U_{42}	U_{43}	U_{44}
U_{41}	1.000	1.000	2.000	1.000
U_{42}	1.000	1.000	2.000	1.000
U_{43}	0.500	0.500	1.000	0.500
U_{44}	1.000	1.000	2.000	1.000

intelligent fuzzy comprehensive evaluation model, namely, model of $M(\circ, \oplus)$.

The calculation method of the first-level fuzzy comprehensive evaluation result is shown in the following formula:

$$B_k = A_k \circ R_k = (Bk_1, Bk_2, Bk_3, Bk_4), \quad k = (1, 2, 3, 4), \quad (14)$$

where A_k is the weight of the index layer and R_k is the first-level fuzzy relation matrix.

The calculation method of the second-level fuzzy comprehensive evaluation result is shown in the following formula:

$$B = A \circ B_k = (b_1, b_2, b_3, b_4) \quad (k = 1, 2, 3, 4), \quad (15)$$

where A is the weight of the criterion layer and B_k is the first-level comprehensive evaluation result.

4. Rationality Verification of the Intelligent Model

4.1. *Example Overview.* The total length of the tunnel in cold regions is 2 950 m, the annual average precipitation in the tunnel site is 392.8 mm, the annual average temperature is 6.2°C , the extreme maximum temperature is 37.9°C , the extreme minimum temperature is -27.9°C , the maximum freezing depth of soil is 192 cm, the annual average wind speed is 1.8 m/s, and the maximum snow thickness is 18 cm. Underground water is relatively rich, mainly bedrock fissure water.

4.2. *Matrix of Fuzzy Relation.* According to the geological data and monitoring data on-site, the value of influencing factors of frost damage in the tunnel portal section is shown in Table 9.

4.3. *Operation of the First-Level Intelligent Fuzzy Comprehensive Evaluation Model.* Firstly, the influencing factors of frost damage in the tunnel portal are substituted into the membership function, and the fuzzy relation matrix R is obtained. Then, the first-level fuzzy comprehensive evaluation result is obtained by using the weighted average evaluation model:

TABLE 8: Weight relationship between criterion level and index level.

Criteria layer	Weight	Index layer	Weight	Target weight
U_1 (temperature condition)	0.29	Temperature outside the tunnel	0.1	0.029
		Ground temperature of the surrounding rock	0.4	0.116
		Driving density	0.3	0.087
		Wind speed in the tunnel	0.2	0.058
U_2 (hydrological condition)	0.29	Void area length of the surrounding rock between lining	0.49	0.1421
		Annual precipitation	0.10	0.029
		Blockage rate of the drain pipe	0.25	0.0725
		Waterproof design of three seams	0.16	0.0464
U_3 (surrounding rock condition)	0.13	Buried depth	0.08	0.0104
		Fracture rate of the surrounding rock	0.38	0.0494
		Lining strength	0.23	0.0299
		Dissolution and invasion of the surrounding rock	0.31	0.0403
U_4 (engineering measure condition)	0.29	Design issues	0.23	0.0667
		Construction issues	0.53	0.1537
		Operation and maintenance problems	0.18	0.0522
		Remedial measures	0.06	0.0174

TABLE 9: Value of influencing factors of frost damage in the portal section.

Influencing factors of frost damage	Measured value
Temperature outside the tunnel/ $^{\circ}\text{C}$	-12.8
Ground temperature of the surrounding rock/ $^{\circ}\text{C}$	7.0
Driving density/(pairs/h)	3.0
Wind speed in the tunnel/(m/s)	1.8
Void area length of the surrounding rock between lining/m	4.2
Annual precipitation/mm	392.8
Blockage rate of the drain pipe	0.1
Waterproof design of three seams	0.85
Buried depth/m	50
Fracture rate of the surrounding rock	1.5
Lining strength	0.8
Dissolution and invasion of the surrounding rock	0.3
Design issues	0.8
Construction issues	0.8
Operation and maintenance problems	0.9
Remedial measures	0.9

$$U_1 = W_{U_1} \circ R_1 = (0.1 \ 0.4 \ 0.3 \ 0.2) \circ \begin{bmatrix} 0.22 & 0.78 & 0 & 0 \\ 0 & 0 & 0.4 & 0.6 \\ 0.5 & 0.5 & 0 & 0 \\ 0.2 & 0.8 & 0 & 0 \end{bmatrix} = (0.212 \ 0.388 \ 0.16 \ 0.24), \quad (16)$$

$$U_2 = W_{U_2} \circ R_2 = (0.49 \ 0.1 \ 0.25 \ 0.16) \circ \begin{bmatrix} 0.4 & 0.6 & 0 & 0 \\ 0.518 & 0.482 & 0 & 0 \\ 1 & 0 & 0 & 0 \\ 1 & 0 & 0 & 0 \end{bmatrix} = (0.6578 \ 0.3422 \ 0 \ 0), \quad (17)$$

$$U_3 = W_{U_3} \circ R_3 = (0.08 \ 0.38 \ 0.23 \ 0.31) \circ \begin{bmatrix} 0 & 0 & 0 & 1 \\ 0 & 0.9 & 0.1 & 0 \\ 0.5 & 0.5 & 0 & 0 \\ 0 & 0 & 0 & 1 \end{bmatrix} = (0.115 \ 0.457 \ 0.038 \ 0.39), \quad (18)$$

$$U_4 = W_{U_4} \circ R_4 = (0.23 \ 0.53 \ 0.18 \ 0.06) \circ \begin{bmatrix} 0.5 & 0.5 & 0 & 0 \\ 0.5 & 0.5 & 0 & 0 \\ 1 & 0 & 0 & 0 \\ 1 & 0 & 0 & 0 \end{bmatrix} = (0.62 \ 0.38 \ 0 \ 0). \quad (19)$$

4.4. *Operation of the Second-Level Intelligent Fuzzy Comprehensive Evaluation Model.* The second level of fuzzy synthesis is as follows:

$$V = W_U \circ R = (0.29 \ 0.29 \ 0.13 \ 0.29) \circ \begin{bmatrix} 0.212 & 0.388 & 0.16 & 0.24 \\ 0.6578 & 0.3422 & 0 & 0 \\ 0.115 & 0.457 & 0.038 & 0.39 \\ 0.62 & 0.38 & 0 & 0 \end{bmatrix} = (0.446992 \ 0.381368 \ 0.05134 \ 0.1203). \quad (20)$$

The maximum membership principle is used to evaluate the calculation results, that is, which value of V is the largest and the frost damage of the tunnel is in which level. It can be seen that the frost damage degree of the tunnel portal section is class I (no frost damage or slight frost damage). It is recommended to set the thermal insulation layer and adopt general ditch in the portal section. The thermal insulation ditch is set up within 500 m of the tunnel portal. Since 2014, only slight freezing phenomenon has been seen at the tunnel portal section, and no obvious frost damage has occurred. The tunnel is in good operation condition, which is consistent with the results of analysis of the intelligent evaluation model proposed in this paper.

5. Conclusion

- (1) Based on the investigation results of 122 seasonal frozen soil tunnels in high-latitude areas of China, four key influencing factors are determined, and an intelligent evaluation system of tunnel frost damage in cold areas is proposed. Taking a tunnel in cold regions as an application example, the scientificity and rationality of the intelligent evaluation system are proved.
- (2) The intelligent fuzzy comprehensive evaluation method can be used to describe the relationship among influencing factors of tunnel frost damage in cold regions, the weight of influencing factors is calculated by analytic hierarchy process, and the main risk sources of tunnel frost damage are found out, which is an efficient and practical method for pre-evaluation.
- (3) By using the subordinate function method, the improvement from qualitative analysis to quantitative index calculation is realized. The blindness of engineering analogy construction is avoided, and the scientificity and accuracy of renovation measures for frost damage have been improved. At the same time,

the research results provide a theoretical basis for the improvement of the intelligent evaluation system of tunnel frost damage in cold regions.

Data Availability

The data used to support the findings of this study are included within the article.

Conflicts of Interest

The authors declare that there are no conflicts of interest regarding the publication of this paper.

Acknowledgments

The authors appreciate the support from the National Natural Science Foundation of China (no. 51778380).

References

- [1] G. Barla, M. Bonini, and M. Semeraro, "Analysis of the behaviour of a yield-control support system in squeezing rock," *Tunnelling and Underground Space Technology Incorporating Trenchless Technology Research*, vol. 26, no. 1, pp. 146–154, 2010.
- [2] W. Yu, W. Wang, X. Chen, and S. Du, "Field investigations of high stress soft surrounding rocks and deformation control," *Journal of Rock Mechanics and Geotechnical Engineering*, vol. 7, no. 4, pp. 421–433, 2015.
- [3] Y. S. Shen, Z. Z. Wang, J. Yu, X. Zhang, and B. Gao, "Shaking table test on flexible joints of mountain tunnels passing through normal fault," *Tunnelling and Underground Space Technology*, vol. 98, Article ID 103299, 2020.
- [4] D.-Y. Wang, J.-S. Qi, G.-Y. Cui, Y. Yang, and J. Chang, "Model test on bearing characteristics of basalt fiber-reinforced concrete lining," *Advances in Materials Science and Engineering*, vol. 2020, no. 03, pp. 1–10, Article ID 3891343, 2020.
- [5] N. Buratti, C. Mazzotti, and M. Savoia, "Post-cracking behaviour of steel and macro-synthetic fibre-reinforced

- concretes," *Construction and Building Materials*, vol. 25, no. 5, pp. 2713–2722, 2010.
- [6] Z. Wang, X.-L. Zhao, G. Xian, G. Wu, R. K. Singh Raman, and S. Al-Saadi, "Durability study on interlaminar shear behaviour of basalt-, glass- and carbon-fibre reinforced polymer (B/G/CFRP) bars in seawater sea sand concrete environment," *Construction and Building Materials*, vol. 156, pp. 985–1004, 2017.
- [7] T. M. Borhan, "Properties of glass concrete reinforced with short basalt fibre," *Materials and Design*, vol. 42, pp. 265–271, 2012.
- [8] T. Kasper, C. Edvardsen, G. Wittneben et al., "Lining design for the district heating tunnel in Copenhagen with steel fibre reinforced concrete segments," *Tunnelling and Underground Space Technology Incorporating Trenchless Technology Research*, vol. 23, no. 5, pp. 574–587, 2007.
- [9] Z. Z. Wang, L. Jiang, and Y. Gao, "Shaking table test of seismic response of immersed tunnels under effect of water," *Soil Dynamics and Earthquake Engineering*, vol. 116, pp. 436–445, 2019.
- [10] Z. Z. Wang, Y. J. Jiang, and C. A. Zhu, "Seismic energy response and damage evolution of tunnel lining structures," *European Journal of Environmental and Civil Engineering*, vol. 23, no. 6, pp. 758–770, 2019.
- [11] J. Branston, S. Das, S. Y. Kenno, C. Taylor, and C. Taylor, "Mechanical behaviour of basalt fibre reinforced concrete," *Construction and Building Materials*, vol. 124, pp. 878–886, 2016.
- [12] Y. V. Lipatov, S. I. Gutnikov, M. S. Manylov, E. S. Zhukovskaya, and B. I. Lazoryak, "High alkali-resistant basalt fiber for reinforcing concrete," *Materials & Design*, vol. 73, pp. 60–66, 2015.
- [13] C. High, H. M. Seliem, A. El-Safty, S. H. Rizkalla, and Rizkalla, "Use of basalt fibers for concrete structures," *Construction and Building Materials*, vol. 96, pp. 37–46, 2015.
- [14] G. Campione, L. La Mendola, A. Monaco, A. Valenza, and V. Fiore, "Behavior in compression of concrete cylinders externally wrapped with basalt fibers," *Composites Part B: Engineering*, vol. 69, pp. 576–586, 2015.
- [15] V. Brik, V. Ramakrishnan, and N. Tolmare, *Performance Evaluation of 3-D Basalt Fibre Reinforced Concrete & Basalt Rod Reinforced Concrete. IDEA Program Final Report*, Transportation Research Board, Washington, DC, USA, 1998.
- [16] H. Wang, L. Yuan, and H. Song, "Experimental study on mechanical property of chopped basalt fiber reinforced concrete," *Building Structure*, vol. 43, no. s2, pp. 562–564, 2013.
- [17] J. Lian, Y. Yang, M. Yang et al., "Experimental research on the mechanical behavior of chopped basalt fiber reinforced concrete," *Industrial Construction*, vol. 37, no. 6, pp. 8–10, 2007.
- [18] J. Sim, C. Park, and D. Y. Moon, "Characteristics of basalt fiber as a strengthening material for concrete structures," *Composites Part B: Engineering*, vol. 36, no. 6-7, pp. 504–512, 2005.
- [19] M. Peng, H. Huang, Q.-he Liao et al., "Test study on basic mechanical properties of basalt fiber reinforced concrete," *Concrete*, vol. 33, no. 1, pp. 74-75, 2012.
- [20] T. Ayub, N. Shafiq, and M. F. Nuruddin, "Mechanical properties of high-performance concrete reinforced with basalt fibers," *Procedia Engineering*, vol. 77, pp. 131–139, 2014.
- [21] C. Jiang, K. Fan, F. Wu, and D. Chen, "Experimental study on the mechanical properties and microstructure of chopped basalt fibre reinforced concrete," *Materials & Design*, vol. 58, pp. 187–193, 2014.

Research Article

Applications of the RST Algorithm to Nonlinear Systems in Real-Time Hybrid Simulation

Yu Tang¹ and Hui Qin ²

¹School of Hydraulic Engineering, Dalian University of Technology, Dalian 116024, China

²State Key Laboratory of Coastal and Offshore Engineering, Dalian University of Technology, Dalian 116024, China

Correspondence should be addressed to Hui Qin; hqin@dlut.edu.cn

Received 1 June 2020; Accepted 11 July 2020; Published 11 August 2020

Guest Editor: Yu-Sheng Shen

Copyright © 2020 Yu Tang and Hui Qin. This is an open access article distributed under the Creative Commons Attribution License, which permits unrestricted use, distribution, and reproduction in any medium, provided the original work is properly cited.

Real-time substructure testing (RST) algorithm is a newly developed integration method for real-time hybrid simulation (RTHS) which has structure-dependent and explicit formulations for both displacement and velocity. The most favourable characteristics of the RST algorithm is unconditionally stable for linear and no iterations are needed. In order to fully evaluate the performance of the RST method in solving dynamic problems for nonlinear systems, stability, numerical dispersion, energy dissipation, and overshooting properties are discussed. Stability analysis shows that the RST method is only conditionally stable when applied to nonlinear systems. The upper stability limit increases for stiffness-softening systems with an increasing value of the instantaneous degree of nonlinearity while decreases for stiffness-hardening systems when the instantaneous degree of nonlinearity becomes larger. Meanwhile, the initial damping ratio of the system has a negative impact on the upper stability limit especially for instantaneous stiffness softening systems, and a larger value of the damping ratio will significantly decrease the upper stability limit of the RST method. It is shown in the accuracy analysis that the RST method has relatively smaller period errors and numerical damping ratios for nonlinear systems when compared with other two well-developed algorithms. Three simplified engineering cases are presented to investigate the dynamic performance of the RST method, and the numerical results indicate that this method has a more desirable accuracy than other methods in solving dynamic problems for both linear and nonlinear systems.

1. Introduction

Real-time hybrid simulation (RTHS) is an advanced technique for assessing the seismic behaviours of structures, especially large-scale and ultralimit complex systems [1–4]. Similar to other hybrid simulation techniques, the original system in a RTHS is divided into two components, including numerical substructures and experimental substructures. The displacement-coordination and force-equilibrium are two principles for the coupling between two components at the interfaces [5]. Both the restoring force calculated from numerical substructures and the resisting force measured from experimental substructures at each time step are fed back to an integration algorithm. Then, the subsequent time-step target displacement applied to the experimental substructure is calculated by solving the step-by-step equation

of motion under external excitations and the reacting forces measured from experimental substructures [6]. “Real-time” is a significant characteristic that makes RTHS different from other hybrid simulations, and the corresponding applications include “real-time calculating of numerical substructures”, “real-time loadings on experiment substructures,” and “real-time transferring the interactions between these substructures.” So far, a few works have focused on the latter two applications. However, with an increasing size and complexity of structural systems, “real-time calculating” becomes more important and the requirement of numerical integration algorithm is higher.

In RTHS, integration algorithms are effective methods to solve discrete equations of motion for structural dynamics [7]. Integration algorithms are usually classified as explicit and implicit based on the expressions of the displacement

and the velocity. In a pseudodynamic testing that quasi-statically imposes the target displacement on the experimental substructures, an integration algorithm is explicit when the displacement for the next time step can be obtained from the response quantities (displacement, velocity, and acceleration) at the current and previous time steps, and otherwise it is implicit [8]. However, the definitions of explicit and implicit algorithms have changed in RTHS, as the loading rate becomes faster or real-time and the velocity of experimental substructures should be feedback for integration. Therefore, an integration algorithm is explicit when both the displacement and velocity for the next time step can be determined as a function of the response quantities at the current and previous time steps. Although various integration algorithms have been used to conduct RTHS, explicit integration algorithms [9–18] are generally preferred over implicit ones [19–23] as they do not involve nonlinear iterations and show a higher calculation efficiency. However, conditional stability limits the application of conventional explicit algorithms in solving structural dynamic problems because it may lead to an extremely small step size for large-number multidegree-of-freedom (MDOF) systems which have high frequency modes.

More and more researchers focus on developing new types of integration algorithms, which can achieve both explicit formulation and unconditional stability at the same time. Chang [24] developed an explicit integration algorithm which is referred to as Chang explicit method (CEM) for pseudodynamic testing, where the expression of displacement is an explicit form. However, when used in RTHS, CEM becomes semiexplicit since the determination of the velocity for the next time step requires knowledge of the unknown acceleration at the next time step. The major difference between CEM and other algorithms lies in the coefficients of difference equations introduced in displacement increment which are functions of initial structural properties and time step rather than constants, making it a structure-dependent algorithm. Chen and Ricles [12] proposed another type of structure-dependent integration algorithm named CR method (CRM) based on discrete control theory. Different from CEM, the expressions for displacement and velocity are both in explicit forms and the coefficients for both displacement increment and velocity increment are functions of initial structural properties and time step. It is noted that CEM and CRM are unconditionally stable for linear and instantaneous stiffness softening systems and possess second order accuracy [25, 26]. Kolay and Ricles [14] introduced a family of explicit direct integration algorithms using discrete control theory, which is named as explicit KR- α algorithm. This method is unconditionally stable for linear and instantaneous stiffness softening systems, and it can control the amount of numerical damping by a single parameter. However, all these favourable attributes are achieved at the expense of degraded accuracy for general structural dynamics problems [27]. Tang and Lou [15] presented a new type of structure-dependent explicit integration algorithm for RTHS using a pole-mapping rule from the discrete domain and named it real-time substructure testing (RST) algorithm. For the RST

method, the structure-dependent coefficients are introduced only in displacement increment while those for velocity increment are constant. Kim and Lee [28] also proposed an explicit integration algorithm with controllable numerical dissipation in the high frequency range, and an extended stability limit and improved spectral characteristics are achieved as well. This method has second-order accuracy but is conditionally stable.

Though the performance of the RST method in solving dynamic problems for linear systems has been well studied, its application to nonlinear systems need to be further discussed and evaluated. In this work, the numerical properties of the RST method in RTHS are discussed for nonlinear structural dynamic problems and compared with other two structure-dependent integration algorithms (i.e., CEM and CRM) since they have quite similar formulations and numerical properties. Firstly, the stability and the upper stability limit of the RST method for nonlinear systems with softening and hardening stiffness are discussed using the spectra radius method. Then, the numerical dispersion and energy dissipation characteristics caused by the numerical damping are evaluated. In addition, the overshooting behaviour [25, 29] of the RST method in displacement is addressed as well. Three different simplified engineering structural systems are presented as numerical examples to demonstrate the computational stability and accuracy of the RST method when compared with other algorithms.

2. Formulations of Structure-Dependent Integration Algorithms

2.1. Single-Degree-of-Freedom (SDOF) Systems. The differential equation of motion for a SDOF system under external excitations can be expressed in time domain as [30, 31]

$$m_N \ddot{u}(t) + c_N \dot{u}(t) + r_N + R_E(u, \dot{u}) = f(t), \quad (1)$$

$$R_E(u, \dot{u}) = c_E \dot{u}(t) + k_E u(t), \quad (2)$$

where m , c , and k are the mass, viscous damping, and stiffness, respectively; \ddot{u} , \dot{u} , and u are the acceleration, velocity, and displacement, respectively; r_N is the restoring force of the numerical substructure, where $r_N = k_N u(t)$ is for linear systems; $R_E(u, \dot{u})$ is the reacting force measured from the experimental substructure; subscript N and E are the numerical substructure and the experimental substructure; and $f(t)$ is the external exciting force. When discretized by time steps, equation (1) can be written in its discrete form:

$$m_N \ddot{u}_i + c_N \dot{u}_i + r_N(u_i) + R_E(u_i, \dot{u}_i) = f_i, \quad (3)$$

where \ddot{u}_i , \dot{u}_i , and u_i are the acceleration, velocity, and displacement at i th time step, respectively; $R_E(u_i, \dot{u}_i)$ is the reacting force of the experimental substructure at i th time step; and f_i is the external exciting force at i th time step.

The general expressions of the displacement and velocity increments for the RST, CEM, and CRM methods is found to be

$$u_{i+1} = u_i + \alpha_1 \Delta t \dot{u}_i + \alpha_2 \Delta t^2 \ddot{u}_i, \quad (4)$$

$$\dot{u}_{i+1} = \dot{u}_i + \alpha_3 \Delta t \ddot{u}_i + \alpha_4 \Delta t \ddot{u}_{i+1}, \quad (5)$$

where Δt is the chosen integration time step. The coefficients α_1 , α_2 , α_3 , and α_4 for the three methods are

$$\begin{cases} \alpha_1 = \frac{4}{4 + 4\xi\Omega + \Omega^2}, & \alpha_2 = \frac{-8\xi^2 - 2\xi\Omega + 4}{4 + 4\xi\Omega + \Omega^2}, & \alpha_3 = 1, & \alpha_4 = 0, & \text{(RST)}, \\ \alpha_1 = \frac{4 + 4\xi\Omega}{4 + 4\xi\Omega + \Omega^2}, & \alpha_2 = \frac{2}{4 + 4\xi\Omega + \Omega^2}, & \alpha_3 = \alpha_4 = \frac{1}{2}, & & \text{(CEM)}, \\ \alpha_1 = 1, & \alpha_2 = \alpha_3 = \frac{2}{4 + 4\xi\Omega + \Omega^2}, & \alpha_4 = 0 & & \text{(CRM)}, \end{cases} \quad (6)$$

where viscous damping ratio $\xi = \xi_N + \xi_E$, $\xi_N = c_N/2m\omega_n$, $\xi_E = c_E/2m\omega_n$, $\Omega = \Delta t\omega_n = \Delta t\sqrt{(k_N + k_E)/m}$, and ω_n is the natural frequency of the system determined from the initial system.

Obviously, the coefficients in each method are not all constant, and some of them depend on the initial structural properties (ξ and ω_n) and time step Δt . Substituting equation (6) into equation (5), it is seen that CEM is implicit as there is \ddot{u}_{i+1} in the velocity formulation, which is unknown at $(i+1)$ th time step. Substituting equations (4)–(6) into equation (3) gives

$$\tilde{m}\ddot{u}_{i+1} = \tilde{f}_{i+1}, \quad (7)$$

$$\tilde{m} = m + \alpha_4 c \Delta t, \quad (8)$$

$$\begin{aligned} \tilde{f}_{i+1} = & f_{i+1} - c(\dot{u}_i + \alpha_3 \Delta t \ddot{u}_i) \\ & - k(u_i + \alpha_1 \Delta t \dot{u}_i + \alpha_2 \Delta t^2 \ddot{u}_i), \end{aligned} \quad (9)$$

where c and k are the viscous damping coefficient and stiffness of the global structural system, which are equal to $(c_N + c_E)$ and $(k_N + k_E)$, respectively. The velocity of the CEM method at $(i+1)$ th time step can be rewritten in an explicit form as follows:

$$\dot{u}_{i+1} = \dot{u}_i + \alpha_3 \Delta t \ddot{u}_i + \alpha_4 \Delta t \left(\frac{\tilde{f}_{i+1}}{\tilde{m}} \right). \quad (10)$$

2.2. Multidegree-of-Freedom (MDOF) Systems. For a MDOF, the coupled differential equation of motion should be written in a matrix form as follows:

$$\mathbf{M}_N \ddot{\mathbf{U}}_i + \mathbf{C}_N \dot{\mathbf{U}}_i + \mathbf{R}_N (\mathbf{U}_i) + \mathbf{R}_E (\mathbf{U}_i, \dot{\mathbf{U}}_i) = \mathbf{F}_i, \quad (11)$$

where \mathbf{M} , \mathbf{C} , and \mathbf{K} are mass matrix, viscous damping coefficients matrix, and stiffness matrix, respectively; $\ddot{\mathbf{U}}_i$, $\dot{\mathbf{U}}_i$, and \mathbf{U}_i are the acceleration vector, velocity vector, and displacement vector at i th time step, respectively; \mathbf{R}_N is the restoring force matrix of the numerical substructure, where $\mathbf{R}_N = \mathbf{K}_N \mathbf{U}_i$ for linear systems; and \mathbf{R}_E and \mathbf{F}_i are the reacting force matrix of the experimental substructure and the external exciting force vector, respectively.

For simplicity, \mathbf{C} is supposed to be proportional and the orthogonality of modes is available in the following equations. For a MDOF linear system, rewrite equations (4), (5), and (11) in the modal coordinate system as follows:

$$\mathbf{M}^* \dot{\mathbf{Y}}_i + \mathbf{C}^* \dot{\mathbf{Y}}_i + \mathbf{K}^* \mathbf{Y}_i + \mathbf{R}^* = \Phi^T \mathbf{F}_i, \quad (12)$$

$$\mathbf{Y}_{i+1} = \mathbf{Y}_i + \alpha_1^* \Delta t \dot{\mathbf{Y}}_i + \alpha_2^* \Delta t^2 \ddot{\mathbf{Y}}_i, \quad (13)$$

$$\dot{\mathbf{Y}}_{i+1} = \dot{\mathbf{Y}}_i + \alpha_3^* \Delta t \ddot{\mathbf{Y}}_i + \alpha_4^* \Delta t \ddot{\mathbf{Y}}_{i+1}, \quad (14)$$

in which, $\Phi = [\phi_1 \ \phi_2 \ \cdots \ \phi_n]$ is the modal matrix derived from solving the eigenvalue problem; n is the number of modes; $\mathbf{M}^* = \Phi^T \mathbf{M} \Phi$, $\mathbf{C}^* = \Phi^T \mathbf{C} \Phi$, and $\mathbf{K}^* = \Phi^T \mathbf{K} \Phi$ are modal mass matrix, modal diagonal damping matrix, and modal diagonal stiffness matrix, respectively; $\dot{\mathbf{Y}}$, $\ddot{\mathbf{Y}}$, and \mathbf{Y} are the acceleration vector, velocity vector, and displacement vector in modal coordinates, respectively; $\alpha_j^* = \Phi^{-1} \alpha_j \Phi$ ($j = 1, 2, 3, 4$) are the diagonal integration coefficient matrices, and α_j is expressed as follows:

$$\begin{cases} \alpha_1 = \mathbf{D}^{-1} (4\mathbf{M}), & \alpha_2 = \mathbf{D}^{-1} (4\mathbf{M} - \Delta t \mathbf{C} - 2\mathbf{S}^2), & \alpha_3 = 1, & \alpha_4 = 0, & \text{(RST)}, \\ \alpha_1 = 1, & \alpha_2 = \mathbf{D}^{-1} (4\mathbf{M}), & \alpha_3 = \mathbf{D}^{-1} (4\mathbf{M}), & \alpha_4 = 0, & \text{(CRM)}, \\ \alpha_1 = \mathbf{D}^{-1} (\mathbf{M} + 2\Delta t \mathbf{C}), & \alpha_2 = \mathbf{D}^{-1} (2\mathbf{M}), & \alpha_3 = \frac{1}{2}, & \alpha_4 = \frac{1}{2}, & \text{(CEM)}, \end{cases} \quad (15)$$

where $\mathbf{D} = 4\mathbf{M} + 2\Delta t\mathbf{C} + \Delta t^2\mathbf{K}$ and $\mathbf{S} = \mathbf{M}^{*-1} \cdot \mathbf{C}^* \cdot \mathbf{K}^{*-1} \cdot \mathbf{M}^*$.

For a MDOF nonlinear system, equations (12)–(14) are not valid, and the general formulation and coefficients for the three methods should be

$$\mathbf{U}_{i+1} = \mathbf{U}_i + \alpha_1 \Delta t \dot{\mathbf{U}}_i + \alpha_2 \Delta t^2 \ddot{\mathbf{U}}_i, \quad (16)$$

$$\dot{\mathbf{U}}_{i+1} = \dot{\mathbf{U}}_i + \alpha_3 \Delta t \ddot{\mathbf{U}}_i + \alpha_4 \Delta t \ddot{\mathbf{U}}_{i+1}, \quad (17)$$

$$\begin{cases} \alpha_1 = \mathbf{D}_0^{-1}(4\mathbf{M}), & \alpha_2 = \mathbf{D}_0^{-1}(4\mathbf{M} - \Delta t\mathbf{C}_0 - 2\mathbf{S}_0^2), & \alpha_3 = 1, & \alpha_4 = 0 & (\text{RST}), \\ \alpha_1 = 1, & \alpha_2 = \mathbf{D}_0^{-1}(4\mathbf{M}), & \alpha_3 = \mathbf{D}_0^{-1}(4\mathbf{M}), & \alpha_4 = 0 & (\text{CRM}), \\ \alpha_1 = \mathbf{D}_0^{-1}(\mathbf{M} + 2\Delta t\mathbf{C}_0), & \alpha_2 = \mathbf{D}_0^{-1}(2\mathbf{M}), & \alpha_3 = \frac{1}{2}, & \alpha_4 = \frac{1}{2} & (\text{CEM}), \end{cases} \quad (18)$$

where $\mathbf{D}_0 = 4\mathbf{M} + 2\Delta t\mathbf{C}_0 + \Delta t^2\mathbf{K}_0$; $\mathbf{S}_0 = \mathbf{M}^{-1} \cdot \mathbf{C}_0 \cdot \mathbf{K}_0^{-1} \cdot \mathbf{M}$; \mathbf{C}_0 is the damping matrix generally determined from the initial structural properties; and \mathbf{K}_0 is the initial stiffness matrix.

2.3. Stability Analysis of the RST Method in Nonlinear Systems.

The unconditional stability of the RST method for linear elastic systems has been verified by authors [15, 24, 32]. In this section, stability analysis of the RST method for nonlinear systems is mainly carried out and compared with that of the CEM and CRM methods.

In order to realistically reflect the change of stiffness during the test, a parameter, defined as the ratios of the stiffness at the end of each time step k_i over the initial stiffness k_0 , is introduced to monitor this change. That is,

$$\delta_{i+1} = \frac{k_{i+1}}{k_0}, \quad (19)$$

where δ_{i+1} is the instantaneous degree of nonlinearity. When $\delta_{i+1} = 1$, it means that the system is linear, and no stiffness change occurs during the test. When $\delta_{i+1} > 1$, it represents that the instantaneous stiffness becomes harder at the end of the $(i+1)$ th time step, while $0 < \delta_{i+1} < 1$ denotes instantaneous stiffness soften.

From equations (3)–(5), the computing sequence at $(i+1)$ th time step can be written in a recursive matrix form as follows:

$$\mathbf{X}_{i+1} = \mathbf{A}\mathbf{X}_i + \mathbf{L}f_{i+1}, \quad (20)$$

in which, $\mathbf{X}_{i+1} = [u_{i+1}]$, $\mathbf{X}_{i+1} = [u_{i+1}, \Delta t \dot{u}_{i+1}, \Delta t^2 \ddot{u}_{i+1}]^T$ is state vector values at the $(i+1)$ th time step; load factor $\mathbf{L} = [0, 0, \Delta t^2/m]^T$; and amplification matrix \mathbf{A} for each algorithm is found to be

$$\mathbf{A}^{\text{RST}} = \begin{bmatrix} 1 & \alpha_1 & \alpha_2 \\ 0 & 1 & 1 \\ -\Omega_{i+1}^2 & -2\xi\Omega_0 - \alpha_1\Omega_{i+1}^2 & -2\xi\Omega_0 - \alpha_2\Omega_{i+1}^2 \end{bmatrix}, \quad (21)$$

$$\mathbf{A}^{\text{CEM}} = \begin{bmatrix} 1 & \alpha_1 & \alpha_2 \\ \frac{-\Omega_{i+1}^2}{2(1+\xi\Omega_0)} & \frac{2-\alpha_1\Omega_{i+1}^2}{2(1+\xi\Omega_0)} & \frac{1-\alpha_2\Omega_{i+1}^2}{2(1+\xi\Omega_0)} \\ \frac{-\Omega_{i+1}^2}{1+\xi\Omega_0} & \frac{-2\xi\Omega_0 - \alpha_1\Omega_{i+1}^2}{1+\xi\Omega_0} & \frac{-\xi\Omega_0 - \alpha_2\Omega_{i+1}^2}{1+\xi\Omega_0} \end{bmatrix}, \quad (22)$$

$$\mathbf{A}^{\text{CRM}} = \begin{bmatrix} 1 & 1 & \alpha_1 \\ 0 & 1 & \alpha_2 \\ -\Omega_{i+1}^2 & -2\xi\Omega_0 - \Omega_{i+1}^2 & -2\alpha_1\xi\Omega_0 - \alpha_2\Omega_{i+1}^2 \end{bmatrix}. \quad (23)$$

Based on the algorithm stability analysis theory, a stable computation of an integration algorithm can be obtained when the spectral radius $\rho(\mathbf{A}) = \max(|\lambda_{1,2,3}|) \leq 1$, where the eigenvalues $\lambda_{1,2,3}$ can be determined by solving the following eigenvalue problem [31, 32]:

$$|\mathbf{A} - \lambda\mathbf{I}| = \lambda^3 - 2A_1\lambda^2 + A_2\lambda - A_3 = 0, \quad (24)$$

where \mathbf{I} is the identity matrix and A_1 , A_2 , and A_3 are three coefficients indicating half of the trace, sum of principal minors, and determinant of \mathbf{A} , respectively.

After substituting equations (21)–(23) into equation (24), the upper stability limits $[\Omega]$ for the RST, CEM, and CRM methods can be formulized. The variations of $[\Omega]$ for all three methods with δ and the case of $\xi = 0.0, 0.05, 0.2$ are shown in Figure 1. It illustrates that the RST method is conditionally stable for nonlinear systems except for instantaneous stiffness softening systems when $\xi = 0.0$. The upper stability limit $[\Omega]$ of the RST method increases with an increasing value of δ when $0 < \delta < 1$ while decreases with a growth of δ value when $\delta > 1$. The initial damping ratio has a great impact on $[\Omega]$ as well especially for instantaneous stiffness softening systems, and a larger value of ξ will significantly decrease the upper stability limit of the RST method. The variations of $[\Omega]$ with δ for the CEM and CRM methods are also plotted in Figure 1, and both these methods are unconditionally stable when $0 < \delta \leq 1$ while conditionally stable when $\delta > 1$. In particular, the curves for the CRM method are overlapped together for different ξ while that for

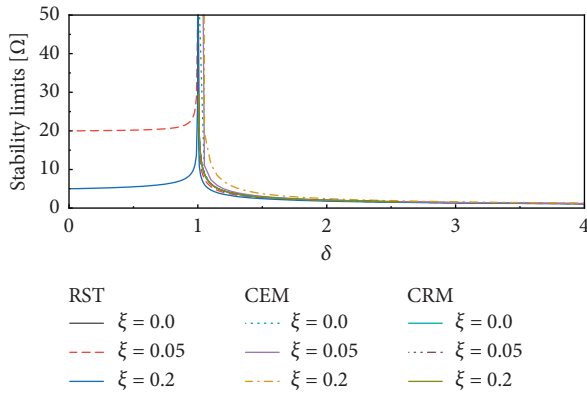


FIGURE 1: Variations of upper stability limits with δ and different values of ξ .

the RST and CEM methods seem to move upward as the value of ξ increases.

3. Accuracy Analysis

Two principal eigenvalues at the $(i + 1)$ th time step for the three structure-dependent integration algorithms are complex conjugate and can be expressed as [33]

$$\lambda_{1,2} = A_1 \pm i\sqrt{A_2 - A_1^2} = \exp\left(-\bar{\xi}_{i+1} \cdot \bar{\Omega}_{i+1} \pm i\bar{\Omega}_{i+1}^D\right), \quad (25)$$

where

$$\left\{ \begin{array}{l} i = \sqrt{-1}, \\ \rho = \sqrt{A_2}, \\ \bar{\Omega}_{i+1} = \bar{\omega}_{i+1} \Delta t, \\ \bar{\Omega}_{i+1}^D = \bar{\Omega}_{i+1} \sqrt{1 - \xi^2} = \arctan\left(\sqrt{\frac{A_2}{A_1^2} - 1}\right), \\ \bar{\xi}_{i+1} = -\frac{\ln(A_2)}{2\bar{\Omega}_{i+1}}, \end{array} \right. \quad (26)$$

in which $\bar{\xi}_{i+1}$ and $\bar{\omega}_{i+1}$ are the numerical damping ratio and frequency related to integration algorithms.

In general, numerical dispersion and energy dissipation characteristics are two indexes evaluating the accuracy of an integration algorithm. The former characteristic is usually expressed by the relative period error $PE = ((\bar{T} - T_n)/T_n) = (\omega_n/\bar{\omega} - 1)$, where $\bar{T} = 2\pi/\bar{\omega}$ and $T_n = 2\pi/\omega_n$ referred to the numerical and exact periods of the systems. The later one can be expressed by the numerical damping ratio $\bar{\xi}$, which is related to amplitude decay in one cycle of free-vibration.

The variations of PE are shown in Figure 2 ($\xi = 0$) and Figure 3 ($\xi = 0.1$) for different δ . It is worth noting that values of PE in all the figures are positive and increase with increasing values of Ω for a given δ , which results in period elongation for the three methods. It is also seen that the

curves are totally overlapped for the RST, CEM, and CRM methods for different values of δ as $\xi = 0$ as well as for $\delta = 1$ as $\xi = 0.1$. Meanwhile, for a specific value of Ω , the RST method possesses the minimum period elongation while the CRM method produces the maximum period elongation for $\delta = 0.5, 2$ as $\xi = 0.1$.

The variations of $\bar{\xi}$ with Ω for the RST, CRM, and CEM methods can be found in equation (26) with A_1 and A_2 derived from equations (21)–(24). It is noteworthy that for $\xi = 0$, A_2 equals to 1 for all the three methods, which leads to $\rho = 1$ and $\bar{\xi} = 0$ in equation (26). This implies that no energy dissipation occurred for the three methods if a zero viscous damping ratio adopted. On the contrary, there will be no amplitude decay for an undamped free vibration. When viscous damping ratio is considered, $\rho_{\infty} = 1$ and the variations of $\bar{\xi}$ with Ω for different δ as $\xi = 0.1$ are shown in Figure 4. For a linear elastic system with viscous damping ratio ($\delta = 1$), $\bar{\xi} = \xi$ for $\Omega = 0$ and then reduces below ξ with increasing Ω , indicating that the viscous damping ratio is not effective in reducing spurious participation of higher modes. Also, the curves for the three methods are totally overlapped in this case, as shown in Figure 4(b). Meanwhile, drastically different phenomena are found for the case of $\delta = 0.5$ and 2.0. In Figure 4(a), the variations of $\bar{\xi}$ with Ω are as similar as the case of $\delta = 1$, but $\bar{\xi} > \xi$ for a small value of produces undesired dissipation in lower modes. In Figure 4(c), $\bar{\xi}$ reduces far below ξ with increasing omega and then increases again in a specific value of Ω . It implies that favourable energy dissipation can be obtained to filter out the spurious participation of higher modes.

4. Overshooting

In general, two primary factors are taken into account for choosing an appropriate time step Δt in the step-by-step integration algorithm in order to perform well in solving structural dynamic problems. The first factor is the highest frequency f_h that is noteworthy in the dynamic analysis, and its value depends both on the higher modal frequency of the system and the effective high frequency of the dynamic load [15]. The second factor is the stability requirement of an integration algorithm. Since the value of a conditionally stable algorithm is strictly limited by upper stability limit, the value of Δt can be easily determined. If an algorithm is unconditionally stable, the value of Δt depends largely on the first factor.

According to the basic theory of structural dynamics, reliable solutions can be achieved when $\Delta t/T \leq 1/10$ ($T = 1/f_h$) [31]. That is, a large time step involving in dynamic analysis, properly speaking, a large value of the ratio of Δt to T will lead to calculation distortion or so called “overshooting.” Actually, the phenomenon that an integration algorithm might overshoot the exact solution in the initial stage of the transient response or in the steady-state response when $\Omega \rightarrow \infty$ has been found and discussed in some papers [25, 29]. Tang and Lou [34] provided a detailed explanation for the issue of overshooting by solving free and forced vibration problems of three

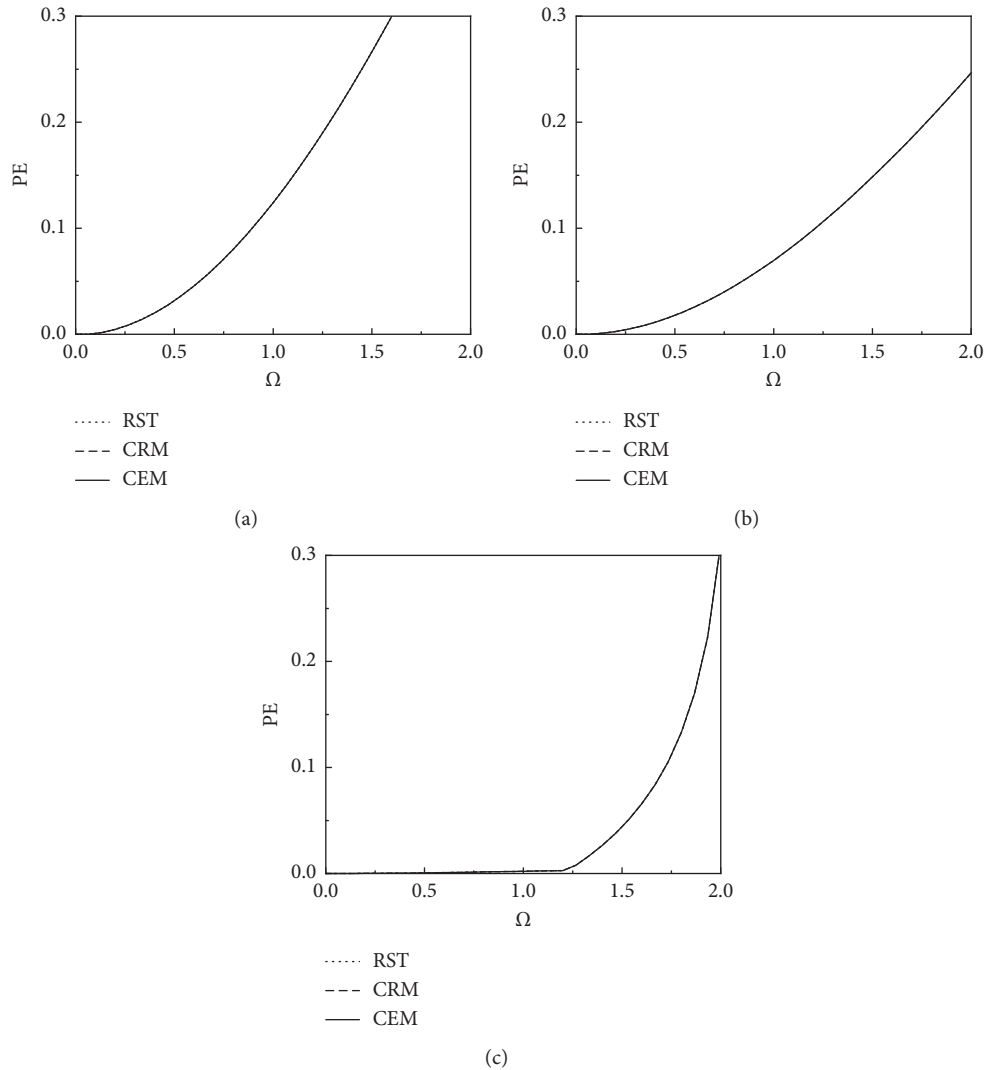


FIGURE 2: Variations of relative period errors with ($\xi = 0$). (a) $\delta = 0.5$. (b) $\delta = 1.0$. (c) $\delta = 2.0$.

single-degree-of-freedom systems with different initial stiffness ($k_0 = 10^2, 10^4, 10^6$) and different values of $\Delta t/T$. It is reasonable to discuss the overshooting issue in zero damping systems as undesirable contaminated responses will be eliminated due to vibration damping. It is noted that overshooting in the steady-state response depends mainly on the rationality of integration time step selection. In a real-time hybrid testing, overshooting will not appear in the entire response for any unconditionally stable integration algorithm as the value of time step Δt is strictly limited by the “real-time” requirement. Therefore, the overshooting property of the three methods will not be discussed in detail herein, and the conclusions made by Tang and Lou [34] will be demonstrated by the following numerical examples.

5. Numerical Simulation of RTHS

In this section, three numerical examples are applied to examine the numerical properties of the RST method when

compared with the CRM and CEM methods for both linear elastic and nonlinear systems.

Example 1. An undamped 4-story building

A linear 4-story shear building with no structural damping is shown in Figure 5. The initial structural properties are $m_1 = 10^8$ kg, $m_2 = 10^5$ kg, $m_3 = 10^5$ kg, $m_4 = 10^3$ kg, and $k = 360 \times 10^7$ N/m. The natural frequencies of the system are 5.9940, 116.95, 306.59, and 1906.9 rad/s for the four modes, respectively; the normalized modal matrix is given by $\Phi = [\phi_1 \ \phi_2 \ \phi_3 \ \phi_4]$, where $\phi_1 = [0.9970 \ 0.9990 \ 1.0000 \ 1.0000]^T$, $\phi_2 = [-0.0002 \ 0.6293 \ 1.0000 \ 1.0000]^T$, $\phi_3 = [0.0006 - 1.5882 \ 0.9412 \ 1.0000]^T$, and $\phi_4 = [-0.0000 \ 0.0001 - 0.0101 \ 1.0000]^T$. It is clear that the system is intentionally designed to have a relatively high frequency for the fourth mode. The first two stories are referred as the experimental substructures while the upper two stories are taken as the numerical substructures.

The free vibration responses of the system subjected to zero initial velocity and displacement $\mathbf{U}_0 = (\phi_1 + \phi_2 + 0.5 \phi_4)$

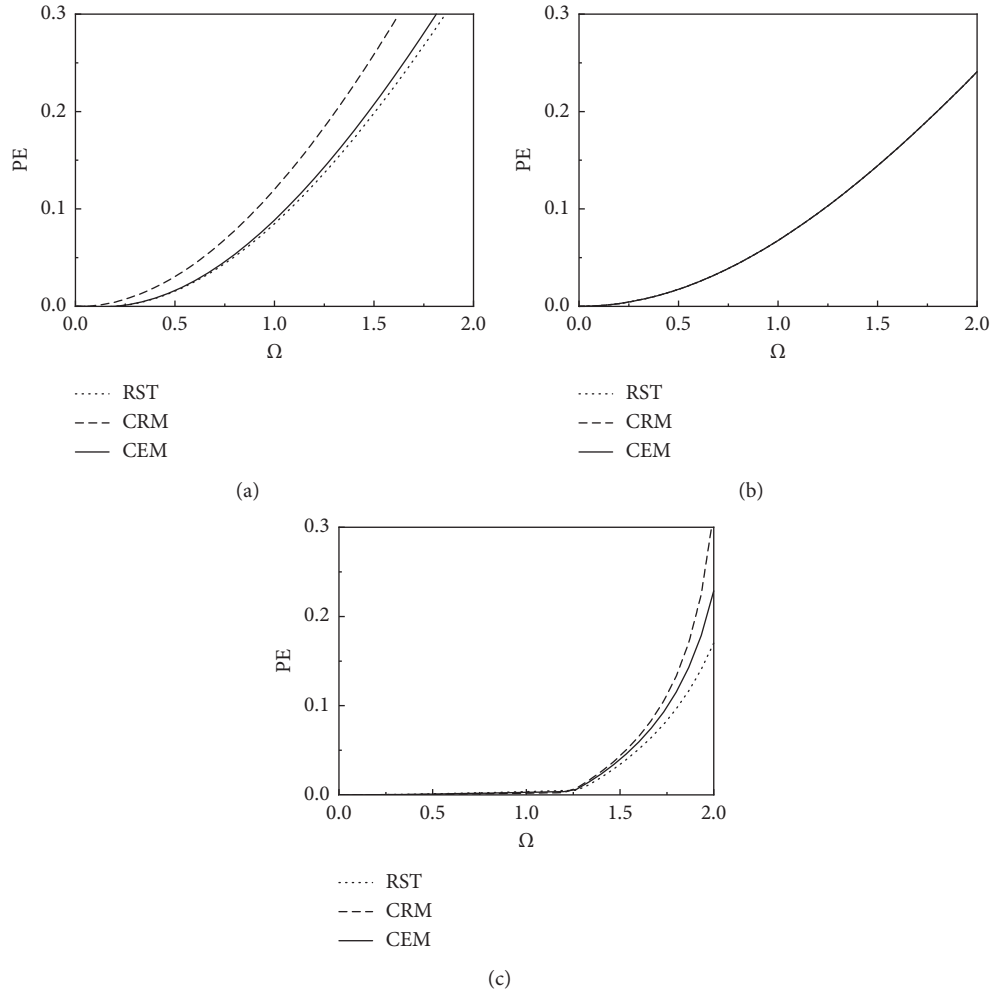


FIGURE 3: Variations of relative period errors with ($\xi=0.1$). (a) $\delta=0.5$. (b) $\delta=1.0$. (c) $\delta=2.0$.

are calculated. The time step of $\Delta t=0.01$ s is employed for RST, CRM, and CEM, and the ratio of $\Delta t/T_4=3.036$. The displacement response obtained from the undamped displacement equation based on the structural dynamics theory [31] is considered as the exact solution. Defining the relative error e (%) as

$$e = \frac{A_{\text{METHOD}} - A_{\text{EXACT}}}{A_{\text{EXACT}}} \times 100, \quad (27)$$

in which A is the peak value of responses derived from each integration algorithm; subscript “METHOD” refers to the RST, CRM, and CEM methods, while “EXACT” refers to the exact solutions, which are calculated by the Newmark method with a time step of 0.005 s for the overall structural system.

It is shown in Figure 6 that all the three methods provide reliable solutions, and the relative errors of the displacement peaks are 1.46% (RST), 2.64% (CRM), and 0.37% (CEM), respectively. The three methods result in a slight period elongation and zero amplification decay, as shown in Figure 6(a), which are consistent with the previous conclusions. The results also indicate that overshooting

behaviours will not appear in a zero damping system if the time step is determined from the perspective of the highest frequency.

Example 2. A 3-story building with a vibration isolator

A linear 3-story shear building with a vibration isolator is shown in Figure 7. In this case, the frame is taken as the numerical substructure while the vibration isolator is supposed to be the experimental substructure. The initial structural properties are $m=160 \times 10^3$ kg, $k_N=360 \times 10^7$ N/m, $k_E=9 \times 10^6$ N/m, $c_N=0$, and $c_E=115 \times 10^5$ N s/m. The natural frequencies of the whole system are 3.7459, 114.10, 212.17, and 277.17 rad/s for the four modes, respectively; the normalized modal matrix is given by $\Phi = [\phi_1 \phi_2 \phi_3 \phi_4]$, where $\phi_1 = [0.9231 \ 0.9231 \ 1.0000 \ 1.0000]^T$, $\phi_2 = [-1.0000 \ -0.5225 \ 0.4245 \ 1.0000]^T$, $\phi_3 = [1.0833 \ -1.0000 \ -1.0833 \ 1.0000]^T$, and $\phi_4 = [-1.0000 \ 2.3657 \ -2.3657 \ 1.0000]^T$.

The seismic performance of the system is studied by exciting the ground acceleration record of EL Centro (1940 NS) with peak ground acceleration (PGA) scaled to 0.8 g. The system is subjected to zero initial velocity and initial displacement. The time step of $\Delta t=0.02$ s is employed for the

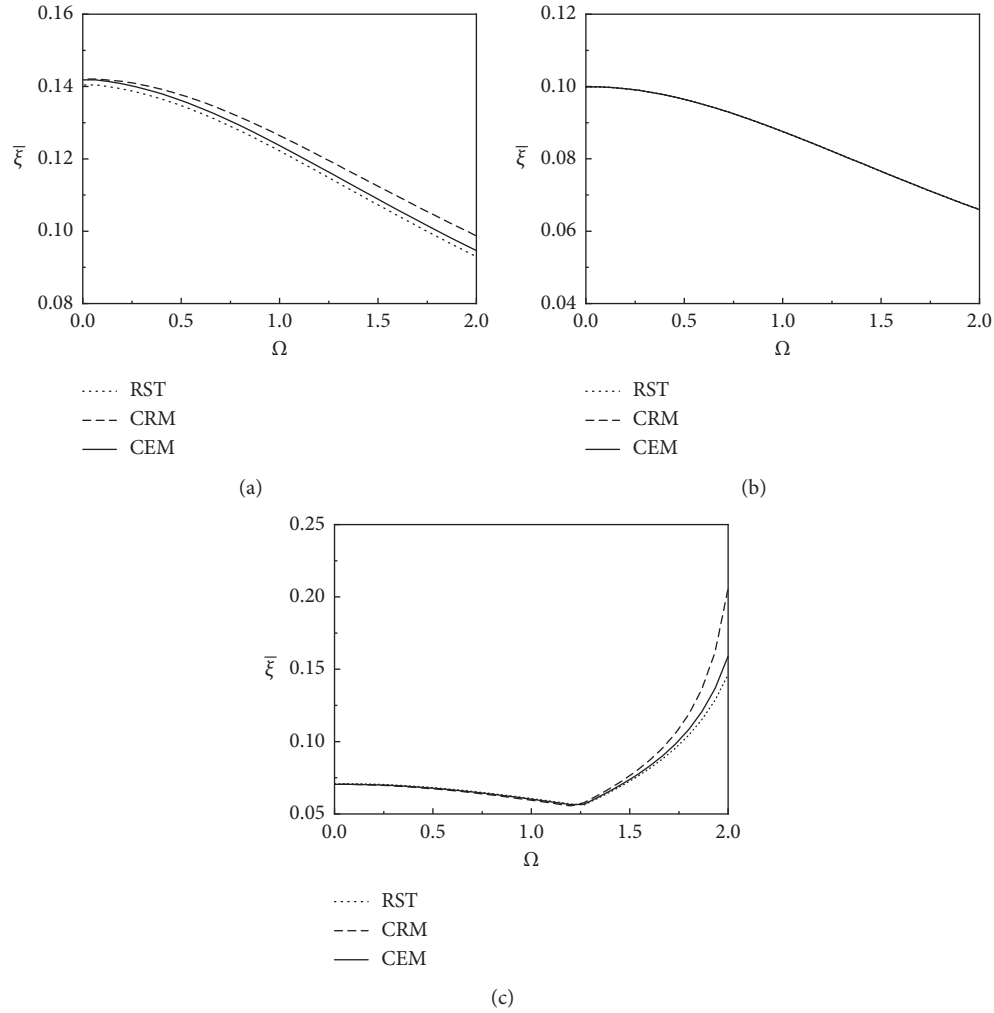


FIGURE 4: Variations of numerical damping ratios with ($\xi=0.1$). (a) $\delta=0.5$. (b) $\delta=1.0$. (c) $\delta=2.0$.

three methods, and the ratio of $\Delta t/T_4 = 0.883$. The responses obtained from the Newmark method with constant average acceleration (N4 algorithm) [15] with a time step of $\Delta t = 0.005$ s is considered as the exact solution for comparisons. Numerical results for the top story are plotted in Figure 8, and the relative errors of the displacement peaks are 0.37% (RST), 0.50% (CRM), and 0.32% (CEM), respectively.

Example 3. A 5-story building with softening stiffness

A 5-story shear building (as shown in Figure 9) with softening stiffness is applied to investigate the performance of the RST, CRM, and CEM methods in a nonlinear system. In this case, the top three stories are taken as the numerical substructure while the first two stories are supposed to be the experimental substructure. The initial structural properties are $m = 10^5$ kg, $k_0 = 10^8$ N/m, and $\xi = 0.05$. The softening stiffness of the system after deformation is intentionally designated as $k_i = k_{i,0} (1 - \sqrt{|\Delta u_i|})$, where subscript i refers to the i th story and Δu_i is the interstory drift for the i th story. The natural initial frequencies of the whole system are 9.001, 26.273, 41.417, 53.206, and 60.684 rad/s for the five modes,

respectively; the normalized modal matrix is given by $\Phi = [\phi_1 \phi_2 \phi_3 \phi_4 \phi_5]$, where $\phi_1 = [0.2828 \ 0.5263 \ 0.7368 \ 0.8947 \ 1.0000]^T$, $\phi_2 = [-0.8235 \ -1.1176 \ -0.5882 \ 0.3160 \ 1.0000]^T$, $\phi_3 = [1.3571 \ 0.3837 \ -1.2143 \ -0.7143 \ 1.0000]^T$, $\phi_4 = [1.7000 \ -1.4000 \ -0.5372 \ 1.9000 \ -1.0000]^T$, and $\phi_5 = [-1.8614 \ 3.1643 \ -3.5366 \ 2.6059 \ -1.0000]^T$. Assuming Rayleigh damping [31], the damping matrix of the system and the proportionality factors are given by

$$\mathbf{C}_0 = a_0 \mathbf{M} + a_1 \mathbf{K}_0, \quad (28)$$

$$\begin{pmatrix} a_0 \\ a_1 \end{pmatrix} = \frac{2\xi}{\omega_1 + \omega_2} \begin{pmatrix} \omega_1 \omega_2 \\ 1 \end{pmatrix}. \quad (29)$$

The seismic responses of the system with zero initial conditions is studied by exciting the ground acceleration record of EL Centro (1940 NS) with peak ground acceleration (PGA) scaled to 0.9 g. The results obtained from N4 algorithm with a time step $\Delta t = 0.005$ s is considered as the exact solution for comparisons. The time step of $\Delta t = 0.02$ s is employed for the RST, CRM, and CEM

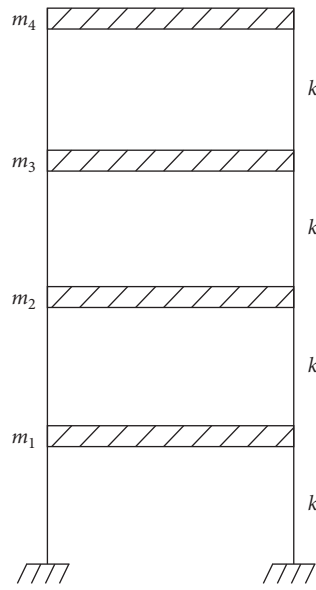


FIGURE 5: Numerical modelling of a 4-story shear building.

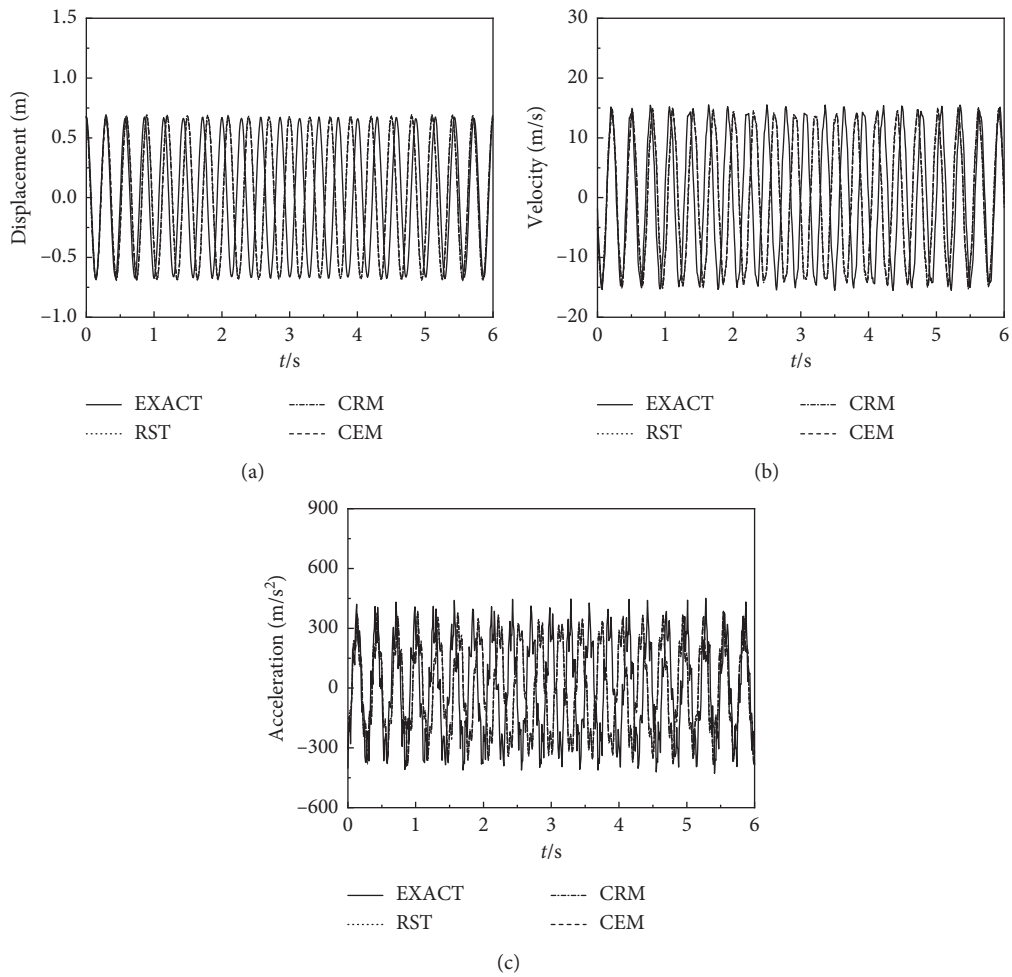


FIGURE 6: Free vibration responses for the 4th story of the system. (a) Displacement. (b) Velocity. (c) Acceleration.

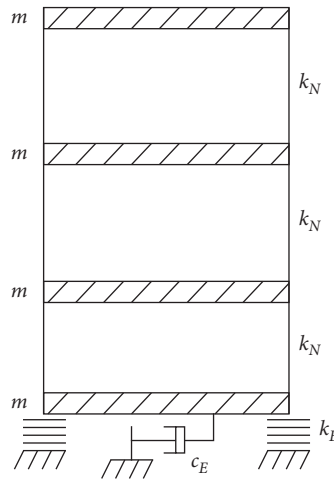


FIGURE 7: Numerical modelling of a 3-story shear building with a vibration isolator.

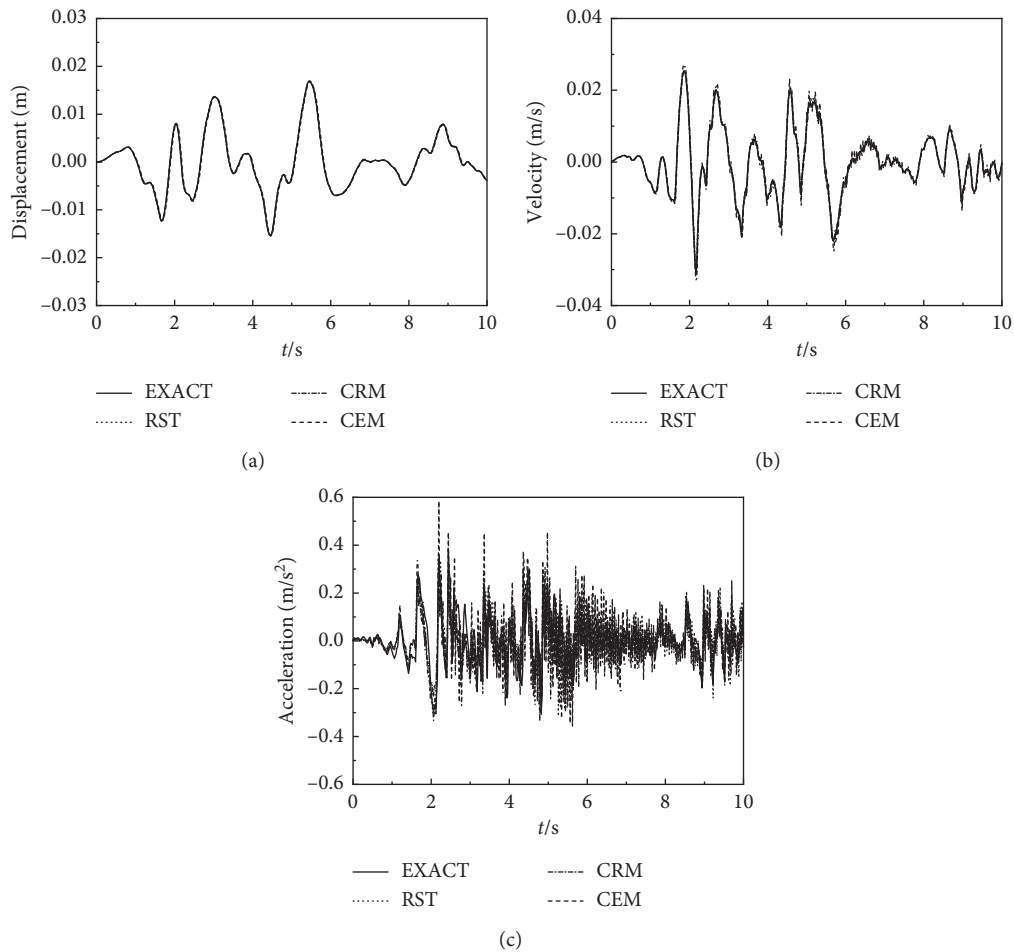


FIGURE 8: Seismic responses for the 3rd story of the system. (a) Displacement. (b) Velocity. (c) Acceleration.

methods, and the ratio of $\Delta t/T_5=0.1933$. Seismic responses for the 5th story and the shear force-displacement curves for the 1st story are plotted in Figures 10 and 11. It

is seen that all the methods can result in acceptable solutions for the nonlinear variation of the stiffness and overshooting behaviours do not appear as well. The

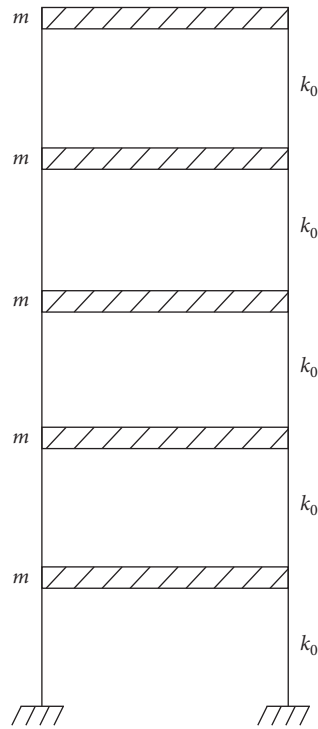


FIGURE 9: Numerical modelling of a 5-story shear building with softening stiffness.

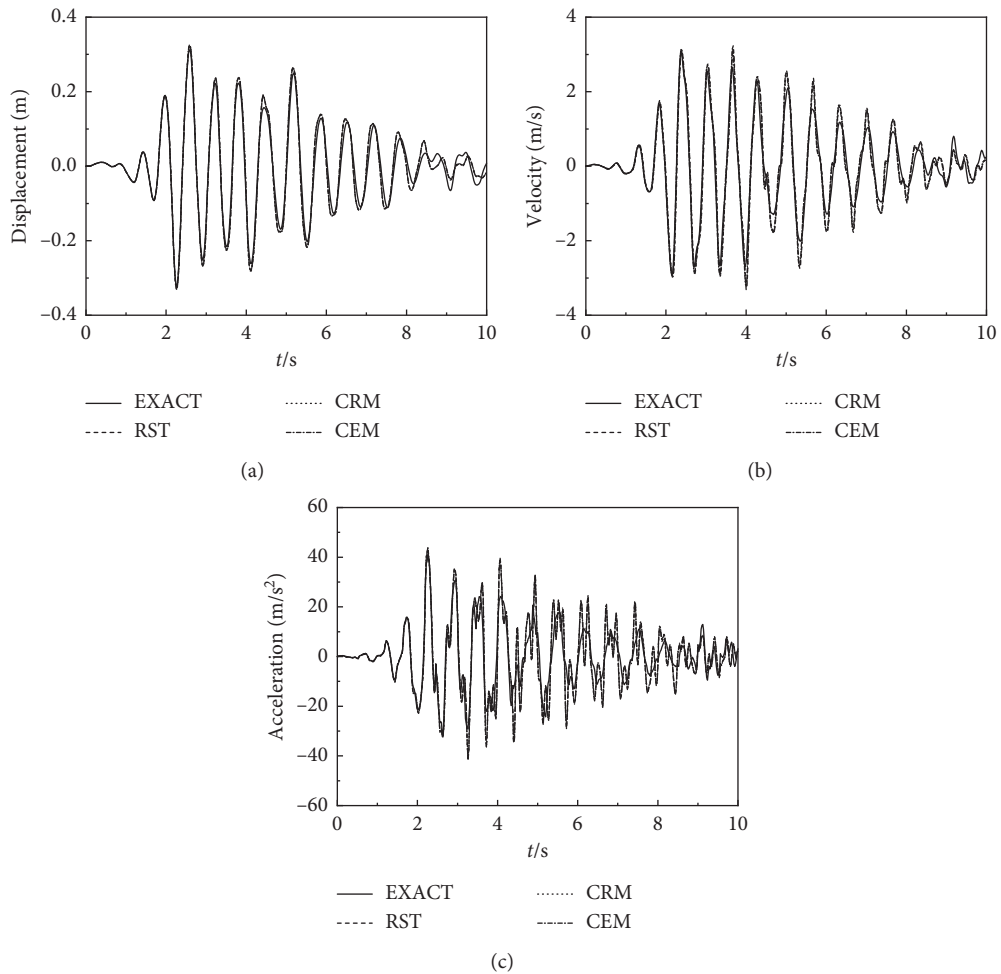


FIGURE 10: Seismic responses for the 5th story of the system. (a) Displacement. (b) Velocity. (c) acceleration.

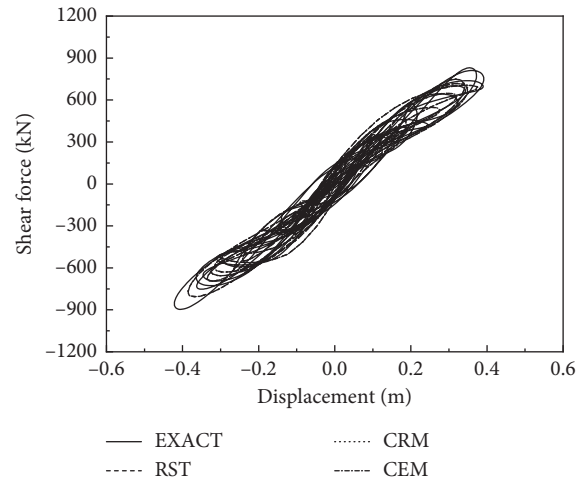


FIGURE 11: Hysteretic loops for the 1st story.

relative errors of the displacement peaks for the RST, CRM, and CEM methods are 3.98%, 4.05%, and 3.97%, respectively.

6. Conclusions

Applications of the RST method to nonlinear systems in RTHS have been evaluated and compared with other two structure-dependent explicit integration algorithms, i.e., the CRM and CEM methods, since they have quite similar formulations and numerical properties. Stability analysis indicates that the RST method is only conditionally stable when applied to nonlinear systems, and the instantaneous degree of nonlinearity will exert great influence on the upper stability limit of the method. For stiffness-softening systems, the upper stability limit increases with an increasing value of the instantaneous degree of nonlinearity, while for stiffness-hardening systems, it decreases when the instantaneous degree of nonlinearity becomes larger. Meanwhile, the initial damping ratio of the system has a negative impact on the upper stability limit especially for instantaneous stiffness softening systems, and a larger value of the damping ratio will significantly decrease the upper stability limit of the RST method.

Three simplified engineering structural systems are presented as numerical examples to demonstrate the computational stability, accuracy, and overshooting behaviours of the three methods. Numerical results demonstrate that overshooting behaviours will not appear if the time step is reasonably chosen for integration. It is also illustrated that the RST and CEM method have a better accuracy than the CRM method in solving dynamic problems for both linear and nonlinear systems. However, as the velocity of the CEM method is in an implicit form, the RST method provides more benefits in computational efficiency as both the displacement and velocity are in an explicit form.

Data Availability

The data used to support the findings of this study are included within the article. The results of this paper can be verified according to the data and methods given in the paper.

Conflicts of Interest

The authors declare that there are no conflicts of interest regarding the publication of this paper.

Acknowledgments

This paper was based upon work supported by the National Natural Foundation of China (Grant nos. 41904095, 51979027, and 51908048), Natural Science Foundation of Hebei Province (Grant no. E2019210350), Natural Science Foundation of Shaanxi Province (Grant nos. 2019JQ-021), State Key Laboratory of Mechanical Behavior and System Safety of Traffic Engineering Structures at Shijiazhuang Tiedao University (Grant nos. ZZ2020-04), and Fundamental Research Funds for the Central Universities (Grant nos. DUT19JC23 and DUT19RC(4)020).

References

- [1] C. N. Lim, S. A. Neild, D. P. Stoten, D. Drury, and C. A. Taylor, "Adaptive control strategy for dynamic substructuring tests," *Journal of Engineering Mechanics*, vol. 133, no. 8, pp. 864–873, 2007.
- [2] X. Drury and C. Griffith, "An overview of hybrid simulation implementations in NEES projects," *Engineering Structures*, vol. 56, pp. 1439–1451, 2013.
- [3] B. Fu, H. Jiang, and T. Wu, "Experimental study of seismic response reduction effects of particle damper using substructure shake table testing method," *Structural Control & Health Monitoring*, vol. 26, no. 2, e2295 pages, 2019.
- [4] B. Fu, H. Jiang, and T. Wu, "Comparative studies of vibration control effects between structures with particle dampers and tuned liquid dampers using substructure shake table testing methods," *Soil Dynamics and Earthquake Engineering*, vol. 121, pp. 421–435, 2019.
- [5] B. M. Phillips and B. F. Spencer, "Model-based multiactuator control for real-time hybrid simulation," *Journal of Engineering Mechanics*, vol. 139, no. 2, pp. 219–228, 2013.
- [6] A. P. Darby, A. Blakeborough, and M. S. Williams, "Real-time substructure tests using hydraulic actuator," *Journal of Engineering Mechanics*, vol. 125, no. 10, pp. 1133–1139, 1999.

- [7] A. P. Darby, A. Blakeborough, and M. S. Williams, "Improved control algorithm for real-time substructure testing," *Earthquake Engineering & Structural Dynamics*, vol. 30, no. 3, pp. 431–448, 2001.
- [8] S. A. Mahin and P. s. B. Shing, "Pseudodynamic method for seismic testing," *Journal of Structural Engineering*, vol. 111, no. 7, pp. 1482–1503, 1985.
- [9] S.-Y. Chang, "Improved numerical dissipation for explicit methods in pseudodynamic tests," *Earthquake Engineering & Structural Dynamics*, vol. 26, no. 9, pp. 917–929, 1997.
- [10] M. Nakashima and N. Masaoka, "Real-time on-line test for MDOF systems," *Earthquake Engineering & Structural Dynamics*, vol. 28, no. 4, pp. 393–420, 1999.
- [11] B. Wu, H. Bao, J. Ou et al., "Stability and accuracy of the central difference method for real-time substructure testing," *Earthquake Engineering & Structural Dynamics*, vol. 34, pp. 271–288, 2005.
- [12] C. Chen and J. M. Ricles, "Development of direct integration algorithms for structural dynamics using discrete control theory," *Journal of Engineering Mechanics*, vol. 134, no. 8, pp. 676–683, 2008.
- [13] S.-Y. Chang, "An explicit method with improved stability property," *International Journal for Numerical Methods in Engineering*, vol. 77, no. 8, pp. 1100–1120, 2009.
- [14] C. Kolay and J. M. Ricles, "Development of a family of unconditionally stable explicit direct integration algorithms with controllable numerical energy dissipation," *Earthquake Engineering & Structural Dynamics*, vol. 43, no. 9, pp. 1361–1380, 2014.
- [15] Y. Tang and M. Lou, "New unconditionally stable explicit integration algorithm for real-time hybrid testing," *Journal of Engineering Mechanics*, vol. 143, no. 7, pp. 1–14, 2017.
- [16] J. Guo, W. Zhao, Y. Du et al., "New method for real-time hybrid testing with a global iteration strategy," *Journal of Engineering Mechanics*, vol. 144, no. 12, Article ID 04018218, 2018.
- [17] C. Kolay and J. M. Ricles, "Improved explicit integration algorithms for structural dynamic analysis with unconditional stability and controllable numerical dissipation," *Journal of Earthquake Engineering*, vol. 23, no. 5, pp. 771–792, 2019.
- [18] B. Fu, D. Feng, and H. Jiang, "A new family of explicit model-based integration algorithms for structural dynamic analysis," *International Journal of Structural Stability and Dynamics*, vol. 19, no. 5, Article ID 1950053, 2019.
- [19] N. Newmark, "A method of computation for structural dynamics," *Journal of Engineering Mechanics*, vol. 85, no. 3, pp. 67–94, 1959.
- [20] C. Thewalt and S. Mahin, "An unconditionally stable hybrid pseudodynamic algorithm," *Earthquake Engineering & Structural Dynamics*, vol. 24, pp. 723–731, 1995.
- [21] B. Wu, Q. Wang, and P. Benson Shing, "Equivalent force control method for generalized real-time substructure testing with implicit integration," *Earthquake Engineering & Structural Dynamics*, vol. 36, no. 9, pp. 1127–1149, 2007.
- [22] Z. Ou, B. Wu, O. S. Bursi, and Y. G. Ding, "An effective online delay estimation method based on a simplified physical system model for real-time hybrid simulation," *Smart Structures and Systems*, vol. 14, no. 6, pp. 1247–1267, 2014.
- [23] M. Xu, J. Rajasankar, and N. R. Iyer, "Numerical assessment of step-by-step integration methods in the paradigm of real-time hybrid testing," *Earthquakes and Structures*, vol. 8, no. 6, pp. 1325–1348, 2015.
- [24] S.-Y. Chang, "Explicit pseudodynamic algorithm with unconditional stability," *Journal of Engineering Mechanics*, vol. 128, no. 9, pp. 935–947, 2002.
- [25] S. Chang, "Comparison of structure-dependent explicit methods for time integration," *International Journal of Structural Stability and Dynamics*, vol. 15, no. 3, pp. 1–20, 2015.
- [26] B. Fu, C. Kolay, J. Ricles, H. Jiang, and T. Wu, "Stability analysis of substructure shake table testing using two families of model-based integration algorithms," *Soil Dynamics and Earthquake Engineering*, vol. 126, p. 105777, 2019.
- [27] C. Jiang and J. Ricles, "Response to Maxam and Tamma's discussion (eqe-18-0306) to Kolay and Ricles's paper, "development of a family of unconditionally stable explicit direct integration algorithms with controllable numerical energy dissipation," *Earthquake Engineering & Structural Dynamics*, vol. 48, pp. 482–485, 2018.
- [28] W. Kim and J. H. Lee, "An improved explicit time integration method for linear and nonlinear structural dynamics," *Computers & Structures*, vol. 206, pp. 42–53, 2018.
- [29] S.-Y. Chang, "Improved formulations of the CR and KR methods for structural dynamics," *Earthquake Engineering and Engineering Vibration*, vol. 17, no. 2, pp. 343–353, 2018.
- [30] J. Butcher, *Numerical Methods for Ordinary Differential Equations*, John Wiley, Hoboken, NJ, USA, 2003.
- [31] R. Clough and J. Penzien, "Dynamics of Structures," Higher Education Press, Beijing, China, 2011.
- [32] S.-Y. Chang, "Improved explicit method for structural dynamics," *Journal of Engineering Mechanics*, vol. 133, no. 7, pp. 748–760, 2007.
- [33] A. Chopra, "Dynamics of Structures: Theory and Applications to Earthquake Engineering," Prentice-Hall, Upper Saddle River, NJ, USA, 2001.
- [34] Y. Tang and M. Lou, "Closure to "new unconditionally stable explicit integration algorithm for real-time hybrid testing" by Yu Tang and Menglin Lou," *Journal of Engineering Mechanics*, vol. 144, no. 10, pp. 1–11, 2018.